

UNIVERSIDAD DE CANTABRIA

Escuela Técnica Superior de Ingenieros  
Industriales y de Telecomunicación



Ph.D. THESIS / TESIS DOCTORAL

Ultrafast laser processing of transparent  
materials for photonic sensing and imaging  
applications

*Procesado con láser ultrarrápido de materiales transparentes  
para aplicaciones fotónicas de detección e imagen*

AUTHOR: Pablo Roldán Varona  
SUPERVISORS: José Miguel López Higuera  
Luis Rodríguez Cobo

Santander, September 2023

Copyright © 2023 Pablo Roldán Varona

UNIVERSIDAD DE CANTABRIA

*Ultrafast laser processing of transparent materials for photonic sensing and imaging applications*

Final version: June 23, 2023

## Declaration / Certificado de los Directores de la Tesis

**José Miguel López Higuera, Ph.D.**, Full Professor at the University of Cantabria, and  
**Luis Rodríguez Cobo, Ph.D.**, Researcher at the University of Cantabria

HEREBY STATE THAT

The Thesis entitled “**Ultrafast laser processing of transparent materials for photonic sensing and imaging applications**” has been carried out by **Mr. Pablo Roldán Varona** in the Photonics Engineering Group of the University of Cantabria, under our supervision, and it meets the requirements for doctoral work.

---

**D. José Miguel López Higuera**, Catedrático de la Universidad de Cantabria, y **D. Luis Rodríguez Cobo**, Investigador de la Universidad de Cantabria

HACEN CONSTAR

Que la Tesis titulada “**Procesado con láser ultrarrápido de materiales transparentes para aplicaciones fotónicas de detección e imagen**” ha sido realizada por **D. Pablo Roldán Varona** en el Grupo de Ingeniería Fotónica de la Universidad de Cantabria, bajo nuestra dirección, y que reúne las condiciones exigidas a los trabajos de doctorado.

Santander, September 2023

José Miguel López Higuera

Luis Rodríguez Cobo

## Evaluation committee

PHD THESIS: Ultrafast laser processing of transparent materials for photonic sensing and imaging applications

AUTHOR: Pablo Roldán Varona  
*Ph.D. candidate in Telecommunication Engineering*

SUPERVISORS: José Miguel López Higuera  
*Full Professor at the University of Cantabria*  
Luis Rodríguez Cobo  
*Researcher at the University of Cantabria*

Evaluation committee that judged the PhD Thesis:

President	Secretary	Vocal
.....	.....	.....
.....	.....	.....
.....	.....	.....

The evaluation committee agrees to award the qualification of: .....

Santander, ..... September 2023

# Abstract

Ultrafast laser processing of transparent materials has been a transformative force, driving considerable innovation across diverse fields like photonics, telecommunications, microfluidics, medicine, biochemistry, among many others. The foundation of this technology lies in the interaction between intense femtosecond laser pulses and matter, which induces precise, internal structural modifications within transparent materials without any consequential impact in the vicinity. This capability has opened up new horizons, allowing for the creation of intricate 3-dimensional microstructures essential for novel device development. When used in conjunction with chemical etching, it is possible to extract these internal structures, thus further expanding the scope of potential applications. This thesis is immersed in the realm of femtosecond laser processing of transparent materials, with special emphasis on fused silica, pivoting on the notion of exploiting its potential for advancing the domain of optical fibre sensors and optofluidic devices. This technology's application holds promise for transforming the landscape of photonics, delivering novel methodologies and avenues for sensing, imaging and device fabrication, offering advancements that could resonate across a spectrum of scientific disciplines.

The initial segment of the thesis establishes a robust groundwork, elucidating the crucial concepts and techniques for later chapters. It starts with an emphasis on the research significance, motivation, and goals. Subsequently, it delves into the fundamental principles of ultrafast laser-matter interactions, a crucial underpinning for the material discussed in following chapters. The discussion then pivots towards microfluidics, examining the implications of device miniaturisation to micrometer scales, while also addressing relevant materials and fabrication methods. Lastly, the different experimental configurations used in the fabrication of optofluidic devices are explored, along with an overview of the various characterisation techniques utilised.

Upon establishing the foundation, the thesis delves into the contributions made during the research. These are primarily bifurcated into two categories: those that involved the use of femtosecond lasers for direct inscription on optical fibres to develop sensors; and those that employed a combination of ultrafast laser inscription with chemical etching. This integration enables the extraction of tailor-made glass devices suitable for both sensing and imaging applications.

The precision and efficiency of laser processing in the fabrication of optical sensors can be significantly impacted by optical aberrations. These aberrations can disrupt the focus of femtosecond laser pulses, affecting the quality of the manufactured device. However, methods such as the slit beam shaping technique have been employed to control these aberrations and to shape the refractive index profile of optical structures, thus improving the performance of plane-by-plane fibre Bragg gratings and in-fibre cladding waveguides. This technique has enabled the creation of advanced optical fibre sensors. Optical fibres, recognised for their high sensitivity, quick response times, and immunity to electromagnetic interference, have become vital tools in sensing applications. Different types of fibres have been used to create distinct sensors. Standard step-index silica fibres have been a common choice. Research conducted with standard fibres has significantly contributed to the development of multiparametric sensors using Mach-Zehnder interferometers in combination with fiber Bragg gratings and waveguides, as well as lab-in-fibre sensors integrated in surgical needles for biomedical applications. In contrast to standard fibres, specialty fibres possess unique properties, making them ideal for crafting specific types of sensors.

Examples include tapered fibres, polarisation-maintaining fibres, hollow-core fibres, and fibres using non-standard materials such as fluoride or phosphate glass. These specialty fibres have facilitated the development of unique, highly capable sensors, expanding the possibilities within the realm of optical fibre sensing. Contributions have particularly impacted the development of sensors based on hollow-core fibres for liquid level sensing and perfluorinated polymer optical fibres as refractometers of aqueous solutions.

In relation to the second part of the thesis, ultrafast laser assisted etching in fused silica enables high etching rates, which are typically dependent on the light polarisation. This etching process, however, has faced challenges in achieving dynamic polarisation control for non-planar surfaces and 3D structures. In this thesis, a novel femtosecond laser inscription regime has been identified where etching rates are independent of the light polarisation. In this regime, few pulses inscriptions are employed, as they exhibit a low degree of anisotropy as compared to higher number of pulses, thus enabling the polarisation insensitivity whose mechanisms are discussed. Consequently, complex 3D structures, characterised by challenging inter-plane angles, can be fabricated without dynamic polarisation control.

As a result of a first stay at the Institute of Photonics and Quantum Sciences (Edinburgh, UK), further advancements in the use of ultrafast laser fabrication have been made in the field of real-time fluorescence endomicroscopy. An endoscopic fibre platform for selective plane illumination microscopy has been developed, featuring an ultrafast laser fabricated end-cap integrated with a polymer coherent fibre bundle and an epifluorescence microscope. This platform overcomes the traditional challenges of polymer fibre fluorescence, demonstrating improved image contrast and reduction of out-of-focus features in an *ex vivo* human lung.

In the field of molecular sensing, Bloch surface waves have been recognised for their potential, particularly on the surface of a one-dimensional photonic crystal. Bloch surface waves, which are tunable across the visible-UV range, offer unique advantages over surface plasmon polaritons. An innovative photonic chip, fabricated during the stay conducted at Institute of Photonics and Nanotechnology (Milan, Italy), incorporates a 1D photonic crystal and enhances the overlap of dispersion relations across a wide spectral range. This development opens up new opportunities in molecular sensing, offering the ability to investigate resonant electronic states of molecules.

In conclusion, this thesis represents a significant contribution to the field of ultrafast laser processing of transparent materials and its engineering applications. Despite the progress made, there is still a wide horizon for exploration in the field. Future studies could delve further into understanding the process that allows high etching rates independent of polarisation, providing a more concrete scientific basis for this discovery. Additionally, expanding the range of materials suitable for the ultrafast laser inscription and chemical etching process could uncover new applications and devices, pushing the boundaries of this exciting field. The cutting-edge devices and techniques presented herein pave the way towards a future where the fusion of photonics and fluidics can effectively cater to intricate sensing and manipulation needs at the microscale.

The research and development efforts culminating in this thesis have received significant validation from the global scientific community. Prior to sharing our findings in international forums and journals, a rigorous analysis of their potential industrial applications was conducted, taking necessary measures to protect intellectual property rights. As an outcome of this extensive research, a UK patent application has been filed, 24 articles have been published in scientific journals, and more than 35 conference contributions have been made.

## Resumen

El procesado láser ultrarrápido de materiales transparentes ha sido una fuerza transformadora, impulsando una considerable innovación en diversos campos como la fotónica, las telecomunicaciones, la microfluídica, la medicina, o la bioquímica, entre muchos otros. La base de esta tecnología radica en la interacción entre pulsos láser ultrarrápidos y la materia, induciendo modificaciones estructurales internas precisas en los materiales transparentes sin ningún impacto considerable en los alrededores del volumen focal. Esta capacidad ha abierto nuevos horizontes, permitiendo la creación de microestructuras tridimensionales complejas, esenciales para el desarrollo de nuevos dispositivos. Cuando se utiliza en conjunto con el revelado químico, es posible extraer estas estructuras internas, ampliando así el alcance de las posibles aplicaciones. Esta tesis se sumerge en el campo del procesado con láseres de femtosegundo de materiales transparentes, con especial énfasis en la sílice fundida, pivotando sobre la idea de explotar su potencial para avanzar en el dominio de los sensores de fibra óptica y los dispositivos optofluídicos. La aplicación de esta tecnología promete transformar el panorama de la fotónica, proporcionando nuevas metodologías y vías para la detección, la imagen y la fabricación de dispositivos, ofreciendo avances que podrían impactar en un amplio espectro de disciplinas científicas.

El segmento inicial de la tesis establece una base sólida, elucidando los conceptos y técnicas cruciales para los capítulos posteriores. Comienza enfatizando sobre la importancia del campo de investigación, la motivación y los objetivos. Posteriormente, se adentra en los principios fundamentales de las interacciones láser-materia, un soporte crucial para el contenido discutido en los siguientes capítulos. La discusión luego pivota hacia la microfluídica, examinando las implicaciones de la miniaturización del dispositivo a escalas de  $\mu\text{m}$ , mientras también aborda los materiales y métodos de fabricación más relevantes. Por último, se exploran las diferentes configuraciones experimentales utilizadas en la fabricación de dispositivos optofluídicos, junto con una descripción general de las diversas técnicas de caracterización empleadas.

Tras establecer los fundamentos, la tesis se adentra en las contribuciones realizadas. Estas se bifurcan principalmente en dos categorías: aquellas que implicaron el uso de láseres de femtosegundo para la inscripción directa en fibras ópticas para el desarrollo de sensores; y aquellas que emplearon una combinación de inscripción con láseres ultrarrápidos y revelado químico. Esta integración permite la extracción de dispositivos de sílice hechos a medida adecuados tanto para aplicaciones de detección como de imagen.

La precisión y eficiencia del procesado láser en la fabricación de sensores ópticos puede verse significativamente afectada por las aberraciones ópticas. Estas aberraciones pueden degradar el enfoque de los pulsos láser de femtosegundo, afectando la calidad del dispositivo fabricado. Sin embargo, se han empleado métodos como la técnica *slit beam shaping* para controlar estas aberraciones y dar forma al perfil de índice de refracción de las estructuras ópticas, mejorando así el rendimiento de las redes de Bragg en fibra y de las guías de ondas de cubierta en fibra. Esta técnica ha permitido la creación de sensores de fibra óptica avanzados. Las fibras ópticas, reconocidas por su alta sensibilidad, tiempos de respuesta rápidos e inmunidad a las interferencias electromagnéticas, se han convertido en herramientas vitales en las aplicaciones de detección. Se han utilizado diferentes tipos de fibras para crear sensores. Las fibras de sílice estándar de salto de índice han sido una elección común. La investigación realizada con este tipo

de fibras ha contribuido significativamente al desarrollo de sensores multiparamétricos utilizando interferómetros Mach-Zehnder en combinación con redes de Bragg en fibra y guías de ondas, así como sensores *lab-in-fibre* integrados en agujas quirúrgicas para aplicaciones biomédicas. En contraste con las fibras estándar, las fibras especiales poseen propiedades únicas, lo que las hace ideales para la elaboración de ciertos tipos de sensores. Ejemplos incluyen fibras cónicas, fibras mantenedoras de polarización, fibras de núcleo hueco y fibras que utilizan materiales no estándar como fluoruros o fosfatos. Estas fibras especiales han facilitado el desarrollo de sensores únicos, expandiendo las posibilidades dentro del ámbito de la detección con fibras ópticas. Las contribuciones han dado lugar al desarrollo de sensores basados en fibras de núcleo hueco para la detección de niveles de líquido y fibras ópticas de polímero perfluorinado para la fabricación de refractómetros de soluciones acuosas.

En relación con la segunda parte de la tesis, el ataque químico asistido por láser ultrarrápido en sílice permite altas tasas de revelado químico, que generalmente dependen de la polarización de la luz. Sin embargo, este proceso de grabado ha enfrentado desafíos para lograr el control dinámico de la polarización para superficies que no son planas y estructuras 3D. Se ha identificado un nuevo régimen de inscripción con láser de femtosegundo donde las tasas de ataque químico son independientes de la polarización de la luz. En este régimen, se emplean inscripciones de pocos pulsos, ya que exhiben un bajo grado de anisotropía en comparación con un mayor número de pulsos, lo que permite la insensibilidad a la polarización, discutiendo los posibles mecanismos detrás de este hallazgo. En consecuencia, se pueden fabricar estructuras 3D complejas, caracterizadas por planos con ángulos desafiantes, sin controlar dinámicamente la polarización.

Como resultado de una primera estancia en el *Instituto de Fotónica y Ciencias Cuánticas* (Edimburgo, Reino Unido), se han realizado avances en el uso de la fabricación láser ultrarrápida en el campo de la endomicroscopía de fluorescencia en tiempo real. Se ha desarrollado una plataforma de fibra endoscópica para la microscopía de iluminación de plano selectivo, que cuenta con una estructura de sílice fabricada con láser ultrarrápido e integrada en una fibra de imagen de plástico, así como un microscopio de epifluorescencia. Esta plataforma supera los problemas tradicionales de la autofluorescencia generada por fibras de polímero, demostrando una mejora del contraste de la imagen y la reducción de aquellos elementos que se encuentran fuera de foco, todo ello evaluado en pulmones humanos *ex vivo*.

En el campo de la detección molecular, las ondas de superficie de Bloch han sido reconocidas por su potencial, particularmente en la superficie de un cristal fotónico unidimensional. Las ondas de superficie de Bloch, que son sintonizables a lo largo del rango visible-UV, ofrecen ventajas únicas sobre los polaritones de plasmón de superficie. Un chip fotónico optofluídico, fabricado durante la estancia realizada en el *Instituto de Fotónica y Nanotecnología* (Milán, Italia), incorpora un cristal fotónico 1D y mejora la superposición de las relaciones de dispersión en un amplio rango espectral. Este desarrollo abre nuevas oportunidades en la detección molecular, ofreciendo la capacidad de investigar estados electrónicos resonantes de las moléculas.

En conclusión, esta tesis representa una contribución significativa al campo del procesado láser ultrarrápido de materiales transparentes y sus aplicaciones de ingeniería. A pesar del progreso realizado, todavía hay un amplio horizonte para la exploración en el campo. Los estudios futuros podrán ahondar más en la comprensión del proceso físico que permite altas tasas de ataque químico independientes de la polarización, proporcionando una base científica más concreta para este descubrimiento. Además, expandir el rango de materiales adecuados

para el proceso de inscripción láser ultrarrápido y revelado químico permitirá descubrir nuevas aplicaciones y dispositivos, empujando los límites en este campo. Los dispositivos y técnicas de vanguardia presentados aquí allanan el camino hacia un futuro donde la fusión de la fotónica y la fluídica puede satisfacer eficazmente las necesidades de detección y manipulación en escala micrométrica.

Los esfuerzos de investigación y desarrollo que culminan en esta tesis han recibido una validación significativa de la comunidad científica global. Antes de compartir nuestros hallazgos en foros y revistas internacionales, se realizó un análisis riguroso de sus posibles aplicaciones industriales, tomando las medidas necesarias para proteger los derechos de propiedad intelectual. Como resultado de esta extensa investigación, se ha presentado una solicitud de patente en el Reino Unido, se han publicado 24 artículos en revistas científicas y se han realizado más de 35 contribuciones a conferencias.

# Acknowledgments

11 de Junio de 2023, en algún punto entre Tokio y Munich.

Una vez escrito todo este documento, llega el momento de acordarse, o simplemente de seguir acordándose, de las personas que han contribuido a que en estos cuatro años no sólo los trabajos que conforman este documento, así como el documento, hayan llegado a buen puerto, sino que también han hecho que haya podido progresar como persona desde lo que era en 2019 hasta lo que soy en 2023, en muchos aspectos. Aunque el proceso de escritura haya sido un sprint final de cinco o seis semanas, merece la pena dedicar un poquito de tiempo a escribir estas líneas.

En primer lugar, gracias a mis directores. A José Miguel por haberme aceptado en el grupo y, fundamentalmente, por haberme dado siempre la confianza para ejecutar todas las ideas que tenía en el láser. La he sentido desde el primer momento. Obviamente también a Luis, ya no como director sino como amigo. Has sido el pilar fundamental de todo esto. Sabes lo que tienes que hacer para dar el último empujón a esta línea y aspirar a cosas que hace dos años eran impensables. Pero las imágenes que primero se me vienen a la cabeza no son de trabajo, sino de cervezas, bicis, buceo, cervezas, cafés, y más cervezas. Has estado cuando tenías que estar.

También me gustaría agradecer al Grupo de Ingeniería Fotónica, desde el primero al último. Lleva siendo mi casa prácticamente seis años, y son muchas las cosas positivas que me llevaré de este grupo humano. A *Femtoteam*, con Mario y Algorri a la cabeza. Mario, eres la persona más brillante que me he encontrado en mi corto periplo investigador, nadie me ha hecho estar tan motivado y con tantas ganas de descubrir cosas nuevas. Y nadie me ha hecho cuestionarme (ni seguro que me hará) a las 3 de la mañana pasando por un pueblo de Burgos si la línea espectral  $D_2$  de Raman es consecuencia del número de anillos con tres Si en la estructura de la silica, o por la reducción del ángulo entre sus enlaces. Algorri, otro tío brillante, especialmente cuando el sol se empieza a poner. Lo mismo te habla de la resonancia del campo en un dieléctrico, que de cómo saber si un cubata es bueno por el sonido de los hielos. MVP desde el primer día.

A Marian, porque soy muy consciente de que pocas personas se alegran tanto por mí como tú; a María, por estar siempre pendiente de que no quedará de gestionar ni un papel de los muchos que se me olvidaban; a Adolfo, porque eres un espejo en el que uno puede mirarse en esto de investigar; a Chus, por hacerme emboscadas en los muritos de Piélagos; y a David, por enseñarme todos los entresijos del láser cuando empezaba en esto. Al dúo dinámico de *Ay Meri*, Marina e Isma. Hemos reído y llorado juntos, y no hemos dejado un solo tema sin hablar delante de un mediano, un solo con sacarina, y un cortado. Sois muy grandes. En general, gracias a todos los que están y han pasado por el grupo estos cuatro años.

From Edinburgh, I can only speak wonders. Probably, if there is someone who has been a turning point in these four years, it is Robert Thomson. From him, I have learned about well-understood research, understanding why we do what we do, and the importance of being motivated in our work. He exudes knowledge and approachability. And he is the driving force behind the ideas and projects we have for the future. I am eager to keep inserting fibres into lungs. But from Edinburgh, I also take with me many other people. To Jacopo, for making a completely new place feel like home, you quickly became a friend. To Helen, for your joyfulness both outside and inside of work, and for always helping me whenever I have needed it, even when

we were thousands of kilometres apart. To Calum, for being the go-to person in femtosecond lasers, as many times I felt like a little child who loses a tooth and does not know what to do.

De Milán también he de agradecer a un montón de gente, empezando por Rebeca. La palabra 'trabajadora' lleva tu foto en el diccionario. Te he visto más veces en la *Cappa* un viernes por la tarde con tus quimijuegos de cristales y HF, que el cartel de que la máquina de café está averiada. Ha sido un verdadero placer que me enseñes un poco de todo lo que sabes. 1 hora de conversación con un *machiatto* delante se me hacía muy poco, la verdad. Sé que malgastar mi último día de láser para hacer muñecos de nieve de 100  $\mu\text{m}$  te sacó una sonrisa. I would also like to thank Roberto Osellame for accepting me into the group and for taking time out of his busy schedule to evaluate a proposal with very few days of margin. Actually, *grazie mille* to everyone in the group, I could mention practically all of you. To Serena as well, for being the host in Abiategrasso after having been the host in Dolomites 8 months earlier. And to the *Piano Piano Team*, led by my favorite crazy person Francesco Bianco, because we didn't leave any corner of the mountain unexplored in the Como, Lecco, Bellagio, Mandello, and Bellano area. Lastly, but certainly not least, I would like to thank Unai, Itziar, and Irantzu, three great friends that Milan has given me.

De Pamplona, aunque no haya estado haciendo estancia, creo que es justo y necesario hablar de Rosana y Mikel. Rose y la estrella Mikelin. Zipi y Zape. Dos cracks, con todo lo que incluye esa palabra. Todo lo que diga de ellos va a ser poco. En Varsovia, Nouredinne, Michal y Pawel hicieron que el mes allí en Polonia fuera una gran experiencia vital.

Me gustaría agradecer también a todos mis amigos y a mi familia. Día 3650, mis padres siguen sin saber a qué me dedico, pero al menos le ponen empeño en tratar de entenderlo. A mi hermana, porque creo que somos imparables cuando queremos. A mi abuelo, porque sigue dándome risas y lecciones cada vez que piso Santa María. Y a mis abuelos que ya no están, sé que estaríais orgullosos de todo esto. A los Roldán, sobre todo a mi tía Chefa, y a los Varona, especialmente a Maria Jesús, Beatriz y Óscar.

Y vamos a cerrar esto con una auténtica máquina, un terremoto que arrasa por donde pasa. La competitividad hecha persona: me quiere ganar haciendo figuras cuando sabe que es imposible. Ningún reto se le pone por delante. Corre maratones de montaña, kilómetros verticales, nada travesías en mar abierto, sube El Caracol con bicis de 20 kg, se tira por pistas rojas en su segundo día de esquí. Es analítica e inteligente. Ha ido saltando vallas desde pequeña, cada vez más altas. Ella aún no sabe que va a conseguir lo que le de la gana. Se le da especialmente bien sonreír. Se llama Fátima y es quien me hace feliz.

## Funding

The financial support for this thesis has been provided by the following entities and actions:

- Ministerio de Ciencia, Innovación y Universidades through PhD grant in the FPU (Formación de Profesorado Universitario) program (FPU18/02797).
- Ministerio de Ciencia e Innovación and Agencia Estatal de Investigación through research project *Dispositivos y sistemas fotónicos. Sensores para estructuras inteligentes y evaluación no destructiva I* (PID2019-107270RB-C21).
- Agencia Estatal de Investigación through research project *Sensores fotónicos para seguridad y protección* (TEC2016-76021-C2-2-R).
- Ministerio de Universidades through a research grant for a 3-month stay at Heriot-Watt University (Edinburgh, UK) (EST19/00956).
- Ministerio de Universidades through a research grant for a 3-month stay at Institute of Photonics and Nanotechnologies (Milan, Italy) (EST22/00034).
- NAWA Prom Programme through a research grant for a 1-month stay at Military University of Technology (Warsaw, Poland) (POWR.03.03.00-IP.08-00-P13/18).
- Organismo Autónomo Parques Nacionales of Ministerio para la Transición Ecológica y el Reto Demográfico through research project *Parques nacionales marítimos virtuales para monitorización de los efectos del cambio climático* (2470S/2017 and 2493S/2017).

# Contents

<b>Contents</b>	<b>I</b>
<b>List of Figures</b>	<b>V</b>
<b>List of Tables</b>	<b>XIX</b>
<b>List of Acronyms</b>	<b>XX</b>
<b>I Preliminary</b>	<b>1</b>
<b>1 Introduction</b>	<b>2</b>
1.1 Motivation . . . . .	3
1.2 Objectives . . . . .	6
1.3 Document structure . . . . .	7
References . . . . .	10
<b>2 Fundamentals of ultrafast laser processing of transparent materials</b>	<b>13</b>
2.1 Mechanisms of material modification . . . . .	14
2.1.1 Free electron plasma generation . . . . .	15
2.1.2 Relaxation and modification of the material . . . . .	16
2.2 Sample irradiation parameters . . . . .	19
References . . . . .	21
<b>3 Fundamentals of optofluidic platforms</b>	<b>25</b>
3.1 Materials and fabrication techniques . . . . .	27
3.1.1 Ultrafast laser assisted etching technique . . . . .	28
3.2 Physics and scaling in microfluidics . . . . .	30
3.2.1 Continuity and Navier-Stokes equation . . . . .	31
3.2.2 Dimensionless numbers . . . . .	32
3.2.3 Relevant considerations in microfluidic devices . . . . .	33
References . . . . .	36
<b>4 Experimental setups and methods</b>	<b>40</b>
4.1 Fabrication setups . . . . .	41
4.1.1 Femtosecond laser writing . . . . .	41
4.1.2 Chemical etching . . . . .	43
4.2 Simulations tools . . . . .	43
4.3 Characterisation techniques . . . . .	44
4.3.1 Quantitative phase microscopy . . . . .	44
4.3.2 Refracted near field profilometry . . . . .	45

4.3.3	Raman spectroscopy . . . . .	46
	References . . . . .	48
<b>II</b>	<b>Ultrafast laser direct writing (ULDW)</b>	<b>50</b>
<b>5</b>	<b>Enhancement of ULDW–based passive in-fibre structures</b>	<b>51</b>
5.1	Optical aberrations and light focusing issues . . . . .	52
5.1.1	Astigmatism in optical fibres . . . . .	54
5.2	Cross-section control of refractive index changes . . . . .	58
5.2.1	Slit beam shaping technique . . . . .	58
5.2.2	Astigmatic beam shaping technique . . . . .	59
5.2.3	Spatiotemporal focusing . . . . .	60
5.2.4	Multiscan technique . . . . .	60
5.2.5	Adaptive optics . . . . .	61
5.3	Slit beam shaping technique for Pl-b-Pl FBGs . . . . .	62
5.3.1	Background . . . . .	62
5.3.2	Control of the cross-section of the focal volume . . . . .	64
5.3.3	Pulse energy setting . . . . .	66
5.3.4	Experimental results and discussion . . . . .	68
5.3.5	Conclusions . . . . .	72
5.4	Slit beam shaping technique for symmetric CWGs . . . . .	73
5.4.1	Background . . . . .	73
5.4.2	Fs laser inscription of CWGs . . . . .	74
5.4.3	Structure design and simulations . . . . .	76
5.4.4	Experimental results and discussion . . . . .	79
5.4.5	Conclusions . . . . .	82
	References . . . . .	84
<b>6</b>	<b>Standard fibre–based sensors</b>	<b>92</b>
6.1	Background of OFSSs . . . . .	93
6.2	In-fibre MZI for multiparameter sensing . . . . .	94
6.2.1	Background . . . . .	94
6.2.2	Theory and sensor design . . . . .	95
6.2.3	Manufacturing . . . . .	97
6.2.4	Experimental results and discussion . . . . .	102
6.2.5	Cross-sensitivity . . . . .	104
6.2.6	Conclusions . . . . .	105
6.3	Reflection-based LIF sensor integrated in a surgical needle . . . . .	106
6.3.1	Background . . . . .	106
6.3.2	Theory and sensor design . . . . .	107
6.3.3	Finite element simulation . . . . .	108
6.3.4	Manufacturing . . . . .	110
6.3.5	Experimental results and discussion . . . . .	112

6.3.6	Conclusions . . . . .	114
	References . . . . .	115
<b>7</b>	<b>Specialty fibre-based sensors</b>	<b>119</b>
7.1	Liquid level sensor using capillary fibres and dynamic FPIs . . . . .	120
7.1.1	Background . . . . .	120
7.1.2	Sensor structure and manufacturing parameters . . . . .	122
7.1.3	Operating principle . . . . .	123
7.1.4	Results and discussion . . . . .	125
7.1.5	Conclusions . . . . .	130
7.2	Perfluorinated POF-based refractometer for water solutions . . . . .	130
7.2.1	Background . . . . .	130
7.2.2	Optical structure design . . . . .	131
7.2.3	BPM simulations . . . . .	132
7.2.4	Operating principle . . . . .	137
7.2.5	Experimental results . . . . .	138
7.2.6	Discussion . . . . .	142
7.2.7	Conclusions . . . . .	142
	References . . . . .	143
<b>III</b>	<b>Ultrafast laser assisted etching (ULAE)</b>	<b>149</b>
<b>8</b>	<b>Polarisation-independent ULAE in fused silica</b>	<b>150</b>
8.1	Point defects in SiO <sub>2</sub> glass . . . . .	151
8.1.1	Frenkel defects . . . . .	153
8.1.2	Dangling-bond defects . . . . .	154
8.2	Etching mechanisms in SiO <sub>2</sub> glass . . . . .	155
8.2.1	Nanograting-driven etching . . . . .	156
8.2.2	Non nanograting-driven etching . . . . .	157
8.3	Experimental setup and protocol . . . . .	158
8.4	Etching rate results . . . . .	160
8.4.1	Definition of $N$ -dependent regimes . . . . .	160
8.4.2	Low $N$ regime ( $N < 15 \mu\text{m}^{-1}$ ) . . . . .	161
8.4.3	Moderate $N$ regime ( $15 \leq N < 100 \mu\text{m}^{-1}$ ) . . . . .	165
8.4.4	High $N$ regime ( $N > 100 \mu\text{m}^{-1}$ ) . . . . .	165
8.5	Discussion about ER and polarisation dependence . . . . .	165
8.6	Etching mechanisms in polarisation-independent regime . . . . .	167
8.7	Conclusions . . . . .	170
	References . . . . .	171
<b>9</b>	<b>SPIM using polymer coherent fibre bundles</b>	<b>175</b>
9.1	Background . . . . .	176
9.2	Overview of the SPIM probe platform . . . . .	177

9.3	Epifluorescence microscope setup . . . . .	179
9.3.1	Optical design of the axicon-based microscope . . . . .	180
9.4	SPIM probe: design and fabrication . . . . .	182
9.4.1	End-cap design: 3D CAD modelling . . . . .	182
9.4.2	End-cap fabrication: ULI-CE . . . . .	183
9.5	SPIM probe characterisation . . . . .	184
9.5.1	Fluorescence of PMMA CFB . . . . .	185
9.5.2	Simulation of light field . . . . .	186
9.5.3	Core crosstalk . . . . .	188
9.6	Imaging . . . . .	191
9.6.1	Image processing . . . . .	191
9.6.2	Evaluation with a tissue phantom . . . . .	194
9.6.3	Demonstration in <i>ex vivo</i> human lung . . . . .	196
9.7	Discussion . . . . .	197
9.8	Conclusions . . . . .	198
	References . . . . .	200
<b>10</b>	<b>Molecular sensing with Bloch surface waves</b>	<b>205</b>
10.1	Surface waves . . . . .	206
10.1.1	Surface plasmon polaritons (SPPs) . . . . .	207
10.1.2	Bloch surface waves (BSWs) . . . . .	207
10.2	Circular dichroism spectroscopy . . . . .	210
10.3	1DPC for superchiral SWs . . . . .	211
10.4	Optofluidic platform . . . . .	212
10.4.1	Design . . . . .	213
10.4.2	Fabrication . . . . .	215
10.5	Experimental setup . . . . .	216
10.6	Preliminary measurements of molecular chirality . . . . .	218
10.6.1	Chiral molecules . . . . .	218
10.6.2	Measurements . . . . .	218
10.7	Conclusions . . . . .	220
	References . . . . .	222
<b>IV</b>	<b>Final remarks and future lines of work</b>	<b>225</b>
<b>11</b>	<b>Conclusions and future lines</b>	<b>226</b>
	<b>List of Publications</b>	<b>230</b>
	<b>References in alphabetical order</b>	<b>241</b>

# List of Figures

## 1 Introduction

- 1.1 **(a)**  $75 \times 75 \times 2$  mm fused silica plate on which the 1978 movie *Superman* was inscribed using ultrafast lasers, as a proof of concept for Microsoft’s Project Silica. The glass stores 75.6 GB of data along with error redundancy codes. Photo by Jonathan Banks for Microsoft [44]. **(b)** Potential multifunctional catheter capable of performing widefield imaging, tissue interrogation, and multi-site aspiration, among other functions. . . . . 5
- 1.2 General structure of the thesis, detailing the association of each topic with the different chapters in the document. Key: ULDW – Ultrafast laser direct writing, ULAE – Ultrafast laser assisted etching, SBST – Slit beam shaping technique, FBG – Fibre Bragg grating, CWG – Cladding waveguide, SMF – Single-mode fibre, MZI – Mach-Zehnder Interferometer, LIF – Lab-in-fibre, POF – Polymer optical fibre, SPIM – Selective plane illumination microscopy, CFB – Coherent fibre bundle, BSW – Bloch surface wave. . . . . 8

## 2 Fundamentals of ultrafast laser processing of transparent materials

- 2.1 Schematic illustration of the effects caused by **(a)** a short laser pulse ( $\sim$  ns), and **(b)** an ultra-short laser pulse (ps, fs). Adapted from [4]. . . . . 14
- 2.2 Non-linear photoionisation processes that underpin femtosecond laser machining [12]. These processes include: **(a)** multiphoton ionisation, where multiple photons are absorbed simultaneously; **(b)** tunnel ionisation, which involves electrons tunnelling through an energy barrier; and **(c-d)** avalanche ionisation, a sequence of events that starts with **(c)** the absorption of free carriers, and **(d)** is followed by impact ionisation. Adapted from [4]. . . . . 15
- 2.3 Physical phenomena during the interaction of a femtosecond laser pulse with a transparent material. Despite light absorption occurs on a femtosecond timescale, subsequent transformations in the material can continue even microseconds after the initial interaction. Adapted from [2]. . . . . 17
- 2.4 Potential modifications induced in fused silica by femtosecond laser irradiation. **(a)** Type I [10], **(b)** Type II [35], **(c)** Type X [14], and **(d)** Type III [36]. Scale bars in **a-d** are 25  $\mu$ m, 1  $\mu$ m, 200 nm, and 10  $\mu$ m, respectively. Reprinted with permission of the indicated references. . . . . 18

## 3 Fundamentals of optofluidic platforms

3.1	Illustration showing lab-on-chip devices inscribed with fs lasers on fused silica substrates in their state prior to the wet chemical etching process. These are the <b>(a)</b> first and <b>(b)</b> second version of a chip designed for phytoplankton analysis in water, a research work currently being undertaken by the Photonics Engineering Group. The colour corresponds to the diffraction generated by the multiple scans performed by the laser. For each chip, (left) a photograph is shown after its inscription, (right) as well as the 3D model designed with Solidworks 2019 SP4.0 and rendered with Blender 3.2. . . . .	26
3.2	Illustration of the creation of microchannels in fused silica (optical fibre) using the ULAE technique. <b>(a)</b> Step 1: Permanent Type II modification in the sample by non-linear absorption of focused femtosecond laser pulses. <b>(b)</b> Step 2: Wet chemical etching of the laser-modified region generates a microfluidic channel with a given aspect ratio. Adapted from [26]. . . . .	29
<b>4 Experimental setups and methods</b>		
4.1	Schematic of the femtosecond laser inscription setup (Key: PBS – polarisation beam splitter, BE – beam expander, BR – beam reducer, HS – harmonic separator, BBO - beta barium borate crystal, C – CCD camera, TL – tube lens, DM – dichroic mirror, AL – aspheric lens, $\lambda/2$ – half waveplate, $\lambda/4$ – quarter waveplate). Red colour corresponds to 1030 nm light, while green light represents 515 nm wavelength. Beam shutters, mirrors, illumination elements, as well as alignment irises are not shown in the schematic. . . . .	41
4.2	Temporal measurement of the pulse from the BlueCut fs laser used an autocorrelator. The 370 fs corresponds to the Gaussian adjustment of the pulse autocorrelation ( $\tau = \tau_a/\sqrt{2}$ , being $\tau_a$ the FWHM pulse duration of autocorrelation). . .	42
4.3	Measurement process of refracted near field profilometry on the end face of an optical fibre. Adapted from [13]. . . . .	46
<b>5 Enhancement of ULDW–based passive in-fibre structures</b>		
5.1	Ray tracing analysis using OpticStudio Zemax considering an objective lens with a NA of 0.5. The lens was focused on three different scenarios: <b>(a)</b> planar object with $n = 1.45$ , positioned 30 $\mu\text{m}$ above the working distance, <b>(b)</b> circular object with the same RI positioned at the same location, and <b>(c)</b> circular object with the same RI positioned at the working distance with its centre aligned. $\lambda = 1030$ nm is considered. Adapted from [1]. . . . .	55
5.2	<b>(a)</b> Distribution of intensity along the material at the centre of the beam varies with the propagation distance for stigmatic and astigmatic beams. Intensity has been normalised to the maximum intensity of the stigmatic beam. <b>(b)</b> Focal volume for both beams, where the astigmatic focal volume does not exceed intensities higher than the normalised 10%. $\lambda = 1030$ nm and $n = 1.45$ are considered. Adapted from [1]. . . . .	56

5.3	(a) Femtosecond laser inscription in a fibre with and without astigmatic correction at a pulse energy of 470 nJ. (b) Comparison of the phase change versus pulse energy for inscribed lines with and without astigmatic compensation when focused at the fibre core, as well as 30 $\mu\text{m}$ below the surface without astigmatic correction. Adapted from [1]. . . . .	57
5.4	Waist radius ( $w_0$ ) and Rayleigh length ( $z_0$ ) for different numerical apertures and substrates, assuming $\lambda = 1030$ nm. The ratio $z_0/w_0$ is also presented. In essence, the higher the substrate's refractive index or the lower the numerical aperture, the greater the asymmetry in the focal volumes. . . . .	59
5.5	Direct-write methods of FBG inscription with fs laser. (a) Point-by-point (PbP), (b) line-by-line (LbL), and (c) plane-by-plane (Pl-b-Pl). Adapted from [2]. . . .	63
5.6	Relationship between $D_x$ and $D_y$ as a function of $D_x$ to obtain a circular cross-section of the focal volume in the $YZ$ plane. A substrate with $n = 1.47$ and a focal length of the objective lens $f = 8$ mm has been used. Adapted from [2]. . .	65
5.7	$YZ$ plane of the focal volume for $D_x/D_y$ ratios of (a) 1, (b) 6, (c) 12 and (d) 20. The white circle represents the core of the optical fibre. A substrate with $n = 1.47$ and a focal length of the objective lens $f = 8$ mm has been used. Adapted from [2].	66
5.8	Evolution of intensity on the $Z$ axis ( $x = y = 0$ ) with focus on the center of the SMF core ( $z = 62.5$ $\mu\text{m}$ ). Different $D_x/D_y$ ratios are depicted. Adapted from [2].	67
5.9	(a) Demonstration of the laser pulse evolution through a 1.5 mm width slit, illustrating the definition of $E_p$ and $(E_p)_{eff}$ . (b) Plot of $E_p$ versus slit width ( $s$ ) to preserve a constant $(E_p)_{eff}$ . Adapted from [2]. . . . .	67
5.10	Normalised energy deposited in the focal volume, considering (a) the $YZ$ ( $x = 0$ ), and (b) $XY$ ( $z = 0$ ) planes. The $YZ$ plane represents the core cross-section, while the $XY$ plane illustrates a longitudinal section of the fibre. The results are shown with and without energy compensation (solid and dotted lines, respectively), as described in this section. Distinct colours indicate various integration regions of energy fluence. Adapted from [2]. . . . .	68
5.11	Mean phase change and modification width for varying slit widths ( $s$ ) are presented. The phase change decreases in accordance with an exponential fit ( $R^2 = 0.9982$ ). Adapted from [2]. . . . .	69
5.12	(a) Transverse phase profile for pristine and $s = \{1, 3\}$ mm, and (b) phase change parallel to grating inscription for $s = \{1, 2, 3\}$ mm. Adapted from [2]. . . . .	70
5.13	FBGs inscribed in the core of an SMF-28 fibre with (a) $s = 1$ mm (Pl-b-Pl), and (b) and $s = 3$ mm (PbP). Scale bars in a-b are 20 $\mu\text{m}$ . Adapted from [2]. . . . .	70
5.14	(a) Reflection and (b) transmission spectra of FBGs inscribed with $s = \{1, 1.5, 2, 3\}$ mm. These spectra consist of 2,001 data points with a 50-point average. Adapted from [2]. . . . .	71
5.15	Variation of the FWHM and reflectivity as a function of the slit width. Adapted from [2]. . . . .	72
5.16	Polarisation dependent loss (PDL) of PbP ( $s = 3$ mm, $D_x/D_y = 1$ ) and Pl-b-Pl ( $s = 1$ mm, $D_x/D_y = 3$ ) FBGs. Adapted from [2]. . . . .	72
5.17	Illustration of the process of CWG inscription using the slit beam shaping method with the assistance of index-matching oil. Adapted from [3]. . . . .	75

LIST OF FIGURES

5.18	Illustration of the simulated and fabricated optical structure. This structure involves the evanescent coupling of light from the core of a single-mode fibre to each of the four cores of a multicore fibre. This coupling is achieved by utilising symmetric cladding waveguides. Adapted from [3]. . . . .	76
5.19	The focal volume and intensity profile at the $Z$ focus plane are depicted in the $YZ$ plane. The focusing conditions are demonstrated for three scenarios: <b>(a)</b> without a slit, <b>(b)</b> with a slit of width $a = 500 \mu\text{m}$ , and <b>(c)</b> with a slit of width $a = 500 \mu\text{m}$ , along with two scans performed with a $2.5 \mu\text{m}$ offset in the $Y$ direction. An objective lens with a focal length of $f = 8 \text{ mm}$ is used, along with the application of refractive index adaptation using index-matching oil. Adapted from [3]. . . . .	77
5.20	Normalised $\text{LP}_{01}$ coupled to the CWG is analysed with a fixed length $L_3$ of $50 \mu\text{m}$ . Two scenarios are considered: <b>(a)</b> varying $L_1$ (with $L_2$ fixed at $1 \text{ mm}$ ), and <b>(b)</b> varying $L_2$ (with $L_1$ fixed at $200 \mu\text{m}$ ). The shaded regions represent the optimal design values. <b>(c, left)</b> Filled 2D contour plot of the normalised $\text{LP}_{01}$ power of the simulated structure. This structure is defined by cutting the fibre indicated in Fig. 5.18 using an $XY$ plane that includes the longitudinal axes of the SMF core and two MCF cores. <b>(c, right)</b> Evolution of the normalised $\text{LP}_{01}$ power along the $X$ axis is depicted. It shows the power in the SMF core and in the combined region of the CWG and MCF core (considering only one core). The shaded region indicates the section where evanescent wave coupling takes place. Adapted from [3]. . . . .	78
5.21	Fs laser inscription setup used to manufacture cladding waveguides in optical fibres. Slit beam shaping technique is employed. Assembly was carried out using SolidWorks 2019 SP4.0 software with components from Thorlabs, Inc. Adapted from [3]. . . . .	80
5.22	<b>(a)</b> Microscope image of the initial part of the CWG, specifically focusing on its coupling section. The transverse separation from the SMF core measures $1 \mu\text{m}$ . <b>(b)</b> Microscope image of the coupling section of the CWG, where red light ( $\lambda = 633 \text{ nm}$ ) is introduced at the distal end of the fibre. <b>(c)</b> Microscope image of the end-face of the SMF fibre, revealing the cross-section of the CWG. Scale bars in <b>a-c</b> are $25 \mu\text{m}$ . Adapted from [3]. . . . .	81
5.23	<b>(a)</b> Microscope image showcasing the splice zone between the SMF and the MCF. The focus of the image is directed towards MCF core <sub>1</sub> , revealing the corresponding CWG. Although slightly out of focus, the presence of MCF core <sub>2</sub> and its associated CWG can also be observed. <b>(b)</b> Microscope image of the end face of the MCF fibre after manufacturing the complete structure of Fig. 5.18. Red light ( $\lambda = 633\text{nm}$ ) is introduced at the distal end of the fibre to aid visualization. Scale bars in <b>a-b</b> are $25 \mu\text{m}$ . Adapted from [3]. . . . .	81
5.24	Transverse phase profile measured with QPM for a cladding waveguide inscribed at $y = -30 \mu\text{m}$ . Adapted from [3]. . . . .	82
5.25	<b>(a)</b> Microscope image of the multicore fibre, with a P1-b-P1 FBG inscribed in each of the two focused cores. <b>(b)</b> Reflection spectrum resulting from the structure depicted in Fig. 5.18, with a $1 \text{ mm}$ long FBG inscribed in each core of the MCF. Scale bar in <b>a</b> is $25 \mu\text{m}$ . Adapted from [3]. . . . .	82

## 6 Standard fibre-based sensors

6.1	Schematic illustration of the all-in-fibre 6 mm optical device. Adapted from [1]. . . . .	96
6.2	Schematic illustration of the multiscan technique. Cross-section view of SMF, with multiple inscriptions for the manufacture of the CWG. Index-matching oil is used. Adapted from [1]. . . . .	97
6.3	Schematic diagram of the simulated structures, with the parameters indicated in Table 6.3. <b>(a)</b> S-Bend transition, <b>(b)</b> and straight transition. Adapted from [1]. . . . .	98
6.4	<b>(a)</b> Normalised transmission of LP <sub>01</sub> mode based on separation angle ( $\theta$ ) for straight and S-Bend transitions. <b>(b)</b> S-Bend example with $L_1 = 650 \mu\text{m}$ ( $\theta = 3.52^\circ$ ). <b>(c)</b> S-Bend example with $L_1 = 1000 \mu\text{m}$ ( $\theta = 2.29^\circ$ ). Adapted from [1]. . . . .	98
6.5	<b>(a)</b> SMF end face of the waveguide captured with a CCD camera. <b>(b)</b> 3D RI profile measured with a RI Profiler. <b>(c)</b> Core and CWG RI Y profile ( $Z = 0 \mu\text{m}$ ). <b>(d)</b> CWG and filament RI Z profile ( $Y = 40 \mu\text{m}$ ). Adapted from [1]. . . . .	99
6.6	<b>(a)</b> Phase profile measured with QPM for waveguides formed by 1, 5 and 10 scans. <b>(b)</b> CWG-cladding phase change based on the number of scans that form the waveguide. Adapted from [1]. . . . .	100
6.7	<b>(a)</b> MZI transmission spectra for waveguides formed between 1 and 5 scans. <b>(b)</b> FSR and increment in the effective RI difference depending on the number of scans that make up the CWG (1–5 scans). The region 1400–1550 nm is selected for the determination of the FSR. Adapted from [1]. . . . .	101
6.8	<b>(a)</b> Transmission spectra of the complete MZI (5 scans) without and with the FBG inscription in the core. Inset: zoom of Bragg resonance. <b>(b)</b> Longitudinal view of the MZI cladding section together with the FBG inscription in the core. Adapted from [1]. . . . .	101
6.9	<b>(Left Y axis)</b> Wavelength shift of a interference dip of the MZI developed in this work for temperatures between 23°C and 800°C (continuous line), and wavelength shift of a interference dip of the MZI developed in [28] for temperatures between 23°C and 650°C, with fit and translation (scale factor $\alpha$ ) to the measurements of the present work (dotted lines). <b>(Right Y axis)</b> Bragg wavelength shift for temperatures between 23°C and 800°C. The sensitivities ( $k_T$ ) as well as the effect of the annealing are indicated. Adapted from [1]. . . . .	102
6.10	Wavelength shift of a MZI interference dip when immersing the fibre in liquids of different refractive index. Adapted from [1]. . . . .	104
6.11	<b>(a)</b> Dip wavelength shift when a curvature sweep is performed. Two sets of measurements are made. <b>(b)</b> Bragg and dip wavelength shift when a strain sweep is applied. Adapted from [1]. . . . .	105
6.12	Cross sensitivity of curvature and strain. The graph is obtained by varying one measurand while the other is fixed. Adapted from [1]. . . . .	106
6.13	Schematic illustration of the manufactured LIF sensor. It contains an in-fibre air bubble (Fabry-Perot cavity) and a P1-b-P1 FBG in the tapered final section of the fibre. The sensor is integrated into a $\varnothing 400 \mu\text{m}$ surgical needle. Adapted from [3]. . . . .	107

LIST OF FIGURES

6.14 Simulation of the electric field in circular air cavities of diameter **(a)** 50  $\mu\text{m}$ , **(b)** 70  $\mu\text{m}$ , **(c)** and 90  $\mu\text{m}$  within an SMF, **(d)** together with the ideal case of a square bubble with 90  $\mu\text{m}$  side. **(e)** Loss and reflection spectrum for each case is presented. Adapted from [3]. . . . . 109

6.15 **(a)** Simulated  $E^*(x)$  value (Equation 6.15) in circular air cavity of 70  $\mu\text{m}$  diameter, **(b)** with the section after the bubble emphasised (0–40  $\mu\text{m}$ ). Adapted from [3]. . . . . 110

6.16 Schematic of the LIF sensor manufacturing process. **(a-c)** In-fibre air microcavity generation, **(d)** fibre end tapering, **(e)** and Pl-b-Pl FBG inscription. Adapted from [3]. . . . . 111

6.17 **(a)** Microscope images of LIF sensing elements: in-fibre air micro-cavity and Pl-b-Pl FBG, and its integration into the  $\varnothing 400 \mu\text{m}$  surgical needle. **(b)** Reflection spectra of the complete LIF sensor, both manufactured and simulated, as well as that corresponding only to the manufactured air cavity. Adapted from [3]. . . . . 112

6.18 **(a)** Measured axial strain sensitivity of air cavity ( $(\kappa_\epsilon)_{\text{FP}} = 6.69 \text{ pm}/\mu\epsilon$ ) and FBG ( $(\kappa_\epsilon)_{\text{FBG}} = 8.38 \text{ pm}/\mu\epsilon$ ). **(b)** Simulated (1.3–1.4) and measured (1.33–1.35) SRI sensitivity ( $(\kappa_{\text{SRI}})_{\text{FBG}} = 11.5 \text{ nm}/\text{RIU}$ ) of the FBG. **(c)** COMSOL simulation of the sensor’s SRI sensitivity for different taper waist diameter. Adapted from [3]. 113

**7 Specialty fibre-based sensors**

7.1 Schematic view of the manufactured sensor. It is based on a 1.55 mm long HCF with four holes fabricated by femtosecond laser ablation. This structure behaves as a liquid level sensor through the dynamic variation of the Fabry-Perot cavity length that forms the liquid within the fibre. Adapted from [6]. . . . . 122

7.2 Microscope image of the HCF spliced to SMF sections ( $\times 20$  objective lens), with a zoom of the splice section ( $\times 50$  objective lens). A schematic of the HCF-SMF splice process is also depicted. Adapted from [6]. . . . . 122

7.3 **(a)** Top view microscope image ( $\times 50$  objective lens) of the processed HCF, with the square  $25 \times 25 \mu\text{m}$  hole. **(b)** Side view microscope image ( $\times 20$  objective lens) of the hole corresponding to the final section of the processed HCF. **(c)** Schematic of the fs laser manufacturing process of the holes. 20 planes are made from the fibre surface to the hollow-core. Each plane corresponds to 8 laser scans of 25  $\mu\text{m}$  in length. Adapted from [6]. . . . . 123

7.4 Schematic explanation of the manufactured sensor, with the interferometric contribution of the different Fabry-Perot cavities: air section, liquid section and both combined. Adapted from [6]. . . . . 124

7.5 Illustration of the experimental setup used to regulate the liquid level in the hollow-core fibre. Adapted from [6]. . . . . 125

7.6 **(a)** Reflection spectra of the no-hole HCF (Fig. 7.2), and the 4-hole HCF (Fig. 7.3 **b**). **(b)** FFT amplitude from the spectra of Fig. 7.6 **a**, as well as the one corresponding to the simulated structure. Adapted from [6]. . . . . 126

7.7 **(a)** Examples of measured reflection spectra for water levels of 200  $\mu\text{m}$ , 700  $\mu\text{m}$  and 1200  $\mu\text{m}$ , respectively. **(b)** FFT amplitude of measured spectra corresponding to water levels of 100  $\mu\text{m}$ , 400  $\mu\text{m}$ , 700  $\mu\text{m}$ , 1000  $\mu\text{m}$  and 1300  $\mu\text{m}$ . Adapted from [6]. 127

7.8	(a) Experimental FFT amplitude measured for water levels in the HCF between 100 $\mu\text{m}$ and 1400 $\mu\text{m}$ , with a spacing of 100 $\mu\text{m}$ . (b) Simulated FFT amplitude for water levels in the HCF between 100 $\mu\text{m}$ and 1400 $\mu\text{m}$ . Adapted from [6]. . . . .	127
7.9	(a) Estimated cavity length (air and water) and relative error for different real water levels. (b) Estimated cavity length (air and water) and relative error for different simulated water levels. Adapted from [6]. . . . .	128
7.10	(a) Experimental FFT amplitude measured for different liquids in the HCF with a liquid level of 30 $\mu\text{m}$ . (b) Experimental FFT amplitude measured for different liquids in the HCF with a liquid level of 1300 $\mu\text{m}$ . Adapted from [6]. . . . .	129
7.11	(a) Estimated refractive index of the HCF liquid whose level is at 300 $\mu\text{m}$ . (b) Estimated refractive index of the HCF liquid whose level is at 1300 $\mu\text{m}$ . Adapted from [6]. . . . .	129
7.12	Schematic illustration of the CYTOP-based optical structure. Adapted from [9].	132
7.13	Geometric parameters that define the (a) major axis and (b) minor axis of the ellipse generated in the XY plane (Fig. 7.12). Adapted from [9]. . . . .	133
7.14	Schematic of the fibre in the $Z$ -plane (no transformation) and in the $W$ -plane (conformal mapping applied) for (a) unpolished ( $R$ -sweep simulation), (b) and polished (at $\Psi = 90^\circ$ ) fibre ( $\epsilon$ -sweep simulation). Refractive index profiles are depicted for each case (with and without transformation). Adapted from [9]. . . . .	135
7.15	RSoft simulation of the resulting field in the fibre cross-section at $\Psi = 90^\circ$ for bending radii of (a) 2 mm, (b) 4 mm, (c) 5 mm, (d) 6 mm, (e) 10 mm and (f) 20 mm. The attenuation obtained at the end of the curvature ( $\Psi = 180^\circ$ ) for each radius is 31 dB, 16.3 dB, 12.7 dB, 9.7 dB, 5.1 dB and 2.7 dB, respectively. The boundaries corresponding to core (dotted line) and cladding (solid line) are also depicted. Adapted from [9]. . . . .	136
7.16	(a) RSoft simulation of fibre losses ( $L$ ) due to curvature ( $R = 5$ mm) as a function of polishing depth ( $\epsilon$ ) and surrounding refractive index. (b) $\partial L/\partial \text{SRI}$ of the values represented in a. The SRI range between 1.318 and 1.336 is highlighted, due to its remarkable sensitivity. Adapted from [9]. . . . .	136
7.17	Diagram of 1D diffraction grating. The diffraction orders in transmission and reflection are depicted. It is assumed that there is no cladding (removed in polishing). Adapted from [9]. . . . .	137
7.18	(a) $5\times$ microscope image of the ellipse generated as a result of polishing, showing both cladding and core, as well as overlapping. $20\times$ microscope images (b) before (c) and after diffraction grating inscription of the region indicated in (a) are also shown. (d) Image of the complete CYTOP-based optical structure. Scale bar in a is 500 $\mu\text{m}$ , and in b-c it is 100 $\mu\text{m}$ . Adapted from [9]. . . . .	138
7.19	(a) Transmission spectra when the structure is immersed in liquids with different RI. The 6 peaks and valleys on which the tracking in sensing is performed are highlighted. (b) Wavelength shift ( $\Delta\lambda$ ) of each of the 6 peaks/valleys for the liquids used, with their quadratic fit and error bars (CL=95%). (c) Simulation and experimental transmission losses for $\lambda = 1550$ nm, as well as experimental results for $\lambda = 1500$ nm and $\lambda = 1600$ nm, with the associated error bars (CL=95%). Adapted from [9]. . . . .	140

- 7.20 Wavelength shift ( $\Delta\lambda$ ) of each peak/valley as a function of temperature. The structure has been immersed in water ( $n_L = 1.3153$ ), and a temperature sweep between 23°C and 40°C has been performed. A linear fit is made, with the slope of each fit. It should be noted that the wavelength step in the spectrum is 50 pm. Adapted from [9]. . . . . 141

## 8 Polarisation-independent ULAE in fused silica

- 8.1 Overview of the main optical absorption bands in synthetic glassy SiO<sub>2</sub> that stem from intrinsic defects and typical dopants/impurities. The spectral position and FWHM of the bands are represented by the centre and width of the bars. Only the oxygen vacancy band (which peaks at 7.6 eV) is observable in  $\alpha$ -quartz crystal among these bands. For optical applications in the visible to deep-UV ranges, the bands associated with dangling oxygen (NBOHC) and silicon bonds (E'-center) are the most prominent and problematic. Adapted from [5]. . . . . 152
- 8.2 Schematic illustration of **(a)** a 6-membered ring ((Si-O)<sub>6</sub>) and a 3-membered planar ring ((Si-O)<sub>3</sub>) in amorphous SiO<sub>2</sub>. **(b)** Vacancy-interstitial type defects, **(c)** and basic dangling-bond type defects observed in SiO<sub>2</sub>. Adapted from [5]. . . 153
- 8.3 SEM images of nanograting structures formed along the writing direction with laser polarisation **(a)** parallel  $\parallel$  and **(b)** perpendicular  $\perp$  to the writing direction. The samples are etched for 20 min in 0.5% HF. Reprinted with permission from [12]. **(c)** Field-emission gun SEM images of the porous region of the nanoplanes, with the polarisation aligned parallel to the direction of writing. Reprinted with permission from [11]. . . . . 157
- 8.4 SEM images of the nanostructures that have emerged within the zones that underwent fs laser irradiation for **(a)** pulse energy of 1  $\mu$ J and parallel polarisation, **(b)** pulse duration of 10 ps and an energy of 8  $\mu$ J under circular polarisation conditions, and **(c)** when using a pulse delay of  $\Delta t = 1000$  fs and parallel polarisation. Images are reprinted from [30], [31], and [32], respectively. . . . . 158
- 8.5 Illustration of optical setup used for ultrafast laser inscription (Key: BE – beam expander (2 $\times$ ), C – CCD camera, TL – tube lens, DM – dichroic mirror, AL – 0.4 NA aspheric lens). Adapted from [1]. . . . . 159
- 8.6 **(top)** Fluorescence intensity of the R6G within the microchannels for  $\circlearrowleft$ ,  $\perp$  and  $\parallel$  polarisations for several pulses,  $N$ , **(bottom)** and corresponding optical microscope image. The images are not to scale.  $E_p=600$  nJ and PRR=120 kHz. Adapted from [1]. . . . . 160
- 8.7 **(a-b)** ERs for  $\circlearrowleft$ ,  $\parallel$  and  $\perp$  polarisation for **(a)**  $E_p=300$  nJ and **(b)** 600 nJ. The etching time is 4 hours, and the PRR is 120 kHz. **(c-d)** ER ratio of  $\perp$  and  $\circlearrowleft$  polarisation with respect to  $\parallel$  polarisation for **(c)**  $E_p=300$  nJ and **(d)** 600 nJ. The region where the ER is independent of polarisation is highlighted. The mean values are shown whereas the shaded regions are the standard deviations of two measurements. Adapted from [1]. . . . . 161
- 8.8 ERs for transversal  $\perp$  and longitudinal  $\parallel$  polarisation for several pulse repetition rates (PRRs) and different pulse energies ( $E_p$ ) as a function of the number of pulses ( $N$ ). Adapted from [1]. . . . . 162

- 8.9 **(a-c)** SEM images of the cross section of laser affected zone using  $\perp$  polarisation at 600 nJ and 120 kHz for pulses **(a)**  $N=5 \mu\text{m}^{-1}$ , **(b)**  $N=20 \mu\text{m}^{-1}$  **(c)** and  $N=100 \mu\text{m}^{-1}$ . Red squares indicate the region shown in the bottom row images with higher magnification. After inscription, the sample was polished and etched for 2 minutes in NaOH solution (5 wt%). Scale bars in **(a-c)** are 1  $\mu\text{m}$ . **(d)** Optical images of the microchannels placed between two crossed polarisers and illuminated with  $660 \pm 10 \text{ nm}$  light (filtered halogen lamp). **(e)** Maximum intensity measured at different number of pulses, whose values are averaged from 150 different points along the laser affected zone whereas the shaded regions represent the standard deviations. The samples were positioned at an angle ( $x$ - $y$ ) where the maximum birefringence intensity was measured ( $45^\circ$ ). Each symbol in **(d)** corresponds to a fringe (microchannel) in **(e)**. The microchannels are separated by 20  $\mu\text{m}$ . The pulse energy is 600 nJ at 120 kHz. Note that reducing the pulses exhibits a less homogeneous birefringence along the laser inscription. The higher intensity at high number of pulses for the longitudinal case indicates the LAZ contains higher domains with material modification, possibly arising from a more homogeneous and ordered damage because the nanogratings length is restricted to the beam waist. Adapted from [1]. . . . . 163
- 8.10 Comparison of **(a)** ERs and **(b)** ER ratios using two different etching solutions (NaOH and KOH) for different pulse energies and PRRs. Both etching solutions yield similar ERs and trends with the number of pulses, hence the mechanisms behind etching are likely the same. The highest ERs correspond to the nanogratings regime for NaOH and by setting the polarisation perpendicular to the beam writing direction. Note that different samples than those of Fig. 8.8 have been used for NaOH obtaining comparable results. Etching time was four hours for NaOH solution of 5 wt% and KOH of 40 wt%. Adapted from [1]. . . . . 164
- 8.11 Polarisation etching rate contrast calculated from the difference between  $\perp$  and  $\parallel$  average etching rates at two different  $E_p$ . Solid lines depict the etching rates for  $\perp$ , while dashed lines show the etching rate contrast. Lower  $E_p$  (180 nJ) and higher PRRs (240 kHz and 480 kHz tested) than the one used for polarisation independence (120 kHz and  $E_p \geq 240 \text{ nJ}$ ) retrieve traditional high polarisation contrast at a few pulses. Adapted from [1]. . . . . 166
- 8.12 **(a)** Curved and **(b)** square-wave microchannels inscribed at a depth of 70  $\mu\text{m}$ . Solid circles show the final penetration of the etching after 4 hours in a NaOH solution (5 wt%). Scale bars are 100  $\mu\text{m}$ . Adapted from [1]. . . . . 167
- 8.13 **(a)** SEM image and **(b)** photograph of the stellated octahedron. Scale bars are 200  $\mu\text{m}$  for SEM picture and 500  $\mu\text{m}$  for the photograph. Adapted from [1]. . . . 168
- 8.14 Resultant absorbance present in pristine fused silica, as well as in a modified substrate processed at 600 nJ and 120 kHz by raster scanning (1  $\mu\text{m}$  spacing) fs laser pulses at high speed ( $N = 5 \mu\text{m}^{-1}$ ) and using  $\parallel$  polarisation. The results shown are presented without annealing, and after annealings of 2 hours at  $600^\circ\text{C}$  and  $900^\circ\text{C}$ . A deuterium UV lamp and a high-sensitivity UV spectrometer Maya2000 Pro from OceanOptics are employed. . . . . 168
- 8.15 ERs for  $\parallel$  polarisation at 600 nJ and 120 kHz in modified fused silica substrate with no annealing, and after 2 hours at  $600^\circ\text{C}$  and  $900^\circ\text{C}$ . Etching of four hours in 5 w% at  $85^\circ\text{C}$  is considered. Shadow areas correspond to the standard deviation of two measurements. . . . . 169

- 8.16 Raman spectra of the cross-section of LAZ are shown for **(a)** no annealing, and after annealing for 2 hours at **(b)** 600°C and **(c)** 900°C. **(d)** Microscope image of the LAZ cross-section is provided. Filled contour 2D plots depict the normalised D<sub>2</sub> Raman band area (using a two-point baseline correction algorithm) for the LAZ cross-section under the following conditions: **(e)** no annealing, and after annealing for 2 hours at **(f)** 600°C and **(g)** 900°C. The experimental parameters used are 600 nJ pulse energy, 120 kHz PRR, || polarisation, and  $N = 5 \mu\text{m}^{-1}$ . The scale bar in **d** is 4  $\mu\text{m}$ . Spectra were acquired using a confocal Raman microscope NRS-4500 (JASCO Inc.) equipped with a 532 nm laser excitation source. . . . . 169

**9 SPIM using polymer coherent fibre bundles**

- 9.1 Schematic illustration of the SPIM probe platform for lung imaging. The SPIM probe is intended to be introduced through the working channel of a standard bronchoscope. **(a)** The diameter of the SPIM probe (1.9 mm) is narrow enough to reach the alveolar space for structural imaging of endogenous fluorescent tissue. **(b)** The custom-made fused silica end-cap secured to the distal end of a PMMA imaging fibre. **(c)** Cross-section of the end-cap when in contact with tissue showing its operational principle. The end-cap is fabricated in two parts, 1 and 2, between which is a thin mirrored surface. Illumination from a laser guided by the outer fibre cores is reflected by the mirrored surface towards the centre of the distal tip, generating a light-sheet perpendicular to the direction of observation. Fluorescence from a sample in the front recess of the distal tip is collected through the central column of cores. Adapted from [1]. . . . . 178
- 9.2 **(a)** Schematic of the imaging fibre MCL-1500-1.75 (Asahi Kasei) and its key dimensions: fibre diameter, core diameter, and spacing between cores. **(b)** Subset of cores used to provide the excitation (70  $\mu\text{m}$  outer ring), and central column of cores used to collect the sample fluorescence ( $\varnothing$  1.36 mm). . . . . 178
- 9.3 Schematic of the proximal end instrumentation (Key: (L) – 485 nm fibre coupled laser, (L<sub>1</sub>) – lens, (BE) – beam expander, (Ex) – excitation filter, (M) – mirror, (L<sub>ax</sub>) – axicon lens, (L<sub>2</sub>) – lens, (L<sub>3</sub>) – lens; (Mask) – silver-coated optical mask, (DM) – dichroic mirror, (L<sub>obj</sub>) – objective lens, (Obj.) – object plane and location of proximal end of SPIM probe, (Em) – emission filter, (L<sub>5</sub>) – tube lens, (C) – CMOS monochrome camera, (L<sub>4</sub>) – tube lens). **(a)** The entire SPIM probe platform consists of the SPIM probe (packaged end-cap shown in photo) coupled to an axicon lens-based epifluorescence microscope and a PC for real-time imaging. **(b)** Epifluorescence microscope which enables the SPIM probe. Note that the greyed-out illumination path is an integrated WF epifluorescence microscope which was used for characterisation experiments and is not a part of the SPIM probe platform. **(c)** 3D view with real optical elements of the axicon-lens based epifluorescence microscope (the WF arm in Fig. (b) is not included here). Adapted from [1] and [2]. . . . . 180
- 9.4 **(a)** Schematic of an axicon lens showing the ring-shaped beam that propagates after the overlap region (Bessel beam region). **(b)** Error made when using the approximation  $t \approx r$  for different values of  $\alpha$ , the exact value being given in Eq. 9.2.  $n = 1.4632$  (UV fused silica at  $\lambda = 485 \text{ nm}$ ) and  $r = 77 \mu\text{m}$  are considered. 181

- 9.5 End-cap design. **(a)** Illustration of the SPIM probe. Inset shows an SEM image (taken with Phenom Pro, Thermo Fisher Scientific) of a region of the end face of the fibre. Scale bar is 50  $\mu\text{m}$ . **(b)** 3D cross-sectional slice of the designed end-cap. The top and bottom parts are shown slightly separated, to indicate the location of a mirrored surface between the two parts. **(c)** 2D CAD drawing of the end-cap.  $R$  refers to radius of curvature. Dimensions are shown to scale. Figures **(a-b)** are made using Blender 3.2, while Fig. **c** is based on the model made with Solidworks 2019 SP4.0, which can be found in [4]. Adapted from [1]. . . . . 183
- 9.6 Polarisation control techniques used in the different laser inscriptions that result in the end cap. **(a)** The vertical surfaces (inscribed while moving in  $Z$ ) present a surface-matched polarisation technique, while the horizontal surfaces (inscribed with constant  $Z$ ) are inscribed with a static polarisation state, being  $E_y$  in this case. **(b)** Appearance of the end-cap in a top view ( $XY$  plane). The arrows show the polarisation direction in the surface-matched polarisation inscriptions, which depends on the angular position. . . . . 184
- 9.7 End-cap fabrication. **(a)** Ultrafast laser inscription. (left) Side and (centre) top view micrograph of the end-cap inscribed in the fused silica substrate. (right) Image of a  $10 \times 10 \times 1$  mm fused silica substrate where twelve end caps are inscribed. **(b)** Micrographs of the (left) bottom and (centre) top parts of the end-cap, after KOH etching process. (right) Micrograph of the bottom part of the end-cap in a slightly oblique position. **(c)** Assembly. (left) Image of the two parts of the end-cap glued together. A silver thin film is located on the surface between the two parts, as depicted in the illustration in Fig. 9.5 **b**. (centre) Image of the end-cap bonded to the PMMA CFB. (right) Image of two end cap samples attached to different illuminated PMMA CFBs, one of them with the protective shrink tubing. Scale bars in **(a)** are 300  $\mu\text{m}$ . Scale bars in **(b-c)** are 400  $\mu\text{m}$ . Adapted from [1]. . . . . 185
- 9.8 Measurement of fibre core fluorescence. **(a)** Fluorescence emission spectra of the cores of the PMMA CFB. Plot shows PMMA fibre cores exhibiting a strong green fluorescence (black line) which coincides with endogenous tissue emission band (blue fill). The silica fibre exhibits a weak, broad fluorescence (red dashed line). Dashed vertical line represents the excitation filter edge. Relative fluorescence units (RFU) refers to fluorescence counts per metre of fibre. **(b)** Epifluorescence system used to measure the fluorescence emission spectra of the cores of the PMMA CFB and the silica CFB when pumped with a 485 nm laser (Key: (L) – 485 nm fibre coupled laser, (L<sub>1-5</sub>) – lenses, (Ex) – excitation filter, (DM) – dichroic mirror, (C) – camera, (Spec.) – spectrometer). Adapted from [1]. . . . 186
- 9.9 Simulations of light fields in WF and SPIM cases. **(a)** Illustration depicting arrangement of the  $4 \times 1.35$  mm  $ZY$  rectangular detector in the simulation for both WF (flood illumination without end cap) and SPIM (ring illumination with end cap) cases. **(b)** 2D simulated excitation light intensity profile in the detector plane using both WF and SPIM illumination. Absorption/scattering have not been taken into account. Dotted white line at  $z = 170$   $\mu\text{m}$  on the SPIM profile represents the end of the end-cap. **(c)** Integrated intensity as a function of distance ( $I(z) = (L_y)^{-1} \int_y I(y, z) \cdot dy$ , with  $L_y = 1.35$  mm) for WF and SPIM illumination. Front recess region ( $z \leq 170$   $\mu\text{m}$ ) is shown as grey fill. Adapted from [1]. . . . . 187

- 9.10 Optical system used for illuminating (laser at 515 nm) a single core within a coherent fibre bundle by butt-coupling, and recording the coupling of light across its immediate and extended neighbouring cores by means of an unsaturated image. 188
- 9.11 Experimental measurement of the core crosstalk of the PMMA CFB. **(a)** Number of modes per core in the PMMA CFB as a function of  $\lambda$ . **(b)** Example of a coupling spread pattern, highlighting the excited core (515 nm wavelength), as well as the first three neighbouring layers. **(c)** Box plot with the relative power in the excited core, as well as in each of the three neighbouring layers, either for the whole layer or for an individual core. Adapted from “Supplementary Information” in [1]. . . . . 189
- 9.12 Simulation measurement of the core crosstalk of the PMMA CFB. **(a)** Field existing at the beginning of propagation, corresponding to a multimode launched field in the central core. **(b)** Field existing at the end of propagation (1 m). Scale bars in **(a-b)** are 10  $\mu\text{m}$ . Adapted from “Supplementary Information” in [1]. . . . 190
- 9.13 Simulation of the transmission of an image along a 1 m long MCL-1500-1.75 imaging fibre. The existing field at the distal end of the fibre is superimposed with the contour of the transmitted images (dotted red lines). The transmitted images are an **(a)** off-centre cross, **(b)** four asymmetrically positioned elliptical dots, and **(c)** a capital letter “A”. Scale bars in **(a-c)** are 100  $\mu\text{m}$ . . . . . 191
- 9.14 Widefield and SPIM images showing improved contrast and a reduction of out-of-focus features. **(a-h)** Corresponding FOVs acquired in WF and SPIM modality. Raw images demonstrate the strong fibre fluorescence which is present in the WF case. The clear ring present in the raw SPIM images is backscattered fibre fluorescence as a result of pumping the excitation light down these cores. Processed images demonstrate qualitatively improved imaging using the SPIM probe. Scale bar is 500  $\mu\text{m}$ . Evaluation of the images (a-d) is shown in Fig. 9.15. Adapted from [1]. . . . . 193
- 9.15 Evaluation of WF and SPIM images. **(a-d)** Line profiles across images shown in Fig. 9.14 a-d demonstrate reduced out-of-focus background and improved contrast of SPIM. Insets show image and line plotted (dashed white line). (Left) and (middle) WF and SPIM image, respectively, with measured background (yellow dashed line), raw image (orange dotted line) and image with subtracted background (blue solid line). (right) Normalised WF (red dashed line) and SPIM (purple solid line) line profiles after background subtraction. Grey fill in each plot corresponds to areas shown by grey arrows where background features are less visible in SPIM. Brightness and contrast of inset images have been adjusted for visibility. Line profiles were taken on raw data and then smoothed using a Savitzky-Golay filter (window=29, polynomial order=2). Adapted from [1]. . . . 195
- 9.16 Representative examples of *ex vivo* human lung tissue. **(a)** Lung tissue sample imaged on the benchtop using the SPIM probe at 5 fps. **(b)** Mechanically ventilated, whole *ex vivo* human lungs imaged through the SPIM probe at 7 fps. The alveolar space is reached via a transbronchial pass. Images and videos have been processed as described in “Image processing” subsection. Scale bar is 500  $\mu\text{m}$ . Adapted from [1]. . . . . 196

## 10 Molecular sensing with Bloch surface waves

10.1	Illustration of the evanescent wave at the surface of a generic 1DPC in a Kretschmann configuration [16], and the BSW propagating through the interface between the two media. . . . .	207
10.2	<b>(a)</b> Dispersion relation (frequency vs. wavevector) of a homogeneous material with a refractive index $n = 1.45$ . The structure does not exhibit any band gap. <b>(b)</b> Dispersion relation of a 1DPC with a refractive index contrast of $n_{high}/n_{low} = 1.4$ . The thickness of both materials is equal. The index contrast leads to the formation of a band gap, characterised by frequency ranges where no states exist. In both graphs, the shaded area represents the continuum of allowed bands where electromagnetic waves can propagate, while frequencies within the band gap correspond to evanescent waves. The bottom line is the light line. The MIT Photonic-Bands (MPB) package has been utilised to calculate the definite-frequency eigenstates of Maxwell's equations within a semi-infinite 1DPC. This computation was achieved by applying the supercell method [22] and the plane wave expansion (PWE) method [23]. . . . .	208
10.3	<b>(a)</b> Diagram illustrating the 1DPC, with the incident TE and TM polarised waves depicted at the lower section, and the corresponding TE and TM surface modes displayed at the upper section. Layers of different RI are distinguished by different colours. <b>(b)</b> Scanning electron microscopy (SEM) image (Hitachi S4800) of the truncated 1DPC, shown in a cross-section view. The brightness contrast between layers arises from the contrasting atomic weights of the $Ta_2O_5$ (lighter) and $SiO_2$ (darker). Scale bar in <b>b</b> is 500 nm. Adapted from [6]. . . . .	211
10.4	Dispersion relation of the 1DPC depicted in Fig. 10.3 for <b>(a)</b> TE polarisation, <b>(d)</b> TM polarisation, and <b>(c)</b> the overlap of these two graphs. The shaded area represents the continuum of allowed bands where electromagnetic waves can propagate. Light lines in water and BK7 are also shown. The MPB package has been utilised to calculate the definite-frequency eigenstates of Maxwell's equations [22, 23]. Adapted from [20]. . . . .	212
10.5	Physical arrangement of the different elements comprising the sensor platform. The figure is created using Blender 3.2. . . . .	213
10.6	<b>(a)</b> Physical dimensions of the microfluidic chamber. <b>(b)</b> Two-phase flow simulation of the filling of the chamber with a flow rate of 25 $\mu\text{L}/\text{min}$ after 3.5 seconds. The chamber design was carried out using Solidworks 2019 SP4.0, and the simulation was performed using Comsol Multiphysics. . . . .	214
10.7	Illustration of a tube plugged into the 3D reservoir of the top fused silica plate. . . . .	214
10.8	<b>(a-e)</b> Illustration of some of the different stages involved in the fabrication of the chip. The figures are created using Blender 3.2. . . . .	216
10.9	<b>(a)</b> Image of the $20 \times 20 \times 2$ mm fused silica glass after the fs laser inscription of the mask used in the UV polymerisation stage of the SU8 layer. <b>(b)</b> Image of the final optofluidic chip. It is equivalent to the illustration in Fig. 10.8 <b>e</b> . . . . .	216

## LIST OF FIGURES

10.10	(a) Schematic of the experimental setup for CD measurements of the sample (Key: L – 405 nm fibre laser, $L_1$ – collimation lens, $\lambda/2$ – half waveplate, $\lambda/4$ – quarter waveplate, BS – beam splitter, GTP – Glan-Taylor polariser, PM – photoelastic modulator, $L_2$ – semicylindrical BK7 lens, S – sample mounted on a rotating holder, $L_3$ – signal capture lens, $D_1$ – intensity detector, $D_2$ – reflectivity detector, LIA – lock-in amplifier). (b) Illustration of the optofluidic platform assembled with the semicylindrical lens and the microfluidic tubes placed in the reservoirs. The figure is created using Blender 3.2. (c) Image of the photonic chip mounted on the rotating holder in the actual setup. The chamber has been filled with custom chiral molecules o-MR-PEA (o-methyl red conjugates with chiral 1-phenyl-ethyamine). . . . .	217
10.11	(a) o-MR-(R)-PEA molecule represented in a 2D structure. (b) Molar extinction coefficient spectrum obtained from the absorption spectrum of a 200 $\mu\text{M}$ solution of the (R) enantiomer. Its peak centred in the blue region of the spectrum, which is the desired range for the 1DPC. Adapted from [20]. . . . .	218
10.12	(a) Optimal amplitude signal of the 1DPC under normal incidence without fluid in the chamber. (b) Optimal amplitude and reflectivity signals of the 1DPC when the chamber is filled with the solvent (acetonitrile). Adapted from [20]. . . . .	219
10.13	(a) Amplitude signal, (b) phase, and (c) CD signal from solvent and both (R) and (S) enantiomers. Adapted from [20]. . . . .	220

## List of Publications

A.1 Graph showing relevant information of the journal articles published during the four years of the thesis (from October 2019 to September 2023). Each circle corresponds to the publication of an article. If it is filled, it is a paper related to the PhD work, otherwise it is empty. The size of the circle indicates the authorship order, going from largest (1<sup>st</sup> author) to smallest (4<sup>th</sup> author). The colour refers to the quartile of the journal where it is published. The Y-axis indicates the impact factor of the journal. Similarly, the temporal periods where an international stay was carried out are highlighted, and the number of journal articles published in each of the four years of the thesis is shown in the format  $(\alpha, \beta)$ , where  $\alpha$  is the number of papers related to the PhD work, and  $\beta$  is the rest. 230

# List of Tables

3.1	Comparison of diverse material options for the fabrication of microfluidic platforms. ●●● is equivalent to 'positive', ●●○ is equivalent to 'moderate', and ●○○ is equivalent to 'negative'. Adapted from [8, 16]. . . . .	27
3.2	Classification of microfluidic fabrication techniques. Adapted from [8, 17]. . . . .	28
3.3	Scaling of physical phenomena with length ( $L$ ) and consequences for microfluidic devices. . . . .	34
5.1	Comparison of the characteristics among various methods of inscribing waveguides using ultrafast lasers. . . . .	76
6.1	Compilation of parameters measured with CWG-MZI existing in the literature. . . . .	95
6.2	Overview of inscription parameters utilised for CWG-MZI reported in the literature. . . . .	95
6.3	Parameters used in the CWG simulations (FE-BPM in RSoft). . . . .	98
7.1	Table comparing liquid detection sensors found in the literature. . . . .	121
7.2	Studies focusing on fs laser-assisted manufacture of optical structures in CYTOP fibres. . . . .	131
7.3	Simulation parameters used in RSoft for both cases ( $R$ sweep and $\epsilon$ sweep). . . . .	133
7.4	Solute concentration, $n_D$ and $n(1550 \text{ nm})$ of the liquids used in the experiments. . . . .	139
7.5	Parameters of the quadratic and linear fits of the six curves depicted in Fig. 7.19 <b>b</b> . . . . .	139
9.1	Required focal lengths for the lens ( $L_2$ ) depending on the different axicon lens options from Thorlabs. . . . .	182
A.1	Number of journal articles published during the thesis, highlighting those works that are closely related to the PhD work, as well as the others. The average values of authorship order, impact factor, and quartile are shown. . . . .	239
A.2	Summary of publications and their relationship with thesis contributions. This table only includes works closely related to the topics conducted in this thesis. . . . .	240

# List of Acronyms

<b>1DPC</b>	One-Dimensional Photonic Crystal	<b>ETP</b>	European Technology Platform
<b>2PP</b>	Two-Photon Polymerisation	<b>EU</b>	European Union
<b>AO</b>	Adaptive Optics	<b>FACS</b>	Fluorescence Activated Cell Sorter
<b>API</b>	Application Programming Interface	<b>FBE<math>\mu</math></b>	Fluorescence Fibre-Bundle Endomicroscopy
<b>AR</b>	Antiresonant	<b>FBG</b>	Fibre Bragg Grating
<b>BE</b>	Beam Expander	<b>FCA</b>	Free Carrier Absorption
<b>BPM</b>	Beam Propagation Method	<b>FDTD</b>	Finite-Difference Time-Domain
<b>BS</b>	Beam Splitter	<b>FEFD</b>	Finite-Element Frequency-Domain
<b>BSW</b>	Bloch Surface Wave	<b>FEM</b>	Finite Element Method
<b>CAD</b>	Computer Aided Design	<b>FFT</b>	Fast Fourier Transform
<b>CCD</b>	Charge-Coupled Device	<b>FIB</b>	Focused Ion Beam
<b>CD</b>	Circular Dichroism	<b>FLCPA</b>	Fibre Laser Chirped Pulse Amplifier
<b>CFB</b>	Coherent Fibre Bundle	<b>FLICE</b>	Femtosecond Laser Irradiation followed by Chemical Etching
<b>CL</b>	Confidence Level	<b>FOV</b>	Field Of View
<b>CLTE</b>	Coefficient of Linear Thermal Expansion	<b>FPI</b>	Fabry-Perot Interferometer
<b>CMOS</b>	Complementary Metal-Oxide-Semiconductor	<b>FSR</b>	Free Spectral Range
<b>CMT</b>	Coupled Mode Theory	<b>FWHM</b>	Full Width at Half Maximum
<b>COG</b>	Centre Of Gravity	<b>GDD</b>	Group Delay Dispersion
<b>CW</b>	Continuous Wave	<b>GI</b>	Graded-Index
<b>CWG</b>	Cladding Waveguide	<b>GTP</b>	Glan-Taylor Polariser
<b>CYTOP</b>	Cyclic Transparent Optical Polymer	<b>HCF</b>	Hollow Core Fibre
<b>DL</b>	Detection Limit	<b>HWP</b>	Half Waveplate
<b>DM</b>	Deformable Mirror	<b>IoT</b>	Internet of Things
<b>DM</b>	Dichroic Mirror	<b>IR</b>	Infrared
<b>DMD</b>	Digital Mirror Device	<b>KET</b>	Key Enabling Technology
<b>EC</b>	European Commission	<b>LbL</b>	Line-by-Line
<b>ER</b>	Etching Rate	<b>LAZ</b>	Laser-Affected-Zone

<b>LIA</b>	Lock-In-Amplifier	<b>RFU</b>	Relative Fluorescence Unit
<b>LIF</b>	Lab-In-Fibre	<b>RI</b>	Refractive Index
<b>LOC</b>	Lab-On-Chip	<b>RIC</b>	Refractive Index Change
<b>LPG</b>	Long Period Grating	<b>RIU</b>	Refractive Index Unit
<b>MCF</b>	Multicore Fibre	<b>RNF</b>	Refracted Near Field
<b>MEMS</b>	Micro-Electro-Mechanical System	<b>ROC</b>	Radius of Curvature
<b>MFD</b>	Mode Field Diameter	<b>SA</b>	Spherical Aberration
<b>MI</b>	Michelson Interferometer	<b>SBST</b>	Slit Beam Shaping Technique
<b>MZI</b>	Mach-Zehnder Interferometer	<b>SD</b>	Standard Deviation
<b>NA</b>	Numerical Aperture	<b>SEM</b>	Scanning Electron Microscope
<b>NBOHC</b>	Non-Bridging Oxygen Hole Centre	<b>SHG</b>	Second Harmonic Generation
<b>NF</b>	Net Fluence	<b>SLD</b>	Super-Luminiscent Diode
<b>NG</b>	Nanograting	<b>SLM</b>	Spatial Light Modulator
<b>ODC</b>	Oxygen Deficiency Centre	<b>SMF</b>	Single-Mode Fibre
<b>OFS</b>	Optical Fibre Sensor	<b>SPIM</b>	Selective Plane Illumination Microscopy
<b>OPD</b>	Optical Path Difference	<b>SPP</b>	Surface Plasmon Polariton
<b>OSA</b>	Optical Spectrum Analyser	<b>SRI</b>	Surrounding Refractive Index
<b>OSNR</b>	Optical Signal-To-Noise Ratio	<b>STE</b>	Self-Trapped Exciton
<b>OTDR</b>	Optical Time Domain Reflectometry	<b>STF</b>	Spatiotemporal Focusing
<b>PbP</b>	Point-by-Point	<b>SW</b>	Surface Wave
<b>Pl-b-Pl</b>	Plane-by-Plane	<b>TE</b>	Transverse Electric
<b>PCF</b>	Photonic Crystal Fibre	<b>TFBG</b>	Tilted Fibre Bragg Grating
<b>PEEK</b>	Polyetheretherketone	<b>THG</b>	Third Harmonic Generation
<b>PDL</b>	Polarisation Dependent Loss	<b>TM</b>	Transverse Magnetic
<b>PDMS</b>	Polydimethylsiloxane	<b>ULAE</b>	Ultrafast Laser Assisted Etching
<b>PL</b>	Photoluminescence	<b>ULDW</b>	Ultrafast Laser Direct Writing
<b>PMMA</b>	Poly(Methyl Methacrylate)	<b>ULI</b>	Ultrafast Laser Inscription
<b>POF</b>	Polymer Optical Fibre	<b>ULI-CE</b>	Ultrafast Laser Inscription and Chemical Etching
<b>PRR</b>	Pulse Repetition Rate	<b>UV</b>	Ultraviolet
<b>PSF</b>	Point Spread Function	<b>VIS</b>	Visible
<b>PWE</b>	Plane Wave Expansion	<b>WBG</b>	Waveguide Bragg Grating
<b>QPM</b>	Quantitative Phase Microscopy	<b>WG</b>	Waveguide
<b>QWP</b>	Quarter Waveplate	<b>WF</b>	Widefield

# PART I

## PRELIMINARY

This first part of the thesis provides a foundational understanding of the essential knowledge and techniques that form the basis for the subsequent chapters. It begins with an introduction that highlights the significance, motivation, and objectives of the research. The second chapter explores the principles of ultrafast laser-matter interaction, laying the groundwork for the following chapters. Next, the focus shifts to microfluidic platforms, discussing the impact of scaling down devices to micrometer dimensions and addressing relevant materials and manufacturing techniques. Finally, the different experimental setups used for fabricating optofluidic devices are presented, as well as an overview of the characterisation techniques employed. Overall, this part serves as a comprehensive introduction and sets the stage for the in-depth exploration of the thesis topic in subsequent parts.

The chapters included in this part are:

- Chapter 1: Introduction.
- Chapter 2: Fundamentals of ultrafast laser processing of transparent materials.
- Chapter 3: Fundamentals of optofluidic platforms.
- Chapter 4: Experimental setups and methods.

# 1

## Introduction

---

<b>1.1</b>	<b>Motivation</b>	<b>3</b>
<b>1.2</b>	<b>Objectives</b>	<b>6</b>
<b>1.3</b>	<b>Document structure</b>	<b>7</b>
	<b>References</b>	<b>10</b>

---

**K** EY enabling technologies (KETs) are deemed by the European Commission (EC) as technologies that are essential for European economic growth and job creation. They are considered to be of exceptional importance due to their capacity to drive innovation across multiple industries and sectors, including those that are not typically associated with high-tech innovation. In 2009, the EC identified photonics, alongside nanotechnology, micro- and nano-electronics, industrial biotechnology, advanced materials, and advanced manufacturing technologies as the six KETs [1]. In 2018, the EC redefined the 6 KETs as a result of the introduction of artificial intelligence, and security and connectivity as two new KETs, as well as expanding the biotechnology KET to a broader term known as life-science technologies. However, it was also indicated that the European Union (EU) must continue to prioritise advanced manufacturing technologies, advanced materials and nanotechnologies, micro-/nano-electronics, and photonics [2]. Photonics, the science and technology of light, is integral to these KETs due to its wide-ranging applications and potential to drive innovation. Photonics technologies are essential for the functioning of many devices and systems in fields as diverse as healthcare [3, 4], communications [5], energy [6], and manufacturing [7, 8], among others. The EC recognises the critical role of photonics in addressing societal challenges, such as climate change, energy efficiency, and health, and its ability to contribute to the competitiveness of European industry.

Similarly, in the USA, photonics is recognised as an “essential” and “facilitating” technology [9], reflecting its capacity to enable advancements in a diverse range of sectors. The National Photonics Initiative in the USA was launched to highlight the importance of photonics and promote its integration into research and industrial applications [10]. The initiative recognises that

photonics is at the heart of countless technologies and industries and, as such, plays a crucial role in driving economic growth and societal progress [11, 12].

Alternatively stated, the European technology platform (ETP) Photonics21 is a significant consortium that brings together Europe’s prominent photonics industries and key R&D stakeholders. Its primary ambition is to reinforce Europe’s leadership in formulating and implementing photonics technologies across a diverse range of application domains. These include, but are not limited to, information and communication technologies, illumination, industrial fabrication, life science, safety, and even areas such as education and training. As a platform, Photonics21 facilitates interaction and collaboration between industry and academic stakeholders, thereby shaping the strategic trajectory of photonics research and innovation within Europe [13]. In its strategic roadmap, the Multiannual Strategic Roadmap 2021–2027 [14], recognises photonics as a key driver for economic growth and as a solution to societal challenges. It has identified several focus areas, such as information and communication, industrial production, life sciences and health, emerging lighting, electronics and displays, security, metrology and sensors, design and manufacturing of components and systems. The roadmap highlights the importance of research and innovation in photonics to meet the objectives of the EU’s Green Deal and Digital Strategy, as well as the United Nations’s Sustainable Development Goals [15]. It is also noteworthy that, according to a 2020 report [16], with a global growth rate of 7%, photonics is outpacing many other high-tech industries in terms of expansion. For instance, the growth rates of the IT industry (4.5%), Medtech (4.9%), and Microelectronics (4%) fall behind that of photonics.

As the field of action for this thesis, the importance of photonics as a key enabling technology is widely recognised by both the European Commission and the United States, and it forms a crucial part of strategies to drive economic growth and address societal challenges. Subsequently, the motivation behind the conducted thesis is detailed, with ultrafast laser microfabrication serving as the core focus.

Within the context of this work, it seems pertinent to me to point out a concerning fact about the country where this thesis has been carried out, Spain. In 2019, the global photonics market accounted for €654,000 million, of which €103,000 million belonged to Europe (15.75%) [16]. However, Spain only contributed €2,400 million, representing a mere 2.3% of the total European share. There are six countries in Europe with a larger market: Germany (40%), the UK (15%), France (15%), the Netherlands (6%), Italy (5%), and Switzerland (4%). While the GDP ratio between these countries and Spain is 3 (Germany), 2.2 (UK), 2.07 (France), 0.7 (Netherlands), 1.48 (Italy), and 0.56 (Switzerland); the ratio between the volume of the photonics market of these countries and that of Spain is 17 (Germany), 6.5 (UK), 6.37 (France), 2.58 (Netherlands), 2.16 (Italy), and 1.8 (Switzerland), respectively. The disparity is striking. There is a worrying lack of companies in the field of photonics in Spain and an alarming neglect concerning public and private funding for research in general, and photonics research in particular.

## 1.1 Motivation

One of the exciting domains within photonics is ultrafast laser microfabrication, the core focus of this thesis. Ultrafast laser microfabrication is a rapidly evolving field that provides a unique platform for creating intricate microstructures with high precision [17]. It has been instrumental

## 1.1. Motivation

in forging new paths in the post-processing of optical materials, enabling the development of innovative sensors, devices, and photonic subsystems.

A striking example of the transformative potential of ultrafast laser microfabrication is Microsoft’s Project Silica [18–20]. This project utilises femtosecond lasers to write data into fused silica glass (Fig. 1.1 a), a durable and stable medium, opening up new possibilities for long-term data storage [21, 22], being able to save up to 7 bits per voxel (128 encoding possibilities in less than  $1 \mu\text{m}^3$ ) [23]. By using ultrafast laser pulses to create a 3D optical data storage system, Microsoft’s Project Silica is revolutionising the future of data archiving, promising unparalleled durability and longevity for information storage ( $>10,000$  years).

In the emerging field of quantum computing, ultrafast lasers play a pivotal role in the generation and manipulation of quantum states of light, a fundamental requirement for efficient and scalable quantum devices [7, 24]. This technology can facilitate the production of high-quality structures needed for quantum bits or “qubits”. By writing complex, three-dimensional waveguides in non-linear crystals, ultrafast lasers aid in quantum information processing. Additionally, these lasers can precisely control quantum states, critical for quantum logic operations [25].

The role of ultrafast laser microfabrication is also becoming a game-changer in the context of Industry 4.0 [26], which is characterised by the integration of digital, physical, and biological systems. In the context of additive manufacturing, ultrafast lasers are essential for high-resolution 3D printing of micro- and nano-scale structures, due to their unique ability to process materials with minimal thermal side effects [27, 28]. Furthermore, the ability to inscribe sensors directly into industrial components can enable real-time monitoring and predictive maintenance, crucial for the smart factories of the future. Thus, ultrafast lasers are not just a tool but a cornerstone technology enabling the transition to Industry 4.0 [29].

Among the myriad of instances where ultrafast laser microfabrication holds substantial significance, its applications in medicine, biomedicine, and biochemistry are particularly transformative. Ultrafast lasers are unlocking unexplored avenues in diagnosis, treatment, and foundational research, altering the landscape of these fields in profound ways.

In the broader field of biochemistry, ultrafast lasers are fundamental to techniques like optogenetics, where light is used to control cells in living tissue, often neurons [30], to better understand biological processes. Furthermore, ultrafast lasers are being used for mass spectrometry in proteomics, allowing for the identification and quantification of proteins, an essential process in understanding cellular functions [31]. Moreover, originating from the pioneering efforts of Bonner, Sweet, Hulett, and Herzenberg at Stanford University in the late 1960s, and their subsequent patent in 1972, the fluorescence activated cell sorter (FACS) instrument laid the foundation for what we now know as flow cytometry [32]. This technique, which swiftly examines the physical and chemical attributes of particles in a fluid as they traverse through one or more lasers, is experiencing a revolution through the advent of ultrafast lasers. These lasers facilitate the advent of multi-photon flow cytometry, characterised by its ability for deeper tissue penetration, reduced phototoxicity, and minimised autofluorescence [33]. This innovation proves pivotal for biomedical applications necessitating cell sorting and analysis, such as immunology, haematology, and cancer diagnostics. The ultrafast lasers’ precise microfabrication competencies are integral to the creation of microfluidic devices used in these applications [34]. They enable the manipulation and control of fluids at the microscopic level, leading to the emergence of the lab-on-chip device paradigm [35, 36].

In diagnostics, ultrafast lasers are essential for advanced imaging techniques like multi-photon microscopy, which allows for non-invasive, real-time imaging of living tissues at unprecedented depths and resolutions [37, 38]. This is of major importance in understanding disease progression and response to treatments at a cellular level. In treatment, ultrafast lasers are being used for example in refractive eye surgery, providing benefits of improved accuracy and fewer side effects. Beyond ophthalmology, they are being developed for use in minimally invasive surgery [39], where their precision can limit damage to surrounding tissues and enhance patient recovery.

On the other hand endomicroscopy, an imaging technique that provides histological information in real-time during endoscopic procedures [40], is another area where ultrafast lasers are making a substantial impact. They are used in the fabrication of miniaturised, high-resolution imaging devices, such as fibre-based probes [41, 42]. Ultrafast lasers are employed in direct laser writing, *e.g.*, ultrafast laser assisted etching or multi-photon polymerisation, to create complex photonic structures that comprise multifunctional catheters, leading to endomicroscopy probes with enhanced capabilities (Fig. 1.1 b). This technique is especially important for fields like gastroenterology and pulmonology [43], where it can aid in the early detection and treatment of conditions like cancer.

All in all, the influence of ultrafast lasers within the medical field is profound, instigating a revolution in these sectors with their precision, versatility, and potential for novel discovery, forming a central pillar of the goals of this thesis. The extensive range of their applications, combined with the depth of their impact, underscores their escalating importance within life sciences, rendering advancements in ultrafast laser technology a pressing priority.

Given the importance and potential of ultrafast laser microfabrication, it is critical to continue to advance this technology. As such, this thesis aims to contribute to that endeavour, exploring novel methods and techniques in ultrafast laser processing of transparent materials, primarily fused silica, for photonics sensing and imaging applications. The research within these pages not only adds to our scientific understanding but also opens the door to potential applications that could have profound implications for society, industry, and medicine.

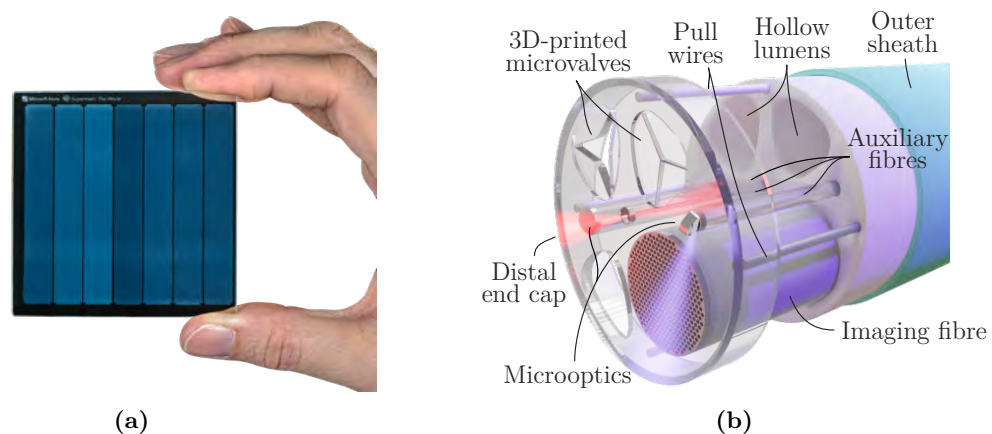


**Figure 1.1.** (a)  $75 \times 75 \times 2$  mm fused silica plate on which the 1978 movie *Superman* was inscribed using ultrafast lasers, as a proof of concept for Microsoft’s Project Silica. The glass stores 75.6 GB of data along with error redundancy codes. Photo by Jonathan Banks for Microsoft [44]. (b) Potential multifunctional catheter capable of performing widefield imaging, tissue interrogation, and multi-site aspiration, among other functions.

## 1.2 Objectives

The main objective of this thesis is to apply the principles of ultrafast laser processing of transparent materials to the advancement of fibre optic sensors, as well as optofluidic devices and glass-formed 3D structures when laser inscription is followed by chemical etching. Although this work contains aspects related to fundamental physics – especially regarding the reasoning behind achieving high etching rates independent of polarisation with low number of pulses per  $\mu\text{m}$ , the vast majority of covered aspects are related to the practical application of ultrafast laser technology to, from an engineering point of view, obtain sensors or develop devices that enhance performance in specific areas.

The primary goals of this thesis have been shaped by several critical elements recognised in the previous state-of-the-art that demand further research exploration. The objectives, focusing only on those that require practical laboratory development, can be divided into two main groups: those that solely use ultrafast lasers for direct inscription, mainly for the development of optical fibre sensors; and those that, in addition to inscription with ultrafast lasers – primarily on fused silica plates – use chemical etching for the extraction of specific structures or devices. These latter objectives define the most original and impactful goals of the thesis.

- **To conduct an in-depth study of the state-of-the-art fundamentals of ultrafast laser processing of transparent materials.**

This will encompass a comprehensive review and analysis of current theories, methodologies, techniques, and applications in this field. The exploration will focus on understanding the principles underlying ultrafast laser-matter interaction, the role of pulse duration, intensity, wavelength, and polarisation, as well as the material properties that influence the processing outcomes, placing special emphasis on fused silica. Special attention will be given to the intricacies of non-linear optical phenomena such as multi-photon absorption and other non-linear effects observed in femtosecond laser processing.

- **To improve the experimental setups for ultrafast laser processing and chemical etching of the Photonics Engineering Group.**

Starting from the experimental setup associated with the femtosecond laser that the research group presented in 2019, it is endowed with a series of capabilities, among which the generation of the second harmonic wavelength (515 nm) for the generation of more precise refractive index changes can be highlighted, as well as the control of the laser beam's polarisation state during inscription. Likewise, the infrastructure for undertaking chemical etching of glass is incorporated, adapted for KOH and NaOH.

- **To design and manufacture multiparametric optical fibre sensors based on standard and specialty fibers.**

Firstly, building upon the existing state-of-the-art in the Gaussian beam focusing for optical fibres, the aim is to enhance the inscription technique in terms of limiting optical aberrations (primarily astigmatism) and improving the performance of fibre Bragg gratings and in-fibre waveguides.

Based on Type I, II, and III modifications, new fibre structures will be proposed and conceived for sensing different parameters, whether they are physical, chemical, or biochemical. Among the optical structures, waveguides and fibre Bragg gratings can be highlighted,

whose performance will be enhanced through new manufacturing techniques. Microchannels or microcavities, integrated within the fibre, will allow the development of lab-in-fibre devices suitable for multiple applications. The sensors will be based on single-mode fibres, unless specific characteristics are required that certain specialty fibre possess.

- **To achieve polarisation-independent ultrafast laser assisted etching and apply it in the manufacture of tailor-made devices specifically designed for imaging and sensing applications.**

Traditionally, to achieve high etching rates in fused silica, the polarisation must be arranged linearly and perpendicular to the writing direction. However, this not only complicates experimental setups when etching non-planar surfaces or 3D structures, but it also practically prevents optimal inscription. An exhaustive investigation into the cutting-edge developments in ultrafast laser-assisted etching, alongside point defects in fused silica, will lead to the identification of a femtosecond laser inscription regime that eradicates the dependence between etching rate and polarisation.

By enhancing the technique, the aim is to manufacture the following photonic devices:

- ▷ An ultrafast laser fabricated silica-glass end cap for selective plane illumination lung endomicroscopy using polymer imaging fibres.
- ▷ A custom 1D photonic crystal-based optofluidic chip fabricated through ultrafast laser inscription for real-time molecular chirality sensing.

### 1.3 Document structure

This thesis is structured into four main parts. The first part compiles all the materials and methods required to understand the core contributions and papers. The second and third parts contain the new ideas and results that have been published by the authors. They have been divided to cover those contributions that solely employ direct inscriptions with an ultrafast laser (Part II: October 2019–July 2021) or employ the ultrafast laser in combination with chemical etching (Part III: August 2021–September 2023), respectively. The final part refers to the conclusions of the work, as well as other techniques and methods that should be studied in the near future. The list of publications related to the development of this thesis is also included. Figure 1.2 schematically illustrates the connection between the most significant blocks of the work, indicating their location within the document.

**Part I (Preliminary)** is focused on detailing the essential knowledge and techniques that are utilised across the rest of the thesis.

- **Chapter 1 (Introduction)** introduces the theme of the thesis, placing special emphasis on its significance, motivation, and objectives.
- **Chapter 2 (Fundamentals of ultrafast laser processing of transparent materials)** provides a comprehensive exploration of the underlying principles, mechanisms, and techniques involved in ultrafast laser-matter interaction, laying the groundwork for the subsequent chapters.

### 1.3. Document structure

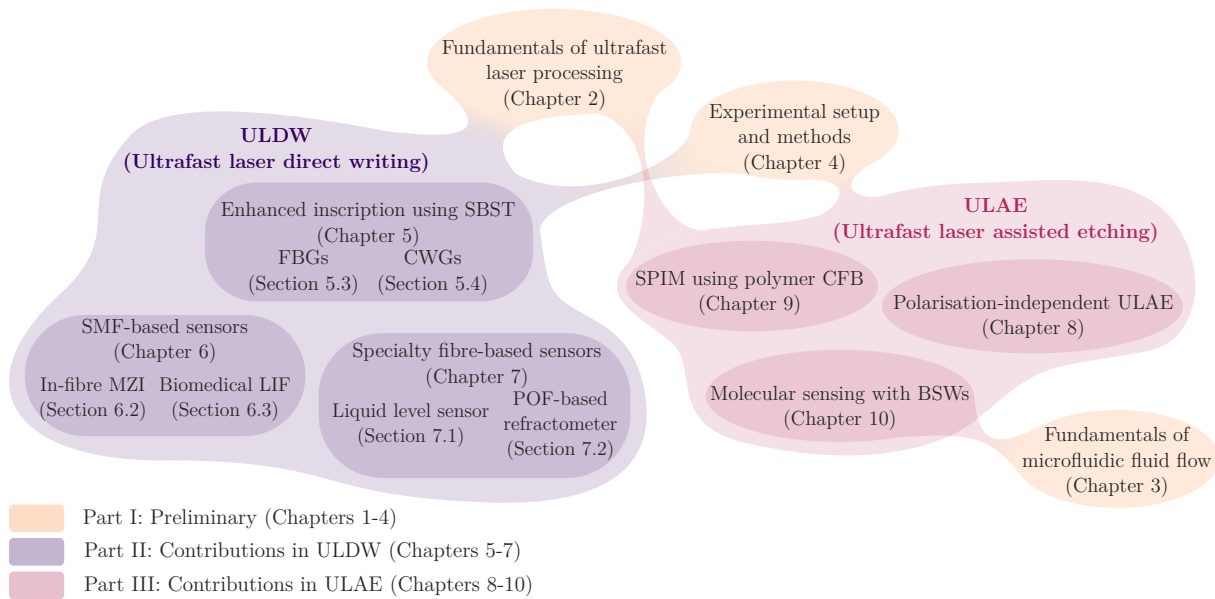


**Figure 1.2.** General structure of the thesis, detailing the association of each topic with the different chapters in the document. Key: ULDW – Ultrafast laser direct writing, ULAE – Ultrafast laser assisted etching, SBST – Slit beam shaping technique, FBG – Fibre Bragg grating, CWG – Cladding waveguide, SMF – Single-mode fibre, MZI – Mach-Zehnder Interferometer, LIF – Lab-in-fibre, POF – Polymer optical fibre, SPIM – Selective plane illumination microscopy, CFB – Coherent fibre bundle, BSW – Bloch surface wave.

- **Chapter 3 (Fundamentals of optofluidic platforms)** briefly examines the fluid dynamics in microchannels to enhance the understanding of chapter 10. Scaling down devices to micrometer dimensions significantly influences fluid physics, as the relative significance of forces acting on fluids undergoes a drastic change in the microenvironment compared to the macroscopic world. The most relevant materials and manufacturing techniques in microfluidic platforms are also addressed.
- **Chapter 4 (Experimental setups and methods)** presents a comprehensive description of the different setups utilised for the fabrication of optofluidic devices, which involve two phases and, consequently, two experimental configurations: (1) irradiation using a femtosecond laser source, and (2) wet chemical etching. Furthermore, a brief overview of the characterisation techniques employed in specific studies within the thesis is presented.

**Part II (Ultrafast laser direct writing (ULDW))** encompasses the contributions made in the field of optical fibre sensors using direct inscriptions with ultrafast lasers. It gathers the results obtained in the first half of the thesis, spanning from October 2019 to July 2021.

- **Chapter 5 (Enhancement of ULDW-based passive in-fibre structures)** contains relevant information about the challenges encountered when depositing focused ultrashort pulses within the bulk of a transparent material. It also discusses techniques to achieve specific focal volumes. Specifically, it delves into studies where the performance of fibre Bragg gratings and cladding waveguides is enhanced using the slit beam shaping technique.
- **Chapter 6 (Standard fibre-based sensors)** documents the works where sensors based on standard telecommunications optical fibres are fabricated. Specifically, it presents a

multiparametric sensor composed of a Mach-Zehnder interferometer and a fibre Bragg grating inscribed in the sensing arm. Additionally, a lab-in-fibre device integrated into a surgical needle for detecting axial strain and surrounding refractive index is also presented.

- **Chapter 7 (Specialty fibre-based sensors)** includes the research on fabricating sensors based on specialty fibres. It features the integration of a level liquid sensor within a hollow-core fibre, as well as the development of a refractometer optimised for water-based solutions using a perfluorinated polymer fibre.

**Part III (Ultrafast laser assisted etching (ULAE))** compiles the contributions made using the technology that combines ultrafast laser inscription and wet chemical etching. It covers the time period from August 2021 until the end of the thesis in September 2023.

- **Chapter 8 (Polarisation-independent ULAE in fused silica)** explores the advancements in the discovery of a new regime of femtosecond laser inscription that, in fused silica and using NaOH (or KOH), enables a high etching rate independent of the employed polarisation. Although a physical explanation of the process is yet to be established, and ongoing research is being conducted in this regard, the chapter includes insights and evidence that can shed light on its origin.
- **Chapter 9 (SPIM using polymer coherent fibre bundles)** documents the outcomes resulting from the research stay conducted in 2021 at Heriot-Watt University in Edinburgh (UK). It presents a powerful novel method for enabling selective plane illumination endomicroscopy in human lung tissue using polymer imaging fibres. This approach exploits an ultrafast laser fabricated silica end cap placed at the distal end of the polymer imaging fibre. The technique employed effectively addresses the issue of autofluorescence from both the imaged tissue and the fibre.
- **Chapter 10 (Molecular sensing with Bloch surface waves)** comprises the results associated with the research stay conducted in 2022 at the Institute of Photonics and Nanotechnology in Milan (Italy). Despite being preliminary data, the chapter describes the design and fabrication of a photonic chip that utilises Bloch surface waves excited in a 1D photonic crystal dielectric. It is anticipated that this chip has the potential to detect molecular chirality through circular dichroism spectroscopy.

**Part IV (Final remarks and future lines of work)** concludes the work with the most notable conclusions and outlines future lines of action.

- **Chapter 11 (Conclusions and future lines)** presents the key highlights of the research conducted as well as the crucial lines of action envisaged based on the findings.

The thesis strives to be self-contained, given its multidisciplinary nature. However, references are provided whenever feasible to allow the reader to delve deeper into each specific topic. Moreover, the digital version of this book includes interactive links to individual sections, enabling the reader to establish connections between different chapters and navigate seamlessly between the book and cited publications.

## References

- [1] European Commission, *Preparing for our future: Developing a common strategy for key enabling technologies in the EU*, 2009.
- [2] European Commission and Directorate-General for Research and Innovation, *Re-finding industry : defining innovation*. Publications Office, 2018. DOI: 10.2777/927953.
- [3] Rogers, C. *et al.*, “A universal 3D imaging sensor on a silicon photonics platform,” *Nature*, vol. 590, no. 7845, pp. 256–261, Feb. 2021. DOI: 10.1038/s41586-021-03259-y.
- [4] Haroun, A. *et al.*, “Progress in micro/nano sensors and nanoenergy for future AIoT-based smart home applications,” *Nano Express*, vol. 2, no. 2, p. 022005, Apr. 2021. DOI: 10.1088/2632-959x/abf3d4.
- [5] Zhu, D. *et al.*, “Integrated photonics on thin-film lithium niobate,” *Advances in Optics and Photonics*, vol. 13, no. 2, pp. 242–352, May 2021. DOI: 10.1364/aop.411024.
- [6] Sun, K. *et al.*, “Three-dimensional direct lithography of stable perovskite nanocrystals in glass,” *Science*, vol. 375, no. 6578, pp. 307–310, Jan. 2022. DOI: 10.1126/science.abj2691.
- [7] Madsen, L. S. *et al.*, “Quantum computational advantage with a programmable photonic processor,” *Nature*, vol. 606, no. 7912, pp. 75–81, Jun. 2022. DOI: 10.1038/s41586-022-04725-x.
- [8] Solntsev, A. S., Agarwal, G. S., and Kivshar, Y. S., “Metasurfaces for quantum photonics,” *Nature Photonics*, vol. 15, no. 5, pp. 327–336, Apr. 2021. DOI: 10.1038/s41566-021-00793-z.
- [9] National Photonics Initiative *et al.*, *Lighting the Path to a Competitive Secure Future*, 2014.
- [10] National Photonics Initiative, *Photonics: Enabling American Innovation, Competition and Security*, 2017.
- [11] “For a brighter tomorrow,” *Nature Photonics*, vol. 7, no. 7, pp. 501–501, Jun. 2013. DOI: 10.1038/nphoton.2013.180.
- [12] National Research Council, *Optics and Photonics: Essential Technologies for Our Nation*. Washington, DC: The National Academies Press, 2013, ISBN: 978-0-309-26377-1. DOI: 10.17226/13491. [Online]. Available: <https://nap.nationalacademies.org/catalog/13491/optics-and-photonics-essential-technologies-for-our-nation>.
- [13] Photonics21, *A critical Key Enabling Technology for Europe Role and impact of Photonics in H2020 Report*, 2017.
- [14] Photonics21, *Europe’s age of light! How photonics will power growth and innovation*, 2019.
- [15] Photonics21, *Market Data and Industry Report 2020. NextPho21: Implementing the European Photonics21 PPP strategy*, 2020.
- [16] Photonics21, *Update of the Strategic Roadmap Europe’s age of light! How photonics will power growth and innovation*, 2020.

- [17] Gattass, R. R. and Mazur, E., “Femtosecond laser micromachining in transparent materials,” *Nature Photonics*, vol. 2, no. 4, pp. 219–225, Apr. 2008. DOI: 10.1038/nphoton.2008.47. [Online]. Available: <https://doi.org/10.1038/nphoton.2008.47>.
- [18] <https://www.microsoft.com/en-us/research/project/project-silica/>, Accessed: 2023-05-16.
- [19] Anderson, P. *et al.*, “Glass: A New Media for a New Era?” In *10th USENIX Workshop on Hot Topics in Storage and File Systems (HotStorage 18)*, Boston, MA: USENIX Association, Jul. 2018. [Online]. Available: <https://www.usenix.org/conference/hotstorage18/presentation/anderson>.
- [20] Chatzieleftheriou, A., Stefanovici, I., Narayanan, D., Thomsen, B., and Rowstron, A., “Could cloud storage be disrupted in the next decade?” In *Proceedings of the 12th USENIX Conference on Hot Topics in Storage and File Systems*, 2020, pp. 25–25.
- [21] Zhang, J., Gecevičius, M., Beresna, M., and Kazansky, P. G., “Seemingly Unlimited Lifetime Data Storage in Nanostructured Glass,” *Physical Review Letters*, vol. 112, no. 3, p. 033901, Jan. 2014. DOI: 10.1103/physrevlett.112.033901.
- [22] Zhang, J., Čerkauskaitė, A., Drevinskas, R., Patel, A., Beresna, M., and Kazansky, P. G., “Eternal 5D data storage by ultrafast laser writing in glass,” in *SPIE Proceedings*, Klotzbach, U., Washio, K., and Arnold, C. B., Eds., SPIE, Mar. 2016. DOI: 10.1117/12.2220600.
- [23] Internal conversations with Peter Kazansky at PULMM 2023, Nikko, Japan.
- [24] Mahmudlu, H. *et al.*, “Fully on-chip photonic turnkey quantum source for entangled qubit/qudit state generation,” *Nature Photonics*, Apr. 2023. DOI: 10.1038/s41566-023-01193-1.
- [25] Crespi, A. *et al.*, “Integrated photonic quantum gates for polarization qubits,” *Nature Communications*, vol. 2, no. 1, Nov. 2011. DOI: 10.1038/ncomms1570.
- [26] Thoss, A. and Haefner, C., “The age of the laser has only just begun,” *Laser Focus World*, Jan. 2022. [Online]. Available: <https://www.laserfocusworld.com/industrial-laser-solutions/article/14222482/the-age-of-the-laser-has-only-just-begun>.
- [27] Courvoisier, F., “Ultrafast Laser Micro-Nano Structuring of Transparent Materials with High Aspect Ratio,” in *Handbook of Laser Micro- and Nano-Engineering*, Springer International Publishing, 2020, pp. 1–37. DOI: 10.1007/978-3-319-69537-2\_33-1.
- [28] <https://microrelleus.com/case-studies/>, Accessed: 2023-05-16.
- [29] Kagermann, H. and Wahlster, W., “Ten Years of Industrie 4.0,” *Sci*, vol. 4, no. 3, p. 26, Jun. 2022. DOI: 10.3390/sci4030026.
- [30] Yizhar, O., Fenno, L. E., Davidson, T. J., Mogri, M., and Deisseroth, K., “Optogenetics in Neural Systems,” *Neuron*, vol. 71, no. 1, pp. 9–34, Jul. 2011. DOI: 10.1016/j.neuron.2011.06.004.
- [31] Puig, M., “Advanced microscopy to resolve the higher-order organization of the exocyst,” Ph.D. dissertation, Universitat Pompeu Fabra, 2023.
- [32] Bonner, W. A., Hulett, H. R., Sweet, R. G., and Herzenberg, L. A., “Fluorescence Activated Cell Sorting,” *Review of Scientific Instruments*, vol. 43, no. 3, pp. 404–409, Mar. 1972. DOI: 10.1063/1.1685647.

## References

- [33] Rozhina, E. *et al.*, “Comparative cytotoxicity of kaolinite, halloysite, multiwalled carbon nanotubes and graphene oxide,” *Applied Clay Science*, vol. 205, p. 106 041, May 2021. DOI: 10.1016/j.clay.2021.106041.
- [34] Bragheri, F. *et al.*, “Optofluidic integrated cell sorter fabricated by femtosecond lasers,” *Lab on a Chip*, vol. 12, no. 19, p. 3779, 2012. DOI: 10.1039/c21c40705a.
- [35] Wang, X. *et al.*, “Enhanced cell sorting and manipulation with combined optical tweezer and microfluidic chip technologies,” *Lab on a Chip*, vol. 11, no. 21, p. 3656, 2011. DOI: 10.1039/c11c20653b.
- [36] Parker, H. E. *et al.*, “A Lab-in-a-Fiber optofluidic device using droplet microfluidics and laser-induced fluorescence for virus detection,” *Scientific Reports*, vol. 12, no. 1, Mar. 2022. DOI: 10.1038/s41598-022-07306-0. [Online]. Available: <https://doi.org/10.1038/s41598-022-07306-0>.
- [37] Liu, W., Chia, S.-H., Chung, H.-Y., Greinert, R., Kärtner, F. X., and Chang, G., “Energetic ultrafast fiber laser sources tunable in 1030–1215 nm for deep tissue multi-photon microscopy,” *Optics Express*, vol. 25, no. 6, pp. 6822–6831, Mar. 2017. DOI: 10.1364/oe.25.006822.
- [38] Marini, M. *et al.*, “Microlenses Fabricated by Two-Photon Laser Polymerization for Cell Imaging with Non-Linear Excitation Microscopy,” *Advanced Functional Materials*, p. 2213926, Mar. 2023. DOI: 10.1002/adfm.202213926.
- [39] Hoy, C. L. *et al.*, “Clinical Ultrafast Laser Surgery: Recent Advances and Future Directions,” *IEEE Journal of Selected Topics in Quantum Electronics*, vol. 20, no. 2, pp. 242–255, Mar. 2014. DOI: 10.1109/jstqe.2013.2287098.
- [40] Perperidis, A., Dhaliwal, K., McLaughlin, S., and Vercauteren, T., “Image computing for fibre-bundle endomicroscopy: A review,” *Medical Image Analysis*, vol. 62, p. 101 620, 2020, ISSN: 1361-8415. DOI: <https://doi.org/10.1016/j.media.2019.101620>. [Online]. Available: <https://www.sciencedirect.com/science/article/pii/S136184151830639X>.
- [41] Ross, C. A. *et al.*, “A Miniature Fibre-Optic Raman Probe Fabricated by Ultrafast Laser-Assisted Etching,” *Micromachines*, vol. 11, no. 2, p. 185, Feb. 2020. DOI: 10.3390/mi11020185.
- [42] Wood, H. A. C. *et al.*, “Tri-mode optical biopsy probe with fluorescence endomicroscopy, Raman spectroscopy, and time-resolved fluorescence spectroscopy,” *Journal of Biophotonics*, vol. 16, no. 2, Sep. 2022. DOI: 10.1002/jbio.202200141.
- [43] Roldán-Varona, P. *et al.*, “Selective plane illumination optical endomicroscopy with polymer imaging fibers,” *APL Photonics*, vol. 8, no. 1, p. 016 103, Jan. 2023. DOI: 10.1063/5.0130486.
- [44] <https://news.microsoft.com/source/features/innovation/ignite-project-silica-superman/>, Accessed: 2023-05-17.

# 2

## Fundamentals of ultrafast laser processing of transparent materials

---

<b>2.1</b>	<b>Mechanisms of material modification . . . . .</b>	<b>14</b>
2.1.1	Free electron plasma generation . . . . .	15
2.1.2	Relaxation and modification of the material . . . . .	16
<b>2.2</b>	<b>Sample irradiation parameters . . . . .</b>	<b>19</b>
<b>References</b>	<b>. . . . .</b>	<b>21</b>

---

**I**N an era where the demand for precision and miniaturisation in material processing is at an all-time high, the role of ultrafast lasers, particularly in the context of transparent materials, is more significant than ever. The interaction of intense laser beams with these materials allows localised modifications of their properties, enabling precision micro- or even nano-machining [1]. This capability is not restricted to merely absorbing materials but extends to transparent ones as well, capitalising on different physical effects of light-matter interaction [2].

The heart of this chapter lies in the exploration of ultrafast laser writing, a technology that has emerged as a powerful tool in both fundamental and applied research. This encompasses a myriad of fields, ranging from advanced integrated optics and material science to life sciences and photonic sensor development [3]. The ultra-short pulses characteristic of femtosecond (fs) lasers offer distinct advantages in material processing, including nano-metric precision and a diminished impact from thermal effects, microcracks, or surface damage that are commonly associated with lasers of longer pulse duration, as depicted in Fig. 2.1.

Pioneered by Davis *et al.* in 1996 [5], ultrafast laser processing of transparent materials has seen widespread interest from the scientific community, leading to the refinement and advancement of the technique [6]. This process relies on a focused pulsed laser beam to permanently modify the transparent material in its focal region, leading to local property changes that

## 2.1. Mechanisms of material modification

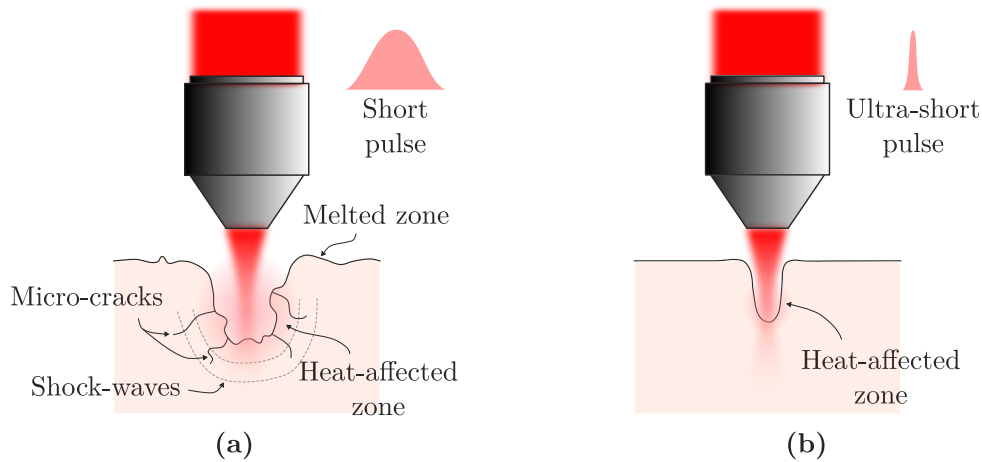


**Figure 2.1.** Schematic illustration of the effects caused by (a) a short laser pulse ( $\sim$  ns), and (b) an ultra-short laser pulse (ps, fs). Adapted from [4].

could culminate in an increased refractive index, birefringent modifications, or even material removal [7]. The beauty of this technique lies in its adaptability. Like a pen writing on a sheet, this technique inscribes the layout of 3D photonic circuits in the substrate by moving the sample under laser irradiation. It offers advantages such as being mask-less (which facilitates rapid prototyping), adaptable to a variety of materials including glasses, crystals, and polymers, and the ability to produce three-dimensional structures by precisely controlling the sample's translation during laser irradiation.

The expanding range of ultrafast laser-based applications is equally impressive. It has found value in optofluidic applications, particularly since the discovery of the increased etching selectivity of the irradiated region by Marcinkevičius *et al.* in 2001 [8], which facilitates microchannel formation through a two-step process: laser irradiation followed by chemical etching [9–11]. This combination of direct writing and microchannel formation can generate devices where both fluidic and optical components can exhibit 3D geometries, reducing fabrication complexity and ensuring excellent alignment between the components.

This chapter thus presents a comprehensive exploration of the principles, techniques, and emerging trends in ultrafast laser processing of transparent materials, preparing the reader for the deeper explorations and analyses that will follow in the subsequent chapters.

## 2.1 Mechanisms of material modification

The interaction between laser and material is a complex process, with a comprehensive model to fully explain fs laser processing still yet to be formulated. This process can be roughly segmented into three stages: (1) initial generation of a free electron plasma in the focal area, (2) subsequent energy relaxation to the lattice, and finally, (3) the modification of the material [7, 12].

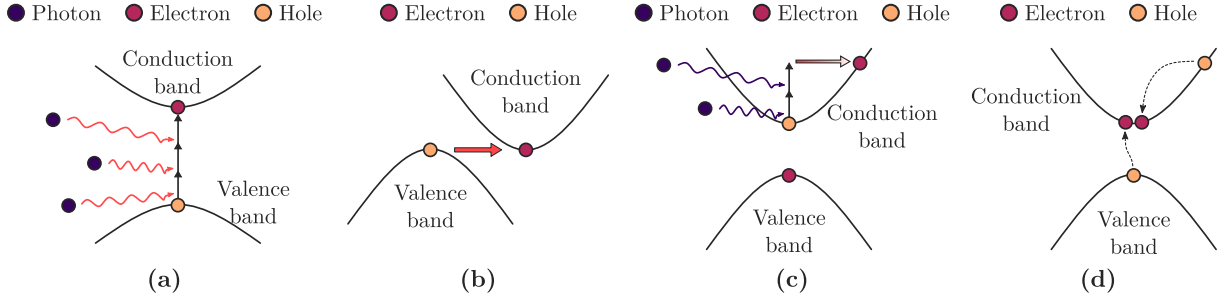


**Figure 2.2.** Non-linear photoionisation processes that underpin femtosecond laser machining [12]. These processes include: (a) multiphoton ionisation, where multiple photons are absorbed simultaneously; (b) tunnel ionisation, which involves electrons tunnelling through an energy barrier; and (c-d) avalanche ionisation, a sequence of events that starts with (c) the absorption of free carriers, and (d) is followed by impact ionisation. Adapted from [4].

### 2.1.1 Free electron plasma generation

It is critical to note that fs laser pulses, with wavelengths in the visible or near-infrared range, carry photons with insufficient energy to be linearly absorbed by glasses and other materials, as there are no permissible electronic transitions for such energy levels. Consequently, valence electrons are promoted to the conduction band via non-linear photoionisation, caused by multiphoton ionisation or tunnel ionisation, or a combination of both.

#### Non-linear photoionisation

Non-linear effects associated with photoionisation, such as multiphoton ionisation and tunnel ionisation, are outlined. Multiphoton ionisation encompasses the simultaneous absorption of numerous photons that excite an electron in the valence band, which subsequently promotes it to the conduction band, thereby leaving a hole in the valence band (Fig. 2.2 a). The number of photons ( $n_p$ ) required to elevate an electron to the conduction band must satisfy the following condition:

$$n_p \frac{hc}{\lambda} \geq E_{gap}. \quad (2.1)$$

This condition indicates that the combined energy of the photons must exceed the forbidden band's energy ( $E_{gap}$ ). For example, fused silica has a band gap of 9 eV. This indicates that at a laser wavelength of 1030 nm, a minimum of eight photons are necessary to stimulate an electron into the conduction band. This photoionisation mechanism prevails under conditions of low laser intensities and high laser frequencies.

On the other hand, when the laser intensity is high and the frequency is low, the dominant non-linear photoionisation mechanism is associated with the tunnel effect. The strong field distorts the band structure, diminishing the potential barrier between the valence and conduction bands. As a result, there are direct band-to-band transitions (Fig. 2.2 b).

Both processes linked with non-linear photoionisation are connected through the Keldysh parameter, defined by Keldysh in 1968 [13]:

## 2.1. Mechanisms of material modification

$$\gamma = \frac{\nu}{e} \sqrt{\frac{m_e c n \epsilon_0 E_{gap}}{I}}. \quad (2.2)$$

This involves the laser frequency ( $\nu$ ), the focal intensity of the pulse ( $I$ ), the electron's effective mass ( $m_e$ ), the fundamental electron charge ( $e$ ), the speed of light ( $c$ ), the refractive index of the material ( $n$ ), and the permittivity in free space ( $\epsilon_0$ ). Based on the value of Keldysh parameter, there are three potential scenarios: (1) if  $\gamma \gg 1.5$ , the dominant mechanism is multiphoton ionisation; (2) if  $\gamma \ll 1.5$ , the dominant mechanism is ionisation by the tunnel effect; and (3) if  $\gamma \approx 1.5$ , photoionisation is a combination of both multiphoton ionisation and the tunnel effect.

### Avalanche photoionisation

Avalanche photoionisation takes place when electrons in the conduction band absorb photons, leading to a carrier's excitation from one state to another within the same band, a process known as free carrier absorption (FCA). After absorbing multiple photons in sequence, the energy of an electron in the conduction band can exceed the band's minimum energy by a margin greater than the forbidden band energy ( $E_{gap}$ ) (Fig. 2.2 c). At this stage, this electron can ionise another electron from the valence band via impact, resulting in two conduction band electrons at minimum energy (Fig. 2.2 d). These two electrons may then absorb more photons through FCA, ionising valence band electrons and creating an exponential surge in the number of conduction band electrons, producing a self-perpetuating avalanche effect as long as the laser field retains its strength.

However, it should be noted that the initiation of avalanche ionisation necessitates a specific number of conduction band electrons, which can be supplied by one of the non-linear photoionisation processes, such as multiphoton absorption and/or tunneling effect. The density of conduction band electrons will grow through avalanche photoionisation until the plasma frequency nears the laser frequency. At this juncture, the plasma becomes highly absorbent. The electron density when the plasma frequency matches the laser frequency is known as the critical density of free electrons (around  $10^{13}$  W/cm<sup>2</sup> in glass). After this point, notable changes in the material begin to occur.

This underscores the value of fs lasers in executing this process consistently and uniformly. In fact, longer pulses ( $\sim$  ns) trigger strong avalanche ionisation, but are unable to generate seed electrons through non-linear absorption due to limited peak intensities, thus they depend on random material defects. Consequently, it is unachievable to deterministically control the creation of the free electron plasma with longer pulses, which might experience significant variations from one point to another.

### 2.1.2 Relaxation and modification of the material

As depicted in Fig. 2.3, following irradiation, the energised plasma relaxes and transfers energy to the lattice within a few picoseconds, leading to its alteration [2]. It is worth noting that the modification timescale is lengthier than other involved physical phenomena: indeed, material modifications can happen up to microseconds after the pulse absorption. As absorption and

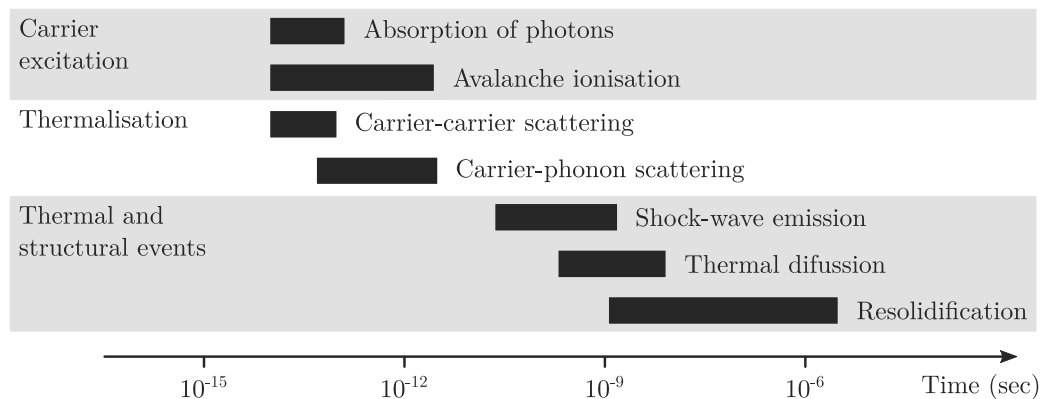


**Figure 2.3.** Physical phenomena during the interaction of a femtosecond laser pulse with a transparent material. Despite light absorption occurs on a femtosecond timescale, subsequent transformations in the material can continue even microseconds after the initial interaction. Adapted from [2].

energy relaxation occur in different temporal windows, they can be viewed as two separate phenomena. The precise process that leads to changes in the material is not entirely understood. Several mechanisms have been proposed as contributors to material modification, including colour centre formation, material densification, structural modification, and ion migrations. The precise combination and relative contributions of these mechanisms are heavily dependent on the material and irradiation properties. Some of the specific defects associated with fused silica are explored more exhaustively in chapter 8.

Numerous studies have been published on the observable morphological changes [7, 12], which can essentially be categorised into four distinct types. These morphological changes, briefly explained below, depend on both laser parameters (pulse energy, pulse duration, pulse repetition rate, wavelength, polarisation, scanning speed) and material properties (bandgap energy, thermal conductivity). In fused silica, Types I, II and III of morphological changes can be observed simply by varying the incident energy of the laser. This is not the case with Type X, which occurs, among other factors, within a specific range of pulse duration [14].

### Type I. Smooth refractive index increase.

The smooth refractive index change induced by fs laser radiation is likely due to a combination of three effects – colour centre formation, densification (structural change) and thermal treatment (melting) of the glass [12]. Optical waveguide devices are fabricated using laser parameters that result in this regime of modification [10, 15–19] (Fig. 2.4 a).

The thermal model suggests that the energy deposited in the focal volume leads to rapid local heating and modification. Because this heating process is localised, the glass cools very quickly. In fused silica, this rapid quenching from a high temperature often results in an increase in density, explaining the observed increase in refractive index [4, 20]. However, different experiments have shown inconsistencies in this model, indicating that thermal heating is not the sole mechanism responsible for refractive index changes.

Another theory posits that the creation of colour centres through radiation can alter the refractive index. High electron density, resulting from non-linear absorption mechanisms, could lead to the formation of different types of substrate defects [21]. Research has identified evidence

## 2.1. Mechanisms of material modification

of colour centre formation in regions modified by femtosecond lasers, potentially contributing to changes in refractive index. However, experiments show that eliminating these colour centres does not fully restore the original index, indicating they do not produce the majority of the refractive index change.

The structural change model suggests that changes in the refractive index might be due to densification and strain in the glass caused by femtosecond laser radiation. For example, fused silica has large 5- and 6-fold ring structures dominant in its network. After ultrafast laser exposure, lower rank ring structures are seen (3- and 4-membered rings), indicating elevated energy and densification of the glass. This densification seems to correlate with refractive index changes. However, it has been noted that densification alone cannot account for the entire change in the refractive index.

### **Type II. Self-ordered sub-wavelength nanograting.**

It has been demonstrated that the fs laser can induce nanoporous structures in modified regions of fused silica. These structures depend on the polarisation of the fs laser writing beam [22, 23]. They are also found to be self-ordered and periodic (as small as 20 nm in size and 140 nm in periodicity,  $\Lambda \approx \lambda/2n$ ), and are arranged perpendicular to the electric field vector of a linearly polarised femtosecond laser writing beam [24–26] (Fig. 2.4 **b**).

These nanostructures alternate between regions of marginally increased and decreased density. This periodic change in material composition within the irradiated volume results in birefringent refractive index alterations [22, 27]. Additionally, Auger electron spectroscopy of these regions revealed varying oxygen concentrations across the irradiated area [28], indicating that these periodic nanostructures consist of alternately distributed oxygen-deficient regions.

As detailed in Type I modification, besides point defects generation [21, 23–25, 29], the material experiences induced stress resulting in densification [30–32]. As the pulse-to-pulse distance reduces, the glass starts to decompose [33]. This decomposition eventually results in a net expansion of the volume [34]; and self-organised nanostructures emerge with an orientation strongly dependent on the light polarisation, the so-called nanogratings.

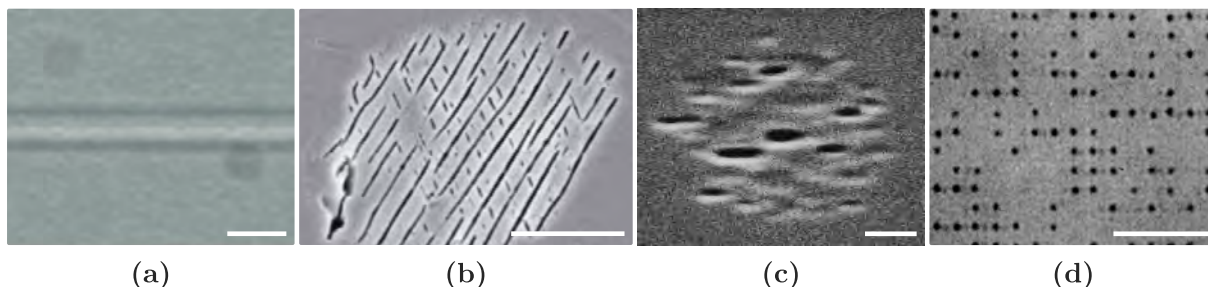


**Figure 2.4.** Potential modifications induced in fused silica by femtosecond laser irradiation. (a) Type I [10], (b) Type II [35], (c) Type X [14], and (d) Type III [36]. Scale bars in **a-d** are 25  $\mu\text{m}$ , 1  $\mu\text{m}$ , 200 nm, and 10  $\mu\text{m}$ , respectively. Reprinted with permission of the indicated references.

**Type X. High-transmission birefringent structure.**

This transformation encompasses randomly distributed nanopores which are elongated in a direction perpendicular to polarisation [14] (Fig. 2.4 c). These nanopores give rise to controllable birefringent structures with transmittance as lofty as 99% in both the visible and near-infrared spectrum, and exceeding 90% in the ultraviolet (UV) spectrum down to 330 nm. These observed anisotropic nanoporous silica structures differ markedly from nanogratings produced by fs lasers (Type II) and conventional nanoporous silica. A suggested mechanism for this process is nanocavitation, initiated by the formation of interstitial oxygen via multiphoton and avalanche defect ionisation [14]. This is discussed in chapter 8.

**Type III. Void.**

When exposed to very high intensity laser, the modified area of the material can exhibit damage or even form voids due to the processes of avalanche and continuous impact ionisation. This results in the creation of a localised plasma in the focal area, which leads to rising temperatures. As the plasma's temperature increases, a significant charge separation occurs, creating immense pressure. This pressure is intense enough to trigger what is known as a Coulomb explosion, or a microexplosion, which then produces a shock wave. As this explosion takes place within the material's bulk, the shock wave disperses matter and energy away from the focal point, thus compressing the surrounding material and leaving a less dense or hollow central region, known as a void [16] (Fig. 2.4 d). The existence of these shock waves during femtosecond laser modification using high pulse energies is backed by the observed emission of acoustic or pressure waves from the focal point. These voids have been utilised in the production of devices like optical memory units [36], fibre Bragg gratings (FBGs), and 2D waveguide arrays.

**2.2 Sample irradiation parameters**

Let us delve into the parameters that greatly affect the interaction between light and material during sample irradiation [16, 37]. Pulse energy ( $E_p$  [ $\mu\text{J}$ ]), fluence ( $F$  [ $\text{J}/\text{mm}^2$ ]), and peak intensity ( $I_{peak}$  [ $\text{W}/\text{mm}^2$ ]) are examined [38]. These factors are interrelated as shown in the following equations [39, 40]:

$$E_p = \int_{t_0}^{t_0+\tau} P(t)dt = \frac{P_{avg}}{\text{PRR}}, \quad (2.3) \quad F = \frac{2 \cdot E_p \cdot \text{PRR}}{\pi \cdot w_0 \cdot \nu}, \quad (2.4)$$

$$I_{peak} = \alpha \frac{F}{\tau}, \quad (2.5)$$

where  $\tau$  is the pulse duration, PRR is the pulse repetition rate,  $P$  is the instantaneous power,  $P_{avg}$  is the average power,  $w_0$  is the beam waist radius,  $\nu$  is the writing speed, and  $\alpha$  is a non-dimensional factor that relies on the time-structured shape of the pulse.

The beam waist ( $w_0$ ) gives the laser spot dimension ( $2w_0$ ) when a sample, with refractive index  $n$ , is exposed to a focused laser beam of wavelength  $\lambda$ , and an objective lens with numerical aperture NA. The beam quality factor ( $M^2$ ) accounts for the discrepancy between actual beam

## 2.2. Sample irradiation parameters

propagation and that of a Gaussian beam. The depth of focus ( $2z_0$ ) is twice the Rayleigh parameter ( $z_0$ ), and is essential as it influences the size and shape of the laser modification in the material [41, 42].

$$w_0 = \frac{M^2\lambda}{\pi\text{NA}}, \quad (2.6)$$

$$z_0 = \frac{M^2n\lambda}{\pi\text{NA}^2}. \quad (2.7)$$

Optical aberrations, such as chromatic and spherical aberrations, can markedly affect these parameters [43]. They often lead to an elongated focal volume in glass when the beam originates from air, and this impact intensifies as the beam focus goes further into the glass. Chapter 5 provides a detailed explanation of the various types of aberrations that can occur when focusing a laser pulse within a substrate, along with diverse strategies that can mitigate these aberrations.

Pulse duration lengthening due to material dispersion is another critical factor. This mainly happens when the pulse goes through thick glass layers present in aberration-compensated objectives, reducing the peak intensity and changing the inscription conditions of the material. This effect becomes negligible for pulse durations of a few hundreds of femtoseconds ( $\sim 300$  fs) or longer but can be significant for particularly short laser pulses (tens of fs long), which may necessitate proper pulse pre-compensation [44].

The writing geometry also plays a pivotal role, influencing the shape of the laser modifications. There are two main approaches: transverse and longitudinal writing, in which the sample is scanned orthogonally or parallelly to the beam direction [16, 45]. Each approach has its pros and cons, affecting the cross-section of the induced modification, potential aberrations, and the fabrication of structures at different depths. These aspects are also covered in chapter 5.

## References

- [1] Sugioka, K. and Cheng, Y., “Ultrafast lasers – reliable tools for advanced materials processing,” *Light: Science & Applications*, vol. 3, no. 4, e149–e149, Apr. 2014. DOI: 10.1038/lsa.2014.30.
- [2] Gattass, R. R. and Mazur, E., “Femtosecond laser micromachining in transparent materials,” *Nature Photonics*, vol. 2, no. 4, pp. 219–225, Apr. 2008. DOI: 10.1038/nphoton.2008.47. [Online]. Available: <https://doi.org/10.1038/nphoton.2008.47>.
- [3] Sugioka, K., Ed., *Handbook of Laser Micro- and Nano-Engineering*. Springer International Publishing, 2021. DOI: 10.1007/978-3-030-63647-0.
- [4] Roldan-Varona, P., “Post-processing of optical fibres using femtosecond lasers,” M.S. thesis, Universidad de Cantabria, Jul. 2019. [Online]. Available: <http://hdl.handle.net/10902/16620>.
- [5] Davis, K. M., Miura, K., Sugimoto, N., and Hirao, K., “Writing waveguides in glass with a femtosecond laser,” *Optics Letters*, vol. 21, no. 21, pp. 1729–1731, Nov. 1996. DOI: 10.1364/ol.21.001729.
- [6] Stoian, R. and Bonse, J., Eds., *Ultrafast Laser Nanostructuring*. Springer International Publishing, 2023. DOI: 10.1007/978-3-031-14752-4.
- [7] Eaton, S. M., Cerullo, G., and Osellame, R., “Fundamentals of Femtosecond Laser Modification of Bulk Dielectrics,” in *Topics in Applied Physics*, Springer Berlin Heidelberg, Dec. 2011, pp. 3–18. DOI: 10.1007/978-3-642-23366-1\_1.
- [8] Marcinkevičius, A. *et al.*, “Femtosecond laser-assisted three-dimensional microfabrication in silica,” *Optics Letters*, vol. 26, no. 5, pp. 277–279, Mar. 2001. DOI: 10.1364/ol.26.000277.
- [9] Bellouard, Y., Said, A., Dugan, M., and Bado, P., “Fabrication of high-aspect ratio, micro-fluidic channels and tunnels using femtosecond laser pulses and chemical etching,” *Optics Express*, vol. 12, no. 10, pp. 2120–2129, 2004. DOI: 10.1364/opeX.12.002120.
- [10] Osellame, R., Hoekstra, H. J. W. M., Cerullo, G., and Pollnau, M., “Femtosecond laser microstructuring: An enabling tool for optofluidic lab-on-chips,” *Laser & Photonics Reviews*, vol. 5, no. 3, pp. 442–463, Feb. 2011. DOI: 10.1002/lpor.201000031.
- [11] Sugioka, K. *et al.*, “Femtosecond laser 3D micromachining: A powerful tool for the fabrication of microfluidic, optofluidic, and electrofluidic devices based on glass,” *Lab on a Chip*, vol. 14, no. 18, pp. 3447–3458, 2014. DOI: 10.1039/c4lc00548a.
- [12] Ams, M. *et al.*, “Investigation of Ultrafast Laser–Photonic Material Interactions: Challenges for Directly Written Glass Photonics,” *IEEE Journal of Selected Topics in Quantum Electronics*, vol. 14, no. 5, pp. 1370–1381, 2008. DOI: 10.1109/jstqe.2008.925809.
- [13] Keldysh, L. V., “Ionization in the field of a strong electromagnetic wave,” *Sov. Phys. JETP*, vol. 20, no. 5, pp. 1307–1314, 1965.
- [14] Sakakura, M., Lei, Y., Wang, L., Yu, Y.-H., and Kazansky, P. G., “Ultralow-loss geometric phase and polarization shaping by ultrafast laser writing in silica glass,” *Light: Science & Applications*, vol. 9, no. 1, Feb. 2020. DOI: 10.1038/s41377-020-0250-y.

## References

- [15] Eaton, S. M. *et al.*, “Transition from thermal diffusion to heat accumulation in high repetition rate femtosecond laser writing of buried optical waveguides,” *Optics Express*, vol. 16, no. 13, pp. 9443–9458, Jun. 2008. DOI: 10.1364/oe.16.009443.
- [16] Eaton, S. M., Cerullo, G., and Osellame, R., “Fundamentals of femtosecond laser modification of bulk dielectrics,” *Topics in Applied Physics*, vol. 123, pp. 3–18, 2012. DOI: 10.1007/978-3-642-23366-1\_1/COVER. [Online]. Available: [https://link.springer.com/chapter/10.1007/978-3-642-23366-1\\_1](https://link.springer.com/chapter/10.1007/978-3-642-23366-1_1).
- [17] Waltermann, C., Doering, A., Köhring, M., Angelmahr, M., and Schade, W., “Cladding waveguide gratings in standard single-mode fiber for 3D shape sensing,” *Optics Letters*, vol. 40, no. 13, pp. 3109–3112, 2015, ISSN: 0146-9592. DOI: 10.1364/OL.40.003109. [Online]. Available: <https://www.osapublishing.org/abstract.cfm?URI=ol-40-13-3109>.
- [18] Ams, M., Marshall, G. D., Spence, D. J., and Withford, M. J., “Slit beam shaping method for femtosecond laser direct-write fabrication of symmetric waveguides in bulk glasses,” *Optics Express*, vol. 13, no. 15, pp. 5676–5681, 2005. DOI: 10.1364/opex.13.005676.
- [19] Roldan-Varona, P., Rodriguez-Cobo, L., and Lopez-Higuera, J. M., “Slit Beam Shaping Technique for Femtosecond Laser Inscription of Symmetric Cladding Waveguides,” *IEEE Journal of Selected Topics in Quantum Electronics*, vol. 27, no. 6, p. 4400208, Nov. 2021. DOI: 10.1109/jstqe.2021.3092438.
- [20] Lancry, M., Régnier, E., and Poumellec, B., “Fictive temperature in silica-based glasses and its application to optical fiber manufacturing,” *Progress in Materials Science*, vol. 57, no. 1, pp. 63–94, Jan. 2012. DOI: 10.1016/j.pmatsci.2011.05.002.
- [21] Skuja, L., Hirano, M., Hosono, H., and Kajihara, K., “Defects in oxide glasses,” *physica status solidi (c)*, vol. 2, no. 1, pp. 15–24, Jan. 2005. DOI: 10.1002/pssc.200460102.
- [22] Shimotsuma, Y., Kazansky, P. G., Qiu, J., and Hirao, K., “Self-Organized Nanogratings in Glass Irradiated by Ultrashort Light Pulses,” *Physical Review Letters*, vol. 91, no. 24, p. 247405, Dec. 2003. DOI: 10.1103/physrevlett.91.247405.
- [23] Wang, Y., Cavillon, M., Ollier, N., Poumellec, B., and Lancry, M., “An Overview of the Thermal Erasure Mechanisms of Femtosecond Laser-Induced Nanogratings in Silica Glass,” *physica status solidi (a)*, vol. 218, no. 12, p. 2100023, Apr. 2021. DOI: 10.1002/pssa.202100023.
- [24] Lancry, M., Poumellec, B., Desmarchelier, R., and Bourguignon, B., “Oriented creation of anisotropic defects by IR femtosecond laser scanning in silica,” *Optical Materials Express*, vol. 2, no. 12, pp. 1809–1821, Nov. 2012. DOI: 10.1364/ome.2.001809.
- [25] Richter, S., Heinrich, M., Döring, S., Tünnermann, A., Nolte, S., and Peschel, U., “Nanogratings in fused silica: Formation, control, and applications,” *Journal of Laser Applications*, vol. 24, no. 4, p. 042008, Sep. 2012. DOI: 10.2351/1.4718561.
- [26] Ramirez, L. P. R. *et al.*, “Tuning the structural properties of femtosecond-laser-induced nanogratings,” *Applied Physics A*, vol. 100, no. 1, pp. 1–6, Apr. 2010. DOI: 10.1007/s00339-010-5684-2.
- [27] Sudrie, L., Franco, M., Prade, B., and Mysyrowicz, A., “Study of damage in fused silica induced by ultra-short IR laser pulses,” *Optics Communications*, vol. 191, no. 3-6, pp. 333–339, May 2001. DOI: 10.1016/s0030-4018(01)01152-x.

- [28] Hirao, K., Shimotsuma, Y., Qiu, J., and Miura, K., “Femtosecond laser induced phenomena in glasses and photonic device applications,” *MRS Proceedings*, vol. 850, 2004. DOI: 10.1557/proc-850-mm2.1.
- [29] Chan, J. W., Huser, T., Risbud, S., and Krol, D. M., “Structural changes in fused silica after exposure to focused femtosecond laser pulses,” *Optics Letters*, vol. 26, no. 21, pp. 1726–1728, Nov. 2001. DOI: 10.1364/ol.26.001726.
- [30] Sugiura, H. and Yamadaya, T., “Raman scattering in silica glass in the permanent densification region,” *Journal of Non-Crystalline Solids*, vol. 144, pp. 151–158, Jan. 1992. DOI: 10.1016/s0022-3093(05)80395-3.
- [31] Bellouard, Y., Barthel, E., Said, A. A., Dugan, M., and Bado, P., “Scanning thermal microscopy and Raman analysis of bulk fused silica exposed to lowenergy femtosecond laser pulses,” *Optics Express*, vol. 16, no. 24, pp. 19 520–19 534, Nov. 2008. DOI: 10.1364/oe.16.019520.
- [32] Champion, A. and Bellouard, Y., “Direct volume variation measurements in fused silica specimens exposed to femtosecond laser,” *Optical Materials Express*, vol. 2, no. 6, pp. 789–798, May 2012. DOI: 10.1364/ome.2.000789.
- [33] Lancry, M., Poumellec, B., Canning, J., Cook, K., Poulin, J.-C., and Brisset, F., “Ultrafast nanoporous silica formation driven by femtosecond laser irradiation,” *Laser & Photonics Reviews*, vol. 7, no. 6, pp. 953–962, Jul. 2013. DOI: 10.1002/lpor.201300043.
- [34] Bellouard, Y. *et al.*, “Stress-state manipulation in fused silica via femtosecond laser irradiation,” *Optica*, vol. 3, no. 12, pp. 1285–1293, Nov. 2016. DOI: 10.1364/optica.3.001285.
- [35] Taylor, R., Hnatovsky, C., and Simova, E., “Applications of femtosecond laser induced self-organized planar nanocracks inside fused silica glass,” *Laser & Photonics Review*, vol. 2, no. 1-2, pp. 26–46, Apr. 2008. DOI: 10.1002/lpor.200710031.
- [36] Glezer, E. N. *et al.*, “Three-dimensional optical storage inside transparent materials,” *Optics Letters*, vol. 21, no. 24, pp. 2023–2025, Dec. 1996. DOI: 10.1364/ol.21.002023.
- [37] Paiè, P., “Femtosecond laser micromachining of optofluidic glass chips for biophotonic applications,” Ph.D. dissertation, Politecnico di Milano, 2016.
- [38] Krol, D. M., “Femtosecond laser modification of glass,” *Journal of Non-Crystalline Solids*, vol. 354, no. 2-9, pp. 416–424, Jan. 2008. DOI: 10.1016/j.jnoncrysol.2007.01.098.
- [39] Rajesh, S. and Bellouard, Y., “Towards fast femtosecond laser micromachining of glass, effect of deposited energy,” in *Conference on Lasers and Electro-Optics 2010*, OSA, 2010. DOI: 10.1364/cleo.2010.jtud18.
- [40] Rajesh, S. and Bellouard, Y., “Towards fast femtosecond laser micromachining of fused silica: The effect of deposited energy,” *Optics Express*, vol. 18, no. 20, pp. 21 490–21 497, Sep. 2010. DOI: 10.1364/oe.18.021490.
- [41] Thomas, J., Voigtländer, C., Becker, R. G., Richter, D., Tünnermann, A., and Nolte, S., “Femtosecond pulse written fiber gratings: A new avenue to integrated fiber technology,” *Laser & Photonics Reviews*, vol. 6, no. 6, pp. 709–723, Feb. 2012. DOI: 10.1002/lpor.201100033.
- [42] Will, M., Nolte, S., Chichkov, B. N., and Tünnermann, A., “Optical properties of waveguides fabricated in fused silica by femtosecond laser pulses,” *Applied Optics*, vol. 41, no. 21, pp. 4360–4363, Jul. 2002. DOI: 10.1364/ao.41.004360.

## References

- [43] Salter, P. S. and Booth, M. J., “Adaptive optics in laser processing,” *Light: Science & Applications*, vol. 8, no. 1, p. 110, Nov. 2019. DOI: 10.1038/s41377-019-0215-1.
- [44] Osellame, R. *et al.*, “Optical properties of waveguides written by a 26 MHz stretched cavity Ti:sapphire femtosecond oscillator,” *Optics Express*, vol. 13, no. 2, pp. 612–620, 2005. DOI: 10.1364/opex.13.000612.
- [45] Low, D. K. Y., Xie, H., Xiong, Z., and Lim, G. C., “Femtosecond laser direct writing of embedded optical waveguides in aluminosilicate glass,” *Applied Physics A*, vol. 81, no. 8, pp. 1633–1638, Nov. 2005. DOI: 10.1007/s00339-005-3324-z.

# 3

## Fundamentals of optofluidic platforms

---

<b>3.1</b>	<b>Materials and fabrication techniques</b>	<b>27</b>
3.1.1	Ultrafast laser assisted etching technique	28
<b>3.2</b>	<b>Physics and scaling in microfluidics</b>	<b>30</b>
3.2.1	Continuity and Navier-Stokes equation	31
3.2.2	Dimensionless numbers	32
3.2.3	Relevant considerations in microfluidic devices	33
	<b>References</b>	<b>36</b>

---

**E**NGENDERING a profound transformation in the realms of chemistry and biology, devices referred to as lab-on-chip (LOC) or lab-in-fibre (LIF) systems, have sparked widespread intrigue [1–4]. Notwithstanding their diminutive size, typically extending from a few millimetres to centimetres, these systems serve as multi-functional platforms encompassing an array of laboratory procedures [5, 6].

The driving force of these devices lies within their intricate network of microchannels. These pathways, barely thicker than a human hair, offer an exquisite control over minuscule liquid volumes (generally between nL to fL), opening the gates for a new discipline – *microfluidics*. This fascinating field studies fluid properties within these small structures, shedding light on new phenomena that govern fluid behaviour at the microscale [5, 7, 8], a concept that will be explored in depth later in this chapter.

The origins of these microfluidic devices trace back to the evolution of microanalytical techniques, like capillary electrophoresis and gas-phase chromatography. As a legacy of the Cold War, there was a necessity to create compact, field-deployable systems for detecting chemical and biological threats – thus microfluidic devices emerged [9]. These factors along with advancements in molecular biology during the 1980s and the progress of photolithographic techniques have contributed to the development of lab-on-chip systems. In the last couple of decades, the scientific community has shown a surge in interest for these innovative devices. They offer sev-

eral advantages [5, 6], such as a reduction in reagent and sample usage, expedited measurement times, and lower risks of contamination due to minimal human interference. These systems even allow for point-of-care measurements [10], a significant departure from the traditional requirement of fully-equipped laboratories. The versatility and potential of these devices indeed promises a revolution in the scientific landscape.

Emerging from the intricate domain of microfluidics, we encounter a fascinating and synergistic field known as *optofluidics*. In essence, optofluidics beautifully marries the principles of optics, which involves controlling and manipulating light, with microfluidics, which pertains to controlling and manipulating fluids on a microscopic scale. It investigates the dynamic interplay between light and fluids and the multifaceted applications that result from this unique intersection [11, 12]. From fluid-controlled tunable micro-lenses to light-guided optothermal effects, the field of optofluidics offers a promising frontier for technological advancements in a plethora of applications including lab-on-a-chip technologies [4], biomedical imaging [13], chemical analyses [14], and more. The potential applications of these devices are vast. From chemical sensing to protein and DNA analysis, the possibilities are expanding. A recent focal point in microfluidic research is the analysis of living cells. With the ability to easily achieve single-cell resolution, these devices are instrumental in unveiling new knowledge about cellular heterogeneity, a crucial consideration for areas such as cancer research, drug discovery, and diagnostics [15]. A couple of examples of lab-on-chip platforms fabricated using fs lasers can be viewed in Fig. 3.1.

The evolution of fabrication methodologies for these systems will also be discussed in this chapter. Primarily, the use of femtosecond lasers and chemical etching as a novel fabrication technique will be explored. As the traditional silicon-based fabrication method proved both expensive and unsuitable for biophotonic applications due to its opacity to visible wavelengths, the need for alternate materials and methodologies arose.

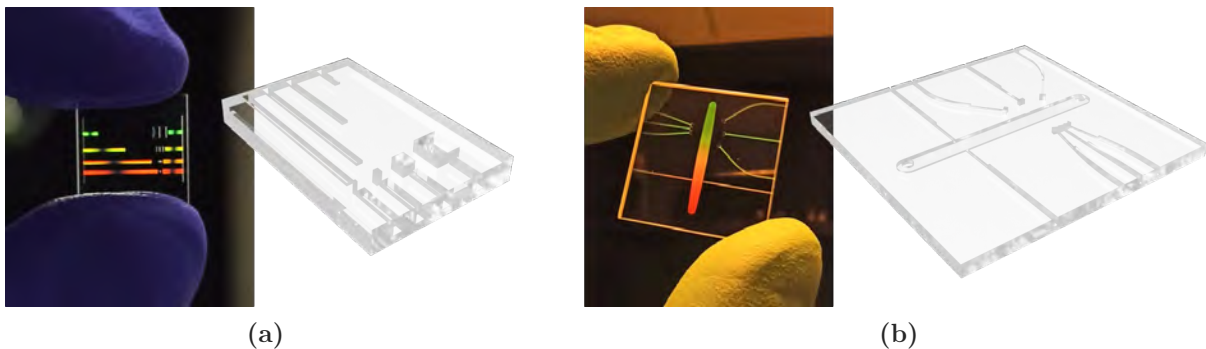


**Figure 3.1.** Illustration showing lab-on-chip devices inscribed with fs lasers on fused silica substrates in their state prior to the wet chemical etching process. These are the (a) first and (b) second version of a chip designed for phytoplankton analysis in water, a research work currently being undertaken by the Photonics Engineering Group. The colour corresponds to the diffraction generated by the multiple scans performed by the laser. For each chip, (left) a photograph is shown after its inscription, (right) as well as the 3D model designed with Solidworks 2019 SP4.0 and rendered with Blender 3.2.

### 3.1 Materials and fabrication techniques

Different types of materials, each with their distinct properties, are used for the fabrication of microfluidic devices [8, 16]. Some of the most commonly used materials are presented in Table 3.1. These materials each have their inherent advantages and drawbacks, hence, the choice of material should be aligned with the expected characteristics of the final fluidic device. The selected material also dictates the possible fabrication techniques [8, 17], which are also summarised in Table 3.2.

While the diversity and quality of materials for microfluidic applications are continually expanding [16], as are fabrication techniques offering greater resolution and repeatability for the final device, our focus will be on glassy materials, as they form the core interest of this thesis.

Glass is characterised by its chemical inertness, thermal stability, electrical insulation, rigidity, biological compatibility, and straightforward surface functionalisation [17–19]. These attributes allow to handle extreme conditions like elevated temperatures, high pressures, and harsh solvents [18]. Glass also offers exceptional optical transparency and the ability to integrate active components [8]. This extends beyond incorporating valves and pumps made from other materials, like silicon, polymers, and hydrogel, but also allows the integration of the glass itself as an active component using ultra-thin glass sheets. Its transparency enables optical detection, and its thermal and chemical stability allows efficient cleaning post-experimentation, either by heating or chemical washing. In terms of composition, these substrates are typically crafted from soda-lime glass, borosilicate glass, or fused silica [17].

While glass holds numerous merits and is relatively cheap, its use in microfabrication presents several hurdles. The conversion of glass into chips is not only a costly process but also labour-intensive and often requires the use of clean-room facilities. This consequently restricts the

**Table 3.1.** Comparison of diverse material options for the fabrication of microfluidic platforms. ●●● is equivalent to 'positive', ●●○ is equivalent to 'moderate', and ●○○ is equivalent to 'negative'. Adapted from [8, 16].

Feature	Metal	Silicon	Glass	Ceramics	Elastomers (PDMS)	Thermoplastics (PMMA)	Hydrogels
Low cost	●●●	●○○	●○○	●●●	●●○	●●●	●●●
Ease fabrication	●●●	●○○	●○○	●●●	●●●	●●○	●●○
Mechanical properties	●●●	●●●	●●●	●○○	●●●	●●●	●●○
Ease sterilisation		●●●	●●●	●○○	●●●	●●●	●○○
Oxygen permeability		●○○	●○○	●●●	●●●	●●○	●●●
Biocompatibility		●●●	●●●	●●○	●●●	●●●	●●●
Optical clarity	●○○	●○○	●●●	●○○	●●○	●●●	●●●
Smallest channel ( $\mu\text{m}$ )		< 1	< 1	> 1	< 1	< 0.1	> 1
Low absorption		●●●	●●●	●●●	●●●	●●●	●●○
Rapid prototyping		●●○	●○○	●○○	●○○	●●●	●●○
Tunable fluorescence	●○○	●○○	●○○	●○○	●●●	●○○	●●○
Cell ingrowth	●○○	●○○	●○○	●○○	●○○	●○○	●●●
Flexibility	●○○	●○○	●○○	●○○	●●●	●●○	●●●

### 3.1. Materials and fabrication techniques

**Table 3.2.** Classification of microfluidic fabrication techniques. Adapted from [8, 17].

Process	Material removing techniques	Material depositing techniques
Chemical	Electrochemical discharge machining	Silicon surface micromachining
	Wet etching	Lithography
	Dry etching	Inkjet 3D printing Powder 3D printing Direct writing 2D virtual hydrophilic channels
Mechanical	Micro-milling	Injection molding Hot embossing
	Micro-grinding	
	Micro-abrasive air-jet machining	
	Micro-abrasive water-jet machining	
	Ultrasonic machining Xurography	
Laser-based	Photothermal process	Selective laser sintering Stereolithography Two-photon polymerisation (2PP)
	Ultrashort pulse process	
	Absorbent material process	
	Photochemical modification process Laser direct machining	
Other	Focused ion beam (FIB)	Forming process
		Soft lithography
		Layer-to-layer manufacturing
		Layer-on-layer manufacturing
		Fused deposition modeling 2.5-Dimensional printing

scope of applications for glass microfluidic devices. However, there is an emerging laser-based technique, known as ultrafast laser-assisted etching (ULAE), also referred to as femtosecond laser irradiation followed by chemical etching (FLICE). Building on the concepts detailed in the preceding chapter, this method facilitates swift prototyping and high-resolution fabrication of glass-based chips, utilising a wet etching technique. The Part III of this thesis is based on this technique.

#### 3.1.1 Ultrafast laser assisted etching technique

Femtosecond lasers, apart from their application in direct writing of optical structures, open up opportunities for the direct creation of microfluidic channels in fused silica through a technique known as ULAE [20]. This approach involves a two-step process: initially, the sample undergoes irradiation with focused femtosecond laser pulses (Fig. 3.2 a), followed by wet etching of the laser-modified zone (Fig. 3.2 b). For this second step, hydrofluoric acid (HF) has traditionally been employed [11]. However, more recently, the use of bases such as potassium hydroxide (KOH) or sodium hydroxide (NaOH) has gained prominence [21, 22]. Occasionally, an intermediate step is included between the two processes, involving a thermal annealing of the structure [23]. This action refines the modifications induced by the laser, diminishing roughness, thereby facilitating acid diffusion across the treated area. The laser irradiation escalates the etching rate by up to three orders of magnitude [24], paving the way for high-aspect ratio (length to diameter

ratio) channel manufacture, and for the formation of 3D geometrical fluidic devices in glass substrates [25].

As previously outlined, there exist four distinct types of material modifications. Particularly at reduced laser fluence (Type I), a smooth increase in the refractive index can be accomplished, beneficial for the guidance of light. An increase in the etching rate of these regions has also been observed [27, 28]. This phenomenon is attributed to the densification, induced by the reduction of the Si–O–Si bond angle within the modified area [28]. It has been demonstrated that the etching rate is proportional to the induced refractive index increment. However, at elevated laser fluence (Type II), nanogratings begin to emerge, leading to an enhanced etching selectivity – up to three orders of magnitude in comparison to pristine fused silica, which can be proficiently employed for the creation of microchannels. Selectivity is defined as the ratio between the etching rate of laser-processed material and that of the pristine material.

The state of the art concerning etching rate and selectivity, along with the mechanisms associated with the increase in etching rate, are thoroughly discussed in chapter 8.

An additional factor that shapes the etching process is the fact that the attack of the solution action is not confined solely to the laser affected zones [29]. It also gradually attacks the non-irradiated material, thereby influencing the final shape of the fabricated microchannels. As a result, irradiating a straight line and subsequently exposing it to the solutions yields a conical microchannel (Fig. 3.2 b). As the solution penetrates along the irradiated area, it also interacts with the surrounding glass, broadening the microchannel’s cross-section beginning at the access point [30]. The diameter expansion is directly proportional to the solution exposure duration, which is the longest at the channel start and the shortest at the channel end. This particular issue is significantly more problematic when employing HF, as it exhibits an etching rate in pristine silica of approximately  $\sim 10 \mu\text{m/h}$  (20 vol%, 35°C) in comparison to the  $1 \mu\text{m/h}$  of KOH (37.5 wt%, 85°C) [29], or the  $0.5 \mu\text{m/h}$  of NaOH (5 wt%, 85°C) [20].

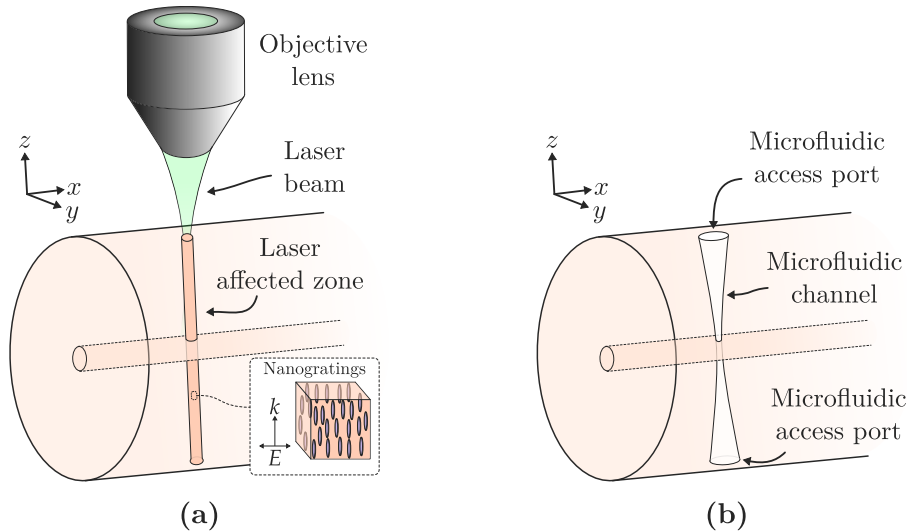
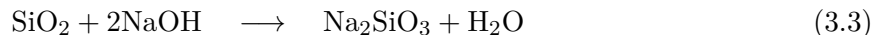
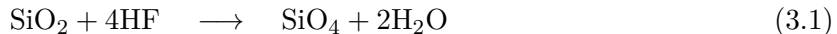


**Figure 3.2.** Illustration of the creation of microchannels in fused silica (optical fibre) using the ULAE technique. (a) Step 1: Permanent Type II modification in the sample by non-linear absorption of focused femtosecond laser pulses. (b) Step 2: Wet chemical etching of the laser-modified region generates a microfluidic channel with a given aspect ratio. Adapted from [26].

### 3.2. Physics and scaling in microfluidics

The specific chemical reactions depicting the interaction of HF, KOH and NaOH with fused silica are presented below:



Continuous replacement of the etching solution within the etched cavity with fresh solution is critical for maintaining the etching rate. This process can be facilitated by using an ultrasonic bath (for HF [31]) or a magnetic stirrer (for KOH [32], NaOH [21]). However, the longer and thinner the structure to be etched is, the more challenging it becomes to replace the exhausted solution [12]. It is noteworthy that unlike when using HF, there is no observed saturation in the length of the microchannel when KOH or NaOH is used.

The temperature and concentration of the solution play crucial roles in the etching process and the severity of the solution attack [29]. These parameters must be thoughtfully optimised in accordance with the specific design requirements of the device. A solution with high concentration can yield long microchannels, but these often have a low aspect ratio. Conversely, a solution with lower concentration can result in a device with a larger aspect ratio, but the maximum attainable length of the device tends to be smaller in this case.

Surface roughness is a significant characteristic of a microchannel, as it can potentially restrict the application of femtosecond laser-fabricated microchannels. For instance, it can affect the transparency of channel content imaging [13], increase light scattering from the channel surface – which is problematic for optical manipulation, and influence sample adhesion to the surface, thereby impacting biological experiments. The roughness is typically found to be in the range of a few hundred nanometers on the channel bottom surface [33]. Thermal treatments, involving heating the glass in ovens [34], or with oxyhydrogen (OH) flames [35], have been successfully employed to smoothen the surface, reducing the residual roughness to a few tens of nanometers or even less. Despite these promising outcomes, the method poses certain challenges. For one, the process could potentially damage the external glass surface [34], making the microchannel optically inaccessible. Moreover, the high temperatures could alter the optical properties of the waveguides, necessitating post-treatment irradiation, which complicates the fabrication process of optofluidic devices. It has also been noted that the writing direction greatly affects the quality of the channel walls [20].

## 3.2 Physics and scaling in microfluidics

The field of microfluidics centres around the manipulation of fluids at microscale levels, where the dynamics of fluid behaviour can differ considerably from what we observe in macroscopic systems [7, 8, 36, 37]. In contrast to macroscopic flows, microfluidic flows occur at length scales that are orders of magnitude smaller, offering unique advantages that include faster operation, size reduction, and diminished fluid requirements. Furthermore, the control of energy inputs and outputs, such as heat generated from a chemical reaction, becomes more manageable due to the significantly larger surface-to-volume ratio, a characteristic of microscale systems [7, 38].

### 3.2.1 Continuity and Navier-Stokes equation

A fluid, whether a gas or a liquid, is subject to continuous deformation when external forces are applied. The fundamental distinction between these two states of matter is associated with their density ( $\rho$ ). For gases, the considerable relative distance between molecules allows to regard them as compressible. Conversely, the density in liquids approaches that of solids, enabling us to typically treat them as incompressible. Therefore,  $\rho$  in a liquid is perceived as a constant over space and time.

The behaviour of fluids is governed by two primary equations [39]: the Continuity Equation and the Navier-Stokes Equation, which is essentially Newton Second Law applied to fluid mechanics:

#### o The Continuity Equation

This equation is derived from the principle of conservation of mass. It states that the rate at which mass enters a system is equal to the rate at which it leaves the system, plus the rate of change of mass within the system. In terms of fluid dynamics, it essentially says that in any steady state flow system, the mass flowing into any section of a channel must equal the mass flowing out [7]. If the fluid is incompressible, this simplifies to the statement that the velocity of the fluid times the cross-sectional area it is flowing through must remain constant. It essentially says that the net inflow of fluid volume into any region of space is zero [39], maintaining the mass conservation principle:

$$\nabla \cdot \mathbf{v} = 0, \quad (3.4)$$

where  $\mathbf{v}$  is the velocity vector of the fluid and  $\nabla \cdot$  denotes the divergence operator.

#### o The Navier-Stokes Equation

This equation express the conservation of momentum (Newton Second Law) for fluid motion. In their most general form (assuming Newtonian, incompressible fluid), it is:

$$\rho \left( \frac{\partial \mathbf{v}}{\partial t} + \mathbf{v} \cdot \nabla \mathbf{v} \right) = -\nabla p + \mu \nabla^2 \mathbf{v} + \rho \mathbf{g}, \quad (3.5)$$

where  $t$  is time,  $p$  is pressure,  $\rho$  is the fluid density,  $\mu$  is the fluid viscosity,  $\nabla$  is the gradient operator,  $\nabla^2$  is the Laplacian operator, *i.e.*, the divergence of the gradient, or  $\nabla \cdot \nabla$ , and  $g$  is the acceleration due to gravity.

The left-hand side of the equation represents the inertia forces (the time rate of change of momentum), and the right-hand side represents the forces acting on the fluid, namely pressure forces ( $-\nabla p$ ), viscous forces ( $\mu \nabla^2 \mathbf{v}$ ), and body forces (like gravity,  $\rho \mathbf{g}$ ).

Now, let us consider a specific situation – a steady, incompressible, laminar flow of a Newtonian fluid through a long, straight pipe with a constant cross-section. In this case, the complexity of the Navier-Stokes equations can be reduced significantly, leading to Poiseuille’s law [39]. There are several key assumptions to consider:

- o Steady flow: The flow rate is constant in time, so it is possible to drop the time-dependent term from the Navier-Stokes equation.

### 3.2. Physics and scaling in microfluidics

- Fully-developed flow: The flow profile is fully developed, which means the velocity profile does not change along the length of the pipe.
- No-slip condition: The velocity at the pipe wall is zero due to viscous effects.
- Incompressible, Newtonian fluid: The fluid density is constant, and the stress in the fluid is linearly proportional to the strain rate.
- Long pipe and small radial gradient of pressure: The pressure gradient is constant in time and only changes in the axial direction (along the length of the pipe), not radially.

Under these assumptions, the velocity only varies across the radial direction – from the centre to the wall of the pipe, and it is constant along the length and circumference of the pipe. As a result, the Continuity Equation is automatically satisfied. Furthermore, the Navier-Stokes equations reduce to a much simpler form, which is a second-order ordinary differential equation. This equation can be integrated twice with the boundary conditions to get the velocity distribution, which is parabolic, with maximum velocity along the centreline of the pipe. Finally, integrating this velocity profile across the microchannel cross-sectional area gives the volumetric flow rate  $Q$  [ $\mu\text{m}^3/\text{s}$ ] (Poiseuille’s law):

$$Q = \frac{\pi \Delta p R^4}{8 \mu L}, \quad (3.6)$$

being  $\Delta p$  the pressure difference between the two ends of the microchannel,  $R$  the diameter of the microchannel, and  $L$  the length of the microchannel.

#### 3.2.2 Dimensionless numbers

The model of flow presented by Poiseuille’s law may serve as a reasonable estimate of an actual flow scenario, provided that it is feasible to overlook the non-linear term in the Navier-Stokes equation,  $\mathbf{v} \cdot \nabla \mathbf{v}$ , within the practical application in question. In terms of solver stability while addressing a microfluidics problem utilising finite element methods, it is crucial to pay attention to two essential dimensionless numbers: the Reynolds number ( $Re$ ), and the Peclet number ( $Pe$ ).

The Peclet number is significant as it describes the relative impact of convection compared to diffusion, whether in terms of heat (Equation 3.7) or mass (Equation 3.8) transfer. Meanwhile, the Reynolds number (Equation 3.9) signifies the comparative influence of the convective inertia term versus viscosity within the context of the Navier-Stokes equations.

$$Pe \text{ (heat flow)} = \frac{\rho c_p v L}{\kappa}, \quad (3.7)$$

$$Pe \text{ (mass transport)} = \frac{v L}{D}, \quad (3.8)$$

$$Re = \frac{\text{inertial forces}}{\text{viscous forces}} = \frac{\rho v L}{\mu}. \quad (3.9)$$

where  $L$  is the length scale of the problem,  $v$  is the flow velocity,  $c_p$  is the heat capacity at constant pressure,  $\kappa$  is the thermal conductivity, and  $D$  is the diffusion constant. Numerical

instabilities may occur when the Reynolds or Peclet number exceeds one. These instabilities typically present themselves as spurious oscillations within the solution.

In situations where the Reynolds numbers are low (typically  $Re < 1000$ ), viscous forces dominate, causing any disturbances to be damped out. This results in a phenomenon known as laminar flow [38], which is primarily used to model slow-moving fluid in environments free from abrupt changes in geometry, material distribution, or temperature. When solving for such scenarios, the Navier-Stokes equations are utilised without the need for a turbulence model. Conversely, at high Reynolds numbers where the damping in the system is minimal, disturbances have the potential to grow via non-linear interactions. If the Reynolds number is sufficiently high ( $Re > 1000$ ), this can result in a chaotic state known as turbulence.

However, for exceptionally low Reynolds numbers ( $Re \ll 1$ ) another regime called creeping flow, or Stokes flow, comes into play. This flow regime is commonly encountered in microfluidics applications, where viscous forces largely rule the flow behaviour [40]. The equations governing creeping flow are identical to those for laminar flow, albeit with the additional assumption of an insignificant inertia term. This flow is characterised by a predominance of viscous forces to the extent that the contribution from the inertia term can be considered negligible.

Creeping flow problems are notably simpler to solve compared to laminar flow problems. It is the only case where Poiseuille flow can be used to approximate the fluid motion, as it is possible to neglect the time dependent term of the left-hand side of the Equation 3.5. Therefore, it is envisaged that the fluid reaction to modifications in the flow condition is instantaneous, and the properties of the fluid exhibit time reversibility. A crucial feature of this flow regime is that fluids moving alongside each other do not mix; instead, mixing predominantly occurs via diffusion.

### Intertial microfluidics

Neglecting the role of fluid inertia in microfluidic systems, simply because of the laminar nature of the flow, can often lead to errors. In fact, even at moderate fluid velocities, inertial effects have a significant impact on both fluids and particles [41]. To provide a practical example, considering a 100  $\mu\text{m}$  wide microchannel filled with water ( $\rho \approx 1000 \text{ kg/m}^3$  and  $\mu \approx 1 \text{ mPa}$ ) flowing at a speed of 10 mm/s. In this scenario,  $Re \approx 1$ , indicating a regime in which passive manipulation of fluids and particles can be achieved efficiently. Due to this, inertial fluid effects are gaining increased recognition and are starting to be utilised in commercial lab-on-chip systems [42]. Despite this, the field is still in its infancy, with many aspects yet to be fully explored or comprehensively understood.

#### 3.2.3 Relevant considerations in microfluidic devices

One of the fascinating aspects of microfluidics lies in the altering significance of physical properties as the length scale ( $L$ ) of fluid flow reduces [43]. Properties that scale with the surface area become increasingly dominant over those scaling with the volume of the flow. This shift in scaling results in viscous forces generated by shear over isovelocity surfaces, which scale as  $L^2$ , overpowering inertial forces, which scale volumetrically as  $L^3$ . Consequently, as stated above, these flows are characterised by low Reynolds numbers ( $Re$ ), indicating the predominance of

### 3.2. Physics and scaling in microfluidics

**Table 3.3.** Scaling of physical phenomena with length ( $L$ ) and consequences for microfluidic devices.

Property	Length scaling	Consequences
Inertial forces	$L^3$	The predominance of viscosity over inertia results in flow that is characteristically laminar or creeping. The absence of convection contributes to the difficulty in achieving efficient mixing.
Viscous forces	$L^2$	
Volume	$L^3$	Properties related to the surface escalate in significance compared to those linked to volume, due to the high surface area to volume ratios.
Area	$L^2$	
Laplace pressure	$L^{-1}$	In two-phase flows, the effects of surface tension become the predominant influencing factors.
Capillary force	$L^{-1}$	
Permeability of porous media	$L^2$	Darcy law applies.
Diffusion time scale	$L^2$	Diffusive mixing is feasible, albeit considerably slower compared to convection.
Electric field	$L^{-1}$	There is potential to leverage a variety of electrokinetic phenomena to propel the fluid flow.
Knudsen number	$L^{-1}$	Gas flows at the microscale are typically rarefied.

laminar or creeping (Stokes) flow regimes.

When dealing with the presence of multiple phases, the effects of surface tension start to take precedence over those of gravity and inertia at smaller scales. Factors such as Laplace pressure, capillary force, and Marangoni forces are all inversely proportional to the length scale ( $L^{-1}$ ) [44].

Moreover, flow can also occur through porous media at microscale geometries. The permeability of a porous medium, which is proportional to the square of the average pore radius ( $L^2$ ), often results in a flow that is dominated by friction when the pore size ( $\sim L$ ) falls within the micron range [45]. Darcy's law can be applied in such cases. The Brinkman equation is also suitable for modelling intermediate flows.

At the microscale level, fluid flow can be influenced by various electro-hydrodynamic effects. The strength of the electric field for a given applied voltage is inversely proportional to  $L$ , which allows the application of relatively large fields to the fluid using moderate voltages. Processes such as electro-osmosis, electrophoresis, dielectrophoresis and magnetophoresis can move charged or polarised particles in the fluid [46–48]. Manipulating contact angles via the electrowetting phenomenon is also achievable in microscale devices [44].

In the case of laminar flows, mixing becomes quite challenging, leading to mass transport that is often limited by diffusion [49]. Despite the fact that diffusion time is proportional to the square of the length scale ( $L^2$ ), it is generally a slow process in microfluidic systems. This has implications for the transport of chemicals and subsequently for reactions within these systems [50, 51].

As the length scale of the flow approaches the intermolecular length scale, complex kinetic

effects start to play a significant role [52]. In gases, the Knudsen number ( $Kn = \lambda/L$ ), which is the ratio of the molecular mean free path ( $\lambda$ ) to the flow geometry size ( $L$ ), scales with  $L^{-1}$ . For  $Kn < 0.01$ , the Navier-Stokes equations with no-slip boundary conditions typically provide a good description of the fluid flow. For  $0.01 < Kn < 0.1$ , the slip flow regime applies and the Navier-Stokes equations with appropriate slip boundary conditions can be used to model the flow. When the Knudsen number exceeds 0.1, a fully kinetic approach is needed for accurate modelling.

The primary concepts and phenomena detailed here is conveniently compiled and presented for ease of understanding in Table 3.3.

## References

- [1] Haque, M., Lee, K. K. C., Ho, S., Fernandes, L. A., and Herman, P. R., “Chemical-assisted femtosecond laser writing of lab-in-fibers,” *Lab on a Chip*, vol. 14, no. 19, pp. 3817–3829, 2014. DOI: 10.1039/c41c00648h.
- [2] Paiè, P., “Femtosecond laser micromachining of optofluidic glass chips for biophotonic applications,” Ph.D. dissertation, Politecnico di Milano, 2016.
- [3] Haque, M., “Chemical-Assisted Femtosecond Laser Writing of Lab-in-Fiber Sensors,” Ph.D. dissertation, University of Toronto, 2014.
- [4] Sugioka, K. *et al.*, “Femtosecond laser 3D micromachining: A powerful tool for the fabrication of microfluidic, optofluidic, and electrofluidic devices based on glass,” *Lab on a Chip*, vol. 14, no. 18, pp. 3447–3458, 2014. DOI: 10.1039/c41c00548a.
- [5] Stone, H. A., Stroock, A. D., and Ajdari, A., “Engineering Flows in Small Devices: Microfluidics Toward a Lab-on-a-Chip,” *Annual Review of Fluid Mechanics*, vol. 36, no. 1, pp. 381–411, Jan. 2004. DOI: 10.1146/annurev.fluid.36.050802.122124.
- [6] Sackmann, E. K., Fulton, A. L., and Beebe, D. J., “The present and future role of microfluidics in biomedical research,” *Nature*, vol. 507, no. 7491, pp. 181–189, Mar. 2014. DOI: 10.1038/nature13118.
- [7] Squires, T. M. and Quake, S. R., “Microfluidics: Fluid physics at the nanoliter scale,” *Reviews of Modern Physics*, vol. 77, no. 3, pp. 977–1026, Oct. 2005. DOI: 10.1103/revmodphys.77.977.
- [8] Niculescu, A.-G., Chircov, C., Bîrcă, A. C., and Grumezescu, A. M., “Fabrication and Applications of Microfluidic Devices: A Review,” *International Journal of Molecular Sciences*, vol. 22, no. 4, p. 2011, Feb. 2021. DOI: 10.3390/ijms22042011.
- [9] Convery, N. and Gadegaard, N., “30 years of microfluidics,” *Micro and Nano Engineering*, vol. 2, pp. 76–91, Mar. 2019. DOI: 10.1016/j.mne.2019.01.003.
- [10] Li, Z. *et al.*, “Fully integrated microfluidic devices for qualitative, quantitative and digital nucleic acids testing at point of care,” *Biosensors and Bioelectronics*, vol. 177, p. 112952, Apr. 2021. DOI: 10.1016/j.bios.2020.112952.
- [11] Bragheri, F. *et al.*, “Optofluidic integrated cell sorter fabricated by femtosecond lasers,” *Lab on a Chip*, vol. 12, no. 19, p. 3779, 2012. DOI: 10.1039/c21c40705a.
- [12] Osellame, R., Maselli, V., Vazquez, R. M., Ramponi, R., and Cerullo, G., “Integration of optical waveguides and microfluidic channels both fabricated by femtosecond laser irradiation,” *Applied Physics Letters*, vol. 90, no. 23, p. 231118, Jun. 2007. DOI: 10.1063/1.2747194.
- [13] Paiè, P., Vázquez, R. M., Osellame, R., Bragheri, F., and Bassi, A., “Microfluidic Based Optical Microscopes on Chip,” *Cytometry Part A*, vol. 93, no. 10, pp. 987–996, Sep. 2018. DOI: 10.1002/cyto.a.23589.
- [14] Basiri, A. *et al.*, “Microfluidic devices for detection of RNA viruses,” *Reviews in Medical Virology*, vol. 31, no. 1, pp. 1–11, Aug. 2020. DOI: 10.1002/rmv.2154.

- [15] Ma, C., Peng, Y., Li, H., and Chen, W., “Organ-on-a-Chip: A New Paradigm for Drug Development,” *Trends in Pharmacological Sciences*, vol. 42, no. 2, pp. 119–133, Feb. 2021. DOI: 10.1016/j.tips.2020.11.009.
- [16] Ren, K., Zhou, J., and Wu, H., “Materials for Microfluidic Chip Fabrication,” *Accounts of Chemical Research*, vol. 46, no. 11, pp. 2396–2406, Jun. 2013. DOI: 10.1021/ar300314s.
- [17] Hwang, J., Cho, Y. H., Park, M. S., and Kim, B. H., “Microchannel Fabrication on Glass Materials for Microfluidic Devices,” *International Journal of Precision Engineering and Manufacturing*, vol. 20, no. 3, pp. 479–495, Mar. 2019. DOI: 10.1007/s12541-019-00103-2.
- [18] Singh, A., Malek, C. K., and Kulkarni, S. K., “Development in microreactor technology for nanoparticle synthesis,” *International Journal of Nanoscience*, vol. 09, no. 01n02, pp. 93–112, Feb. 2010. DOI: 10.1142/s0219581x10006557.
- [19] Martins, J. P., Torrieri, G., and Santos, H. A., “The importance of microfluidics for the preparation of nanoparticles as advanced drug delivery systems,” *Expert Opinion on Drug Delivery*, vol. 15, no. 5, pp. 469–479, Mar. 2018. DOI: 10.1080/17425247.2018.1446936.
- [20] Casamenti, E., Pologhini, S., and Bellouard, Y., “Few pulses femtosecond laser exposure for high efficiency 3D glass micromachining,” *Optics Express*, vol. 29, no. 22, pp. 35 054–35 066, Oct. 2021. DOI: 10.1364/oe.435163. [Online]. Available: <https://doi.org/10.1364/oe.435163>.
- [21] Ochoa, M., Roldán-Varona, P., Algorri, J. F., López-Higuera, J. M., and Rodríguez-Cobo, L., “Polarisation-independent ultrafast laser selective etching processing in fused silica,” *Lab on a Chip*, vol. 23, no. 7, pp. 1752–1757, 2023. DOI: 10.1039/d3lc00052d.
- [22] Ross, C. A., MacLachlan, D. G., Choudhury, D., and Thomson, R. R., “Optimisation of ultrafast laser assisted etching in fused silica,” *Optics Express*, vol. 26, no. 19, pp. 24 343–24 356, Sep. 2018. DOI: 10.1364/oe.26.024343. [Online]. Available: <https://doi.org/10.1364/oe.26.024343>.
- [23] Sugioka, K., “Hybrid femtosecond laser three-dimensional micro- and nanoprocessing: A review,” *International Journal of Extreme Manufacturing*, vol. 1, no. 1, p. 012 003, Apr. 2019. DOI: 10.1088/2631-7990/ab0eda.
- [24] Hermans, M., “Selective, Laser-Induced Etching of Fused Silica at High Scan-Speeds Using KOH,” *Journal of Laser Micro/Nanoengineering*, vol. 9, no. 2, pp. 126–131, Jun. 2014. DOI: 10.2961/jlmm.2014.02.0009.
- [25] Piacentini, S., Bragheri, F., Corrielli, G., Vázquez, R. M., Paié, P., and Osellame, R., “Advanced photonic and optofluidic devices fabricated in glass via femtosecond laser micromachining [Invited],” *Optical Materials Express*, vol. 12, no. 10, pp. 3930–3945, Sep. 2022. DOI: 10.1364/ome.463715.
- [26] Pallarés-Aldeiturriaga, D., Roldán-Varona, P., Rodríguez-Cobo, L., and López-Higuera, J. M., “Optical Fiber Sensors by Direct Laser Processing: A Review,” *Sensors*, vol. 20, no. 23, p. 6971, Dec. 2020. DOI: 10.3390/s20236971.
- [27] Taylor, R. *et al.*, “Ultra-high resolution index of refraction profiles of femtosecond laser modified silica structures,” *Optics Express*, vol. 11, no. 7, p. 775, Apr. 2003. DOI: 10.1364/oe.11.000775.

## References

- [28] Bellouard, Y., Said, A., Dugan, M., and Bado, P., “Fabrication of high-aspect ratio, micro-fluidic channels and tunnels using femtosecond laser pulses and chemical etching,” *Optics Express*, vol. 12, no. 10, pp. 2120–2129, 2004. DOI: 10.1364/opex.12.002120.
- [29] Seidel, H., Csepregi, L., Heuberger, A., and Baumgärtel, H., “Anisotropic Etching of Crystalline Silicon in Alkaline Solutions: I . Orientation Dependence and Behavior of Passivation Layers,” *Journal of The Electrochemical Society*, vol. 137, no. 11, pp. 3612–3626, Nov. 1990. DOI: 10.1149/1.2086277.
- [30] Vishnubhatla, K. C., Bellini, N., Ramponi, R., Cerullo, G., and Osellame, R., “Shape control of microchannels fabricated in fused silica by femtosecond laser irradiation and chemical etching,” *Optics Express*, vol. 17, no. 10, pp. 8685–8695, May 2009. DOI: 10.1364/oe.17.008685.
- [31] Sima, F., Sugioka, K., Vázquez, R. M., Osellame, R., Kelemen, L., and Ormos, P., “Three-dimensional femtosecond laser processing for lab-on-a-chip applications,” *Nanophotonics*, vol. 7, no. 3, pp. 613–634, Feb. 2018. DOI: 10.1515/nanoph-2017-0097.
- [32] Roldán-Varona, P. *et al.*, “Selective plane illumination optical endomicroscopy with polymer imaging fibers,” *APL Photonics*, vol. 8, no. 1, p. 016103, Jan. 2023. DOI: 10.1063/5.0130486.
- [33] Butkutė, A. *et al.*, “Optimization of selective laser etching (SLE) for glass micromechanical structure fabrication,” *Optics Express*, vol. 29, no. 15, pp. 23487–23499, Jul. 2021. DOI: 10.1364/oe.430623.
- [34] Sala, F., Paié, P., Vázquez, R. M., Osellame, R., and Bragheri, F., “Effects of Thermal Annealing on Femtosecond Laser Micromachined Glass Surfaces,” *Micromachines*, vol. 12, no. 2, p. 180, Feb. 2021. DOI: 10.3390/mi12020180.
- [35] Ross, C. A. *et al.*, “A Miniature Fibre-Optic Raman Probe Fabricated by Ultrafast Laser-Assisted Etching,” *Micromachines*, vol. 11, no. 2, p. 185, Feb. 2020. DOI: 10.3390/mi11020185.
- [36] Shang, L., Cheng, Y., and Zhao, Y., “Emerging Droplet Microfluidics,” *Chemical Reviews*, vol. 117, no. 12, pp. 7964–8040, May 2017. DOI: 10.1021/acs.chemrev.6b00848.
- [37] Beebe, D. J., Mensing, G. A., and Walker, G. M., “Physics and Applications of Microfluidics in Biology,” *Annual Review of Biomedical Engineering*, vol. 4, no. 1, pp. 261–286, Aug. 2002. DOI: 10.1146/annurev.bioeng.4.112601.125916.
- [38] Pethig, R. and Smith, S., *Introductory Bioelectronics*. Wiley, Sep. 2012. DOI: 10.1002/9781118443293.
- [39] Song, Y., Zhao, X., Tian, Q., and Liang, H., “Fundamental Concepts and Physics in Microfluidics,” in *Microfluidics: Fundamental, Devices and Applications*, Wiley-VCH Verlag GmbH & Co. KGaA, Jan. 2018, pp. 19–111. DOI: 10.1002/9783527800643.ch2.
- [40] Ku, M. J. H. *et al.*, “Imaging viscous flow of the Dirac fluid in graphene,” *Nature*, vol. 583, no. 7817, pp. 537–541, Jul. 2020. DOI: 10.1038/s41586-020-2507-2.
- [41] Zhang, J. *et al.*, “Fundamentals and applications of inertial microfluidics: A review,” *Lab on a Chip*, vol. 16, no. 1, pp. 10–34, 2016. DOI: 10.1039/c51c01159k.
- [42] Amini, H., Lee, W., and Carlo, D. D., “Inertial microfluidic physics,” *Lab on a Chip*, vol. 14, no. 15, p. 2739, 2014. DOI: 10.1039/c41c00128a.

- [43] Chen, L. *et al.*, “Millifluidics, microfluidics, and nanofluidics: Manipulating fluids at varying length scales,” *Materials Today Nano*, vol. 16, p. 100 136, Dec. 2021. DOI: 10.1016/j.mtnano.2021.100136.
- [44] Gennes, P.-G. de, Brochard-Wyart, F., and Quéré, D., *Capillarity and Wetting Phenomena*. Springer New York, 2004. DOI: 10.1007/978-0-387-21656-0.
- [45] Grathwohl, P., *Diffusion in Natural Porous Media: Contaminant Transport, Sorption/Desorption and Dissolution Kinetics*. Springer US, 1998. DOI: 10.1007/978-1-4615-5683-1.
- [46] Harrison, D. J., Fluri, K., Seiler, K., Fan, Z., Effenhauser, C. S., and Manz, A., “Micro-machining a Miniaturized Capillary Electrophoresis-Based Chemical Analysis System on a Chip,” *Science*, vol. 261, no. 5123, pp. 895–897, Aug. 1993. DOI: 10.1126/science.261.5123.895.
- [47] Nazeer, M. *et al.*, “Theoretical study of MHD electro-osmotically flow of third-grade fluid in micro channel,” *Applied Mathematics and Computation*, vol. 420, p. 126 868, May 2022. DOI: 10.1016/j.amc.2021.126868.
- [48] Dongre, C. *et al.*, “Fluorescence monitoring of microchip capillary electrophoresis separation with monolithically integrated waveguides,” *Optics Letters*, vol. 33, no. 21, pp. 2503–2505, Oct. 2008. DOI: 10.1364/ol.33.002503.
- [49] Tadevosyan, K., Iglesias-García, O., Mazo, M. M., Prósper, F., and Raya, A., “Engineering and Assessing Cardiac Tissue Complexity,” *International Journal of Molecular Sciences*, vol. 22, no. 3, p. 1479, Feb. 2021. DOI: 10.3390/ijms22031479.
- [50] Mo, Y. *et al.*, “Microfluidic electrochemistry for single-electron transfer redox-neutral reactions,” *Science*, vol. 368, no. 6497, pp. 1352–1357, Jun. 2020. DOI: 10.1126/science.aba3823.
- [51] Vasala, A., Hytönen, V. P., and Laitinen, O. H., “Modern Tools for Rapid Diagnostics of Antimicrobial Resistance,” *Frontiers in Cellular and Infection Microbiology*, vol. 10, Jul. 2020. DOI: 10.3389/fcimb.2020.00308.
- [52] Regenauer-Lieb, K., “An immersed boundary-lattice Boltzmann method for gaseous slip flow,” *Physics of Fluids*, vol. 32, no. 1, p. 012 002, Jan. 2020. DOI: 10.1063/1.5126392.

# 4

## Experimental setups and methods

---

<b>4.1</b>	<b>Fabrication setups</b>	<b>41</b>
4.1.1	Femtosecond laser writing	41
4.1.2	Chemical etching	43
<b>4.2</b>	<b>Simulations tools</b>	<b>43</b>
<b>4.3</b>	<b>Characterisation techniques</b>	<b>44</b>
4.3.1	Quantitative phase microscopy	44
4.3.2	Refracted near field profilometry	45
4.3.3	Raman spectroscopy	46
	<b>References</b>	<b>48</b>

---

**I**N this chapter, readers will learn about the tools and methods used in the research carried out in this thesis. A key facet of this chapter is the unique fabrication setup, which integrates the high-precision ultrafast laser with the comprehensive functionality of a chemical hood used for wet etching. This robust combination caters to a broad spectrum of microfabrication requirements, aligning with the multifaceted demands of the research. Attention is also accorded to the description of the simulation tools employed, as well as the characterisation techniques, specifically the quantitative phase microscopy (QPM), refracted near field (RNF) profilometry, and Raman spectroscopy. These are of paramount importance in corroborating our findings and hypotheses, thereby anchoring the subsequent analysis. By engendering a thorough understanding of these experimental methodologies, the aim is to create a rigorous context in which the outcomes and significance of this research can be fully comprehended and critically assessed.

## 4.1 Fabrication setups

### 4.1.1 Femtosecond laser writing

Here, the optical setup for making modifications in glass substrates using a femtosecond laser is briefly introduced. It can be understood to represent the most important experimental configuration of the thesis, being the most used, both in the creation of structures using direct-write, as well as employing the ULAE technique. The setup shown in Fig. 4.1 is what has been formed in the Photonic Engineering Group in Santander, as a result of this thesis. It is worth noting, however, that the experimental configurations used during research stays in Edinburgh (Institute of Photonics and Quantum Sciences) and Italy (Institute of Photonics and Nanotechnology) are very similar.

Regarding the laser source, in Santander there is a fibre laser chirped pulse amplifier (FLCPA) from the Cazadero series of Calmar Laser, model FLCPA-03U-20. This laser allows for the generation of variable pulse energies (with a maximum of approximately 5  $\mu\text{J}$ ), as well as the ability to modify the pulse repetition rate (PRR) thanks to an additional controller made with an STM32 microcontroller, which can go from a maximum PRR of 1 MHz to a single pulse configuration. The wavelength and pulse duration are 1030 nm and 370 fs, respectively.

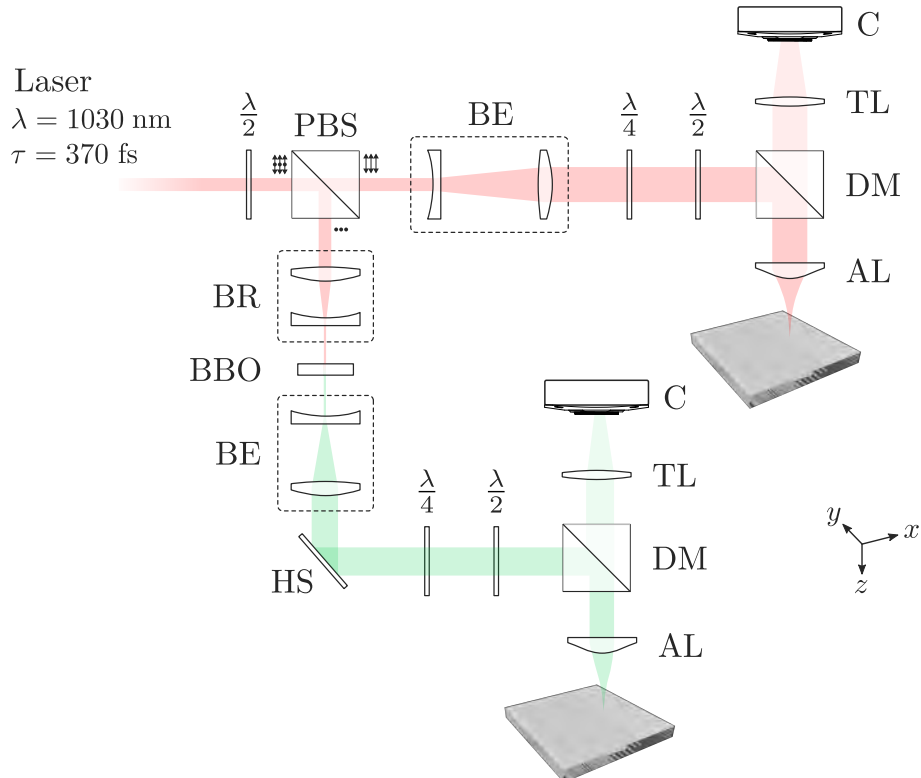


**Figure 4.1.** Schematic of the femtosecond laser inscription setup (Key: PBS – polarisation beam splitter, BE – beam expander, BR – beam reducer, HS – harmonic separator, BBO - beta barium borate crystal, C – CCD camera, TL – tube lens, DM – dichroic mirror, AL – aspheric lens,  $\lambda/2$  – half waveplate,  $\lambda/4$  – quarter waveplate). Red colour corresponds to 1030 nm light, while green light represents 515 nm wavelength. Beam shutters, mirrors, illumination elements, as well as alignment irises are not shown in the schematic.

#### 4.1. Fabrication setups

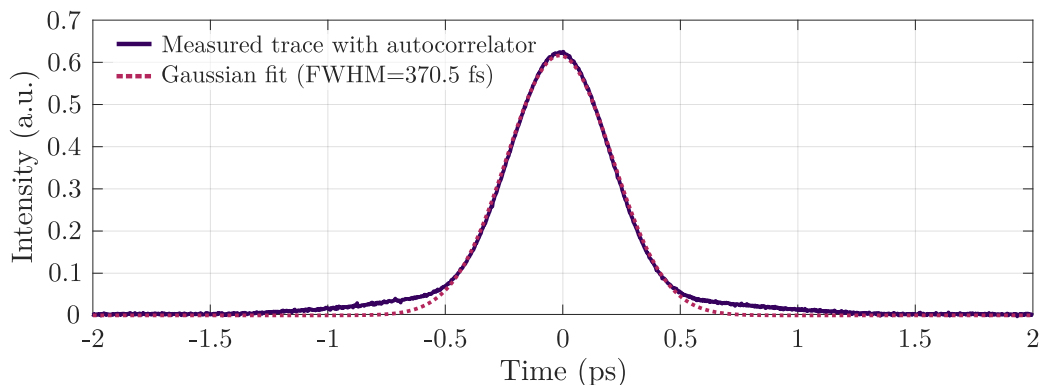


**Figure 4.2.** Temporal measurement of the pulse from the BlueCut fs laser used an autocorrelator. The 370 fs corresponds to the Gaussian adjustment of the pulse autocorrelation ( $\tau = \tau_a/\sqrt{2}$ , being  $\tau_a$  the FWHM pulse duration of autocorrelation).

In Edinburgh, on the other hand, the BlueCut laser from Menlo Systems GmbH was primarily used, with equivalent parameters. This fibre-based laser has a wavelength of 1030 nm, variable pulse energy up to 10  $\mu$ J, with selectable PRRs between 250 kHz, 500 kHz, 1 MHz, and 2 MHz [1–3]. The pulse duration is also 370 fs (see Fig. 4.2). In Milan, the ytterbium fibre-based laser Satsuma from Amplitude System was used. Although the laser wavelength is 1030 nm, inscriptions were made using 515 nm due to a second harmonic generation process carried out prior to the focusing optics [4, 5]. The pulse duration can be varied, but 280 fs was used at the laser output, degraded to  $\sim$  350 fs after the intermediate optics. The repetition rate, also modifiable by a pulse picker, was mainly fixed to 1 MHz. The maximum output power of this laser is 10 W.

The initial beam is split into two paths: the infrared (IR) and the visible (VIS) path. This is achieved by using a combination of a half waveplate (HWP) and a polarisation cube. Given that the output of the laser has a linear polarisation, the HWP allows for rotation of the polarisation plane, so that power can be directed either to the IR path or to the VIS path. Due to the presence of manual shutters on both optical paths following the polarisation cube, this pair of optical elements can also be used for external pulse energy control.

Concerning the IR beam, the beam diameter is enlarged using a beam expander in order to cover the input pupil of the focusing objective lens (or the diameter of the aspherical focusing lens). There is also a combination of half and quarter waveplates that allow for complete control of the inscription polarisation: linear, circular, or elliptical. It is worth noting that the HWP is placed on a mount that rotates at a speed of 5 Hz, which enables the positioning of optimal linear polarisations in real-time inscriptions, something crucial in the ULAE technique for etching 3D complex structures.

On the other hand, the VIS path also has complete control of polarisation, but prior to this, a second harmonic generation (SHG) process takes place using a non-linear crystal made of beta barium borate (BBO,  $\beta$ -BaB<sub>2</sub>O<sub>4</sub>). To increase the conversion efficiency, the beam energy is spatially concentrated using a beam reducer, and the diameter is later restored with a beam expander. The fundamental wavelength is eliminated through a harmonic separator. It is important to note that the components used in the setup are characterised by a reduced group delay dispersion (GDD), in order to minimise pulse duration degradation.

The movement of the sample is carried out using a computer-controlled 3D (XYZ) stage with nanoresolution, from Aerotech. The alignment of the sample in relation to the laser beam (either IR or VIS) is fine-tuned using a machine vision system. This system uses a charge-coupled device (CCD) camera to capture the image of the fibre with transmission illumination, or the laser back-reflection from the sample, especially when using fused silica plates. Power control is achieved either directly through the laser or via a combination of a half waveplate and polarisation beam splitter, which are situated along the initial beam path.

### 4.1.2 Chemical etching

For the creation of microchannels, microfluidic devices, or simply for removing the areas previously processed by the laser, a secondary stage of chemical etching is required, as was explained in the previous chapter. This is carried out in a fireproof fume hood which captures any vapors that may arise during this wet etching process. For safety reasons, this stage is performed exclusively within the fume hood. However, depending on the type of solution used to extract the previously modified fused silica, a specific protocol is followed.

In both Santander (where this thesis has been carried out) and Edinburgh (where a 3-month stay was completed in 2021 as described in chapter 9), aqueous solutions of KOH or NaOH, both bases, are used. To maintain a consistent solute concentration throughout the process, a magnetic stirrer is used. Temperature control is also exercised, and in this case, it is kept at 85 °C. It is noteworthy to mention that the concentrations used for KOH-based solutions and NaOH-based solutions are 37.5 wt% and 5 wt%, respectively.

In contrast, during the 3-month stay in Milan in 2022 (chapter 10), aqueous solutions of HF were used, at 20 v%. Here, the exposure of the glass sample to the acid needs to be carried out in an ultrasonic bath to facilitate the etching process. The sonic bath has a temperature control set at 35 °C.

Regardless of whether an acid or a base is used, the samples are sonicated for five minutes in a solution of deionised water and isopropyl alcohol. Likewise, prior to wet etching, if the sample is not clean, it can be lightly sonicated in acetone, and then rinsed with deionised water. It is important to note that fused silica was consistently used throughout this thesis, which is why the chosen chemical compounds are as stated. The beakers used in the etching process are made of polytetrafluoroethylene (PTFE), a material resistant to the solution.

## 4.2 Simulations tools

Simulation tools are crucial instruments in the field of photonics, specifically in the design and optimisation of sensors and devices. These tools provide a numerical platform to investigate the interactions between light and matter, circumventing the time and resource-intensive process of direct experimentation [6]. Comsol Multiphysics, RSoft Photonic, and Zemax OpticStudio are key commercial softwares employed in this thesis, each offering unique methodologies for examining photonic systems. Although additional methods have been utilised, the three fundamental ones upon which the majority of the work is based involve the use of geometrical optics, finite-difference time-domain (FDTD) method, and the beam propagation method (BPM). Now

### 4.3. Characterisation techniques

each method is briefly developed, as they are not the main objective of this thesis.

Geometrical optics, used through Zemax, simplifies light propagation into rays, following straight paths until they interact with a surface. This method is most effective when dealing with systems where the wavelength of light ( $\lambda$ ) is much smaller than the size of the components. Its main advantage lies in its simplicity and computational efficiency, although it does not accurately model diffraction, interference or polarisation effects, making it less effective for nano-scale or highly integrated photonic systems. However, in this thesis, it will primarily be used to model the reflection that occurs in certain designed structures.

The finite-difference time-domain method, used both in Comsol and RSoft, is a powerful technique for modelling time-dependent electromagnetic fields. It is a full-wave method that can capture complex behaviours like scattering, interference, diffraction, and non-linear effects, making it ideal for studying wave propagation in nanostructures and complex geometries. However, FDTD requires substantial computational resources and can be time-consuming, especially for large or long-range systems. It is a rigorous solution to Maxwell equations and does not have any approximations or theoretical restrictions.

Lastly, the beam propagation method, also available in RSoft, is designed for analysing waveguide devices and wave propagation in structures that vary slowly along the propagation direction. It is computationally efficient for these specific applications and can effectively model interference and diffraction. However, its main limitation is that it cannot accurately handle abrupt structural changes or highly scattering systems.

## 4.3 Characterisation techniques

Characterisation plays a vital role in material processing and the validation of experimental results, allowing for precise measurements of the properties of a given material or structure. In the context of fs laser processing, it becomes even more critical to characterise the modified samples to gain insight into changes in optical properties. This data serves multiple purposes: it provides a quality check for inscribed structures, guides the selection of laser parameters for future designs, and assists in generating reliable simulations.

This section introduces the most important characterisation methods utilised in this research. Not all methods are covered, but the ones that are crucial to the understanding of this work are presented. Techniques such as refracted near field profilometry and quantitative phase microscopy are employed for determining refractive index or phase – which is proportional to the refractive index, respectively. Moreover, Raman spectroscopy provides valuable information about the internal structure that can shed light on various modifications, such as structural expansion or stress relief [7], specially relevant in chapter 8.

### 4.3.1 Quantitative phase microscopy

Quantitative phase microscopy (QPM) is a powerful imaging technique that allows to measure the optical phase shift induced by a transparent or semi-transparent sample [8, 9], such a glass substrate or an optical fibre. This method has become especially useful in the field of biological and materials sciences, due to its non-invasive and label-free nature [10].

In a traditional light microscope, contrast comes from absorption or scattering of light, which often requires staining or tagging of the sample. However, in QPM, contrast is generated from the delay (or phase shift) that light experiences when passing through a sample compared to the surrounding medium [11]. This phase shift is proportional to the refractive index of the sample, allowing for quantitative analysis of the sample structure and composition:

$$\Delta n = \frac{\lambda}{2\pi \cdot \Delta z} \Delta\phi, \quad (4.1)$$

where  $\lambda$  is the wavelength of the illumination source (typically monochromatic),  $\Delta\phi$  is the phase change,  $\Delta n$  is the refractive index change, and  $\Delta z$  is the RIC length.

This technique relies in the intensity transport equation [9] (Equation 4.2). The equation demonstrates that phase retrieval is possible when there is a known change in intensity in its propagating direction. To achieve this, three conventional intensity images are used - one in focus and two others defocused by a certain degree, denoted by  $\delta z$  [8]. This process can be executed with a standard, well-illuminated transmission microscope equipped with a step platform that can accurately adjust the level of defocusing.

$$k \frac{\partial I(\vec{r})}{\partial z} = -\nabla \cdot (I(\vec{r}) \nabla \phi(\vec{r})). \quad (4.2)$$

In this equation,  $I$  represents the intensity,  $z$  is the propagation direction,  $k$  is the wavenumber,  $\nabla$  is the gradient operator, and  $\phi$  represents the phase.

### 4.3.2 Refracted near field profilometry

Refracted near field (RNF) profilometry is a characterisation technique used to measure the refractive index profile of optical fibres and waveguides. It provides a non-destructive and direct way to ascertain the refractive index variation across the radial profile of an optical waveguide.

The principle of RNF is based on the near-field scanning technique. A probe scans the exit face of the waveguide or fibre under test, collecting the light that comes out. This light consists of a set of guided modes, each propagating at a specific angle determined by the local refractive index. Because of Snell's law, the refracted light beams are deviated at different angles based on their corresponding refractive indices [12].

By analysing the distribution of refracted light intensities at different angles, one can reconstruct the refractive index profile of the fibre or waveguide. An important prerequisite for accurate results is the use of a monochromatic light source to ensure that the measured refraction angles are only due to the refractive index variations and not due to wavelength-dependent effects.

Figure 4.3 shows a schematic of the measurement process. It can be observed that  $\theta_2$  corresponds to the refracted incident angle on the circumference of the disk. This angle corresponds to the input angle  $\theta_1$ . Between this angle  $\theta_1$  and  $(\theta_1)_{max}$ , the refracted light is not blocked by the disk and, therefore, is captured by the detector. The relationship between the angle  $\theta_2$  and

### 4.3. Characterisation techniques

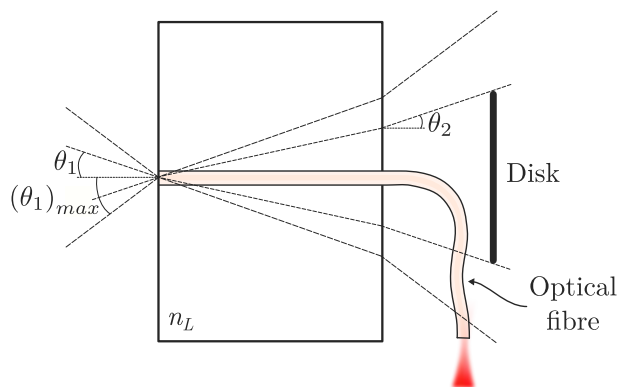


**Figure 4.3.** Measurement process of refracted near field profilometry on the end face of an optical fibre. Adapted from [13].

$\theta_1$  can be determined by applying Snell's law to the liquid cell, obtaining:

$$n^2(r) = \sin^2(\theta_1) + n_L^2 - \sin^2(\theta_2). \quad (4.3)$$

Taking into account that  $n_L$  and  $\theta_2$  are fixed during the measurement, a change in  $n(r)$  causes a variation in the angle  $\theta_1$ . Considering that the detector located behind the disk measures the output beam power for  $\theta \geq \theta_2$ , and that this amount is equivalent to  $P(\theta_1)$  (input beam power associated with the angle  $\theta_1$ ), disregarding possible losses, it is obtained:

$$P(\theta_1) = P(0) \left( 1 - \frac{\tan^2(\theta_1)}{\tan^2(\theta_1)_{max}} \right) \approx P(0) \left( 1 - \frac{\sin^2(\theta_1)}{\sin^2(\theta_1)_{max}} \right). \quad (4.4)$$

Given that the variation in the refractive index in the fibre is very small ( $\sim 1\%$  or even less), the following approximation can be made:

$$n(r) = n(0) + \delta(r) \longrightarrow n^2(r) = n^2(0) + 2n(0)\delta(r) + \delta^2(r) \stackrel{\approx 0}{\simeq} 2n(0)n(r) - n^2(0). \quad (4.5)$$

Combining equations 4.3, 4.4 y 4.5, the following relation is obtained:

$$P(\theta_1) \simeq a_1 - a_2 \cdot n(r), \quad (4.6)$$

being  $a_1$  and  $a_2$  constant values. It is deduced that the power of the refracted light cone is proportional to the refractive index of the focused point. Thus, using this technique and performing a sweep over the diameter of the fibre or waveguide, the detected optical power provides the refractive index profile.

#### 4.3.3 Raman spectroscopy

Raman spectroscopy is a spectroscopic technique used to study vibrational, rotational, and other low-frequency modes in a system. It provides a molecular fingerprint of a material, allowing to identify the chemical composition and structure of a sample [7, 14, 15].

The method is based on Raman scattering. When light interacts with a molecule, most

photons are scattered in an elastic manner, meaning their energy (and thus wavelength) remains unchanged. However, a small fraction of the light (typically around 1 photon in  $10^6$ – $10^8$ ) is scattered inelastically, meaning the photons' energy changes. This change in energy corresponds to a transition in the vibrational or rotational energy of the molecules in the sample.

In a Raman spectroscopy experiment, a laser is shone on a sample and the scattered light is collected and analysed. The energy of the inelastically scattered light is compared to the energy of the incoming laser light. The difference in energy is called the Raman shift and is specific to the chemical bonds and symmetry of the molecules, providing a spectrum that serves as a unique fingerprint of the sample. As it is a non-destructive technique, the sample can be studied in its natural state without the need for any prior preparation [16].

## References

- [1] Ross, C. A., MacLachlan, D. G., Choudhury, D., and Thomson, R. R., “Optimisation of ultrafast laser assisted etching in fused silica,” *Optics Express*, vol. 26, no. 19, pp. 24 343–24 356, Sep. 2018. DOI: 10.1364/oe.26.024343. [Online]. Available: <https://doi.org/10.1364/oe.26.024343>.
- [2] Ross, C. A. *et al.*, “A Miniature Fibre-Optic Raman Probe Fabricated by Ultrafast Laser-Assisted Etching,” *Micromachines*, vol. 11, no. 2, p. 185, Feb. 2020. DOI: 10.3390/mi11020185.
- [3] Roldán-Varona, P. *et al.*, “Selective plane illumination optical endomicroscopy with polymer imaging fibers,” *APL Photonics*, vol. 8, no. 1, p. 016 103, Jan. 2023. DOI: 10.1063/5.0130486.
- [4] Marini, M. *et al.*, “Microlenses Fabricated by Two-Photon Laser Polymerization for Cell Imaging with Non-Linear Excitation Microscopy,” *Advanced Functional Materials*, p. 2213926, Mar. 2023. DOI: 10.1002/adfm.202213926.
- [5] Ciriolo, A. G. *et al.*, “Microfluidic devices for quasi-phase-matching in high-order harmonic generation,” *APL Photonics*, vol. 7, no. 11, p. 110 801, Nov. 2022. DOI: 10.1063/5.0118199.
- [6] Rahman, A. and Agrawal, A., *Finite element modeling methods for photonics*. Artech House, 2013.
- [7] Bellouard, Y., Barthel, E., Said, A. A., Dugan, M., and Bado, P., “Scanning thermal microscopy and Raman analysis of bulk fused silica exposed to lowenergy femtosecond laser pulses,” *Optics Express*, vol. 16, no. 24, pp. 19 520–19 534, Nov. 2008. DOI: 10.1364/oe.16.019520.
- [8] Bellair, C. J. *et al.*, “Quantitative phase amplitude microscopy IV: Imaging thick specimens,” *Journal of Microscopy*, vol. 214, no. 1, pp. 62–69, Apr. 2004. DOI: 10.1111/j.0022-2720.2004.01302.x.
- [9] Barty, A., Nugent, K. A., Paganin, D., and Roberts, A., “Quantitative optical phase microscopy,” *Optics Letters*, vol. 23, no. 11, pp. 817–819, Jun. 1998. DOI: 10.1364/ol.23.000817.
- [10] Curl, C. L. *et al.*, “Refractive index measurement in viable cells using quantitative phase-amplitude microscopy and confocal microscopy,” *Cytometry Part A*, vol. 65A, no. 1, pp. 88–92, 2005. DOI: 10.1002/cyto.a.20134.
- [11] Mehta, D. S., Butola, A., and Singh, V., *Quantitative Phase Microscopy and Tomography*. IOP Publishing, Dec. 2022. DOI: 10.1088/978-0-7503-3987-2.
- [12] White, K. I., “Practical application of the refracted near-field technique for the measurement of optical fibre refractive index profiles,” *Optical and Quantum Electronics*, vol. 11, no. 2, pp. 185–196, Mar. 1979. DOI: 10.1007/bf00624397.
- [13] Roldan-Varona, P., “Post-processing of optical fibres using femtosecond lasers,” M.S. thesis, Universidad de Cantabria, Jul. 2019. [Online]. Available: <http://hdl.handle.net/10902/16620>.

- [14] Sugiura, H. and Yamadaya, T., “Raman scattering in silica glass in the permanent densification region,” *Journal of Non-Crystalline Solids*, vol. 144, pp. 151–158, Jan. 1992. DOI: 10.1016/s0022-3093(05)80395-3.
- [15] Chan, J. W., Huser, T., Risbud, S., and Krol, D. M., “Structural changes in fused silica after exposure to focused femtosecond laser pulses,” *Optics Letters*, vol. 26, no. 21, pp. 1726–1728, Nov. 2001. DOI: 10.1364/ol.26.001726.
- [16] Fernández-Manteca, M. G. *et al.*, “Automatic classification of *Candida* species using Raman spectroscopy and machine learning,” *Spectrochimica Acta Part A: Molecular and Biomolecular Spectroscopy*, vol. 290, p. 122270, Apr. 2023. DOI: 10.1016/j.saa.2022.122270.

# PART II

## ULTRAFAST LASER DIRECT WRITING (ULDW)

This part showcases the contributions made in the field of optical fibre sensors using direct inscriptions with ultrafast lasers. The results obtained in the first half of the thesis, spanning from October 2019 to July 2021, are consolidated in this part of the document. Significant advancements are presented regarding the challenges encountered when depositing focused ultrashort pulses within transparent materials. Techniques for achieving specific focal volumes are explored, leading to enhanced performance in fibre Bragg gratings and cladding waveguides using the slit beam shaping technique. Furthermore, the fabrication of sensors based on standard telecommunications optical fibres and specialty fibres is documented. These sensors encompass a range of applications, including multiparametric sensing, lab-in-fibre devices integrated into surgical needles, liquid level sensing within hollow-core fibres, and refractometers optimised for water-based solutions using perfluorinated polymer fibres. Overall, the part showcases the progress achieved in the development of optical fibre sensors through direct inscriptions with ultrafast lasers.

The chapters included in this part are:

- Chapter 5: Enhancement of ULDW-based passive in-fibre structures.
- Chapter 6: Standard fibre-based sensors.
- Chapter 7: Specialty fibre-based sensors.

# 5

## Enhancement of ULDW-based passive in-fibre structures

---

<b>5.1</b>	<b>Optical aberrations and light focusing issues</b>	<b>52</b>
5.1.1	Astigmatism in optical fibres	54
<b>5.2</b>	<b>Cross-section control of refractive index changes</b>	<b>58</b>
5.2.1	Slit beam shaping technique	58
5.2.2	Astigmatic beam shaping technique	59
5.2.3	Spatiotemporal focusing	60
5.2.4	Multiscan technique	60
5.2.5	Adaptive optics	61
<b>5.3</b>	<b>Slit beam shaping technique for PI-b-PI FBGs</b>	<b>62</b>
5.3.1	Background	62
5.3.2	Control of the cross-section of the focal volume	64
5.3.3	Pulse energy setting	66
5.3.4	Experimental results and discussion	68
5.3.5	Conclusions	72
<b>5.4</b>	<b>Slit beam shaping technique for symmetric CWGs</b>	<b>73</b>
5.4.1	Background	73
5.4.2	Fs laser inscription of CWGs	74
5.4.3	Structure design and simulations	76
5.4.4	Experimental results and discussion	79
5.4.5	Conclusions	82
	<b>References</b>	<b>84</b>

---

**O**PTICAL aberrations in laser processing can significantly degrade the precision and efficiency of the process. These aberrations occur when light fails to converge at a single point due to non-uniform refractive index distribution, often caused by imperfections in optical compo-

## 5.1. Optical aberrations and light focusing issues

nents or by the medium through which the light is passing. This disrupts the focusing of light and introduces distortion, changing the form of the focal intensity distribution and potentially affecting the quality of the fabricated device.

The two first sections of the chapter will address theoretical-practical aspects related to the problems that arise when inscribing optical structures using ultrashort laser pulses tightly focused within transparent materials. Specifically, the section 5.1 will present the main optical aberrations that occur, as well as ways to limit them in laser manufacturing, considering, among others, the work developed by Pallarés *et al.* [1]. On the other hand, the section 5.2 deals with the different practical methods used to control the cross-section of the refractive index change (RIC) induced in the material, *i.e.*, the refractive index profile of the optical structure to be manufactured.

Among the different ways of controlling the focal volume of ultrashort focused pulses is the slit beam shaping technique (SBST). In sections 5.3 and 5.4, two works carried out by Roldán *et al.* are developed, corresponding to the use of this technique for the inscription of plane-by-plane FBGs [2], as well as symmetric cladding waveguides as transitions for the evanescent coupling of light from the core of single-mode fibres (SMF) to the cores of multicore fibres [3], respectively.

## 5.1 Optical aberrations and light focusing issues

Inscribing transparent materials with ultrafast lasers is an important tool in the ever-evolving field of waveguide-based photonic devices. However, challenges persist despite significant strides made in waveguide writing and application. A primary concern lies in the management of optical aberrations and light focusing issues during the inscription process. The ultrafast laser direct writing technique, while providing 3D fabrication capabilities, encounters difficulties in achieving low insertion loss, symmetric mode fields, and reduced propagation loss. Furthermore, the phenomena of filamentation and self-focusing can alter energy-deposition behaviour and resultant microstructures, limiting its performance [4].

The types of aberrations typically encountered in laser processing can be classified into two main categories: chromatic and monochromatic (or Seidel) aberrations.

### Chromatic aberrations

This type of aberration arises due to the dependency of a material's refractive index on the wavelength of light. Different wavelengths of light refract differently when they pass through an optical material, causing them to focus at different points along the optical axis. This results in coloured fringes around the image, reducing its quality. In most laser processing applications, chromatic aberration is indeed not a significant concern because lasers usually output light at a single wavelength. This is why chromatic aberration is most noticeable in broadband light sources that encompass multiple wavelengths, like supercontinuum lasers.

However, it is worth noting that even in a single-wavelength laser system, chromatic aberration could potentially become an issue in certain scenarios. For example, in ultrafast lasers, the ultrashort pulse will have a broad spectrum despite being centred around a single wavelength.

In such cases, the dispersion caused by chromatic aberration could affect the pulse shape and duration [5], which can be significant in precision applications. Another case where chromatic aberration could be significant is when the laser system uses second harmonic generation (SHG), third harmonic generation (THG), or other non-linear optical processes that effectively create new wavelengths from the original laser beam [6]. The different generated wavelengths, if they are not removed from the optical path, could then focus at different points due to chromatic aberration, affecting the overall process.

### Monochromatic aberrations

These aberrations are caused by the geometrical properties of the material and include five primary types:

- **Spherical aberration (SA)**

The most troublesome aberration in ultrafast laser processing is SA. Spherical aberration is a prevalent issue when a tightly focused femtosecond laser irradiates a glass [7, 8]. The RI mismatch between air and glass distorts the energy distribution in the focus, leading to modified volumes' shape alterations [9]. Increasing numerical aperture, focusing depth, or the refractive index of the substrate exacerbates SA, resulting in focus distortion [10].

The use of immersion techniques, specifically water-immersion and oil-immersion, are highly effective methods to reduce spherical aberrations [11]. Both techniques function by replacing the air between the lens and the sample with a medium that closely matches the refractive index of the lens. This adjustment minimises the refractive index mismatch that causes SA. They are particularly useful for high-resolution writing because the use of lenses with a very high NA is feasible.

- **Astigmatism** → this type of aberration is due to the material having different focal lengths in different meridians. Astigmatism causes points of light off the optical axis to form lines of light in the focal plane. In the context of laser processing, this could be seen in the form of focal splitting, particularly when working with samples that have an irregular or curved surface, like an optical fibre, as will be seen later [1].
- **Coma** → coma or *comatic* aberration occurs when off-axis light rays focus at different points, resulting in a “comet-like” tail. This typically occurs when a point source of light is not positioned directly in front of the optical system.
- **Distortion** → distortion aberration does not affect focus but changes the shape of the image. Pincushion distortion swells the center of the image, while barrel distortion squeezes it.
- **Field Curvature** → field curvature aberration is when the best focus is not a flat plane but a curved one. This results in the center and edge of the field of view not being in focus at the same time.

### Other types of aberrations

Other types of aberrations commonly encountered in laser processing occur at the edges of samples [12]. This is particularly the case when the laser is used to write transverse waveguides. These aberrations relate to the parts of the fabrication laser that focus through different facets of the sample, leading to a phenomenon known as focal splitting. Furthermore, when focusing occurs inside birefringent media [13], where different polarisation modes couple to different refractive indices, additional focal splitting can occur.

### Aberration correction

While identifying aberrations can be quite intricate in broad optical systems, in the context of laser processing applications the process can be simplified significantly. The prime factor to consider, in many instances, is the depth-dependent spherical aberration [4, 10]. By tracing the light rays from the focal point back to the objective lens's pupil plane, an analytic formula for the phase of the depth-dependent SA can be derived [14]. This concept allows for the deployment of an adaptive optical component in a plane that is conjugate to the pupil of the objective lens, which can apply the counter-phase. This predictive correction of aberration is sufficient in many circumstances. Nonetheless, when a higher degree of precision in aberration correction is required, a method of focal feedback is essential to fine-tune the correction phase [9, 15, 16].

When it comes to the fabrication of intricate 3D devices, aberration correction proves to be highly advantageous, particularly when the fabrication depth surpasses  $\sim 1$  mm. For fabrications of high resolution, such as two-photon polymerisation, aberrations can have a critical effect [17, 18]. However, the application of aberration correction can significantly amplify the spectral attributes of devices and has demonstrated success in a variety of materials, including lithium niobate and chalcogenides [19, 20]. Additionally, the correction of aberration has revolutionised the process of inscribing 3D conductive graphitic wires beneath the diamond's surface [21], causing a substantial reduction in the resistivity of the wires. This breakthrough paves the way for fabricating radiation detectors and components vital for quantum processing.

#### 5.1.1 Astigmatism in optical fibres

The main challenge encountered when writing structures within optical fibres is the cylindrical shape, which results in significant astigmatism in the focal volume. Consequently, the laser intensity at the focal point is reduced. While immersion techniques can help alleviate this issue, they require a specific microscope objective. Zhou *et al.* proposed an alternative method to mitigate this astigmatism without the need for such objectives [22]. This method has been successfully used in waveguide and FBG inscription [2, 3, 23]. Below, it is briefly described the impact of the astigmatism induced by the optical fibre's geometry on power distribution in the focal volume. It is also presented the phase changes observed in inscriptions using astigmatic correction compared to direct exposure at the fibre core.

According to [24], when a laser pulse with a wavelength  $\lambda$  is tightly focused using a objective lens with a given NA (and a background index  $n_0$ ), onto a planar dielectric sample with a refractive index  $n$ , the width of its waist ( $w_0$ ) and the Rayleigh length ( $z_0$ ) can be determined

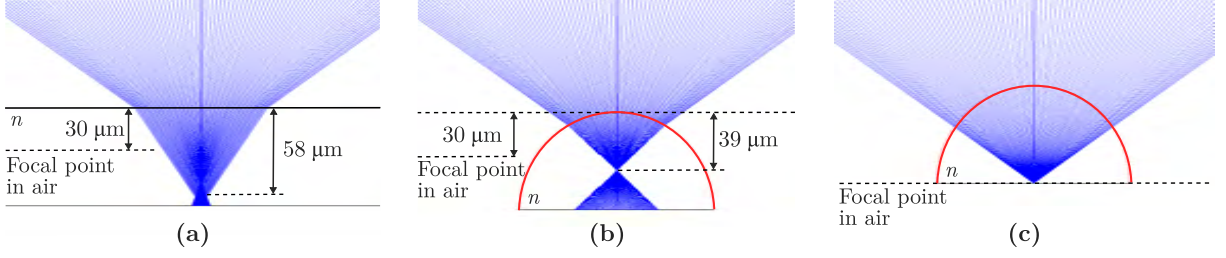


**Figure 5.1.** Ray tracing analysis using OpticStudio Zemax considering an objective lens with a NA of 0.5. The lens was focused on three different scenarios: **(a)** planar object with  $n = 1.45$ , positioned  $30 \mu\text{m}$  above the working distance, **(b)** circular object with the same RI positioned at the same location, and **(c)** circular object with the same RI positioned at the working distance with its centre aligned.  $\lambda = 1030 \text{ nm}$  is considered. Adapted from [1].

using Equations 2.6 and 2.7.

This planar index change already induces a displacement on the focal point perpendicular to the refractive index (RI) quotient  $n/n_0$  in the paraxial region. The focal point is displaced to  $z' = (n/n_0) \cdot z$  (paraxial approximation), where  $z$  is the distance from the interface to the focal point in  $n_0$ . In the majority of ultrafast laser applications, a high NA is employed, in which the paraxial approximation is no longer valid. Therefore, ray trajectories with larger angles will focus below the paraxial approximation, leading to spherical aberrations. Thus, there is a defocusing proportional to the inscription depth and displacement of the focal point. Such loose of focusing is depicted in Fig. 5.1 **a** for a  $\lambda = 1030 \text{ nm}$  light source focused through a  $\text{NA}=0.5$  lens in air and a dielectric medium  $n = 1.45$  with its interface placed  $30 \mu\text{m}$  above focal spot in air.

When the incident light encounters a circular geometry, it undergoes the typical focusing that one would expect from a lens. For instance, if the planar surface shown in Fig. 5.1 **a** is replaced with a circular surface measuring  $125 \mu\text{m}$  in diameter, *e.g.*, the optical fibre diameter, the focal spot would shift  $9 \mu\text{m}$  below, as depicted in Fig. 5.1 **b**. However, there is a special case when the focal spot aligns with the centre of the circumference. In this particular situation, all the rays are perpendicular to the surface of the circumference, resulting in no displacement of the focal spot, as shown in Fig. 5.1 **c**. In this case, the Gaussian waist and Rayleigh length (considering  $M^2 = 1$ ) can be calculated using the following equations [24].

$$w_0 = \frac{\lambda}{n\pi\text{NA}}, \quad (5.1) \quad z_0 = \frac{\lambda}{n\pi\text{NA}^2}. \quad (5.2)$$

When a Gaussian beam is focused inside an optical fibre, the parallel and perpendicular axes to the fibre's axis will display distinct characteristics, resembling an orthogonal astigmatic beam. The distribution of intensity for a basic astigmatic Gaussian beam with a power  $P$  is described in [25].

$$I(z) = \frac{2P}{\pi w_x(z)w_y(z)} e^{-2\left(\left(\frac{x}{w_x(z)}\right)^2 + \left(\frac{y}{w_y(z)}\right)^2\right)}, \quad (5.3)$$

$$w_i(z) = w_{0i} \sqrt{1 + \left(\frac{z - z_{0i}}{z_0}\right)^2}. \quad (5.4)$$

## 5.1. Optical aberrations and light focusing issues

When comparing the beam intensity along the  $z$  direction at the centre of an astigmatic beam generated by an optical fibre and a stigmatic beam produced by a planar sample, the latter demonstrates a higher intensity concentrated in a lower region. This observation is illustrated in Fig. 5.2 **a** using the provided parameters. The intensity distribution of the astigmatic beam reveals two peaks corresponding to the positions of minimal waist, whereas the stigmatic intensity distribution displays a single peak with a significantly greater magnitude compared to the maximum of the astigmatic beam. Figure 5.2 **b** presents the focal volume of the stigmatic and astigmatic beams at different intensities, all normalised to the maximum intensity of the stigmatic beam. It is important to note that the astigmatic focal volume does not contain intensities higher than 10% of the normalised maximum, requiring higher laser pulse energies to induce modifications to the material. Consequently, this increases the modification threshold of the astigmatic beam.

### Phase study

An experimental characterisation of this aberration has been studied by analysing the phase of induced refraction index changes. Line inscription was carried out using a femtosecond laser chirped pulse amplifier from Calmar ( $\lambda = 1030$  nm, 370 fs, PRR=120 kHz). The pulses were focused through a Mitutoyo  $\times 100/\text{NA}=0.5$  objective lens, using a conventional SMF-28 placed on a nano-resolution movable stage from Aerotech. To mitigate astigmatism in the focal volume, the approach introduced by Zhou *et al.* [22] was employed. This method involves the use of a drop of index-matching oil surrounding the fibre, sandwiched between a slide and a coverslip.

The impact of astigmatism removal is evident in Fig. 5.3 **a**, which shows two intensity images of inscribed lines with a pulse energy of 470 nJ (at a speed of 0.1 mm/s). The width of the pattern inscribed with direct exposure is significantly narrower than that of its corrected counterpart. Furthermore, the modification appears smoother, without the sharp details typically associated with high fluence inscriptions.

For a more quantitative analysis, the phase change was determined using QPM [26], with a  $\delta = \pm 3$   $\mu\text{m}$  defocusing. Several lines were inscribed at speeds of 0.1 mm/s, with pulse energies

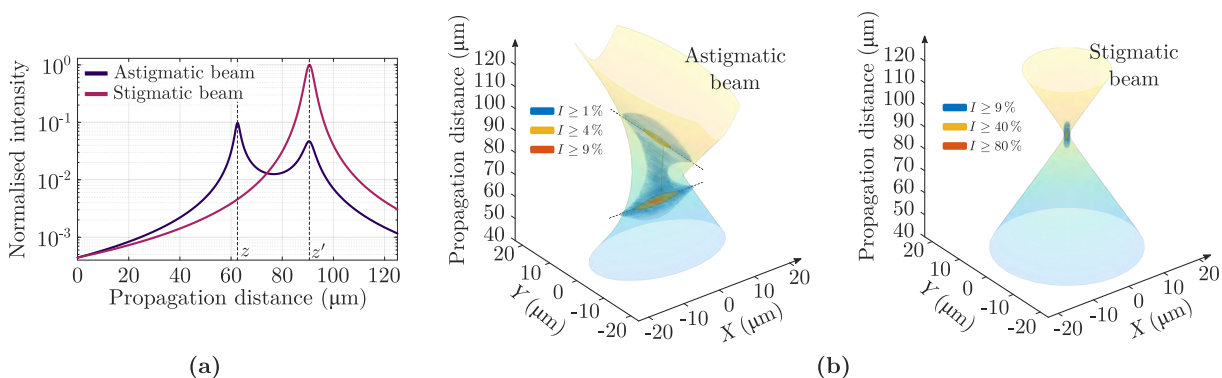


**Figure 5.2.** (a) Distribution of intensity along the material at the centre of the beam varies with the propagation distance for stigmatic and astigmatic beams. Intensity has been normalised to the maximum intensity of the stigmatic beam. (b) Focal volume for both beams, where the astigmatic focal volume does not exceed intensities higher than the normalised 10%.  $\lambda = 1030$  nm and  $n = 1.45$  are considered. Adapted from [1].

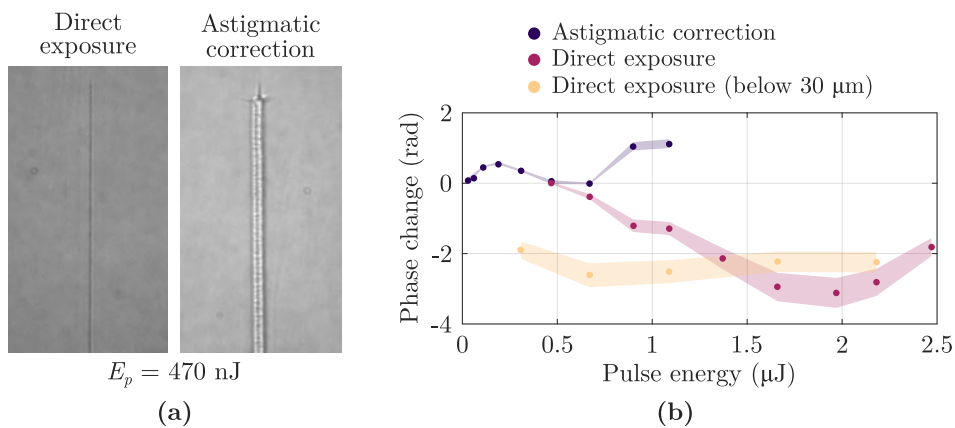


**Figure 5.3.** (a) Femtosecond laser inscription in a fibre with and without astigmatic correction at a pulse energy of 470 nJ. (b) Comparison of the phase change versus pulse energy for inscribed lines with and without astigmatic compensation when focused at the fibre core, as well as 30  $\mu\text{m}$  below the surface without astigmatic correction. Adapted from [1].

ranging from 0–2.5  $\mu\text{J}$ , both with and without astigmatic correction. The results are shown in Fig. 5.3 b, where the first phase changes occur at 60 nJ with astigmatic correction, while direct exposure requires 470 nJ. This corresponds to an approximate factor of 10. The most notable distinction between the two types of inscription is their sign: astigmatic beams produce a negative change, while corrected beams produce a positive phase change.

The inscription exhibits four regions. The first region, ranging from 0–0.31  $\mu\text{J}$ , is characterised by a smooth, positive Type I RIC. From 0.31–0.67  $\mu\text{J}$ , the width of the lines increases, with an exterior region exhibiting a high phase change and an interior region displaying a lower phase change. As the pulse energies increase, the structure becomes more complex, with positive change predominating despite the formation of secondary structures with negative indices. Filamentation is likely to occur in this regime. For pulse energies higher than 1.09  $\mu\text{J}$ , the pulse damages the coverslip, leading to measurement errors in the phase change.

In contrast, direct exposure results in a negative index change that is thinner than its corrected counterpart. Initially, a smooth negative RIC is observed until 1.09  $\mu\text{J}$ , after which the focal volume experiences an abrupt negative phase increase before stabilising at 1.97  $\mu\text{J}$ . The phase change then decreases monotonically. The inscribed lines in this region exhibit filamentation, with the length of the filaments dependent on the writing speed. These filaments can exhibit positive RIC in specific zones, making them capable of guiding light [27]. Additionally, inscriptions were performed with and without astigmatism correction at a focal point 30  $\mu\text{m}$  below the fibre surface. In this case, the degree of astigmatism is significantly lower, allowing for a high phase change of 0.31  $\mu\text{m}$  (below the modification threshold for the same parameters focused at the core). However, the phase change remains relatively stable with laser fluence. Filamentation occurs throughout this region, with filament lengths exceeding those observed in the core counterpart.

From the above discussion, it is evident that astigmatism correction not only reduces the modification threshold but also enables the creation of smooth Type I RICs that would not be achievable otherwise. These changes are beneficial for waveguide inscription, particularly for multiscan inscription [23], as well as for grating inscription [2], as it is presented in the following sections.

## 5.2 Cross-section control of refractive index changes

The refractive index profile of the focal volume – or cross-section – of an optical waveguide is a pivotal property that governs the number and properties of the transverse modes supported by the waveguide. Accordingly, precise control of the waveguide cross-section is paramount in optimising the performance of the waveguide device.

Addressing the issues stated in the previous section is critical for the creation of complex reconfigurable photonic circuits, vital for highly integrated on-chip devices with multifunctionality [28]. Also, the demand for fabricating waveguides (WGs) with high uniformity and efficiency is on the rise [29], pushing for better control over the highly non-linear process in WG writing and setup stability [30]. To advance the development and wide-scale implementation of integrated photonic devices, it is crucial to confront the challenges at hand.

The direction of substrate translation during inscription has a significant impact on the waveguide cross-section. Longitudinal writing geometry, where the substrate moves along the laser beam’s direction, and transverse writing geometry, where it moves perpendicular to it, yield different results. When inscribing using a circular Gaussian beam (and single pulse regime, *i.e.*, no thermal accumulation) and longitudinal geometry, the waveguide core’s cross-sectional size corresponds directly to the beam waist diameter (twice the value of beam waist radius given in Equation 2.6). In transverse geometry, the waveguide core size is also related to the beam waist diameter, but the size along the  $Z$ -axis correlates with the Rayleigh length (Equation 2.7).

As expected, waveguides inscribed using longitudinal geometry are inherently circular due to the laser beam’s rotational symmetry. However, the waveguide length is confined to the focusing lens’s working distance. Additionally, varying the focus depth inside the sample alters the SA imparted on the laser beam by the substrate, which in turn changes the electric field distribution around the focus and the form of the modification along the waveguide. Hence, the more versatile transverse writing geometry has garnered more attention. However, it is worth noting that waveguides inscribed in the single pulse regime using transverse writing geometry exhibit significant asymmetry unless the beam waist radius is close to the light’s free space wavelength divided by the substrate’s RI. Achieving such a small spot size would require a focusing NA close to the refractive index (see Fig. 5.4). However, creating such small waveguides often results in poor confinement of the guided mode, particularly at telecommunication wavelengths (1.3 and 1.55  $\mu\text{m}$ ), considering that the maximum RIC of ultrafast laser inscribed waveguides is usually limited to about 0.5% in most materials. Thus, for many applications, the waveguide’s width must be increased to support the mode adequately. The following discussion highlights some of the cutting-edge experimental techniques developed to control the cross-section of ultrafast laser-inscribed structures [31].

### 5.2.1 Slit beam shaping technique

There are multiple ways to control the cross-section of the focal volume, through a variation in the beam waist ratio. However, most of them require additional optics, such as astigmatic beam shaping, active optics or spatiotemporal focussing techniques, so alignment can be a major problem. Initially utilised in the creation of embedded microchannels with symmetric cross-sections [32]. Not long after its initial application, the technique was adapted for the inscription

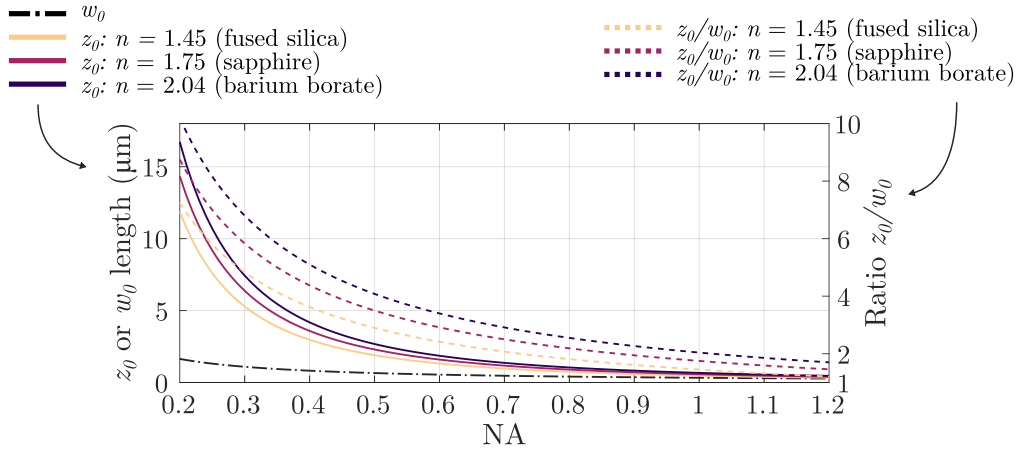


**Figure 5.4.** Waist radius ( $w_0$ ) and Rayleigh length ( $z_0$ ) for different numerical apertures and substrates, assuming  $\lambda = 1030$  nm. The ratio  $z_0/w_0$  is also presented. In essence, the higher the substrate's refractive index or the lower the numerical aperture, the greater the asymmetry in the focal volumes.

of optical waveguides [33].

The slit beam technique consists in modifying the beam previously to the objective lens by introducing a slit (see Fig. 5.21), which offers greater simplicity and control than previous techniques. The focal volume of a focused Gaussian beam is defined by the waist radius ( $w_0$ ) and the Rayleigh length ( $z_0$ ):

$$w_{0i} = \frac{\lambda}{\pi \text{NA}_i} \simeq \frac{\lambda f}{\pi D_i}, \quad \forall i = \{x, y\}. \quad (5.5)$$

$$z_{0i} = \frac{n\lambda}{\pi \text{NA}_i^2}, \quad \forall i = \{x, y\}. \quad (5.6)$$

where NA is the numerical aperture of the objective lens,  $f$  its focal length,  $D_i$  beam diameter at the lens input in axis  $i$ ,  $\lambda$  the laser wavelength, and  $n$  the refractive index of the substrate. Therefore,  $w_0$  and  $z_0$  can vary in each axis ( $X$ ,  $Y$ ) if the NA is different in each axis, *i.e.*, if the diameter of the input beam ( $D$ ) is different in each axis.

The slit is aligned with the direction of sample translation, effectively reducing the NA of the focusing in the plane that is perpendicular to the axis of the waveguide. This means that the slit has control over the beam waist ratio, and therefore, the symmetry of the waveguide. Unlike the astigmatic beam shaping method, the slit beam shaping technique allows for an easier and more flexible control of the beam waist ratio, which can be achieved using an adjustable slit. It is important, however, to acknowledge that this technique is not efficient in terms of power, as the slit obstructs a substantial portion of the pulse energy. In sections 5.3 and 5.4, this technique is used for the fabrication of FBGs and in-fibre cladding waveguides.

### 5.2.2 Astigmatic beam shaping technique

The astigmatic beam shaping technique, pioneered by Cerullo *et al.* in 2002 [34], employs an astigmatic optical system, typically involving cylindrical lenses, to shape the laser beam before it is focused onto the substrate. Essentially, this technique modifies the shape of the inscription laser beam, thereby controlling the shape of the modified region [35]. It capitalises on the fact

## 5.2. Cross-section control of refractive index changes

that the waveguide's width remains independent of the  $X$ -axis beam waist diameter, allowing for a reduction in the waveguide's  $Z$ -axis width by focussing tightly along the  $X$ -axis. In practice, this approach requires a careful balance between beam waist ratios and astigmatic difference (the offset in the focal planes for  $w_{0x}$  and  $w_{0y}$  [1]). The primary aim is to control the region of highest intensity, typically found in the plane corresponding to the smallest spot ( $w_{0x}$ ), by adjusting the astigmatic difference.

Achieving the desired waveguide symmetry in practice is more complex than it might seem theoretically. To inscribe a waveguide with a symmetric cross-section, a beam waist ratio ( $w_{0y}/w_{0x}$ ) of approximately 10 would be required, which demands a high demagnification cylindrical telescope. This presents practical challenges as it would be difficult to align, and introduce aberrations. Cerullo *et al.* proposed a solution to this issue [34]: by adjusting the astigmatic difference, a symmetric waveguide could be inscribed using beam waist ratios of only 2 to 3.

However, it is important to remember that while astigmatic beam shaping can significantly improve the symmetry of the inscribed waveguides, it may not completely eliminate all forms of asymmetry, as other factors such as spherical aberration, and self-focusing. Therefore, it is often used in conjunction with other techniques or adaptive optical elements for the best results.

### 5.2.3 Spatiotemporal focusing

Astigmatic and slit beam shaping techniques, despite their proven success, have certain drawbacks. One of them is that they are not ideal for creating waveguides with non-linear paths as the cross-section of the waveguide alters with the shift in the sample translation direction. An alternative that provides a solution to this is the spatiotemporal focusing technique (STF), first applied by He *et al.* [36]. This technique offers a distinct advantage as it controls the Rayleigh range of the focus, independent of the beam waists that are focused. As a result, STF could facilitate the creation of optical waveguides with a symmetrical cross-section, regardless of the direction of sample translation.

In the STF method, a spectral chirp is applied across the beam before it reaches the objective lens. This chirp decreases the spectral bandwidth of the pulse at each point across the beam, leading to the temporal stretching of the pulse [36–38]. The complete restoration of the pulse duration can only occur in the focal region, where the spectral components of the pulse spatially converge again. This means the pulse is focused both in space and time by the objective lens.

### 5.2.4 Multiscan technique

In multiscan technique, the cross-section is constructed by scanning many times the substrate through the focus of the laser beam. By combining the lines of modified material induced by each scan it is possible to correct not only the asymmetry of the waveguide, but also its refractive index. This is because the structure of the material depends strongly on its thermal history. The fast cooling suffered by the material after each scan involves an increase in the fictive temperature which, in the case of fused silica (unlike common glass), implies densification [39, 40], and therefore an increase in the refractive index of the waveguide formed by multiple scans.

The waveguide manufacture consists in multiple inscriptions with sub-micron displacements

perpendicular to both the laser beam propagation axis and waveguide axis between each scan [41] (see Fig. 6.2). This *inscribe-and-move* process ends when the structure with the required geometrical properties is obtained, typically when the desired waveguide width is achieved.

### 5.2.5 Adaptive optics

Adaptive optics (AO), originally engineered for astronomical applications, are now showing their potential in ultrafast laser processing. They offer enhanced functionality and flexibility, powering laser processing systems' capabilities. As stated in the review conducted by Salter and Booth in 2019 [4], by employing just one adaptive component, it is feasible to rectify aberrations that occur when focusing within the workpiece [42, 43], adjust the focal intensity distribution for the specific fabrication procedure [44–46], and provide parallelisation to decrease processing durations [47]. This is particularly advantageous for applications that utilise ultrafast lasers for three-dimensional manufacturing. An adaptive optical component allows manipulation over the fabrication laser beam, making it possible to dynamically update it during processing [4]. These adaptive elements can modify the phase, amplitude, and/or polarisation of the fabrication beam, offering numerous possibilities for enhanced control over the laser fabrication process.

The incorporation of AO with laser fabrication can yield numerous benefits, either by controlling the spatial and temporal intensity distribution at the laser focus or through adaptive parallelisation of the process. AO can correct optical aberrations that cause distortions in light focusing, which consequently changes the form of the focal intensity distribution. Even without optical aberrations, adaptive optical elements can facilitate the complex shaping of the laser focus, which can be adjusted during fabrication to produce different shapes for different parts of a device. Addressing a major challenge in laser writing, the point-based nature of the process that can result in extended processing times, adaptive optical elements can be used. These elements can divide a beam and simultaneously create multiple foci through a single lens for parallel processing [18, 48]. The reconfigurability of the element allows for updates to the spot pattern during processing, enabling the creation of large, complex structures.

There exists a range of reconfigurable optical elements capable of altering a beam's properties across its profile. Liquid crystal-based spatial light modulators (SLMs) are the most prevalent adaptive elements [18, 42, 47], owing to their ease of use, operational flexibility, and high resolution. These devices can continuously modulate the output state of the laser beam. Digital mirror devices (DMDs), developed on micro-electromechanical system (MEMS) platform, offer amplitude modulation by steering light into or out of the laser beam path [48]. Despite their high-speed switching capability, they do come with limitations, including the binary nature of the amplitude modulation. Another type of adaptive element is deformable mirrors (DMs), which consist of a highly reflective surface that can be shaped by forces from an array of actuators [49]. These mirrors are not affected by polarisation and have a good reflectance over a broad range of wavelengths.

In conclusion, AO technology has the potential to transform laser processing by providing superior control over the laser fabrication process. This will not only enhanced the performance of optical devices but also expanded their potential applications in the field of integrated photonics.

## 5.3 Slit beam shaping technique for Pl-b-Pl FBGs

This section discusses the creation of plane-by-plane (Pl-b-Pl) fibre Bragg gratings using a single pulse, achieved by using a longitudinal slit to shape the laser beam and widen the focal volume in the transverse direction of the fibre. This allows for 2D modifications of the refractive index, where the width and height depend on the slit width and pulse energy, respectively. The relationship between the diameter of the Gaussian laser beam and the slit width is determined mathematically to obtain a circular cross-section. The experimental results show that Pl-b-Pl FBGs with a  $D_x/D_y$  ratio of 3 produce positive and uniform refractive index changes, which is an improvement over the negative and uneven changes seen with point-by-point (PbP) FBGs. Pl-b-Pl FBGs also have lower transmission losses (0.3 dB) and better reflectivity and full-width-at-half-maximum (FWHM) due to their broader modification of the core cross-section. The relationship between these three parameters and the slit width is found to be monotonic. The study also evaluates the polarisation dependence of the FBGs.

### 5.3.1 Background

FBGs written with femtosecond lasers exhibit a great interest given the increased temperature resistance and also a better flexibility of wavelength and composition, thanks to their characteristic high peak power densities that makes possible to achieve non-linear ionisation at arbitrary locations [50, 51]. Besides, FBGs can not only be manufactured with the phase mask technique [52], but also can be produced with the direct-write technique, which is far more versatile than phase mask (works only for a given period and wavelength), being attractive for multiplexing applications [3, 53].

Within the direct-write technique [54], there are three types of inscription, namely, point-by-point, line-by-line (LbL) and plane-by-plane. The first one, PbP, essentially consists in the inscription within the fibre core of a line parallel to the fibre axis. The line is inscribed with a writing speed  $v = \Lambda \cdot \text{PRR}$  where  $\Lambda$  is the grating period and PRR the pulse repetition rate [24], allowing single pulses to be deposited with proper separation (Fig. 5.5 a). This type of inscription is simple and straightforward. However, it usually exhibits strong broadband losses [55, 56], lower grating strength and also the coupling of higher order modes. To limit the latter, any refractive index change must precisely coincide with the longitudinal axis of the optical fibre, requiring precise alignment. This can be explained through the Coupled Mode Theory (CMT) and the transversal coupling constant between two modes [57]:

$$\kappa_{ab} = \iint 2\epsilon_0 \cdot \Delta n_m(x, y) \cdot n(x, y) \cdot \mathbf{E}_a^T(x, y) \cdot \mathbf{E}_b^{T*}(x, y) \cdot dx dy. \quad (5.7)$$

Here, if  $\Delta n_m(x, y)$  covers the entire cross-section of the fibre homogeneously (being constant), then the orthogonality relation will exclude coupling between different modes. However, if  $\Delta n_m(x, y)$  is asymmetric as the laser modification does not cover the entire core cross-section, then light will be decoupled to higher  $m$  and  $l$  modes [24].

The LbL technique was first employed by Zhou *et al.* [58] and is depicted in Fig. 5.5 b. Here, instead of a single inscription, several lines are inscribed perpendicular to the longitudinal axis. This method is significantly slower than PbP, but covers more cross-section of the core,

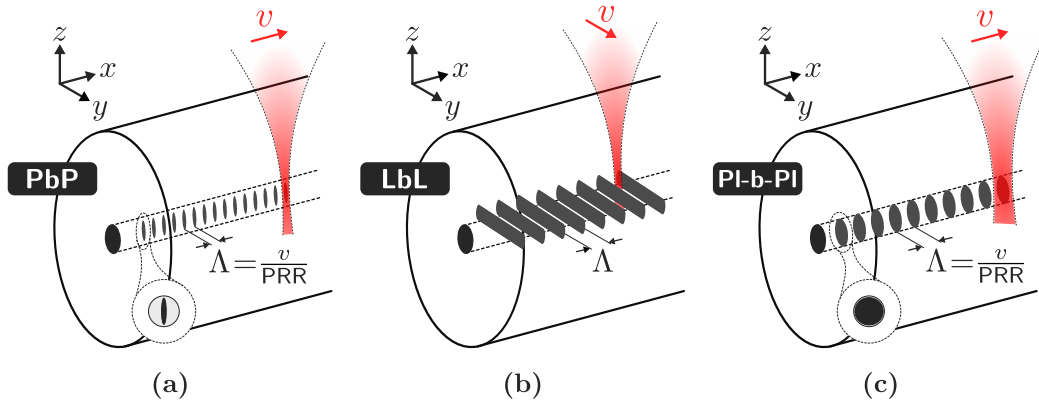


**Figure 5.5.** Direct-write methods of FBG inscription with fs laser. (a) Point-by-point (PbP), (b) line-by-line (LbL), and (c) plane-by-plane (PI-b-PI). Adapted from [2].

reducing the amount of cladding modes coupled. However, the line geometry is quite exploited to manufacture tilted FBGs where cladding modes are enhanced, allowing sensitivity to external changes. This larger and also smoother area can allow lower broadband losses, which depend on the length and roughness of the lines. Furthermore, the LbL inscription method allows the manufacture of relatively complex structures, by allowing flexible control over each inscribed line (*e.g.*, induced refractive index change [59]).

Finally, the PI-b-PI method involves the inscription of a plane that produces a quasi-homogeneous 2D refractive index change in the core (or cladding) cross-section [60]. This method involves flexible control of the width (direction of the  $Y$  axis in Fig. 5.5) and height ( $Z$  axis) of the planes, since the thickness of the plane ( $X$  axis) is defined by the laser wavelength and the numerical aperture of the objective lens. Thus, width and height of equal dimensions are possible. PI-b-PI method, depicted in Figure 5.5 c, was first reported in 2016 by Theodosiou *et al.* [53], and has subsequently been used in multiple applications, such as polymer optical fibres [61], or the inscription of gratings and interferometric in-fibre components [62, 63]. Another attractive way to achieve such control is by shaping the focal volume into a plane, thus writing planes in a single pulse in a similar way to PbP method. This was successfully achieved by Lu *et al.* by means of a cylindrical lens before the microscope objective, which induces astigmatism in the focal volume [64]. This concept is quite similar to the astigmatic beam shaping technique, where a cylindrical telescope modifies the resulting Rayleigh range after the microscope lens in order to achieve circular waveguides [35]. Another method to get planar modifications with a single pulse is the slit beam method, employed by Ams *et al.* to carry out waveguides [33]. Here, the cylindrical telescope is replaced by a simple slit before the objective lens, being more compact and requiring much less adjustment, but with a higher pulse energy requirement. The use of a slit was also used to reduce the focal volume distortions caused by the induced astigmatism due to the cylindrical fibre geometry [65].

In this section the slit beam method will be employed to generate PI-b-PI gratings with a single pulse. Here, one step further is taken by shaping the beam to a more adequate geometry in order to achieve higher quality inscription. For such purpose, a theoretical revision will be performed to select the most adequate slit width for the current setup. Then, the inscribed gratings will be characterised using quantitative phase microscopy to compare geometry and refractive index change of the new PI-b-PI gratings with their PbP counterpart. Finally, the

### 5.3. Slit beam shaping technique for PI-b-PI FBGs

transmission and reflection spectra are presented, as well as the polarisation dependent losses (PDL), in order to study the improvements achieved with this new method.

#### 5.3.2 Control of the cross-section of the focal volume

Based on the spatial axis arrangement depicted in Fig. 5.5, if a planar modification of the fibre core is required, then the focused beam waist of the  $Y$  axis ( $w_{0y}$ ) must be enlarged. This requires a reduction in the NA and, consequently, the beam diameter ( $D_y$ ) along that axis (see Equation 5.5). As a result, the slit is oriented along the  $X$  axis, and its width ( $s$ ) determines  $D_y$ .

Following the slit, the resulting diffractive effect can be modelled as an elliptic Gaussian beam, which redistributes optical energy around the focus [66]. However, assuming an elliptical Gaussian beam at the input of the objective lens requires the distance between the slit and the objective lens to always be less than the Rayleigh range ( $d_R = s^2/\lambda$ ), where  $s$  is the slit width. By operating in the near-field regime, Fraunhofer diffraction can be neglected. To simplify the calculation and ignore this effect, the energy distribution around the focal volume can be expressed as:

$$I(x, y, z) = \frac{I_0 \cdot w_{0x} w_{0y}}{w_x(z) w_y(z)} e^{-2 \left[ \left( \frac{x}{w_x(z)} \right)^2 + \left( \frac{y}{w_y(z)} \right)^2 \right]}, \quad (5.8)$$

with

$$w_i(z) = w_{0i} \sqrt{1 + \left( \frac{z}{z_{0i}} \right)^2}, \quad z_{0i} = \frac{n\lambda}{\pi \text{NA}_i^2}, \quad \forall i = \{x, y\},$$

where  $z_0$  is the Rayleigh length, and  $n$  is the refractive index of the substrate. Using a paraxial approach and assuming that the beam reaching the slit (located before the objective lens) is a circular Gaussian beam, an analytical process is performed to establish the  $D_x/D_y$  ratios that result in a circular cross-section in the  $YZ$  plane. In contrast to [33], no initial assumption is made regarding the relationship between  $D_x$  and  $D_y$ .

Assuming that  $y_{I/2}$  represents the distance on the  $Y$  axis from the focal point at which the intensity decreases by a factor of 2, and  $z_{I/2}$  represents the equivalent distance on the  $Z$  axis, a circular cross-section is achieved when  $y_{I/2} = z_{I/2}$  (following the half-width-half-maximum approach). Starting from Equation 5.8, the derivation proceeds as follows:

- $Y$  AXIS ( $x = 0, z = 0$ )

$$I(0, y_{I/2}, 0) = \frac{I_0}{2} = I_0 \cdot e^{-\frac{2y_{I/2}^2}{w_{0y}^2}}.$$

$$y_{I/2} = w_{0y} \sqrt{\frac{\ln(2)}{2}}. \quad (5.9)$$

- $Z$  AXIS ( $x = 0, y = 0$ )

$$I(0, 0, z_{I/2}) = \frac{I_0}{2} = I_0 \frac{1}{\sqrt{1 + \left(\frac{z_{I/2}}{z_{0x}}\right)^2} \sqrt{1 + \left(\frac{z_{I/2}}{z_{0y}}\right)^2}}.$$

$$\left(z_{I/2}^2 + z_{0x}^2\right) \left(z_{I/2}^2 + z_{0y}^2\right) = 4z_{0x}^2 z_{0y}^2. \quad (5.10)$$

By setting  $y_{I/2}$  from Equation 5.9 equal to  $z_{I/2}$  from Equation 5.10, an expression is obtained that depends on  $D_x$  and  $D_y$  (see Equation 5.11). The comparison of these results to those presented in [33], where it is assumed that  $D_x > 3D_y$ , is illustrated in Fig. 5.6.

$$\left(1 + \alpha \frac{D_x^4}{D_y^2}\right) \left(1 + \alpha D_y^2\right) = 4, \quad \text{with} \quad \alpha = \frac{\ln(2)}{2n^2 f^2}. \quad (5.11)$$

The results obtained can be adjusted to the expression shown below, which offers a coefficient of determination  $R^2 = 0.9994$  for values of  $D_x$  between 1 mm and 12 mm.

$$\frac{D_x}{D_y} \simeq 33.97 \cdot [D_x(\text{mm})]^{-0.993}. \quad (5.12)$$

Using a slit can substantially enhance the symmetry of the cross-section, however, this comes at the expense of reduced efficiency due to the loss of initial pulse energy. This trade-off indicates that achieving a circular cross-section may not be desirable in certain situations, such as in this study, where efficiency is significantly compromised. To solve this problem, there exist alternatives that necessitate intricate optical alignment, but can surmount this limitation, as reported in previous works [35, 67].

Next, based on simulations performed, the  $YZ$  plane of the focal volume for different  $D_x/D_y$  ratios is presented (Fig. 5.7), depicting the variations of its ellipticity. The circular cross-section is obtained for  $D_x/D_y = 12$ , which corresponds to the result shown in Fig. 5.6 for  $D_x = 3$  mm.

Finally, the impact of efficiency is demonstrated. Fig. 5.8 portrays the variation in intensity along the fibre (focusing the core) at  $x = y = 0$ . It is observed that a  $D_x/D_y = 2$  ratio leads to a 28% reduction in intensity at the focal point when compared to the case without a slit. Conversely, achieving a circular cross-section ( $D_x/D_y = 12$ ) results in only 0.8% of the energy

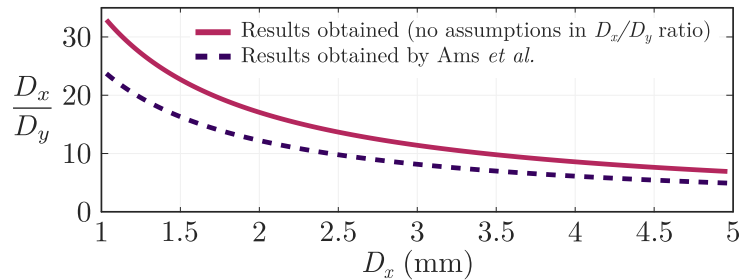


**Figure 5.6.** Relationship between  $D_x$  and  $D_y$  as a function of  $D_x$  to obtain a circular cross-section of the focal volume in the  $YZ$  plane. A substrate with  $n = 1.47$  and a focal length of the objective lens  $f = 8$  mm has been used. Adapted from [2].

### 5.3. Slit beam shaping technique for PI-b-PI FBGs

at the focal point compared to the situation without the slit. The significantly higher laser pulse energy required to obtain a circular cross-section is due to the slit obstructing most of the power.

#### 5.3.3 Pulse energy setting

For FBG inscriptions, a commercially available femtosecond fibre laser chirped pulse amplifier from Calmar laser has been employed, which functions at 1030 nm, with a 370 fs pulse duration and a variable PRR of 1 Hz to 120 kHz. To ensure a clear wavefront, laser pulses pass through an iris diaphragm ( $\varnothing$  3 mm), followed by an adjustable slit positioned along the  $X$  axis, the direction of inscription, as previously discussed.

Next, the pulses are focused using a Mitutoyo objective lens with  $NA = 0.42$  and a magnification of  $\times 50$ . A slide supports the stretched optical fibre, covered with a coverslip, and separated by an index-matching oil that helps mitigate fibre-induced aberrations [22]. The sample is mounted on an Aerotech XYZ motor stage with nano-resolution capability. To achieve correct positioning and visualisation of the fibre, transmission illumination and a CCD camera are used.

The primary consideration to bear in mind is that the pulse energy at the laser output ( $E_p$ ) is not equivalent to the amount that ultimately reaches the sample. To account for this, the effective pulse energy ( $(E_p)_{eff}$ ) will be used to denote the energy that passes through the slit. For comparing inscribed structures with varying slit widths,  $(E_p)_{eff}$  must remain constant to avoid altering the induced laser energy in the focal volume. Given that the incident pulse energy follows a Gaussian spatial distribution ( $M^2 < 1.1$ ),

$$E_p(x, y) = A \cdot e \left[ - \left( \frac{x^2}{2\sigma_x^2} + \frac{y^2}{2\sigma_y^2} \right) \right], \quad (5.13)$$

with a beam diameter 2.5 mm ( $1/e^2$ ), it is crucial to specify the light transmission percentage

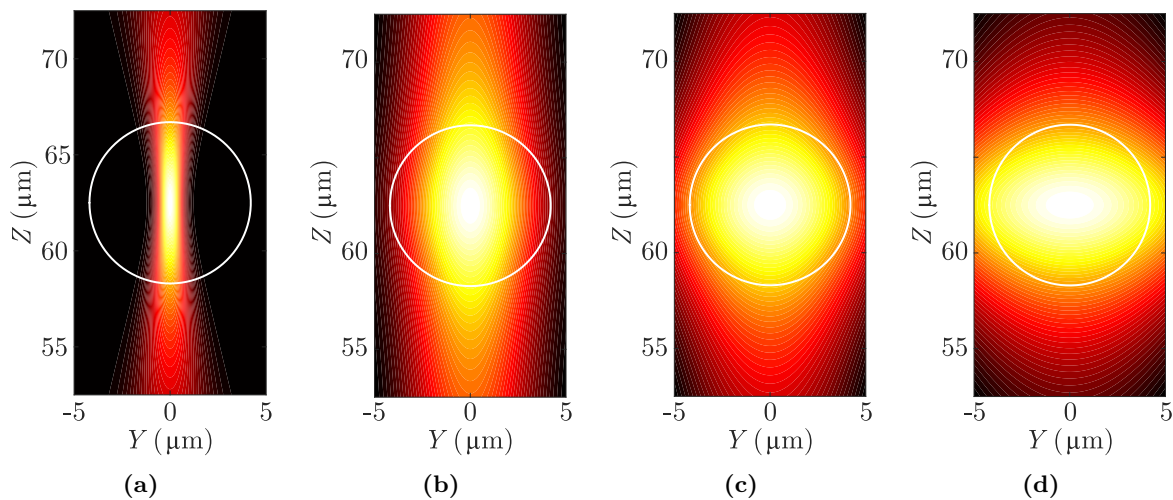


**Figure 5.7.**  $YZ$  plane of the focal volume for  $D_x/D_y$  ratios of (a) 1, (b) 6, (c) 12 and (d) 20. The white circle represents the core of the optical fibre. A substrate with  $n = 1.47$  and a focal length of the objective lens  $f = 8$  mm has been used. Adapted from [2].

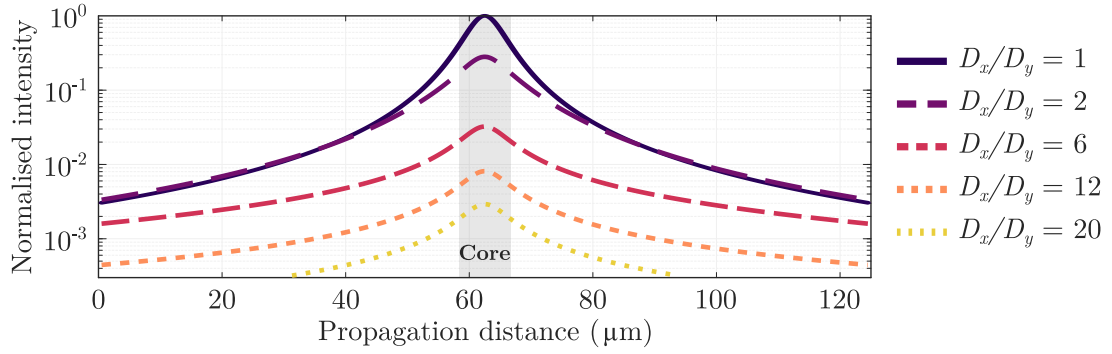


**Figure 5.8.** Evolution of intensity on the  $Z$  axis ( $x = y = 0$ ) with focus on the center of the SMF core ( $z = 62.5 \mu\text{m}$ ). Different  $D_x/D_y$  ratios are depicted. Adapted from [2].

through the slit, which is dependent on its width ( $s$ ), and to determine the pulse energy for each  $s$  value such that  $(E_p)_{eff}$  remains constant.

For inscribing the FBGs, the effective pulse energy will be  $2.84 \mu\text{J}$ . The required incident pulse energy is illustrated in Fig. 5.9.

The objective of this study is to compare PbP and Pl-b-Pl FBGs inscribed with identical energy in the focal volume, guaranteeing that the deposited energy in the focal volume is nearly identical for any  $D_x/D_y$  ratio. As shown in Fig. 5.10, the detailed energy compensation (effective pulse energy) ensures that the same energy is available in the focal volume. The fluence integrated into the integration regions displayed in the  $YZ$  (Fig. 5.10 a) and  $XY$  (Fig. 5.10 b) planes is explicitly presented. Both scenarios, with and without energy compensation, are compared. PbP has higher fluence in smaller focal volumes, whereas Pl-b-Pl focal volumes contain lower and smoother fluence. Consequently, smaller integration regions result in more energy in PbP than in Pl-b-Pl. Nonetheless, the energy deposited in the focal volume is considered identical for both cases. For larger ratios, the integration region should be enlarged.

An alternative approach would be to equalise the energy fluence at the focal volume's center. This would involve increasing the energy deposited in the focal volume as  $D_x/D_y$  increases. However, even if the focal point's intensity is equalised, PbP's smaller focal volume width would

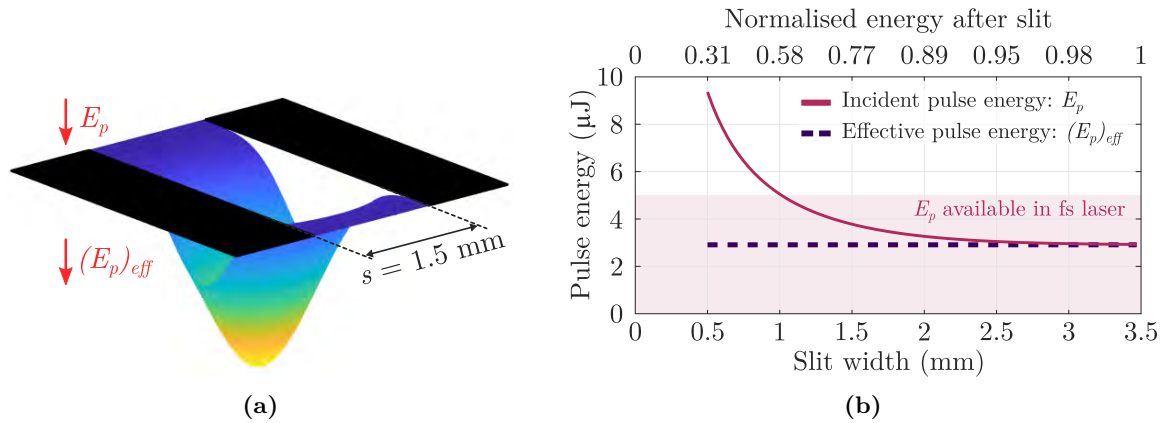


**Figure 5.9.** (a) Demonstration of the laser pulse evolution through a  $1.5 \text{ mm}$  width slit, illustrating the definition of  $E_p$  and  $(E_p)_{eff}$ . (b) Plot of  $E_p$  versus slit width ( $s$ ) to preserve a constant  $(E_p)_{eff}$ . Adapted from [2].

### 5.3. Slit beam shaping technique for PI-b-PI FBGs

lead to more localised stress at the core and lower grating strength.

FBGs will be performed in an SMF-28 core using slit widths of 1 mm, 1.5 mm, 2 mm and 3 mm, which requires incident pulse energies of 4.93  $\mu\text{J}$ , 3.69  $\mu\text{J}$ , 3.19  $\mu\text{J}$  and 2.88  $\mu\text{J}$ , respectively. The laser PRR is set to 30 Hz, and the period of the FBGs takes a value of  $\Lambda = 2.15 \mu\text{m}$ , resulting in the 4<sup>th</sup> order (C-band). As such, the writing speed is  $v = \Lambda \cdot \text{PRR} = 64.5 \mu\text{m/s}$ .

#### 5.3.4 Experimental results and discussion

##### QPM characterisation

Once inscribed the aforementioned gratings, a phase study can be performed to contrast with the theoretical results. It should be noted that the refractive index is proportional to the phase ( $n \propto \phi$ ). Quantitative phase microscopy is a relatively straightforward method to retrieve phase images from intensity images exploiting the intensity transport equation [26]. The average phase change ( $\Delta\phi$ ) and width of the gratings depending on the slit width ( $s$ ) are depicted in Fig. 5.11.

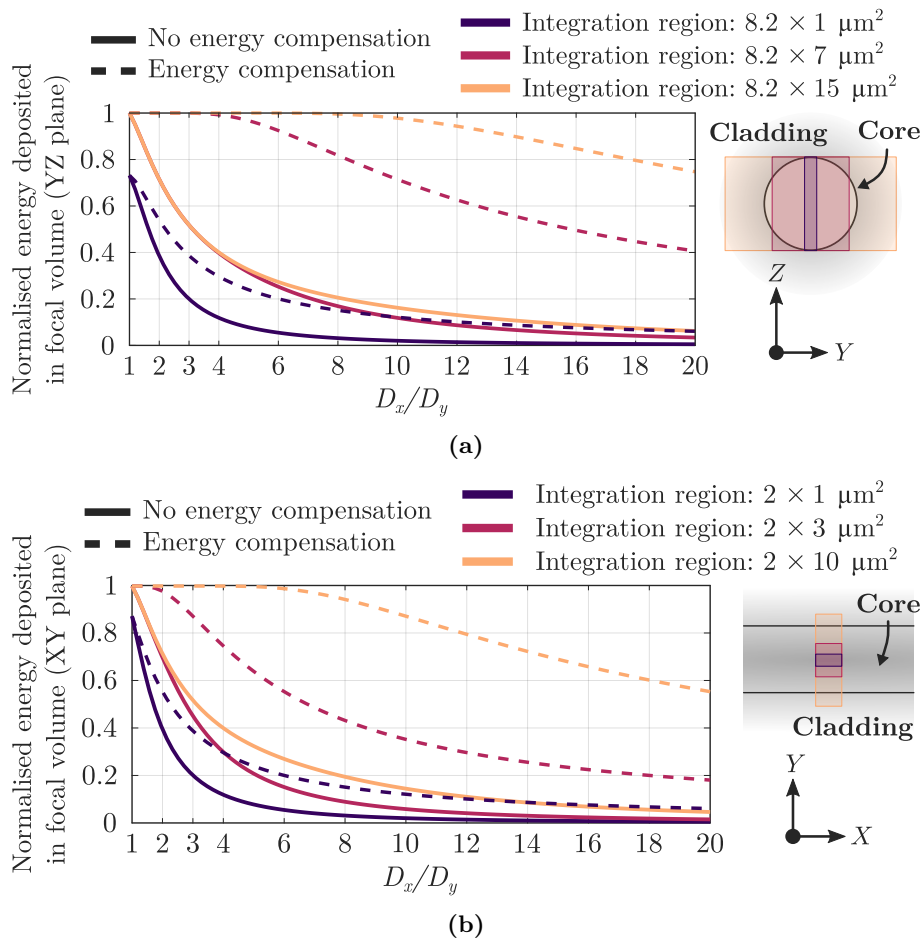


**Figure 5.10.** Normalised energy deposited in the focal volume, considering (a) the YZ ( $x = 0$ ), and (b) XY ( $z = 0$ ) planes. The YZ plane represents the core cross-section, while the XY plane illustrates a longitudinal section of the fibre. The results are shown with and without energy compensation (solid and dotted lines, respectively), as described in this section. Distinct colours indicate various integration regions of energy fluence. Adapted from [2].

Here, first and foremost, the inscription width increases for  $D_x/D_y > 1.5$  up to a 3 factor ( $s = 1$  mm), which is almost the core width. Besides, another interesting property of  $D_x/D_y > 2$  ratios is its positive phase change compared with higher slit values, where the PbP counterpart shows higher but negative phase changes. These modifications become more inhomogeneous, as shown in the transversal profile of Fig. 5.12 a. In fact, the phase change decreases with an exponential curve ( $R^2 = 0.9982$ ). Figure 5.12 b depicts three phase profiles corresponding to a pristine fibre and  $s = \{1, 3\}$  mm. The  $s = 1$  mm inscription not only produces a positive phase change as indicated above, but also generates a homogeneous modification compared with  $s = 3$  mm.

The amplitude of the phase change has also been investigated. As shown in Fig. 5.12 b, the amplitude for  $s = 1$  mm is weak compared to larger slit widths such as 2 mm and 3 mm, which have approximately equal amplitudes, with  $s = 2$  mm exhibiting a slightly more sinusoidal phase change profile. In these PbP cases, the focal volume is more compact, resulting in higher phase changes due to expansion. Additionally, the surrounding area exhibits stress associated with an index change of opposing sign and without grating modulation. Based on Equation 5.7, a higher index amplitude ( $\Delta n_m$ ) could suggest a higher coupling coefficient. However, the lower cross-section and the stress region must also be considered. In particular, the RIC surrounding the grating can induce losses that compromise ideal transmission and reflection. This will be discussed further in the next section.

It appears that all inscriptions correspond to Type I changes in the material. According to the literature, Type II corresponds to a birefringent change in the refractive index, caused by the formation of nanogratings in the material. However, multiple studies [51, 68] have shown that the interaction of two or more pulses is required to achieve such a change. This makes the existence of nanogratings in the FBGs unlikely. In summary, PbP FBGs exhibit more birefringent behavior due to the asymmetry of their focal volume and the more localised stress in the core. On the other hand, Pl-b-Pl FBGs, while still exhibiting induced stress, show markedly inferior anisotropic behavior. Additionally, the generated planes exhibit a more symmetrical and homogeneous change.

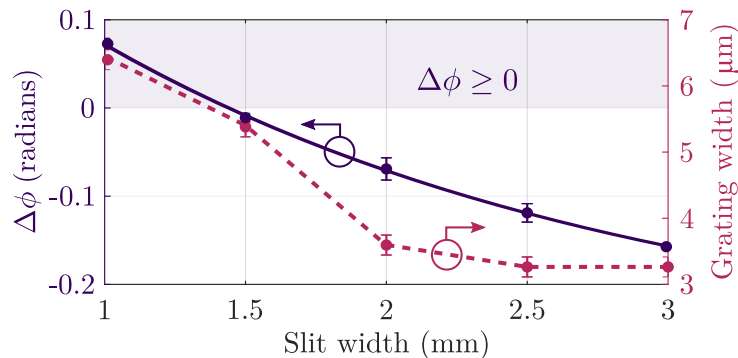


**Figure 5.11.** Mean phase change and modification width for varying slit widths ( $s$ ) are presented. The phase change decreases in accordance with an exponential fit ( $R^2 = 0.9982$ ). Adapted from [2].

### 5.3. Slit beam shaping technique for PI-b-PI FBGs

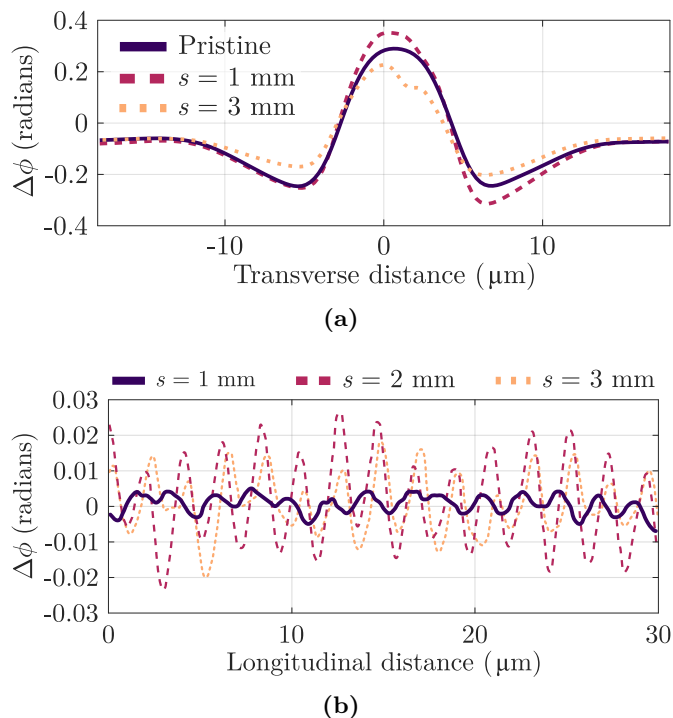


**Figure 5.12.** (a) Transverse phase profile for pristine and  $s = \{1, 3\}$  mm, and (b) phase change parallel to grating inscription for  $s = \{1, 2, 3\}$  mm. Adapted from [2].

### PI-b-PI FBGs with slit beam shaping technique

The use of the slit beam technique enables precise control over the period of the PI-b-PI FBGs, as well as the width and height of the planes, depending on the pulse energy and slit width, respectively. This allows for some flexibility in the performance of the optical structure.

The FBGs were characterised using the pulse energies and slit widths described in subsection 5.3.3. The results of inscribing with slit widths of 1 mm ( $D_x/D_y \simeq 3$ ) and 3 mm ( $D_x/D_y \simeq 1$ ) are presented in Fig. 5.13. As the effective pulse energy is constant, an increase in plane width can be observed as the slit width decreases. PbP FBGs are achieved when the slit width is similar to the diameter of the laser beam ( $1/e^2$ ), which is approximately 2.5 mm.

The FBGs, with a length  $L = 1$  mm (inscription time  $\sim 15$  sec/FBG), have been characterised both in reflection and transmission using a broadband light source (HP 83437A) and an

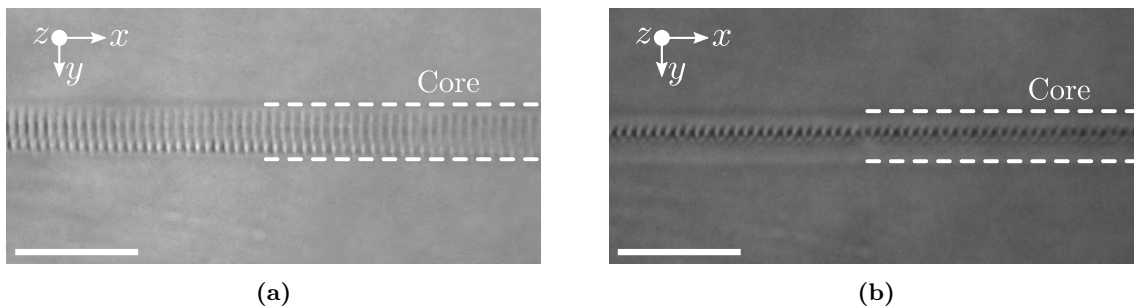


**Figure 5.13.** FBGs inscribed in the core of an SMF-28 fibre with (a)  $s = 1$  mm (PI-b-PI), and (b) and  $s = 3$  mm (PbP). Scale bars in **a-b** are 20  $\mu\text{m}$ . Adapted from [2].

optical spectrum analyser (Anritsu MS9740A) with 30 pm resolution. Reflection and transmission spectra are depicted in Fig. 5.14 for slit widths  $s = \{1, 1.5, 2, 3\}$  mm.

The increase in broadband losses as the inscription approaches a PbP is noteworthy, with 4 dB transmission losses for the PbP and 0.3 dB for the  $D_x/D_y \simeq 3$  Pl-b-Pl inscription (Fig. 5.13 a). These losses, which are better than those reported in the literature [58], are consistent with the phase results discussed in subsection 5.3.4, where the stress region and lower cross-section play a major role. PbP ( $s = 3$  mm) reflection is approximately 6 dB higher than Pl-b-Pl ( $s = 1$  mm), but the results presented here are intended to show the tendency of varying the slit width. By choosing the appropriate energies, it is possible to manufacture high-performance FBGs using both PbP and Pl-b-Pl methods.

The reduction of slit width clearly improves both FWHM and reflectivity. These trends are shown in Fig. 5.15, where FWHM decreases with increasing  $D_x/D_y$ , while reflectivity increases monotonically. For  $s = 1$  mm ( $\kappa L \approx 0.65$ , where  $\kappa$  is the coupling constant), reflectivity can reach  $-5$  dB and FWHM can be around 0.69 nm. The increase in reflectivity can be attributed to the increase in width and the reduction in losses, which allows more light to propagate through the entire grating length. Likewise, the reduction in FWHM is consistent with smaller slit widths where the cross-section is not only larger but also more homogeneous, as shown in Fig. 5.12 b. Therefore, the presented method for inscribing Pl-b-Pl gratings leads to a higher quality index modulation, resulting in a better performance.

To validate the obtained results, the polarisation-dependence of PbP ( $s = 3$  mm) and Pl-b-Pl

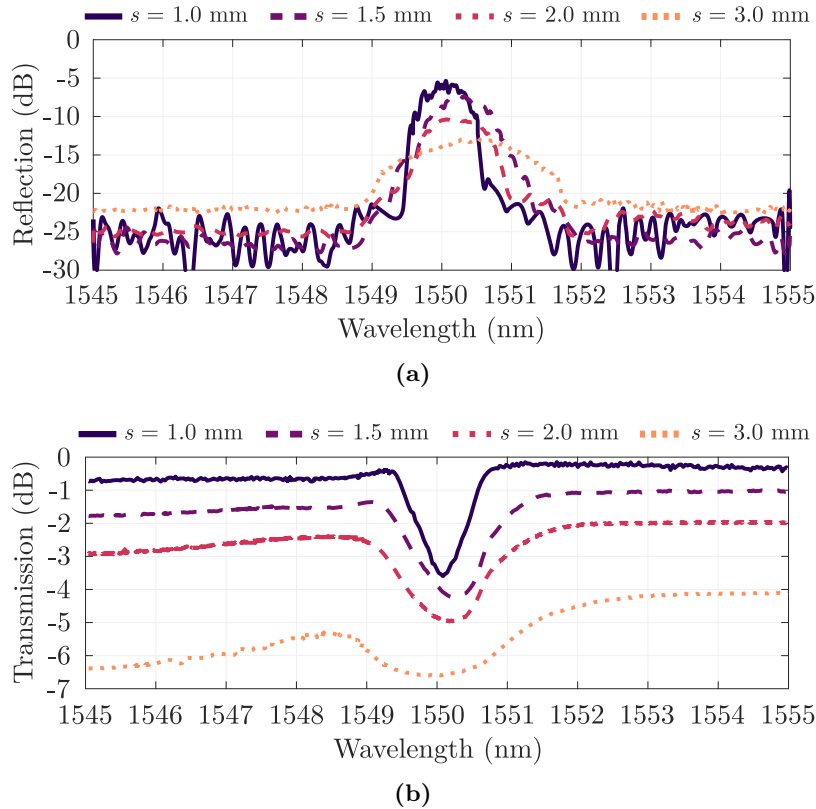


**Figure 5.14.** (a) Reflection and (b) transmission spectra of FBGs inscribed with  $s = \{1, 1.5, 2, 3\}$  mm. These spectra consist of 2,001 data points with a 50-point average. Adapted from [2].

### 5.3. Slit beam shaping technique for PI-b-PI FBGs

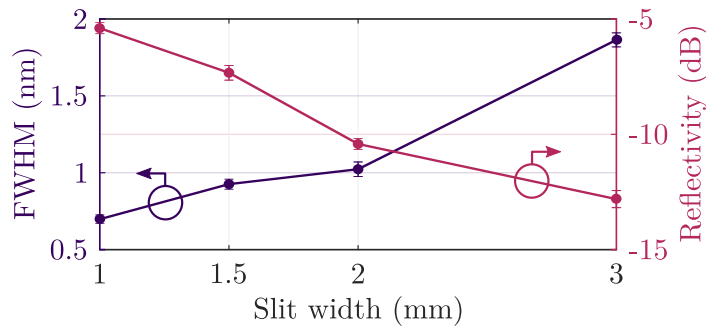


**Figure 5.15.** Variation of the FWHM and reflectivity as a function of the slit width. Adapted from [2].

( $s = 1$  mm) FBGs was examined by measuring the maximum change in transmitted or reflected power when the input polarisation state was varied over all polarisation states, as suggested in the literature [69]. A polarisation controller and a broadband light source were used to carry out the measurement. The results, depicted in Fig. 5.16, indicate that the PbP FBG exhibits a greater variation with the polarisation state, mainly due to its higher birefringence and marked transverse asymmetry. In contrast, the PI-b-PI FBG has a significantly lower polarisation-dependent loss ( $\sim 1.5$  dB) because of its more symmetric structure. The Bragg wavelength shift of the different polarisation states was always less than 70 pm.

### 5.3.5 Conclusions

A novel technique for inscribing plane-by-plane FBGs has been introduced and experimentally validated. The method involves using a slit located before the objective lens to induce quasi-homogeneous two-dimensional RICs, with flexible control over the width and height of the grating plane. Despite lower energy efficiency than other methods, the technique boasts high inscription speed as a plane is induced with each laser pulse. The resulting spectral response outperforms that of PbP and LbL methods in terms of losses, FWHM, and reflectivity. Additionally, PI-b-PI FBGs exhibit significantly reduced polarisation dependence. Phase characterisation of these modifications revealed smooth and uniform changes in PI-b-PI FBGs with  $D_x/D_y = 3$ , in contrast to the negative and inhomogeneous changes of PbP FBGs produced by Gaussian laser beams without previous shaping.

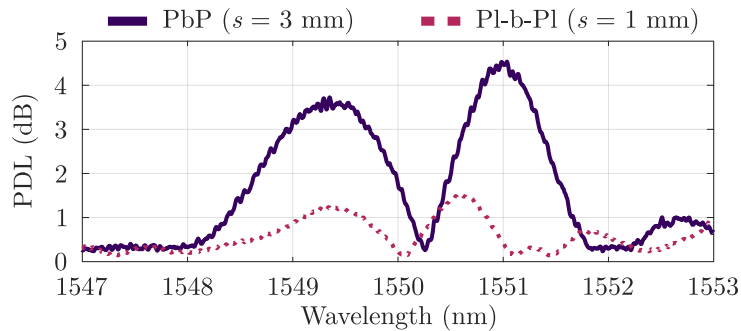


**Figure 5.16.** Polarisation dependent loss (PDL) of PbP ( $s = 3$  mm,  $D_x/D_y = 1$ ) and PI-b-PI ( $s = 1$  mm,  $D_x/D_y = 3$ ) FBGs. Adapted from [2].

## 5.4 Slit beam shaping technique for symmetric CWGs

This section aims to contribute to the field of advanced manufacturing by focusing on the design, simulation, and manufacturing of symmetric cladding waveguides within optical fibres using ultrafast lasers. The proposed technique employs the slit beam shaping method. These cladding waveguides (CWGs) possess distinctive characteristics, including low losses (measuring approximately 0.21 dB/cm), a quasi-step-index refractive index profile, and a circular cross-section. The primary objective of these waveguides is to facilitate the efficient coupling of evanescent light from the core of a single-mode fibre to each of the four cores within a multicore fibre. This work seeks to advance the capabilities of optical fibre technology and its applications in a broader context. It is important to note that the primary motivation of this research lies in the advancements and possibilities within the field of photonics and advanced manufacturing.

### 5.4.1 Background

The integration of advanced production techniques with smart technologies, commonly known as Industry 4.0 or the 4<sup>th</sup> industrial revolution, aims to enhance the performance and efficiency of industry processes and services [70, 71]. These smart technologies encompass a wide range of innovations, including advanced robotics, big data, Internet of Things (IoT) [72], the “maker” culture [73], cognitive technologies [74], nanotechnology, and photonics, among others.

Photonics, particularly the field of light science and technology, holds significant importance in the broader context of advanced manufacturing, beyond the scope of Industry 4.0. The application of light-based technologies spans multiple domains. Firstly, the development of devices, subsystems, and networks based on optical technologies enables advanced communications within the industry, facilitating the interconnection of different smart architectures. Additionally, light-based sensors play a prominent role in automating the collection of physical, chemical, and biological information from the environment, enabling precise actions. Lastly, advanced light-based manufacturing, such as the micro-fabrication of 3D optical structures using femtosecond (fs) lasers, holds significant industrial applicability [75, 76].

In advanced manufacturing using fs lasers, waveguides are widely fabricated optical structures due to their applicability in the field of photonic sensors [76]. The optical interconnection of diverse sensor structures enables the generation of sensors that are more comprehensive and efficient [23, 77], which are of great importance in various applications.

This work applies the principles of advanced manufacturing and laser inscription techniques to design, simulate, and manufacture a light-based sensor. To accommodate different optical structures within a confined space, a multicore fibre (MCF) composed of four cores is utilised. Each core receives light through a CWG that achieves evanescent coupling with the core of an SMF. These waveguides, featuring a relatively circular cross-section, are manufactured using the slit beam shaping technique [2, 33]. To the best of the author’s knowledge, this is the first application of this method to inscribe symmetric waveguides in optical fibres.

## 5.4. Slit beam shaping technique for symmetric CWGs

### 5.4.2 Fs laser inscription of CWGs

During the last 20 years the fabrication of waveguides using ultrafast lasers in bulk glasses has been extensively studied [33, 78–81]. However, there is relatively less literature available on the manufacture of waveguides in optical fibres. Inscribing waveguides in optical fibres presents significant challenges, including the size of the waveguides and their coupling efficiency with the fibre core and other structures. However, the primary difficulty arises from the cylindrical geometry of the fibre.

Within fibre optic manufacturing, there are several approaches to waveguide inscription, as indicated in the review by Pallarés *et al.* [82]. One approach involves inscribing waveguides without correcting the cylindrical aberrations of the fibre, resulting in what is known as filamented waveguides [27]. This method utilises high pulse energies, causing Type II modifications. The modified region within the focal volume exhibits a negative RIC, while the filament below possesses a positive RIC ( $\sim 10^{-2}$ ), acting as a waveguide. However, this structure has a clearly asymmetric cross-section, leading to poor performance and mechanical robustness.

In an alternative approach, the cylinder lens effect of the fibre surface can be overcome by using AO [4] and/or index-matching oil in the fibre [83], which can be used together. AO enables the spatial shaping of a laser beam in terms of amplitude, polarisation, and phase, providing great flexibility in aberration correction and beam shaping. Regarding the use of index-matching oil, it is important to differentiate between oil immersion [84, 85] and surrounding the fibre with oil and placing a coverslip on top [23, 62, 86].

Since the width of the waveguide is generally much greater than the waist radius of the Gaussian beam focus (focal volume) [76], different approximations are necessary to achieve the appropriate size and shape. In the context of using index-matching oil, the common practice is to employ the multiscan technique [23, 62, 86]. This technique involves controlling the width (and shape) of the waveguide through multiple scans. Additionally, the waveguide's refractive index change can be controlled by appropriately overlapping the scans [23]. Although this significantly increases the inscription time, it allows for slight control over the waveguide's cross-section without adding complexity to the optical setup.

Beam shaping techniques offer an alternative means of controlling the cross-sectional shape of the waveguide without the need for multiple laser scans. While these techniques cannot be strictly considered adaptive optics, they enable slight corrections to the cross-section of the focal volume [76]. Among these techniques, the slit beam shaping technique stands out.

#### Slit beam shaping technique

As previously described in Equations 5.5 and 5.6, the focal volume of a focused Gaussian beam is determined by the waist radius ( $w_0$ ) and the Rayleigh length ( $z_0$ ).  $w_0$  and  $z_0$  can vary in  $X$  and  $Y$  if the NA is different in each axis, *i.e.*, if the diameter of the input beam ( $D$ ) is different in each axis. Ultimately, if the input beam to the objective lens is elliptical, an asymmetric focal volume is achieved in the radial axis of the laser beam. An adjustable slit positioned before the objective lens is one method to achieve an approximation of an elliptical beam.

Assuming that the longitudinal axis of the fibre is oriented in the direction of the  $X$  axis,

and that the cladding waveguides must be oriented in that axis, a circular cross-section in the  $YZ$  plane is required (Fig. 5.17). Hence, to increase  $w_{0y}$  or, equivalently, reduce  $D_y$  at the input of the objective lens, a slit can be positioned along the  $X$  axis. The adjustable slit width  $a$  on the  $Y$  axis allows for the assumption of an elliptical beam in the near field of the refractive element, specifically when the distance between the slit and the objective lens falls within the Rayleigh range [87].

$$d_{slit-lens} < d_R = \frac{a^2}{\lambda}. \quad (5.14)$$

The use of the slit beam shaping method for manufacturing CWGs offers several significant advantages over other techniques, such as multiscan. Firstly, it provides a notably shorter inscription time. Secondly, it allows for greater control over the waveguide cross-section, while adding minimal complexity to the optical setup.

The slit beam shaping method was originally proposed by Ams *et al.* in 2005 for inscribing circular waveguides in phosphate glass bulk [33]. This technique has also been employed on PMMA substrates [88]. In subsequent years, the performance of the inscribed waveguides has been improved by combining the method with active optical elements like SLMs [89, 90] or utilising other techniques such as spatio-temporal focusing [37], always in bulk materials.

It is worth noting that the slit beam shaping technique has not been limited to fs laser waveguide inscription alone. In 2020, as detailed in the previous section, Roldán *et al.* utilised this method to manufacture enhanced plane-by-plane FBGs, achieving planar refractive index changes that completely covered the fibre core, thereby improving the performance of the gratings [2].

In summary, Table 5.1 provides a comparison of some key characteristics of the waveguide inscription techniques discussed in this section.

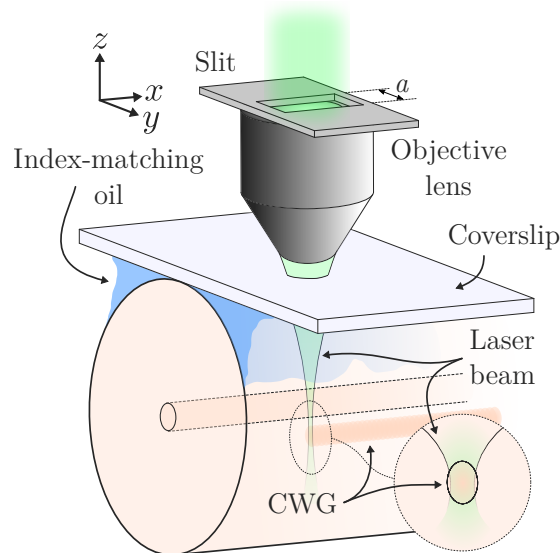


**Figure 5.17.** Illustration of the process of CWG inscription using the slit beam shaping method with the assistance of index-matching oil. Adapted from [3].

#### 5.4. Slit beam shaping technique for symmetric CWGs

**Table 5.1.** Comparison of the characteristics among various methods of inscribing waveguides using ultrafast lasers.

	Direct-write (filamented)	Index-matching oil		Adaptive optics
		Multiscan	Slit beam method	
Aberration free	No	Yes	Yes	Yes
Inscription time	●○○	●●●	●○○	●○○
Cross-section control	○○○	●○○	●○○	●●●
Light transmission	●○○	●●○	●●○	●●●
Optical complexity	○○○	○○○	●○○	●●●

#### 5.4.3 Structure design and simulations

The primary objective of this study is to demonstrate, for the first time, the feasibility of producing smooth and circular waveguides in optical fibers using the aforementioned slit beam shaping technique. To serve as a proof of concept, the optical structure depicted in Fig. 5.18 is designed, simulated, and manufactured. This structure facilitates the coupling of light from the SMF core to each of the MCF cores through evanescent wave coupling.

CWGs consist of three distinct sections. The first section is a straight segment, denoted by length  $L_1$ , which runs parallel to the SMF core and is positioned as close to it as possible. This section facilitates evanescent wave coupling without inducing modifications on the core, thus minimising losses and enabling the placement of multiple optical structures along the fibre. The second section, with a length of  $L_2$ , comprises an S-Bend that guides the light from the SMF core to the cladding. Finally, the light is coupled to the MCF core through the last straight section, denoted by length  $L_3$ .

As previously described, the slit beam method enables the production of highly circular waveguide cross-sections [2]. For a 2.5 mm diameter ( $1/e^2$ ) circular Gaussian beam, Figure 5.19 depicts the focal volume in the  $YZ$  plane and the intensity curve in the focal plane  $Z$  ( $z = 62.5 \mu\text{m} \rightarrow$  fibre centre). The three scenarios presented are as follows: without the use of

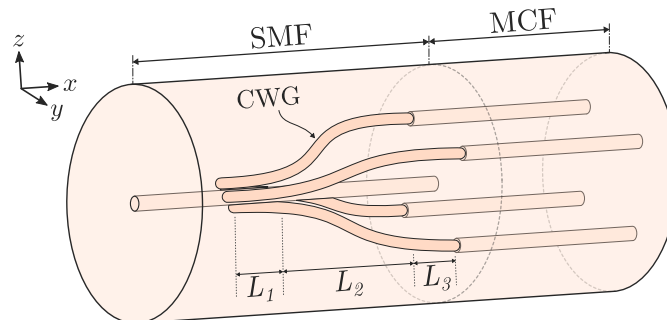


**Figure 5.18.** Illustration of the simulated and fabricated optical structure. This structure involves the evanescent coupling of light from the core of a single-mode fibre to each of the four cores of a multicore fibre. This coupling is achieved by utilising symmetric cladding waveguides. Adapted from [3].

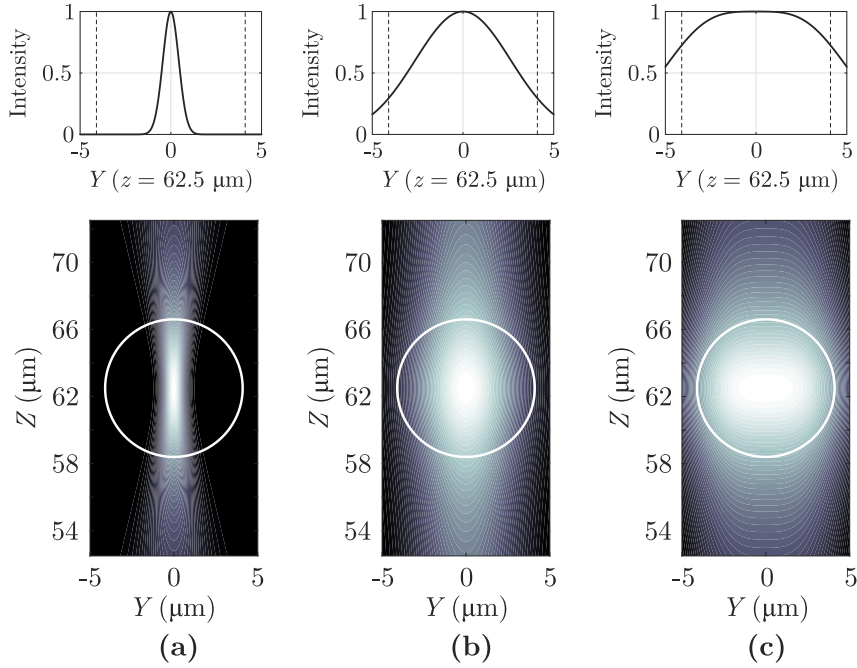


**Figure 5.19.** The focal volume and intensity profile at the  $Z$  focus plane are depicted in the  $YZ$  plane. The focusing conditions are demonstrated for three scenarios: **(a)** without a slit, **(b)** with a slit of width  $a = 500 \mu\text{m}$ , and **(c)** with a slit of width  $a = 500 \mu\text{m}$ , along with two scans performed with a  $2.5 \mu\text{m}$  offset in the  $Y$  direction. An objective lens with a focal length of  $f = 8 \text{ mm}$  is used, along with the application of refractive index adaptation using index-matching oil. Adapted from [3].

a slit (Fig. 5.19 a), with a  $500 \mu\text{m}$  slit (Fig. 5.19 b), and using a  $500 \mu\text{m}$  slit with two scans and a  $2.5 \mu\text{m}$   $Y$  offset (Fig. 5.19 c). The white circle represents the circumference that defines the SMF core, providing a relative perspective on the waveguide dimensions.

When examining Fig. 5.19 b in detail, it becomes apparent that the laser energy distribution at the focal point produces a more circular cross-section. However, it appears insufficient in terms of matching the CWG diameter to that of the fibre core. To address this, two approaches can be considered to achieve a similar width to the core with a pronounced symmetry. The first approach involves reducing the slit width ( $a$ ), theoretically achieving the desired result with a value of approximately  $170 \mu\text{m}$ . Nevertheless, in practice, this approach proves challenging as it requires significantly higher laser pulse energy than what is available in our setup due to the low energy transmission through the narrow slit. The second option, as depicted in Fig. 5.19 c, involves performing two scans with a slight offset in the  $Y$  direction. By employing this method, it can be observed that a CWG width comparable to the core, along with a circular symmetry in the cross-section, can be achieved.

Furthermore, when considering the cumulative focal intensity of both scans, it is evident that it exhibits a more even distribution compared to the case of a single scan. In this way, taking into account that the quantitative RIC is a function dependent on the pulse energy (in silica [76]), which correlates to the energy density within the focal volume, the intensity profile provides insight into the refractive index profile of the CWG. Based on this observation, conducting two scans yields a quasi-step-index CWG, while a single scan results in a profile characteristic of a graded-index structure. The verification of this distinction will be carried out subsequently through QPM measurements.

#### 5.4. Slit beam shaping technique for symmetric CWGs

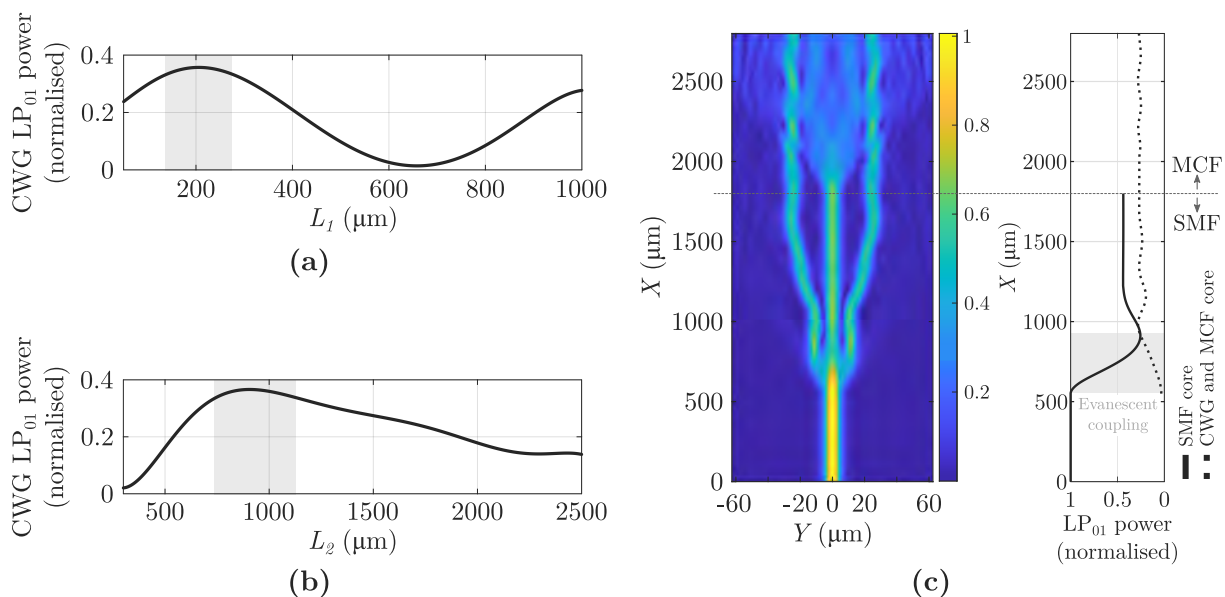


**Figure 5.20.** Normalised  $LP_{01}$  coupled to the CWG is analysed with a fixed length  $L_3$  of  $50 \mu\text{m}$ . Two scenarios are considered: **(a)** varying  $L_1$  (with  $L_2$  fixed at  $1 \text{ mm}$ ), and **(b)** varying  $L_2$  (with  $L_1$  fixed at  $200 \mu\text{m}$ ). The shaded regions represent the optimal design values. **(c, left)** Filled 2D contour plot of the normalised  $LP_{01}$  power of the simulated structure. This structure is defined by cutting the fibre indicated in Fig. 5.18 using an  $XY$  plane that includes the longitudinal axes of the SMF core and two MCF cores. **(c, right)** Evolution of the normalised  $LP_{01}$  power along the  $X$  axis is depicted. It shows the power in the SMF core and in the combined region of the CWG and MCF core (considering only one core). The shaded region indicates the section where evanescent wave coupling takes place. Adapted from [3].

Subsequently, simulations are conducted to determine the optimal lengths of sections  $L_1$ ,  $L_2$ , and  $L_3$  for the CWG. The finite element BPM within the RSoft software is employed for this purpose. A 2D structure is defined, representing a longitudinal plane of the fibre from Fig. 5.18 that includes the axial axes of the SMF core and two cores of the MCF (with a separation of  $50 \mu\text{m}$  between the MCF cores in that plane). The refractive index profile of the CWGs is quasi-step-index, and the coupling section is positioned  $1 \mu\text{m}$  away from the SMF core in the transverse direction. The parameter  $L_3$  is set to a value of  $50 \mu\text{m}$ , while  $L_1$  and  $L_2$  are the parameters whose lengths are subject to optimisation.

Figure 5.20 **a** illustrates the normalised power of the  $LP_{01}$  mode coupled in a CWG as a function of the length of the coupling section  $L_1$ . It is evident that the optimal length lies around  $200 \mu\text{m}$ . By utilising this value for  $L_1$  and conducting a sweep in  $L_2$ , as shown in Fig. 5.20 **b**, it is determined that the optimal S-Bend length is approximately  $1 \text{ mm}$ . Shorter lengths result in significant power losses due to the abrupt change in light direction, while longer lengths lead to a transition so gradual that back-coupling to the SMF core occurs. According to the simulation, the proposed design enables the coupling of approximately  $36\%$  of the  $LP_{01}$  power in a CWG. However, it should be noted that in practical applications, the losses experienced by the manufactured CWGs and the non-ideal nature of the cross-section mean that each CWG will not achieve a power coupling of approximately  $36\%$  of the SMF core power. As a result, the manufacturing of the CWG is performed using the optimal values obtained from the simulation.

Figure 5.20 **c** presents a 2D contour plot representing the normalised  $LP_{01}$  power of the simulated structure with the selected parameter values:  $L_1 = 200 \mu\text{m}$ ,  $L_2 = 1 \text{ mm}$ , and  $L_3 =$

50  $\mu\text{m}$ . Additionally, the plot indicates the  $\text{LP}_{01}$  power evolution along the  $X$  axis within the SMF core, as well as within one of the arms composed of the CWG and MCF core. Notably, the graph highlights the region of coupling through evanescent wave interaction.

#### 5.4.4 Experimental results and discussion

##### Ultrafast laser inscription parameters

All subsequent inscriptions have been made using a commercial fibre laser chirped pulse amplifier provided by Calmar. The FLCPA operates at a wavelength of 1030 nm and produces pulses lasting 370 fs. The laser beam, with a diameter of 2.5 mm (at  $1/e^2$  intensity), passes through a 3 mm iris diaphragm to ensure a clean wavefront. It then proceeds through a slit aligned along the  $X$ -axis (adjustable on the  $Y$ -axis) as described in [2]. The laser beam is tightly focused using a Mitutoyo objective lens with a NA of 0.42 and a magnification of  $\times 50$ . The fibre sample is coated with an index-matching oil as outlined in [83] and positioned on a nano-resolution XYZ motor stage provided by Aerotech.

Based on previous studies and experimental measurements, it is deduced that circular polarisation enhances the light transmission in direct-write waveguides, leading to reduced roughness and losses [91]. Consequently, a quarter-wave plate is inserted into the optical path of the laser beam. The complete experimental setup is illustrated in Fig. 5.21. Regarding the inscription parameters, the CWGs are generated using a laser pulse energy of 0.52  $\mu\text{J}$  (prior to the slit), and a PRR of 120 kHz, resulting in 1,000 pulses/ $\mu\text{m}$ . The slit has a width of  $a = 500 \mu\text{m}$ , and two separate laser scans are performed for each CWG with a 2.5  $\mu\text{m}$  offset along the  $Y$ -axis.

##### CWG properties and cross-section

The cladding waveguide that has been manufactured possesses the dimensions  $L_1$ ,  $L_2$ , and  $L_3$  as previously specified. Its width is 8.1  $\mu\text{m}$ , which is similar to the core width. The transverse separation from the SMF core in the coupling section ( $L_1$ ) is approximately 1  $\mu\text{m}$ , as depicted in Fig. 5.22 **a**. This close proximity enables significant evanescent wave coupling, as evidenced by the image shown in Fig. 5.22 **b**. When red light ( $\lambda = 633 \text{ nm}$ ) is introduced into the SMF, it couples with the guided modes within the waveguide, and the power contribution increases along the coupling section ( $L_1$ ) of the CWG. The scattering of red light (indicative of waveguide losses) provides a visual indication of the amount of coupled light.

At this stage, the waveguide losses have been estimated using image processing techniques similar to those employed in Fig. 5.22 **b**. Assuming that the roughness of the CWG remains relatively constant throughout the waveguide, it is possible to establish a proportional relationship between scattering and guiding losses, as long as the power level in the waveguide remains consistent. By analysing the scattered light captured by the complementary metal-oxide-semiconductor (CMOS) camera and comparing it with the fibre transmission in various differential measurements, an estimation of the losses can be obtained. The estimated loss value for the manufactured CWGs is approximately 0.21 dB/cm.

#### 5.4. Slit beam shaping technique for symmetric CWGs

The cross-section of the CWG is depicted in the end-face image shown in Fig. 5.22 **c**. It is apparent that the dimensions of the CWG closely resemble those of the SMF core, exhibiting clear circular symmetry. In fact, its shape corresponds to the analytically determined focal volume described in Fig. 5.19 **c**, which takes into account the slit width and the  $Y$  offset (resulting from two scans) utilised during the manufacturing process.

After specifying the properties of the cladding waveguide, the structure illustrated in Fig. 5.18 is fabricated. The outcome of this fabrication process is depicted in Fig. 5.23. In Fig. 5.23 **a**, the region corresponding to the splice between the SMF and MCF is displayed. By focusing the image on the upper cores of the MCF, specifically MCF core<sub>1</sub>, the waveguides associated with those cores can be observed. Ideally, the power coupled into each MCF core should be 25%. However, as shown in Fig. 5.23 **b**, when red light is introduced at the distal end of the fibre (resulting in multimode behaviour for that wavelength), three of the cores exhibit similar power coupling (presumably corresponding to the LP<sub>31</sub> mode), while one core seems to have a higher power level (possibly indicating the presence of the LP<sub>12</sub> mode). Nevertheless, it should be noted that the CWGs produced are intended for use in the 3<sup>rd</sup> window of optical communications, where monomode behaviour is desired. The obtained results are highly promising and reliable.

#### QPM characterisation

Lastly, it is essential to characterise the RIC of the optical waveguide or at least obtain a relative value in comparison to the core. There are various approaches to accomplish this, one of which is QPM. As explained previously, this method enables the quantification of the phase alteration that transpires when light passes through an optically dense medium, such as an optical fibre [26]. Consequently, a phase image can be extracted from three intensity images: one in focus ( $\delta z = 0$ ) and the other two slightly out of focus at  $\pm\delta z$ . It is important to note that the phase change ( $\Delta\phi$ ) and the RIC ( $\Delta n$ ) are linked by the well-established relationship:

$$\Delta n = \frac{\lambda}{2\pi \cdot z} \Delta\phi, \quad (5.15)$$

where  $\lambda$  is the wavelength of the illumination source (453 nm), and  $z$  is the RIC length.

Figure 5.24 depicts the  $Y$  phase change profile of a SMF with a CWG inscribed at  $y = -30 \mu\text{m}$ , with the manufacturing parameters indicated above. It is observed that the phase change profiles of both core and CWG are similar, and therefore, their RI. Additionally, it can be seen that the RIC value is marginally higher in the CWG, albeit remaining within the order of magnitude of  $10^{-3}$ . This RIC is well-suited for achieving low-loss transmission in waveguides.

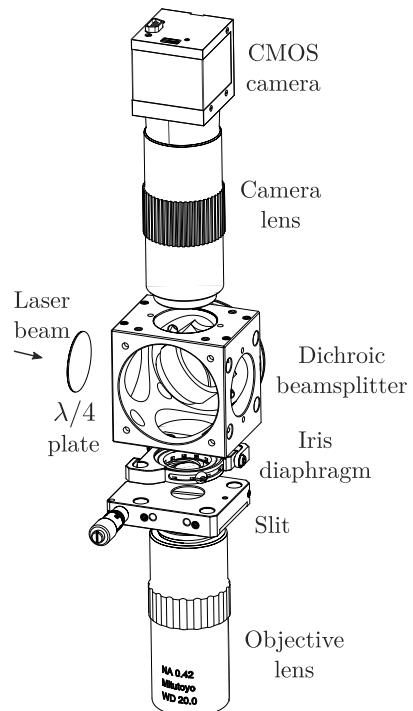


**Figure 5.21.** Fs laser inscription setup used to manufacture cladding waveguides in optical fibres. Slit beam shaping technique is employed. Assembly was carried out using SolidWorks 2019 SP4.0 software with components from Thorlabs, Inc. Adapted from [3].

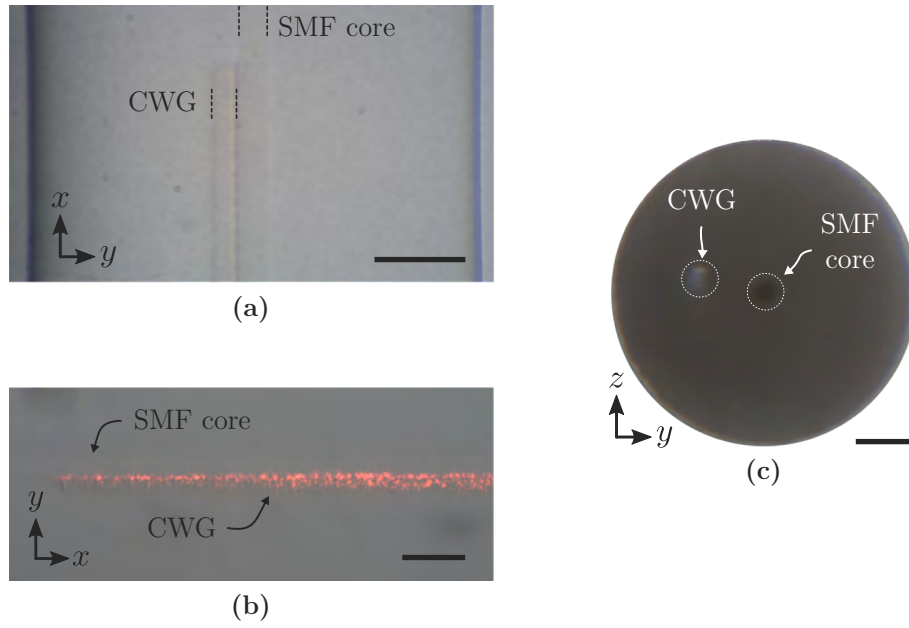


**Figure 5.22.** (a) Microscope image of the initial part of the CWG, specifically focusing on its coupling section. The transverse separation from the SMF core measures  $1\ \mu\text{m}$ . (b) Microscope image of the coupling section of the CWG, where red light ( $\lambda = 633\ \text{nm}$ ) is introduced at the distal end of the fibre. (c) Microscope image of the end-face of the SMF fibre, revealing the cross-section of the CWG. Scale bars in **a-c** are  $25\ \mu\text{m}$ . Adapted from [3].

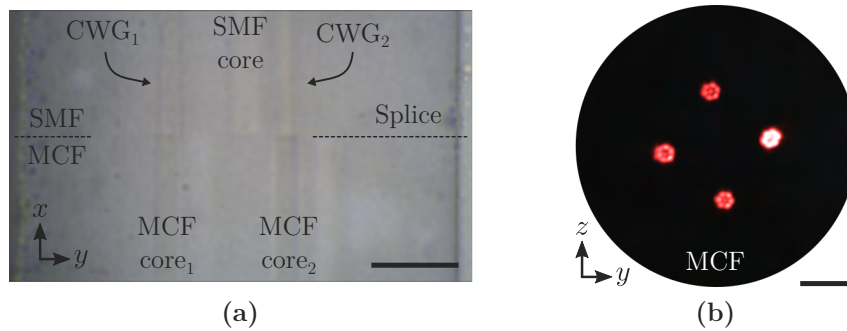


**Figure 5.23.** (a) Microscope image showcasing the splice zone between the SMF and the MCF. The focus of the image is directed towards MCF core<sub>1</sub>, revealing the corresponding CWG. Although slightly out of focus, the presence of MCF core<sub>2</sub> and its associated CWG can also be observed. (b) Microscope image of the end face of the MCF fibre after manufacturing the complete structure of Fig. 5.18. Red light ( $\lambda = 633\ \text{nm}$ ) is introduced at the distal end of the fibre to aid visualization. Scale bars in **a-b** are  $25\ \mu\text{m}$ . Adapted from [3].

### Application as a sensor

Lastly, as a final aspect of this study, a brief overview of its application as an optical sensor structure is presented. In addition to the schematic representation in Fig. 5.18, four FBGs are inscribed, with one placed in each core of the MCF. These FBGs have a length of  $1\ \text{mm}$ . What makes them unique is the method of their fabrication, which follows the same slit beam shaping technique employed for manufacturing CWGs. This ensures that the refractive index contrast induced by each laser pulse fully covers the cross-section of the respective core, as depicted in Fig. 5.25 **a**. This type of FBG is referred to as PI-b-PI FBGs [2]. The inscription setup used for this purpose is the same as shown in Fig. 5.21.

#### 5.4. Slit beam shaping technique for symmetric CWGs

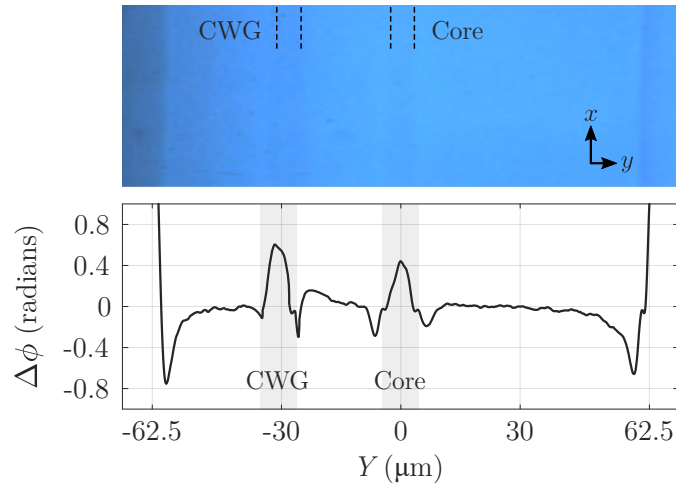


**Figure 5.24.** Transverse phase profile measured with QPM for a cladding waveguide inscribed at  $y = -30 \mu\text{m}$ . Adapted from [3].

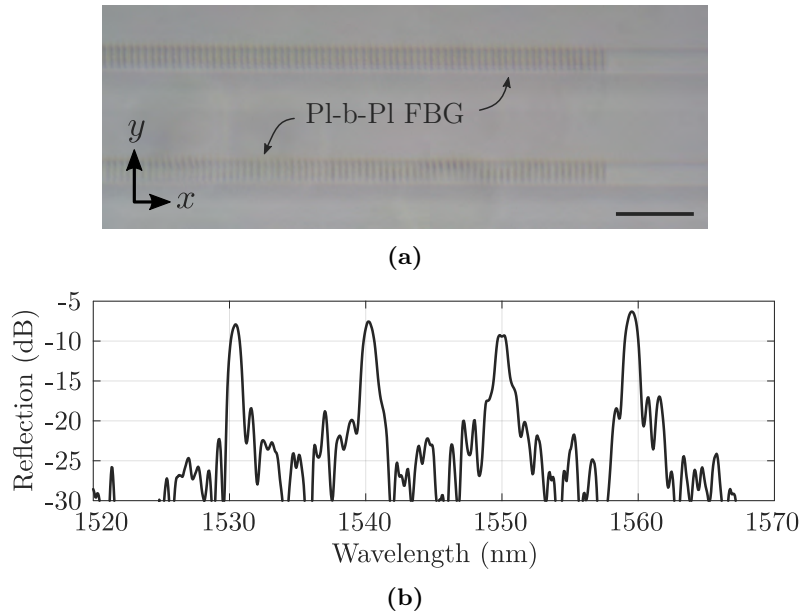


**Figure 5.25.** (a) Microscope image of the multicore fibre, with a PI-b-PI FBG inscribed in each of the two focused cores. (b) Reflection spectrum resulting from the structure depicted in Fig. 5.18, with a 1 mm long FBG inscribed in each core of the MCF. Scale bar in **a** is  $25 \mu\text{m}$ . Adapted from [3].

For each FBG, a laser pulse energy of  $1.09 \mu\text{J}$  (before the slit), a slit width of  $500 \mu\text{m}$ , a PRR of 300 Hz, and a specific grating period were employed. The chosen period ensures that the fourth order of the FBG generates Bragg wavelengths at 1530 nm, 1540 nm, 1550 nm, and 1560 nm, as clearly observed in the reflection spectrum displayed in Fig. 5.25 **b**.

#### 5.4.5 Conclusions

In this study, the slit beam shaping technique is employed for the first time to inscribe waveguides in optical fibres using femtosecond lasers. The research encompasses the design, simulation, and manufacturing of a structure consisting of four cladding waveguides, enabling evanescent

light coupling from the core of a single-mode fibre to each core of a multicore fibre. The manufactured cladding waveguides exhibit noteworthy characteristics, including an 8.1  $\mu\text{m}$  width (for single-mode behaviour in the C-Band), a circular cross-section, and estimated losses of 0.21 dB/cm. Furthermore, they possess a slightly higher RIC compared to the core, falling within the same order of magnitude, and demonstrate a quasi-step-index refractive index profile. The inscription parameters and waveguide design variables have been optimised through simulations. The significant potential of these waveguides for the advanced manufacturing of compact light-based sensors opens up vast possibilities within the context of Industry 4.0.

## References

- [1] Pallarés-Aldeiturriaga, D., Roldán-Varona, P., Rodríguez-Cobo, L., and Lopez-Higuera, J. M., “Astigmatism compensation for waveguide inscription in optical fiber by femtosecond lasers,” in *Seventh European Workshop on Optical Fibre Sensors*, Kalli, K., Brambilla, G., and O’Keeffe, S. O., Eds., SPIE, Aug. 2019. DOI: 10.1117/12.2539835.
- [2] Roldan-Varona, P., Pallares-Aldeiturriaga, D., Rodriguez-Cobo, L., and Lopez-Higuera, J. M., “Slit Beam Shaping Technique for Femtosecond Laser Inscription of Enhanced Plane-by-Plane FBGs,” *Journal of Lightwave Technology*, vol. 38, no. 16, pp. 4526–4532, Aug. 2020. DOI: 10.1109/jlt.2020.2992568.
- [3] Roldan-Varona, P., Rodriguez-Cobo, L., and Lopez-Higuera, J. M., “Slit Beam Shaping Technique for Femtosecond Laser Inscription of Symmetric Cladding Waveguides,” *IEEE Journal of Selected Topics in Quantum Electronics*, vol. 27, no. 6, p. 4400208, Nov. 2021. DOI: 10.1109/jstqe.2021.3092438.
- [4] Salter, P. S. and Booth, M. J., “Adaptive optics in laser processing,” *Light: Science & Applications*, vol. 8, no. 1, p. 110, Nov. 2019. DOI: 10.1038/s41377-019-0215-1.
- [5] Cui, Z. *et al.*, “Dynamic chromatic aberration pre-compensation scheme for ultrashort petawatt laser systems,” *Optics Express*, vol. 27, no. 12, pp. 16812–16822, May 2019. DOI: 10.1364/oe.27.016812.
- [6] Filippi, A. *et al.*, “Multimodal label-free ex vivo imaging using a dual-wavelength microscope with axial chromatic aberration compensation,” *Journal of Biomedical Optics*, vol. 23, no. 09, p. 091403, Mar. 2018. DOI: 10.1117/1.jbo.23.9.091403.
- [7] Marcinkevičius, A., Mizeikis, V., Juodkazis, S., Matsuo, S., and Misawa, H., “Effect of refractive index-mismatch on laser microfabrication in silica glass,” *Applied Physics A: Materials Science & Processing*, vol. 76, no. 2, pp. 257–260, Feb. 2003. DOI: 10.1007/s00339-002-1447-z.
- [8] Sun, Q., Jiang, H., Liu, Y., Zhou, Y., Yang, H., and Gong, Q., “Effect of spherical aberration on the propagation of a tightly focused femtosecond laser pulse inside fused silica,” *Journal of Optics A: Pure and Applied Optics*, vol. 7, no. 11, pp. 655–659, Oct. 2005. DOI: 10.1088/1464-4258/7/11/006.
- [9] Maclair, C., Mermillod-Blondin, A., Huot, N., Audouard, E., and Stoian, R., “Ultrafast laser writing of homogeneous longitudinal waveguides in glasses using dynamic wavefront correction,” *Optics Express*, vol. 16, no. 8, pp. 5481–5492, Apr. 2008. DOI: 10.1364/oe.16.005481.
- [10] Bisch, N., Guan, J., Booth, M. J., and Salter, P. S., “Adaptive optics aberration correction for deep direct laser written waveguides in the heating regime,” *Applied Physics A*, vol. 125, no. 5, Apr. 2019. DOI: 10.1007/s00339-019-2635-4.
- [11] Hampson, K. M. *et al.*, “Adaptive optics for high-resolution imaging,” *Nature Reviews Methods Primers*, vol. 1, no. 1, Oct. 2021. DOI: 10.1038/s43586-021-00066-7.
- [12] Salter, P. S. and Booth, M. J., “Focussing over the edge: Adaptive subsurface laser fabrication up to the sample face,” *Optics Express*, vol. 20, no. 18, pp. 19978–19989, Aug. 2012. DOI: 10.1364/oe.20.019978.

- [13] Karpinski, P., Shvedov, V., Krolkowski, W., and Hnatovsky, C., “Laser-writing inside uniaxially birefringent crystals: Fine morphology of ultrashort pulse-induced changes in lithium niobate,” *Optics Express*, vol. 24, no. 7, pp. 7456–7476, Mar. 2016. DOI: 10.1364/oe.24.007456.
- [14] Booth, M. J., Neil, M. A. A., and Wilson, T., “Aberration correction for confocal imaging in refractive-index-mismatched media,” *Journal of Microscopy*, vol. 192, no. 2, pp. 90–98, Nov. 1998. DOI: 10.1111/j.1365-2818.1998.99999.x.
- [15] Jesacher, A., Marshall, G. D., Wilson, T., and Booth, M. J., “Adaptive optics for direct laser writing with plasma emission aberration sensing,” *Optics Express*, vol. 18, no. 2, pp. 656–661, Jan. 2010. DOI: 10.1364/oe.18.000656.
- [16] Hering, J., Waller, E. H., and Freymann, G. V., “Automated aberration correction of arbitrary laser modes in high numerical aperture systems,” *Optics Express*, vol. 24, no. 25, pp. 28 500–28 508, Nov. 2016. DOI: 10.1364/oe.24.028500.
- [17] Marini, M. *et al.*, “Microlenses Fabricated by Two-Photon Laser Polymerization for Cell Imaging with Non-Linear Excitation Microscopy,” *Advanced Functional Materials*, p. 2213926, Mar. 2023. DOI: 10.1002/adfm.202213926.
- [18] Conci, C. *et al.*, “A Miniaturized Imaging Window to Quantify Intravital Tissue Regeneration within a 3D Microscaffold in Longitudinal Studies,” *Advanced Optical Materials*, vol. 10, no. 7, p. 2101103, Feb. 2022. DOI: 10.1002/adom.202101103.
- [19] Wang, P., Qi, J., Liu, Z., Liao, Y., Chu, W., and Cheng, Y., “Fabrication of polarization-independent waveguides deeply buried in lithium niobate crystal using aberration-corrected femtosecond laser direct writing,” *Scientific Reports*, vol. 7, no. 1, Jan. 2017. DOI: 10.1038/srep41211.
- [20] Cumming, B. P., Turner, M. D., Schröder-Turk, G. E., Debbarma, S., Luther-Davies, B., and Gu, M., “Adaptive optics enhanced direct laser writing of high refractive index gyroid photonic crystals in chalcogenide glass,” *Optics Express*, vol. 22, no. 1, pp. 689–698, Jan. 2014. DOI: 10.1364/oe.22.000689.
- [21] Sun, B., Salter, P. S., and Booth, M. J., “High conductivity micro-wires in diamond following arbitrary paths,” *Applied Physics Letters*, vol. 105, no. 23, p. 231105, Dec. 2014. DOI: 10.1063/1.4902998.
- [22] Zhou, K., Shen, F., Yin, G., and Zhang, L., “Optical fiber micro-devices made with femtosecond laser,” in *Advanced Photonics 2016 (IPR, NOMA, Sensors, Networks, SPCom, SOF)*, OSA, 2016. DOI: 10.1364/sensors.2016.sew3d.1.
- [23] Roldán-Varona, P., Pallarés-Aldeiturriaga, D., Rodríguez-Cobo, L., and López-Higuera, J. M., “All-in-fiber multiscan Mach-Zehnder interferometer assisted by core FBG for simultaneous multi-parameter sensing,” *Optics & Laser Technology*, vol. 132, p. 106459, Dec. 2020. DOI: 10.1016/j.optlastec.2020.106459.
- [24] Thomas, J., Voigtländer, C., Becker, R. G., Richter, D., Tünnermann, A., and Nolte, S., “Femtosecond pulse written fiber gratings: A new avenue to integrated fiber technology,” *Laser & Photonics Reviews*, vol. 6, no. 6, pp. 709–723, Feb. 2012. DOI: 10.1002/lpor.201100033.
- [25] Kochkina, E., “Stigmatic and Astigmatic Gaussian Beams in Fundamental Mode Path-length Signal Estimates,” Ph.D. dissertation, Leibniz Universität Hannover, 2013.

## References

- [26] Bellair, C. J. *et al.*, “Quantitative phase amplitude microscopy IV: Imaging thick specimens,” *Journal of Microscopy*, vol. 214, no. 1, pp. 62–69, Apr. 2004. DOI: 10.1111/j.0022-2720.2004.01302.x.
- [27] Pallares-Aldeiturriaga, D., Rodriguez-Cobo, L., Quintela, A., and Lopez-Higuera, J. M., “Curvature Sensor Based on In-Fiber Mach-Zehnder Interferometer Inscribed with Femtosecond Laser,” *Journal of Lightwave Technology*, vol. 35, no. 21, pp. 4624–4628, 2017, ISSN: 0733-8724. DOI: 10.1109/JLT.2017.2756103.
- [28] Yoo, S. J. B., Guan, B., and Scott, R. P., “Heterogeneous 2D/3D photonic integrated microsystems,” *Microsystems & Nanoengineering*, vol. 2, no. 1, Aug. 2016. DOI: 10.1038/micronano.2016.30.
- [29] Pont, M. *et al.*, “Quantifying  $n$ -Photon Indistinguishability with a Cyclic Integrated Interferometer,” *Physical Review X*, vol. 12, no. 3, p. 031033, Sep. 2022. DOI: 10.1103/physrevx.12.031033.
- [30] Butcher, H. L., MacLachlan, D. G., Lee, D., Thomson, R. R., and Weidmann, D., “Demonstration and characterization of ultrafast laser-inscribed mid-infrared waveguides in chalcogenide glass IG2,” *Optics Express*, vol. 26, no. 8, pp. 10930–10943, Apr. 2018. DOI: 10.1364/oe.26.010930.
- [31] Thomson, R. R., Psaila, N. D., Bookey, H. T., Reid, D. T., and Kar, A. K., “Controlling the Cross-section of Ultrafast Laser Inscribed Optical Waveguides,” in *Femtosecond Laser Micromachining: Photonic and Microfluidic Devices in Transparent Materials*, Osellame, R., Cerullo, G., and Ramponi, R., Eds. Berlin, Heidelberg: Springer Berlin Heidelberg, 2012, pp. 93–125, ISBN: 978-3-642-23366-1. DOI: 10.1007/978-3-642-23366-1\_5. [Online]. Available: [https://doi.org/10.1007/978-3-642-23366-1\\_5](https://doi.org/10.1007/978-3-642-23366-1_5).
- [32] Cheng, Y. *et al.*, “Control of the cross-sectional shape of a hollow microchannel embedded in photostructurable glass by use of a femtosecond laser,” *Optics Letters*, vol. 28, no. 1, pp. 55–57, Jan. 2003. DOI: 10.1364/ol.28.000055.
- [33] Ams, M., Marshall, G. D., Spence, D. J., and Withford, M. J., “Slit beam shaping method for femtosecond laser direct-write fabrication of symmetric waveguides in bulk glasses,” *Optics Express*, vol. 13, no. 15, pp. 5676–5681, 2005. DOI: 10.1364/opex.13.005676.
- [34] Cerullo, G. *et al.*, “Femtosecond micromachining of symmetric waveguides at 15  $\mu\text{m}$  by astigmatic beam focusing,” *Optics Letters*, vol. 27, no. 21, pp. 1938–1940, Nov. 2002. DOI: 10.1364/ol.27.001938.
- [35] Osellame, R. *et al.*, “Femtosecond writing of active optical waveguides with astigmatically shaped beams,” *Journal of the Optical Society of America B*, vol. 20, no. 7, p. 1559, Jul. 2003. DOI: 10.1364/josab.20.001559.
- [36] He, F. *et al.*, “Fabrication of microfluidic channels with a circular cross section using spatiotemporally focused femtosecond laser pulses,” *Optics Letters*, vol. 35, no. 7, pp. 1106–1108, Mar. 2010. DOI: 10.1364/ol.35.001106.
- [37] He, F. *et al.*, “Independent control of aspect ratios in the axial and lateral cross sections of a focal spot for three-dimensional femtosecond laser micromachining,” *New Journal of Physics*, vol. 13, no. 8, p. 083014, Aug. 2011. DOI: 10.1088/1367-2630/13/8/083014.

- [38] Vitek, D. N. *et al.*, “Spatio-temporally focused femtosecond laser pulses for nonreciprocal writing in optically transparent materials,” *Optics Express*, vol. 18, no. 24, pp. 24 673–24 678, Nov. 2010. DOI: 10.1364/oe.18.024673.
- [39] Brückner, R., “Properties and structure of vitreous silica. I,” *Journal of Non-Crystalline Solids*, vol. 5, no. 2, pp. 123–175, Nov. 1970. DOI: 10.1016/0022-3093(70)90190-0.
- [40] Chan, J. W., Huser, T. R., Risbud, S. H., Hayden, J. S., and Krol, D. M., “Waveguide fabrication in phosphate glasses using femtosecond laser pulses,” *Applied Physics Letters*, vol. 82, no. 15, pp. 2371–2373, Apr. 2003. DOI: 10.1063/1.1565708.
- [41] Roldán-Varona, P., Pallarés-Aldeiturriaga, D., Rodríguez-Cobo, L., and López-Higuera, J. M., “Hybrid Mach-Zehnder interferometer manufactured by femtosecond laser multiscan technique,” in *Seventh European Workshop on Optical Fibre Sensors*, Kalli, K., Brambilla, G., and O’Keeffe, S. O., Eds., SPIE, Aug. 2019. DOI: 10.1117/12.2538813.
- [42] McArthur, S. R., Thomson, R. R., and Ross, C. A., “Investigating focus elongation using a spatial light modulator for high-throughput ultrafast-laser-induced selective etching in fused silica,” *Optics Express*, vol. 30, no. 11, pp. 18 903–18 918, May 2022. DOI: 10.1364/oe.454280.
- [43] McArthur, S. R., Siliprandi, J., MacLachlan, D. G., Benoît, A., Thomson, R. R., and Ross, C. A., “Ultrafast laser inscription of efficient volume Bragg gratings deep in fused silica using active wavefront shaping,” *Optical Materials Express*, vol. 12, no. 9, pp. 3589–3599, Aug. 2022. DOI: 10.1364/ome.462654.
- [44] Kuang, Z., Li, J., Edwardson, S., Perrie, W., Liu, D., and Dearden, G., “Ultrafast laser beam shaping for material processing at imaging plane by geometric masks using a spatial light modulator,” *Optics and Lasers in Engineering*, vol. 70, pp. 1–5, Jul. 2015. DOI: 10.1016/j.optlaseng.2015.02.004.
- [45] Häfner, T., Strauß, J., Roider, C., Heberle, J., and Schmidt, M., “Tailored laser beam shaping for efficient and accurate microstructuring,” *Applied Physics A*, vol. 124, no. 2, Jan. 2018. DOI: 10.1007/s00339-017-1530-0.
- [46] Wang, A. *et al.*, “Mask-Free Patterning of High-Conductivity Metal Nanowires in Open Air by Spatially Modulated Femtosecond Laser Pulses,” *Advanced Materials*, vol. 27, no. 40, pp. 6238–6243, Sep. 2015. DOI: 10.1002/adma.201503289.
- [47] Zandrini, T., Shan, O., Parodi, V., Cerullo, G., Raimondi, M. T., and Osellame, R., “Multi-foci laser microfabrication of 3D polymeric scaffolds for stem cell expansion in regenerative medicine,” *Scientific Reports*, vol. 9, no. 1, Aug. 2019. DOI: 10.1038/s41598-019-48080-w.
- [48] Geng, Q., Wang, D., Chen, P., and Chen, S.-C., “Ultrafast multi-focus 3-D nanofabrication based on two-photon polymerization,” *Nature Communications*, vol. 10, no. 1, May 2019. DOI: 10.1038/s41467-019-10249-2.
- [49] Thomson, R. R. *et al.*, “Shaping ultrafast laser inscribed optical waveguides using a deformable mirror,” *Optics Express*, vol. 16, no. 17, pp. 12 786–12 793, Aug. 2008. DOI: 10.1364/oe.16.012786.
- [50] Günter, P. and Huignard, J.-P., Eds., *Photorefractive Materials and Their Applications 2*. Springer New York, 2007. DOI: 10.1007/0-387-34081-5.

## References

- [51] Dürr, Florian, “Laser-induced stress changes in optical fibers,” en, 2005. DOI: 10.5075/EPFL-THESIS-3314.
- [52] Mihailov, S. J. *et al.*, “Bragg Gratings Written in All-SiO<sub>2</sub> and Ge-Doped Core Fibers With 800-nm Femtosecond Radiation and a Phase Mask,” *Journal of Lightwave Technology*, vol. 22, no. 1, pp. 94–100, Jan. 2004. DOI: 10.1109/jlt.2003.822169.
- [53] Theodosiou, A. *et al.*, “Modified fs-Laser Inscribed FBG Array for Rapid Mode Shape Capture of Free-Free Vibrating Beams,” *IEEE Photonics Technology Letters*, vol. 28, no. 14, pp. 1509–1512, Jul. 2016. DOI: 10.1109/1pt.2016.2555852.
- [54] Martinez, A., Dubov, M., Khrushchev, I., and Bennion, I., “Direct writing of fibre Bragg gratings by femtosecond laser,” *Electronics Letters*, vol. 40, no. 19, p. 1170, 2004. DOI: 10.1049/el:20046050.
- [55] Williams, R. J., Krämer, R. G., Nolte, S., and Withford, M. J., “Femtosecond direct-writing of low-loss fiber Bragg gratings using a continuous core-scanning technique,” *Optics Letters*, vol. 38, no. 11, pp. 1918–1920, May 2013. DOI: 10.1364/ol.38.001918.
- [56] Williams, R. J., Jovanovic, N., Marshall, G. D., Smith, G. N., Steel, M. J., and Withford, M. J., “Optimizing the net reflectivity of point-by-point fiber Bragg gratings: The role of scattering loss,” *Optics Express*, vol. 20, no. 12, pp. 13 451–13 456, May 2012. DOI: 10.1364/oe.20.013451.
- [57] Erdogan, T., “Fiber grating spectra,” *Journal of Lightwave Technology*, vol. 15, no. 8, pp. 1277–1294, 1997. DOI: 10.1109/50.618322.
- [58] Zhou, K., Dubov, M., Mou, C., Zhang, L., Mezentsev, V. K., and Bennion, I., “Line-by-Line Fiber Bragg Grating Made by Femtosecond Laser,” *IEEE Photonics Technology Letters*, vol. 22, no. 16, pp. 1190–1192, Aug. 2010. DOI: 10.1109/1pt.2010.2050877.
- [59] Goebel, T. A. *et al.*, “Realization of aperiodic fiber Bragg gratings with ultrashort laser pulses and the line-by-line technique,” *Optics Letters*, vol. 43, no. 15, pp. 3794–3797, Aug. 2018. DOI: 10.1364/ol.43.003794.
- [60] Roberge, A., Loranger, S., Boisvert, J.-S., Monet, F., and Kashyap, R., “Femtosecond laser direct-writing of high quality first-order Bragg gratings with arbitrary complex apodization by phase modulation,” *Optics Express*, vol. 30, no. 17, p. 30 405, Aug. 2022. DOI: 10.1364/oe.465331.
- [61] Theodosiou, A., Lacraz, A., Stassis, A., Koutsides, C., Komodromos, M., and Kalli, K., “Plane-by-Plane Femtosecond Laser Inscription Method for Single-Peak Bragg Gratings in Multimode CYTOP Polymer Optical Fiber,” *Journal of Lightwave Technology*, vol. 35, no. 24, pp. 5404–5410, Dec. 2017. DOI: 10.1109/jlt.2017.2776862.
- [62] Theodosiou, A., Ioannou, A., and Kalli, K., “All-in-Fiber Cladding Interferometric and Bragg Grating Components Made via Plane-by-Plane Femtosecond Laser Inscription,” *Journal of Lightwave Technology*, vol. 37, no. 18, pp. 4864–4871, Sep. 2019. DOI: 10.1109/jlt.2019.2925263.
- [63] Ioannou, A., Theodosiou, A., Caucheteur, C., and Kalli, K., “Direct writing of plane-by-plane tilted fiber Bragg gratings using a femtosecond laser,” *Optics Letters*, vol. 42, no. 24, pp. 5198–5201, Dec. 2017. DOI: 10.1364/ol.42.005198.

- [64] Lu, P. *et al.*, “Plane-by-Plane Inscription of Grating Structures in Optical Fibers,” *Journal of Lightwave Technology*, vol. 36, no. 4, pp. 926–931, Feb. 2018. DOI: 10.1109/jlt.2017.2750490.
- [65] Lai, Y., Chen, Y., and Cheong, M. W. O., “Low-loss, high reflectivity, first-order, pitch-by-pitch fiber Bragg grating fabrication in truly free-standing single-mode fiber,” *Journal of Physics: Conference Series*, vol. 679, p. 012055, Feb. 2016. DOI: 10.1088/1742-6596/679/1/012055.
- [66] Moh, K. J., Tan, Y. Y., Yuan, X.-C., Low, D. K. Y., and Li, Z. L., “Influence of diffraction by a rectangular aperture on the aspect ratio of femtosecond direct-write waveguides,” *Optics Express*, vol. 13, no. 19, pp. 7288–7297, 2005. DOI: 10.1364/opex.13.007288.
- [67] Lammers, K. *et al.*, “Nanograting based birefringent retardation elements in integrated photonic circuits,” in *Laser-based Micro- and Nanoprocessing XIV*, Klotzbach, U., Kling, R., and Watanabe, A., Eds., SPIE, Mar. 2020. DOI: 10.1117/12.2544786.
- [68] Lancry, M., Poumellec, B., Canning, J., Cook, K., Poulin, J.-C., and Brisset, F., “Ultrafast nanoporous silica formation driven by femtosecond laser irradiation,” *Laser & Photonics Reviews*, vol. 7, no. 6, pp. 953–962, Jul. 2013. DOI: 10.1002/lpor.201300043.
- [69] Caucheteur, C., Guo, T., and Albert, J., “Polarization-Assisted Fiber Bragg Grating Sensors: tutorial and Review,” *Journal of Lightwave Technology*, vol. 35, no. 16, pp. 3311–3322, Aug. 2017. DOI: 10.1109/jlt.2016.2585738.
- [70] Lasi, H., Fettke, P., Kemper, H.-G., Feld, T., and Hoffmann, M., “Industry 4.0,” *Business & Information Systems Engineering*, vol. 6, no. 4, pp. 239–242, Jun. 2014. DOI: 10.1007/s12599-014-0334-4.
- [71] Xu, L. D., Xu, E. L., and Li, L., “Industry 4.0: State of the art and future trends,” *International Journal of Production Research*, vol. 56, no. 8, pp. 2941–2962, Mar. 2018. DOI: 10.1080/00207543.2018.1444806.
- [72] Zhang, C. and Chen, Y., “A Review of Research Relevant to the Emerging Industry Trends: Industry 4.0, IoT, Blockchain, and Business Analytics,” *Journal of Industrial Integration and Management*, vol. 05, no. 01, pp. 165–180, Feb. 2020. DOI: 10.1142/s2424862219500192.
- [73] Hamada, T., “Determinants of Decision-Makers’ Attitudes toward Industry 4.0 Adaptation,” *Social Sciences*, vol. 8, no. 5, p. 140, May 2019. DOI: 10.3390/socsci8050140.
- [74] Romero, D., Bernus, P., Noran, O., Stahre, J., and Fast-Berglund, Å., “The Operator 4.0: Human Cyber-Physical Systems & Adaptive Automation Towards Human-Automation Symbiosis Work Systems,” in *IFIP Advances in Information and Communication Technology*, Springer International Publishing, 2016, pp. 677–686. DOI: 10.1007/978-3-319-51133-7\_80.
- [75] Gattass, R. R. and Mazur, E., “Femtosecond laser micromachining in transparent materials,” *Nature Photonics*, vol. 2, no. 4, pp. 219–225, Apr. 2008. DOI: 10.1038/nphoton.2008.47. [Online]. Available: <https://doi.org/10.1038/nphoton.2008.47>.
- [76] Osellame, R., Cerullo, G., and Ramponi, R., Eds., *Femtosecond Laser Micromachining*. Springer Berlin Heidelberg, 2012. DOI: 10.1007/978-3-642-23366-1.

## References

- [77] Roldán-Varona, P., Rodríguez-Cobo, L., and López-Higuera, J. M., “Reflection-based lab-in-fiber sensor integrated in a surgical needle for biomedical applications,” *Optics Letters*, vol. 45, no. 18, pp. 5242–5245, Sep. 2020. DOI: 10.1364/ol.399407.
- [78] Will, M., Nolte, S., Chichkov, B. N., and Tünnermann, A., “Optical properties of waveguides fabricated in fused silica by femtosecond laser pulses,” *Applied Optics*, vol. 41, no. 21, pp. 4360–4363, Jul. 2002. DOI: 10.1364/ao.41.004360.
- [79] Siebenmorgen, J., Calmano, T., Petermann, K., and Huber, G., “Highly efficient Yb:YAG channel waveguide laser written with a femtosecond-laser,” *Optics Express*, vol. 18, no. 15, pp. 16 035–16 041, Jul. 2010. DOI: 10.1364/oe.18.016035.
- [80] Valle, G. D., Taccheo, S., Osellame, R., Festa, A., Cerullo, G., and Laporta, P., “1.5  $\mu\text{m}$  single longitudinal mode waveguide laser fabricated by femtosecond laser writing,” *Optics Express*, vol. 15, no. 6, pp. 3190–3194, 2007. DOI: 10.1364/oe.15.003190.
- [81] Babu, B. H. *et al.*, “Stress-induced optical waveguides written by an ultrafast laser in  $\text{Nd}^{3+}$ ,  $\text{Y}^{3+}$  co-doped  $\text{SrF}_2$  crystals,” *Applied Optics*, vol. 58, no. 4, pp. 984–990, Jan. 2019. DOI: 10.1364/ao.58.000984.
- [82] Pallarés-Aldeiturriaga, D., Roldán-Varona, P., Rodríguez-Cobo, L., and López-Higuera, J. M., “Optical Fiber Sensors by Direct Laser Processing: A Review,” *Sensors*, vol. 20, no. 23, p. 6971, Dec. 2020. DOI: 10.3390/s20236971.
- [83] Lai, Y., Zhou, K., Zhang, L., and Bennion, I., “Microchannels in conventional single-mode fibers,” *Optics Letters*, vol. 31, no. 17, pp. 2559–2561, Aug. 2006. DOI: 10.1364/ol.31.002559.
- [84] Li, W. W., Chen, W. P., Wang, D. N., Wang, Z. K., and Xu, B., “Fiber inline Mach–Zehnder interferometer based on femtosecond laser inscribed waveguides,” *Optics Letters*, vol. 42, no. 21, pp. 4438–4441, 2017, ISSN: 0146-9592. DOI: 10.1364/OL.42.004438. [Online]. Available: <https://www.osapublishing.org/abstract.cfm?URI=ol-42-21-4438>.
- [85] Zhang, Y., Lin, C., Liao, C., Yang, K., Li, Z., and Wang, Y., “Femtosecond laser-inscribed fiber interface Mach–Zehnder interferometer for temperature-insensitive refractive index measurement,” *Optics Letters*, vol. 43, no. 18, pp. 4421–4424, 2018, ISSN: 0146-9592. DOI: 10.1364/ol.43.004421.
- [86] Waltermann, C., Doering, A., Köhring, M., Angelmahr, M., and Schade, W., “Cladding waveguide gratings in standard single-mode fiber for 3D shape sensing,” *Optics Letters*, vol. 40, no. 13, pp. 3109–3112, 2015, ISSN: 0146-9592. DOI: 10.1364/OL.40.003109. [Online]. Available: <https://www.osapublishing.org/abstract.cfm?URI=ol-40-13-3109>.
- [87] Adams, C. S. and Hughes, I. G., *Optics f2f*. Oxford University PressOxford, Dec. 2018. DOI: 10.1093/oso/9780198786788.001.0001.
- [88] Sowa, S., Watanabe, W., Tamaki, T., Nishii, J., and Itoh, K., “Symmetric waveguides in poly(methyl methacrylate) fabricated by femtosecond laser pulses,” *Optics Express*, vol. 14, no. 1, pp. 291–297, 2006. DOI: 10.1364/opex.14.000291.
- [89] Qi, J. *et al.*, “Fabrication of polarization-independent single-mode waveguides in lithium niobate crystal with femtosecond laser pulses,” *Optical Materials Express*, vol. 6, no. 8, pp. 2554–2559, Jul. 2016. DOI: 10.1364/ome.6.002554.

- [90] Salter, P. S. *et al.*, “Adaptive slit beam shaping for direct laser written waveguides,” *Optics Letters*, vol. 37, no. 4, pp. 470–472, Feb. 2012. DOI: 10.1364/ol.37.000470.
- [91] Ams, M., Marshall, G. D., and Withford, M. J., “Study of the influence of femtosecond laser polarisation on direct writing of waveguides,” *Optics Express*, vol. 14, no. 26, pp. 13 158–13 163, 2006. DOI: 10.1364/oe.14.013158.

# 6

## Standard fibre-based sensors

---

<b>6.1</b>	<b>Background of OFSs . . . . .</b>	<b>93</b>
<b>6.2</b>	<b>In-fibre MZI for multiparameter sensing . . . . .</b>	<b>94</b>
6.2.1	Background . . . . .	94
6.2.2	Theory and sensor design . . . . .	95
6.2.3	Manufacturing . . . . .	97
6.2.4	Experimental results and discussion . . . . .	102
6.2.5	Cross-sensitivity . . . . .	104
6.2.6	Conclusions . . . . .	105
<b>6.3</b>	<b>Reflection-based LIF sensor integrated in a surgical needle . . . . .</b>	<b>106</b>
6.3.1	Background . . . . .	106
6.3.2	Theory and sensor design . . . . .	107
6.3.3	Finite element simulation . . . . .	108
6.3.4	Manufacturing . . . . .	110
6.3.5	Experimental results and discussion . . . . .	112
6.3.6	Conclusions . . . . .	114
	<b>References . . . . .</b>	<b>115</b>

---

**O**PTICAL fibres are widely used in sensing applications due to their high sensitivity, fast response time, and immunity to electromagnetic interference. Since the beginning of this century, femtosecond laser inscription has emerged as a powerful tool for fabricating optical fibre sensors with improved performance and unique features. Making a very rough classification, these sensors can be differentiated according to whether they are made using standard fibres or specialty fibres. This chapter covers the works related to the former type, while the next chapter addresses specialty fibre-based sensors.

It should be noted that the definition of the term *standard fibre* may vary depending on the context, and there is no widely accepted definition. However, in the context of optical fibres, it generally refers to a basic step-index fibre made with a standard material like silica, with typical values for parameters such as core size and numerical aperture. Specifically, in this chapter,

we refer to the standard telecommunication fibre, single-mode fibre (@1550 nm) with a core diameter of 8.2  $\mu\text{m}$  and a numerical aperture of 0.11 (@1550 nm).

Section 6.1 provides a brief historical background of optical fibre sensors (OFSs), which is relevant for this chapter as well as the next one. This chapter also presents the research conducted by Roldán *et al.*, which is discussed in sections 6.2 [1, 2], and 6.3 [3]. It is worth noting that there are other works on single-mode fibre-based sensors that have been conducted but are not elaborated in this book [4]. Moreover, the review conducted by Pallarés *et al.* offers a summary of such sensors documented in literature for readers who want to explore the topic further [5].

## 6.1 Background of OFSs

In 1961, Snitzer demonstrated the resonant cavity behaviour of optical fibres [6], which sparked significant research interest in the transducing properties of optical fibres [7–11]. This research ultimately led to the development of OFSs in the mid-1970s, which boasted numerous benefits compared to other sensing methods, including immunity to electrical interference, low transmission loss, remote sensing capability, and high sensitivity that could outperform other sensors by 10-100 dB in some cases [12]. Initially, OFS configurations were based on interferometric schemes (*e.g.*, Fabry-Perot interferometer (FPI), Michelson interferometer (MI), Mach-Zehnder interferometer (MZI), and Sagnac interferometer), which provided a single measurement per sensor (point sensing) [11]. Later on, the development of FBG technology emerged from photosensitivity research conducted by Hill *et al.* in 1978 [13]. This technology allowed for more compact structures with higher signal-to-noise ratios and was commercialised in the 1990s. FBGs are now one of the most widely used OFS methods due to their durability, wavelength multiplexing capabilities, linear behaviour, small size (a few millimetres), and ability for mass production [14].

In addition to point sensing, optical time domain reflectometry (OTDR), demonstrated in the late 1980s, enabled the development of distributed sensors in the field of OFSs [15]. These sensors use Raman, Brillouin, or Rayleigh fibre backscattering to detect changes along the entire fibre with resolutions initially as low as 1 metre, which have since been improved to cm-level resolutions [16]. The oil and gas sector accounts for 46% of the total distributed sensor market due to the suitability of these sensors for monitoring long structures such as pipelines and oil or gas wells [17]. While point sensing was initially more popular, distributed sensing caught up by 2008 and surpassed it by 2014 [12].

This trend of optical fibre sensors dominating the market is expected to continue due to the development of compact transducer structures and specialty fibres that allow for the measurement of new parameters beyond temperature, strain, and magnetic field [10]. These advances are particularly useful in medical and biological applications where probe size is a limitation, and tiny transducer structures such as lab-in-fibre (LIF) or lab-on-chip (LOC) platforms are being developed to monitor multiple parameters [3, 18–20]. Additionally, point structures like FBGs and reflectors can be combined with distributed sensing to create quasi-distributed sensing, which refines sensing and adds additional measurement to key positions [21].

Laser technology has been used commercially since the 1970s and offers a range of possibilities to modify the intrinsic properties of optical fibre [22]. Ultrafast laser technologies, which have

## 6.2. In-fibre MZI for multiparameter sensing

matured over the past 50 years, allow for precise micro-scale changes and the development of compact, high-transduction structures [23]. This offers new opportunities for expanding the industrial and medical market for OFS.

## 6.2 In-fibre MZI for multiparameter sensing

This section showcases a femtosecond laser-inscribed hybrid cladding waveguide Mach-Zehnder interferometer (CWG-MZI) sensor. The CWG was inscribed using an aberration-compensation technique and the multiscan method, resulting in a phase shift that varies depending on the number of sweeps performed, thereby controlling the free spectral range (FSR) of the interference pattern. The temperature characterisation revealed a lower and proportional RIC compared to previously reported CWG-MZIs, indicating less degradation at high temperatures. The CWG's proximity to the cladding/air boundary also provides good RI sensitivity. Finally, curvature and strain were measured simultaneously without being affected by cross-sensitivity due to the FBG inscribed in the reference arm using the point-by-point (PbP) technique.

### 6.2.1 Background

The manufacturing of reliable and compact devices in optical fibre exhibits an increased demand due to their intrinsic properties and the possibility of monitoring several parameters simultaneously in a single device [5, 24, 25]. For this purpose, CWGs are a key technology to enhance the complexity and possibilities of optical fibre sensors [25]. The manufacture of waveguides as the optical interconnection structure of different sensor elements has enabled the development of more advanced sensor structures, such as optical couplers, waveguide Bragg gratings (WBGs), or interferometers, in their different forms [26, 27]. One of the most straightforward patterns that can be manufactured with CWGs is an in-fibre MZI. Its main operation principle consists in a CWG decoupling light from core and then coupling it back in order to act as a sensing arm of a MZI instead of using conventional cladding modes. These interferometers are quite versatile, can measure different parameters and offer the possibility to adjust their sensitivity. They are attractive not only for its enhanced behaviour compared to conventional MZI [28], but also for being a solid step to future next-gen waveguide based devices [29].

This type of interferometers were introduced by several authors independently, measuring different parameters, but not all of them together, as it is done in this work; thus, proving its intrinsic versatility. Table 6.1 shows the sensitivities achieved for each parameter in each work. The temperature was measured in a low range (25–100 °C), except in one case [28], achieving sensitivities higher than conventional FBGs. Curvature and strain have been measured in different works independently when these parameters exhibit a high cross-sensitivity. In this work, the joint discrimination of both parameters is undertaken. Moreover, the refractive index has only been studied once, in [30], with great uncertainty.

In addition to measuring different parameters, the manufacturing of these devices depends on each application. The analysis of the different inscription parameters used in the manufacture of CWGs is therefore worth highlighting. In Table 6.2, the reported inscription parameters and types of the waveguides for the previous works are summarised. A common trend observed is the use of low to moderate pulse repetition rates, typically ranging from 5 to 200 kHz, and 500–1200

**Table 6.1.** Compilation of parameters measured with CWG-MZI existing in the literature.

Ref.	Temperature	Curvature	Strain	RI
[28]	Non linear (50 – 650 °C)	–	–	–
[31]	0.22 nm/°C (20 – 90 °C)	–	4.89 pm/ $\mu\epsilon$	–
[30]	0.6 nm/°C (25 – 100 °C)	–	–	60 nm/RIU <sup>a</sup>
[29]	0.49 nm/°C (50 – 60 °C)	(with FBG)	(with FBG)	(with FBG)
[28]	0.023 nm/°C (25 – 180 °C)	9.49 nm/m <sup>-1</sup>	–	–

<sup>a</sup> RI Range: 1.33 – 1.34.

pulses/ $\mu\text{m}$ . There are three types of inscriptions depending on the method employed to deal with the wavefront distortion caused by the cylindrical geometry of optical fibres. Waveguides can be inscribed without addressing the distortion, exploiting the filamentation effect [28]. As a solution to induced aberration, they can also be inscribed with an oil-immersed objective [30, 31], or employing other arrangements such as the one employed in [2, 29]. This level of versatility further motivates the need for extensive characterisation of RIC and its effects on the transmission spectra of MZIs.

In this study, a 6-mm CWG-MZI was produced using the multiscan technique, which offers a more comprehensive characterisation compared to previous literature. The focus of the characterisation is on the phase change with each scan, which provides an efficient means of controlling the FSR. As a significant innovation, we analytically describe the degradation ratio of the manufactured waveguide (multiscan technique) compared to that based on filamentation for high temperatures, in order to justify the advantages of this inscription method. Furthermore, addressing the cross-sensitivity is necessary due to the number of parameters that this interferometer can measure. To achieve this, an FBG is inscribed in the reference arm. Thus, a hybrid MZI is demonstrated and used for simultaneous strain and bending measurements, two parameters that share a strong cross-sensitivity as previously mentioned. Additionally, the sensor’s ability to distinguish the surrounding refractive index (SRI) is also demonstrated.

## 6.2.2 Theory and sensor design

In a simple way, MZIs are based on the optical path difference (OPD) that arises when a beam of light is divided into two optical paths, one of which is taken as a reference, while the other acts as a sensor element. When the MZI is manufactured in an optical fibre, it can be understood that the fundamental mode of the core (reference) is decoupled to a secondary mode that propagates during a distance  $L$  in a cladding waveguide (sensing element), until it is coupled again, deriving

**Table 6.2.** Overview of inscription parameters utilised for CWG-MZI reported in the literature.

Ref.	Inscription method	NA	$\lambda$ (nm)	PRR (kHz)	$\frac{\text{pulses}}{\mu\text{m}}$	$\tau$ (fs)	$E_p$ ( $\mu\text{J}$ )
[31]	Oil immersion	$\times 100, 1.25$	800	5	500	35	0.5
[30]	Oil immersion	$\times 60, 1.4$	532	200	1000	250	0.12
[29]	Adaptive optics	$\times 100, 0.42$	517	50	1000	220	0.11
[28]	Filamented waveguide	$\times 100, 0.5$	1030	120	1200	370	1.09

## 6.2. In-fibre MZI for multiparameter sensing

in an OPD that causes an interference defined by the well-known expression (detailed in [32])

$$I \approx I_c + I_{wg} + 2\sqrt{I_c I_{wg}} \cos\left(\frac{2\pi\Delta n L}{\lambda} + \phi_0\right), \quad (6.1)$$

where  $I_c$  and  $I_{wg}$  represent fundamental (core) and secondary (waveguide) irradiance, respectively,  $\Delta n = |n_c - n_{wg}|$  corresponds to the effective mode index difference between both modes,  $L$  is the length of the waveguide through which the secondary mode propagates, and  $\phi_0$  the initial phase.

The transmission spectrum has a sinusoidal shape in which local minima (known as interference dips) shifts are used to quantify the measured parameter,

$$\lambda_{dip} = \frac{2\pi \cdot \Delta n \cdot L}{\pi(2m + 1) - \phi_0}. \quad (6.2)$$

Likewise, the free spectral range can be controlled during the inscription of the waveguide, since it depends on its refractive index. FSR is defined as the spectral distance between two successive transmitted intensity maxima or minima for a given wavelength  $\lambda_0$ :

$$FSR \approx \frac{\lambda_0^2}{\Delta n \cdot L}. \quad (6.3)$$

The proposed sensor design is depicted in Fig. 6.1. Secondary mode guidance was achieved by inscribing in a SMF a cladding waveguide whose path length is  $L \approx 2 \cdot L_1 + L_2$ , where  $L_1$  refers to the S-Bend section that decouples the light from the core towards the straight cladding section  $L_2$ , separated from the core by a transversal distance  $d$ , to be subsequently coupled back to the core under an identical S-Bend. The separation angle of the S-Bend section ( $\theta = \arctan(d/L_1)$ ) is proportional to the waveguide coupling losses.

Parallel to the MZI cladding section, a FBG of length  $L_g$  was inscribed in the core through the point-by-point (PbP) inscription method [25]. The capacity to perform gratings of period  $\Lambda \simeq 1 \mu\text{m}$  allows to have a 2<sup>nd</sup>-order Bragg wavelength in the S-band ( $\lambda_B = \frac{2}{m} n_{eff} \Lambda$  with  $m = 2$ ). The grating period ( $\Lambda$ ) is controlled by  $\Lambda = v/PRR$ , where  $v$  is the writing speed, and PRR is the pulse repetition rate of the laser.

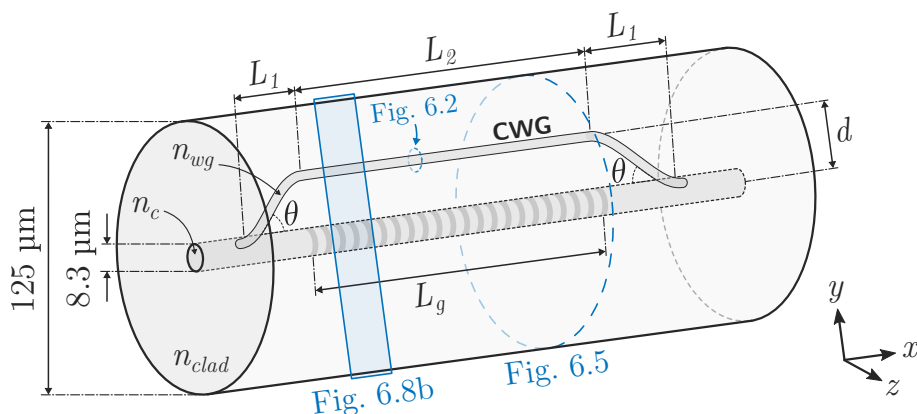


**Figure 6.1.** Schematic illustration of the all-in-fibre 6 mm optical device. Adapted from [1].

### Waveguide inscription: multiscan technique

The waveguide manufacture is schematically depicted in Fig. 6.2. It is based on the multiscan technique, through which multiple inscriptions are made, with sub-micron displacements ( $s$ ) perpendicular to both the laser beam propagation axis and fibre axis between each CWG scan [2]. This *inscribe-and-move* process ends when the structure with the required geometrical properties is obtained, typically when the desired waveguide width ( $R$ ) is achieved. To ensure optimal conditions, a series of MZIs were conducted to study the values of various parameters.

### 6.2.3 Manufacturing

All inscriptions were performed using a commercial femtosecond fibre laser chirped pulse amplifier from Calmar lasers, operating at 1030 nm, with a 370 fs pulse duration and a variable PRR from 1 Hz to 120 kHz. Laser pulses were focused through an  $\times 100$ , NA=0.5 objective lens from Mitutoyo. The stripped and stretched optical fibre was placed on a slide and covered by a coverslip [33]. As shown in Fig. 6.2, there was an index-matching oil in the middle that allows to eliminate the cylindrical aberration inherent to the fibre when in-fibre processing is carried out. The slide that contains the fibre was placed on a platform located on a nano-resolution XYZ motor stage from Aerotech. Using a CCD camera and a white light source that illuminates the platform, it was possible to accurately visualize and determine the fibre position.

### Cladding waveguide

One of the crucial aspects of the MZI is the light coupling from the core (reference arm) to the CWG (sensing arm). Regarding its design,  $\theta$  parameter is essential, determined by  $d$  and  $L_1$  (see Fig. 6.1). Among the many existing structures for the coupling of light, two stand out in the existing literature [26]: transition in curve (S-Bend) or transition in straight section. The simulations were performed using finite element beam propagation method (FE-BPM) from RSoft commercial software (version 2019.05), in order to select the most suitable geometry. The parameters used in the simulation are shown in Table 6.3. A sweep was performed on  $L_1$ . The schematic diagrams with the notation used in the simulated structures are depicted in Fig. 6.3, which also corresponds to the coupling section of Fig. 6.1.

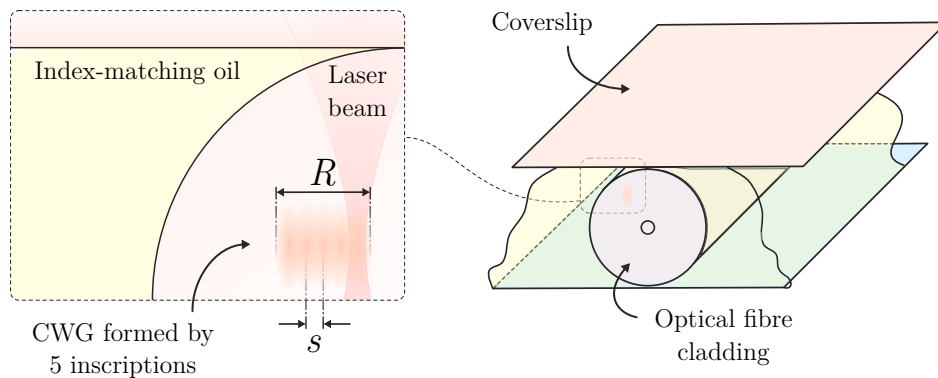


**Figure 6.2.** Schematic illustration of the multiscan technique. Cross-section view of SMF, with multiple inscriptions for the manufacture of the CWG. Index-matching oil is used. Adapted from [1].

## 6.2. In-fibre MZI for multiparameter sensing

**Table 6.3.** Parameters used in the CWG simulations (FE-BPM in RSoft).

$n_{clad}$	1.4661
$d$	40 $\mu\text{m}$
$R$	4 $\mu\text{m}$
$\Delta n_{wg}$	$5 \cdot 10^{-3}$
Mode	LP <sub>01</sub>
$L_1$	[250, 5000] $\mu\text{m}$

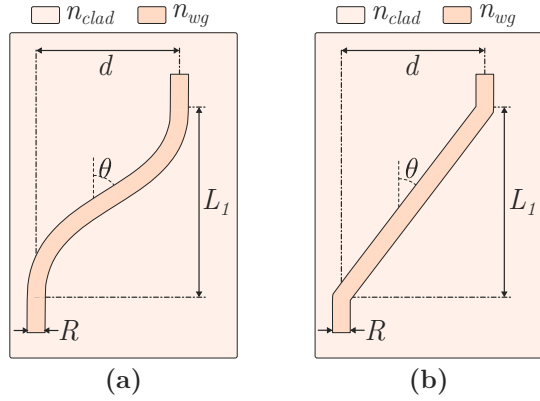


**Figure 6.3.** Schematic diagram of the simulated structures, with the parameters indicated in Table 6.3. (a) S-Bend transition, (b) and straight transition. Adapted from [1].

Taking into account that, due to physical restrictions, it is interesting to make a compact sensor, values of  $L_1 < 1500 \mu\text{m}$  are chosen. In that case S-Bend transitions are more appropriate than straight transitions, limiting losses in the coupling. In Fig. 6.4, the simulation results are shown.

After modelling and experimental inscriptions, it has been found that the following parameters cause a cladding waveguide with the appropriate symmetry and light guidance. The S-Bend sections have a length  $L_1 = 1 \text{ mm}$  (Fig. 6.4 c), while the cladding section has a length  $L_2 = 4 \text{ mm}$ , identical to the length  $L_g$  of the FBG located in the core. The MZI cladding section is transversally separated  $d = 40 \mu\text{m}$  from the core, which results in a S-Bend transition angle of  $\theta = 2.29^\circ$ . This angular value limits the coupling losses of the S-Bend section.

Regarding inscription parameters, cladding waveguides have been manufactured using a pulse energy of 0.19  $\mu\text{J}$ , a PRR of 60 kHz and 800 pulses/ $\mu\text{m}$  ( $v = 75 \mu\text{m/s}$ ).

In Fig. 6.5, the fibre end face for a waveguide formed by 5 scans is depicted. The space between those scans is  $s = 0.2 \mu\text{m}$ , originating a waveguide structure with a width  $R \simeq 4 \mu\text{m}$ .

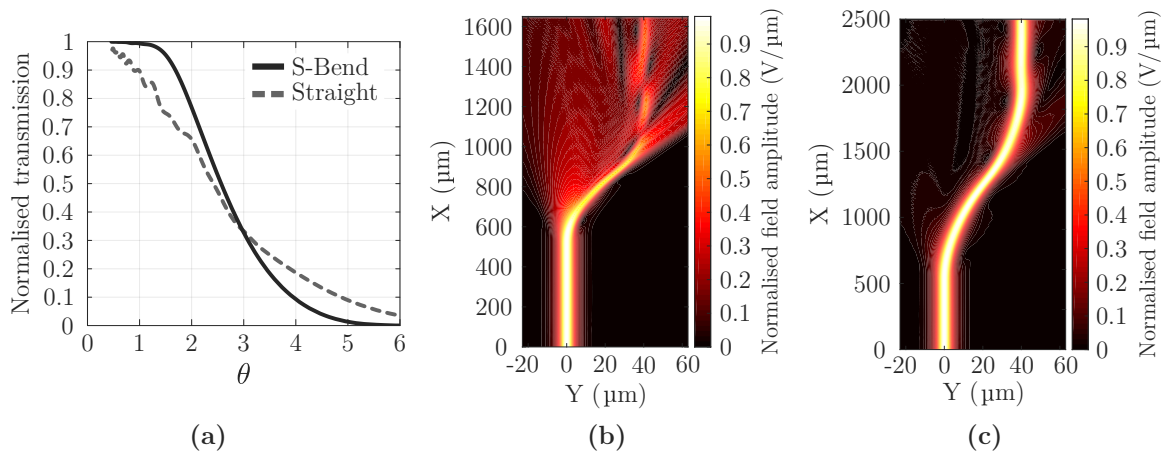


**Figure 6.4.** (a) Normalised transmission of LP<sub>01</sub> mode based on separation angle ( $\theta$ ) for straight and S-Bend transitions. (b) S-Bend example with  $L_1 = 650 \mu\text{m}$  ( $\theta = 3.52^\circ$ ). (c) S-Bend example with  $L_1 = 1000 \mu\text{m}$  ( $\theta = 2.29^\circ$ ). Adapted from [1].

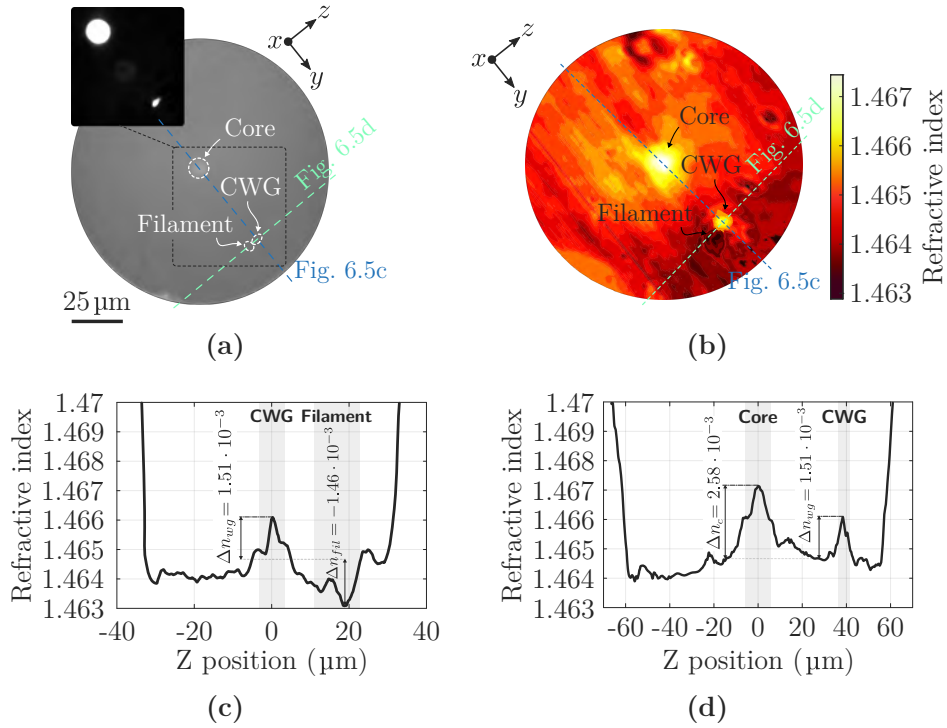


**Figure 6.5.** (a) SMF end face of the waveguide captured with a CCD camera. (b) 3D RI profile measured with a RI Profiler. (c) Core and CWG RI Y profile ( $Z = 0 \mu\text{m}$ ). (d) CWG and filament RI Z profile ( $Y = 40 \mu\text{m}$ ). Adapted from [1].

By illuminating the distal end of the fibre sample with a white light source, two light spots are observed, corresponding to the core and the CWG (Fig. 6.5 a). It can be seen that the CWG presents a remarkable circular symmetry. Figure 6.5 b shows the 3D profile of the fibre end-face, with the regions corresponding to the core, the CWG and the filament generated during the laser processing. For this, RNF profilometry was obtained with Sira Electro-Optics optical fibre refractive index profiler.

Figure 6.5 c is intended to show the RI profile in the core and the CWG, the latter presenting an RI change of  $\Delta n_{wg} = 1.51 \cdot 10^{-3}$ . If an RI profile is made on the  $Z$  axis in the region of the CWG ( $Y = d = 40 \mu\text{m}$ ), it can be distinguished the zones corresponding to the CWG and the filament generated during inscription. Since aberration compensation was used in the inscription process, the RI change is positive in the focal volume, whereas it is negative in the filamented region ( $\Delta n_{fil} = -1.46 \cdot 10^{-3}$ ). In case of not using adaptive optics, the RI change is negative in the focal volume and positive in the filament [28].

On the other hand, waveguides were also characterised through the QPM technique. As explained in the chapter 4, it is a microscopy method that quantifies the phase change that occurs when the light that illuminates the platform passes an optically dense sample as is the optical fibre [34]. It must be noted that the phase change and the RI change are proportional, being related by the well-known relation

$$\Delta(\Delta n) = \frac{\lambda}{2\pi \cdot z} \Delta\phi, \quad (6.4)$$

where  $\lambda$  is the wavelength of the light source (550 nm), and  $z$  is the region with different RI.

## 6.2. In-fibre MZI for multiparameter sensing

In order to obtain an exhaustive study of inscribed waveguides by multiscan technique, the phase change associated with waveguides formed between 1 and 10 scans was characterised. QPM has been used with a defocusing of  $\delta z = 3 \mu\text{m}$  and a  $\times 100$ ,  $\text{NA} = 0.5$  Mitutoyo objective lens. The experimental results of Fig. 6.6 determine that the lines of modified material induced by each scan cause an increment in the phase change of the waveguide, until reaching a point at which said change tends to stabilise (9 scans). On average, the overlap between consecutive scans is  $\sim 72.24\%$ . The phase increase is due to the densification caused by the increment in the fictive temperature during multiscan inscription. In a simplified way, two sections with the following slopes can be established:

$$m = \frac{\Delta(\Delta\phi)}{\Delta(\#\text{scans})} = \begin{cases} 94.71 \frac{\text{mrad}}{\text{scan}}, & \forall \#\text{scans} \in \mathbb{N} \cap [1, 8]. \\ 0 \frac{\text{rad}}{\text{scan}}, & \forall \#\text{scans} \in \mathbb{N} \cap [9, \infty). \end{cases} \quad (6.5)$$

The CWG inscription of Fig. 6.5 was stopped  $\sim 10 \mu\text{m}$  before the cleaved end of the fibre, which is why RNF indicates a lower RI change in the CWG than in the core, while QPM indicates a higher phase change in the waveguide than in the core (for 5 scans).

### Mach-Zehnder Interferometer

From now on, waveguides formed by 5 scans will be used to manufacture the MZI, with a refractive index change similar to the core (Fig. 6.6), and with a circular symmetry that favours light guidance. A greater number of scans would result in structures with an almost rectangular cross-section, hindering the light coupling. The MZI was also characterised during multiscan inscription. A broadband light source (HP 83437A), and an optical spectrum analyser (Anritsu MS9740A) were used in a transmission configuration.

Figure 6.7 **a** shows the MZI transmission spectra when the secondary path is formed between 1 and 5 scans. It is noteworthy that the losses caused by the inscription of the sensor are relatively low, standing at approximately 6 dB. Likewise, Fig. 6.7 **b** shows the variation of the FSR with the number of waveguide scans. FSR values have been extracted from Fig. 6.7 **a** from the spectral distance between two successive transmitted intensity maxima or minima. Emphasis is placed on the idea that the multiscan technique is a potential way to control the properties

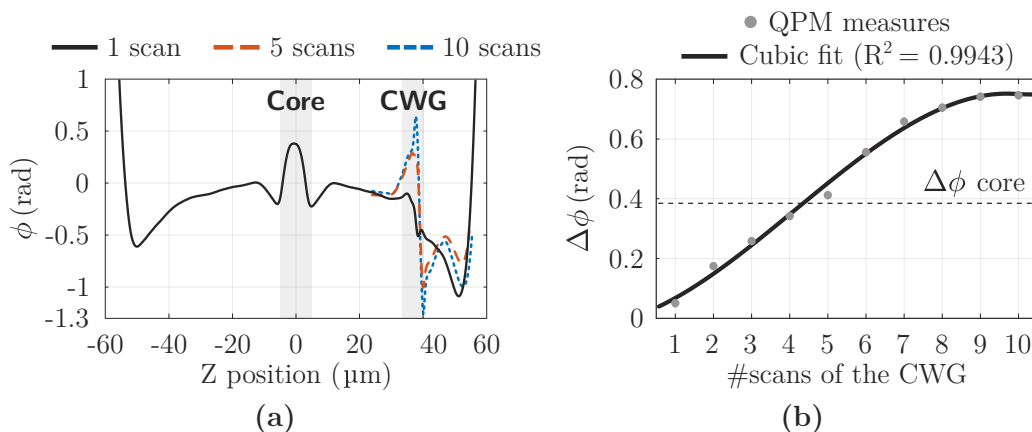


**Figure 6.6.** (a) Phase profile measured with QPM for waveguides formed by 1, 5 and 10 scans. (b) CWG-cladding phase change based on the number of scans that form the waveguide. Adapted from [1].

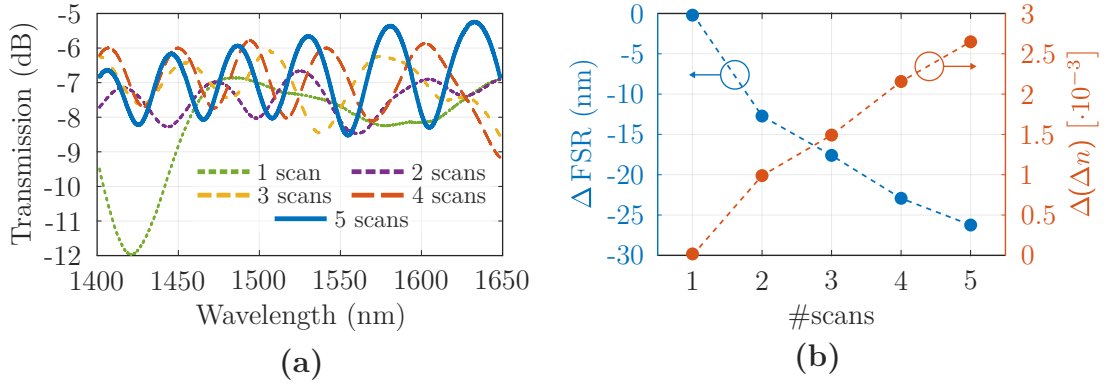


**Figure 6.7.** (a) MZI transmission spectra for waveguides formed between 1 and 5 scans. (b) FSR and increment in the effective RI difference depending on the number of scans that make up the CWG (1–5 scans). The region 1400–1550 nm is selected for the determination of the FSR. Adapted from [1].

of an MZI, especially the light coupling and the FSR. According to the relationship shown in Equation 6.14, reducing the FSR has an associated increase in  $\Delta n$ . From this equation, taking  $L \simeq 2L_1 + L_2 = 6$  mm and  $\lambda_0 = 1500$  nm, the incremental values of  $\Delta n$  are obtained (Fig. 6.7 b). For a CWG formed by 5 scans, a  $\Delta(\Delta n)$  close to  $3 \cdot 10^{-3}$  is obtained (taking 1 scan as reference), which approximates the RI change associated with the core, thus validating the results obtained with QPM (Fig. 6.6 b).

### Mach-Zehnder with FBG

The next step is to inscribe the FBG in the core using the PbP method. The manufactured FBG is associated with Type II grating [35]. The laser is configured with a pulse energy of 0.47  $\mu$ J and a PRR of 10 Hz. The grating period is  $\Lambda = 1.051$   $\mu$ m, which results in a writing speed  $v = 10.51$   $\mu$ m/s. Its length is  $L_g = 4$  mm, being located parallel to the MZI cladding section. A 2<sup>nd</sup>-order Bragg wavelength of  $\lambda_B = 1516.9$  nm is generated, as it is depicted in Fig. 6.8 a. The FWHM is  $\sim 1.19$  nm.

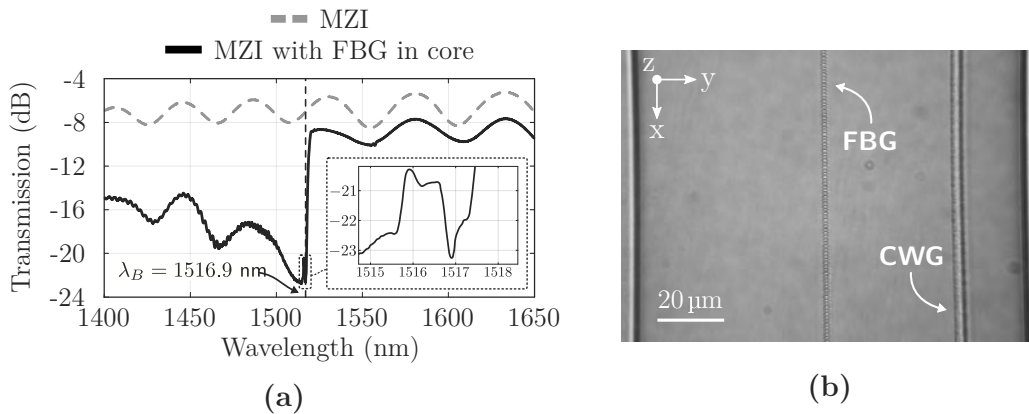


**Figure 6.8.** (a) Transmission spectra of the complete MZI (5 scans) without and with the FBG inscription in the core. Inset: zoom of Bragg resonance. (b) Longitudinal view of the MZI cladding section together with the FBG inscription in the core. Adapted from [1].

### 6.2.4 Experimental results and discussion

First, a temperature analysis will be carried out in order to perform an even more complete characterisation of the behaviour of the waveguide. In order to achieve this, a comparison is made with the MZI developed by Pallarés-Aldeiturriaga *et al.* [28]. The MZI mentioned presents a filamentary propagation and a birefringent RIC (Type II  $\rightarrow \Delta n_{wg} < 0$ ) as a type of permanent modification in the material [23], with a secondary optical path length  $L = 300 \mu\text{m}$ . In both cases, an identical temperature cycle has been carried out: it is climbed in steps of  $50^\circ\text{C}$  to  $800^\circ\text{C}$ , remaining stable for 10 minutes in each step. It should be noted that the Type II MZI is only evaluated up to  $650^\circ\text{C}$ , the temperature at which the structure is erased. A notable difference is that, in this paper, a pre-annealing has been carried out by placing the device 6 hours at  $200^\circ\text{C}$ . The purpose is to improve the repeatability of the sensor in a medium-high temperature range, as well as to eliminate laser-induced stress changes from the structure.

The experimental results, together with those collected from the study carried out in [28], are shown in Fig. 6.9. It is depicted the shift of the interference dips ( $\Delta\lambda_{dip}$ ) of both MZIs, and the Bragg wavelength shift ( $\Delta\lambda_{Bragg}$ ) corresponding to the FBG. The process of annealing is appreciated in the temperature steps, in which, remaining the temperature stable for 10 min, a shift of  $\lambda_{dip}$  occurs. This is a consequence of the stress relaxation that takes place in the waveguide. As the stress can cause anisotropic and inhomogeneous distribution of the refractive index in the waveguide, the annealing process originates a better behavior of the MZI, since the refractive index is smoothed. Although annealing occurs in both MZIs, the phenomenon is more pronounced in the one manufactured in this work, as it presents a significantly higher sensitivity.

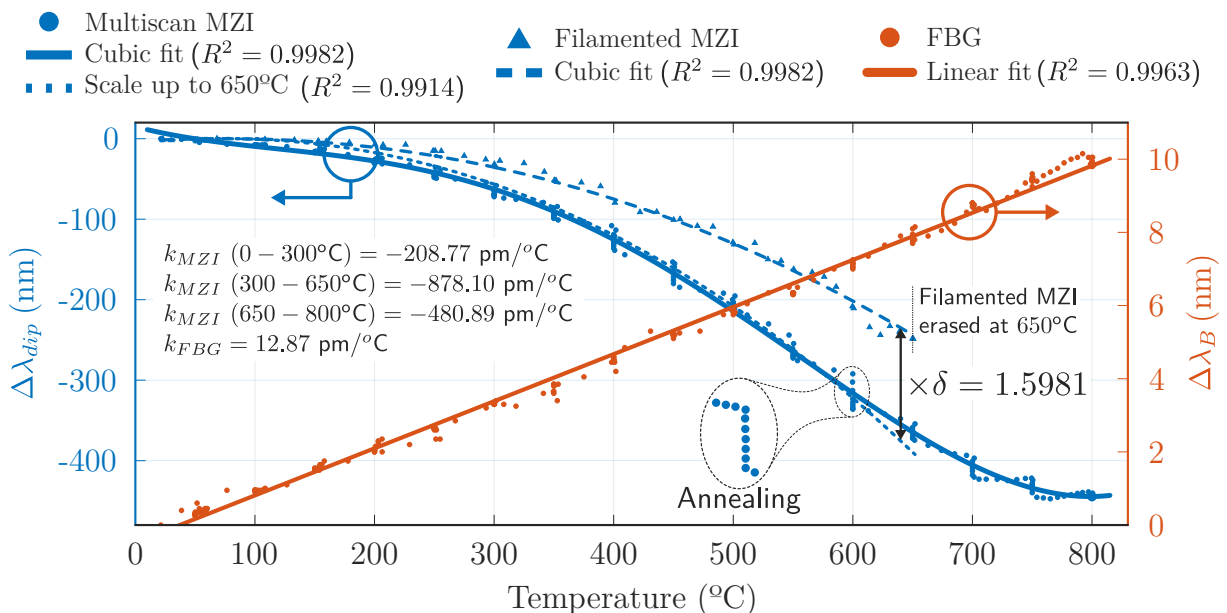


**Figure 6.9.** (Left Y axis) Wavelength shift of a interference dip of the MZI developed in this work for temperatures between  $23^\circ\text{C}$  and  $800^\circ\text{C}$  (continuous line), and wavelength shift of a interference dip of the MZI developed in [28] for temperatures between  $23^\circ\text{C}$  and  $650^\circ\text{C}$ , with fit and translation (scale factor  $\alpha$ ) to the measurements of the present work (dotted lines). (Right Y axis) Bragg wavelength shift for temperatures between  $23^\circ\text{C}$  and  $800^\circ\text{C}$ . The sensitivities ( $k_T$ ) as well as the effect of the annealing are indicated. Adapted from [1].

The cubic fit of the filamented MZI measurements presents a remarkable coincidence ( $R^2 = 0.9914$ ) with the cubic fit of the multiscan MZI measurements when applying a scale factor  $\delta = 1.5981$ . This fact has a very important implication, which is developed below.

In order to establish a common starting point between the two MZIs, it is considered  $(\lambda_{dip})_1(T) = (\lambda_{dip})_2(T)$  at a temperature  $T$ , referring 1 to multiscan MZI and 2 to filamented MZI. According to Equation 6.2:

$$(\Delta n_{wg})_1(T) \cdot \gamma_1 = (\Delta n_{wg})_2(T) \cdot \gamma_2, \quad (6.6)$$

$$\text{with } \gamma_i \frac{2\pi L_i}{\pi(2m_i + 1) - \phi_i}, \quad \text{being } L_i = \begin{cases} 6 \text{ mm}, & i = 1. \\ 300 \text{ }\mu\text{m}, & i = 2. \end{cases}$$

Defining  $(\Delta \lambda_{dip})_i(T)$  as

$$(\Delta \lambda_{dip})_i(T) = (\lambda_{dip})_i(T) - (\lambda_{dip})_i(23^\circ\text{C}) = f_i(T), \quad (6.7)$$

$$\begin{cases} f_1(T) = \delta \cdot f_2(T) \rightarrow \text{Cubic fit multiscan MZI} \\ f_2(T) \rightarrow \text{Cubic fit filamented MZI} \end{cases} \quad (6.8)$$

Taking increments on Equation 6.2, and applying the equality of Eq. 6.7

$$(\Delta \lambda_{dip})_i(T) = [\Delta (\Delta n_{wg})]_i(T) \cdot \gamma_i = f_i(T). \quad (6.9)$$

Finally, according to the relationship indicated in Equation 6.8, the following equality is obtained

$$[\Delta (\Delta n_{wg})]_1(T) = \gamma \cdot [\Delta (\Delta n_{wg})]_2(T), \quad \gamma = \delta \frac{\gamma_2}{\gamma_1}. \quad (6.10)$$

Thus, it is demonstrated that the variation of the RI with the temperature, for the waveguides of both MZI (filamented Type II, and multiscan Type I), are related through a constant of proportionality  $\gamma$ . From the data obtained with the RNF Profiler, simulations have been applied by means of the finite element method (FEM) in order to obtain the effective mode index difference. In this way, it is possible to estimate  $\gamma$  from Equation 6.6, taking  $T = 23^\circ\text{C}$ , temperature at which the RI measurements of the waveguides have been made.

The obtained result is coherent insofar as the MZI based on the elementary propagation presents a RI change higher than the MZI made by multiscan technique, so it has a degradation  $\gamma^{-1} = 2.6129$  higher. Hence, at  $650^\circ\text{C}$  the filamented MZI is erased, while the MZI developed in this work is still maintained at  $800^\circ\text{C}$ .

## Refractive Index

The  $40 \text{ }\mu\text{m}$  separation of the CWG (multiscan technique) from the core causes a high sensitivity of the MZI to the surrounding RI. Due to this, the MZI was immersed in six different liquids with variations in its refractive index of the order of  $10^{-3}$ . Specifically, these are solutions with sugar concentrations (solute) of 0, 20, 40, 60, 80 and 100 grams per 100 grams of water (solvent). The refractive index of each liquid has been measured with the Krüss Optronic DR-6100 refractometer. The measurement process has been carried out by fixing the fibre and

## 6.2. In-fibre MZI for multiparameter sensing

surrounding it with the different liquids.

In Fig. 6.10 the wavelength shift of the MZI interference dips is observed for the six liquids. Air has been taken as the reference point ( $RI = 1 \rightarrow \Delta\lambda_{dip} = 0$ ). The developed MZI has a sensitivity of  $k_{RI} = 86.52$  nm/RIU (refractive index unit) (higher than [30] at that RI range), being able to detect minimal variations of the medium surrounding the fibre.

The operational principle behind the behavior is easily justifiable from Eq. 6.2, since it is the variation of  $\lambda_{dip}$  that is monitored during the measurement. By placing the waveguide near the outside of the fibre, if it is immersed in a liquid with a refractive index higher than that of the air, the effective RI of the waveguide ( $\Delta n_{wg}$ ) is increased, causing an increase in  $\lambda_{dip}$ , and in turn, a decrease of the free spectral range.

### 6.2.5 Cross-sensitivity

Finally, after having sensed temperature and refractive index, the cross-sensitivity of two different parameters is studied. In order to exploit the advantages that the MZI and the FBG provide jointly, joint discrimination of strain ( $\epsilon$ ) and curvature ( $\kappa$ ) is proposed. Knowing the variations of both parameters and having their sensitivities, the Bragg and dip wavelength shifts are given by:

$$\begin{bmatrix} \Delta\lambda_B \\ \Delta\lambda_{dip} \end{bmatrix} = \begin{bmatrix} k_{\kappa_B} & k_{\epsilon_B} \\ k_{\kappa_{dip}} & k_{\epsilon_{dip}} \end{bmatrix} \begin{bmatrix} \Delta\kappa \\ \Delta\epsilon \end{bmatrix}, \quad (6.11)$$

being  $k_{\kappa}$  and  $k_{\epsilon}$  the curvature and strain sensitivities, both being specified for the FBG ( $k_{_B}$ ) and the MZI ( $k_{_{dip}}$ ).

With respect to the curvature, two measurement sets have been made, as it is depicted in Fig. 6.11 a. To perform the measurements, the fibre is clamped on two platforms separated an initial distance  $L_f = 15.2$  cm, being the sensor at the midpoint. One platform remains fixed while the other moves on the X axis. The bending direction must be produced on the Y axis, since the sensitivity obtained is maximum (see Fig. 6.11 a). An estimate of the curvature is achieved through the circumference relation [36]:

$$L_f - x = L_f \cdot \text{sinc}\left(\frac{L_f \cdot \kappa}{2}\right), \quad (6.12)$$

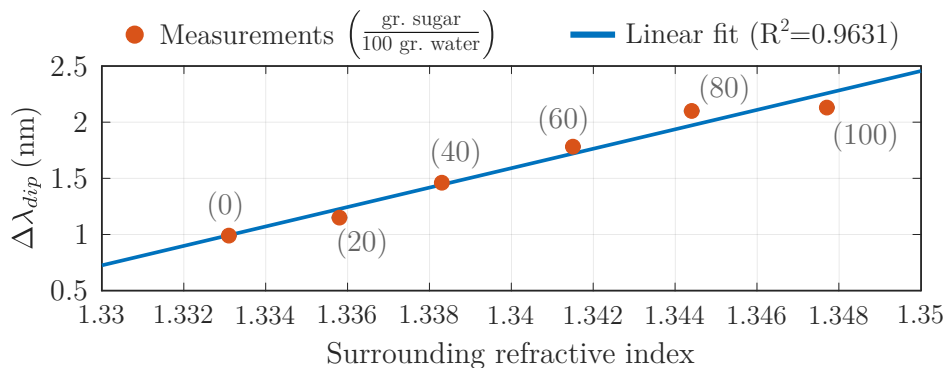


**Figure 6.10.** Wavelength shift of a MZI interference dip when immersing the fibre in liquids of different refractive index. Adapted from [1].

where  $x$  refers to the shift of the movable platform on the X axis, and  $\kappa = \frac{1}{R}$  is the curvature, the inverse of bending radius  $R$  towards bending axis. The sensitivities obtained are  $k_{\kappa_B} = -0.0914 \text{ nm/m}^{-1}$  and  $k_{\kappa_{dip}} = -30.2578 \text{ nm/m}^{-1}$ . The variation of  $k_{\kappa_{dip}}$  between both measurement sets is 2.4%.

To carry out strain measurements, a fibre section of 15.2 cm length is fixed at both ends, with the sensor in the middle. Subsequently, the fibre is fixed from one point and strained from the other. It is stretched in steps of 0.03 mm to reach 0.63 mm, which results in a maximum strain of  $\sim 4150 \mu\epsilon$ . According to the results shown in Fig. 6.11 b, the sensitivity obtained for the FBG and the MZI is  $k_{\epsilon_B} = 0.7683 \text{ pm}/\mu\epsilon$  and  $k_{\epsilon_{dip}} = 0.9839 \text{ pm}/\mu\epsilon$ , respectively.

At this point, from Eq. 6.11, both measurands can be obtained from the Bragg and dip wavelengths by calculating the inverse matrix of the relation, obtaining the next equality:

$$\begin{bmatrix} \Delta\kappa \\ \Delta\epsilon \end{bmatrix} = \frac{1}{D} \begin{bmatrix} k_{\epsilon_{dip}} & -k_{\epsilon_B} \\ -k_{\kappa_{dip}} & k_{\kappa_B} \end{bmatrix} \begin{bmatrix} \Delta\lambda_B \\ \Delta\lambda_{dip} \end{bmatrix}, \quad (6.13)$$

where  $D = k_{\kappa_B} k_{\epsilon_{dip}} - k_{\kappa_{dip}} k_{\epsilon_B}$  is the matrix determinant.

In Fig. 6.12, the cross-sensitivity of strain and curvature is depicted. It has been obtained by varying a measurand while the other is fixed. For this, the experimental data of Fig. 6.11 has been used. The applied sweeps show no curvature ( $\kappa = 0$ ) or strain ( $\epsilon = 0$ ), and are depicted (black dotted lines) against the values estimated from the experimental data after applying Eq. 6.13 (dots). Likewise, a linear fit is indicated (color lines) in order to evaluate the error committed. When  $\kappa$  sweep is applied (blue), there is an error of  $\sim 7.8\%$  between the real and estimated  $\kappa$  value from the experimental data. Also, the estimated strain (should be null) varies with the curvature according to  $-13.4 \mu\epsilon/\text{m}^{-1}$ . On the other hand, when strain sweep is applied (orange), the error between the real and estimate strain is  $\sim 1.1\%$ . In this case, the estimated curvature varies with the strain according to  $0.00476 \text{ m}^{-1}/\mu\epsilon$ .

## 6.2.6 Conclusions

In this work a hybrid CWG MZI with a FBG inscribed both by a femtosecond laser has been demonstrated. The CWG has been inscribed employing the multiscan technique that allows control of both width and RIC, as the latter increases with the increment of fictive temperature

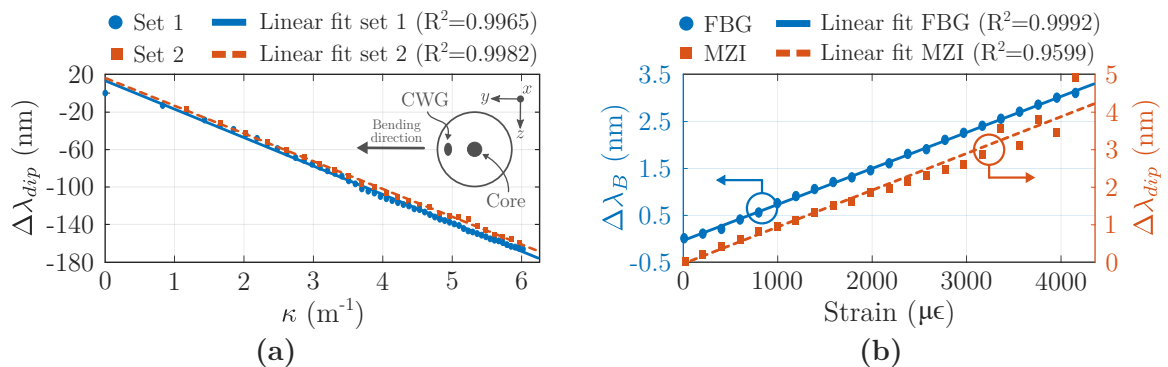


**Figure 6.11.** (a) Dip wavelength shift when a curvature sweep is performed. Two sets of measurements are made. (b) Bragg and dip wavelength shift when a strain sweep is applied. Adapted from [1].

### 6.3. Reflection-based LIF sensor integrated in a surgical needle

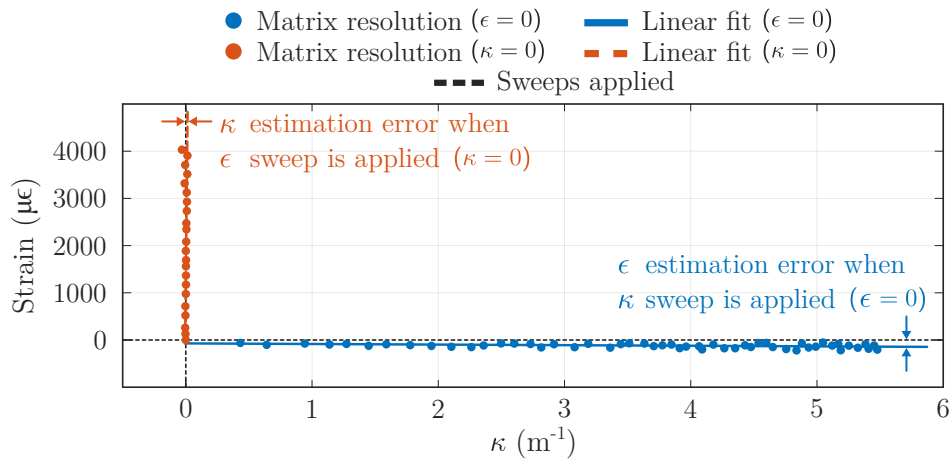


**Figure 6.12.** Cross sensitivity of curvature and strain. The graph is obtained by varying one measurand while the other is fixed. Adapted from [1].

produced by each scan. In this way, the number of scans is a way to control FSR of the MZI. The temperature characterisation of the multiscan waveguide reveals a shift (compared to the filamented waveguide) attributed to a decrement of RIC of the CWG caused by annealing. This change ratio has been proven to be proportional to the one exhibited by filament waveguides, being the latter more degraded with temperature. In addition, given the proximity of CWG to the cladding/air boundary, the interferometer exhibits higher sensitivity to RI than previously reported MZIs at 1.33–1.35 range. The FBG inscribed at the reference arm has been employed to independently measure both curvature and strain with cross-sensitivities as low as  $-13.4 \mu\epsilon/m^{-1}$  and  $0.00476 m^{-1}/m\epsilon$ .

## 6.3 Reflection-based LIF sensor integrated in a surgical needle

Lab-in-fibre (LIF) sensors have recently emerged as a novel approach in various fields, including optofluidics, due to their capability to integrate multiple sensor elements that account for various physical phenomena in a compact space. This work proposes the creation of a multi-parameter sensing device by combining an in-fibre air microcavity with a PI-b-PI FBG. This sensor is reflection-based, less than 300  $\mu\text{m}$  in length, situated at the end of an SMF, and integrated into a surgical needle for use in biomedical applications. This paper presents the first ultra-short LIF sensor designed under the “*touch and measure*” method. The prototype is capable of detecting both axial tensile strain (6.69  $\text{pm}/\mu\epsilon$  in the air cavity) and the surrounding refractive index (11.5  $\text{nm}/\text{RIU}$  in FBG) simultaneously.

### 6.3.1 Background

In recent years, there has been a substantial growth in the advancement of lab-on-a-chip platforms, leading to significant impacts in diverse fields such as biology, chemistry, clinical procedures, and more [37, 38]. These platforms offer wide functionality by integrating multiple sensor elements in a compact space, leading to the emergence of LIF systems that leverage the benefits of optical fibres to create multifunctional sensing elements [20]. The presence of the fibre core

as a waveguide allows optimal interconnection of different optofluidic sensor components [39].

Femtosecond lasers are commonly used to create three-dimensional structures in optical fibres due to their simplicity and flexibility in inscribing patterns directly into the bulk volume of transparent materials [40]. The induced RICs can create gratings or waveguides, leading to optofluidic microchannels (via selective chemical etching), all of which have great potential in biomedical applications. It is essential that sensors used in such applications exhibit a reflection detection mode to facilitate minimally invasive procedures.

Several studies have integrated in-fibre air cavities and FBGs to enable multi-parameter sensing. Notably, Liao *et al.* manufactured two sensors in 2010 [41] and 2013 [42]. The first sensor comprises an FBG with an integrated Mach-Zehnder interferometer formed by a half-core trough-hole (transmission detection mode) [41]. The second sensor is a tunable phase-shifted FBG based on an in-grating through-hole bubble (reflection detection mode) [42]. However, these sensors are 4 mm and 5 mm long, respectively, more than 13 times greater than the sensor manufactured in this work, and have lower strain sensitivity ( $0.48 \text{ pm}/\mu\epsilon$ ).

### 6.3.2 Theory and sensor design

This work presents the detailed design and manufacture process of a highly compact LIF sensor integrated into a surgical needle for multiparameter sensing. The sensor is located within an SMF and consists of an in-fibre air bubble that acts as a Fabry-Perot microcavity, along with a plane-by-plane fibre Bragg grating situated at the tapered fibre end (as shown in Fig. 6.13). Using this device, clinicians can determine the contact of the fibre with a tissue and measure the SRI using a “*touch and measure*” approach. This is the first ultra-short reflection-based LIF sensor (less than  $500 \mu\text{m}$ ) capable of simultaneously detecting axial tensile strain and SRI. To optimise the final structure and verify experimental results, a numerical study of light propagation through the sensor elements is conducted.

The air bubble can be understood as an in-fibre Fabry-Perot interferometer. There are many more configurations apart from the air cavity used in the present work, such as hollow tubes, hollow-core photonic crystal fibres or tapered optical fibres. All of them stand out for their high sensitivity in a structure of small dimensions, as well as for a linear response and a potential

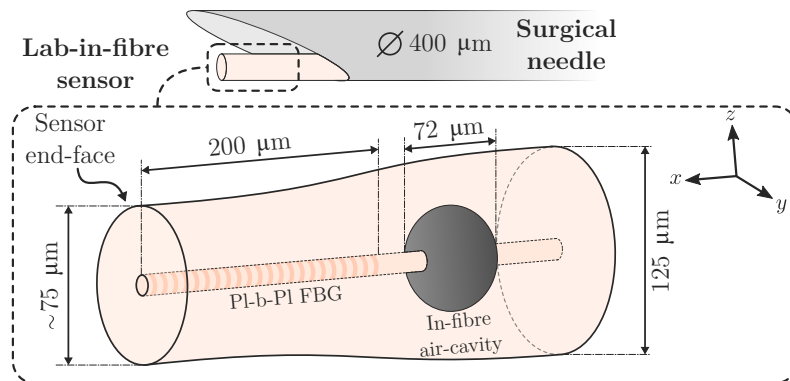


**Figure 6.13.** Schematic illustration of the manufactured LIF sensor. It contains an in-fibre air bubble (Fabry-Perot cavity) and a PI-b-Pi FBG in the tapered final section of the fibre. The sensor is integrated into a  $\varnothing 400 \mu\text{m}$  surgical needle. Adapted from [3].

reflection-based detection mode [43].

In the manufactured LIF, the air microcavity allows the axial strain to be detected in the fibre end (“*touch*”). This parameter is protected from cross-sensitivity error with radial strain, since the fibre is embedded in the needle. The incident light that is transmitted by the fibre core is reflected in each of the two fibre-air interfaces ( $|\text{RIC}| \simeq 0.45$ ). Both optical paths recombine in reflection, resulting in an interference pattern whose free spectral range (FSR) is defined by the well-known equation:

$$\text{FSR} \simeq \frac{\lambda^2}{n \cdot 2L}, \quad \text{with} \quad \begin{cases} n = 1 \text{ (cavity refractive index)} \\ L = \varnothing \text{ cavity (diameter)} \end{cases}, \quad (6.14)$$

where  $2L$  is the optical path difference.

The second structure corresponds to the FBG located in the tapered fibre section (between air bubble and fibre end-face). The fibre tapering process makes it possible to increase the SRI sensitivity (“*measure*”). Its length is small enough that the Bragg wavelength ( $\lambda_B$ ) reflection is greater than the interference pattern of the in-fibre air cavity ( $\simeq 1\%$  of the incident light power).

### 6.3.3 Finite element simulation

The physical dimensions and the relative positioning of each sensor element has been optimised from the electromagnetic point of view in order to maximise reflection, limiting losses as much as possible. To this end, simulations using finite element BPM have been carried out in the Comsol Multiphysics software. The maximum element size in the mesh is  $0.19 \mu\text{m}$  ( $\leq \lambda/8$ ).

The most restrictive element in terms of losses is the in-fibre air bubble. Consequently, a study of the electric field is performed by varying the cavity diameter and the wavelength (operating in C-Band). Specifically, it is performed a study for circular air-cavities of  $50 \mu\text{m}$ ,  $70 \mu\text{m}$  and  $90 \mu\text{m}$  in diameter, as well as a square bubble (unreal) with  $90 \mu\text{m}$  side. The electromagnetic study, shown in Fig. 6.14, has been carried out in the wavelength range between  $1520 \text{ nm}$  and  $1570 \text{ nm}$ . Based on the results, it can be seen that the square bubble configuration exhibits the optimal performance in terms of reflection and losses, making it the proof-of-concept for an ideal behaviour (Fig. 6.14 **b**). This is because the RIC interface of the two reflective surfaces is perfectly perpendicular to the longitudinal axis of the fibre. In this way, reflections towards the cladding, which lead to losses, are minimised. These unwanted reflections towards cladding increase as the cavity diameter decreases, as observed in the simulations corresponding to circular cavities. The power confinement in the central part of the bubble (and therefore in the posterior section of the fibre core) improves as the bubble diameter increases, up to the ideal case. Likewise, cavity lengths of  $45.26 \mu\text{m}$ ,  $70.69 \mu\text{m}$  and  $90.35 \mu\text{m}$  have been determined by post-processing the FSR of the reflection patterns of the circular air cavities (Fig. 6.14 **e**). It corresponds to relative errors ( $\epsilon_r$ ) of  $9.4\%$ ,  $0.9\%$  and  $0.4\%$ , respectively, with respect to the real values, verifying the validity of the simulations carried out. From a trade-off between performance (reflection and losses) and robustness of the sensor against breakage, the manufactured LIF will present an air micro-cavity with a diameter  $\sim 70 \mu\text{m}$ .

Based on the detailed results, the initial point of the FBG must be placed at the optimum point to limit the total length of the LIF sensor, while maximising its reflection performance.

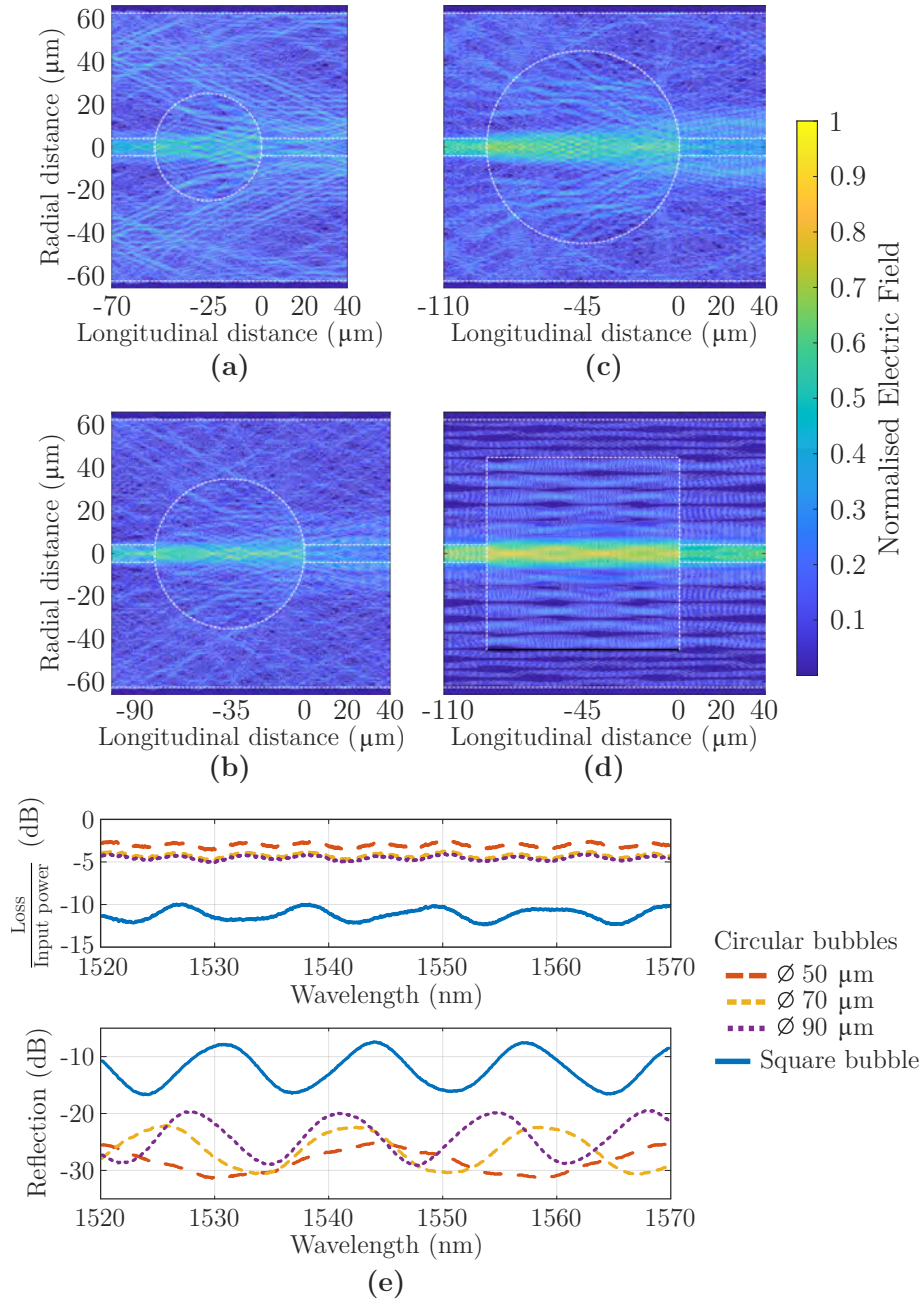


**Figure 6.14.** Simulation of the electric field in circular air cavities of diameter (a) 50 μm, (b) 70 μm, (c) and 90 μm within an SMF, (d) together with the ideal case of a square bubble with 90 μm side. (e) Loss and reflection spectrum for each case is presented. Adapted from [3].

Consequently, the following function  $E^*(x)$  is defined, which refers to the average electric field (in wavelength) in the longitudinal axis of the fibre ( $y = z = 0$ ) (Comsol cutline core is required):

$$E^*(x) = \frac{1}{50 \text{ nm}} \int_{1520 \text{ nm}}^{1570 \text{ nm}} |E(\lambda, x, y = 0, z = 0)| d\lambda, \quad (6.15)$$

$$\forall x, \lambda \in \mathbb{R} : 1520 \text{ nm} \leq \lambda \leq 1570 \text{ nm}.$$

where  $E(\lambda, x, y, z)$  refers to the electric field. The reference point on the  $X$  axis ( $x = 0$ ) is located at the end of the air micro-cavity.

### 6.3. Reflection-based LIF sensor integrated in a surgical needle

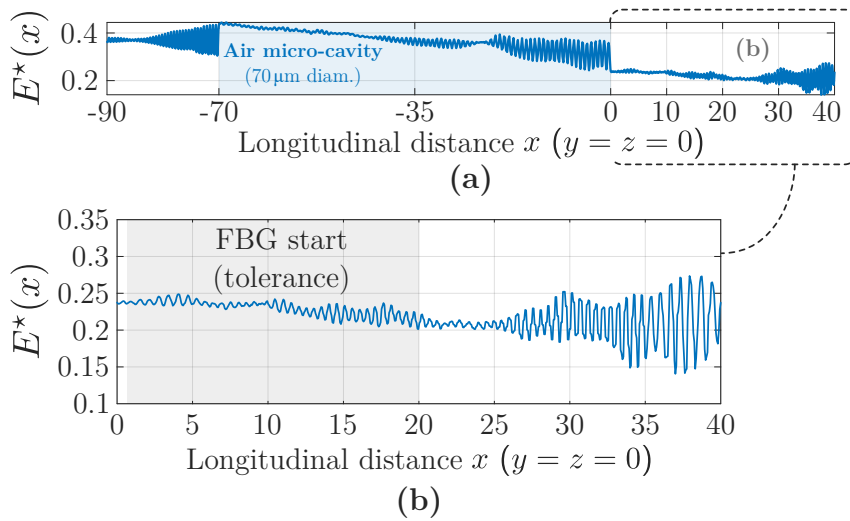


**Figure 6.15.** (a) Simulated  $E^*(x)$  value (Equation 6.15) in circular air cavity of 70  $\mu\text{m}$  diameter, (b) with the section after the bubble emphasised (0–40  $\mu\text{m}$ ). Adapted from [3].

In Fig. 6.15, it is depicted the value of  $E^*(x)$  for the simulated  $\varnothing 70$   $\mu\text{m}$  circular air cavity (bubble later manufactured). Focusing on the section after the bubble (Fig. 6.15), the electric field is more tightly confined to the core centre ( $y = z = 0$ ) in the first  $\sim 20$   $\mu\text{m}$  (the final interference is due to the simulation fibre end, located at 40  $\mu\text{m}$ ). This aspect is also slightly appreciated in Fig. 6.14. In order to maximise reflection efficiency, it is important to take advantage of this area by locating the beginning of the FBG.

#### 6.3.4 Manufacturing

A commercial fs fibre laser from Calmar was used for the inscriptions made in this work. The operating wavelength is 1030 nm, with a pulse duration of 370 fs, and a maximum pulse energy of 5  $\mu\text{J}$ . The beam is tightly focused with a long working distance objective lens from Mitutoyo (NA=0.42). The fibre samples are mounted on a high-precision air-bearing XYZ translation stage (Aerotech) that allows controlled movement during the inscription procedure. In order to avoid the cylindrical aberrations inherent to the fibre, it is surrounded by an index-matching oil [44].

The manufacturing process of the sensor device can be divided into three differentiated stages: in-fibre air microcavity generation, fibre end tapering, and inscription of the P1-b-P1 FBG. The stages are depicted schematically in Fig. 6.16.

Since the subsequent FBG inscription will be done with the fs laser, it is also used to generate the bubble inside the fibre. In this way, the use of special optical fibres (hollow core fibres, photonic crystal fibres) is avoided, as well as the dangerous acid corrosion in case of using chemical etching. Initially, there are two cleaved Corning SMF-28 sections. In the core of one end-face section a micro-hole is made with the fs laser. Both the hole properties and the splice characteristics (time and current of the electric arc discharge) determine the air-cavity size [42].

Empirical determination of laser inscription parameters is carried out to obtain the optimal diameter as predicted by the numerical model. A 3  $\mu\text{m}$  diameter micro-hole is generated from 120 pulses with  $E_p = 2.7$   $\mu\text{J}$  (Fig. 6.16 a). Then, based on a commercial fusion splicer (Fujikura

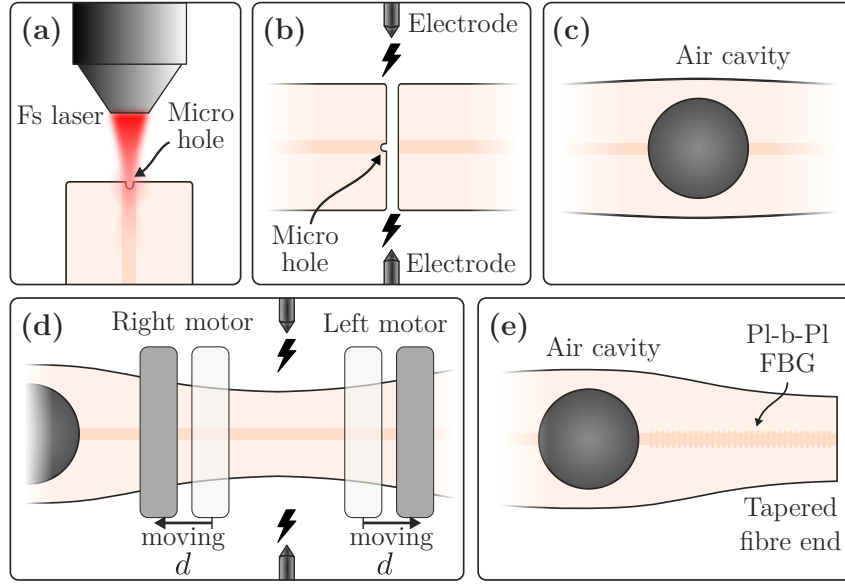


**Figure 6.16.** Schematic of the LIF sensor manufacturing process. (a-c) In-fibre air microcavity generation, (d) fibre end tapering, (e) and PI-b-PI FBG inscription. Adapted from [3].

FSM-100P), a splice is performed using an arc of 1500 ms and 25% of the maximum current (Fig. 6.16 b). The result of the splice is a 72  $\mu\text{m}$  diameter in-fibre air cavity (Fig. 6.16 c). After manufacturing a set of 10 bubble samples, the repeatability is characterised by a standard deviation of 3.76  $\mu\text{m}$ .

The second stage in the manufacturing process refers to the non-adiabatic tapering of the fibre end. The splice electrodes are placed 300  $\mu\text{m}$  apart from the location of the in-fibre bubble. Subsequently, an electric arc discharge of 3,000 ms and 15% of the maximum current is applied. While performing the arc, the right and left fibre holders move backward to each other a distance  $d$  in order to apply an axial tensile stress (Fig. 6.16 d). Parameter  $d$  defines the subsequent waist of the tapered fibre generated. After a series of tests performed,  $d = 30 \mu\text{m}$  is applied, causing a diameter of the fibre end of  $\sim 75 \mu\text{m}$ .

Finally, the fibre is cleaved and an FBG is inscribed between the point determined by simulation and the fibre end. The plane-by-plane inscription method is used, which is achieved by means of the slit beam shaping technique [45]. In this way, the width and depth of the 2D refractive index change induced in the material is controllable by the slit width and pulse energy, respectively. With this, a 200  $\mu\text{m}$  FBG is inscribed 18  $\mu\text{m}$  after the bubble. The period is  $\Lambda = 1.61 \mu\text{m}$ , which generates the 3<sup>rd</sup> order in the C-Band (around 1545 nm). The pulse energy of the laser is 5  $\mu\text{J}$ . However, only 25.1% crosses the slit and is absorbed non-linearly by the fibre. This is because the slit width is set to 400  $\mu\text{m}$ , while the diameter of the Gaussian laser beam is 2.5 mm ( $1/e^2$ ). According to the measurements made with the quantitative phase microscopy (QPM) technique, the Type I RIC estimated for the modifications generated with the fs laser is  $\Delta n \simeq 5 \cdot 10^{-3}$  ( $\Delta n \propto \Delta\phi$ , with  $\phi$  being the induced phase change) [45]. A slightly greater  $\Delta n$  is undertaken to maximise the grating reflection, at the cost of slightly increasing the losses.

### 6.3.5 Experimental results and discussion

Once the optical fibre sensor is manufactured, it is inserted into a  $\varnothing 400\ \mu\text{m}$  surgical needle, and is fixed using epoxy resin. It is important to note that the sensor, being located near the fibre end, is susceptible to breakage when contacting solid surfaces. Consequently, the fibre end-face is placed  $\sim 200\ \mu\text{m}$  before the needle end. In this way, the needle itself acts as a fibre protection. Another option would be to place the FBG before the bubble, so that changes of the end-face do not vary the sensor response.

During the inscription, the reflection spectra of the different manufacturing stages are obtained using a broadband light source (HP 83437A) and an optical spectrum analyser (Anritsu MS9740A, 30 pm resolution). The spectra measured after finishing the manufacturing stages (c) and (e) are depicted in Fig. 6.17 b. Likewise, the simulation result of the complete lab-in-fibre sensor (after (e) stage) is shown, verifying the experimental result. Detection of the FBG peak position is performed by first decoupling the contribution of the interference pattern, and then applying a threshold-based centre of gravity (COG) algorithm [46].

The measurement procedure is detailed below. The lab-in-fibre sensor essentially consists of two sensor elements: the in-fibre air microcavity and the Pl-b-Pl FBG. The air bubble is only sensitive to axial strain (insensitive to SRI and temperature, and protected from radial strain by the needle), and has an FSR that takes a value of 16.58 nm (Fig. 6.17 b). This FSR value offers a cavity length of 71.98  $\mu\text{m}$  according to Eq. 6.14 ( $\epsilon_r = 0.03\%$ ), which is consistent with the measurement obtained from the picture of Fig. 6.17 a. On the other hand, FBG is sensitive to both axial strain and SRI (due to fibre end tapering). It is important to maintain

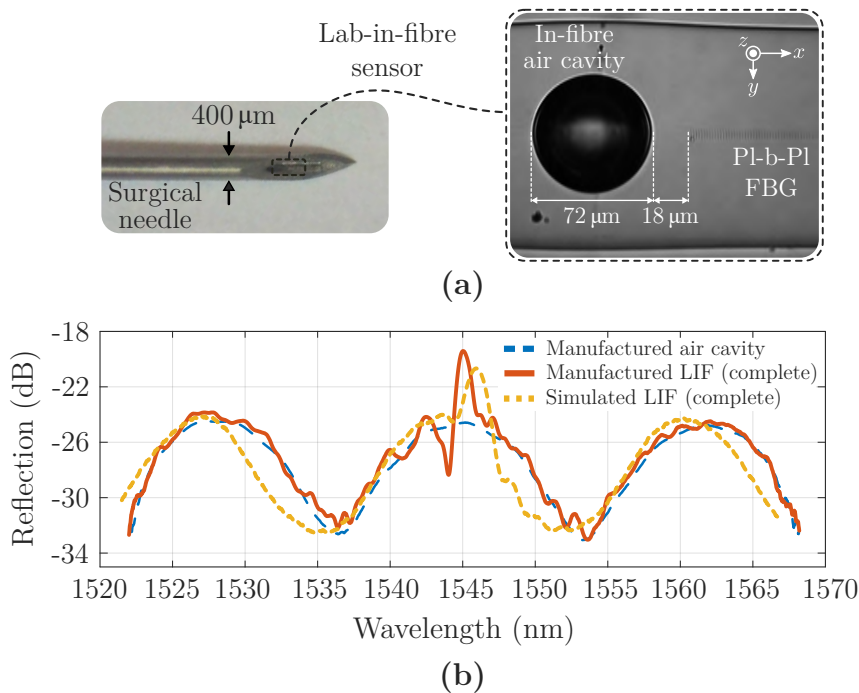


**Figure 6.17.** (a) Microscope images of LIF sensing elements: in-fibre air micro-cavity and Pl-b-Pl FBG, and its integration into the  $\varnothing 400\ \mu\text{m}$  surgical needle. (b) Reflection spectra of the complete LIF sensor, both manufactured and simulated, as well as that corresponding only to the manufactured air cavity. Adapted from [3].

a stable temperature compared to the reference temperature, as the sensor is also sensitive to temperature changes.

However, it should be noted that a second cavity between the bubble and fibre end is also strictly manifested in the spectrum. It has a cavity length of  $\sim 218 \mu\text{m}$  (FSR=3.75 nm), being slightly sensitive to axial strain and SRI. Despite this, such a low FSR value induces high measurement errors, and it is additionally dispensable for this two-parameter detection, so it will not be taken into account. Therefore, the detection problem can be expressed mathematically as follows:

$$\begin{bmatrix} \Delta\lambda_B \\ \Delta \text{FSR} \end{bmatrix} = \begin{bmatrix} (\kappa_\varepsilon)_{\text{FBG}} & (\kappa_{\text{SRI}})_{\text{FBG}} \\ (\kappa_\varepsilon)_{\text{FP}} & (\kappa_{\text{SRI}})_{\text{FP}} \end{bmatrix} \begin{bmatrix} \Delta\varepsilon \\ \Delta \text{SRI} \end{bmatrix}, \quad (6.16)$$

where  $\kappa_\varepsilon$  and  $\kappa_{\text{SRI}}$  are the axial strain and SRI sensitivities, respectively, both being specified for the FBG and the in-fibre bubble (Fabry-Perot cavity, FP).  $\Delta\lambda_B$  refers to the Bragg wavelength shift, and  $\Delta\text{FSR}$  corresponds to the FSR variation of air cavity.

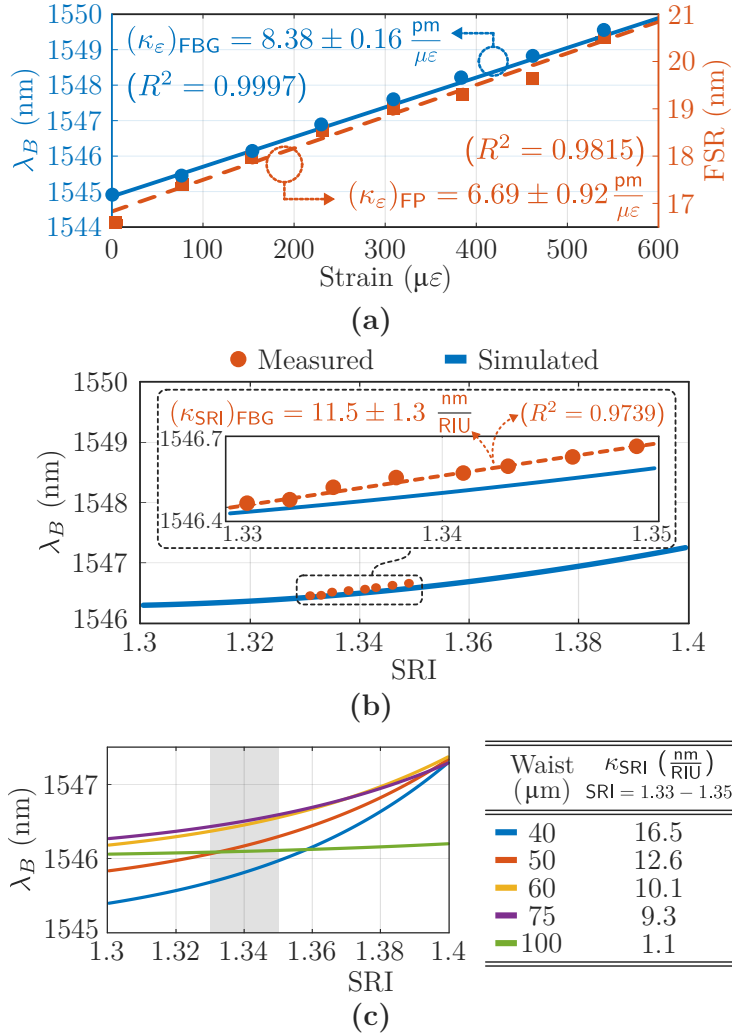


**Figure 6.18.** (a) Measured axial strain sensitivity of air cavity ( $(\kappa_\varepsilon)_{\text{FP}} = 6.69 \text{ pm}/\mu\varepsilon$ ) and FBG ( $(\kappa_\varepsilon)_{\text{FBG}} = 8.38 \text{ pm}/\mu\varepsilon$ ). (b) Simulated (1.3–1.4) and measured (1.33–1.35) SRI sensitivity ( $(\kappa_{\text{SRI}})_{\text{FBG}} = 11.5 \text{ nm}/\text{RIU}$ ) of the FBG. (c) COMSOL simulation of the sensor's SRI sensitivity for different taper waist diameter. Adapted from [3].

### 6.3. Reflection-based LIF sensor integrated in a surgical needle

In order to determine the various sensitivities ( $\kappa_{\_}$ ), measurements have been conducted to evaluate the response of the sensor to changes in both axial strain and the surrounding refractive index (using various sugar concentrations in water). The results obtained are depicted in Fig. 6.18. The strain measurement setup is as follows: the fibre end is fixed, and a fibre point located 13 cm from the end is fixed to a translation stage. A tensile strain is applied to the LIF sensor by moving the translation stage away from the fixed one in steps of 0.01 mm (at room temperature). The axial strain suffered by the sensor when touching an object/tissue has been determined to vary between 200  $\mu\epsilon$  and 400  $\mu\epsilon$ . On the other hand,  $\lambda_B$  shift due to SRI has been experimentally measured in the range 1.33–1.35, and simulated using Comsol (Finite-Element Frequency-Domain, FEFD) in the range 1.3–1.4. Likewise, the response of the sensor to the SRI for different waist diameter of the non-adiabatic tapered fibre has also been evaluated using Comsol FEFD simulations (Fig. 6.18 c). The trade-off that exists between robustness and SRI sensitivity is observed. A more abrupt tapered fibre end (lower waist) causes more interaction of the modal field with the area around the fibre, increasing sensitivity.

#### 6.3.6 Conclusions

To summarise, this work describes the development and fabrication of a LIF sensor integrated into a surgical needle at the end of a single mode fibre. The sensor is compact, with a length of less than 300  $\mu\text{m}$ , and comprises an in-fibre air micro-cavity and a plane-by-plane FBG that was inscribed using a femtosecond laser. The reflection detection mode enables the sensor to be used in biomedical applications, with minimal invasiveness during the measurement process. The sensor follows a “*touch and measure*” approach, detecting the surrounding refractive index of a fluid upon contact with an object/tissue. The sensor exhibits sensitivities of 6.69 pm/ $\mu\epsilon$  for axial strain (*touch*) and 11.5 nm/RIU for SRI (*measure*) in the range of 1.33–1.35.

## References

- [1] Roldán-Varona, P., Pallarés-Aldeiturriaga, D., Rodríguez-Cobo, L., and López-Higuera, J. M., “All-in-fiber multiscan Mach-Zehnder interferometer assisted by core FBG for simultaneous multi-parameter sensing,” *Optics & Laser Technology*, vol. 132, p. 106 459, Dec. 2020. DOI: 10.1016/j.optlastec.2020.106459.
- [2] Roldán-Varona, P., Pallarés-Aldeiturriaga, D., Rodríguez-Cobo, L., and López-Higuera, J. M., “Hybrid Mach-Zehnder interferometer manufactured by femtosecond laser multiscan technique,” in *Seventh European Workshop on Optical Fibre Sensors*, Kalli, K., Brambilla, G., and O’Keeffe, S. O., Eds., SPIE, Aug. 2019. DOI: 10.1117/12.2538813.
- [3] Roldán-Varona, P., Rodríguez-Cobo, L., and López-Higuera, J. M., “Reflection-based lab-in-fiber sensor integrated in a surgical needle for biomedical applications,” *Optics Letters*, vol. 45, no. 18, pp. 5242–5245, Sep. 2020. DOI: 10.1364/ol.399407.
- [4] Roldán-Varona, P., Pallarés-Aldeiturriaga, D., Rodríguez-Cobo, L., and López-Higuera, J. M., “Reflected power-based 2D bending sensor using femtosecond laser FBG inscription in multicore fiber,” in *Seventh European Workshop on Optical Fibre Sensors*, Kalli, K., Brambilla, G., and O’Keeffe, S. O., Eds., SPIE, Aug. 2019. DOI: 10.1117/12.2538794.
- [5] Pallarés-Aldeiturriaga, D., Roldán-Varona, P., Rodríguez-Cobo, L., and López-Higuera, J. M., “Optical Fiber Sensors by Direct Laser Processing: A Review,” *Sensors*, vol. 20, no. 23, p. 6971, Dec. 2020. DOI: 10.3390/s20236971.
- [6] Snitzer, E., “Proposed Fiber Cavities for Optical Masers,” *Journal of Applied Physics*, vol. 32, no. 1, pp. 36–39, Jan. 1961. DOI: 10.1063/1.1735955.
- [7] Hill, K. O. and Meltz, G., “Fiber Bragg grating technology fundamentals and overview,” *Journal of Lightwave Technology*, vol. 15, no. 8, pp. 1263–1276, 1997. DOI: 10.1109/50.618320.
- [8] Norton, S. M., Erdogan, T., and Morris, G. M., “Coupled-mode theory of resonant-grating filters,” *Journal of the Optical Society of America A*, vol. 14, no. 3, pp. 629–639, Mar. 1997. DOI: 10.1364/josaa.14.000629.
- [9] Lopez-Higuera, J. M., Rodriguez-Cobo, L., Quintela-Incera, A., and Cobo, A., “Fiber Optic Sensors in Structural Health Monitoring,” *Journal of Lightwave Technology*, vol. 29, no. 4, pp. 587–608, Feb. 2011. DOI: 10.1109/jlt.2011.2106479.
- [10] Giallorenzi, T. *et al.*, “Optical fiber sensor technology,” *IEEE Journal of Quantum Electronics*, vol. 18, no. 4, pp. 626–665, Apr. 1982. DOI: 10.1109/jqe.1982.1071566.
- [11] Arditty, H. J. and Lefèvre, H. C., “Sagnac effect in fiber gyroscopes,” *Optics Letters*, vol. 6, no. 8, pp. 401–403, Aug. 1981. DOI: 10.1364/ol.6.000401.
- [12] Ferreira, M. F. S. *et al.*, “Roadmap on optical sensors,” *Journal of Optics*, vol. 19, no. 8, p. 083 001, Jul. 2017. DOI: 10.1088/2040-8986/aa7419.
- [13] Hill, K. O., Fujii, Y., Johnson, D. C., and Kawasaki, B. S., “Photosensitivity in optical fiber waveguides: Application to reflection filter fabrication,” *Applied Physics Letters*, vol. 32, no. 10, pp. 647–649, May 1978. DOI: 10.1063/1.89881.
- [14] Méndez, A., “Fiber Bragg grating sensors: a market overview,” in *Third European Workshop on Optical Fibre Sensors*, SPIE, Jul. 2007. DOI: 10.1117/12.738334.

## References

- [15] Dakin, J. P., Pratt, D. J., Bibby, G. W., and Ross, J. N., “Temperature Distribution Measurement Using Raman Ratio Thermometry,” in *SPIE Proceedings*, SPIE, Jan. 1986. DOI: 10.1117/12.949798.
- [16] Lu, P. *et al.*, “Distributed optical fiber sensing: Review and perspective,” *Applied Physics Reviews*, vol. 6, no. 4, p. 041302, Sep. 2019. DOI: 10.1063/1.5113955.
- [17] Light Wave Venture, Ed., *Information 2015 Photonic Sensor Consortium Market Survey Report*. Gatekeepers Inc, 2015.
- [18] Light Wave Venture, Ed., *Distributed and Single Point Fiber Optic Sensing Systems Forecast: A Photonic Sensor Consortium Market Survey Report*. Gatekeepers Inc, 2019.
- [19] Roldán-Varona, P. *et al.*, “Selective Plane Illumination Optical Endomicroscopy with Polymer Imaging Fibres,” in *Conference on Lasers and Electro-Optics*, Optica Publishing Group, 2022. DOI: 10.1364/cleo\_si.2022.sm31.2.
- [20] Haque, M., Lee, K. K. C., Ho, S., Fernandes, L. A., and Herman, P. R., “Chemical-assisted femtosecond laser writing of lab-in-fibers,” *Lab on a Chip*, vol. 14, no. 19, pp. 3817–3829, 2014. DOI: 10.1039/c4lc00648h.
- [21] Laarossi, I., Roldán-Varona, P., Quintela-Incera, M. A., Rodríguez-Cobo, L., and López-Higuera, J. M., “Ultrahigh temperature and strain hybrid integrated sensor system based on Raman and femtosecond FBG inscription in a multimode gold-coated fiber,” *Optics Express*, vol. 27, no. 26, pp. 37122–37130, Dec. 2019. DOI: 10.1364/oe.27.037122.
- [22] Gattass, R. R. and Mazur, E., “Femtosecond laser micromachining in transparent materials,” *Nature Photonics*, vol. 2, no. 4, pp. 219–225, Apr. 2008. DOI: 10.1038/nphoton.2008.47. [Online]. Available: <https://doi.org/10.1038/nphoton.2008.47>.
- [23] Osellame, R., Cerullo, G., and Ramponi, R., Eds., *Femtosecond Laser Micromachining*. Springer Berlin Heidelberg, 2012. DOI: 10.1007/978-3-642-23366-1.
- [24] Haque, M., “Chemical-Assisted Femtosecond Laser Writing of Lab-in-Fiber Sensors,” Ph.D. dissertation, University of Toronto, 2014.
- [25] Waltermann, C., Doering, A., Köhring, M., Angelmahr, M., and Schade, W., “Cladding waveguide gratings in standard single-mode fiber for 3D shape sensing,” *Optics Letters*, vol. 40, no. 13, pp. 3109–3112, 2015, ISSN: 0146-9592. DOI: 10.1364/OL.40.003109. [Online]. Available: <https://www.osapublishing.org/abstract.cfm?URI=ol-40-13-3109>.
- [26] Grenier, J. R., Haque, M., Fernandes, L. A., Lee, K. K. C., and Herman, P. R., “Femtosecond Laser Inscription of Photonic and Optofluidic Devices in Fiber Cladding,” in *Planar Waveguides and other Confined Geometries*, Springer New York, Sep. 2014, pp. 67–110. DOI: 10.1007/978-1-4939-1179-0\_4.
- [27] Shah, L., Arai, A. Y., Eaton, S. M., and Herman, P. R., “Waveguide writing in fused silica with a femtosecond fiber laser at 522 nm and 1 MHz repetition rate,” *Optics Express*, vol. 13, no. 6, pp. 1999–2006, 2005. DOI: 10.1364/opex.13.001999.
- [28] Pallares-Aldeiturriaga, D., Rodríguez-Cobo, L., Quintela, A., and López-Higuera, J. M., “Curvature Sensor Based on In-Fiber Mach-Zehnder Interferometer Inscribed with Femtosecond Laser,” *Journal of Lightwave Technology*, vol. 35, no. 21, pp. 4624–4628, 2017, ISSN: 0733-8724. DOI: 10.1109/JLT.2017.2756103.

- [29] Theodosiou, A., Ioannou, A., and Kalli, K., “All-in-Fiber Cladding Interferometric and Bragg Grating Components Made via Plane-by-Plane Femtosecond Laser Inscription,” *Journal of Lightwave Technology*, vol. 37, no. 18, pp. 4864–4871, Sep. 2019. DOI: 10.1109/jlt.2019.2925263.
- [30] Zhang, Y., Lin, C., Liao, C., Yang, K., Li, Z., and Wang, Y., “Femtosecond laser-inscribed fiber interface Mach–Zehnder interferometer for temperature-insensitive refractive index measurement,” *Optics Letters*, vol. 43, no. 18, pp. 4421–4424, 2018, ISSN: 0146-9592. DOI: 10.1364/ol.43.004421.
- [31] Li, W. W., Chen, W. P., Wang, D. N., Wang, Z. K., and Xu, B., “Fiber inline Mach–Zehnder interferometer based on femtosecond laser inscribed waveguides,” *Optics Letters*, vol. 42, no. 21, pp. 4438–4441, 2017, ISSN: 0146-9592. DOI: 10.1364/OL.42.004438. [Online]. Available: <https://www.osapublishing.org/abstract.cfm?URI=ol-42-21-4438>.
- [32] Chen, P., Shu, X., and Sugden, K., “Ultra-compact all-in-fiber-core Mach-Zehnder interferometer,” *Optics Letters*, vol. 42, no. 20, pp. 4059–4062, Oct. 2017. DOI: 10.1364/ol.42.004059.
- [33] Zhou, K., Shen, F., Yin, G., and Zhang, L., “Optical fiber micro-devices made with femtosecond laser,” in *Advanced Photonics 2016 (IPR, NOMA, Sensors, Networks, SPCom, SOF)*, OSA, 2016. DOI: 10.1364/sensors.2016.sew3d.1.
- [34] Bellair, C. J. *et al.*, “Quantitative phase amplitude microscopy IV: Imaging thick specimens,” *Journal of Microscopy*, vol. 214, no. 1, pp. 62–69, Apr. 2004. DOI: 10.1111/j.0022-2720.2004.01302.x.
- [35] Canning, J., “Fibre gratings and devices for sensors and lasers,” *Laser & Photonics Review*, vol. 2, no. 4, pp. 275–289, Aug. 2008. DOI: 10.1002/lpor.200810010.
- [36] Zhang, S., Zhang, W., Gao, S., Geng, P., and Xue, X., “Fiber-optic bending vector sensor based on Mach-Zehnder interferometer exploiting lateral-offset and up-taper,” *Optics Letters*, vol. 37, no. 21, pp. 4480–4482, Oct. 2012. DOI: 10.1364/ol.37.004480.
- [37] Wu, J., Dong, M., Rigatto, C., Liu, Y., and Lin, F., “Lab-on-chip technology for chronic disease diagnosis,” *npj Digital Medicine*, vol. 1, no. 1, pp. 1–11, Apr. 2018. DOI: 10.1038/s41746-017-0014-0.
- [38] Rahman, M., Stott, M. A., Li, Y., Hawkins, A. R., and Schmidt, H., “Single-particle analysis with 2D electro-optical trapping on an integrated optofluidic device,” *Optica*, vol. 5, no. 10, pp. 1311–1314, Oct. 2018. DOI: 10.1364/optica.5.001311.
- [39] Madani, A. *et al.*, “Optical microtube cavities monolithically integrated on photonic chips for optofluidic sensing,” *Optics Letters*, vol. 42, no. 3, pp. 486–489, Jan. 2017. DOI: 10.1364/ol.42.000486.
- [40] Malinauskas, M. *et al.*, “Ultrafast laser processing of materials: From science to industry,” *Light: Science & Applications*, vol. 5, no. 8, e16133–e16133, Mar. 2016. DOI: 10.1038/lsa.2016.133.
- [41] Liao, C. R., Wang, Y., Wang, D. N., and Yang, M. W., “Fiber In-Line Mach–Zehnder Interferometer Embedded in FBG for Simultaneous Refractive Index and Temperature Measurement,” *IEEE Photonics Technology Letters*, vol. 22, no. 22, pp. 1686–1688, Nov. 2010. DOI: 10.1109/lpt.2010.2079924.

## References

- [42] Liao, C. *et al.*, “Tunable phase-shifted fiber Bragg grating based on femtosecond laser fabricated in-grating bubble,” *Optics Letters*, vol. 38, no. 21, pp. 4473–4476, Oct. 2013. DOI: 10.1364/ol.38.004473.
- [43] Liu, S. *et al.*, “High-sensitivity strain sensor based on in-fiber rectangular air bubble,” *Scientific Reports*, vol. 5, no. 1, p. 7624, Jan. 2015. DOI: 10.1038/srep07624.
- [44] Lai, Y., Zhou, K., Zhang, L., and Bennion, I., “Microchannels in conventional single-mode fibers,” *Optics Letters*, vol. 31, no. 17, pp. 2559–2561, Aug. 2006. DOI: 10.1364/ol.31.002559.
- [45] Roldan-Varona, P., Pallares-Aldeiturriaga, D., Rodriguez-Cobo, L., and Lopez-Higuera, J. M., “Slit Beam Shaping Technique for Femtosecond Laser Inscription of Enhanced Plane-by-Plane FBGs,” *Journal of Lightwave Technology*, vol. 38, no. 16, pp. 4526–4532, Aug. 2020. DOI: 10.1109/jlt.2020.2992568.
- [46] Ganziy, D., Jespersen, O., Woyessa, G., Rose, B., and Bang, O., “Dynamic gate algorithm for multimode fiber Bragg grating sensor systems,” *Applied Optics*, vol. 54, no. 18, pp. 5657–5661, Jun. 2015. DOI: 10.1364/ao.54.005657.

# 7

## Specialty fibre-based sensors

---

<b>7.1</b>	<b>Liquid level sensor using capillary fibres and dynamic FPIs . . . . .</b>	<b>120</b>
7.1.1	Background . . . . .	120
7.1.2	Sensor structure and manufacturing parameters . . . . .	122
7.1.3	Operating principle . . . . .	123
7.1.4	Results and discussion . . . . .	125
7.1.5	Conclusions . . . . .	130
<b>7.2</b>	<b>Perfluorinated POF-based refractometer for water solutions . . . . .</b>	<b>130</b>
7.2.1	Background . . . . .	130
7.2.2	Optical structure design . . . . .	131
7.2.3	BPM simulations . . . . .	132
7.2.4	Operating principle . . . . .	137
7.2.5	Experimental results . . . . .	138
7.2.6	Discussion . . . . .	142
7.2.7	Conclusions . . . . .	142
	<b>References . . . . .</b>	<b>143</b>

---

**S**PECIALTY fibres are generally defined as optical fibres that have at least one unique property that sets them apart from *standard fibres*. These properties can place specialty fibres into various categories, some of which are presented below.

Some examples of these fibres include tapered fibres [1], polarisation-maintaining fibres (*e.g.*, spun fibres, PANDA fibres, and bow-tie fibres) [2], chirally-coupled-core fibres [3] (which have a core surrounded by one or more satellite cores that are chirally wound around it), hollow-core fibres (*e.g.*, photonic crystal fibres [4], negative curvature fibres [5], and capillary fibres [6]), active fibres (fibres doped with laser-active ions, such as erbium-doped fibres, ytterbium-doped fibres) [7], triple-clad and double-clad fibres [8], radiation-resistant fibres, solarisation-resistant fibres, and fibres that use non-standard materials (*e.g.*, fluoride fibres, phosphate glass fibres, polymer fibres [9]).

## 7.1. Liquid level sensor using capillary fibres and dynamic FPIs

Due to the wide range of special properties that these fibres can possess, it is often preferred to use more specific terms rather than a generic term like *specialty fibres*. The works related to hollow-core fibres (section 7.1) and perfluorinated polymer optical fibres (section 7.2), as described in contributions [6] and [9], respectively, are covered in this chapter. While other works utilising specialty fibres in this thesis are not included here, they can be found in [7, 10, 11]. Moreover, some biomedical photonic sensors existing in the literature and based mainly on specialty fibres can be found in the review conducted by Ochoa *et al.* [12].

## 7.1 Liquid level sensor using capillary fibres and dynamic FPIs

In this section, a novel optical fibre sensor capable of measuring both the liquid level and its refractive index is designed, manufactured and demonstrated through simulations and experimentally. For this, a silica capillary hollow-core fibre is used. The fibre, with a sensing length of 1.55 mm, has been processed with a femtosecond laser, so that it incorporates four holes in its structure. In this way, the liquid enters the air core, and it is possible to perform the sensing through the Fabry-Perot cavities that the liquid generates. The detection mode is set to reflection. With a resolution of 4  $\mu\text{m}$  (liquid level), it is in the state-of-the-art of this type of sensor. The system is designed with the capability to measure the level of immiscible liquids in the future, *i.e.*, liquids that form layered structures. This feature could be valuable in identifying the presence of impurities in tanks.

### 7.1.1 Background

Optical fibre sensors have traditionally been used in multiple application fields, such as biology, industry, communications, chemistry, or clinical procedures in medicine. The possibility of discriminating different physical, chemical or biological parameters in complex or inaccessible environments makes its presence very relevant today, with a great capacity of improvement. In recent years, what is known as lab-in-fibre has begun to take on a notable importance. A LIF sensor is characterised by providing a wide functionality by integrating in relatively small dimensions a large number of sensor elements [13–16]. Typically, these are optical structures that allow small volumes ( $\mu\text{L}$ , nL) of biological fluids and liquids to be interrogated [13, 15, 17]. In an optical fibre, this type of optofluidic structures are favoured by the presence of the fibre core as a waveguide that allows the different elements to be optimally interconnected.

Typically there are two options for sensing fluids located around the fibre: by guiding the light to the cladding [18, 19] (or by modifying the geometry of the fibre [20, 21]), or by entering the fluid inside the fibre [13, 15, 22, 23]. The latter notably improves sensitivity, and has been achieved through the manufacture of microchannels or microfluidic reservoirs [13]. However, it is also possible to use optical fibres whose characteristics allow to dynamically introduce fluids into the core, such as hollow-core fibres (HCFs). This type of fibre, which has been used mostly in applications such as fibre lasers [24–26], or non-linear optics [27], is also a very useful platform for use as a sensor [28, 29]. There are multiple types of HCFs, among which are hollow-core photonic band gap fibre [30], hole-assisted dual-core fibre [31], two-core hollow eccentric fibre [32], single hole twin eccentric cores fibre [33], or silica capillary, among others. This last fibre type is cheaper than the rest of the other fibre types and allows splicing without collapsing air regions.

Within the large number of parameters that can be measured, the detection of the liquid level with optical fibres is a really useful application in corrosive environments (such as car batteries or chemical processing), or with flammable liquids (such as fuel tanks). Table 7.1 lists the most relevant works in the literature regarding liquid level detection.

Although it is possible to use structures such as long period gratings (LPGs) [34] or fibre Bragg gratings (FBGs) [35] to perform the liquid level sensing, it is common to use HCFs to perform this type of sensing, due to the advantages that they present with regard to the handling of liquids, mentioned above. Photonic crystal fibres (PCFs) have been used [36], as well as more special fibres based on reflection originated by Bragg resonance [37], with sensitivities in both cases of 1.1 dB/mm (transmission). In recent years, silica tubes have been used, with different air core diameters, and sensing lengths between 1 and 2 cm. Likewise, the use of antiresonant (AR) mechanism [38, 39] for detection has been common in such works. Liu *et al.* developed in 2019 the first liquid level sensor whose resolution was below  $\mu\text{m}$  ( $\sim 0.7 \mu\text{m}$ ), with a sensing length of 4.73 mm [40]. The sensor, also based on AR mechanisms, uses power variations in transmission for its detection.

As far as the author is aware, this work contains the first liquid level sensor that features a reflection detection mode, and uses Fabry-Perot mechanisms to perform sensing. For this, a silica capillary is used. The creation of four holes using a femtosecond laser allows for the ingress of the liquid into the air core. Although the sensing length is shorter than in other reported works, a resolution of 4  $\mu\text{m}$  is achieved, and it allows simultaneously determining both the liquid level and its refractive index. However, it is important to note that the Fabry-Perot dual-cavity (air-liquid) concept is mentioned by Lee *et al.* in 2015 [43].

**Table 7.1.** Table comparing liquid detection sensors found in the literature.

Ref.	Optical fibre	Sensing length	Operation principle	Parameter	Sensitivity	Resolution <sup>a</sup> (liq. level)
[41]	$\varnothing 75 \mu\text{m}$ silica capillary	18 mm	AR mechanism	Liq. level	0.4 dB/mm	25 $\mu\text{m}$
[40]	$\varnothing 30 \mu\text{m}$ silica capillary	4.73 mm	AR mechanism	Liq. level	0.014 dB/ $\mu\text{m}$	0.71 $\mu\text{m}$
[37]	Hollow core Bragg fibre	18 mm	Bragg reflection	Liq. level	1.1 dB/mm	9.1 $\mu\text{m}$
[42]	MMF-HCF-FBG	18 mm	MZI FBG	Liq. level Temperature	1.145 nm/mm 15 pm/ $^{\circ}\text{C}$	26.2 $\mu\text{m}$
[34]	SMF with LPG	40 mm	LPG ( $\Lambda=400 \mu\text{m}$ )	Liq. level	4.8%/mm (RI=1.456)	33 $\mu\text{m}$
[35]	SMF with FBG	24 mm	Etched FBG	Liq. level	2.56 dB/mm	3.9 $\mu\text{m}$
[36]	Hollow-core PCF	10 mm	AR mechanism	Liq. level Temperature	1.1 dB/mm -0.48 nm/ $^{\circ}\text{C}$	9.1 $\mu\text{m}$
This work	$\varnothing 60 \mu\text{m}$ silica capillary	1.55 mm	Dynamic FPs	Liq. level SRI	$1.13 \cdot 10^{-3} \text{ nm}^{-1}/\mu\text{m}$ (@ 1.3-1.4)	4 $\mu\text{m}$

<sup>a</sup> A wavelength resolution of 30 pm and intensity resolution of 0.01 dB (typical detector) are considered as reference.

### 7.1.2 Sensor structure and manufacturing parameters

Figure 7.1 illustrates the schematic design of the sensor, which consists of a 1.55 mm long HCF connected at each end to separate sections of a SMF. The HCF has undergone femtosecond laser processing to create various holes that connect the hollow-core to the surrounding medium. It is worth mentioning that the HCF has a hollow-core with a diameter of 60  $\mu\text{m}$ .

First, to perform the splice between HCF and SMF, the electric arc is not performed at the intersection, but slightly offset towards the side of the SMF ( $d \simeq 100 \mu\text{m}$  in Fig. 7.2), and with the ends of both fibres in close proximity. Likewise, the electric arc is shorter (1 sec) and less intense (18% of maximum current) than a normal splice, in order not to collapse the hollow-core. The result of the splice can be seen in Fig. 7.2. The contact surface of the hollow-core with the SMF core is flat, so losses are significantly reduced.

Next, the four holes that communicate the hollow-core with the surrounding medium are manufactured. These holes are located as shown in Fig. 7.1. It can be seen that the separation between each hole and the ends of the HCF is unique. This fact is important, as will be explained later in section 7.1.3 subsection. For its manufacture, a commercial femtosecond fibre laser chirped pulse amplifier from Calmar laser is used [44, 45]. It operates at 1030 nm, and the pulses are tightly focused by a Mitutoyo objective lens ( $\times 50$ ,  $\text{NA}=0.42$ ). The sample, placed on an XYZ motor stage from Aerotech, is illuminated in transmission and displayed by a CMOS camera.

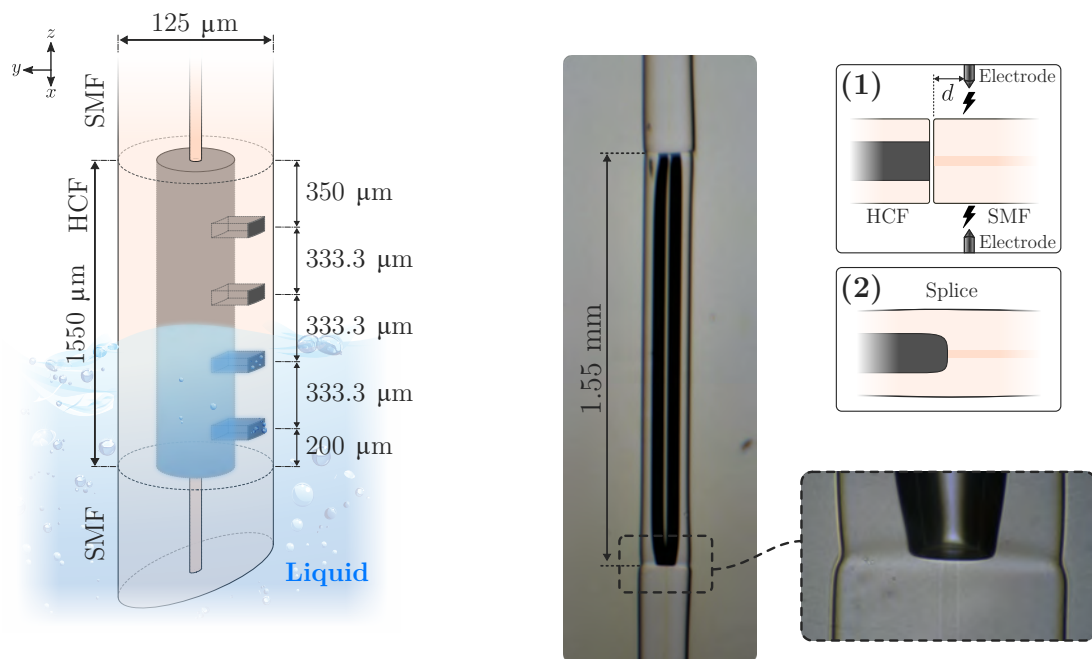


**Figure 7.1.** Schematic view of the manufactured sensor. It is based on a 1.55 mm long HCF with four holes fabricated by femtosecond laser ablation. This structure behaves as a liquid level sensor through the dynamic variation of the Fabry-Perot cavity length that forms the liquid within the fibre. Adapted from [6].

**Figure 7.2.** Microscope image of the HCF spliced to SMF sections ( $\times 20$  objective lens), with a zoom of the splice section ( $\times 50$  objective lens). A schematic of the HCF-SMF splice process is also depicted. Adapted from [6].

The holes have dimensions of  $25 \times 25 \mu\text{m}$  (square shape) (Fig. 7.3 a), going from the outside of the fibre to the hollow-core, so they have a depth of  $\sim 32.5 \mu\text{m}$  (Fig. 7.3 b). For its manufacture, a laser pulse energy of  $2.77 \mu\text{J}$  is used, as well as a PRR of 60 kHz. The inscription process outlined in Fig. 7.3 c is followed: the square shape of the hole is based on the inscription of 8 lines of  $25 \mu\text{m}$  each, and  $3.125 \mu\text{m}$  separated from each other. The writing speed is  $v = 2 \mu\text{m}/\text{sec}$ , so 30,000 pulses (PRR/ $v$ ) are deposited for each  $\mu\text{m}$  of the fibre. Once the 8 lines have been inscribed, which define the plane located on the outer surface of the fibre, the laser inscription is repeated in a plane located  $2 \mu\text{m}$  below, and so on until the inscription of 20 planes is made. The result obtained is shown in Figs. 7.3 a and 7.3 c. The separation between planes has been defined in such a way that the focal volume of the focused laser beam allows the material existing between both planes to be ablated. Given the objective lens used (NA=0.42), the Rayleigh length of the Gaussian beam focus (using the paraxial approximation [46]) is  $y_0 = 2.7 \mu\text{m}$ . Consequently, the successive planes are arranged so that they are  $2 \mu\text{m}$  apart, causing the focal volumes in both positions to be slightly overlapping.

### 7.1.3 Operating principle

The operation principle of the manufactured sensor is based on interferometry. The 1.55 mm HCF acts as a single Fabry-Perot cavity when there is no liquid, or as a multi-cavity when liquid enters the fibre through the holes, as depicted in Fig. 7.4. In the latter case, the incident light that goes through the SMF core is reflected by the three surfaces present in the hollow-core fibre:  $\text{core}_{\text{SMF}}\text{-air}_{\text{HCF}}$ ,  $\text{air}_{\text{HCF}}\text{-liquid}_{\text{HCF}}$ , and  $\text{liquid}_{\text{HCF}}\text{-core}_{\text{SMF}}$ . Consequently, there are three cavities, corresponding to the different combinations offered by these three existing surfaces in the HCF.

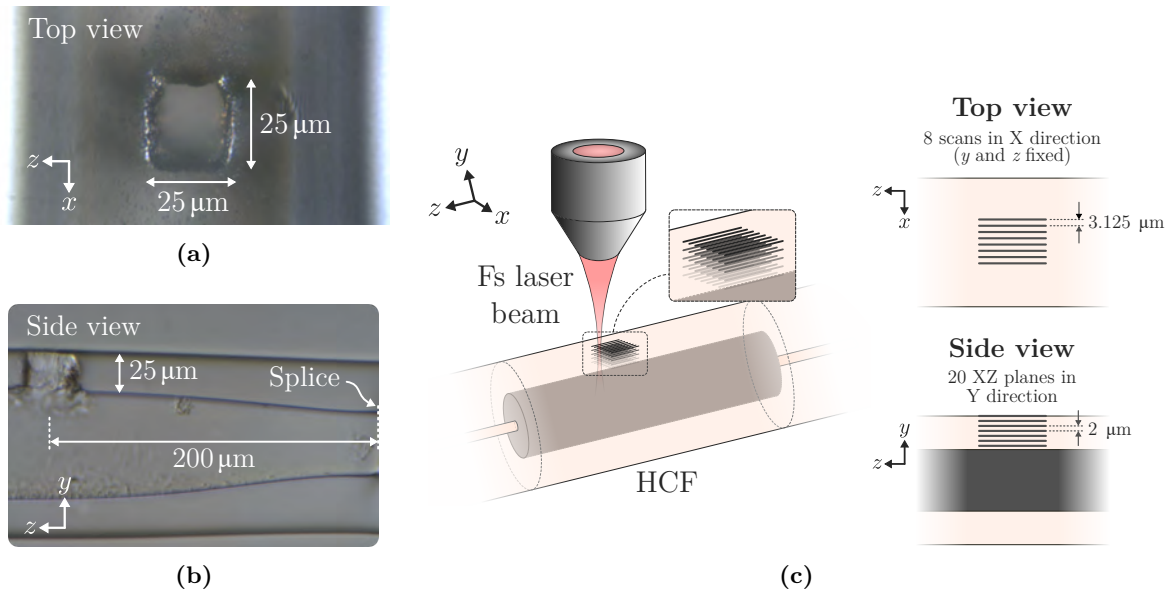


**Figure 7.3.** (a) Top view microscope image ( $\times 50$  objective lens) of the processed HCF, with the square  $25 \times 25 \mu\text{m}$  hole. (b) Side view microscope image ( $\times 20$  objective lens) of the hole corresponding to the final section of the processed HCF. (c) Schematic of the fs laser manufacturing process of the holes. 20 planes are made from the fibre surface to the hollow-core. Each plane corresponds to 8 laser scans of  $25 \mu\text{m}$  in length. Adapted from [6].

## 7.1. Liquid level sensor using capillary fibres and dynamic FPIs

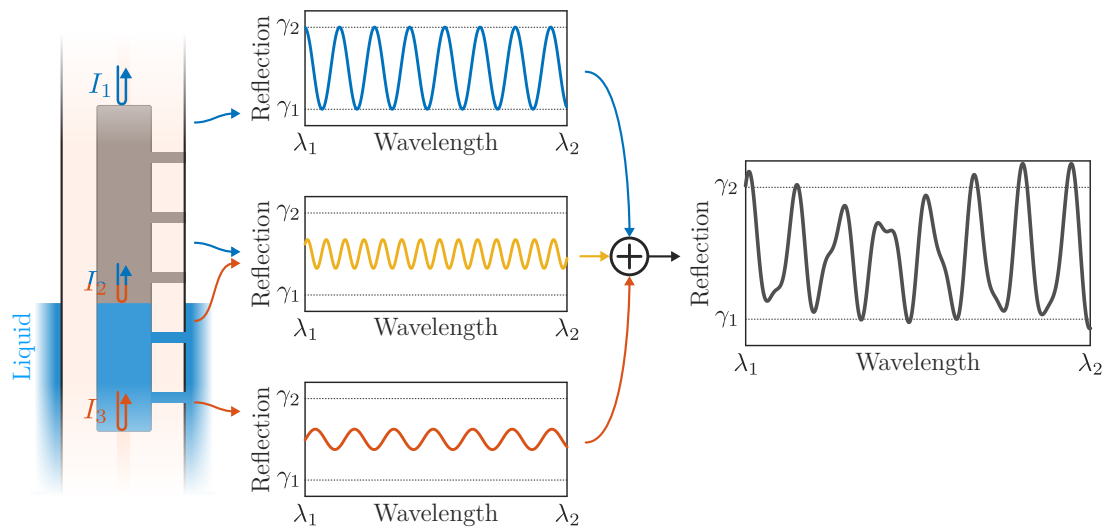


**Figure 7.4.** Schematic explanation of the manufactured sensor, with the interferometric contribution of the different Fabry-Perot cavities: air section, liquid section and both combined. Adapted from [6].

These optical paths recombine in reflection, resulting in the interference pattern given by the next equation:

$$\begin{aligned}
 I = & I_1 + I_2 + I_3 + \underbrace{2\sqrt{I_1 I_2} \cos\left(\frac{2\pi n_{air} \cdot 2L_{air}}{\lambda} + \phi_{air}\right)}_{\text{Air section of HCF}} + \underbrace{2\sqrt{I_2 I_3} \cos\left(\frac{2\pi n_{liquid} \cdot 2L_{liquid}}{\lambda} + \phi_{liquid}\right)}_{\text{Liquid section of HCF}} + \\
 & + \underbrace{2\sqrt{I_1 I_3} \cos\left(\frac{2\pi n_{HCF} \cdot 2L_{HCF}}{\lambda} + \phi_{HCF}\right)}_{\text{HCF section (air and liquid)}} + \underbrace{\sum_i \gamma_i \cdot \cos(\varphi_i)}_{\text{AR and other contributions}}, \\
 \text{where } & n_{air} = 1, \quad L_{HCF} = 1550 \mu\text{m}, \quad L_{HCF} = L_{air} + L_{liquid}, \\
 n_{HCF} = & \frac{t_{air}}{t_{air} + t_{liquid}} n_{air} + \frac{t_{liquid}}{t_{air} + t_{liquid}} n_{liquid}, \\
 t_{air} = & 2 \cdot L_{air} \frac{n_{air}}{c}, \quad t_{liquid} = 2 \cdot L_{liquid} \frac{n_{liquid}}{c}.
 \end{aligned} \tag{7.1}$$

$I_1$ ,  $I_2$  and  $I_3$  correspond to the light intensities reflected by the three mentioned surfaces;  $\lambda$  is the wavelength of the incident light;  $L_{air}$ ,  $L_{liquid}$  and  $L_{HCF}$  are the length of the cavities corresponding to the cavities formed in the HCF (air, liquid, and combination, respectively) ( $2L_{\_}$  is the difference of optical paths); and  $n_{air}$ ,  $n_{liquid}$  and  $n_{HCF}$  are the refractive indices of the cavities.  $n_{HCF}$ , effective refractive index of the cavity that forms the complete HCF (with air and liquid), must be computed taking into account the time that the light is in air ( $t_{air}$ ) and liquid ( $t_{liquid}$ ).  $c$  is the speed of light in vacuum.

The last term refers to intensity contributions whose importance is not relevant in this case. Fundamentally, it corresponds to the antiresonant mechanisms that take place in a structure such as SMF-HCF-SMF when hollow-core fibre has a length greater than what is known as the critical length ( $L_c$ ) [38, 39]. In this work, only Fabry-Perot mechanisms will be used.

It is important to note that the final section of the SMF is cleaved at an angle, as depicted in Fig. 7.1, thus avoiding unwanted reflections that could lead to other cavities. Consequently,

the FSR of the three dominant interference patterns corresponds to the following expression:

$$FSR_i = \frac{\lambda_m \lambda_{m+1}}{2 \cdot n_i \cdot L_i}, \quad \text{where} \quad \lambda_m = \frac{2 \cdot n_i \cdot L_i}{m}, \quad i \in \{\text{air, liquid, HCF}\}, \quad m \in \mathbb{N}. \quad (7.2)$$

These FSR values, and therefore the refractive index of the liquid and its level (length of the cavities), can be obtained from the higher-order modes of the fast Fourier transform (FFT) of the spectral signal. To do this, it is essential to start from a known state. Hence, in the design, the holes have been made so that if there is liquid up to the level of each hole, the cavities that they create have unique lengths for each hole. However, HCF is typically considered to be liquid free in the initial state. The liquid filling process is noticeably slower than the spectra capture frequency, making it possible to track from the reference spectrum.

### 7.1.4 Results and discussion

#### Experimental setup

The experimental measurement setup must be such as to ensure a resolution of  $\mu\text{m}$  in the liquid level of the HCF. For this, a syringe pump manufactured by 3D printing and controlled by an Arduino platform is used [47]. The vision system consists of a CCD camera and a  $\times 10$  Mitutoyo objective lens. Figure 7.5 depicts the complete setup used. With the syringe used (10 mL), the minimum volume of liquid that the stepper motor can move is  $1 \mu\text{L}$ , and with the beaker and the vision system used, that  $\mu\text{L}$  of liquid displacement in the syringe causes a movement of  $0.65 \mu\text{m}$  in the liquid level of the beaker. Consequently, filling the  $1.55 \text{ mm}$  of the HCF implies a liquid displacement of  $2.37 \text{ mL}$  from the syringe. Moreover, the reflection spectra are obtained using a broadband light source (HP 83437A) and an optical spectrum analyser (OSA) (Anritsu MS9740A,  $30 \text{ pm}$  resolution). The only consideration to take into account in choosing the light source is that it offers a power density such that the interfering signal reflected by

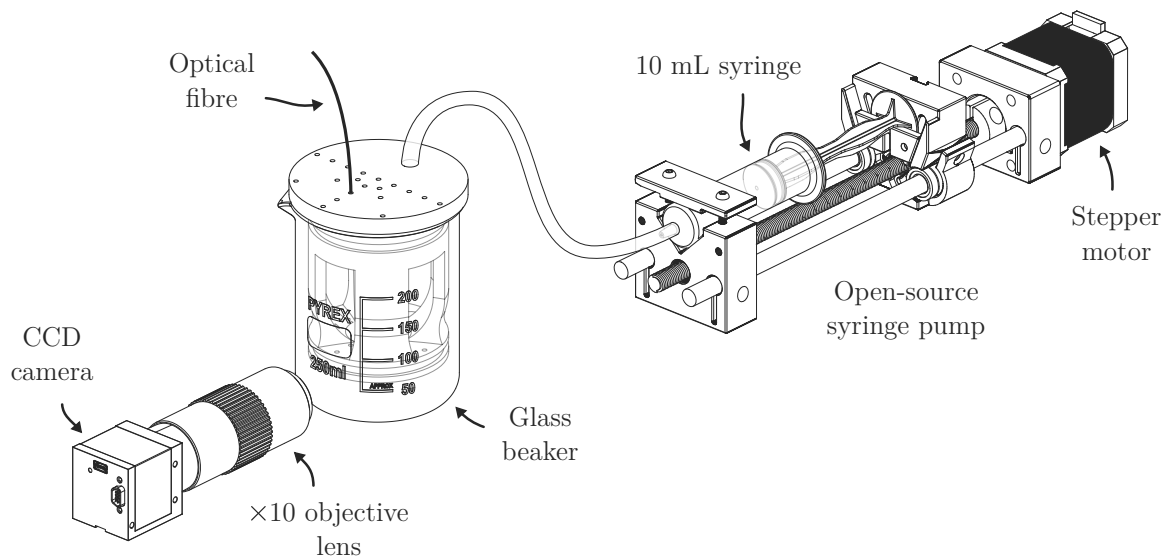


**Figure 7.5.** Illustration of the experimental setup used to regulate the liquid level in the hollow-core fibre. Adapted from [6].

the sensor is above the noise level, with a relatively high optical signal-to-noise ratio (OSNR). For this, it is important to highlight that, based on simulations carried out using the finite element bidirectional beam propagation method (bidirectional BPM) of RSoft software, there is a  $\sim 11.6\%$  back-coupling efficiency from the silica capillary back to SMF (LP<sub>01</sub> guided mode).

## Experimental and simulated results

As mentioned above, the designed and manufactured sensor allows not only to determine the liquid level in the structure, but also the refractive index of the liquid. Consequently, the experimental results carried out, which are shown below, comprise two large groups. First, for different water levels, the real liquid level has been compared with the estimated one. Second, both the liquid level and the refractive index have been determined for different liquids. In both cases, simulations have been carried out using bidirectional BPM of RSoft software. The sensor does not measure temperature and, therefore, is not able to compensate for deviations in its value. Consequently, the experiments must be carried out at a constant temperature from the first reference measurement.

The spectral characterisation of the manufactured structure is presented in Fig. 7.6. In Fig. 7.6 **a**, the spectral response of the HCF without holes is depicted (Fig. 7.2), as well as the response when HCF has been processed with the fs laser (four holes inscribed). The introduction of holes is seen to result in increased losses and reduced amplitude of the interference pattern. Moreover, in both scenarios, an interferometric contribution with a lower frequency component is evident, attributed to AR mechanisms, in addition to the Fabry-Perot cavity associated with the HCF. Figure 7.6 **b** shows the FFT amplitude of the spectra in Fig. 7.6 **a**, as well as the one corresponding to the simulation of the structure. The realization of the holes does not modify the spatial frequency but only the amplitude of the spectral contribution of the Fabry-Perot cavity. The dominant spatial frequency has a value of  $1.3 \text{ nm}^{-1}$ , which corresponds to a cavity length of  $\sim 1550 \text{ }\mu\text{m}$  (real HCF length).

Fig. 7.7 depicts the experimental spectra for different levels of liquid in the HCF ( $200 \text{ }\mu\text{m}$ ,  $700 \text{ }\mu\text{m}$  and  $1200 \text{ }\mu\text{m}$ ) (Fig. 7.7 **a**), as well as the resulting FFT spectra for liquid levels of  $100 \text{ }\mu\text{m}$ ,  $400 \text{ }\mu\text{m}$ ,  $700 \text{ }\mu\text{m}$ ,  $1000 \text{ }\mu\text{m}$  and  $1300 \text{ }\mu\text{m}$  (Fig. 7.7 **b**). The liquid is water, with a refractive index of 1.318. It is important to note that during the filling of the HCF, it is

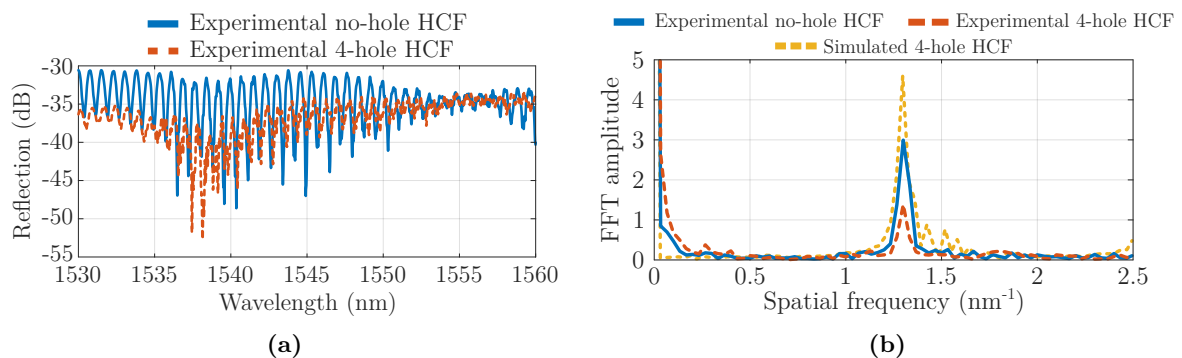


**Figure 7.6.** (a) Reflection spectra of the no-hole HCF (Fig. 7.2), and the 4-hole HCF (Fig. 7.3 b). (b) FFT amplitude from the spectra of Fig. 7.6 a, as well as the one corresponding to the simulated structure. Adapted from [6].

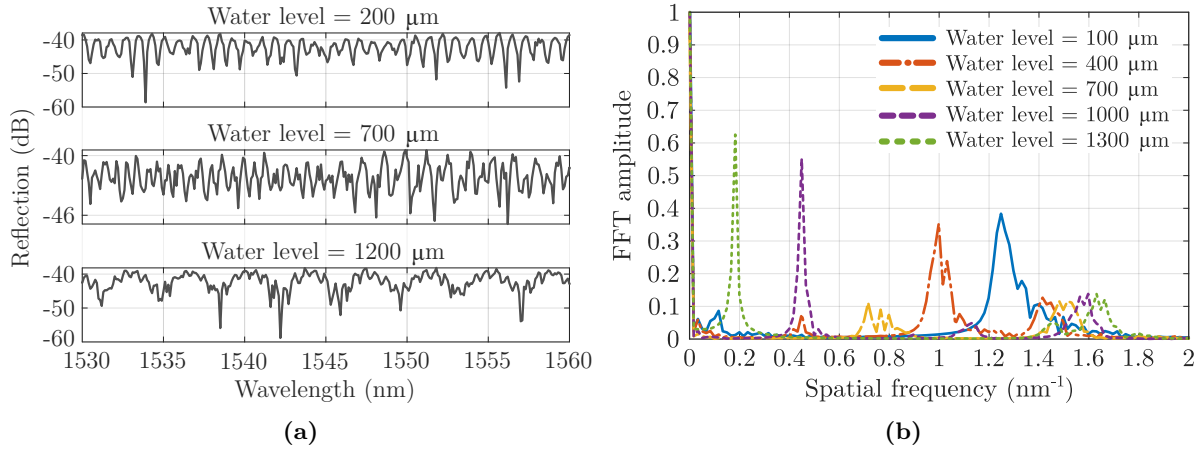


**Figure 7.7.** (a) Examples of measured reflection spectra for water levels of 200 μm, 700 μm and 1200 μm, respectively. (b) FFT amplitude of measured spectra corresponding to water levels of 100 μm, 400 μm, 700 μm, 1000 μm and 1300 μm. Adapted from [6].

necessary to wait approximately  $\sim 90$  seconds ( $25 \times 25$  μm hole) in order to stabilise the liquid and thus obtain a stable spectral pattern. Larger holes cause faster filling [48], but greater degradation in the amplitude of the interference spectral signal. Moreover, filled contour plots of the spatial frequency corresponding to liquid levels between 100 μm and 1400 μm measured experimentally (Fig. 7.8 a) and by simulation (Fig. 7.8 b) are presented.

In the FFT spectra, the presence of three large contributions can be observed, corresponding to the air, water, and joint cavities (complete HCF), as previously indicated in Equation 7.1. In this work, unlike those indicated in the introduction, the spatial frequency shift is evaluated, and not the power variation due to the uncertainty that this parameter may present. The sensitivities determined for the experimental and simulation measurements are:  $-8.89 \cdot 10^{-4}$  nm<sup>-1</sup>/μm and  $-8.19 \cdot 10^{-4}$  nm<sup>-1</sup>/μm (air cavity),  $11.3 \cdot 10^{-4}$  nm<sup>-1</sup>/μm and  $10.9 \cdot 10^{-4}$  nm<sup>-1</sup>/μm (water cavity), and  $2.28 \cdot 10^{-4}$  nm<sup>-1</sup>/μm and  $2.75 \cdot 10^{-4}$  nm<sup>-1</sup>/μm (both cavities), respectively.

From Equations 7.1 and 7.2, it is possible to determine the length of the cavity in each case. If the refractive index of the liquid is known, as in this case, the lengths of the air and liquid cavities

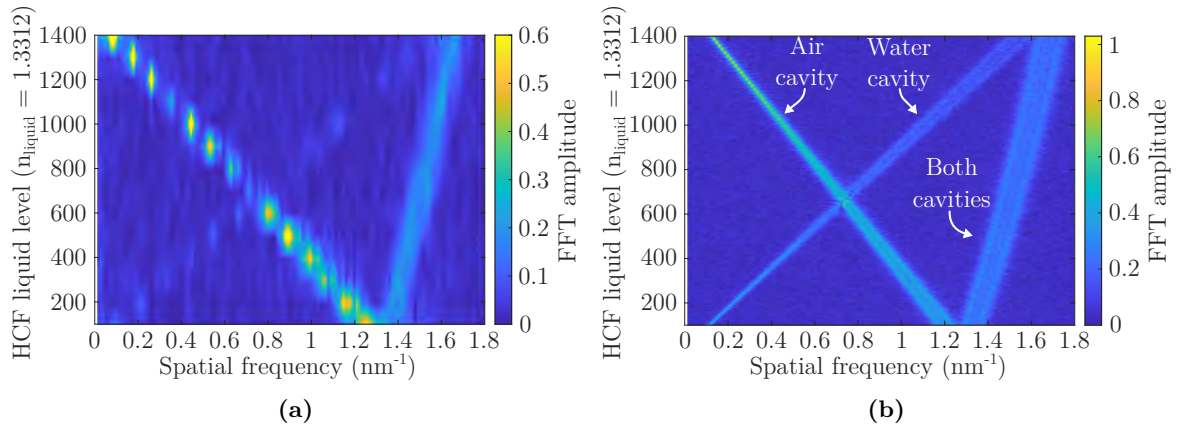


**Figure 7.8.** (a) Experimental FFT amplitude measured for water levels in the HCF between 100 μm and 1400 μm, with a spacing of 100 μm. (b) Simulated FFT amplitude for water levels in the HCF between 100 μm and 1400 μm. Adapted from [6].

## 7.1. Liquid level sensor using capillary fibres and dynamic FPIs

can be obtained directly. In Fig. 7.9, the cavity lengths extracted from the spatial frequency are depicted, as well as the relative error committed, both for the experimental and simulation results. The slope corresponding to the real-estimated water level curve takes values  $\gamma = 1.027$  (experimental) and  $\gamma = 0.9951$  (simulation). Furthermore, the experimental measurements have shown that the relative error in estimating the liquid level is consistently less than 2.5%, indicating the accuracy of the results. The resolution, in this case, depends exclusively on the OSA, since the span and the number of points in the measurements determine the frequency spacing in the FFT spectrum. For the configuration used, the frequency resolution obtained is  $0.00333 \text{ nm}^{-1}$ , which corresponds to a resolution of  $4 \text{ }\mu\text{m}$  in the liquid level. Although the spectral resolution of the OSA is the most important contribution regarding the calculation of the detection limit (DL) [49], two types of noise contributions must be taken into account [50]: amplitude noise (shot and thermal noise of the photodetector, and light source relative intensity noise), and spectral noise (thermal variation, and thermal-induced fluctuations because of the liquid in the capillary fibre), the latter being the most important in this case. Considering water as a liquid, as well as a  $\mathcal{N}(25, 9)$  temperature distribution during the measurements, the DL obtained is  $4.42 \text{ }\mu\text{m}$  (compared to the value of  $2.95 \text{ }\mu\text{m}$  in the absence of noise). On the other hand, sensor repeatability is adequate. The relative error made between the values obtained by increasing and decreasing the liquid level, as well as by complete liquid removal and re-injection is less than 2%, with respect to the values in Fig. 7.9 a.

Subsequently, experimental measurements have been carried out with Cargille liquids of refractive indices between 1.3 and 1.4 (increment of 0.01), in order to determine both parameters (liquid level and RI) simultaneously. The liquid levels where the measurements have been made are  $300 \text{ }\mu\text{m}$  and  $1300 \text{ }\mu\text{m}$ . The resulting FFT spectra for those liquid levels are depicted in Fig. 7.10.

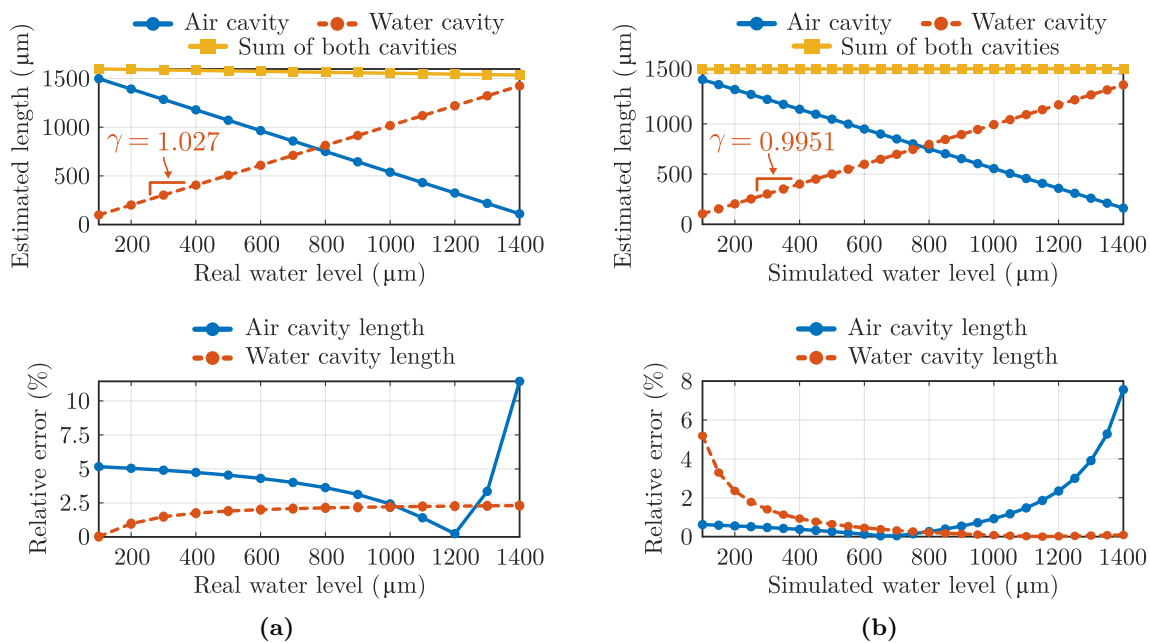


**Figure 7.9.** (a) Estimated cavity length (air and water) and relative error for different real water levels. (b) Estimated cavity length (air and water) and relative error for different simulated water levels. Adapted from [6].

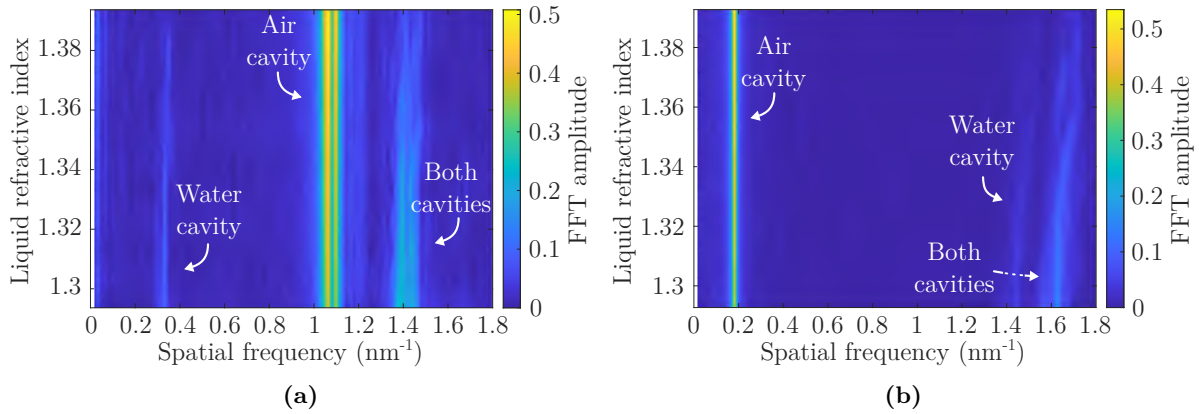


**Figure 7.10.** (a) Experimental FFT amplitude measured for different liquids in the HCF with a liquid level of 300  $\mu\text{m}$ . (b) Experimental FFT amplitude measured for different liquids in the HCF with a liquid level of 1300  $\mu\text{m}$ . Adapted from [6].

It can be seen that, in both cases, the frequency corresponding to the air cavity remains fixed. The change of liquid in the cavity only affects the two remaining contributions. For detection, the air cavity length is first determined from its spatial frequency. Subsequently, the length of the liquid cavity is deduced by knowing the HCF length. For the cases presented, liquid cavity lengths of 287.25  $\mu\text{m}$  (it should be 300  $\mu\text{m}$ ) and 1327.29  $\mu\text{m}$  (it should be 1300  $\mu\text{m}$ ) have been determined, which offer relative errors of 4.25% and 2.1%, respectively.

Once the length of the liquid cavity is known, it is possible to extract the refractive index of the cavity from the corresponding spatial frequency (Equation 7.2). Figure 7.11 depicts the estimated RI, as well as the absolute error made, for the two cases presented in Fig. 7.10. The sensitivities of the spatial frequency corresponding to the liquid cavity are 0.2296  $\text{nm}^{-1}/\text{RIU}$  (liquid level of 300  $\mu\text{m}$ ) and 1.1099  $\text{nm}^{-1}/\text{RIU}$  (1300  $\mu\text{m}$ ). The absolute error made is always lower than the order of the measurement step, so the sensor can be valid to offer an indicative measure of the liquid whose level is being evaluated. In any case, the precision in detecting the liquid level or the RI will be significantly higher when the other parameter is known. In this

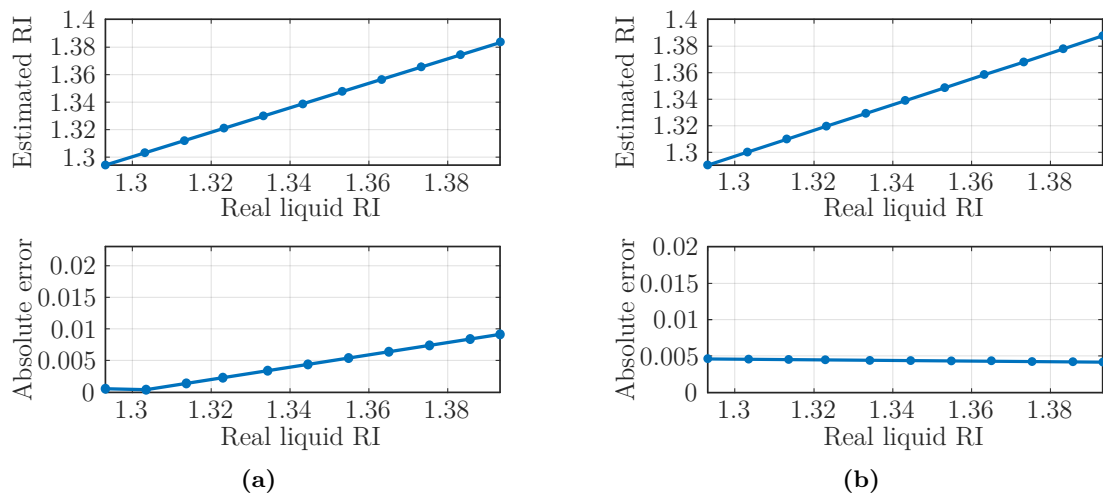


**Figure 7.11.** (a) Estimated refractive index of the HCF liquid whose level is at 300  $\mu\text{m}$ . (b) Estimated refractive index of the HCF liquid whose level is at 1300  $\mu\text{m}$ . Adapted from [6].

## 7.2. Perfluorinated POF–based refractometer for water solutions

case, the worst scenario has been presented, in which none of the parameters are known.

### 7.1.5 Conclusions

In this section, a novel sensor to evaluate the liquid level and its refractive index was designed, manufactured and experimentally demonstrated. The sensor is based on a 1.55 mm long silica capillary hollow-core fibre ( $\varnothing 60 \mu\text{m}$  core). The sensor section underwent femtosecond laser processing to create four holes, enabling the liquid to enter the HCF’s air core. This technique enhances sensitivity compared to previous works, and enables the utilisation of dynamic Fabry-Perot mechanisms for reflective sensing, which is unprecedented in liquid level sensing. With a liquid level resolution of  $4 \mu\text{m}$ , the sensitivity obtained experimentally is  $11.3 \cdot 10^{-4} \text{ nm}^{-1}/\mu\text{m}$  (spatial frequency shift), and its ability to measure liquids whose refractive index is between 1.3 and 1.4 has been verified. Similarly, the simulations have been validated by the experimental results.

## 7.2 Perfluorinated POF–based refractometer for water solutions

The use of new CYTOP (Cyclic Transparent Optical Polymer) fibres for the inscription of optical structures and the detection of different parameters has started to gain importance in the last decade. This section presents the design, simulation and manufacture of a CYTOP-based surrounding refractive index sensor for water-based solutions, given its high sensitivity in the range 1.315–1.333 (@1550 nm wavelength). The structure is based on a bent and polished fibre, the polished area being the surface on which a diffraction grating is inscribed with a femtosecond laser. The interaction of the field propagated by the fibre with the grating causes diffraction of certain orders towards the outside, depending, among other things, on the refractive index of the fluid. In addition to a maximum sensitivity of  $-208.8 \text{ nm}/\text{RIU}$ , and a remarkable insensitivity to temperature, it offers a spectral fingerprint of each sensed fluid.

### 7.2.1 Background

A great attention and research effort have been drawn to the transducing properties of optical fibres, which has made possible a breakthrough in the last 50 years with respect to optical fibre sensors, whether in glass fibre [51] or plastic optical fibre (POF) [52, 53]. The development of new fibre materials with enhanced optical properties has led to their widespread use in various fields, including engineering, industry, medicine, biochemistry, and more.

Regarding plastic optical fibres, poly(methyl methacrylate) (PMMA) has traditionally been used. The first fibres based on PMMA cores emerged in the 1960s, and their growth has been extraordinary to this day. In contrast to glass fibres, POF stands out for its ease of handling, flexibility, and reduced price [52, 54]. Likewise, the improvement of the manufacturing process has considerably limited their attenuation, and they can be used for short-haul communications or even optical fibre sensors.

However, in the late 1990s Asahi Glass Co (currently ACG Inc.) developed a special type of POF, based on an amorphous fluorinated polymer called CYTOP [55, 56]. It is poly(perfluoro-

butenylvinyl ether). Characterised by a refractive index of  $\sim 1.34$ , it stands out for its compatibility with the aqueous index regime, an important feature for biosensing [12, 57]. Moreover, it has a very low near-infrared attenuation ( $\sim 10$  dB/km) and a transmission bandwidth of up to 1300 nm. It is a graded-index polymer optical fibre (GI-POF), with less modal noise and material dispersion than PMMA fibres [52]. The use of CYTOP fibres began to gain important relevance in the 2010s, so it is a field with a great future projection. In recent years, the inscription of optical structures using fs lasers in CYTOP fibres for the development of OFSS stands out [58]. The most significant works on this topic are listed in Table 7.2. These studies are relatively recent, and a majority of them utilise FBGs as the sensing structure.

In this work, an optical structure based on a perfluorinated POF is designed, simulated and manufactured using a femtosecond laser. Taking advantage of its infrared transmission, the device is used as a highly-sensitive RI sensor in aqueous solutions, thus having potential applicability in the field of biomedicine [12]. To this end, in addition to increasing sensitivity to the external medium by bending the fibre and polishing its cladding, a diffraction grating is inscribed into the previously polished area. The variability of the transmitted diffraction orders provides a spectral fingerprint of the different aqueous solutions, which can be used for the sensing of their refractive index, among others.

## 7.2.2 Optical structure design

The designed optical structure is the one depicted in Fig. 7.12. The dimensions of the CYTOP fibre used are listed below. The graded-index core has a diameter  $d_{core} = 120$   $\mu\text{m}$ , while the cladding has a thickness of 20  $\mu\text{m}$  ( $d_{clad} = 160$   $\mu\text{m}$ ). Likewise, there is a polycarbonate protection overladding with a total diameter  $d_{oc} = 490$   $\mu\text{m}$ . The fibre, measured in transmis-

**Table 7.2.** Studies focusing on fs laser-assisted manufacture of optical structures in CYTOP fibres.

Ref.	Year	Optical structure	Parameter sensed	Sensitivity
[59]	2021	FBG <sup>a</sup>	Temperature	27.5 $\frac{\text{pm}}{\text{°C}}$ (10 – 60 °C)
[60]	2020	FBG	$\gamma$ radiation	–26.2 pm/kGy (0 – 41 kGy)
[61]	2020	FBG and FPI <sup>b</sup>	Bending angle	–3.9 pm/° (0 – 90 °)
[62]	2020	CFBG <sup>c</sup>	Force and liquid level	200 N range 50 cm range
[63]	2019	FBG array	Torque and displacement	$8.8 \cdot 10^{-2} \frac{\text{nm}}{\text{Nm}}$
[64]	2018	FPI	Strain and temperature	1.35 $\frac{\text{pm}}{\mu\epsilon}$ (0 – 5040 $\mu\epsilon$ ) 26.4 $\frac{\text{pm}}{\text{°C}}$ (40 – 60 °C)
[65]	2017	FBG	Vibration	–
[57]	2015	FBG	Strain	1.3 pm/ $\mu\epsilon$ (0 – 50 $\mu\epsilon$ )

<sup>a</sup> Fibre Bragg grating;

<sup>b</sup> Fabry-Perot interferometer;

<sup>c</sup> Chirped FBG.

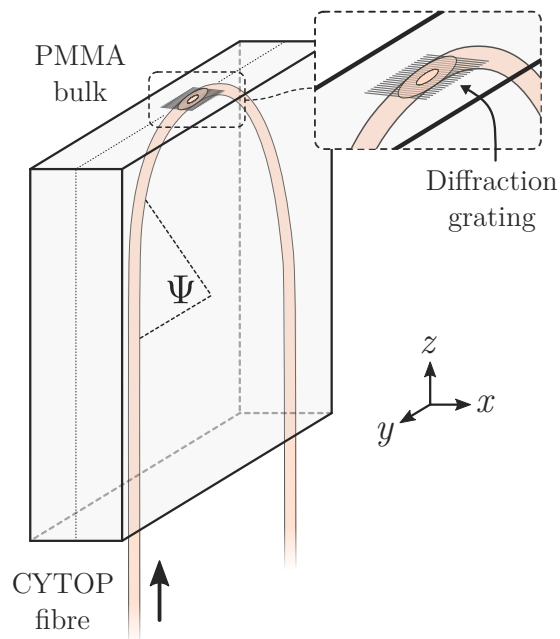


**Figure 7.12.** Schematic illustration of the CYTOP-based optical structure. Adapted from [9].

sion, was placed with a curvature defined by a radius of curvature (ROC)  $R$ . To fix the fibre, two PMMA bulks were manufactured with the groove where the fibre was placed, closing the sandwich-structure with epoxy resin.

Subsequently, the PMMA bulk corresponding to  $\Psi = 90^\circ$  started to be polished (first with ultra-fine grit sandpaper, P4000; and then with 12  $\mu\text{m}$  lapping film).  $\epsilon$  refers to the depth of polish. At the moment in which the outer interface of the fibre is reached,  $\epsilon = 0$ . When polishing continued ( $\epsilon > 0$ ), the polished part of the fibre began to generate an elliptical shape in the XY plane. To determine the polishing depth ( $\epsilon$ ), the dimensions of the ellipse generated were considered, specifically their minor and major axes. The geometric and trigonometric relationships that relate the different design parameters are presented in Fig. 7.13 **a** (for the major axis) and Fig. 7.13 **b** (minor axis) [22]. The expressions that relate  $\epsilon$  and the axes of the ellipse ( $x, y$ ) are shown below:

$$y^2 + \left(R + \frac{d_{oc}}{2} - \epsilon\right)^2 = \left(R + \frac{d_{oc}}{2}\right)^2, \quad (7.3)$$

$$x^2 + \left(\frac{d_{oc}}{2} - \epsilon\right)^2 = \left(\frac{d_{oc}}{2}\right)^2. \quad (7.4)$$

### 7.2.3 BPM simulations

Diffraction grating aside, there are two design parameters:  $R$  and  $\epsilon$ . To obtain the optimal values, finite element simulations are carried out using the BPM with the commercial software RSoft. First, a 3D simulation (in order to obtain the spatial-pattern of the cross-section) is performed by sweeping the radius of curvature ( $R$ ). Subsequently, once the  $R$  value has been chosen, the sweep is performed on the polishing depth ( $\epsilon$ ). In the latter case, by focusing only

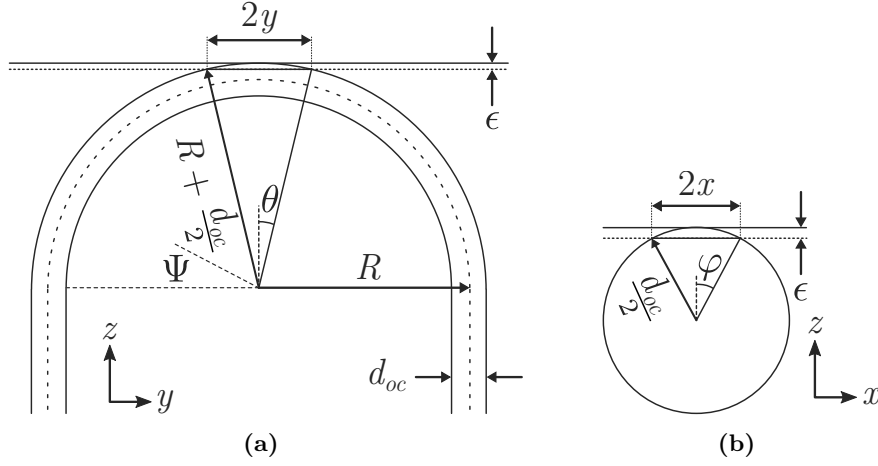


**Figure 7.13.** Geometric parameters that define the (a) major axis and (b) minor axis of the ellipse generated in the XY plane (Fig. 7.12). Adapted from [9].

on the final fibre losses, a 2-D simulation is sufficient. The simulation parameters used in both cases are listed in Table 7.3.

It should be noted that in both cases, in order to make the bending simulation feasible in BPM, a mathematical coordinate transformation called conformal mapping is used [66, 67]. The transformation used, that preserves the angle between oriented curves, is as follows:

$$W = u + iv = f(Z) = f(x + iy) = R \cdot \ln \left( \frac{Z}{R} \right), \quad (7.5)$$

for which

$$\left| \frac{dZ}{dW} \right| = \exp \left( \frac{u}{R} \right). \quad (7.6)$$

In this way, the fibre curvature can be modelled from a tilted refractive index profile, achieving a translation invariance in light propagation direction. The tilted RI profile ( $n_{tilt}$ ) as a consequence of the transformation is obtained by multiplying the actual RI of the material

**Table 7.3.** Simulation parameters used in RSoft for both cases ( $R$  sweep and  $\epsilon$  sweep).

• COMMON PARAMETERS			
$d_{core}$	120 $\mu\text{m}$	$n_{core}(r)$	$1.352\sqrt{1 - 2\Delta\frac{4r^2}{d_{core}^2}}$
$d_{clad}$	160 $\mu\text{m}$	$n_{clad}$	1.34
$d_{oc}$	$\infty$	$n_{oc}$	1.58
$\Psi$	$[0, 180]^\circ$	$\lambda$	1550 nm
• $R$ -SWEEP SIMULATION (3-D)			
$\epsilon$	0 $\mu\text{m}$	$R$	{1 : 10, 20} mm
• $\epsilon$ -SWEEP SIMULATION (2-D)			
$R$	5 mm	$\epsilon$	{0 : 10 : 60} $\mu\text{m}$
SRI	[1, 1.36]		

$r$ : radial distance to the axial axis of the fibre;

$$\Delta = \frac{(n_{core})_{max}^2 - n_{clad}^2}{2(n_{core})_{max}^2}.$$

## 7.2. Perfluorinated POF-based refractometer for water solutions

( $n_{real}$ ) by Equation 7.6:

$$n_{tilt}(u, v) = n_{real}(u, v) \cdot \exp\left(\frac{u}{R}\right) \approx \{d_{clad} \ll R\} \approx n_{real}(u, v) \left(1 + \frac{u}{R}\right). \quad (7.7)$$

Figure 7.14 depicts, for both unpolished ( $R$  sweep, Fig. 7.14 **a**) and polished ( $\epsilon$  sweep, Fig. 7.14 **b**) fibre, a schematic of the fibre in the  $Z$ -plane (no transformation) and in the  $W$ -plane (conformal mapping applied), as well as the corresponding refractive index profiles. The RI profile in Fig. 7.14 **b** corresponds to a polished fibre in the  $\Psi = 90^\circ$  position. Fibre polishing centered at  $\Psi = 90^\circ$  is mathematically associated with the function shown below (defined in the  $Z$ -plane), in polar coordinates. The limits of  $\theta$  are defined from trigonometric relations obtained according to Fig. 7.13 **a**.

$$r(\theta) = \frac{R + \frac{d_{clad}}{2} - \epsilon}{\sin \theta}, \quad \theta \in \left[\frac{\pi}{2} - \alpha, \frac{\pi}{2} + \alpha\right], \quad (7.8)$$

with  $\alpha = \cos^{-1}\left(\frac{R + \frac{d_{clad}}{2} - \epsilon}{R + \frac{d_{clad}}{2}}\right)$ . Accordingly,  $\delta = 2R\alpha$ .

Once conformal mapping has been defined, the simulations are carried out. First of all, regarding the ROC, a value of  $R$  must be chosen such that it causes relevant bending losses. In this case, an increase in attenuation is the basis of many optical sensors, due to the high sensitivity achieved to detect variations in the surrounding medium. Fig. 7.15 depicts the simulated cross-section of the fibre (core and cladding) at  $\Psi = 90^\circ$  (polishing position) for different values of  $R$ .

It can be seen that extremely small  $R$  values (*e.g.*, 2 mm) result in excessive sensing attenuation ( $> 15$  dB), as well as greater ease of fibre breakage. On the other hand, bending radii larger than 6 mm make the power propagate more easily along the axial axis of the GI-POF, with less dependence of the bending losses on the outer refractive index. Consequently, the optimum bending radii are around 5 mm, which is the value chosen. At this specific value, one can observe a significant presence of propagated cladding modes, which will be influenced by the SRI after the polishing process.

For the chosen bending radius value ( $R = 5$  mm), the fibre losses  $L$  (at  $\Psi = 180^\circ$ ) are simulated for the values given in the corresponding part of Table 7.3. Specifically, a sweep is performed on the surrounding refractive index (SRI between 1 and 1.36) for different values of polishing depth ( $\epsilon$  between 0  $\mu\text{m}$  and 60  $\mu\text{m}$  with steps of 10  $\mu\text{m}$ ). The results are plotted in Fig. 7.16.

It can be seen that, together with the fibre curvature itself, the polishing of the cladding contributes to increase the sensitivity to the external medium. However, due to its graded-index refractive index profile, the transverse field travels more confined to the axial axis of the fibre. Consequently, there are no evident differences with increasing polishing depth (only a slight increase in losses), even going into the core ( $\epsilon \geq 20$   $\mu\text{m}$ ). This approach is different from using a step-index fibre as reported by Lomer *et al.* [22]. To inscribe a sufficient number of periods on the diffraction grating, a polish of approximately 50  $\mu\text{m}$ , slightly inside the core, is recommended, as described in the following subsection.

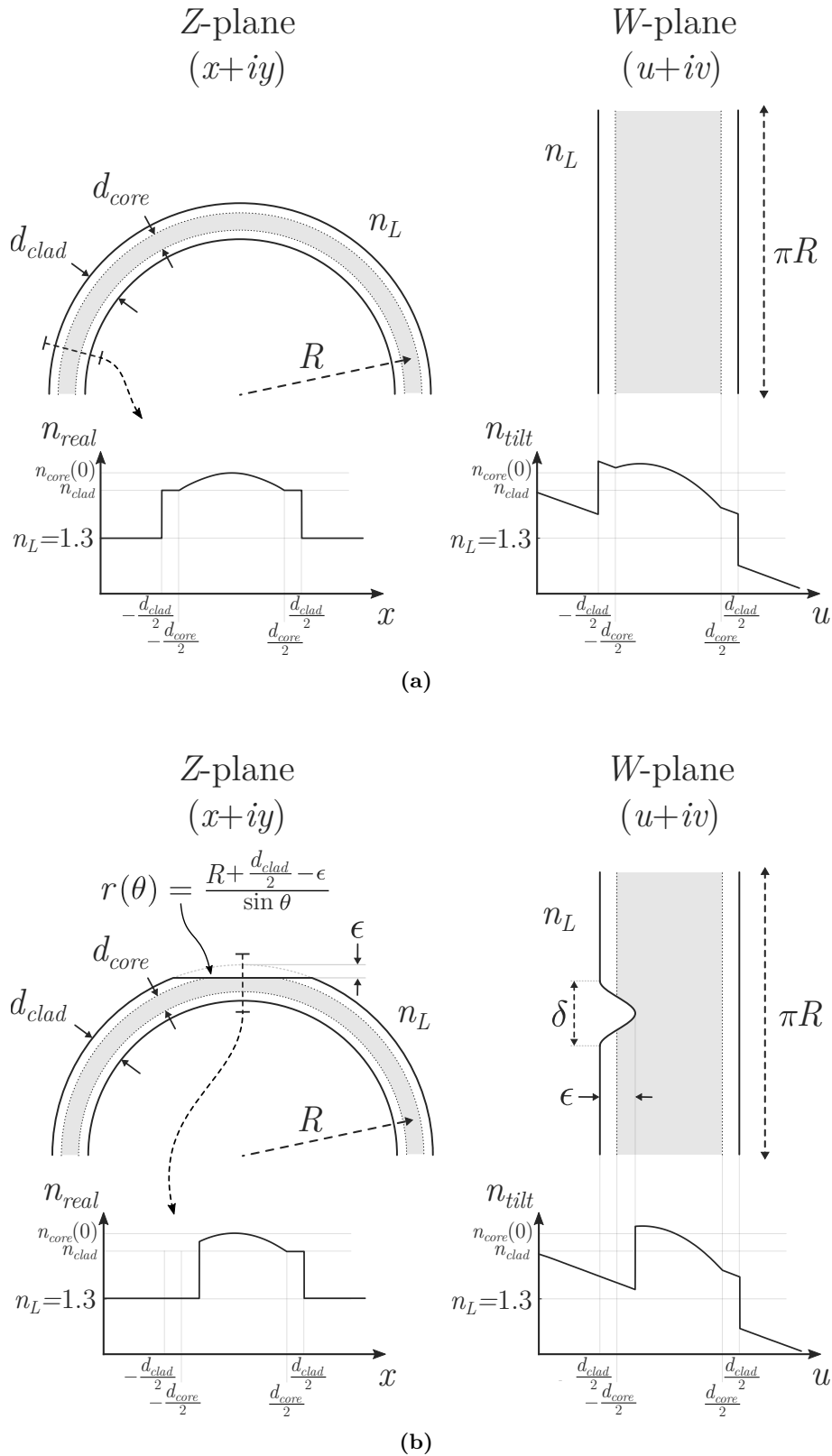


**Figure 7.14.** Schematic of the fibre in the Z-plane (no transformation) and in the W-plane (conformal mapping applied) for (a) unpolished ( $R$ -sweep simulation), (b) and polished (at  $\Psi = 90^\circ$ ) fibre ( $\epsilon$ -sweep simulation). Refractive index profiles are depicted for each case (with and without transformation). Adapted from [9].

## 7.2. Perfluorinated POF-based refractometer for water solutions

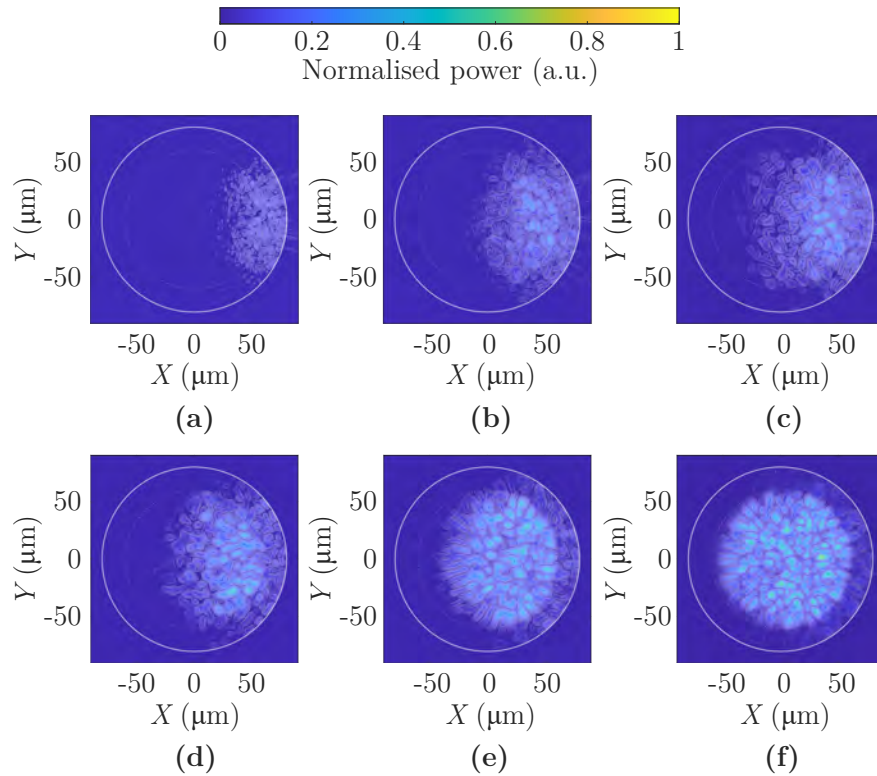


**Figure 7.15.** RSoft simulation of the resulting field in the fibre cross-section at  $\Psi = 90^\circ$  for bending radii of (a) 2 mm, (b) 4 mm, (c) 5 mm, (d) 6 mm, (e) 10 mm and (f) 20 mm. The attenuation obtained at the end of the curvature ( $\Psi = 180^\circ$ ) for each radius is 31 dB, 16.3 dB, 12.7 dB, 9.7 dB, 5.1 dB and 2.7 dB, respectively. The boundaries corresponding to core (dotted line) and cladding (solid line) are also depicted. Adapted from [9].

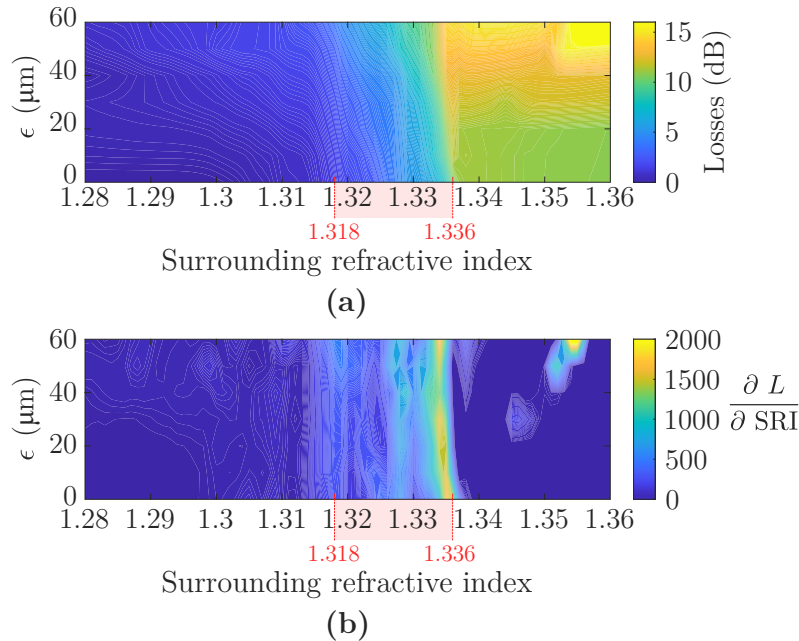


**Figure 7.16.** (a) RSoft simulation of fibre losses ( $L$ ) due to curvature ( $R = 5$  mm) as a function of polishing depth ( $\epsilon$ ) and surrounding refractive index. (b)  $\partial L / \partial \text{SRI}$  of the values represented in a. The SRI range between 1.318 and 1.336 is highlighted, due to its remarkable sensitivity. Adapted from [9].

### 7.2.4 Operating principle

A diffraction grating is inscribed on the polished surface. The angles of the diffracted modes ( $\theta_d$  for transmission, and  $\theta_r$  for reflection) are related to the wavelength ( $\lambda$ ) and grating period ( $\Lambda$ ) through the grating equation, both in the transmission (Equation 7.9) and the reflection region (Equation 7.10).

$$n_L \sin \theta_d = n_{core} \sin \theta_i + \frac{\lambda}{\Lambda} p, \quad p \in \mathbb{Z}. \quad (7.9)$$

$$n_{core} \sin \theta_r = n_{core} \sin \theta_i + \frac{\lambda}{\Lambda} p, \quad p \in \mathbb{Z}. \quad (7.10)$$

$\theta_i$  refers to the angle of the incident wave,  $p$  to the diffraction order,  $n_{core}$  to the core RI, and  $n_L$  to the SRI. These equations only predicts the direction of the modes, not how much power is in them. A schematic of the aforementioned process is shown in Fig. 7.17.

To ensure relevant efficiency in the diffracted orders, a low-order grating ( $\Lambda > \lambda/n_{core}$ ) must be chosen with a period that matches the spectral range to be used ( $\lambda \in [1500 - 1600]$  nm). A grating period of  $\Lambda = 2 \mu\text{m}$  was selected, based on an  $\epsilon$  value of  $50 \mu\text{m}$ . This yields an ellipse with major and minor axes of  $1.42 \text{ mm}$  and  $148 \mu\text{m}$ , respectively, and allows for more than 700 periods to be inscribed, thereby improving the efficiency of the different diffraction orders.

In this case, the appearance of new diffraction orders (as a function of  $\lambda$  and  $n_L$ ) causes a transfer of energy from the old to the new diffraction orders (Rayleigh anomalies [68, 69]). Consequently, there will be transitions or power variations (absorption peaks in short) in the spectrum transmitted and collected in an OSA. This is the main feature to be exploited in the measurement process.

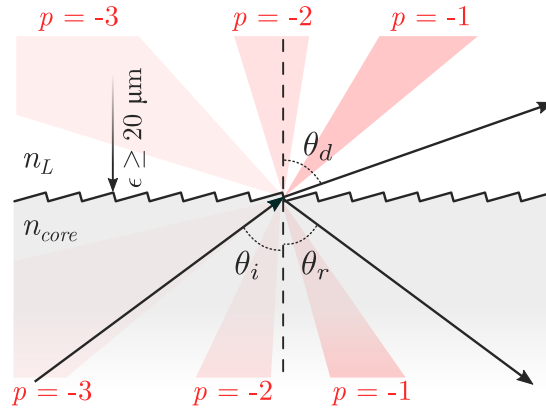


**Figure 7.17.** Diagram of 1D diffraction grating. The diffraction orders in transmission and reflection are depicted. It is assumed that there is no cladding (removed in polishing). Adapted from [9].

### 7.2.5 Experimental results

#### Manufacturing parameters

The inscription of the diffraction grating has been carried out using the following optical setup (also depicted in Fig. 4.1). A commercial fibre laser chirped pulse amplifier from Calmar has been employed. It has a 1030 nm wavelength, and 370 fs pulse duration. However, the laser beam is passed through a barium borate crystal (BBO) in order to generate a 515 nm laser beam (second harmonic generation). After harmonic separation is performed, the previously reduced beam (higher irradiance in the BBO results in higher conversion efficiency) is expanded. The pulse energy is controlled by the combination of  $\lambda/2$  plate and linear polariser. Subsequently, a half-wave plate and a quarter wave-plate are arranged in order to have total control of the polarisation state of the laser beam. Subsequently, an iris diaphragm is placed to provide a clean wavefront. The laser pulses are tightly focused through a NA=0.5,  $\times 100$  Mitutoyo objective lens. The sample is placed on a nano-resolution XYZ motor stage from Aerotech. The inscription process is monitored and visualised using a CMOS camera.

Once the structure is polished with ultra-fine sandpaper, the surface depicted in Fig. 7.18 **a** is obtained. The area corresponding to the cladding corresponds to an ellipse with major and minor axes of 1.41 mm and 148  $\mu\text{m}$ , respectively. According to Equations 7.3 and 7.4, the  $\epsilon$  value is 49.2  $\mu\text{m}$ . Fs laser inscription parameters of the diffraction grating are  $\Lambda = 2 \mu\text{m}$ , grating length of 1.45 mm, grating line length of 160  $\mu\text{m}$ ,  $E_p = 220 \text{ nJ}$ , pulse repetition rate of 30 kHz and 1,000 pulses/ $\mu\text{m}$ . Figure 7.18 **c** depicts an image of the diffraction grating, with the final complete structure in Fig. 7.18 **d**.

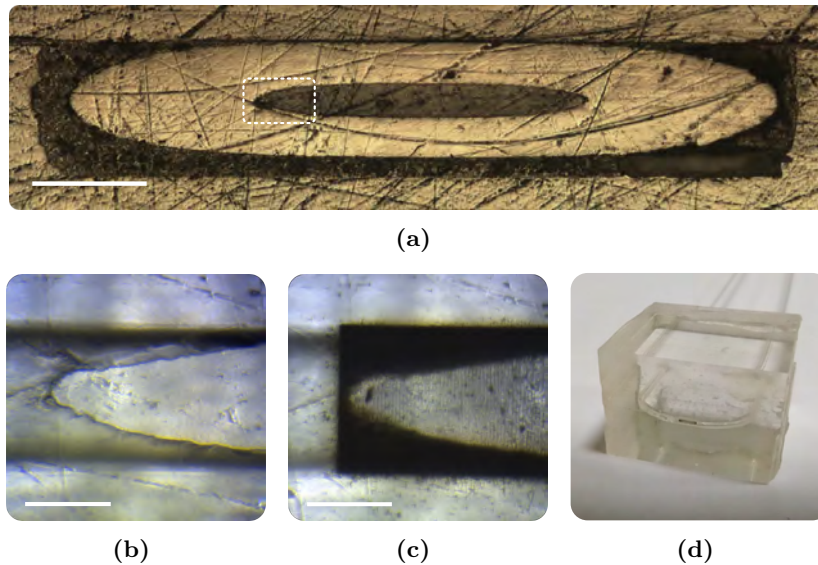


**Figure 7.18.** (a)  $5\times$  microscope image of the ellipse generated as a result of polishing, showing both cladding and core, as well as overcladding.  $20\times$  microscope images (b) before (c) and after diffraction grating inscription of the region indicated in (a) are also shown. (d) Image of the complete CYTOP-based optical structure. Scale bar in **a** is 500  $\mu\text{m}$ , and in **b-c** it is 100  $\mu\text{m}$ . Adapted from [9].

## Sensor application

The functionality of the produced structure as an aqueous solution refractometer is confirmed by conducting transmission measurements using the super-luminescent diode (SLD) S5FC1005S (Thorlabs) and OSA MS9740A (Anritsu) with a resolution of 30 pm. The measurement setup involves a length of approximately 1 m of CYTOP fibre with SMF connections at both ends.

The liquids used in the measurement process are obtained using different ratios of sucrose-aqueous solution. The RI determination of those liquids has been carried out with the Krüss DR6100 refractometer, at a temperature of  $23.9 \pm 0.4^\circ\text{C}$ . The RI values, both measured in the yellow doublet D-line of sodium (589.3 nm) and estimated in C-Band (1550 nm), are presented in Table 7.4. The estimation is made by combining existing literature data [70, 71], and Sellmeier coefficients in water [72]. According to the simulation results in Fig. 7.16, the liquids used are in the RI range of highest sensitivity.

Placing the manufactured structure in a fixed position, it is immersed in the different liquids, obtaining the transmission spectra depicted in Fig. 7.19 **a**. The measurements are repeated five times, with the uncertainty (95% confidence level, CL) depicted in the shaded region of each curve. Processing the spectra, it is observed that there are six points whose tracking consistently gives a discrimination of  $n_L$  with a high sensitivity in the range 1.315–1.33. These are valleys (absorption peaks) 2, 4, 5 and 6 in the figure, and peaks 1 and 3. Figure 7.19 **b** contains the wavelength shift ( $\Delta\lambda$ ) of each of these peaks/valleys for the six liquids used, with the corresponding quadratic fit. In addition to the high coefficient of determination ( $R^2$ ) of the fits, it is worth noting that there are three obvious trends, *i.e.*, peaks with similar behaviour: 1, 2 and 6 have a higher sensitivity in the range  $n_L \in [1.325 - 1.33]$ , 4 has its highest sensitivity in the range 1.315–1.32, while 3 and 5, although they have a lower sensitivity, have a higher linearity over the whole range 1.315–1.33 (Table 7.5).

The fibre losses are also depicted in Fig. 7.19 **c**. For  $\lambda = 1550$  nm, both the experimental results and their quadratic fit, as well as the simulation results (Fig. 7.16 **a**), are shown. Taking

**Table 7.4.** Solute concentration,  $n_D$  and  $n(1550$  nm) of the liquids used in the experiments.

Solute concentration <sup>a</sup>	0 g	20 g	40 g	60 g	80 g	100 g
$n_D^a$	1.3322	1.3353	1.3390	1.3415	1.3438	1.3468
$n(1550$ nm)	1.3153	1.3184	1.3221	1.3246	1.3269	1.3299

<sup>a</sup> C<sub>12</sub>H<sub>22</sub>O<sub>11</sub> grams per 1L H<sub>2</sub>O;

<sup>b</sup>  $n_D = n(589.3$  nm).

**Table 7.5.** Parameters of the quadratic and linear fits of the six curves depicted in Fig. 7.19 **b**.

	QUADRATIC FIT: $a_1 n_L^2 + a_2 n_L + a_3$			LINEAR FIT: $b_1 n_L + b_2$ (only $b_1$ indicated)		
	$a_1$ ( $\frac{\text{nm}^2}{\text{RIU}}$ )	$a_2$ ( $\frac{\text{nm}}{\text{RIU}}$ )	$a_3$ (nm)	$n_L \rightarrow 1.315 - 1.32$	$1.32 - 1.325$	$1.325 - 1.33$
#1	-8556	22510	-14802	-37.56 $\frac{\text{nm}}{\text{RIU}}$	-123.2 $\frac{\text{nm}}{\text{RIU}}$	-208.8 $\frac{\text{nm}}{\text{RIU}}$
#2	-7098	18650	-12250	-54.61 $\frac{\text{nm}}{\text{RIU}}$	-125.6 $\frac{\text{nm}}{\text{RIU}}$	-196.7 $\frac{\text{nm}}{\text{RIU}}$
#3	1020	-2765	1873	-78.21 $\frac{\text{nm}}{\text{RIU}}$	-68 $\frac{\text{nm}}{\text{RIU}}$	-57.8 $\frac{\text{nm}}{\text{RIU}}$
#4	6420	-17100	11380	-179.7 $\frac{\text{nm}}{\text{RIU}}$	-115.5 $\frac{\text{nm}}{\text{RIU}}$	-51.25 $\frac{\text{nm}}{\text{RIU}}$
#5	-1827	4776	-3122	-36.93 $\frac{\text{nm}}{\text{RIU}}$	-55.21 $\frac{\text{nm}}{\text{RIU}}$	-73.49 $\frac{\text{nm}}{\text{RIU}}$
#6	-6879	18080	-11890	-42.53 $\frac{\text{nm}}{\text{RIU}}$	-111.4 $\frac{\text{nm}}{\text{RIU}}$	-180.2 $\frac{\text{nm}}{\text{RIU}}$

## 7.2. Perfluorinated POF-based refractometer for water solutions

into account that the intrinsic losses of the CYTOP fibre have not been taken into account in the simulation, the similarity is remarkable. In fact, the Pearson correlation coefficient between the simulation curve for  $n_L \in [1.315 - 1.333]$  and the quadratic fit of the experimental results

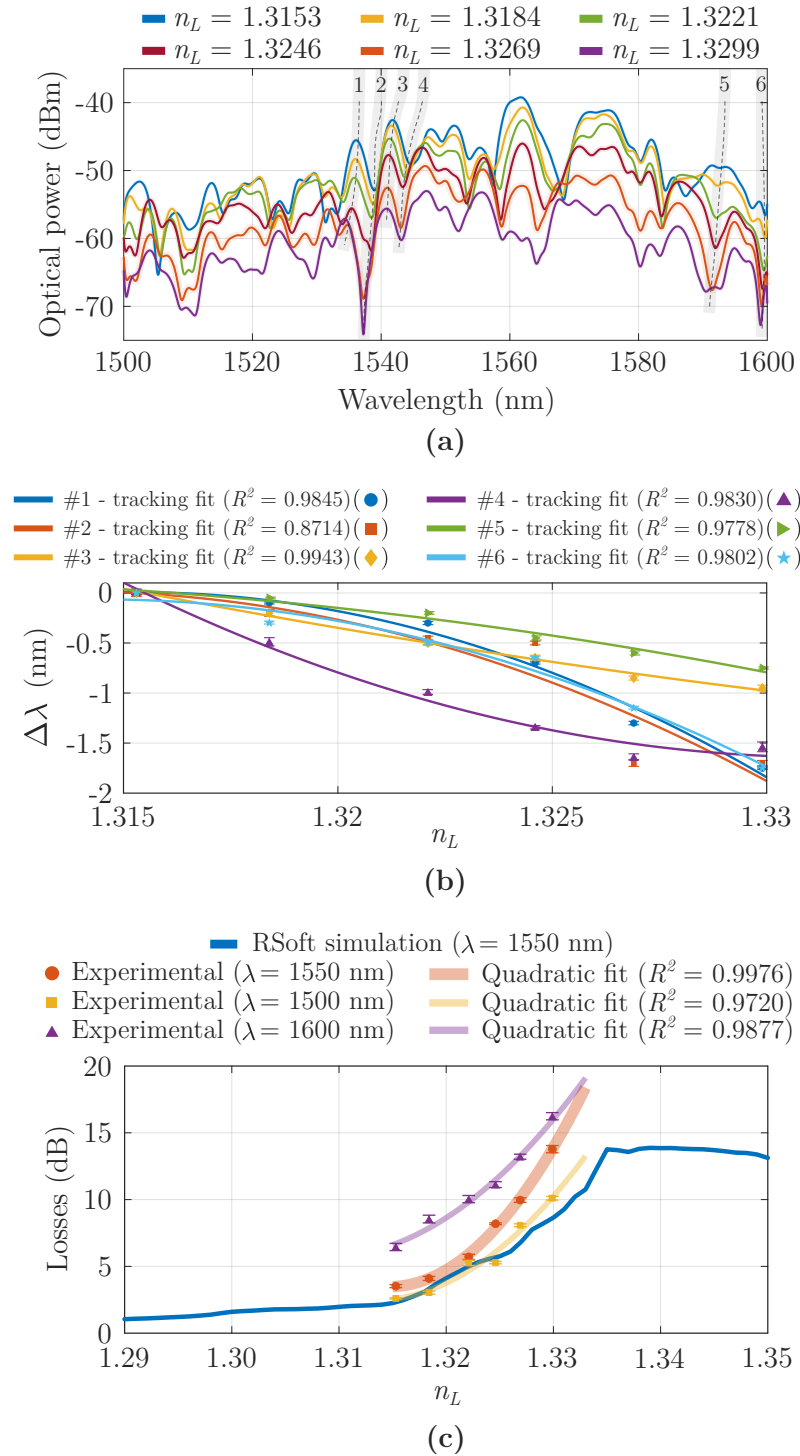


**Figure 7.19.** (a) Transmission spectra when the structure is immersed in liquids with different RI. The 6 peaks and valleys on which the tracking in sensing is performed are highlighted. (b) Wavelength shift ( $\Delta\lambda$ ) of each of the 6 peaks/valleys for the liquids used, with their quadratic fit and error bars (CL=95%). (c) Simulation and experimental transmission losses for  $\lambda = 1550$  nm, as well as experimental results for  $\lambda = 1500$  nm and  $\lambda = 1600$  nm, with the associated error bars (CL=95%). Adapted from [9].

is  $\rho = 0.9799$ . In this range, the sensitivities are 695.9 dB/RIU (experimental measurements) and 422.5 dB/RIU (simulation). Lastly, the trend of experimentally obtained losses for the 1500 and 1600 nm wavelengths is also shown. Considering that sensitivities above 120 nm/RIU are obtained in any of the three defined ranges (Table 7.5), it is possible to sense changes in SRI when they are in the order of  $10^{-3}$  ( $\Delta\lambda \geq 0.12$  nm) or even  $2.5 \cdot 10^{-4}$  ( $\Delta\lambda \geq 30$  pm). Only peak #4 presents an uncertainty higher than the OSA resolution (30 pm), especially in the first of the linear sections defined in Table 7.5. In that range ( $n_L \in [1.315 - 1.32]$ ), the detection occurs for  $\Delta\lambda \geq 57$  pm, but the sensitivity in that section is  $-179.7$  nm/RIU, so it is possible to detect changes in SRI of up to  $\sim 3.1 \cdot 10^{-4}$ . Peaks with a positive concavity, such as #4, are used as sensing points for the lower range of the sensing zone, due to their high sensitivity.

### Temperature cross-sensitivity

Temperature cross-sensitivity significantly affects refractive index measurement by altering the properties of the diffraction grating, particularly its period ( $\Lambda$ ). Firstly, it is important to note that the coefficient of linear thermal expansion (CLTE) of CYTOP is  $\sim 7.4 \cdot 10^{-5}$   $^{\circ}\text{C}^{-1}$ , which is slightly lower than PMMA. Therefore, it is not a relevant factor here, even less so in a temperature range below  $30^{\circ}\text{C}$ . To evaluate the behaviour of the SRI sensor, a temperature sweep between  $23^{\circ}\text{C}$  (room temperature) and  $40^{\circ}\text{C}$  is performed. In the measurement process, the device is immersed in water ( $n_L = 1.3153$ ), and the peaks/valleys indicated in Fig. 7.19 a are tracked. The variation of the refractive index of the liquid in this temperature range is less than  $5 \cdot 10^{-4}$ . The results obtained are depicted in Fig. 7.20. The most pronounced variation is observed at peak #1, with  $1.67$  pm/ $^{\circ}\text{C}$ . In any case, this is a value that can be considered negligible, since it gives rise to an error in the SRI measurement that is in the order of  $10^{-5}$ . It can therefore be concluded that the measurement of the surrounding refractive index is insensitive to the temperature of the fluid.

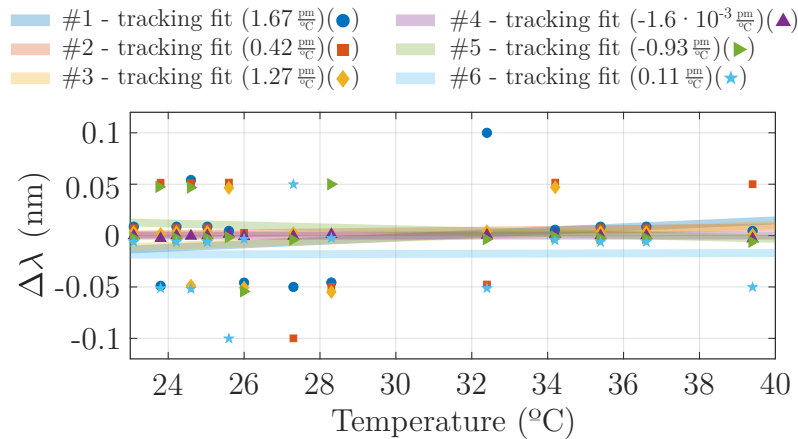


**Figure 7.20.** Wavelength shift ( $\Delta\lambda$ ) of each peak/valley as a function of temperature. The structure has been immersed in water ( $n_L = 1.3153$ ), and a temperature sweep between  $23^{\circ}\text{C}$  and  $40^{\circ}\text{C}$  has been performed. A linear fit is made, with the slope of each fit. It should be noted that the wavelength step in the spectrum is 50 pm. Adapted from [9].

### 7.2.6 Discussion

To conclude this section, it is interesting to briefly outline the main innovations and advantages compared to existing work on fibre-based refractometers. In a 2019 review, Urrutia *et al.* present the state-of-the-art associated with optical fibre refractometers [73], classifying them according to whether they are interferometers, grating-based structures, or resonance-based structures (coating). Although it can be concluded that there is not a great difference in performance between these three groups, it can be highlighted that tilted fibre Bragg gratings (TFBG) have been traditionally used as they are absolute refractometers in a wide wavelength range [74, 75]. Moreover, they are relatively robust and simple, as they do not need specialty fibres, nor modifications of their geometry that degrade their practical use from a commercial point of view. With an accuracy of  $\pm 5 \cdot 10^{-5}$ , the grating-based refractometer presented in [74] indicates that works are beginning to exist that obtain comparable performances to the Abbe refractometer.

TFBG-based refractometers have even been developed on polymer fibres [76]. These are custom PMMA fibres with a core diameter of 8.2  $\mu\text{m}$  and  $\text{NA}=0.23$ , which gives rise to a few-mode behaviour (4 guided modes). Although the performance is lower than silica single-mode fibres, sensitivities of up to  $\sim 13$  nm/RIU are achieved. They also allow to increase their high sensitivity measurement range up to  $\text{SRI}=1.49$ , compared to silica fibres, with a range of up to about  $\text{SRI}=1.45$ .

However, commercially available perfluorinated fibres have a highly multimode behaviour, which makes it impossible to use TFBGs to detect SRI with high accuracy. The great advantage of using polishing in combination with diffraction gratings is that, by eliminating cladding in a curved area, it is possible to induce most of the guided modes to interact with the external medium and condition their propagation as a function of SRI. Also, although these fibres do not allow a high sensitivity region as wide as PMMA fibres, they do have a maximum sensitivity region of around  $\text{SRI}=1.34$ . These fibers are well-suited for applications that involve distinguishing between different aqueous solutions.

### 7.2.7 Conclusions

As far as the author is aware, this is the first work using perfluorinated polymer fibres for the sensing of the surrounding refractive index. This device presents a novel approach to refractive index sensing by using an in-fibre diffraction grating inscribed with a femtosecond laser on a polished curvature zone. This structure modifies the diffraction orders transmitted and reflected by the fibre in response to the surrounding refractive index, resulting in a unique "fingerprint" of the external liquid. The device is designed for use in aqueous solutions and has potential for biomedical applications. Its encapsulated design ensures robust practical use. It has a maximum sensitivity of -208.8 nm/RIU, can detect changes in SRI of around  $2.5 \cdot 10^{-4}$ , and is insensitive to temperature, thus avoiding cross-sensitivity issues.

## References

- [1] Perez-Herrera, R. A. *et al.*, “Microdrilled tapers to enhance optical fiber lasers for sensing,” *Scientific Reports*, vol. 11, no. 1, p. 20 408, Oct. 2021. DOI: 10.1038/s41598-021-00046-7.
- [2] Bashan, G., Diamandi, H. H., Zehavi, E., Sharma, K., London, Y., and Zadok, A., “A forward Brillouin fibre laser,” *Nature Communications*, vol. 13, no. 1, p. 3554, Jun. 2022. DOI: 10.1038/s41467-022-31246-y.
- [3] Ma, X., Zhu, C., Hu, I., Kaplan, A., and Galvanauskas, A., “Single-mode chirally-coupled-core fibers with larger than 50  $\mu\text{m}$  diameter cores,” *Optics Express*, vol. 22, no. 8, pp. 9206–9219, Apr. 2014. DOI: 10.1364/oe.22.009206.
- [4] Bertoncini, A. and Liberale, C., “3D printed waveguides based on photonic crystal fiber designs for complex fiber-end photonic devices,” *Optica*, vol. 7, no. 11, pp. 1487–1494, Oct. 2020. DOI: 10.1364/optica.397281.
- [5] Yerolatsitis, S. *et al.*, “Sub millimetre flexible fibre probe for background and fluorescence free Raman spectroscopy,” *Journal of Biophotonics*, vol. 14, no. 10, e202000488, Jul. 2021. DOI: 10.1002/jbio.202000488.
- [6] Roldán-Varona, P., Pérez-Herrera, R. A., Rodríguez-Cobo, L., Reyes-González, L., López-Amo, M., and López-Higuera, J. M., “Liquid level sensor based on dynamic Fabry-Perot interferometers in processed capillary fiber,” *Scientific Reports*, vol. 11, no. 1, p. 3039, Feb. 2021. DOI: 10.1038/s41598-021-82193-5.
- [7] Roldán-Varona, P. *et al.*, “Compact Optical Fiber Lasers and Optical Fiber Sensors assisted by Femtosecond Laser Inscription of Plane-by-Plane FBGs,” in *Optical Fiber Sensors Conference 2020 Special Edition*, Optica Publishing Group, 2021. DOI: 10.1364/ofs.2020.w4.77.
- [8] Pshenay-Severin, E. *et al.*, “Multimodal nonlinear endomicroscopic imaging probe using a double-core double-clad fiber and focus-combining micro-optical concept,” *Light: Science & Applications*, vol. 10, no. 1, p. 207, Oct. 2021. DOI: 10.1038/s41377-021-00648-w.
- [9] Roldán-Varona, P., Lomer, M., Algorri, J. F., Rodríguez-Cobo, L., and López-Higuera, J. M., “Enhanced refractometer for aqueous solutions based on perfluorinated polymer optical fibres,” *Optics Express*, vol. 30, no. 2, pp. 1397–1409, Jan. 2022. DOI: 10.1364/oe.448111.
- [10] Laarossi, I., Roldán-Varona, P., Quintela-Incera, M. A., Rodríguez-Cobo, L., and López-Higuera, J. M., “Ultrahigh temperature and strain hybrid integrated sensor system based on Raman and femtosecond FBG inscription in a multimode gold-coated fiber,” *Optics Express*, vol. 27, no. 26, pp. 37 122–37 130, Dec. 2019. DOI: 10.1364/oe.27.037122.
- [11] Roldán-Varona, P., Pallarés-Aldeiturriaga, D., Rodríguez-Cobo, L., and López-Higuera, J. M., “Reflected power-based 2D bending sensor using femtosecond laser FBG inscription in multicore fiber,” in *Seventh European Workshop on Optical Fibre Sensors*, Kalli, K., Brambilla, G., and O’Keeffe, S. O., Eds., SPIE, Aug. 2019. DOI: 10.1117/12.2538794.
- [12] Ochoa, M., Algorri, J. F., Roldán-Varona, P., Rodríguez-Cobo, L., and López-Higuera, J. M., “Recent Advances in Biomedical Photonic Sensors: A Focus on Optical-Fibre-Based Sensing,” *Sensors*, vol. 21, no. 19, p. 6469, Sep. 2021. DOI: 10.3390/s21196469.

## References

- [13] Haque, M., Lee, K. K. C., Ho, S., Fernandes, L. A., and Herman, P. R., “Chemical-assisted femtosecond laser writing of lab-in-fibers,” *Lab on a Chip*, vol. 14, no. 19, pp. 3817–3829, 2014. DOI: 10.1039/c41c00648h.
- [14] Roldán-Varona, P., Rodríguez-Cobo, L., and López-Higuera, J. M., “Reflection-based lab-in-fiber sensor integrated in a surgical needle for biomedical applications,” *Optics Letters*, vol. 45, no. 18, pp. 5242–5245, Sep. 2020. DOI: 10.1364/ol.399407.
- [15] Siyu, E., Zhang, Y.-N., Han, B., Zheng, W., Wu, Q.-L., and Zheng, H.-K., “Two-Channel Surface Plasmon Resonance Sensor for Simultaneous Measurement of Seawater Salinity and Temperature,” *IEEE Transactions on Instrumentation and Measurement*, vol. 69, no. 9, pp. 7191–7199, Sep. 2020. DOI: 10.1109/tim.2020.2976405.
- [16] Tian, F., Sukhishvili, S., and Du, H., “Photonic Crystal Fiber as a Lab-in-Fiber Optofluidic Platform,” in *Springer Series in Surface Sciences*, Springer International Publishing, Jul. 2014, pp. 315–334. DOI: 10.1007/978-3-319-06998-2\_15.
- [17] Liao, C. *et al.*, “Femtosecond laser micromachining of microfluidic fiber sensors,” in *2016 15th International Conference on Optical Communications and Networks (ICOON)*, IEEE, Sep. 2016. DOI: 10.1109/icocn.2016.7875603.
- [18] Theodosiou, A., Ioannou, A., and Kalli, K., “All-in-Fiber Cladding Interferometric and Bragg Grating Components Made via Plane-by-Plane Femtosecond Laser Inscription,” *Journal of Lightwave Technology*, vol. 37, no. 18, pp. 4864–4871, Sep. 2019. DOI: 10.1109/jlt.2019.2925263.
- [19] Roldán-Varona, P., Pallarés-Aldeiturriaga, D., Rodríguez-Cobo, L., and López-Higuera, J. M., “All-in-fiber multiscan Mach-Zehnder interferometer assisted by core FBG for simultaneous multi-parameter sensing,” *Optics & Laser Technology*, vol. 132, p. 106 459, Dec. 2020. DOI: 10.1016/j.optlastec.2020.106459.
- [20] Galarza, M., Perez-Herrera, R. A., Leandro, D., Judez, A., and López-Amo, M., “Spatial-frequency multiplexing of high-sensitivity liquid level sensors based on multimode interference micro-fibers,” *Sensors and Actuators A: Physical*, vol. 307, p. 111 985, Jun. 2020. DOI: 10.1016/j.sna.2020.111985.
- [21] Mas, S., Marti, J., and Palaci, J., “Biconical Tapered Fibers Manipulation for Refractive Index and Strain Sensing Applications,” *IEEE Sensors Journal*, vol. 15, no. 3, pp. 1331–1335, Mar. 2015. DOI: 10.1109/jsen.2014.2368146.
- [22] Lomer, M., Quintela, A., López-Amo, M., Zubia, J., and López-Higuera, J. M., “A quasi-distributed level sensor based on a bent side-polished plastic optical fibre cable,” *Measurement Science and Technology*, vol. 18, no. 7, pp. 2261–2267, Jun. 2007. DOI: 10.1088/0957-0233/18/7/061.
- [23] Liao, C. *et al.*, “Tunable phase-shifted fiber Bragg grating based on femtosecond laser fabricated in-grating bubble,” *Optics Letters*, vol. 38, no. 21, pp. 4473–4476, Oct. 2013. DOI: 10.1364/ol.38.004473.
- [24] Xu, M., Yu, F., and Knight, J., “Mid-infrared 1 W hollow-core fiber gas laser source,” *Optics Letters*, vol. 42, no. 20, pp. 4055–4058, Oct. 2017. DOI: 10.1364/ol.42.004055.
- [25] Zhou, Z. *et al.*, “Towards high-power mid-IR light source tunable from 3.8 to 4.5  $\mu\text{m}$  by HBr-filled hollow-core silica fibres,” *Light: Science & Applications*, vol. 11, no. 1, Jan. 2022. DOI: 10.1038/s41377-021-00703-6.

- [26] Mulvad, H. C. H. *et al.*, “Kilowatt-average-power single-mode laser light transmission over kilometre-scale hollow-core fibre,” *Nature Photonics*, vol. 16, no. 6, pp. 448–453, May 2022. DOI: 10.1038/s41566-022-01000-3.
- [27] Millot, G. *et al.*, “Frequency-agile dual-comb spectroscopy,” *Nature Photonics*, vol. 10, no. 1, pp. 27–30, Dec. 2015. DOI: 10.1038/nphoton.2015.250.
- [28] Pérez-Herrera, R. A. *et al.*, “Multiplexing optical fiber Fabry-Perot interferometers based on air-microcavities,” in *Seventh European Workshop on Optical Fibre Sensors*, Kalli, K., Brambilla, G., and O’Keeffe, S. O., Eds., SPIE, Aug. 2019. DOI: 10.1117/12.2540150.
- [29] Pinto, A., Baptista, J., Santos, J., Lopez-Amo, M., and Frazão, O., “Micro-Displacement Sensor Based on a Hollow-Core Photonic Crystal Fiber,” *Sensors*, vol. 12, no. 12, pp. 17497–17503, Dec. 2012. DOI: 10.3390/s121217497.
- [30] Zhang, Z., He, J., Du, B., Zhang, F., Guo, K., and Wang, Y., “Measurement of high pressure and high temperature using a dual-cavity Fabry-Perot interferometer created in cascade hollow-core fibers,” *Optics Letters*, vol. 43, no. 24, pp. 6009–6012, Dec. 2018. DOI: 10.1364/ol.43.006009.
- [31] Yang, J. *et al.*, “In-fiber Mach-Zehnder interferometer with piecewise interference spectrum based on hole-assisted dual-core fiber for refractive index sensing,” *Optics Express*, vol. 26, no. 15, pp. 19091–19099, Jul. 2018. DOI: 10.1364/oe.26.019091.
- [32] Yuan, T. *et al.*, “Long period fiber grating in two-core hollow eccentric fiber,” *Optics Express*, vol. 23, no. 26, pp. 33378–33385, Dec. 2015. DOI: 10.1364/oe.23.033378.
- [33] Ni, W. *et al.*, “Simultaneous implementation of enhanced resolution and large dynamic range for fiber temperature sensing based on different optical transmission mechanisms,” *Optics Express*, vol. 26, no. 14, pp. 18341–18350, Jul. 2018. DOI: 10.1364/oe.26.018341.
- [34] Khaliq, S., James, S. W., and Tatam, R. P., “Fiber-optic liquid-level sensor using a long-period grating,” *Optics Letters*, vol. 26, no. 16, pp. 1224–1226, Aug. 2001. DOI: 10.1364/ol.26.001224.
- [35] Yun, B., Chen, N., and Cui, Y., “Highly Sensitive Liquid-Level Sensor Based on Etched Fiber Bragg Grating,” *IEEE Photonics Technology Letters*, vol. 19, no. 21, pp. 1747–1749, Nov. 2007. DOI: 10.1109/1pt.2007.905093.
- [36] Liu, S., Wang, Y., Hou, M., Guo, J., Li, Z., and Lu, P., “Anti-resonant reflecting guidance in alcohol-filled hollow core photonic crystal fiber for sensing applications,” *Optics Express*, vol. 21, no. 25, pp. 31690–31697, Dec. 2013. DOI: 10.1364/oe.21.031690.
- [37] Wang, Y., Yan, G., Lian, Z., Wu, C., and He, S., “Liquid-level sensing based on a hollow core Bragg fiber,” *Optics Express*, vol. 26, no. 17, pp. 21656–21663, Aug. 2018. DOI: 10.1364/oe.26.021656.
- [38] Zhang, Y., Lin, C., Liao, C., Yang, K., Li, Z., and Wang, Y., “Femtosecond laser-inscribed fiber interface Mach-Zehnder interferometer for temperature-insensitive refractive index measurement,” *Optics Letters*, vol. 43, no. 18, pp. 4421–4424, 2018, ISSN: 0146-9592. DOI: 10.1364/ol.43.004421.
- [39] Sun, W. *et al.*, “Comparative Study on Transmission Mechanisms in a SMF-Capillary-SMF Structure,” *Journal of Lightwave Technology*, vol. 38, no. 15, pp. 4075–4085, Aug. 2020. DOI: 10.1109/jlt.2020.2983910.

## References

- [40] Liu, D. *et al.*, “Sub-micrometer resolution liquid level sensor based on a hollow core fiber structure,” *Optics Letters*, vol. 44, no. 8, pp. 2125–2128, Apr. 2019. DOI: 10.1364/ol.44.002125.
- [41] Liu, S., Tian, J., Liu, N., Xia, J., and Lu, P., “Temperature Insensitive Liquid Level Sensor Based on Antiresonant Reflecting Guidance in Silica Tube,” *Journal of Lightwave Technology*, vol. 34, no. 22, pp. 5239–5243, Nov. 2016. DOI: 10.1109/jlt.2016.2611007.
- [42] Zhang, Y., Zhang, W., Chen, L., Zhang, Y., Wang, S., and Yan, T., “High sensitivity optical fiber liquid level sensor based on a compact MMF-HCF-FBG structure,” *Measurement Science and Technology*, vol. 29, no. 5, p. 055 104, Mar. 2018. DOI: 10.1088/1361-6501/aaac5c.
- [43] Lee, C.-L., Ho, H.-Y., Gu, J.-H., Yeh, T.-Y., and Tseng, C.-H., “Dual hollow core fiber-based Fabry-Perot interferometer for measuring the thermo-optic coefficients of liquids,” *Optics Letters*, vol. 40, no. 4, pp. 459–462, Feb. 2015. DOI: 10.1364/ol.40.000459.
- [44] Gattass, R. R. and Mazur, E., “Femtosecond laser micromachining in transparent materials,” *Nature Photonics*, vol. 2, no. 4, pp. 219–225, Apr. 2008. DOI: 10.1038/nphoton.2008.47. [Online]. Available: <https://doi.org/10.1038/nphoton.2008.47>.
- [45] Itoh, K., Watanabe, W., Nolte, S., and Schaffer, C. B., “Ultrafast Processes for Bulk Modification of Transparent Materials,” *MRS Bulletin*, vol. 31, no. 8, pp. 620–625, Aug. 2006. DOI: 10.1557/mrs2006.159.
- [46] Thomas, J., Voigtländer, C., Becker, R. G., Richter, D., Tünnermann, A., and Nolte, S., “Femtosecond pulse written fiber gratings: A new avenue to integrated fiber technology,” *Laser & Photonics Reviews*, vol. 6, no. 6, pp. 709–723, Feb. 2012. DOI: 10.1002/lpor.201100033.
- [47] Samokhin, A. S., “Syringe Pump Created using 3D Printing Technology and Arduino Platform,” *Journal of Analytical Chemistry*, vol. 75, no. 3, pp. 416–421, Mar. 2020. DOI: 10.1134/s1061934820030156.
- [48] Liao, C. R., Hu, T. Y., and Wang, D. N., “Optical fiber Fabry-Perot interferometer cavity fabricated by femtosecond laser micromachining and fusion splicing for refractive index sensing,” *Optics Express*, vol. 20, no. 20, pp. 22 813–22 818, Sep. 2012. DOI: 10.1364/oe.20.022813.
- [49] Loock, H.-P. and Wentzell, P. D., “Detection limits of chemical sensors: Applications and misapplications,” *Sensors and Actuators B: Chemical*, vol. 173, pp. 157–163, Oct. 2012. DOI: 10.1016/j.snb.2012.06.071.
- [50] White, I. M. and Fan, X., “On the performance quantification of resonant refractive index sensors,” *Optics Express*, vol. 16, no. 2, pp. 1020–1028, 2008. DOI: 10.1364/oe.16.001020.
- [51] Pallarés-Aldeiturriaga, D., Roldán-Varona, P., Rodríguez-Cobo, L., and López-Higuera, J. M., “Optical Fiber Sensors by Direct Laser Processing: A Review,” *Sensors*, vol. 20, no. 23, p. 6971, Dec. 2020. DOI: 10.3390/s20236971.
- [52] Peters, K., “Polymer optical fiber sensors—a review,” *Smart Materials and Structures*, vol. 20, no. 1, p. 013 002, Dec. 2010. DOI: 10.1088/0964-1726/20/1/013002.
- [53] Bilro, L., Alberto, N., Pinto, J. L., and Nogueira, R., “Optical Sensors Based on Plastic Fibers,” *Sensors*, vol. 12, no. 9, pp. 12 184–12 207, Sep. 2012. DOI: 10.3390/s120912184.

- [54] Zubia, J. and Arrue, J., “Plastic Optical Fibers: An Introduction to Their Technological Processes and Applications,” *Optical Fiber Technology*, vol. 7, no. 2, pp. 101–140, Apr. 2001. DOI: 10.1006/ofte.2000.0355.
- [55] Yoshihara, N., “Low-loss, high-bandwidth fluorinated POF for visible to 1.3- $\mu\text{m}$  wavelengths,” in *OFC '98. Optical Fiber Communication Conference and Exhibit. Technical Digest. Conference Edition. 1998 OSA Technical Digest Series Vol.2 (IEEE Cat. No.98CH36177)*, Opt. Soc. America. DOI: 10.1109/ofc.1998.657428.
- [56] Naritomi, M., “CYTOP Amorphous Perfluoropolymer for Low Loss POF,” *POF Asia Pacific Forum '96*, 1996. [Online]. Available: <https://ci.nii.ac.jp/naid/10022381823/en/>.
- [57] Lacraz, A., Polis, M., Theodosiou, A., Koutsides, C., and Kalli, K., “Femtosecond Laser Inscribed Bragg Gratings in Low Loss CYTOP Polymer Optical Fiber,” *IEEE Photonics Technology Letters*, vol. 27, no. 7, pp. 693–696, Apr. 2015. DOI: 10.1109/lpt.2014.2386692.
- [58] Theodosiou, A. and Kalli, K., “Recent trends and advances of fibre Bragg grating sensors in CYTOP polymer optical fibres,” *Optical Fiber Technology*, vol. 54, p. 102079, Jan. 2020. DOI: 10.1016/j.yofte.2019.102079.
- [59] Nan, Y.-G., Kinet, D., Chah, K., Chapalo, I., Caucheteur, C., and Mégret, P., “Ultra-fast fiber Bragg grating inscription in CYTOP polymer optical fibers using phase mask and 400 nm femtosecond laser,” *Optics Express*, vol. 29, no. 16, pp. 25 824–25 835, Jul. 2021. DOI: 10.1364/oe.428592.
- [60] Broadway, C. *et al.*, “CYTOP Fibre Bragg Grating Sensors for Harsh Radiation Environments,” *Sensors*, vol. 19, no. 13, p. 2853, Jun. 2019. DOI: 10.3390/s19132853.
- [61] Leal-Junior, A. G. *et al.*, “FPI-POFBG Angular Movement Sensor Inscribed in CYTOP Fibers With Dynamic Angle Compensator,” *IEEE Sensors Journal*, vol. 20, no. 11, pp. 5962–5969, Jun. 2020. DOI: 10.1109/jsen.2020.2974931.
- [62] Leal-Junior, A. G. *et al.*, “Optimizing Linearity and Sensitivity of 3D-Printed Diaphragms With Chirped FBGs in CYTOP Fibers,” *IEEE Access*, vol. 8, pp. 31 983–31 991, 2020. DOI: 10.1109/access.2020.2973187.
- [63] Leal-Junior, A. G. *et al.*, “Quasi-Distributed Torque and Displacement Sensing on a Series Elastic Actuator’s Spring Using FBG Arrays Inscribed in CYTOP Fibers,” *IEEE Sensors Journal*, vol. 19, no. 11, pp. 4054–4061, Jun. 2019. DOI: 10.1109/jsen.2019.2898722.
- [64] Theodosiou, A., Hu, X., Caucheteur, C., and Kalli, K., “Bragg Gratings and Fabry-Perot Cavities in Low-Loss Multimode CYTOP Polymer Fiber,” *IEEE Photonics Technology Letters*, vol. 30, no. 9, pp. 857–860, May 2018. DOI: 10.1109/lpt.2018.2820381.
- [65] Theodosiou, A., Lacraz, A., Stassis, A., Koutsides, C., Komodromos, M., and Kalli, K., “Plane-by-Plane Femtosecond Laser Inscription Method for Single-Peak Bragg Gratings in Multimode CYTOP Polymer Optical Fiber,” *Journal of Lightwave Technology*, vol. 35, no. 24, pp. 5404–5410, Dec. 2017. DOI: 10.1109/jlt.2017.2776862.
- [66] Schulze, C. *et al.*, “Mode resolved bend loss in few-mode optical fibers,” *Optics Express*, vol. 21, no. 3, pp. 3170–3181, Feb. 2013. DOI: 10.1364/oe.21.003170.
- [67] Pallares-Aldeiturriaga, D., Rodriguez-Cobo, L., Quintela, A., and Lopez-Higuera, J. M., “Curvature Sensor Based on In-Fiber Mach-Zehnder Interferometer Inscribed with Fem-

## References

- tosecond Laser,” *Journal of Lightwave Technology*, vol. 35, no. 21, pp. 4624–4628, 2017, ISSN: 0733-8724. DOI: 10.1109/JLT.2017.2756103.
- [68] Harvey, J. E. and Pfisterer, R. N., “Understanding diffraction grating behavior: Including conical diffraction and Rayleigh anomalies from transmission gratings,” *Optical Engineering*, vol. 58, no. 08, p. 087105, Aug. 2019. DOI: 10.1117/1.oe.58.8.087105.
- [69] Amin, M. S., Yoon, J. W., and Magnusson, R., “Optical transmission filters with coexisting guided-mode resonance and Rayleigh anomaly,” *Applied Physics Letters*, vol. 103, no. 13, p. 131106, Sep. 2013. DOI: 10.1063/1.4823532.
- [70] Saunders, J. E., Sanders, C., Chen, H., and Loock, H.-P., “Refractive indices of common solvents and solutions at 1550 nm,” *Applied Optics*, vol. 55, no. 4, pp. 947–953, Feb. 2016. DOI: 10.1364/ao.55.000947.
- [71] Hale, G. M. and Querry, M. R., “Optical Constants of Water in the 200-nm to 200- $\mu$ m Wavelength Region,” *Applied Optics*, vol. 12, no. 3, pp. 555–563, Mar. 1973. DOI: 10.1364/ao.12.000555.
- [72] Arif, M. F. H. and Biddut, M. J. H., “Enhancement of relative sensitivity of photonic crystal fiber with high birefringence and low confinement loss,” *Optik*, vol. 131, pp. 697–704, Feb. 2017. DOI: 10.1016/j.ijleo.2016.11.203.
- [73] Urrutia, A., Villar, I. D., Zubiate, P., and Zamarreño, C. R., “A Comprehensive Review of Optical Fiber Refractometers: Toward a Standard Comparative Criterion,” *Laser & Photonics Reviews*, vol. 13, no. 11, p. 1900094, Oct. 2019. DOI: 10.1002/lpor.201900094.
- [74] Zhou, W., Zhou, Y., and Albert, J., “A true fiber optic refractometer,” *Laser & Photonics Reviews*, vol. 11, no. 1, p. 1600157, Jan. 2017. DOI: 10.1002/lpor.201600157.
- [75] Liu, Z. *et al.*, “Liquid surface tension and refractive index sensor based on a tilted fiber Bragg grating,” *Journal of the Optical Society of America B*, vol. 35, no. 6, pp. 1282–1287, May 2018. DOI: 10.1364/josab.35.001282.
- [76] Hu, X., Pun, C.-F. J., Tam, H.-Y., Mégret, P., and Caucheteur, C., “Tilted Bragg gratings in step-index polymer optical fiber,” *Optics Letters*, vol. 39, no. 24, pp. 6835–6838, Dec. 2014. DOI: 10.1364/ol.39.006835.

# PART III

## ULTRAFAST LASER ASSISTED ETCHING (ULAE)

Part III showcases the contributions made utilising the technology that combines ultrafast laser inscription and wet chemical etching. This section covers the time period from August 2021 until the completion of the thesis in September 2023. The advancements made during this period are presented. Firstly, a new regime of femtosecond laser inscription is explored, enabling a high etching rate in fused silica using NaOH (or KOH) independent of the employed polarisation. Although a complete understanding of the process is still being researched, insights and evidence are provided to shed light on its origin. Secondly, the outcomes resulting from a research stay conducted in 2021 at Heriot-Watt University in Edinburgh (UK) are documented. A powerful method for selective plane illumination endomicroscopy in human lung tissue is presented, utilising an ultrafast laser-fabricated silica end cap placed at the distal end of a polymer imaging fibre. This approach effectively addresses the issue of autofluorescence from both the imaged tissue and the fibre. Lastly, preliminary data associated with a research stay in 2022 at the Institute of Photonics and Nanotechnology in Milan (Italy) is described. The design and fabrication of a photonic chip utilising Bloch surface waves excited in a dielectric 1D photonic crystal are presented, showcasing the potential for detecting molecular chirality through circular dichroism spectroscopy. The part highlights significant advancements achieved through ultrafast laser assisted etching.

The chapters included in this part are:

- Chapter 8: Polarisation-independent ULAE in fused silica.
- Chapter 9: SPIM using polymer coherent fibre bundles.
- Chapter 10: Molecular sensing with Bloch surface waves.

# 8

## Polarisation-independent ULAE in fused silica

---

<b>8.1</b>	<b>Point defects in SiO<sub>2</sub> glass</b>	<b>151</b>
8.1.1	Frenkel defects	153
8.1.2	Dangling-bond defects	154
<b>8.2</b>	<b>Etching mechanisms in SiO<sub>2</sub> glass</b>	<b>155</b>
8.2.1	Nanograting-driven etching	156
8.2.2	Non nanograting-driven etching	157
<b>8.3</b>	<b>Experimental setup and protocol</b>	<b>158</b>
<b>8.4</b>	<b>Etching rate results</b>	<b>160</b>
8.4.1	Definition of $N$ -dependent regimes	160
8.4.2	Low $N$ regime ( $N < 15 \mu\text{m}^{-1}$ )	161
8.4.3	Moderate $N$ regime ( $15 \leq N < 100 \mu\text{m}^{-1}$ )	165
8.4.4	High $N$ regime ( $N > 100 \mu\text{m}^{-1}$ )	165
<b>8.5</b>	<b>Discussion about ER and polarisation dependence</b>	<b>165</b>
<b>8.6</b>	<b>Etching mechanisms in polarisation-independent regime</b>	<b>167</b>
<b>8.7</b>	<b>Conclusions</b>	<b>170</b>
	<b>References</b>	<b>171</b>

---

**I**N fused silica, ultrafast laser assisted etching enables high chemical etching rates ( $> 300 \mu\text{m}\cdot\text{h}^{-1}$ ) by setting the light polarisation linear and perpendicular to the beam writing direction. However, for many non-planar surfaces and 3D structures, dynamic polarisation control is difficult or not yet possible to implement.

This chapter describes the results corresponding to the identification of a laser inscription regime in which high etching rates are accomplished independently of the light polarisation. In this regime ( $< 15$  pulses/ $\mu\text{m}$ ), etching rates  $\sim 300 \mu\text{m}\cdot\text{h}^{-1}$  (4 hours in NaOH) are measured, including femtosecond-pulse energies corresponding to Type II modifications. Few pulses

inscriptions exhibit a low degree of anisotropy as compared to higher number of pulses, thus enabling the polarisation insensitivity whose mechanisms are discussed in the chapter. To demonstrate the capabilities of the processing, curved and square-wave microchannels are fabricated, together with a complex 3D geometrical structure (stellated octahedron) containing an inter-plane arrangement with challenging angles ( $45^\circ$ ), difficult to achieve even employing dynamic polarisation control.

Two theoretical sections are included prior to the work carried out, with two clear objectives: firstly, to provide a concise overview of the current understanding of intrinsic defects in silica that affect its optical transparency (section 8.1); and secondly, to investigate how these imperfections may be related to the fs laser inscription regime identified in this work through a state-of-the-art review of mechanisms driving high etching rates in  $\text{SiO}_2$  (section 8.2).

The contributions detailed here were published in 2023 by Ochoa *et al.* [1–3], and the data that support the findings of this study can be found in [4]. The study has also been featured on the inside back cover of the Lab on a Chip journal, in its volume 25, issue 7.

## 8.1 Point defects in $\text{SiO}_2$ glass

The study of defects in silica is primarily motivated by its various applications. Silica glass possesses exceptional properties that set it apart from other glassy materials. It is mechanically and chemically durable, and its excellent mid-IR transparency makes it indispensable for long-range, low-loss optical communication fibres. Additionally, silica boasts the highest UV transparency among all glasses, making it the ideal material for UV optics and high-power pulsed laser optics, where the energy of multiphoton excitations must remain lower than the band gap. The longstanding dominance of silicon-based microelectronics is largely facilitated by the high quality and ease of obtaining thin amorphous silicon oxide films on silicon, which have excellent dielectric properties. Silica glass also possesses the best resistance against coloration in radiation environments, making it the material of choice for many space and nuclear energy technology-related optical applications.

However, point defects and impurities in silica can often be detrimental to these applications. While the issue of impurities has largely been resolved, with the most troublesome impurities eliminated to below parts-per-billion levels, intrinsic point defects continue to be a formidable problem. These defects can be preexisting or created by ionizing or particle irradiation, by light or by charge carriers (Fig. 8.1). Despite decades of research, a number of practically important tasks remain unsolved and will be discussed below.

Silica in its glassy form can be viewed as a continuous network comprising relatively rigid, undistorted  $\text{SiO}_4$  tetrahedra that are connected at their corners by shared (“*bridging*”) oxygen atoms. The O–Si–O angle deviates by less than  $4^\circ$  from the expected tetrahedral value of  $109.5^\circ$ . The disorder of the glassy state is primarily accommodated by a continuous distribution in the intertetrahedral Si–O–Si angles, which range from  $120^\circ$  to  $180^\circ$  with a peak at  $144^\circ$ – $150^\circ$ , as well as in the torsional angles. The arrangement of the silica network can be described by the distribution of  $n$ -membered  $(\text{Si-O})_n$  rings (Fig. 8.2 a). The  $\alpha$ -quartz lattice is composed solely of 6- and 8-membered rings, but modeling of amorphous  $\text{SiO}_2$  reveals a range of 3- to 10-membered rings. The statistics of these rings depend on the thermal and radiation history

## 8.1. Point defects in SiO<sub>2</sub> glass

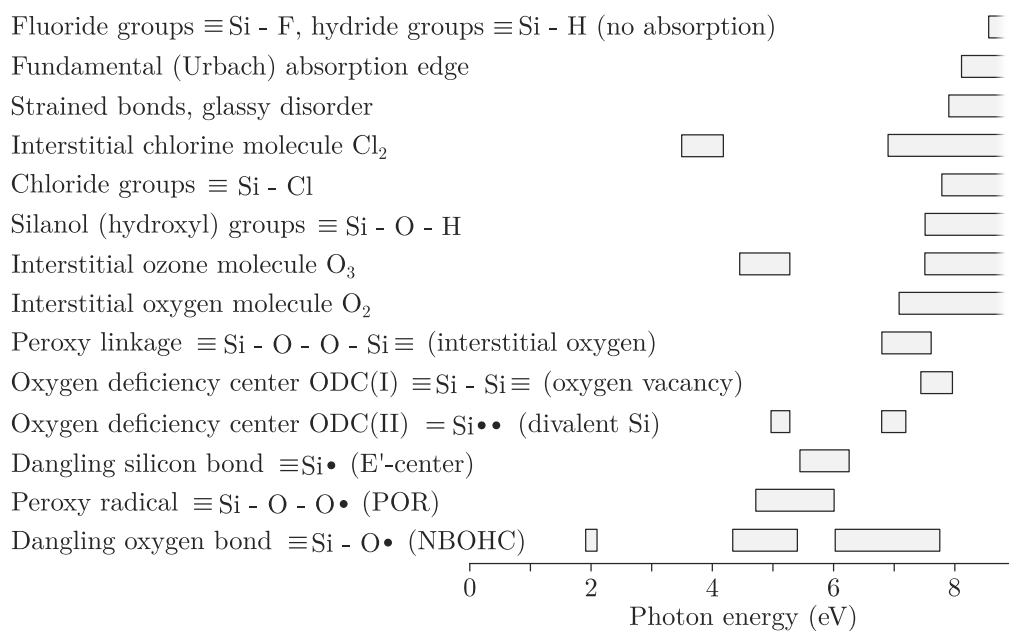


**Figure 8.1.** Overview of the main optical absorption bands in synthetic glassy SiO<sub>2</sub> that stem from intrinsic defects and typical dopants/impurities. The spectral position and FWHM of the bands are represented by the centre and width of the bars. Only the oxygen vacancy band (which peaks at 7.6 eV) is observable in  $\alpha$ -quartz crystal among these bands. For optical applications in the visible to deep-UV ranges, the bands associated with dangling oxygen (NBOHC) and silicon bonds (E'-center) are the most prominent and problematic. Adapted from [5].

of the silica.

Raman spectroscopy can be utilised to directly observe structural modifications such as changes in the inter-tetrahedral Si–O–Si angle or fluctuations in ring statistics (*e.g.*, number of strained bonds in the silica network). The presence of 4- and 3-membered rings results in distinct Raman lines at  $\sim 495\text{ cm}^{-1}$  (D<sub>1</sub> band) and  $\sim 606\text{ cm}^{-1}$  (D<sub>2</sub> band), respectively. In general, when the population of 3- and 4-membered ring structures increases, it indicates a reduction in the overall bond angle and, as a result, the densification of the glass. However, it is important to note that the changes observed in the D<sub>1</sub> and D<sub>2</sub> lines differ slightly between compressed and irradiated glasses. In the case of the latter, the enhancement of the D<sub>2</sub> line is particularly noteworthy.

By utilising this technique, it was discovered that the creation of dangling bonds (E'-centre and NBOHC) is closely linked to the quantity of strained 3-membered rings in silica, *i.e.*, D<sub>2</sub> line in Raman spectrum. Consequently, it seems likely that the generation of non-bridging oxygen hole centre (NBOHC) and E'-centre defects is associated with the densification of the silica glass.

Regarding point defects, some assumptions were made in the past that suggested that the “glass-specific” defects, which are not present in  $\alpha$ -quartz, are located on internal surfaces of the silica network. This was based on the observation that while SiO<sub>4</sub> tetrahedra have the same size in silica glass and  $\alpha$ -quartz, the density of glass is significantly lower (2.20 vs. 2.65 g/cm<sup>3</sup>), indicating the presence of large interstitial spaces. However, extensive studies have confirmed that many of the defects observed in bulk silica are also found on surfaces. The atoms on the surface have weaker binding compared to those in the bulk, and thus, they can be easily displaced under excitation.

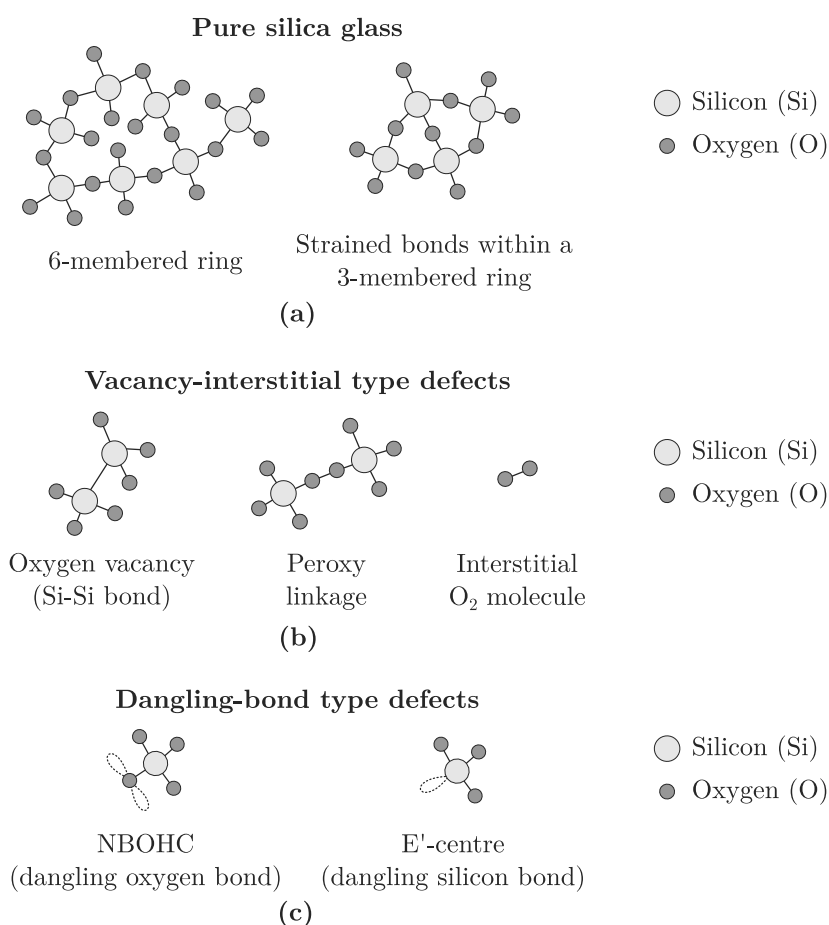


**Figure 8.2.** Schematic illustration of (a) a 6-membered ring ((Si-O)<sub>6</sub>) and a 3-membered planar ring ((Si-O)<sub>3</sub>) in amorphous SiO<sub>2</sub>. (b) Vacancy-interstitial type defects, (c) and basic dangling-bond type defects observed in SiO<sub>2</sub>. Adapted from [5].

Next, we present some types of defects, specifically Frenkel (vacancy-interstitial type) defects, which could be expected to be roughly similar to defects in crystal quartz, and dangling bond type centres, which are closely related to centres observed in surfaces. There will be no mention regarding the role of hydrogen and fluorine dopants in strained bonds.

### 8.1.1 Frenkel defects

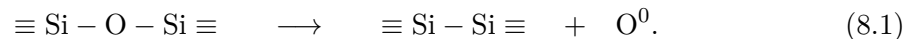
The decomposition of an Si-O-Si bond into an oxygen vacancy and interstitial oxygen species is an inherent defect process in glassy SiO<sub>2</sub>, analogous to the creation of vacancy-interstitial pairs in crystalline materials. In an amorphous material, this is referred to as the “Frenkel defect process”. When fused silica is irradiated with vacuum-UV light or electron beams, oxygen is known to be emitted from its surfaces. However, the spectroscopic signatures of the interstitial oxygen atom are not well-established. Among the different types of Frenkel defects that exist, the following can be highlighted (Fig. 8.2 b):

- **Oxygen vacancy (Si-Si bond):** The Si-Si bond (oxygen deficient center I, ODC(I)) is the most prevalent oxygen-deficiency related defect in SiO<sub>2</sub>. It exhibits diamagnetism and is identified by a strong optical absorption band at 7.6 eV. Neutron beam irradiation

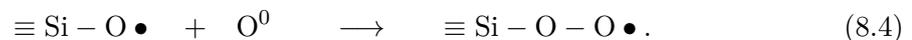
### 8.1. Point defects in SiO<sub>2</sub> glass

and  $\gamma$ -ray exposure trigger the appearance of the 7.6 eV band in both amorphous-SiO<sub>2</sub> and crystalline-SiO<sub>2</sub>, suggesting that the geometry of the Si-Si bond is unaffected by the structural disorder that distinguishes amorphous- and crystalline-SiO<sub>2</sub>. This indicates that a robust Si-Si bond is formed at the vacancy site of O, leading to a significant atomic displacement around it and preserving the distance between Si atoms.

The Frenkel process in amorphous SiO<sub>2</sub> primarily produces interstitial O<sup>0</sup> (oxygen atom) as its intermediate product:



- **Peroxy linkage ( $\equiv \text{Si-O-O-Si}$  bond):** interstitial O<sup>0</sup> is readily incorporated into the amorphous SiO<sub>2</sub> network to form an Si-O-O-Si bond (peroxy linkage, POL). Although POL is anticipated to exhibit a faint optical absorption band at 7.1 eV, there is a lack of knowledge regarding other spectroscopic markers of interstitial O<sup>0</sup>.
- **Interstitial oxygen molecule O<sub>2</sub>:** At room temperature, O<sup>0</sup> in the form of POL is expected to be immobile, but it becomes mobile at  $\geq 200$  °C and transforms into interstitial O<sub>2</sub> (reaction 8.2), NBOHC (reaction 8.3), and peroxy radical (POR) (reaction 8.4):



As previously stated, glassy SiO<sub>2</sub> is a low-density oxide that possesses a significant number of interstices capable of accommodating small molecules. Within these interstices, interstitial O<sub>2</sub> is dissolved and considered the most stable form of excess oxygen species in amorphous SiO<sub>2</sub>. This species is generated as a significant secondary product of the Frenkel process through the dimerisation of interstitial O<sup>0</sup>, which is produced via the mechanism described in reaction 8.1. At or below room temperature, interstitial O<sub>2</sub> exhibits minimal mobility and remains almost immobile. The detection of interstitial O<sub>2</sub> within glassy SiO<sub>2</sub> is achieved using optical absorption, Raman, and photoluminescence (PL) spectroscopies, which rely on the vibronic and electronic transitions in O<sub>2</sub>.

- **Interstitial ozone molecule O<sub>3</sub>:** The formation of interstitial O<sub>3</sub> occurs as a result of the reaction between interstitial O<sub>2</sub> and O<sup>0</sup>. Identification of interstitial O<sub>3</sub> is based on the optical absorption at 4.8 eV and IR phosphorescence of interstitial O<sub>2</sub>, which is created in an excited state due to UV photolysis of interstitial O<sub>3</sub>. Thermal annealing at  $\geq 200$  °C causes interstitial O<sub>3</sub> to decompose quickly.

#### 8.1.2 Dangling-bond defects

Dangling-bond defects of the type depicted in Fig. 8.2 **c** pose the greatest challenge for optical applications of silica. The optical absorption spectrum of irradiated silica is typically dominated by the presence of both dangling oxygen (NBOHC) and silicon (E'-centre) bonds. These point defects can be induced by different types of irradiation, including neutrons, ions, electrons, X-rays,  $\gamma$ -rays, and the most significant for this work, laser photons. The creation of defects

is primarily driven by two mechanisms: elastic collision (direct transfer of kinetic energy of irradiating particles) and electronic excitation (ionisation followed by the decay of excited states).

During the process of electronic excitation due to ultrafast laser irradiation, band-to-band excitation is a critical step that leads to the generation of electron-hole pairs and excitons. In  $\text{SiO}_2$ , the strong electron-lattice interaction readily localises these holes and excitons, resulting in self-trapping. The formation of self-trapped excitons (STE) is extremely fast in  $\text{SiO}_2$ , taking only around 150 fs.

The decay of STEs produces a photoluminescence band at around 2.7 eV – much smaller than energy necessary for band-to-band excitation ( $\sim 9$  eV). This shift of the PL band indicates that there is a significant lattice relaxation around the STEs. This localisation of excited energy and accompanying lattice distortion is a key factor in defect formation in  $\text{SiO}_2$ . The transient absorption of STEs resembles the sum of the optical absorption bands of dangling bond pairs (E'-centre and NBOHC), suggesting the transient formation of these defects.

The E'-centre is the most extensively investigated defect in  $\text{SiO}_2$ , with over 10 different variants discovered. The vast majority of E'-centres share a common characteristic of having a dangling Si bond. This type of defect exhibits a prominent absorption band at 5.8 eV. On the other hand, the absorption spectrum in the visible-to-near-UV regions is dominated by the oxygen dangling bond, NBOHC, with their absorption bands at 2.0 eV and 4.8 eV. These defects are present on the surfaces of silica and can be transformed into surface E'-centres, or peroxy radicals ( $\equiv \text{SiOO}\bullet$ ) by adding an interstitial  $\text{O}^0$  atom.

Although most STEs decay without forming permanent defects, they can be converted to stable defects when formed at heavily distorted sites in the amorphous  $\text{SiO}_2$  network, such as strained Si–O–Si bonds. Consequently, as detailed before, it seems that these point defects lead to a densification of the irradiated material. Femtosecond laser pulses have enough power to induce rapid changes in density and refractive index, even by a single pulse.

## 8.2 Etching mechanisms in $\text{SiO}_2$ glass

Ultrafast laser assisted etching is a widely known manufacturing technique for applications including integrated optics, photonics, and microfluidics. A focused laser beam of short pulses (fs-regime) generates different material modifications depending on –but not only– the pulse energy, pulse width, repetition rates and writing speed [6]. In fused silica, the material modifications can be achieved by solely varying the pulse energy ( $E_p$ ) and they include tiny isotropic refractive index variation (Type I), birefringence (Type II), or voids (Type III) [6, 7]. It is worth noting that in 2020, Sakakura *et al.* published a work on a new type of birefringent modification (referred to as type X) in silica glass, which allows for optical transmission rates of over 99% [8]. Birefringence is highly desirable for controlling the optical properties of the materials at the nm scale. In these cases, such modifications result in self-ordered polarisation-dependent sub-wavelength nanogratings (NGs) [9, 10], formed by nanoporous layers [11]. Controlled NGs have been demonstrated to produce optical elements, *e.g.*, polarisers, nanofluidic channels and nanocapillaries, and have been employed for 3D optical data storage [8, 12–15]. Furthermore, Type II alterations combined with chemical etching enable the fabrication of 3D optical and microfluidic components, or the so-called lab-on-chip and lab-on-fibre devices, featuring high as-

pect ratios and surface qualities. Hence, the 3D fabrication of microfluidic and photonic systems with the capability to build multifunctional platforms have been developed [16–20].

Traditionally, hydrofluoric acid (HF) has been employed as etching solutions [12], but potassium hydroxide (KOH) started to be used a few years ago [21–23]. Alternative solutions were sought to reduce the use of HF, which is one of the most hazardous acids to handle. Although operator safety is increased, KOH, like all alkali metal hydroxides, remains highly corrosive and hazardous when used at high concentrations ( $>5$  mol/L), as in KOH-based ULAE works. Recently, a couple of recent works used sodium hydroxide (NaOH) in fused silica, showing promising high chemical etching rates (ERs) in the laser-affected-zone (LAZ) and lower ERs in pristine material, thus increasing the aspect ratio of the technique [23]. Additionally, not only is the risk reduced for the operator during handling, but the environmental impact also drops drastically, as it has been used at really low concentrations ( $<2$  mol/L).

### 8.2.1 Nanograting–driven etching

It was with the discovery of Type II birefringent periodic nanostructures, *i.e.*, NGs, in 2003 by Shimotsuma *et al.* [10], and their application by Bellouard (2004) [24], and Hnavotsky (2005) [25] to achieve notably high etching selectivity, that ULAE became a highly precise manufacturing technique in multiple fields of photonics. However, fused silica must be processed with a polarisation linear and perpendicular to the writing direction due to the highly anisotropy of the NGs. This is a NG-driven etching process.

As described by Lancry *et al.* in 2013 [11], Type II modifications exhibit strong form birefringence ( $10^{-2}$ ), attributed to the presence of nanostructures known as nanogratings (see Fig. 8.3 **a-b**). Nanogratings are composed of nanoplanes with a sub-wavelength period around  $\lambda/2n$ , which are porous (see Fig. 8.3 **c**) and have an average index lower than typical silica ( $\Delta n \approx -0.20$ ). The formation of nanogratings is explained as a result of rapid decomposition of the glass under localised, high-intensity femtosecond laser radiation, where non-linear, multiphoton-induced photoionisation generates plasma. Due to rapid relaxation, recombination is prevented, and dissociated atomic oxygen instead combines with each other to form molecular oxygen, as observed using Raman microscopy. Some of the molecular oxygen dissolves in the condensed glass, while the remainder becomes trapped within nanovoids. Chemical recombination can only occur at temperatures of 1200 °C for extended periods. These porous nanoplanes lead to densification of the region between them.

The mechanism underlying the etching rate in nanogratings is not fully understood to this day. It is known, as stated above, that the etching is polarisation-dependent, meaning that there is chemical selectivity only when the polarisation direction is linear and perpendicular to the etching direction, ensuring that the nanogratings are aligned parallel to the subsequent microchannel [24, 25]. What is it that allows the NG to increase the chemical selectivity of the processed area by up to a factor of  $\sim 1,000$ ?

Several existing works in the literature state the following. By acknowledging that the LAZ is composed of porous material in the nanogratings, the formation of each nanopore would induce the creation of compressively stressed regions surrounding them. If the stress reaches a sufficiently high level, it would locally result in a mechanical densification [26]. The stress also contributes to variations in the bond angles within the SiO<sub>2</sub> matrix. In fact, the decrease

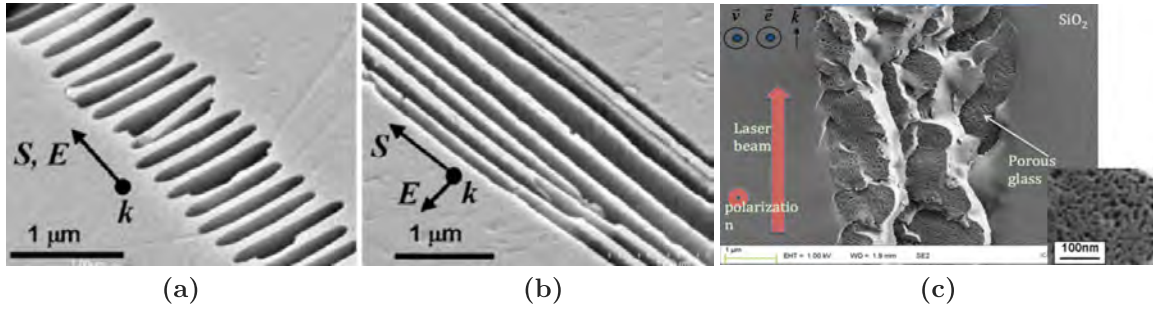


**Figure 8.3.** SEM images of nanograting structures formed along the writing direction with laser polarisation (a) parallel  $\parallel$  and (b) perpendicular  $\perp$  to the writing direction. The samples are etched for 20 min in 0.5% HF. Reprinted with permission from [12]. (c) Field-emission gun SEM images of the porous region of the nanoplanes, with the polarisation aligned parallel to the direction of writing. Reprinted with permission from [11].

in the bridging angle in densified silica enhances the reactivity of oxygen due to the distorted configuration of the oxygen's valence electrons of oxygen (in terms of Lewis base), which explains the faster etching rate in the LAZ [27]. Similarly, in line with the described findings, Tomozawa *et al.* discovered that a higher rate is linked to an increased fictive temperature ( $T_f$ ) of the glass, and consequently, to a higher density [28]. Another possible explanation is the presence of a Si-rich structure in the laser-irradiated area [29], particularly when alkali alkaline solutions such as KOH or NaOH are used.

### 8.2.2 Non nanograting-driven etching

There are also certain studies where relatively high etching rates have been achieved, with a certain level of polarisation independence. However, this has been achieved through very high pulse energies ( $\sim \mu\text{J}$ ), pulse durations in the ps range, or through pulse shaping. In all these scenarios, there seems to be the existence of disordered nanostructures, unlike the self-ordered nanogratings discussed in the previous section which offered a notably high etching rate.

In the first of these cases, Yu *et al.* demonstrate that, for a pulse energy greater than  $2.5 \mu\text{J}$ , an etching rate is achieved with relative polarisation independence (albeit at a rate as low as  $90 \mu\text{m/h}$ ) [30]. This independence is achieved at the expense of a notable drop in the etching rate, due primarily to the transition that occurs from the presence of nanogratings ( $< 1 \mu\text{J}$ ) to completely disordered nanostructures (see Fig. 8.4 a).

Similarly, Li *et al.* also observed polarisation independence, but this was achieved by using pulse durations in the ps range ( $\sim 500 \mu\text{m/h}$  with  $\tau = 10 \text{ ps}$ ) [31]. Randomly oriented nanocracks are reported in this regime (see Fig. 8.4 b). However, the physical mechanism behind the transition from self-organised nanogratings to chaotic nanocracks is not completely understood.

Finally, Yan *et al.* demonstrate etching rates of  $500 \mu\text{m/h}$  with some polarisation independence by introducing temporally shaped pulse trains [32]. Pulse shaping involves pulse trains with double subpulses (pulse delay  $\Delta t > 1 \text{ ps}$ ). Again, it seems that disordered but interconnected nanostructures generated by the pulse train irradiation is what lies behind this regime (see Fig. 8.4 c).

As has been observed, ULAE does have some areas that need improvement. NG-driven

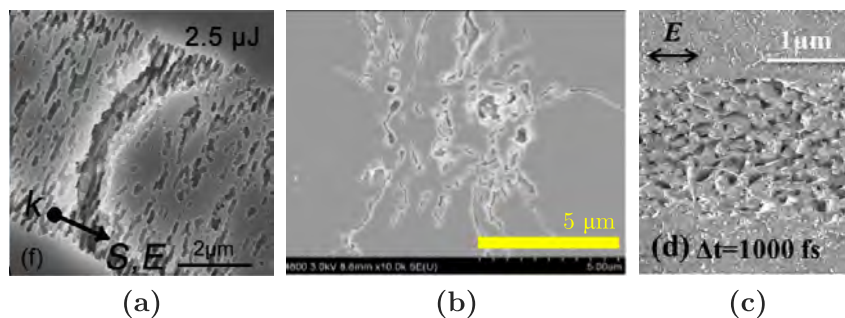


**Figure 8.4.** SEM images of the nanostructures that have emerged within the zones that underwent fs laser irradiation for (a) pulse energy of 1  $\mu\text{J}$  and parallel polarisation, (b) pulse duration of 10 ps and an energy of 8  $\mu\text{J}$  under circular polarisation conditions, and (c) when using a pulse delay of  $\Delta t = 1000$  fs and parallel polarisation. Images are reprinted from [30], [31], and [32], respectively.

etching has allowed the manufacturing of optofluidic devices to expand in less than 20 years in a repetitive and highly precise manner. However, it has the major drawback of needing to control the polarisation of the laser source during inscription. As a result, dynamic polarisation control is necessary [22], which is challenging to achieve for many 3D geometries or non-planar surfaces. From a technological perspective, eliminating polarisation dependence is crucial for simplifying the systems and reducing both processing and etching times. Likewise, the necessity of using a large number of pulses per  $\mu\text{m}$  for nanograting generation leads to low processing speeds.

On the other hand, as stated above, polarisation insensitivity has been reported for picosecond pulse widths and significantly higher pulse energies than those typically used for Type II modifications ( $\mu\text{J}$ -range with  $\text{NA}=0.45$ ) [31]. In fact, such polarisation dependence has been shown to partially diminish with  $E_p$  [13]. However, higher  $E_p$  and longer pulse durations imply collateral damage that negatively affects the aspect ratio, increases roughness, reduces etching rates (ERs), and loses processing precision [7, 12, 24].

Is it possible to achieve polarisation independence in the femtosecond-laser regime using lower pulse energies or simpler strategies? It is widely known that fewer pulses (or lower fluence) reduce anisotropy. But is etching still possible? In this year, 2023, the first two studies achieving polarisation-independent etching using fewer pulses have been reported.

The first of these, carried out by Yao *et al.* [33], uses HF as the chemical agent in etching. As for the fabrication parameters, a laser operating at 780 nm and 120 fs is used, with pulses focused by a 0.55 NA lens. The PRR is kept fixed at 1 kHz, and the minimum pulse energy used (always seeking to operate with the lowest possible pulse energy) is 500 nJ. By varying the speed, they manage to deposit between 17 and 1033 pulses/ $\mu\text{m}$ . The results reveal an etching rate of 150  $\mu\text{m}/\text{h}$  in the low pulse regime, and a notably superior aspect ratio ( $\sim 40$ ) compared to a higher pulse overlapping.

The second study, in this case, uses KOH and NaOH and is detailed in this chapter [1].

### 8.3 Experimental setup and protocol

In this chapter, it is performed a more comprehensive study that enabled the identification of a laser inscription regime in which high ERs can be maintained independently of light polari-

sation and utilising low-energy femtosecond pulses (minimum  $E_p=240$  nJ). NaOH is employed as etching solution to evaluate its performance in ULAE and to expand the scarce literature regarding its use. The laser source is a commercial femtosecond fibre laser chirped pulse amplifier from Calmar, which emits 370 fs-pulses at 1030 nm. The PRR varied from 10 kHz to 480 kHz. The beam is focused onto the sample by an aspheric lens with NA=0.4 (A110TM-B, Thorlabs). The sample is placed on a nano-resolution XYZ motor stage from Aerotech. A CCD camera (DMK 31AG03 Imaging Source) is used to visualise the focused beam on the sample. Three polarisations referenced to the beam writing direction were tested: transversal  $\perp$ , circular  $\odot$  and longitudinal  $\parallel$ . The light polarisation was changed by controlling dynamically half and quarter waveplates (Fig. 8.5).

Pulse energies in a wide range (150 nJ–2  $\mu$ J) were tested (up to 600 nJ are shown), covering net fluences (NF) from tenths to hundreds  $\text{J}\cdot\text{mm}^{-2}$ . The NF is defined as [34, 35]:

$$\text{NF} = \frac{4 \cdot E_p \cdot \text{PRR}}{\pi \cdot \omega \cdot \nu}, \quad (8.5)$$

where  $\omega = 2w_0$  is the beam diameter (1.98  $\mu\text{m}$ ), and  $\nu$  the inscription speed. The number of pulses per  $\mu\text{m}$  ( $N$ ) is defined as  $N = \text{PRR}/\nu$ . To achieve a wide range of  $N$ ,  $\nu$  was adjusted accordingly. The ERs were estimated by measuring the length of a series of microchannels. The channels were inscribed with a single laser scan (same writing direction) in fused silica samples (Spectrosil  $\text{\textcircled{R}}$  2000 from UQG Optics). The channels are separated by 20  $\mu\text{m}$  (otherwise stated) and inscribed at a depth of 70  $\mu\text{m}$ . The single scan covers the entire length of the samples (10 $\times$ 10 $\times$ 1 mm), starting/ending sufficiently away from the edges to avoid any undesirable acceleration/deceleration ramps of the stage. After the inscription, the sample edges were polished and etched for four hours in a 5 wt% NaOH solution at  $85\pm 2$   $^\circ\text{C}$  and magnetically stirred. Then, the samples were heavily rinsed with distilled water.

To confirm the microchannel fabrication (bottom image of Fig. 8.6), one sample was soaked in a solution of isopropyl alcohol and Rhodamine 6G (R6G) dye after etching for 30 minutes [14]. The fluorescence intensity of R6G was detected with a confocal microscope (Nikon AR1) using laser excitation of 561 nm and spectral detection 570–620 nm (top image of Fig. 8.6). To measure the induced birefringence, we obtain optical images of the samples placed between two crossed

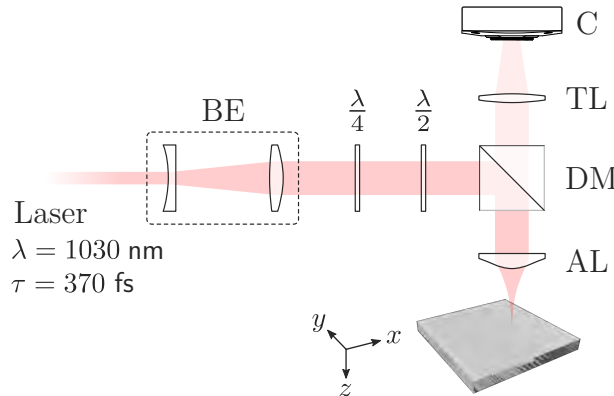


**Figure 8.5.** Illustration of optical setup used for ultrafast laser inscription (Key: BE – beam expander (2 $\times$ ), C – CCD camera, TL – tube lens, DM – dichroic mirror, AL – 0.4 NA aspheric lens). Adapted from [1].

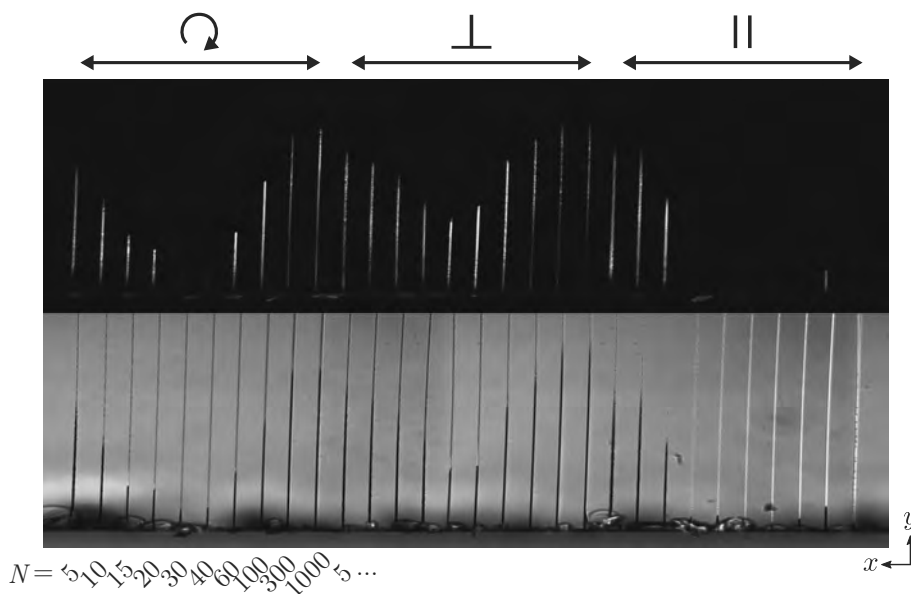


**Figure 8.6.** (top) Fluorescence intensity of the R6G within the microchannels for  $\odot$ ,  $\perp$  and  $\parallel$  polarisations for several pulses,  $N$ , (bottom) and corresponding optical microscope image. The images are not to scale.  $E_p=600$  nJ and PRR=120 kHz. Adapted from [1].

polarisers. The intensity is related to certain degree of birefringence, whereas dark regions indicate isotropic material not affected by the laser [9, 13, 36].

## 8.4 Etching rate results

Figure 8.7 shows the ERs and ER ratios as a function of  $N$  (bottom axes) and  $NF$  (top axes) for  $\perp$ ,  $\odot$  and  $\parallel$  polarisations and two pulse energies: 300 nJ and 600 nJ. PRR is set to 120 kHz. Polarisation insensitivity is found at a low number of pulses ( $N < 15 \mu\text{m}^{-1}$ ), exhibiting high ERs ( $\sim 300\text{--}350 \mu\text{m}\cdot\text{h}^{-1}$ ). The ER reduces at a moderate number of pulses ( $20 < N < 50 \mu\text{m}^{-1}$ ), more than three times for  $\odot$  and  $\parallel$  cases, whereas  $\perp$  decreases only for 600 nJ by 20%. At  $N > 100 \mu\text{m}^{-1}$ , the ERs recover for  $\odot$  and  $\perp$ , reaching the maximum values measured (approximately 15-25% higher than those at the insensitive region). In contrast, the ERs for  $\parallel$  remain low, as expected. Figure 8.8 includes results associated with a more comprehensive study, specifically for PRR values of 10 kHz, 120 kHz, 240 kHz, and 480 kHz, and with pulse energies for each PRR of 180 nJ, 210 nJ, 240 nJ, 270 nJ, 300 nJ, and 600 nJ.

### 8.4.1 Definition of $N$ -dependent regimes

According to Fig. 8.7, we define three regimes, namely low ( $N < 15 \mu\text{m}^{-1}$ ), moderate ( $15 \leq N < 100 \mu\text{m}^{-1}$ ) and high number of pulses ( $N \geq 100 \mu\text{m}^{-1}$ ). In general, upon laser irradiation and prior to any etching, the material undergoes several structural changes in these regimes. Besides point defects generation [5, 13, 37–39], the material experiences induced stress resulting in densification [26, 40, 41]. As the pulse-to-pulse distance reduces, glass decomposition occurs [11] that ultimately yields a net volume expansion [42]; and self-organised nanostructures emerge with an orientation (and order) strongly dependent on the light polarisation.

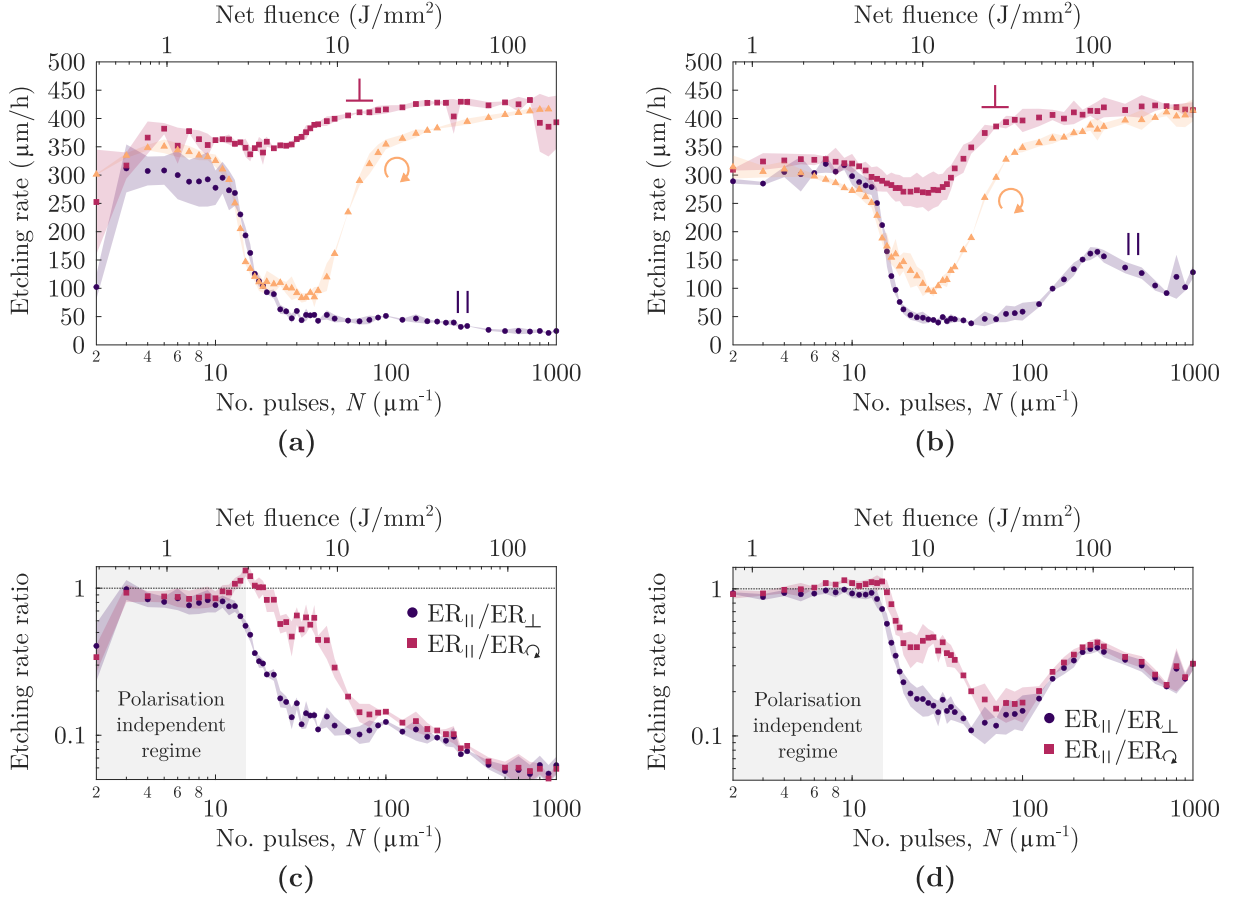


**Figure 8.7.** (a-b) ERs for  $\odot$ ,  $\parallel$  and  $\perp$  polarisation for (a)  $E_p=300$  nJ and (b) 600 nJ. The etching time is 4 hours, and the PRR is 120 kHz. (c-d) ER ratio of  $\perp$  and  $\odot$  polarisation with respect to  $\parallel$  polarisation for (c)  $E_p=300$  nJ and (d) 600 nJ. The region where the ER is independent of polarisation is highlighted. The mean values are shown whereas the shaded regions are the standard deviations of two measurements. Adapted from [1].

At this point, two main questions arise:

- What are the implications of the structural changes on the ERs shown in Fig. 8.7?
- What is the relationship of such changes with the polarisation insensitivity?

We attempt to answer these questions by describing our interpretation of the three regimes identified.

#### 8.4.2 Low $N$ regime ( $N < 15 \mu\text{m}^{-1}$ )

First, at  $N < 15 \mu\text{m}^{-1}$ , the material undergoes densification and point defects are generated. The point defects include E'-centres, NBOHC, and divalent silicon with oxygen deficiency centres, *i.e.*, SiODC (II) [5, 13, 37–39]. The few pulses limit the defects incubation process [43] (null formation of nanogratings, see Fig. 8.9 a), being distributed within a narrow region with certain orientation, but low anisotropic degree as will be shown below [38]. Defects can drive the ERs [23], and their low induced-anisotropy could be behind the high ER at the polarisation insensitive region. However, it should be noted that this relation has not been confirmed, and there may be other factors contributing to this phenomenon. The low-level material anisotropy is

### 8.4. Etching rate results

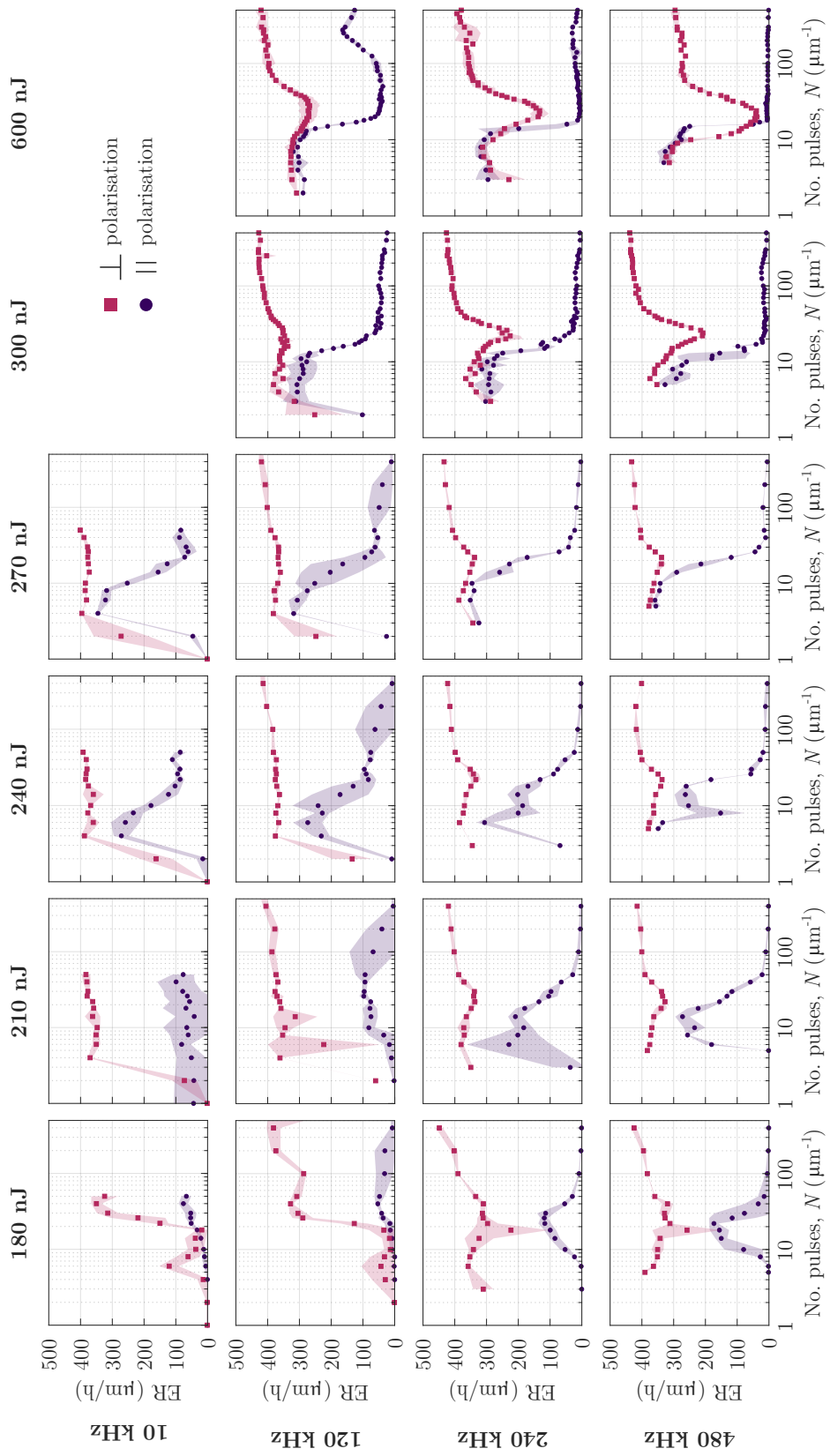


**Figure 8.8.** ERs for transversal  $\perp$  and longitudinal  $\parallel$  polarisation for several pulse repetition rates (PRRs) and different pulse energies ( $E_p$ ) as a function of the number of pulses ( $N$ ). Adapted from [1].

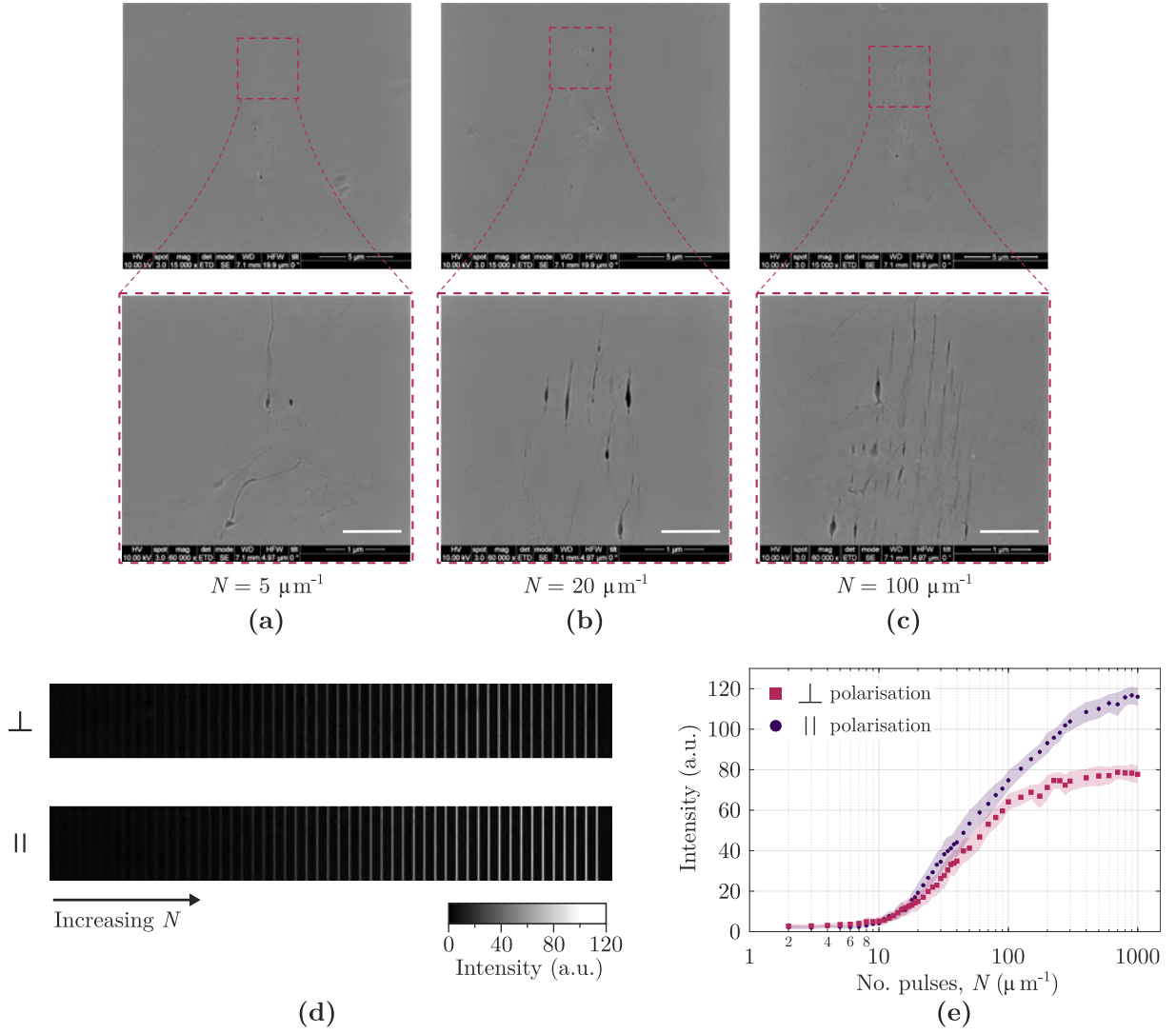


**Figure 8.9.** (a-c) SEM images of the cross section of laser affected zone using  $\perp$  polarisation at 600 nJ and 120 kHz for pulses (a)  $N=5 \mu\text{m}^{-1}$ , (b)  $N=20 \mu\text{m}^{-1}$  (c) and  $N=100 \mu\text{m}^{-1}$ . Red squares indicate the region shown in the bottom row images with higher magnification. After inscription, the sample was polished and etched for 2 minutes in NaOH solution (5 wt%). Scale bars in (a-c) are 1  $\mu\text{m}$ . (d) Optical images of the microchannels placed between two crossed polarisers and illuminated with  $660 \pm 10$  nm light (filtered halogen lamp). (e) Maximum intensity measured at different number of pulses, whose values are averaged from 150 different points along the laser affected zone whereas the shaded regions represent the standard deviations. The samples were positioned at an angle (x-y) where the maximum birefringence intensity was measured ( $45^\circ$ ). Each symbol in (d) corresponds to a fringe (microchannel) in (e). The microchannels are separated by 20  $\mu\text{m}$ . The pulse energy is 600 nJ at 120 kHz. Note that reducing the pulses exhibits a less homogeneous birefringence along the laser inscription. The higher intensity at high number of pulses for the longitudinal case indicates the LAZ contains higher domains with material modification, possibly arising from a more homogeneous and ordered damage because the nanogratings length is restricted to the beam waist. Adapted from [1].

consistent with the slightly lower ER for  $\parallel$  polarisation as compared to  $\perp$  for 300 nJ (Fig. 8.7 a). At  $E_p \geq 600$  nJ (Fig. 8.7 b), the ERs are similar for all cases.

Regarding material densification, it results in decreased angle of Si–O–Si bonds and a higher number of lower order membered rings in the silica network (*e.g.*, 3 and 4) [37]. Lower ordered rings than in an unstrained structure and decreased Si–O–Si angle have been correlated to

#### 8.4. Etching rate results

higher ERs (in HF) [26, 28]. However, it has been recently shown that the etching mechanisms may differ depending on the etching solution, *i.e.* NaOH or KOH, as compared to HF, for which the etching of KOH or NaOH may be less affected by densification [23]. We confirm similar etching rates and trends with  $N$  by using KOH (Fig. 8.10), suggesting that the physical mechanisms behind the etching rates are the same for NaOH and KOH. On the other hand, three-membered rings are precursors of oxygen hole and E'-centres that could also promote etching, as previously mentioned [44]. Thus, with the results described here it appears plausible to expect the polarisation insensitivity is mainly due to a benign anisotropy degree of point defects and, to a lesser extent induced densification. Future investigations could shed more light on the interplay between specific point defects, densification and their contribution to the ER.

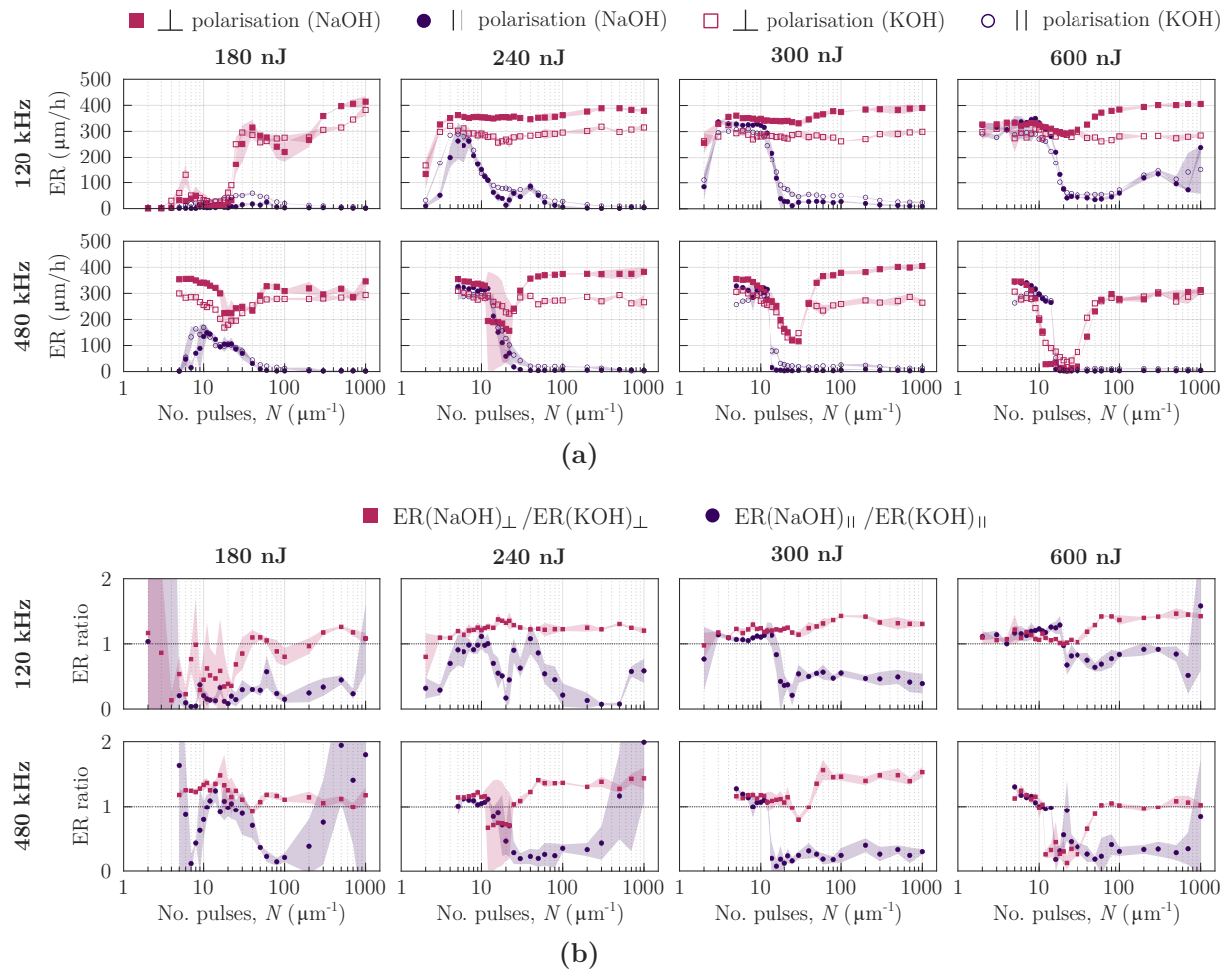


**Figure 8.10.** Comparison of (a) ERs and (b) ER ratios using two different etching solutions (NaOH and KOH) for different pulse energies and PRRs. Both etching solutions yield similar ERs and trends with the number of pulses, hence the mechanisms behind etching are likely the same. The highest ERs correspond to the nanogratings regime for NaOH and by setting the polarisation perpendicular to the beam writing direction. Note that different samples than those of Fig. 8.8 have been used for NaOH obtaining comparable results. Etching time was four hours for NaOH solution of 5 wt% and KOH of 40 wt%. Adapted from [1].

### 8.4.3 Moderate $N$ regime ( $15 \leq N < 100 \mu\text{m}^{-1}$ )

Now, we turn to the transition regime at a moderate number of pulses, *i.e.*,  $15 \leq N < 100 \mu\text{m}^{-1}$ . In this case, there is a polarisation-sensitive ER. For  $N > 10 \mu\text{m}^{-1}$ , nanopores of nm-size are expected to form in nanolayers [11, 42]. The formation of nanopores has been attributed to glass decomposition, for which defects cause oxygen atoms dissociation from the silica structure [11]. Since the number of nanopores and their orientation increase with  $N$  [11], these regions exhibit higher anisotropy that could hinder (or favour) the ER to a greater or lower extent depending on polarisation ( $\circlearrowleft$  or  $\parallel$ ), being consistent with Fig. 8.7.

All in all, we attribute the drastic drop in the ERs for  $\parallel$  polarisation to an increased material anisotropy degree (see [38]) with the number of pulses [13], as will be further supported below. Indeed, the polarisation contrast between  $\perp$  and  $\parallel$  is not surprising because oriented NGs are partially formed under these conditions [42], as confirmed by SEM measurements in our samples (Fig. 8.9 b). Finally, since the formation of nanopores is not related to the presence of nanogratings [42] that could be slightly developed (especially for  $N < 20 \mu\text{m}^{-1}$ , we speculate the moderate ERs (steepest variation in ERs for  $15 < N < 30 \mu\text{m}^{-1}$ ) are due to a mixed impact from low anisotropic point defects, etching solution penetrating through nanopores to highly reactive densified areas, and the little or null formation of nanostructures.

### 8.4.4 High $N$ regime ( $N > 100 \mu\text{m}^{-1}$ )

At  $N > 100$  pulses per  $\mu\text{m}$ , the complete formation of highly oriented NGs occurs (Fig. 8.9 c) [13, 23]. Once the NGs are fully formed, their orientation determines the ER, being highly diminished for  $\parallel$  polarisation. This polarisation contrast is well-known, and can be explained by an uneven ER between alternate regions with modified and unmodified material ( $\sim 0.5 \mu\text{m}\cdot\text{h}^{-1}$  for NaOH [23]) that dramatically slows down the process [25]. For  $\circlearrowleft$  polarisation, disordered nanostructures are expected to fully develop, enabling ERs comparable to  $\perp$ , as reported in [9, 45].

## 8.5 Discussion about ER and polarisation dependence

Hitherto, we have considered the increasing material anisotropy degree with  $N$  as the main responsible of the different ERs and their polarisation sensitivity; either by point defects or assisted by the influence of nanopores and oriented nanostructures. To support this hypothesis in our samples, we perform polarisation microscopy. We measure a certain level of birefringence for  $\perp$  and  $\parallel$  polarisations from  $N = 10 \mu\text{m}^{-1}$  that rapidly increases until it reaches maximum values for  $N > 100 \mu\text{m}^{-1}$  (Fig. 8.9 d-e). As shown by Richter *et al.* [13], the polarisation contrast intensity of the LAZ increases with the pulse energy and the number of pulses, in agreement with Fig. 8.9 d-e and the interpretation of Fig. 8.7 described above. Indeed, the higher degree of material anisotropy is consistent with a high polarisation contrast in etching rate between  $\parallel$  and  $\perp$  or  $\circlearrowleft$  cases. For instance, at  $N = 1000 \mu\text{m}^{-1}$  and 300 nJ (Fig. 8.7 a), the  $\parallel$  ER is more than ten times lower ( $\sim 25 \mu\text{m}\cdot\text{h}^{-1}$ ) than the  $\perp$  case. Furthermore, the birefringence intensity qualitatively agrees with the polarisation contrast between  $\perp$  and  $\parallel$  at the moderate pulse regime ( $15 \leq N < 100 \mu\text{m}^{-1}$ ).

## 8.5. Discussion about ER and polarisation dependence

We now compare our results with the literature. Few works exist regarding the impact of low number of pulses on the ERs in fused silica, especially using NaOH. In this regard, we note that contrary to Casamenti *et al.* results [23], we find high ERs at few pulses for both,  $\perp$  and  $\parallel$ , and using  $E_p \geq 240$  nJ (up to 2  $\mu$ J tested). Casamenti *et al.* showed high polarisation sensitivity (high and low ERs for  $\perp$  and  $\parallel$  polarisations, respectively) for similar pulse energies. Besides setup construction, the main differences between the conditions used for the inscriptions (equal depth) are the PRR, being 333 kHz for [23], and 120 kHz in our case. The second difference is the pulse width: 270 fs in [23] and 370 fs in our case. These pulse widths are similar; both lie above the threshold to produce self-organised nanostructures [46]. Although the slight difference in the pulse width cannot be discarded, it is reasonable to expect a lower influence from this parameter.

Therefore, to investigate a possible cause that explains the discrepancy, we increased the PRR up to 480 kHz and explored lower  $E_p$  (Fig. 8.8). As can be seen in Fig. 8.11, we find similar traditional polarisation sensitivity for  $N < 10 \mu\text{m}^{-1}$  and for 480 kHz (also for 240 kHz as shown in Fig. 8.8), as in [23], but using slightly lower  $E_p = 180$  nJ. There is a high polarisation contrast for low  $N$  (high ERs for  $\perp$ ), which decreases at moderate  $N$  to recover at a high  $N$  (NGs-regime). Hence, the  $E_p$ - and NF-threshold may promote a sufficient incubation of defects that enables high ERs at a few pulses regime.

In turn, increasing the PRR approaches to regimes in which thermal accumulation effects could play a role. Thermal accumulation effects depend mainly on the PRR,  $E_p$ , and  $\nu$  [47]. Indeed, we found higher width of the LAZ for 480 kHz than that of 120 kHz, indicating extended damage originating likely from thermal accumulation effects. Hence, the reconciliation of our results with those of Casamenti *et al.* [23] (only at a few pulses  $N < 10 \mu\text{m}^{-1}$ ) involves the influence of thermal accumulation effects and defects generation. It is worth highlighting that the experiments at higher PRRs show the impact of this parameter on the ERs at the transition regime ( $15 < N < 100 \mu\text{m}^{-1}$ ), being stronger with higher  $E_p$  for the  $\perp$  case. For instance, ERs for 300 nJ and 600 nJ exhibit a steeper drop with PRR increase (see Fig. 8.8). High  $E_p$  in combination with thermal accumulation do not promote polarisation-dependent etching at the

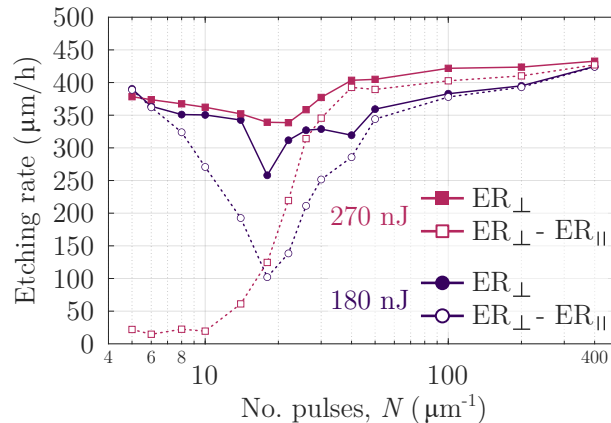


**Figure 8.11.** Polarisation etching rate contrast calculated from the difference between  $\perp$  and  $\parallel$  average etching rates at two different  $E_p$ . Solid lines depict the etching rates for  $\perp$ , while dashed lines show the etching rate contrast. Lower  $E_p$  (180 nJ) and higher PRRs (240 kHz and 480 kHz tested) than the one used for polarisation independence (120 kHz and  $E_p \geq 240$  nJ) retrieve traditional high polarisation contrast at a few pulses. Adapted from [1].

transition regime, requiring an increased  $N$  to recover it [9].

Finally, to demonstrate the capabilities of a few pulses yielding high ERs independent of polarisation, we inscribed curved and square-wave microchannels (Fig. 8.12 a and Fig. 8.12 b). The final penetration of the etching after 4 hours is shown by the solid circles. Both, curved and square-wave microchannels show that  $N = 8 \mu\text{m}^{-1}$  achieves polarisation-independence with an etching rate  $\sim 300 \mu\text{m}\cdot\text{h}^{-1}$ . The polarisation sensitive regime at  $N = 1000 \mu\text{m}^{-1}$  for  $\parallel$  and  $\perp$  polarisations, respectively, exhibit significantly lower ER rates ( $\text{ER} \sim 10 - 35 \mu\text{m}\cdot\text{h}^{-1}$ ), as expected. We further test the polarisation insensitivity along the volume of the fused silica plate by inscribing a mm-size regular compound stellated octahedron (Fig. 8.13). Manufacturing a stellated octahedron within reasonable times is highly complex because it contains twenty-four facets at  $45^\circ$ , the most challenging angle for polarisation-dependent 3D processing. Less than 2.5 hours of etching enabled the detachment of the stellated octahedron from the substrate, consistent with the ERs obtained at the polarisation-independent regime.

## 8.6 Etching mechanisms in polarisation-independent regime

In the regime of interest for this work, characterised by a low number of pulses ( $N < 15 \mu\text{m}^{-1}$ ), the material undergoes several modifications, including densification, formation of defect sites,

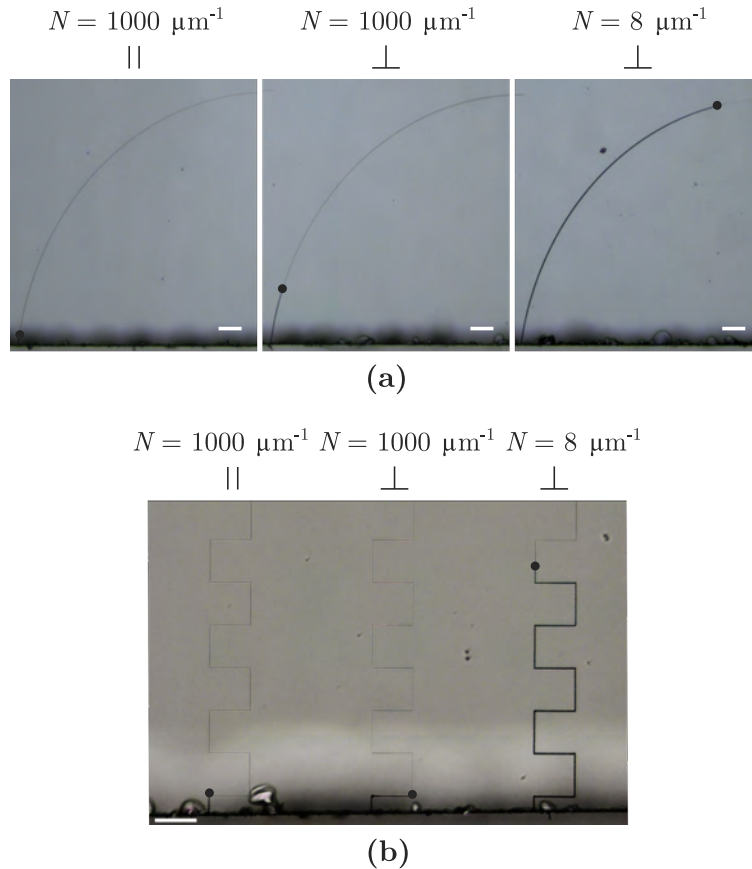


**Figure 8.12.** (a) Curved and (b) square-wave microchannels inscribed at a depth of  $70 \mu\text{m}$ . Solid circles show the final penetration of the etching after 4 hours in a NaOH solution (5 wt%). Scale bars are  $100 \mu\text{m}$ . Adapted from [1].

## 8.6. Etching mechanisms in polarisation-independent regime

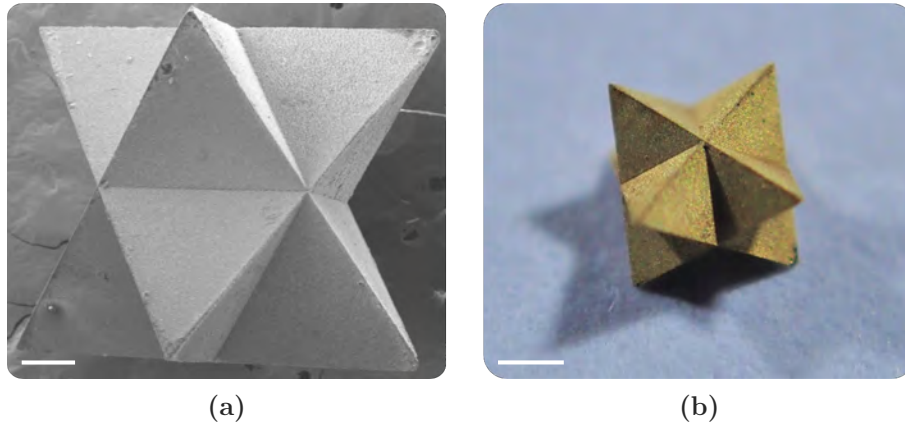


**Figure 8.13.** (a) SEM image and (b) photograph of the stellated octahedron. Scale bars are 200  $\mu\text{m}$  for SEM picture and 500  $\mu\text{m}$  for the photograph. Adapted from [1].

and morphological changes such as the appearance of nanopores. Widespread literature exists regarding the impact of fs laser irradiation and this kind of modifications. Nevertheless, there is no attempt to link the subtle material modifications (in the non-nanograting regime) and the high etching rates in this polarisation-independent regime. Besides, the mechanisms behind high etching rates at a few pulses are not understood, with some literature pointing to the important role of matrix defects [23, 48]. In this section, some preliminary results are included to provide insights into the mechanisms behind the high etching rates in this regime. Absorbance, photoluminescence, and Raman spectroscopy are performed in laser-processed fused silica substrates after thermal annealing treatments. Three annealing temperatures were chosen: 300°C, 600°C and 900°C, such that electronic defects could be annealed ( $> 500^\circ\text{C}$ ) and the structural modifications (*e.g.*, densification) at the laser-affected-zone could be reversed ( $> 900^\circ\text{C}$ ). In this manner, the objective is to connect the high etching rates with specific material modifications caused by the laser.

Photoluminescence and absorbance (Fig. 8.14) signatures associated with electronic defects (*e.g.*, the non-bridging oxygen hole centres with peak at 248 nm) vanish at 600°C, consistent with

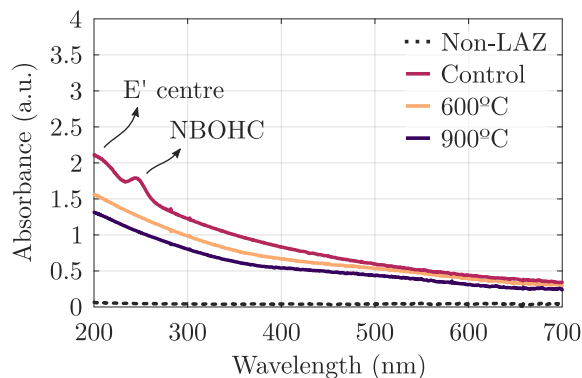


**Figure 8.14.** Resultant absorbance present in pristine fused silica, as well as in a modified substrate processed at 600 nJ and 120 kHz by raster scanning (1  $\mu\text{m}$  spacing) fs laser pulses at high speed ( $N = 5 \mu\text{m}^{-1}$ ) and using  $\parallel$  polarisation. The results shown are presented without annealing, and after annealings of 2 hours at 600°C and 900°C. A deuterium UV lamp and a high-sensitivity UV spectrometer Maya2000 Pro from OceanOptics are employed.

the literature [49]. In contrast, the etching rates (Fig. 8.15) remain high at 600°C and drastically diminish at 900°C. These findings suggest some matrix defects may not be strongly related to the polarisation-independent high etching rates. Instead, other laser-induced structural changes (reversed after 900°C annealing) could be the key drivers at this regime.

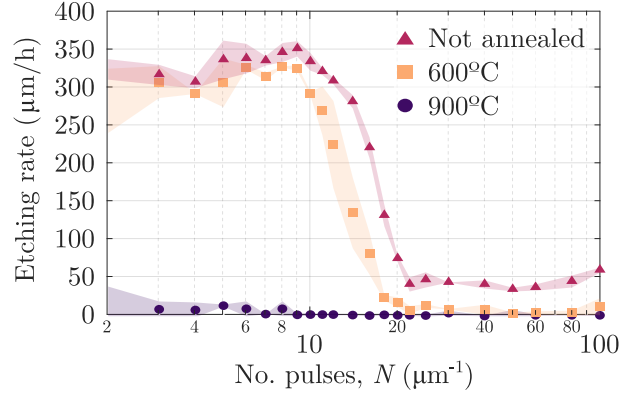


**Figure 8.15.** ERs for  $\parallel$  polarisation at 600 nJ and 120 kHz in modified fused silica substrate with no annealing, and after 2 hours at 600°C and 900°C. Etching of four hours in 5 w% at 85°C is considered. Shadow areas correspond to the standard deviation of two measurements.

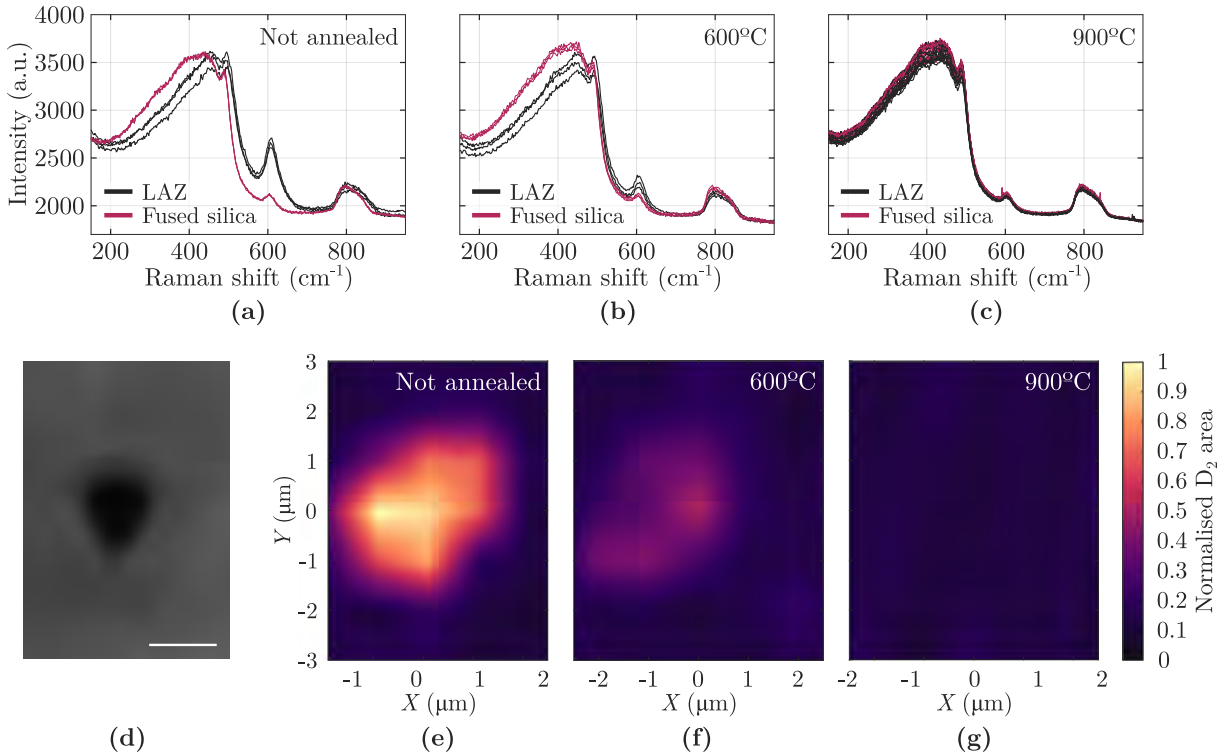


**Figure 8.16.** Raman spectra of the cross-section of LAZ are shown for (a) no annealing, and after annealing for 2 hours at (b) 600°C and (c) 900°C. (d) Microscope image of the LAZ cross-section is provided. Filled contour 2D plots depict the normalised  $D_2$  Raman band area (using a two-point baseline correction algorithm) for the LAZ cross-section under the following conditions: (e) no annealing, and after annealing for 2 hours at (f) 600°C and (g) 900°C. The experimental parameters used are 600 nJ pulse energy, 120 kHz PRR,  $\parallel$  polarisation, and  $N = 5 \mu\text{m}^{-1}$ . The scale bar in **d** is 4  $\mu\text{m}$ . Spectra were acquired using a confocal Raman microscope NRS-4500 (JASCO Inc.) equipped with a 532 nm laser excitation source.

## 8.7. Conclusions

Finally, Raman measurements have been carried out on the cross-section of the modified area for different thermal annealings (600°C and 900°C). The results are shown in Fig. 8.16. It is important to note that the D<sub>2</sub> band (with peak at  $\sim 606 \text{ cm}^{-1}$ ) is significantly increased compared to the pristine silica. This could be attributed to an increase in the number of 3-membered rings as well as a higher number of strained bonds in the silica network, resulting in a reduction in the overall bond angle and, generally, densification of the area. After annealing at 600°C, this densification decreases, and it practically disappears at 900°C, along with the etching. This could suggest as a possible hypothesis that the reason for high etching rates with low-pulse regime (anisotropy structures resulting in polarisation insensitivity) is not so much due to the presence of point defects but primarily due to densification and/or quasi-spherical nanopores precursor to nanogratings with a higher number of pulses.

Although not presented here, ongoing research conducted mainly by Mario Ochoa and Mariela Fernández-Manteca appears to indicate the presence of certain differences in the  $1552 \text{ cm}^{-1}$  band corresponding to O<sub>2</sub>. While it cannot be stated with certainty, this could explain the presence of nanopores in the LAZ. According to the Lewis base, it is the densification of silica that may be behind the etching [27, 50], but this could be caused by laser-induced nanopores, which do not correspond to the simple increase in refractive index characteristic of Type I, as they involve different physical mechanisms [51]. However, this is only a hypothesis that needs to be thoroughly explored to draw conclusions about the mechanism that leads to this regime.

## 8.7 Conclusions

In summary, it is demonstrated the fabrication of complex geometries in fused silica without any requirement of light polarisation control. A wide range of  $E_p$  that achieved high ERs ( $\sim 300 \text{ }\mu\text{m}\cdot\text{h}^{-1}$ ) was employed in the polarisation insensitive regime, including low-energy femtosecond pulses typically employed for Type II (or even Type X) modifications (minimum  $E_p \sim 240 \text{ nJ}$ ). It is also shown that a cumulative effect of the pulses dominates the sensitivity because the transition to a polarisation-sensitive regime occurs at a given number of pulses instead of a given pulse energy or repetition rate within the limits of the investigated ranges. The results presented enable the fabrication of microstructures with high aspect ratios and ERs, avoiding polarisation control.

In the insensitive range, the mechanisms driving the ERs are not determined by NGs (not evident in SEM results as compared to higher  $N$  cases). Instead, a given nanopore density with a low anisotropic degree that results in densification is suggested. The reduction in the bridging angle within densified silica enhances the reactivity of oxygen due to the distorted arrangement of its valence electrons. This deformation of the electron configuration can be understood in the context of the Lewis base. However, further research is needed to better understand the role of densification, nanopore formation, point defects and other mechanisms behind the polarisation-independent high ERs, and their implications on the development of lab-on-chip devices and integrated optics.

## References

- [1] Ochoa, M., Roldán-Varona, P., Algorri, J. F., López-Higuera, J. M., and Rodríguez-Cobo, L., “Polarisation-independent ultrafast laser selective etching processing in fused silica,” *Lab on a Chip*, vol. 23, no. 7, pp. 1752–1757, 2023. DOI: 10.1039/d3lc00052d.
- [2] Ochoa, M., Roldán-Varona, P., Algorri, J. F., López-Higuera, J. M., and Rodríguez-Cobo, L., “Polarisation-independent ultrafast laser selective etching processing in fused silica,” in *Frontiers in Ultrafast Optics: Biomedical, Scientific, and Industrial Applications XXIII*, SPIE, 2023.
- [3] Ochoa, M., Roldán-Varona, P., Fernández-Manteca, M. G., Cobo, A., López-Higuera, J. M., and Rodríguez-Cobo, L., “On the mechanisms enabling polarisation-independent high etching rates in fused silica processed by ultrafast laser selective etching,” in *Progress in Ultrafast Laser Modifications of Materials*, Jun. 2023.
- [4] Ochoa, M., Roldán-Varona, P., Algorri, J. F., López-Higuera, J. M., and Rodríguez-Cobo, L., *Data supporting paper: Polarisation-independent ultrafast laser selective etching processing in fused silica*, 2023. DOI: 10.5281/ZENODO.7129527.
- [5] Skuja, L., Hirano, M., Hosono, H., and Kajihara, K., “Defects in oxide glasses,” *physica status solidi (c)*, vol. 2, no. 1, pp. 15–24, Jan. 2005. DOI: 10.1002/pssc.200460102.
- [6] Eaton, S. M., Cerullo, G., and Osellame, R., “Fundamentals of femtosecond laser modification of bulk dielectrics,” *Topics in Applied Physics*, vol. 123, pp. 3–18, 2012. DOI: 10.1007/978-3-642-23366-1\_1/COVER. [Online]. Available: [https://link.springer.com/chapter/10.1007/978-3-642-23366-1\\_1](https://link.springer.com/chapter/10.1007/978-3-642-23366-1_1).
- [7] Gattass, R. R. and Mazur, E., “Femtosecond laser micromachining in transparent materials,” *Nature Photonics*, vol. 2, no. 4, pp. 219–225, Apr. 2008. DOI: 10.1038/nphoton.2008.47. [Online]. Available: <https://doi.org/10.1038/nphoton.2008.47>.
- [8] Sakakura, M., Lei, Y., Wang, L., Yu, Y.-H., and Kazansky, P. G., “Ultralow-loss geometric phase and polarization shaping by ultrafast laser writing in silica glass,” *Light: Science & Applications*, vol. 9, no. 1, Feb. 2020. DOI: 10.1038/s41377-020-0250-y.
- [9] Taylor, R. S., Hnatovsky, C., Simova, E., Rayner, D. M., Bhardwaj, V. R., and Corkum, P. B., “Femtosecond laser fabrication of nanostructures in silica glass,” *Optics Letters*, vol. 28, no. 12, pp. 1043–1045, Jun. 2003. DOI: 10.1364/ol.28.001043.
- [10] Shimotsuma, Y., Kazansky, P. G., Qiu, J., and Hirao, K., “Self-Organized Nanogratings in Glass Irradiated by Ultrashort Light Pulses,” *Physical Review Letters*, vol. 91, no. 24, p. 247405, Dec. 2003. DOI: 10.1103/physrevlett.91.247405.
- [11] Lancry, M., Poumellec, B., Canning, J., Cook, K., Poulin, J.-C., and Brisset, F., “Ultrafast nanoporous silica formation driven by femtosecond laser irradiation,” *Laser & Photonics Reviews*, vol. 7, no. 6, pp. 953–962, Jul. 2013. DOI: 10.1002/lpor.201300043.
- [12] Hnatovsky, C. *et al.*, “Fabrication of microchannels in glass using focused femtosecond laser radiation and selective chemical etching,” *Applied Physics A*, vol. 84, no. 1-2, pp. 47–61, Apr. 2006. DOI: 10.1007/s00339-006-3590-4.
- [13] Richter, S., Heinrich, M., Döring, S., Tünnermann, A., Nolte, S., and Peschel, U., “Nanogratings in fused silica: Formation, control, and applications,” *Journal of Laser Applications*, vol. 24, no. 4, p. 042008, Sep. 2012. DOI: 10.2351/1.4718561.

## References

- [14] Taylor, R., Hnatovsky, C., and Simova, E., “Applications of femtosecond laser induced self-organized planar nanocracks inside fused silica glass,” *Laser & Photonics Review*, vol. 2, no. 1-2, pp. 26–46, Apr. 2008. DOI: 10.1002/lpor.200710031.
- [15] Wang, H. *et al.*, “100-Layer Error-Free 5D Optical Data Storage by Ultrafast Laser Nanostructuring in Glass,” *Laser & Photonics Reviews*, vol. 16, no. 4, p. 2100563, Jan. 2022. DOI: 10.1002/lpor.202100563.
- [16] Sugioka, K., Cheng, Y., and Midorikawa, K., ““All-in-One” chip fabrication by 3D femtosecond laser microprocessing for biophotonics,” *Journal of Physics: Conference Series*, vol. 59, pp. 533–538, Apr. 2007. DOI: 10.1088/1742-6596/59/1/114.
- [17] Sugioka, K. *et al.*, “Femtosecond laser 3D micromachining: A powerful tool for the fabrication of microfluidic, optofluidic, and electrofluidic devices based on glass,” *Lab on a Chip*, vol. 14, no. 18, pp. 3447–3458, 2014. DOI: 10.1039/c4lc00548a.
- [18] Haque, M., Lee, K. K. C., Ho, S., Fernandes, L. A., and Herman, P. R., “Chemical-assisted femtosecond laser writing of lab-in-fibers,” *Lab on a Chip*, vol. 14, no. 19, pp. 3817–3829, 2014. DOI: 10.1039/c4lc00648h.
- [19] Piacentini, S., Bragheri, F., Corrielli, G., Vázquez, R. M., Paié, P., and Osellame, R., “Advanced photonic and optofluidic devices fabricated in glass via femtosecond laser micromachining [Invited],” *Optical Materials Express*, vol. 12, no. 10, pp. 3930–3945, Sep. 2022. DOI: 10.1364/ome.463715.
- [20] Roldán-Varona, P. *et al.*, “Selective plane illumination optical endomicroscopy with polymer imaging fibers,” *APL Photonics*, vol. 8, no. 1, p. 016103, Jan. 2023. DOI: 10.1063/5.0130486.
- [21] Hermans, M., “Selective, Laser-Induced Etching of Fused Silica at High Scan-Speeds Using KOH,” *Journal of Laser Micro/Nanoengineering*, vol. 9, no. 2, pp. 126–131, Jun. 2014. DOI: 10.2961/jlmm.2014.02.0009.
- [22] Ross, C. A., MacLachlan, D. G., Choudhury, D., and Thomson, R. R., “Optimisation of ultrafast laser assisted etching in fused silica,” *Optics Express*, vol. 26, no. 19, pp. 24343–24356, Sep. 2018. DOI: 10.1364/oe.26.024343. [Online]. Available: <https://doi.org/10.1364/oe.26.024343>.
- [23] Casamenti, E., Pollonghini, S., and Bellouard, Y., “Few pulses femtosecond laser exposure for high efficiency 3D glass micromachining,” *Optics Express*, vol. 29, no. 22, pp. 35054–35066, Oct. 2021. DOI: 10.1364/oe.435163. [Online]. Available: <https://doi.org/10.1364/oe.435163>.
- [24] Bellouard, Y., Said, A., Dugan, M., and Bado, P., “Fabrication of high-aspect ratio, micro-fluidic channels and tunnels using femtosecond laser pulses and chemical etching,” *Optics Express*, vol. 12, no. 10, pp. 2120–2129, 2004. DOI: 10.1364/opex.12.002120.
- [25] Hnatovsky, C., Taylor, R. S., Simova, E., Bhardwaj, V. R., Rayner, D. M., and Corkum, P. B., “Polarization-selective etching in femtosecond laser-assisted microfluidic channel fabrication in fused silica,” *Optics Letters*, vol. 30, no. 14, pp. 1867–1869, Jul. 2005. DOI: 10.1364/ol.30.001867.
- [26] Champion, A. and Bellouard, Y., “Direct volume variation measurements in fused silica specimens exposed to femtosecond laser,” *Optical Materials Express*, vol. 2, no. 6, pp. 789–798, May 2012. DOI: 10.1364/ome.2.000789.

- [27] Marcinkevičius, A. *et al.*, “Femtosecond laser-assisted three-dimensional microfabrication in silica,” *Optics Letters*, vol. 26, no. 5, pp. 277–279, Mar. 2001. DOI: 10.1364/ol.26.000277.
- [28] Agarwal, A. and Tomozawa, M., “Correlation of silica glass properties with the infrared spectra,” *Journal of Non-Crystalline Solids*, vol. 209, no. 1-2, pp. 166–174, Jan. 1997. DOI: 10.1016/s0022-3093(96)00542-x.
- [29] Miura, K., Shimotsuma, Y., Sakakura, M., Kanehira, S., Hamabe, M., and Hirao, K., “Three-dimensional deposition of silicon from silicate glass with dispersed metallic aluminum by a femtosecond laser,” in *SPIE Proceedings*, Voelcker, N. H., Ed., SPIE, Dec. 2006. DOI: 10.1117/12.695925.
- [30] Yu, X. *et al.*, “Tuning etch selectivity of fused silica irradiated by femtosecond laser pulses by controlling polarization of the writing pulses,” *Journal of Applied Physics*, vol. 109, no. 5, p. 053114, Mar. 2011. DOI: 10.1063/1.3555080.
- [31] Li, X. *et al.*, “Polarization-insensitive space-selective etching in fused silica induced by picosecond laser irradiation,” *Applied Surface Science*, vol. 485, pp. 188–193, Aug. 2019. DOI: 10.1016/j.apsusc.2019.04.211.
- [32] Yan, X. *et al.*, “Polarization-independent etching of fused silica based on electrons dynamics control by shaped femtosecond pulse trains for microchannel fabrication,” *Optics Letters*, vol. 39, no. 17, pp. 5240–5243, Aug. 2014. DOI: 10.1364/ol.39.005240.
- [33] Yao, Q. *et al.*, “Polarization-independent microchannel in a high-speed-scan femtosecond laser-assisted etching of fused silica,” *Applied Optics*, vol. 62, no. 2, pp. 291–297, Jan. 2023. DOI: 10.1364/ao.475940.
- [34] Rajesh, S. and Bellouard, Y., “Towards fast femtosecond laser micromachining of glass, effect of deposited energy,” in *Conference on Lasers and Electro-Optics 2010*, OSA, 2010. DOI: 10.1364/cleo.2010.jtud18.
- [35] Rajesh, S. and Bellouard, Y., “Towards fast femtosecond laser micromachining of fused silica: The effect of deposited energy,” *Optics Express*, vol. 18, no. 20, pp. 21490–21497, Sep. 2010. DOI: 10.1364/oe.18.021490.
- [36] Ramirez, L. P. R. *et al.*, “Tuning the structural properties of femtosecond-laser-induced nanogratings,” *Applied Physics A*, vol. 100, no. 1, pp. 1–6, Apr. 2010. DOI: 10.1007/s00339-010-5684-2.
- [37] Chan, J. W., Huser, T., Risbud, S., and Krol, D. M., “Structural changes in fused silica after exposure to focused femtosecond laser pulses,” *Optics Letters*, vol. 26, no. 21, pp. 1726–1728, Nov. 2001. DOI: 10.1364/ol.26.001726.
- [38] Lancry, M., Poumellec, B., Desmarchelier, R., and Bourguignon, B., “Oriented creation of anisotropic defects by IR femtosecond laser scanning in silica,” *Optical Materials Express*, vol. 2, no. 12, pp. 1809–1821, Nov. 2012. DOI: 10.1364/ome.2.001809.
- [39] Wang, Y., Cavillon, M., Ollier, N., Poumellec, B., and Lancry, M., “An Overview of the Thermal Erasure Mechanisms of Femtosecond Laser-Induced Nanogratings in Silica Glass,” *physica status solidi (a)*, vol. 218, no. 12, p. 2100023, Apr. 2021. DOI: 10.1002/pssa.202100023.

## References

- [40] Sugiura, H. and Yamadaya, T., “Raman scattering in silica glass in the permanent densification region,” *Journal of Non-Crystalline Solids*, vol. 144, pp. 151–158, Jan. 1992. DOI: 10.1016/s0022-3093(05)80395-3.
- [41] Bellouard, Y., Barthel, E., Said, A. A., Dugan, M., and Bado, P., “Scanning thermal microscopy and Raman analysis of bulk fused silica exposed to lowenergy femtosecond laser pulses,” *Optics Express*, vol. 16, no. 24, pp. 19 520–19 534, Nov. 2008. DOI: 10.1364/oe.16.019520.
- [42] Bellouard, Y. *et al.*, “Stress-state manipulation in fused silica via femtosecond laser irradiation,” *Optica*, vol. 3, no. 12, pp. 1285–1293, Nov. 2016. DOI: 10.1364/optica.3.001285.
- [43] Liang, F. and Vallée, R., “Physical origin of nanograting formation on fused silica with femtosecond pulses,” *Applied Physics Letters*, vol. 105, no. 13, p. 131 904, Sep. 2014. DOI: 10.1063/1.4896749.
- [44] Awazu, K. and Kawazoe, H., “Strained Si–O–Si bonds in amorphous SiO<sub>2</sub> materials: A family member of active centers in radio, photo, and chemical responses,” *Journal of Applied Physics*, vol. 94, no. 10, pp. 6243–6262, Nov. 2003. DOI: 10.1063/1.1618351.
- [45] Ho, S., Herman, P. R., and Aitchison, J. S., “Single- and multi-scan femtosecond laser writing for selective chemical etching of cross section patternable glass micro-channels,” *Applied Physics A*, vol. 106, no. 1, pp. 5–13, Dec. 2011. DOI: 10.1007/s00339-011-6675-7.
- [46] Hnatovsky, C. *et al.*, “Pulse duration dependence of femtosecond-laser-fabricated nanogratings in fused silica,” *Applied Physics Letters*, vol. 87, no. 1, p. 014 104, Jul. 2005. DOI: 10.1063/1.1991991.
- [47] Eaton, S. M. *et al.*, “Transition from thermal diffusion to heat accumulation in high repetition rate femtosecond laser writing of buried optical waveguides,” *Optics Express*, vol. 16, no. 13, pp. 9443–9458, Jun. 2008. DOI: 10.1364/oe.16.009443.
- [48] Bernard, O., Kraxner, A., Boukhayma, A., Squier, J. A., Enz, C., and Bellouard, Y., “Third-harmonic generation monitoring of femtosecond-laser-induced in-volume functional modifications,” *Optica*, vol. 10, no. 6, pp. 774–782, Jun. 2023. DOI: 10.1364/optica.486746.
- [49] Witcher, J. J., Reichman, W. J., Fletcher, L. B., Troy, N. W., and Krol, D. M., “Thermal annealing of femtosecond laser written structures in silica glass,” *Optical Materials Express*, vol. 3, no. 4, pp. 502–510, Mar. 2013. DOI: 10.1364/ome.3.000502.
- [50] Internal conversations with Saulius Juodkazis at PULMM 2023, Nikko, Japan.
- [51] Internal conversations with Matthieu Lancry at PULMM 2023, Nikko, Japan.

# 9

## SPIM using polymer coherent fibre bundles

---

<b>9.1</b>	<b>Background</b>	<b>176</b>
<b>9.2</b>	<b>Overview of the SPIM probe platform</b>	<b>177</b>
<b>9.3</b>	<b>Epifluorescence microscope setup</b>	<b>179</b>
9.3.1	Optical design of the axicon-based microscope	180
<b>9.4</b>	<b>SPIM probe: design and fabrication</b>	<b>182</b>
9.4.1	End-cap design: 3D CAD modelling	182
9.4.2	End-cap fabrication: ULI-CE	183
<b>9.5</b>	<b>SPIM probe characterisation</b>	<b>184</b>
9.5.1	Fluorescence of PMMA CFB	185
9.5.2	Simulation of light field	186
9.5.3	Core crosstalk	188
<b>9.6</b>	<b>Imaging</b>	<b>191</b>
9.6.1	Image processing	191
9.6.2	Evaluation with a tissue phantom	194
9.6.3	Demonstration in <i>ex vivo</i> human lung	196
<b>9.7</b>	<b>Discussion</b>	<b>197</b>
<b>9.8</b>	<b>Conclusions</b>	<b>198</b>
	<b>References</b>	<b>200</b>

---

**I**MAGING fibres are used to perform real-time fluorescence endomicroscopy *in vivo, in situ*, with the goal of increasing diagnostic information for a plethora of organ systems and diseases. Widefield fibre endomicroscopy systems are simple, cost-effective, and come with fast image acquisition times. However, alternative approaches such as scanning systems produce higher contrast images with intrinsic optical sectioning, improving the visibility of histological features, albeit at the expense of simplicity, cost and acquisition rate.

## 9.1. Background

This chapter describes the development of a selective plane illumination microscopy (SPIM) endoscopic fibre platform consisting of an ultrafast laser fabricated end-cap integrated with a polymer coherent fibre bundle and an epifluorescence microscope. Polymer fibres are known to fluoresce when pumped with blue light, increasing background and noise in images. Our end-cap design circumvents this challenge. We demonstrate a reduction of out-of-focus features along with improved contrast of in-focus features in images of a tissue phantom. Moreover, we demonstrate the utility of our platform for endomicroscopy using a whole *ex vivo* human lung model.

The results presented in this chapter arise as a consequence of the 3-month research stay at the Photonic Instrumentation Group (Institute of Photonics and Quantum Sciences) of the Heriot-Watt University of Edinburgh (UK), under the supervision of Prof. Robert R. Thomson. This chapter follows the corresponding works by Roldán *et al.* [1, 2], and Parker *et al.* [3], as well as the patent application filed on 21<sup>st</sup> April 2022 to the UK Intellectual Property Office with application number GB2205826.7. A dataset with raw data, 3D models, simulations, videos, and other data related to the work can also be accessed in [4].

## 9.1 Background

Optical fibres are used across a range of clinical applications due to their flexibility, small cross-section, and ability to reach remote sites in the body. Coherent fibre bundles (CFBs) are a type of optical fibre used for imaging which consist of an array of many thousands of light-guiding cores [5]. These cores maintain their relative spatial positioning along the length of the bundle, each acting as a pixel in an acquired image. Silica CFBs are used clinically for minimally invasive fluorescence fibre-bundle endomicroscopy (FBE<sub>μ</sub>) of various organs of the body [6, 7], providing the opportunity for a better understanding of biological processes. For example, FBE<sub>μ</sub> has been used within urinary [8, 9], gastrointestinal [10–15], and respiratory systems [16–18], for the identification of neoplasia [8, 13, 15], dysplasia [12], cancer [9, 17], infection [16], or more general histological assessment [10, 11, 14, 18].

Coherent fibre bundles have been used within various endoscopic imaging applications since the late 1950s [19]. However, widespread commercial uptake of CFBs has been hindered by their high cost. Factors determining this cost include the price of the material and the complexity of fabrication. For example, many CFBs are made with highly doped silica cores in order to maximise core-cladding refractive index contrast and minimise core crosstalk, which can have a non-negligible effect on imaging performance [20–22]. Such doping is expensive, although impressive advances have been made to realise inexpensive CFBs using low-cost silica preforms intended for telecoms fibre [21, 23]. Polymer CFBs may be an attractive alternative to silica fibres as they can enable extremely high core-cladding refractive index contrasts, higher diameter CFBs which maintain relative flexibility, and are fabricated using inherently lower cost materials and facilities. However, it is known that polymer CFBs exhibit substantial fluorescence when pumped with blue light, which can be prohibitive for biological fluorescence imaging, particularly at shorter wavelengths, *e.g.*, green imaging. In order to open up the use of polymer CFBs for low-cost FBE<sub>μ</sub>, the issue of polymer CFB fluorescence must be overcome.

In fluorescence FBE<sub>μ</sub>, sample illumination is carried out, conventionally, in either a widefield

(WF) [24–26] or scanning [27–30] modality. Widefield systems may be favourable in clinical scenarios due to simplicity, low cost, and fast acquisition times. However, image contrast is limited by the presence of out-of-focus fluorescence within highly scattering tissue [31]. Scanning systems allow for optical sectioning, reducing unwanted background, but come with inherently more complex and costly optical arrangements and a decrease in image acquisition rate. On the bench, SPIM combines speed and simplicity with optical sectioning and high contrast imaging [32]. With this technique, a thin sheet of excitation light is projected across the focal plane, ensuring that out-of-focus sample is not excited. Accordingly, SPIM requires two orthogonally positioned objectives. To miniaturise and integrate SPIM into the form factor of a fibre-endoscope would therefore require a creative solution. To date, efforts towards miniaturised fibre-based SPIM have been directed towards tissue targets in animal models which can be surgically accessed, such as the brain [33, 34]. Alternative format, *i.e.*, not fibre-based, miniaturised SPIM implantable devices have been developed for animal studies [35, 36]. Although promising, these technologies have cross-sections and optical geometries which are not suitable for minimally invasive delivery through an endoscope in humans.

Ideally, a fluorescence FBE $\mu$  system would combine the benefits of several approaches and be cost-effective, be deployable through a conventional endoscope, produce high contrast images, and have a large field of view (FOV) with fast image acquisition. In pursuit of these key features, we have developed a proof-of-concept *SPIM probe* which consists of a fused silica end-cap and a commercial PMMA CFB. The SPIM probe is functional when operated with a bespoke WF epifluorescence microscope. We refer hereafter to the entire SPIM imaging system as the *SPIM probe platform*. While its name highlights its SPIM functionality, it is important to note that our approach also crucially negates the negative effect of CFB fluorescence. Herein, we describe the fabrication of the end-cap by ultrafast laser inscription and selective chemical etching (ULI-CE) and evaluate its performance using a fluorescent tissue phantom. We present images and video data acquired from a whole *ex vivo* human lung model as a proof-of-concept, whereby the SPIM probe was passed to the distal parenchymal region of the human lung. Thus, we demonstrate that our SPIM probe platform operates within an appropriate regime for the visualisation of tissue autofluorescence. This work represents an important step towards the translation of SPIM to *in vivo* scenarios.

## 9.2 Overview of the SPIM probe platform

The SPIM probe platform combines an in-house developed fused silica end-cap with a PMMA CFB and a custom-built epifluorescence microscope (Figures 9.1 and 9.3). The PMMA CFB we used is the MCL-1500-1.75, from Asahi Kasei Corporation. The CFB has a diameter of 1.5 mm and 13,000 cores, each with a diameter of  $\sim 10.5 \mu\text{m}$  (Fig. 9.2 **a**). The cores are PMMA and the cladding is a fluorinated polymer with refractive indices of 1.49 and 1.4, respectively (as stated by the manufacturer and confirmed with refracted near-field measurement). The core pitch (distance between core centre and nearest neighbour core centre) is  $\sim 12 \mu\text{m}$  (see SEM image in Fig. 9.5 **a**) and the cores have a numerical aperture of 0.5. The CFB is packaged with a polyethylene jacket which results in a full outer diameter of 1.75 mm.

A potential clinical deployment strategy of the SPIM probe into the distal lung via the working channel of a bronchoscope is shown in Fig. 9.1 (left). Due to its small form factor, the

## 9.2. Overview of the SPIM probe platform

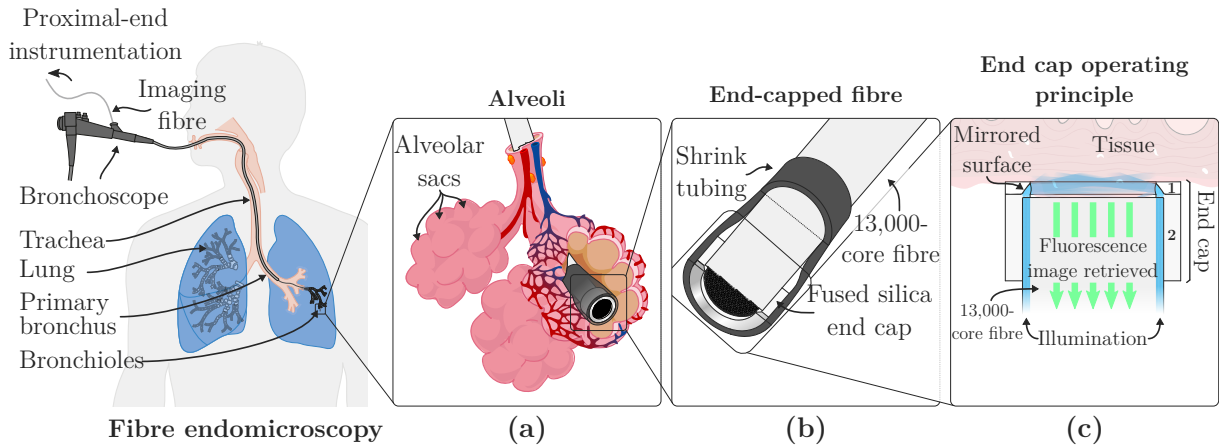


**Figure 9.1.** Schematic illustration of the SPIM probe platform for lung imaging. The SPIM probe is intended to be introduced through the working channel of a standard bronchoscope. **(a)** The diameter of the SPIM probe (1.9 mm) is narrow enough to reach the alveolar space for structural imaging of endogenous fluorescent tissue. **(b)** The custom-made fused silica end-cap secured to the distal end of a PMMA imaging fibre. **(c)** Cross-section of the end-cap when in contact with tissue showing its operational principle. The end-cap is fabricated in two parts, 1 and 2, between which is a thin mirrored surface. Illumination from a laser guided by the outer fibre cores is reflected by the mirrored surface towards the centre of the distal tip, generating a light-sheet perpendicular to the direction of observation. Fluorescence from a sample in the front recess of the distal tip is collected through the central column of cores. Adapted from [1].

SPIM probe can be delivered directly into the alveolar space (Fig. 9.1 a-b) via a transbronchial pass where it can visualise endogenous tissue fluorescence. SPIM functionality arises due to the light path through the probe as described as follows. The end-cap is affixed to the distal end of the PMMA CFB, shown in Fig. 9.1 b (see also a 3D video animation of the end-cap assembly into the polymer CFB in [4]). Tissue depressed into a shallow front recess is excited by an illumination plane orthogonal to the fibre propagation axis (blue light in Fig. 9.1 c) via pump light that is coupled at the proximal end to the outer cores only. Fluorescence induced in the illumination plane is collected through a central imaging array of cores of the CFB (green arrows in Fig. 9.1 c).

The SPIM probe platform acquires images in real-time using proximal-end instrumentation

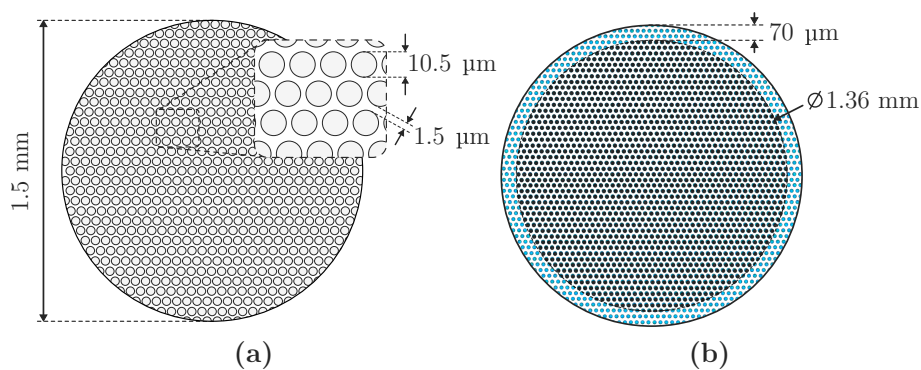


**Figure 9.2.** **(a)** Schematic of the imaging fibre MCL-1500-1.75 (Asahi Kasei) and its key dimensions: fibre diameter, core diameter, and spacing between cores. **(b)** Subset of cores used to provide the excitation (70  $\mu\text{m}$  outer ring), and central column of cores used to collect the sample fluorescence ( $\varnothing$  1.36 mm).

consisting of an epifluorescence microscope and computer (Fig. 9.3 a). Figure 9.3 b-c schematically depicts the epifluorescence microscope. For the purposes of this work, we incorporated a second illumination path to straightforwardly convert the platform's operating modality from SPIM to WF, as desired for characterisation experiments.

### 9.3 Epifluorescence microscope setup

A dual-illumination epifluorescence microscope was constructed, shown schematically in Fig. 9.3 b. The microscope allows for easy switching between optical paths via a rotatable dichroic mirror leading to either ring-illumination or flood-illumination of the proximal end of the fibre for SPIM imaging or WF imaging, respectively. In either arrangement, excitation was provided by a 485 nm laser (L) (LDH-D-C-485 with PDL 800-D driver, PicoQuant) operated in CW mode.

For SPIM imaging the following excitation path was used. A lens ( $L_1$ ) (C230TMD, Thorlabs) was used to collimate the output of a single-mode patchcord (P5-405-FC-2, Thorlabs) connected to the laser. The collimated beam was then expanded using a  $5\times$  beam expander (BE) (GBE05-A, Thorlabs) and passed through an excitation filter (Ex) (FITC-Ex01-Clin-25, Semrock). The light was then reflected via an aluminium mirror (M) (PF10-03-G01, Thorlabs) and passed through an axicon lens with a  $0.9^\circ$  angle of divergence ( $L_{ax}$ ) (AX122-A, Thorlabs). An image plane (Im.) of the ring-shaped beam was then created by a lens ( $L_2$ ) (LA1131-A-ML, Thorlabs). An optical mask (Mask) positioned in the image plane was used to block any stray light in the centre of the ring-shaped beam. This image plane was relay imaged onto the proximal end of the CFB using a second lens ( $L_3$ ) (LA1131-A-ML, Thorlabs) and a  $4\times$  objective lens ( $L_{obj}$ ) (RMS4X, Olympus) via the dichroic (DM) (FITC-Di01-Clin-25x36, Semrock). The optical mask was fabricated via ULI-CE on a 1 mm thick fused silica substrate (UV Grade Corning 7980 0F), onto which a  $\varnothing$  1.36 mm central circle was silver-coated to opacity. The axicon and lenses were selected together to create a ring of illumination on the CFB with a 1.5 mm outer diameter and 70  $\mu\text{m}$  inwardly protruding thickness. Thus, excitation light was only coupled to cores capped by the end-cap mirror (Fig. 9.2 b).

For WF imaging the following excitation path was used. Excitation light from a single-mode patchcord (P5-405-FC-2, Thorlabs) connected to the laser was collimated via a tube lens ( $L_4$ ) (TTL-200-A, Thorlabs) and passed through an excitation filter (Ex) (FITC-Ex01-Clin-25, Semrock). The dichroic mirror (DM) (FITC-Di01-Clin-25x36, Semrock) was angled to redirect this light through the objective lens ( $L_{obj}$ ) (RMS4X, Olympus) onto the proximal end of the CFB. The relative position of the patchcord output and the tube lens was then adjusted to massively defocus the laser spot incident on the CFB until even illumination of the central column of cores was obtained.

In either SPIM or WF mode, fluorescence images were acquired through the same objective lens and dichroic mirror. Subsequently, after an emission filter ( $L_{Em}$ ) (FITC-LP01-Clin-25, Semrock) and a tube lens ( $L_5$ ) (TTL200-A, Thorlabs), the images were captured by a camera with a monochrome CMOS sensor (C) (GS3-U3-32S4M-C, FLIR).

### 9.3. Epifluorescence microscope setup

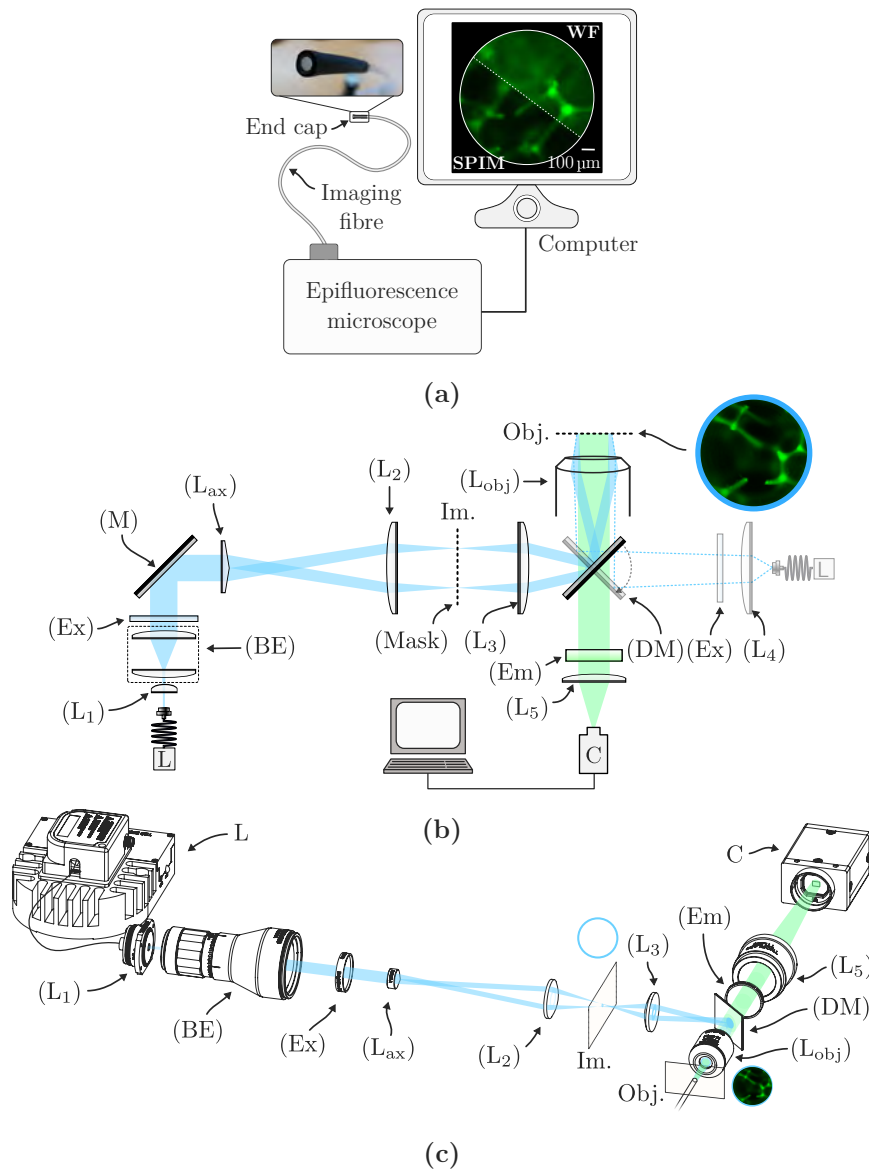


**Figure 9.3.** Schematic of the proximal end instrumentation (Key: (L) – 485 nm fibre coupled laser, (L<sub>1</sub>) – lens, (BE) – beam expander, (Ex) – excitation filter, (M) – mirror, (L<sub>ax</sub>) – axicon lens, (L<sub>2</sub>) – lens, (L<sub>3</sub>) – lens; (Mask) – silver-coated optical mask, (DM) – dichroic mirror, (L<sub>obj</sub>) – objective lens, (Obj.) – object plane and location of proximal end of SPIM probe, (Em) – emission filter, (L<sub>5</sub>) – tube lens, (C) – CMOS monochrome camera, (L<sub>4</sub>) – tube lens). **(a)** The entire SPIM probe platform consists of the SPIM probe (packaged end-cap shown in photo) coupled to an axicon lens-based epifluorescence microscope and a PC for real-time imaging. **(b)** Epifluorescence microscope which enables the SPIM probe. Note that the greyed-out illumination path is an integrated WF epifluorescence microscope which was used for characterisation experiments and is not a part of the SPIM probe platform. **(c)** 3D view with real optical elements of the axicon-lens based epifluorescence microscope (the WF arm in Fig. (b) is not included here). Adapted from [1] and [2].

#### 9.3.1 Optical design of the axicon-based microscope

Working backwards, an illumination ring in the object plane has the following dimensions: inner diameter (ID)  $\varnothing$  1.36 mm, outer diameter (OD)  $\varnothing$  1.5 mm, and thickness 70 μm. The objective (L<sub>obj</sub>) was preselected in combination with the tube lens (L<sub>5</sub>) in the fluorescence emission optical path. The objective lens has an effective focal length of 45 mm.

The lens ( $L_3$ ) was preselected in such a way that it works at  $1.1\times$  magnification from the image plane to the object plane. Therefore, in the image plane, we wanted to produce a ring with approximately: ID  $\approx 1.5$  mm, OD = 1.65 mm, and thickness = 77  $\mu\text{m}$ .

An axicon deflects light according to Snell's Law, which can be used to find the deflection angle ( $\beta$ ):

$$n \cdot \sin(\alpha) = \sin(\alpha + \beta), \quad (9.1)$$

where  $n$  is the refractive index of the lens,  $\alpha$  is the physical angle of the prism, and  $\beta$  is the angle the deflected beam creates with the optical axis. Beyond the Bessel beam region (overlap region in Fig. 9.4 a) of the lens, a ring of light is formed. The thickness of the ring ( $t$ ) remains constant and equivalent to  $r$ . For the wavelength used ( $\lambda = 485$  nm) the refractive index of the lens is  $n = 1.4632$ . Under these conditions, and with  $r = 77$   $\mu\text{m}$ , the thickness of the ring is shown in Fig. 9.4 b for different values of  $\alpha$ . It can be seen that  $t \approx r$  can be considered, especially for small values of  $\alpha$ :

$$t = \frac{r\sqrt{1 - n^2 \sin^2 \alpha}}{\cos \alpha (n \sin^2 \alpha + \cos \alpha \sqrt{1 - n^2 \sin^2 \alpha})} \approx r. \quad (9.2)$$

In the setup depicted in Fig. 9.3 b, the diameter of the image plane ring ( $2R = 1.65$  mm) is the result by the deflection angle ( $\beta$ ) of the axicon ( $L_{\text{ax}}$ ) and the focal length ( $f_{L_2}$ ) of the lens ( $L_2$ ) (see also Fig. 9.4 a):

$$\tan \beta = \frac{r}{f_{L_2}}. \quad (9.3)$$

With  $\beta$ 's available from Thorlabs options of axicons and  $r = 0.825$  mm, Table 9.1 lists the possible focal lengths of the lens ( $L_2$ ). The lens ( $L_2$ ) chosen is the AX122-A ( $\alpha = 2^\circ$ ,  $\beta = 0.9^\circ$ ), not only because of the closeness of its focal length to that required, but also because of the practical reasons for setting up the microscope. In fact, focal lengths less than  $\sim 50$  mm make it difficult to position the different optomechanical components, and distances greater than that begin to create a discrepancy between the required and available focal lengths. Also, the error made in the thickness of the ring is minimised ( $t = 76.96$   $\mu\text{m}$ ,  $r = 77$   $\mu\text{m}$ ).

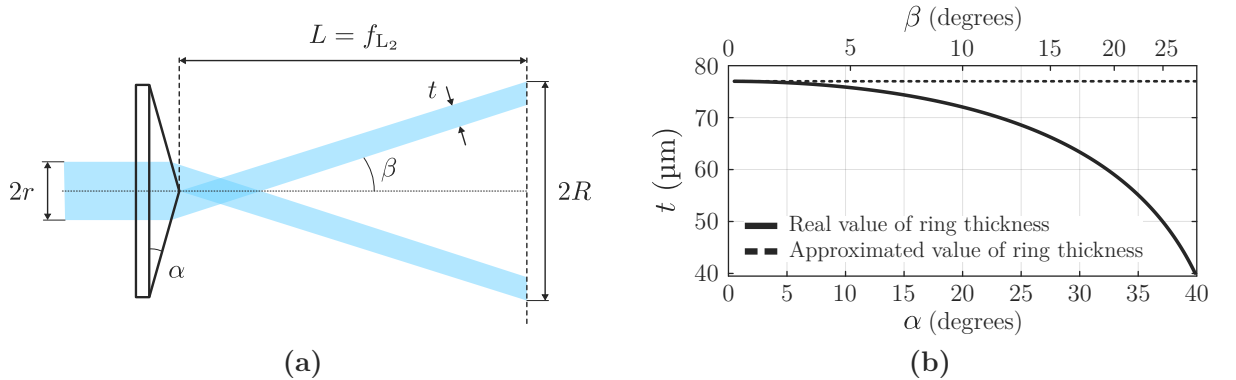


**Figure 9.4.** (a) Schematic of an axicon lens showing the ring-shaped beam that propagates after the overlap region (Bessel beam region). (b) Error made when using the approximation  $t \approx r$  for different values of  $\alpha$ , the exact value being given in Eq. 9.2.  $n = 1.4632$  (UV fused silica at  $\lambda = 485$  nm) and  $r = 77$   $\mu\text{m}$  are considered.

## 9.4. SPIM probe: design and fabrication

**Table 9.1.** Required focal lengths for the lens ( $L_2$ ) depending on the different axicon lens options from Thorlabs.

Item #	$\beta$	$f_{L_2}$	Closest ( $L_2$ ) focal length available
AX1205-A	0.2°	236.3 mm	199.3 mm
AX121-A	0.5°	94.5 mm	99.7 mm
AX122-A	0.9°	52.5 mm	49.8 mm (chosen as the most practical option)
AX125-A	2.3°	20.5 mm	19.9 mm
AX1210-A	4.7°	10.0 mm	–
AX1220-A	10°	4.7 mm	–
AX1240-A	29.9°	1.4 mm	–

Moreover, the thickness of the image plane ring ( $t \approx r$ ) is a result of the magnification from the laser fibre output to the image plane. The laser is fibre coupled and has a mode field diameter (MFD) of  $\sim 4 \mu\text{m}$ , while  $r$  must be  $77 \mu\text{m}$ :

$$\frac{r}{0.5 \cdot \text{MFD}} = \frac{77 \mu\text{m}}{0.5 \cdot 4 \mu\text{m}} = 38.5 \times \text{magnification.} \quad (9.4)$$

The focal lengths of lenses ( $L_1$ ) and ( $L_2$ ) are 4 mm and 50 mm, respectively. Consequently, the magnification is  $f_{L_2}/f_{L_1} = 12.5\times$ . To get the  $38.5\times$  magnification, a beam expander (BE) is needed. BEs (with fixed magnification) were available either at  $3\times$  or  $5\times$ . We chose  $5\times$  BE (resulting in an overall magnification of  $62.5\times$ ) to make sure the ring is large enough. We still used the mask to ensure that there was no light coupled into the imaging region of the fibre.

## 9.4 SPIM probe: design and fabrication

This section explains both the 3D CAD design process of the end cap, as well as the subsequent fabrication, including the steps of fs laser writing, chemical etching, silver coating, and assembly.

### 9.4.1 End-cap design: 3D CAD modelling

The end-cap was designed to be secured to the distal tip of the PMMA CFB and result in SPIM functionality without adding bulkiness (Fig. 9.5 **a**). The design, which can be found in [4], was made using Solidworks software version 2019 SP4.0. Its key functional feature is an annular, angled, mirrored surface which circumscribes the distal end face of the PMMA CFB (Fig. 9.5 **b**) and redirects excitation light into a plane across the FOV. Both the mirrored surface and the peripheral inner surface of the end-cap were given curvatures (radii of curvature 0.45 mm and 0.15 mm, respectively) to prevent excitation light from diverging excessively outside of the imaging region. The mirrored surface protrudes inwardly a distance of  $70 \mu\text{m}$  from the perimeter of the PMMA CFB end face, capping a ring of cores approximately six cores thick. This represents 18% of the total cores in the fibre. As previously discussed, proximally, the epifluorescence system features an axicon lens in order to couple excitation light only into this ring of cores, delivering excitation to the sample at the distal end. The remaining 82% of the cores are reserved for the collection of fluorescence: this equates to a FOV of  $\varnothing 1.36 \text{ mm}$ . The

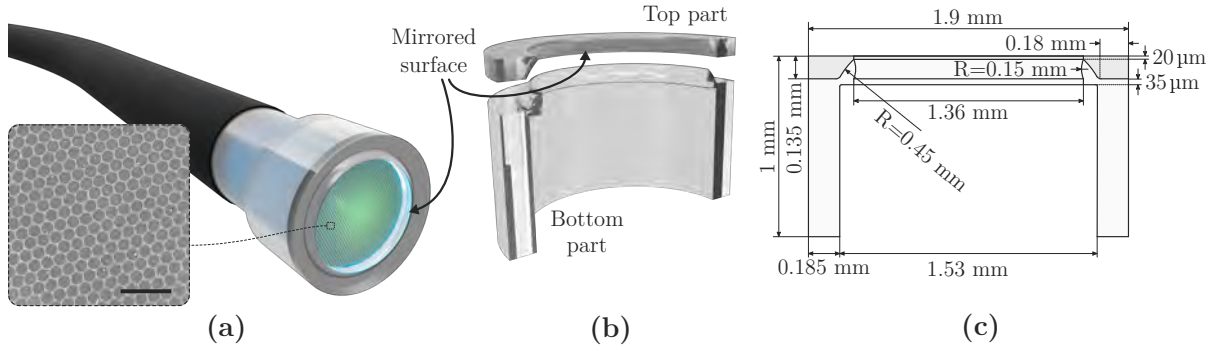


**Figure 9.5.** End-cap design. **(a)** Illustration of the SPIM probe. Inset shows an SEM image (taken with Phenom Pro, Thermo Fisher Scientific) of a region of the end face of the fibre. Scale bar is 50  $\mu\text{m}$ . **(b)** 3D cross-sectional slice of the designed end-cap. The top and bottom parts are shown slightly separated, to indicate the location of a mirrored surface between the two parts. **(c)** 2D CAD drawing of the end-cap.  $R$  refers to radius of curvature. Dimensions are shown to scale. Figures **(a-b)** are made using Blender 3.2, while Fig. **c** is based on the model made with Solidworks 2019 SP4.0, which can be found in [4]. Adapted from [1].

end-cap outer diameter is 1.9 mm (Fig. 9.5 **c**) and can be delivered down the working channel of most commercial bronchoscopes.

#### 9.4.2 End-cap fabrication: ULI-CE

The end-cap fabrication process centres around ULI-CE, also known as ultrafast laser assisted etching (ULAE) [37], or femtosecond laser irradiation followed by chemical etching (FLICE) [38, 39]. As detailed extensively in Chapter 3, ultrafast laser inscription (ULI) [40] is a powerful technology which enables the production of micro-optics with remarkable freedom and precision [41–43]. In this technique, tightly-focused ultra short pulses ( $< 350$  fs) are used to induce nonlinear photoionisation in a dielectric substrate [44–46]. The resulting modified substrate volume is highly localised so that material directly outside of the focal point is largely unaffected. One result of ULI-CE on a substrate is an increased etching rate (up to  $\times 10^3$ ) when compared to pristine material [37, 47]. This effect can be harnessed to “write” 3D structures into bulk material that can then be revealed by wet etching.

In the first part of the fabrication process, the end-cap structure is inscribed into a fused silica substrate as two separate parts (Fig. 9.5 **b**). Femtosecond laser writing was performed using a Menlo Systems BlueCut fibre laser (Menlo Systems GmbH) that delivers 350 fs laser pulses at a central wavelength of 1030 nm. A PRR of 250 kHz and a pulse energy of 250 nJ were used. The inscription speed was 3 mm/s, thus obtaining 83.3 pulses/ $\mu\text{m}$ . To obtain the highest selectivity in the subsequent chemical etching of the structures, the polarisation was set linear and perpendicular to the intended etching direction [37]. As the end-cap inscription is circular, the polarisation was dynamically controlled during laser inscription by rotating a  $\lambda/2$  waveplate. Figure 9.6 shows the direction of polarisation in the inscription of the different parts of the end cap. The laser pulses were tightly focused into the 1 mm thick high purity fused silica glass (UV Grade Corning 7980 0F) using a 0.4 NA aspheric lens (A110TM-B, Thorlabs). The substrate was translated through the laser focus using a motorised nano-resolution XYZ crossed roller bearing stage (Alio Industries), and the stage motion was controlled using ACSPL+ programming language. Figure 9.7 **a** shows micrographs of the fused silica substrate after ULI.

## 9.5. SPIM probe characterisation

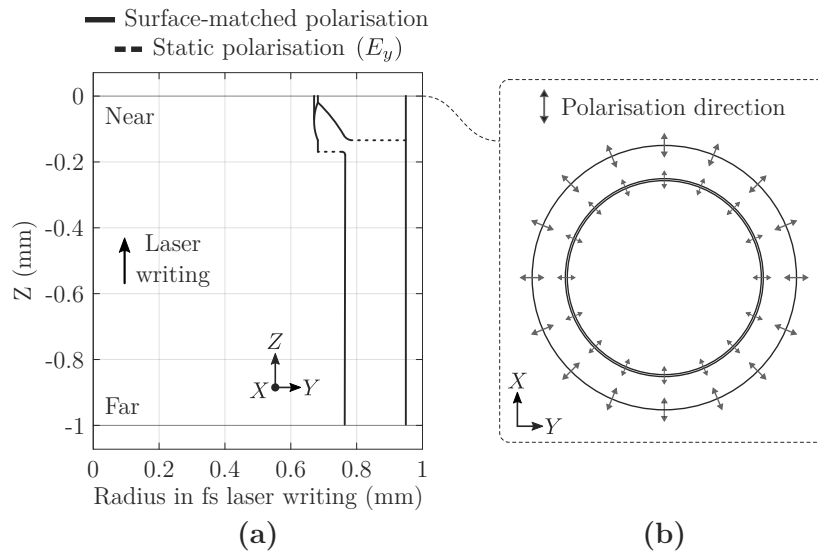


**Figure 9.6.** Polarisation control techniques used in the different laser inscriptions that result in the end cap. **(a)** The vertical surfaces (inscribed while moving in  $Z$ ) present a surface-matched polarisation technique, while the horizontal surfaces (inscribed with constant  $Z$ ) are inscribed with a static polarisation state, being  $E_y$  in this case. **(b)** Appearance of the end-cap in a top view ( $XY$  plane). The arrows show the polarisation direction in the surface-matched polarisation inscriptions, which depends on the angular position.

In the subsequent etching process, the inscribed fused silica glass was immersed for three hours in a magnetically stirred etching solution of KOH diluted with deionised water (8 mol/L, 85°C). The etching time was determined empirically to facilitate easy release of the two parts forming the end-cap, without over-etching. The two parts were individually removed and rinsed with deionised water (see Fig. 9.7 b).

The top part of the end-cap was silver-coated on the surface shown in Fig. 9.5 b by e-beam deposition (MiniLab 080 System, Moorfield Nanotechnology Limited). The coating thickness was  $90 \text{ nm} \pm 10 \text{ nm}$ .

Before assembling the end-cap to the fibre, the two ends of the CFB were polished according to the following procedure: 30 s (1,000-grit sandpaper), 1 min (4,000-grit sandpaper), 2 min (12  $\mu\text{m}$  of grit size lapping film), 3 min (5  $\mu\text{m}$  grade lapping film), 4 min (3  $\mu\text{m}$  grade lapping film), and 5 min (1  $\mu\text{m}$  grade lapping film).

Finally, both parts of the end-cap were assembled using manual translations stages and glued with UV-curable optical adhesive (NOA 61, Norland) (see Fig. 9.7 c – left). Similarly, the end-cap was glued (NOA 68, Norland) to the polished distal end of a 1.5 m length of the fibre (see Fig. 9.7 c – centre), and a flexible heat-shrink tube was attached for protection during experiments (see Fig. 9.7 c – right).

## 9.5 SPIM probe characterisation

Three aspects of the SPIM probe were characterised. Firstly, we quantified the fluorescence emission of the cores in the PMMA CFB when pumped with blue light. Secondly, we simulated the distal-end light field of the SPIM probe and compared it with simulations of the CFB fibre

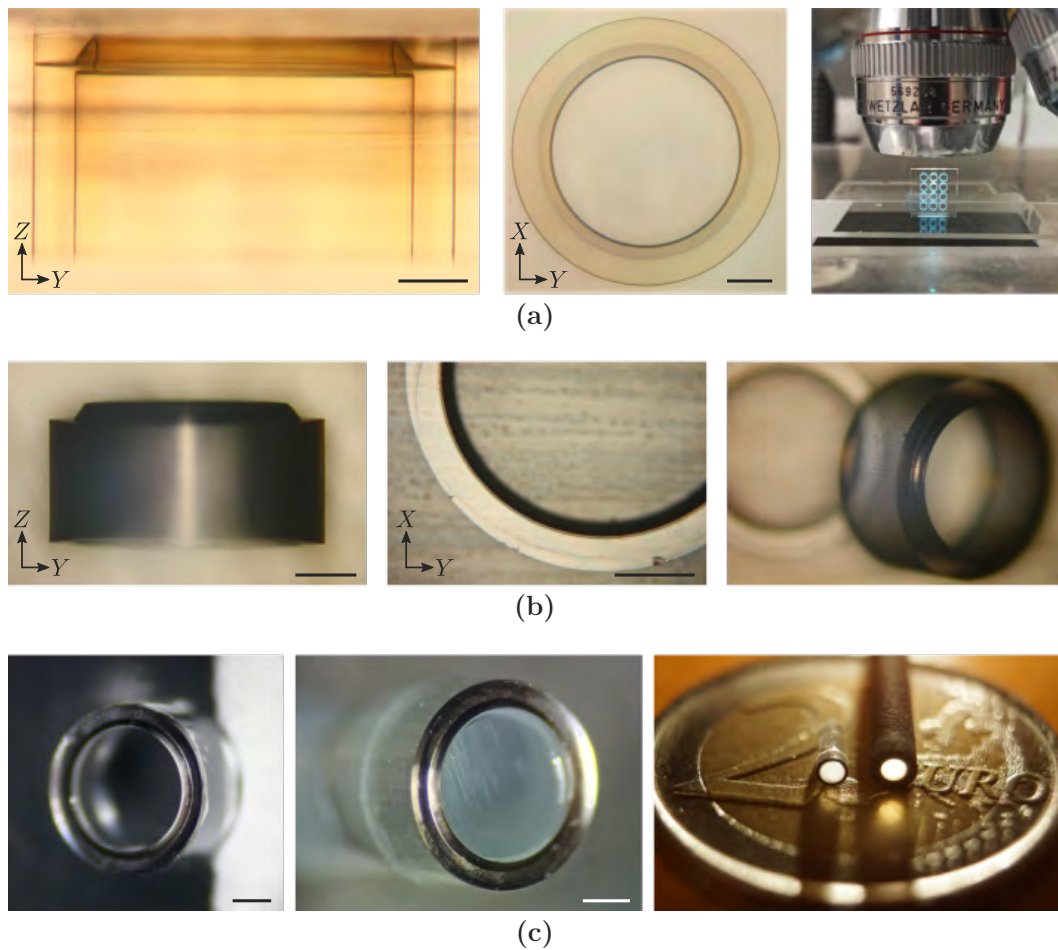


**Figure 9.7.** End-cap fabrication. **(a)** Ultrafast laser inscription. (left) Side and (centre) top view micrograph of the end-cap inscribed in the fused silica substrate. (right) Image of a  $10 \times 10 \times 1$  mm fused silica substrate where twelve end caps are inscribed. **(b)** Micrographs of the (left) bottom and (centre) top parts of the end-cap, after KOH etching process. (right) Micrograph of the bottom part of the end-cap in a slightly oblique position. **(c)** Assembly. (left) Image of the two parts of the end-cap glued together. A silver thin film is located on the surface between the two parts, as depicted in the illustration in Fig. 9.5 b. (centre) Image of the end-cap bonded to the PMMA CFB. (right) Image of two end cap samples attached to different illuminated PMMA CFBs, one of them with the protective shrink tubing. Scale bars in **(a)** are  $300 \mu\text{m}$ . Scale bars in **(b-c)** are  $400 \mu\text{m}$ . Adapted from [1].

when used as a WF imaging fibre. Finally, we investigated the extent of core crosstalk in the PMMA CFB as a means to compare it with silica CFBs.

### 9.5.1 Fluorescence of PMMA CFB

The fluorescence emission from single cores of both the PMMA CFB and a commercial silica CFB (FIGH-30-650S, Fujikura) is shown in Fig. 9.8 a. Figure 9.8 b shows the system used for measuring the fluorescence emission of fibre cores. The output of a fibre-coupled 485 nm laser (L) (LDH-D-C-485 with PDL 800-D driver, PicoQuant) was collimated and coupled into a single core at the proximal end of the CFB via lenses ( $L_1$ ) and ( $L_2$ ) that were selected so that the incident laser spot would not over-fill the core. At the distal end of the fibre, a camera (C) (DCC1645C, Thorlabs) was used to provide feedback for positioning the fibre with respect to the

## 9.5. SPIM probe characterisation

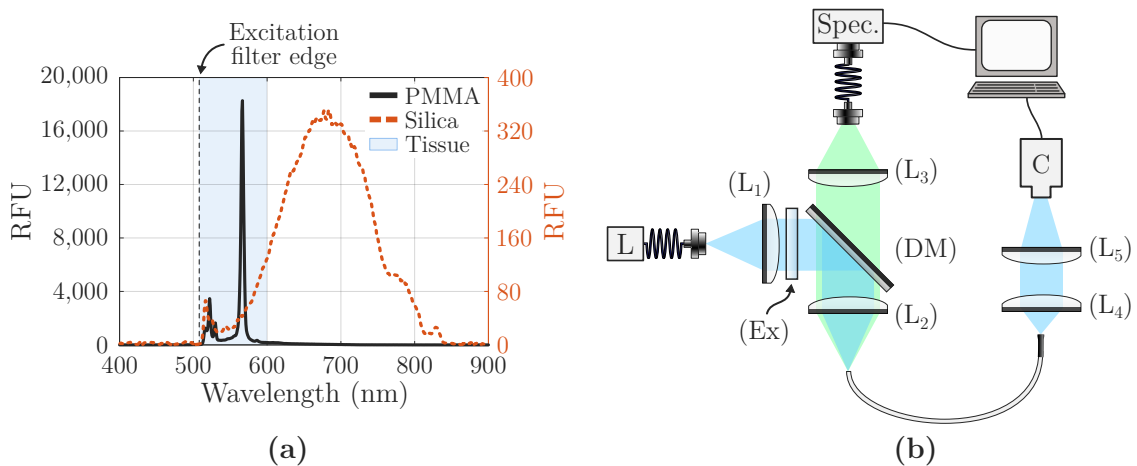


**Figure 9.8.** Measurement of fibre core fluorescence. **(a)** Fluorescence emission spectra of the cores of the PMMA CFB. Plot shows PMMA fibre cores exhibiting a strong green fluorescence (black line) which coincides with endogenous tissue emission band (blue fill). The silica fibre exhibits a weak, broad fluorescence (red dashed line). Dashed vertical line represents the excitation filter edge. Relative fluorescence units (RFU) refers to fluorescence counts per metre of fibre. **(b)** Epifluorescence system used to measure the fluorescence emission spectra of the cores of the PMMA CFB and the silica CFB when pumped with a 485 nm laser (Key: (L) – 485 nm fibre coupled laser, (L<sub>1-5</sub>) – lenses, (Ex) – excitation filter, (DM) – dichroic mirror, (C) – camera, (Spec.) – spectrometer). Adapted from [1].

proximal end laser spot such that the pump light was incident on the core and not the cladding. The laser was operated in CW mode and the power was measured to be 200  $\mu$ W. Backscattered fluorescence induced in the core was then coupled via a multimode fibre (M42L01, Thorlabs) to a spectrometer (Spec.) (QE-Pro VIS, Ocean Optics now Ocean Insight) for readout.

When normalised to the length of the fibre, the fluorescence of the PMMA fibre cores was found to be two orders of magnitude greater than that of the silica fibre cores and overlaps with the emission wavelength range of endogenous tissue fluorophores [48]. Thus, using the same cores to provide excitation and to collect fluorescence, as is done in standard WF imaging techniques, would result in a significant fluorescence background and a decreased signal-to-noise ratio. Indeed, this effect can be seen in Figs. 9.14 and 9.15 and is discussed later. In contrast, the SPIM probe uses separate sets of cores for excitation and collection, avoiding the negative impact of core fluorescence.

### 9.5.2 Simulation of light field

Ray-trace simulations were carried out with the aim of predicting the spatial properties of the excitation plane parallel to the distal end face of the SPIM probe (Fig. 9.9 a bottom). We also simulated the case of the PMMA CFB used in a WF modality, *i.e.*, without an end-cap and with proximal-end flood illumination (Fig. 9.9 a top). A simulated detector perpendicular to the end face of the fibre shows the intensity distribution in these two scenarios.

Zemax OpticStudio software (version 22.2) was used with Matlab (version R2022a Update 1, The MathWorks Inc.) as the application programming interface (API). Standalone mode was the program mode used for the connection between Matlab and Zemax OpticStudio. For the simulations, non-sequential ray-tracing mode was employed. Both end-cap parts were included as CAD parts, and each simulated core was modelled as a source point with an illumination angle

cone defined by the NA of the fibre. A nominal 1 mW was launched at the proximal end of the fibre, with a total of 1,000 rays per core. 485 nm wavelength was employed. It should be noted that neither the attenuation of the PMMA fibre nor its dispersion was taken into account in the simulations. The autofluorescence of the PMMA fibre when excited at the working wavelength was also not considered. Both the 3D model of the end-cap and simulations are included in [4].

The intensity distribution in the 2D detector plane (Fig. 9.9 b) was obtained in the SPIM case using the end-cap with a 70  $\mu\text{m}$  thick ring-illumination (2,337 cores simulated, 100%), and in the WF case using a bare fibre with flood-illumination (10,000 cores simulated placed randomly, 76.92%). The 2D detector plane was oriented as shown in Fig. 9.9 a, *i.e.*, containing the axial axis of the fibre, initiating at the fibre end face, and with dimensions of 1.35 and 4 mm in the Y and Z axes ( $1001 \times 1001$  pixels), respectively. The averaged intensity as a function of propagation distance (Fig. 9.9 c), for both SPIM and WF, was extracted from the intensity distribution in the 2D detector plane, as  $I(z) = (L_y)^{-1} \int_y I(y, z) \cdot dy$ , with  $L_y = 1.35$  mm.

Plots of the intensity distribution in the detector plane (Fig. 9.9 b), and the integrated intensity as a function of distance from the fibre end face (Fig. 9.9 c) allow two key conclusions to be drawn. Firstly, the intensity drop-off as a function of distance is noticeably steeper in SPIM than WF. A 20 dB decay is observed at a distance of  $\sim 0.7$  mm for SPIM and  $\sim 3.3$  mm for WF. Secondly, the power within the front recess of the end-cap ( $z \leq 170$   $\mu\text{m}$ ) is  $\sim 2.97$  times higher than within the equivalent propagation distance in the WF case. According to the simulations, for 1 mW launched into the proximal end of the CFB 0.232 mW will be confined in the front recess of the SPIM probe compared to 0.078 mW in the equivalent 170  $\mu\text{m}$  after the fibre at the distal end in the WF case. For an increased distance of 0.5 mm extending from the fibre end face, the power is 0.448 mW in the SPIM case and 0.194 mW in the WF case. In short, almost half of the power delivered in the SPIM probe is confined in the first 0.5 mm after the fibre. Thus, in the SPIM case, distant features in any given FOV receive less light and more light is contained within the CFB imaging volume. It should be noted that some light exiting the CFB diverges outside of the finite detector plane and is not captured in the simulations.

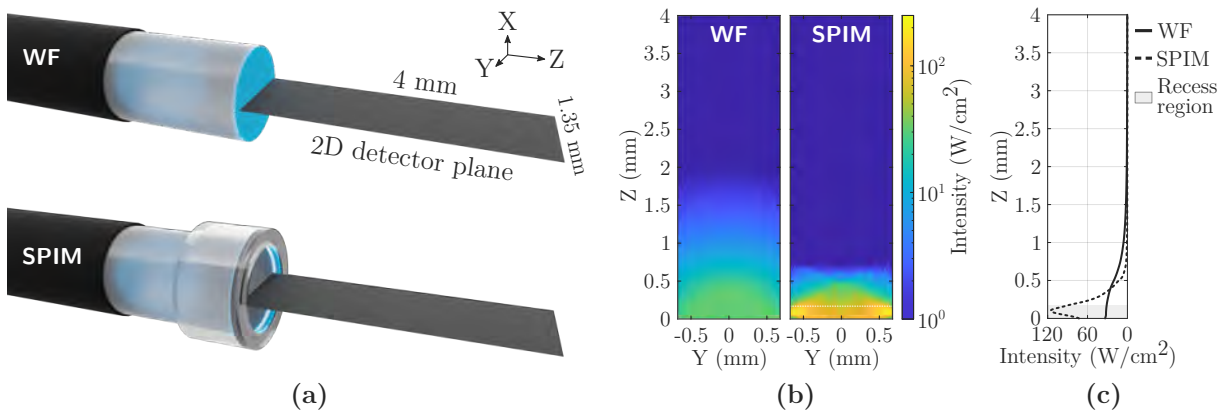


**Figure 9.9.** Simulations of light fields in WF and SPIM cases. (a) Illustration depicting arrangement of the  $4 \times 1.35$  mm  $ZY$  rectangular detector in the simulation for both WF (flood illumination without end cap) and SPIM (ring illumination with end cap) cases. (b) 2D simulated excitation light intensity profile in the detector plane using both WF and SPIM illumination. Absorption/scattering have not been taken into account. Dotted white line at  $z = 170$   $\mu\text{m}$  on the SPIM profile represents the end of the end-cap. (c) Integrated intensity as a function of distance ( $I(z) = (L_y)^{-1} \int_y I(y, z) \cdot dy$ , with  $L_y = 1.35$  mm) for WF and SPIM illumination. Front recess region ( $z \leq 170$   $\mu\text{m}$ ) is shown as grey fill. Adapted from [1].

### 9.5.3 Core crosstalk

Silica CFBs are typically designed with a range in core size as a means to prevent crosstalk [20, 21], a power-coupling between neighbouring cores which degrades imaging performance. The PMMA CFB features very uniform core size ( $10.5\ \mu\text{m}$ ,  $\text{SD}=0.24\ \mu\text{m}$ ) and spacing ( $1.5\ \mu\text{m}$ ,  $\text{SD}=0.15\ \mu\text{m}$ ) (extracted from SEM image of Fig. 9.5 a, and depicted in Fig. 9.2 a).

#### Experimental measurement

Crosstalk of light at 515 nm between cores in the PMMA CFB was measured experimentally on a total of 13 cores. We chose this wavelength as it is representative of the fluorescence originating from the alveolar tissue of a human lung [26, 48], and therefore of the images retrieved with the SPIM probe. As shown in Fig. 9.10, light from a laser (L515A1, Thorlabs) with single mode fibre output (P1-460B-FC-2, Thorlabs) was butt-coupled into a single core of the proximal end of the 1 m long PMMA CFB fibre (MCL-1500-1.75, Asahi). In this way, the cores were underfilled. However, this experiment was not intended to be a complete study of the power cross-coupling of these fibres. In other studies of CFB crosstalk, such as in [20, 21], large data sets were required for valid statistical analysis. This was due to the non-uniformity of the core structure in the CFBs, which also precluded the possibility of simulation. The CFB employed in this work presents almost identical cores which are arranged in a uniform pattern. Thus, we determined that experimentally measuring a small set of cores as well as using simulation to validate our results was appropriate (and possible) to estimate the effect of crosstalk.

The spatial distribution of the light at the distal end of the fibre was imaged with a 7.5 mm focal length lens and a monochrome camera (DCC1545M-GL, Thorlabs). With the help of a micro-positioner at the proximal end of the fibre, different cores were excited and images of crosstalk distribution at the distal end were taken. All non-saturated images were taken with

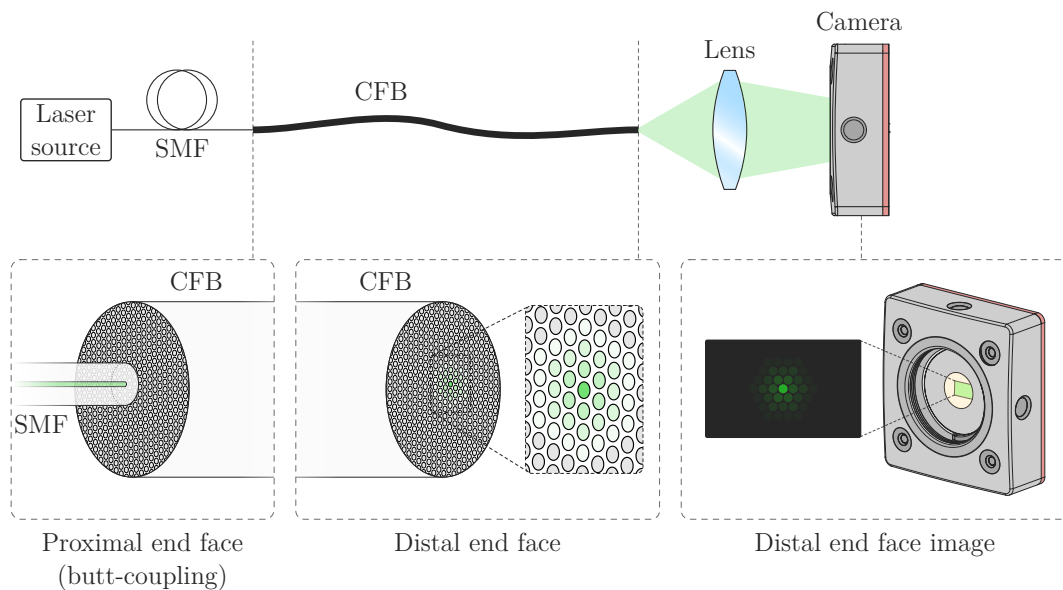


**Figure 9.10.** Optical system used for illuminating (laser at 515 nm) a single core within a coherent fibre bundle by butt-coupling, and recording the coupling of light across its immediate and extended neighbouring cores by means of an unsaturated image.

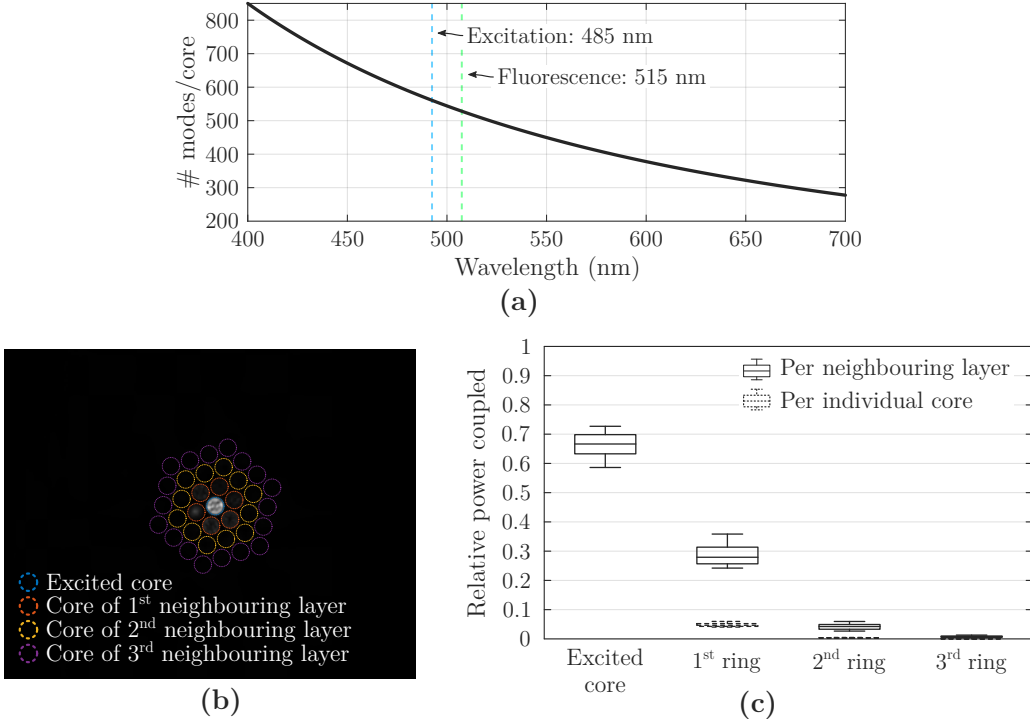


**Figure 9.11.** Experimental measurement of the core crosstalk of the PMMA CFB. **(a)** Number of modes per core in the PMMA CFB as a function of  $\lambda$ . **(b)** Example of a coupling spread pattern, highlighting the excited core (515 nm wavelength), as well as the first three neighbouring layers. **(c)** Box plot with the relative power in the excited core, as well as in each of the three neighbouring layers, either for the whole layer or for an individual core. Adapted from “Supplementary Information” in [1].

an exposure time of 80  $\mu$ s. Figure 9.11 **b** shows an example of the light distribution at the distal end of the fibre upon excitation of a single CFB core.

We found that, despite the uniformity of the core pattern in the PMMA CFB and the number of supported modes of the 10.5  $\mu$ m cores ( $\sim 512$  at 515 nm, Fig. 9.11 **a**), along a 1 m length of fibre,  $66.3\% \pm 2.4\%$  of light coupled into one core of the PMMA CFB remained confined to the core, while the remaining  $\sim 33.7\%$  power-coupled to neighbouring cores. These values are comparable to the available reported measurements of silica CFBs [20, 21]. Thus, it can be expected that image degradation as a result of core crosstalk is no more of a concern using the PMMA CFB than it is using a silica fibre.

The algorithm to obtain the inter-core coupling is detailed below. It is mainly based on the one presented by Perperidis *et al.* [20], with some modifications. The power in the excited core is obtained relative to the power in the three adjacent rings of cores (6, 12 and 18 cores, respectively).

- $I(x, y)$  is the matrix containing the intensity values of the non-saturated end face image, with  $\{x, y \in \mathbb{Z}_0^+ \mid x \leq N_x, y \leq N_y\}$ , where  $N_x$  and  $N_y$  are the number of pixels in width and height, respectively.
- $M_i$  is the mean intensity in ring  $i$ . Ring 0 is the excited core. 3 rings are considered.

$$M_i = \sum_{j=1}^{n_i} \frac{1}{|(x, y) \in c_{i,j}|} \sum_{(x,y) \in c_{i,j}} I(x, y), \quad \forall \{i \in \mathbb{Z}_0^+ \mid i \leq 3\}. \quad (9.5)$$

## 9.5. SPIM probe characterisation

$c_{i,j}$  is the core  $j$  in ring  $i$ , and  $n_i$  the number of cores in ring  $i$  ( $n_0 = 1$ ,  $n_1 = 6$ ,  $n_2 = 12$ , and  $n_3 = 18$ ).

- o The relative power remaining in each ring is:

$$P_i = \frac{M_i}{\sum_{j=0}^3 M_j}, \quad \forall \{i \in \mathbb{Z}_0^+ \mid i \leq 3\}. \quad (9.6)$$

Thus, the power remaining in the excited core ( $P_{nc}$ ) can be extracted, as well as the power coupled to other cores ( $P_c$ ):

$$P_{nc} = \frac{M_0}{\sum_{j=0}^3 M_j}, \quad P_c = \frac{\sum_{j=1}^3 M_j}{\sum_{j=0}^3 M_j}. \quad (9.7)$$

The results obtained are shown in Fig. 9.11 c. The power remaining in the excited core after 1 m of fibre is  $66.29\% \pm 2.43\%$  (confidence level of 95%), with the remaining 33.71% being evanescently coupled to adjacent cores, with the distribution shown in the box plot.

## Simulation

In order to verify the experimental results, the commercial software RSoft Photonics CAD Suite (version 2021.09-1) was used for simulation. Specifically, the advanced finite element beam propagation method was applied within the BeamPROP BPM simulation engine. Within a 3D simulation model, a 2D lattice formed by four hexagonal rings was defined, with the geometrical structure and refractive indices of the PMMA CFB. Only the central core was excited with an input field corresponding to a superposition of all fibre modes supported by the core (equal power and random phase for each mode) (see Fig. 9.12 a). The core crosstalk was evaluated after 1 m of propagation (see Fig. 9.12 b). It should be noted that the mesh grid size took a value of  $\lambda/4$  in the X and Y axes, and  $\lambda/2$  in the Z axis (propagation direction), where  $\lambda = 515$  nm. Neither the attenuation of the PMMA fibre, nor its fluorescence when excited at the working wavelength, nor other effects have been considered in the simulations.

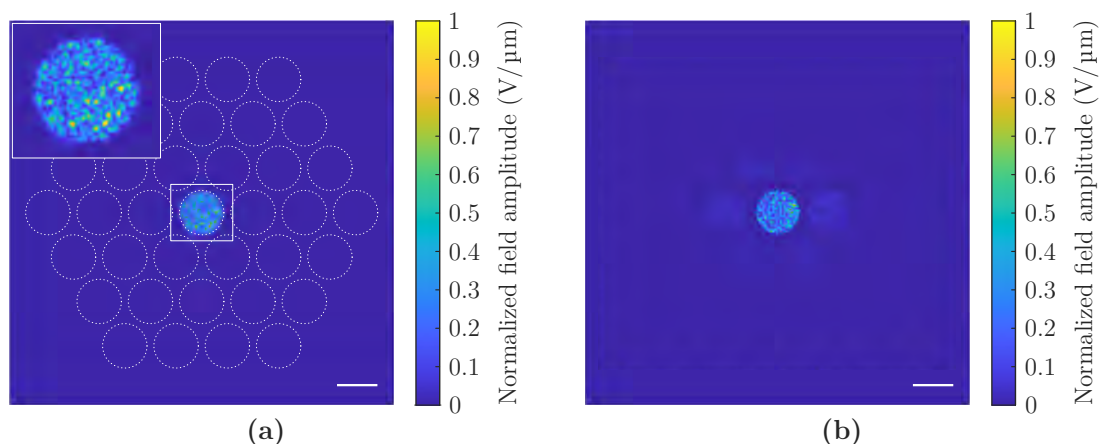


**Figure 9.12.** Simulation measurement of the core crosstalk of the PMMA CFB. **(a)** Field existing at the beginning of propagation, corresponding to a multimode launched field in the central core. **(b)** Field existing at the end of propagation (1 m). Scale bars in **(a-b)** are 10  $\mu\text{m}$ . Adapted from “Supplementary Information” in [1].

According to the simulation results, 52.31% of the power remains in the excited core. The remaining power is distributed according to 27.17%, 14.45% and 6.07%, for the first, second and third neighbouring layers, respectively. This difference with the experimental result can be explained by the fact that in the simulation all the modes of the core are excited and, therefore, power cross-coupling is more likely.

Finally, in Fig. 9.13 the effect of cross coupling is shown when images are sent through 1 m of fibre without any bends. At the proximal end of the fibre three different shapes, corresponding to an off-centre cross (Fig. 9.13 **a**), four asymmetrically positioned elliptical dots (Fig. 9.13 **b**), and a capital letter “A” (Fig. 9.13 **c**), are illuminated by a plane wave with wavelength 515 nm. For this, as in the previous simulation, we have a 3D simulation model using BeamPROP on RSoft. In this case the 2D lattice is formed by a geometrical structure of the PMMA CFB such that it has a rectangular image region of  $612 \times 528 \mu\text{m}$  ( $X \times Y$ ). The total number of simulated cores is 2,500. The rest of the simulation parameters are identical to the previous one.

## 9.6 Imaging

In this section, the SPIM probe is used to verify that the conclusions drawn during the characterisation process result in adequate imaging performance. For this purpose, both a tissue phantom and a human lung tissue are used. Previously, the processing of the images acquired in the experiments is shown and detailed.

### 9.6.1 Image processing

The data consist of images of circular fibres captured in a rectangular format such that there is clipping of the fibre diameter in the horizontal and vertical direction (see Fig. 9.14). The subset

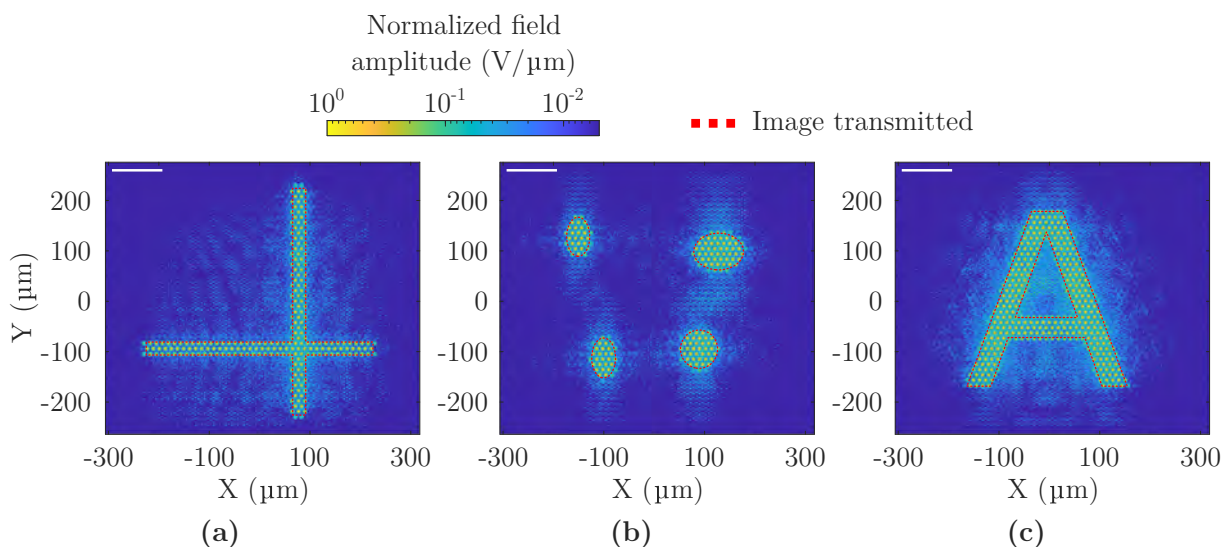


**Figure 9.13.** Simulation of the transmission of an image along a 1 m long MCL-1500-1.75 imaging fibre. The existing field at the distal end of the fibre is superimposed with the contour of the transmitted images (dotted red lines). The transmitted images are an **(a)** off-centre cross, **(b)** four asymmetrically positioned elliptical dots, and **(c)** a capital letter “A”. Scale bars in **(a-c)** are 100 μm.

## 9.6. Imaging

of fibre cores used for excitation in the SPIM case were excluded from the analysis below, as well as the corresponding cores in the WF case. The array of remaining cores, the imaging cores, are referred to collectively below as the fibre FOV. All images were acquired with a monochrome sensor and 8-bit depth in each pixel ( $L = 8$ ). The mathematical notation of each image is shown in Equation 9.8.

$$\mathbf{I}_\alpha \in \mathbb{Z}^{M \times N} : I_\alpha(x, y) \in [0, 2^L - 1] \subset \mathbb{Z}_0^+, \quad \forall \{x \in X, y \in Y\}, \quad (9.8)$$

where  $\alpha$  can refer to the raw image ( $\alpha = r$ ), background image ( $\alpha = b$ ), subtracted image ( $\alpha = s$ ), contrast-optimised image ( $\alpha = c$ ), or filtered image ( $\alpha = f$ ). Likewise,  $X = [1, N] \subset \mathbb{Z}$ , and  $Y = [1, M] \subset \mathbb{Z}$ , where  $N$  and  $M$  refer to the width and height in pixels of the image, respectively. In this case,  $N = 2048$  and  $M = 1536$ .

For visualisation of image data contained in Figs. 9.14, and 9.16, image processing was carried out as follows. The acquired background ( $\mathbf{I}_b$ ) was subtracted from the corresponding raw image ( $\mathbf{I}_r$ ), obtaining  $\mathbf{I}_s$  (Equation 9.9),

$$\mathbf{I}_s = \mathbf{I}_r - \mathbf{I}_b. \quad (9.9)$$

The contrast within the fibre FOV in  $\mathbf{I}_s$  was then enhanced by performing a linear transform of the pixel values, while maintaining the “zero” value, to obtain  $\mathbf{I}_c$ . To determine this transform, we established a “useful” maximum pixel value contained within the fibre FOV,  $l_{adj}$ , which we later used to adjust the image while ignoring dead or anomalously high-valued pixels. For the calculation of  $l_{adj}$ , a histogram of the fibre FOV within  $\mathbf{I}_s$ , defined as  $\mathbf{H}_s$ , was taken. Then, defining  $l_c$  as the modal value within  $\mathbf{H}_s$  we determined  $l_{adj}$  as the maximum pixel value that satisfies  $H_s(l_{adj}) \geq 0.01 \cdot H_s(l_c)$ .

We then apply a linear transform on  $\mathbf{I}_s$  to obtain  $\mathbf{I}_c$  according to Equation 9.10,

$$I_c(x, y) = \begin{cases} (I_s)_{min}, & I_s(x, y) < (I_s)_{min}. \\ \frac{2^L - 1 - (I_s)_{min}}{l_{adj} - (I_s)_{min}} [I_s(x, y) - (I_s)_{min}] + (I_s)_{min}, & (I_s)_{min} \leq I_s(x, y) \leq l_{adj}. \\ 2^L - 1, & I_s(x, y) > l_{adj}. \end{cases} \quad (9.10)$$

In this way, the “zero” value in the fibre FOV is maintained while maximising contrast enhancement of useful information in the image.

Finally, to reduce the prominence of the core pattern in the displayed image, a two-dimensional Weierstrass transform (Gaussian blur with standard deviation  $\sigma = 4$ ) was applied [49], resulting in image ( $\mathbf{I}_f$ ). Figures 9.14, and 9.16 contain processed images ( $\mathbf{I}_f$ ). As can be seen, the computational burden of image processing is significantly light.

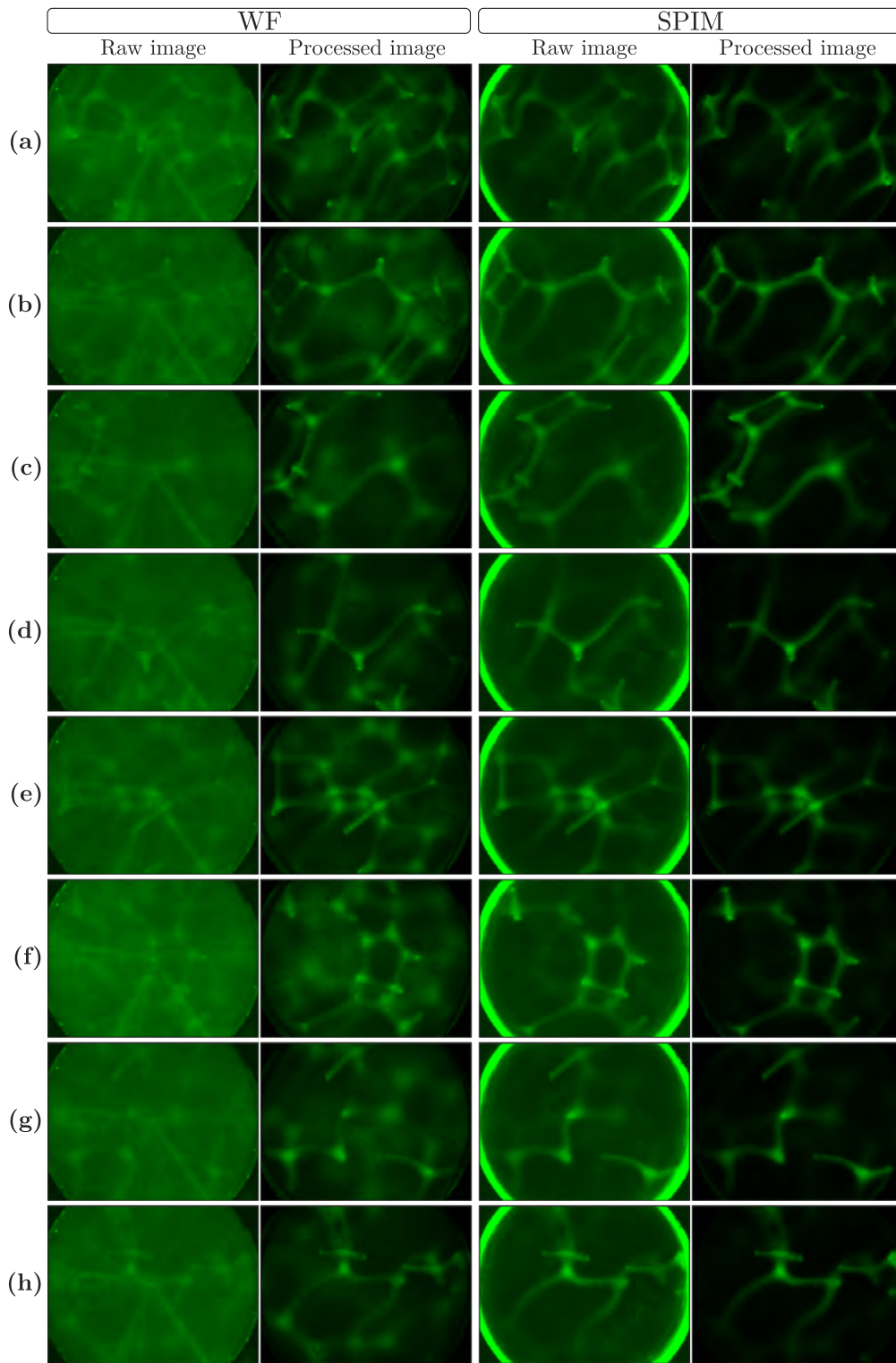


**Figure 9.14.** Widefield and SPIM images showing improved contrast and a reduction of out-of-focus features. (a-h) Corresponding FOVs acquired in WF and SPIM modality. Raw images demonstrate the strong fibre fluorescence which is present in the WF case. The clear ring present in the raw SPIM images is backscattered fibre fluorescence as a result of pumping the excitation light down these cores. Processed images demonstrate qualitatively improved imaging using the SPIM probe. Scale bar is 500  $\mu\text{m}$ . Evaluation of the images (a-d) is shown in Fig. 9.15. Adapted from [1].

### 9.6.2 Evaluation with a tissue phantom

Image characterisation was performed using a polymer sponge (yellow dish sponge) which has a loosely-packed strand structure. The distal end of the CFB and the tissue phantom were secured to separate 3-axis translation stages (MBT616D, Thorlabs), providing a way to precisely locate a FOV and maintain it through sequential image acquisitions. In SPIM/WF mode, the power of the 485 nm laser was set to 1.6 mW as measured between the objective and the proximal fibre face. With the distal end of the CFB retracted from the tissue phantom and non-reflective black card placed between the CFB and the phantom, a background image was taken. The distal end of the CFB was then translated to make contact with the tissue phantom and another image was acquired. Without moving the CFB or the tissue phantom, the fibred laser was coupled to the WF/SPIM illumination path and the dichroic mirror was rotated to flood/ring illuminate the proximal end of the CFB. The laser output power was adjusted, if needed, to achieve 1.6 mW measured between the objective and the proximal fibre face and an image of the phantom was acquired. The CFB was then retracted, black card was used to block the extended light path between the CFB and the phantom, and a background image was acquired. This process thus resulted in a data set containing four images: a FOV image and a background image pair in both SPIM and WF modality. Images were taken with a 200 ms exposure time and a detector gain of 15 dB.

Representative examples of a tissue phantom imaged in both WF and SPIM modality are shown in Fig. 9.14. Raw WF and SPIM images of each FOV are given to demonstrate the significant fluorescence background originating from the PMMA CFB cores. In the WF case, it can be seen that this fluorescence background is severe and obscures many of the image features. Subtraction of the background improves visibility of image features but does not minimise the presence of out-of-focus features within the FOV.

Quantitative evaluation of the tissue phantom images is shown in Fig. 9.15. Line profiles were taken on each of the (a-d) images in a data set using ImageJ [50]. Any displacement of the relative position of the fibre within the image frame was accounted for to ensure that lines were drawn through corresponding image scenes without lateral translation. Any data sets where the phantom itself had moved during data collection were discarded. The data were plotted after being smoothed by a Savitzky-Golay filter [51] with a window-length of 29 and a polynomial order of 2. The filter parameters were determined empirically such that the fibre core pattern present in the data was minimised while preserving the apparent relative signal-to-noise ratio between WF and SPIM data.

Each subfigure contains three plots: (i) The left plot represents a WF image. (ii) The middle plot represents a SPIM image of the same FOV. In these plots, line profiles of the measured background are shown as yellow dashed lines, raw images as orange dotted lines, and images with background subtracted as blue solid lines. (iii) The right plot compares WF (red dotted line) and SPIM (purple solid line) after background subtraction and normalisation. In Fig. 9.15 **a** and **b** random pairs of WF and SPIM images were selected and horizontal line profiles were drawn through the FOV. Several observations can be noted. (i) The measured background in the WF case is higher than in the SPIM case (yellow dashed lines). Furthermore, the background within the SPIM FOV was comparable to the measured camera background itself, except for an uptick in background within  $\sim 100 \mu\text{m}$  of the excitation ring of cores, as can be seen at the

extreme ends of the line profiles. (ii) Out-of-focus features, indicated by grey arrows in images and grey fill in plots, are diminished in the SPIM case. This is particularly clear when comparing normalised WF and SPIM line profiles (red dashed line and purple solid line, respectively). (iii) Signal-to-noise is improved in the SPIM case in comparison to the WF case. In Fig. 9.15 c and d, line profiles within the FOV were preferentially chosen to include out-of-focus features which are clearly present in the WF image and minimised in the SPIM image. Again, grey arrows indicate out-of-focus features in the inset images which are represented in the grey fill regions of the plots. From these results, it is clear that the SPIM probe results in higher contrast images with a reduction in out-of-focus image features.

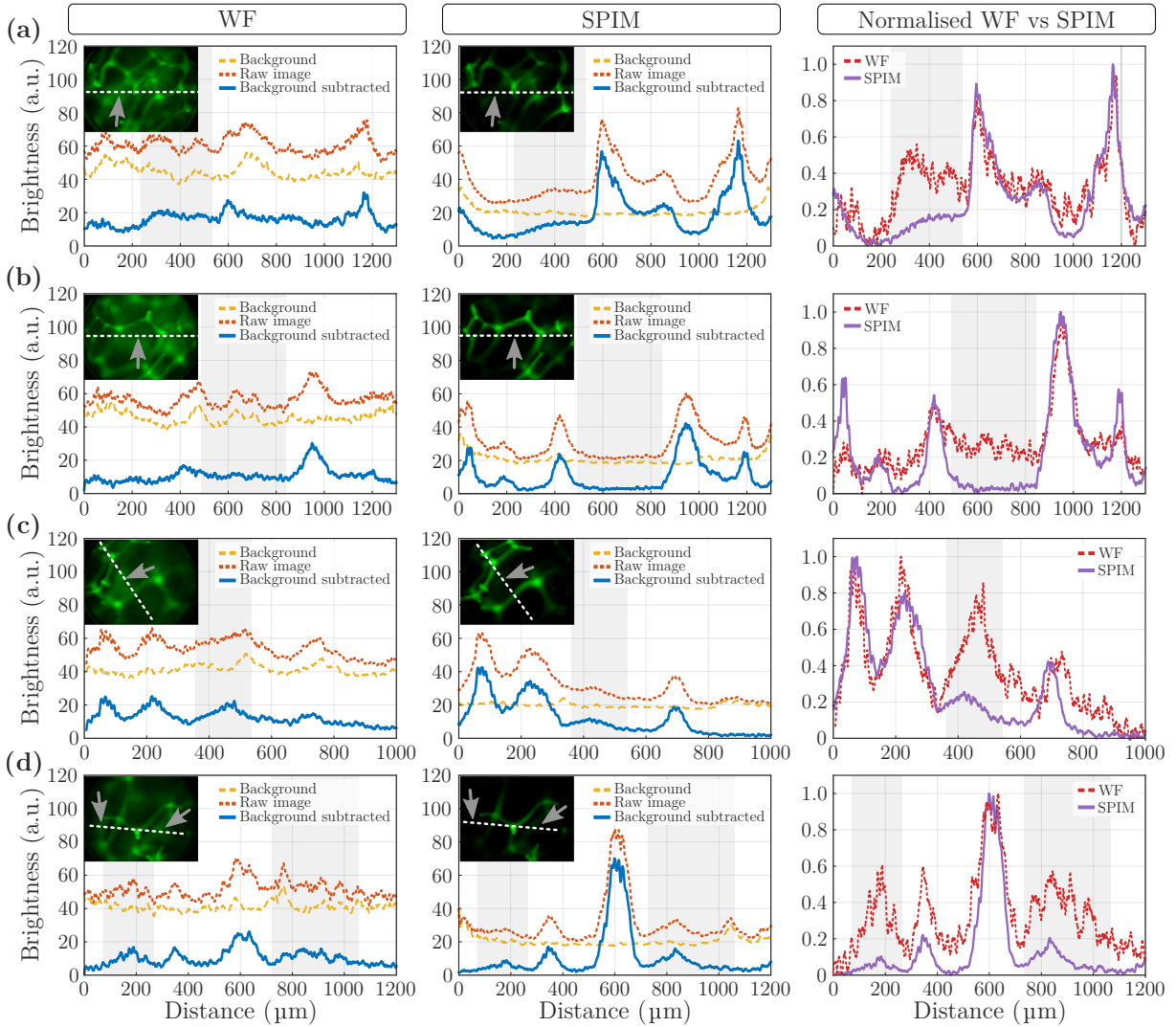


**Figure 9.15.** Evaluation of WF and SPIM images. (a-d) Line profiles across images shown in Fig. 9.14 a-d demonstrate reduced out-of-focus background and improved contrast of SPIM. Insets show image and line plotted (dashed white line). (Left) and (middle) WF and SPIM image, respectively, with measured background (yellow dashed line), raw image (orange dotted line) and image with subtracted background (blue solid line). (right) Normalised WF (red dashed line) and SPIM (purple solid line) line profiles after background subtraction. Grey fill in each plot corresponds to areas shown by grey arrows where background features are less visible in SPIM. Brightness and contrast of inset images have been adjusted for visibility. Line profiles were taken on raw data and then smoothed using a Savitzky-Golay filter (window=29, polynomial order=2). Adapted from [1].

### 9.6.3 Demonstration in *ex vivo* human lung

Finally, as a proof-of-concept demonstrator, we acquired images from human lung tissue at the Queen’s Medical Research Institute (QMRI) in Edinburgh (UK), within the Translational Healthcare Technologies Group. This was done with both excised lung tissue and whole ventilated *ex vivo* lungs, whereby the SPIM probe was delivered into the alveolar space. For the former, a few centimetres of tissue was excised from a lower lobe and placed in a dish. The tissue was punctured as necessary to gain access to the alveolar space. Images were acquired at 200 ms exposure (5 fps) with a detector gain of 15 dB in sets of 200 images. Fibre background images were taken before and after each 200 image set. For the latter, a pair of whole *ex vivo* human lungs were mechanically ventilated (Dräger Savina 300) by securing the ventilator endotracheal tube within the trachea. The SPIM probe was delivered via the endotracheal tube and passed into various regions of the distal lung by an operator, using real-time SPIM probe platform imaging for guidance. Images were acquired at 150 ms exposure (7 fps) with a detector gain of 15 dB in sets of 1,000 images. Fibre background images were taken before and after each 1,000 image set.

Figure 9.16 shows various frames from video capture of excised tissue imaged on the benchtop (Fig. 9.16 a) and of whole lungs imaged via the trachea (Fig. 9.16 b) (see also supplementary videos in [4]). Without the use of exogenous fluorophores, we were able to visualise alveolar tissue in real-time (either 5 fps or 7 fps) using the SPIM probe platform. Due to the dynamic nature of the experiment, it was not possible collect comparable FOVs in WF and SPIM modality. A full quantitative comparative study of the SPIM probe with a WF system is out of the scope of this work, but will be pursued in future.

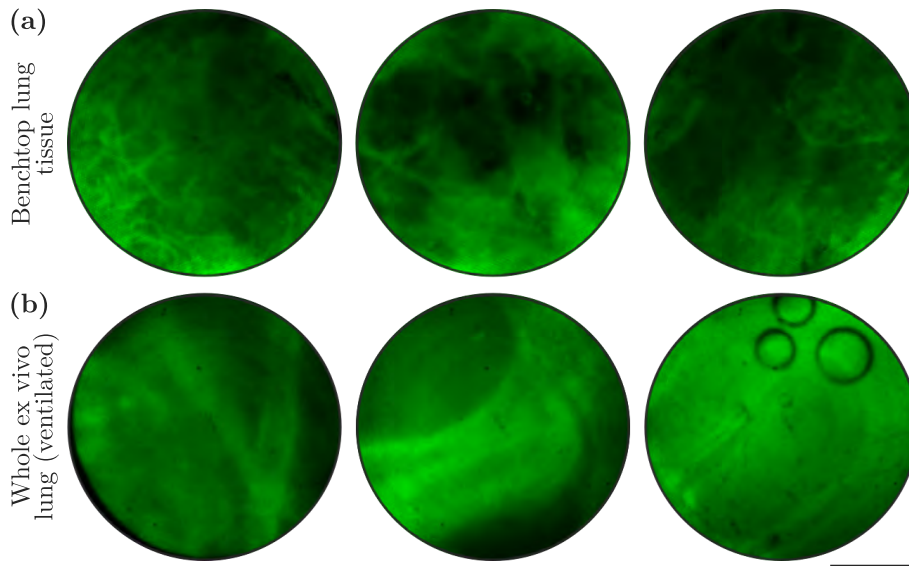


**Figure 9.16.** Representative examples of *ex vivo* human lung tissue. (a) Lung tissue sample imaged on the benchtop using the SPIM probe at 5 fps. (b) Mechanically ventilated, whole *ex vivo* human lungs imaged through the SPIM probe at 7 fps. The alveolar space is reached via a transbronchial pass. Images and videos have been processed as described in “Image processing” subsection. Scale bar is 500  $\mu\text{m}$ . Adapted from [1].

## 9.7 Discussion

In this work, we developed a fused silica end-cap to enable SPIM through a fibre while maintaining a form factor conducive to endoscopic deployment. Our SPIM platform has two key strengths. Firstly, it avoids the effect of PMMA fibre core fluorescence (when pumped with blue light) by using separate excitation and imaging cores. Secondly, it reduces the appearance of out-of-focus features in an imaged sample, which would otherwise decrease image contrast.

As measured, the fluorescence emitted from cores of a PMMA CFB is undesirable. The fluorescence spectrum (Fig. 9.8 a) reveals several strong emission peaks within the typical endogenous fluorescence imaging window ( $\sim 500 \text{ nm} - 600 \text{ nm}$ ). Careful selection of filters could result in removal of these peaks from the images, but with a severe loss of signal. Moreover, regions of minima between the measured emission peaks are still significantly higher than the measured emission from the silica fibre within the same wavelength range. It is important to note the effect of this fibre fluorescence in images. When used in WF mode, the fluorescence emission of the PMMA CFB can be thought of as a DC component in the acquired images. Removing this background is trivial, as we did in Fig. 9.14. However, the fluorescence background adds noise to the image, which is not removed through background subtraction, and can be seen in Fig. 9.15. Thus, using separate cores for excitation and collection is a superior approach for improving the usability of PMMA CFBs. Furthermore, due to the unusually large diameter of polymer fibre, it is possible to subdivide the core array in this way without significantly compromising the FOV. We allocated  $\sim 2,300$  cores to the excitation path ( $\sim 18\%$  of the total cores), leaving a sizable  $1.36 \text{ mm}$  diameter imaging window ( $\sim 82\%$  of the total cores). This is significantly larger than many commercial silica CFBs, for example the Confocal Miniprobes™ range of imaging fibres with FOVs in the range of  $240 \mu\text{m} - 600 \mu\text{m}$  (Mauna Kea Technologies, Paris, France).

Our investigation found that despite the uniformity of the core pattern in the PMMA CFB and the fact that the  $10.5 \mu\text{m}$  cores supported numerous modes,  $66.3\% \pm 2.4\%$  of the light coupled into one core of the PMMA CFB remained confined to that core over a  $1 \text{ m}$  length of fibre (Fig. 9.11 c). The remaining  $\sim 33.7\%$  power was coupled to neighboring cores, which is similar to the results reported for silica CFBs. Hence, we can conclude that image degradation due to core crosstalk is not a more significant issue when using the PMMA CFB than when using a silica fibre [20, 21]. We further supported this conclusion with BPM simulations of rectangular image regions measuring  $612 \times 528 \mu\text{m}$ , where we simulated the transmission of various known shapes over  $1 \text{ m}$  of imaging fibre with the same characteristics as the one used experimentally (MCL-1500-1.75, Asahi Kasei). As depicted in Fig. 9.13, although image contrast is slightly reduced, macroscopic tissue structures in a human lung tissue could still be clearly distinguished, as demonstrated experimentally (Fig. 9.16).

Simulation data show our SPIM end-cap results in good confinement of excitation light in the end-cap front recess (Fig. 9.9 b). Specifically, when integrated over the  $170 \mu\text{m}$  corresponding to the depth of the front recess of the end-cap, the power is  $\sim 2.97$  times greater than in the corresponding propagation distance in the WF case. Furthermore, an intensity decay of  $20 \text{ dB}$  is achieved in just  $\sim 0.7 \text{ mm}$  (Fig. 9.9 c), enabling the optical sectioning capabilities seen here. These results bear out in our comparison of image feature contrast in equivalent WF and SPIM FOVs of a tissue phantom. We selected line profiles through these images and revealed that,

## 9.8. Conclusions

in addition to a reduction in noise as discussed above, the prominence of out-of-focus features is decreased in SPIM images (Fig. 9.15). Additionally, using an *ex vivo* human lung model (Fig. 9.16), we demonstrated that the SPIM probe platform operates with sufficient excitation and collection efficiency to visualise tissue fluorescence *in situ* without the use of any exogenous fluorophores.

Underpinning several of our choices in this work was the goal of achieving a high performance fibre-based imaging probe without high cost. Silica CFBs are available direct from manufacturers, such as Fujikura [52], for  $\sim$  \$100s USD per metre (FIGH-30-650S, \$575 USD per metre). Many of the fabrication steps of the SPIM probe are scalable. Multiple end-caps can be inscribed in a single glass substrate, decreasing both fabrication time and cost. Further reduction in inscription time could be achieved by adopting laser beam shaping techniques [53]. Likewise, etching and silver coating processes can be performed in batches. With appropriate scaling, the manufacturing costs of the end-cap can be considered practically negligible compared to the price of PMMA fibre ( $\sim$  \$30 USD per metre [54]). It is therefore conceivable to consider, even taking into account future regulatory costs associated with translation of a device to the clinic, that such a polymer SPIM probe holds potential as a low-cost, single-use, disposable device. As such, we have avoided the need to overcome challenges related to sterilisation processes, which may add substantial cost or be impossible to perform. For example, while the fused silica end-cap could tolerate an autoclave procedure without issue, the PMMA fibre is irreversibly damaged by temperatures above 60–70 °C and would not survive the autoclaving process. PMMA is routinely used within microfluidics contexts and sterilisation with ethylene oxide [55] could be a viable pathway towards re-usability, although this is beyond the scope of the work.

Finally, we identify several potential areas of improvement. We observed trapped air during *ex vivo* lung imaging (Fig. 9.16 **b** right). Although the air could be dispersed with gentle agitation of the SPIM probe from outside of the lung, small notches integrated in the perimeter of the end-cap design could alleviate this issue without much disruption to the excitation path. Some imaging targets/tissues may benefit from a tighter illumination plane and therefore higher fidelity optical sectioning. This could be achieved by reducing the thickness of the ring of cores used for excitation, provided sufficient illumination is preserved overall. Along similar lines, dynamically addressing separate, thin rings of cores of different diameters, corresponding to a change in the depth of the illumination plane, could allow us to achieve Z-stacking of the FOV (with a reduced acquisition time compared with the current SPIM arrangement).

## 9.8 Conclusions

To summarise, we demonstrated a powerful new approach to enable selective plane illumination microscopy using polymer coherent fibre bundles. This approach exploits an ultrafast laser fabricated silica-glass end cap that was passively aligned onto the distal end of the polymer CFB, and which circumvents the issue of autofluorescence from the polymer CFBs by spatially separating the pump delivery and fluorescence imaging paths. It was also revealed that appearance of out-of-focus features in an imaged sample is decreased.

We believe that our technique has the potential to be an enabling technology for cost-effective microendoscopes in many applications, including FBE $\mu$  of the respiratory system. COVID-19

has demonstrated we urgently need new safe and effective therapies for respiratory infections, and polymer imaging fibres can image across a multi-mm field-of-view while maintaining great flexibility, thus allowing access to the acinar units in the distal lung, providing a view of macroscopic tissue structures to observe cellular signatures. Working with Prof. K. Dhaliwal, Director of the Pandemic Science Hub at the University of Edinburgh, we successfully demonstrated that this technology facilitates high quality endomicroscopic widefield imaging of human lung tissues that are free of background autofluorescence signals from the polymer CFB, opening a new route to enable their exploitation in clinical and experimental medicine applications.

## References

- [1] Roldán-Varona, P. *et al.*, “Selective plane illumination optical endomicroscopy with polymer imaging fibers,” *APL Photonics*, vol. 8, no. 1, p. 016 103, Jan. 2023. DOI: 10.1063/5.0130486.
- [2] Roldán-Varona, P. *et al.*, “Selective Plane Illumination Optical Endomicroscopy with Polymer Imaging Fibres,” in *Conference on Lasers and Electro-Optics*, Optica Publishing Group, 2022. DOI: 10.1364/cleo\_si.2022.sm31.2.
- [3] Parker, H. E. *et al.*, “Selective Plane Illumination Fluorescence Endomicroscopy using a Polymer Imaging Fiber and an End-cap,” in *Biophotonics Congress: Biomedical Optics 2022 (Translational, Microscopy, OCT, OTS, BRAIN)*, Optica Publishing Group, 2022. DOI: 10.1364/translational.2022.tw1b.6.
- [4] Roldán-Varona, P., Ross, C., Thomson, R. R., Tanner, M. G., and Parker, H., *Data supporting paper: Selective Plane Illumination Optical Endomicroscopy with Polymer Imaging Fibres*, 2022. DOI: 10.17861/31F319C0-66EB-41B0-A586-6F2480C85A47.
- [5] Orth, A., Ploschner, M., Wilson, E. R., Maksymov, I. S., and Gibson, B. C., “Optical fiber bundles: Ultra-slim light field imaging probes,” *Science Advances*, vol. 5, no. 4, Apr. 2019. DOI: 10.1126/sciadv.aav1555.
- [6] Flusberg, B. A., Cocker, E. D., Piyawattanametha, W., Jung, J. C., Cheung, E. L. M., and Schnitzer, M. J., “Fiber-optic fluorescence imaging,” *Nature Methods*, vol. 2, no. 12, pp. 941–950, Nov. 2005. DOI: 10.1038/nmeth820. [Online]. Available: <https://doi.org/10.1038/nmeth820>.
- [7] Perperidis, A., Dhaliwal, K., McLaughlin, S., and Vercauteren, T., “Image computing for fibre-bundle endomicroscopy: A review,” *Medical Image Analysis*, vol. 62, p. 101 620, 2020, ISSN: 1361-8415. DOI: <https://doi.org/10.1016/j.media.2019.101620>. [Online]. Available: <https://www.sciencedirect.com/science/article/pii/S136184151830639X>.
- [8] Sonn, G. A. *et al.*, “Optical biopsy of human bladder neoplasia with in vivo confocal laser endomicroscopy,” en, *Journal of Urology*, vol. 182, no. 4, pp. 1299–1305, Oct. 2009. DOI: 10.1016/j.juro.2009.06.039. [Online]. Available: <https://doi.org/10.1016/j.juro.2009.06.039>.
- [9] Liu, J.-J., Droller, M. J., and Liao, J. C., “New optical imaging technologies for bladder cancer: Considerations and perspectives,” en, *Journal of Urology*, vol. 188, no. 2, pp. 361–368, Aug. 2012. DOI: 10.1016/j.juro.2012.03.127. [Online]. Available: <https://doi.org/10.1016/j.juro.2012.03.127>.
- [10] Polglase, A. L., McLaren, W. J., Skinner, S. A., Kiesslich, R., Neurath, M. F., and Delaney, P. M., “A fluorescence confocal endomicroscope for in vivo microscopy of the upper- and the lower-GI tract,” *Gastrointestinal Endoscopy*, vol. 62, no. 5, pp. 686–695, Nov. 2005. DOI: 10.1016/j.gie.2005.05.021. [Online]. Available: <https://doi.org/10.1016/j.gie.2005.05.021>.
- [11] Fugazza, A. *et al.*, “Confocal Laser Endomicroscopy in Gastrointestinal and Pancreatobiliary Diseases: A Systematic Review and Meta-Analysis,” *BioMed Research Interna-*

- tional*, vol. 2016, pp. 1–31, 2016. DOI: 10.1155/2016/4638683. [Online]. Available: <https://doi.org/10.1155/2016/4638683>.
- [12] Krishna, S. G. *et al.*, “EUS-guided confocal laser endomicroscopy: Prediction of dysplasia in intraductal papillary mucinous neoplasms (with video),” *Gastrointestinal Endoscopy*, vol. 91, no. 3, 551–563.e5, Mar. 2020. DOI: 10.1016/j.gie.2019.09.014. [Online]. Available: <https://doi.org/10.1016/j.gie.2019.09.014>.
- [13] Quang, T. *et al.*, “A tablet-interfaced high-resolution microendoscope with automated image interpretation for real-time evaluation of esophageal squamous cell neoplasia,” *Gastrointestinal Endoscopy*, vol. 84, no. 5, pp. 834–841, Nov. 2016. DOI: 10.1016/j.gie.2016.03.1472. [Online]. Available: <https://doi.org/10.1016/j.gie.2016.03.1472>.
- [14] Pierce, M. C., Vila, P. M., Polydorides, A. D., Richards-Kortum, R., and Anandasabapathy, S., “Low-Cost Endomicroscopy in the Esophagus and Colon,” *American Journal of Gastroenterology*, vol. 106, no. 9, pp. 1722–1724, Sep. 2011. DOI: 10.1038/ajg.2011.140. [Online]. Available: <https://doi.org/10.1038/ajg.2011.140>.
- [15] Su, P. *et al.*, “Efficacy of confocal laser endomicroscopy for discriminating colorectal neoplasms from non-neoplasms: A systematic review and meta-analysis,” en, *Colorectal Disease*, vol. 15, no. 1, e1–12, Jan. 2013. DOI: 10.1111/codi.12033. [Online]. Available: <https://doi.org/10.1111/codi.12033>.
- [16] Mills, B. *et al.*, “Molecular detection of Gram-positive bacteria in the human lung through an optical fiber-based endoscope,” *European Journal of Nuclear Medicine and Molecular Imaging*, vol. 48, no. 3, pp. 800–807, Sep. 2020. DOI: 10.1007/s00259-020-05021-4. [Online]. Available: <https://doi.org/10.1007/s00259-020-05021-4>.
- [17] Wellikoff, A. S., Holladay, R. C., Downie, G. H., Chaudoir, C. S., Brandi, L., and Turbat-Herrera, E. A., “Comparison of in vivo probe-based confocal laser endomicroscopy with histopathology in lung cancer: A move toward optical biopsy,” *Respirology*, vol. 20, no. 6, pp. 967–974, Jun. 2015. DOI: 10.1111/resp.12578. [Online]. Available: <https://doi.org/10.1111/resp.12578>.
- [18] Thiberville, L. *et al.*, “Human in vivo fluorescence microimaging of the alveolar ducts and sacs during bronchoscopy,” en, *European Respiratory Journal*, vol. 33, no. 5, pp. 974–985, May 2009. DOI: 10.1183/09031936.00083708. [Online]. Available: <https://doi.org/10.1183/09031936.00083708>.
- [19] Hirschowitz, B., “Endoscopic examination of the stomach and duodenal cap with the fiberscope,” *The Lancet*, vol. 277, no. 7186, pp. 1074–1078, May 1961. DOI: 10.1016/S0140-6736(61)92308-x. [Online]. Available: [https://doi.org/10.1016/S0140-6736\(61\)92308-x](https://doi.org/10.1016/S0140-6736(61)92308-x).
- [20] Perperidis, A. *et al.*, “Characterization and modelling of inter-core coupling in coherent fiber bundles,” *Optics Express*, vol. 25, no. 10, pp. 11932–11953, May 2017. DOI: 10.1364/oe.25.011932. [Online]. Available: <https://doi.org/10.1364/oe.25.011932>.
- [21] Parker, H. E., Perperidis, A., Stone, J. M., Dhaliwal, K., and Tanner, M. G., “Core crosstalk in ordered imaging fiber bundles,” *Optics Letters*, vol. 45, no. 23, pp. 6490–6493, Nov. 2020. DOI: 10.1364/ol.405764. [Online]. Available: <https://doi.org/10.1364/ol.405764>.

## References

- [22] Ortega-Quijano, N., Fanjul-Vélez, F., and Arce-Diego, J. L., “Optical crosstalk influence in fiber imaging endoscopes design,” *Optics Communications*, vol. 283, no. 4, pp. 633–638, Feb. 2010. DOI: 10.1016/j.optcom.2009.10.075. [Online]. Available: <https://doi.org/10.1016/j.optcom.2009.10.075>.
- [23] Stone, J. M., Wood, H. A. C., Harrington, K., and Birks, T. A., “Low index contrast imaging fibers,” *Optics Letters*, vol. 42, no. 8, p. 1484, Apr. 2017. DOI: 10.1364/ol.42.001484. [Online]. Available: <https://doi.org/10.1364/ol.42.001484>.
- [24] Krstajic, N. *et al.*, “Low-cost high sensitivity pulsed endomicroscopy to visualize tricolor optical signatures,” en, *Journal of Biomedical Optics*, vol. 23, no. 7, pp. 1–12, Jul. 2018. DOI: 10.1117/1.JBO.23.7.076005. [Online]. Available: <https://doi.org/10.1117/1.JBO.23.7.076005>.
- [25] Hong, X., Nagarajan, V. K., Mugler, D. H., and Yu, B., “Smartphone microendoscopy for high resolution fluorescence imaging,” en, *Journal of Innovative Optical Health Sciences*, vol. 09, no. 05, p. 1650046, Sep. 2016. DOI: 10.1142/S1793545816500462. [Online]. Available: <https://doi.org/10.1142/S1793545816500462>.
- [26] Parker, H. E. *et al.*, “Fibre-based spectral ratio endomicroscopy for contrast enhancement of bacterial imaging and pulmonary autofluorescence,” *Biomedical Optics Express*, vol. 10, no. 4, pp. 1856–1869, Mar. 2019. DOI: 10.1364/boe.10.001856. [Online]. Available: <https://doi.org/10.1364/boe.10.001856>.
- [27] Gmitro, A. F. and Aziz, D., “Confocal microscopy through a fiber-optic imaging bundle,” *Optics Letters*, vol. 18, no. 8, p. 565, Apr. 1993. DOI: 10.1364/ol.18.000565. [Online]. Available: <https://doi.org/10.1364/ol.18.000565>.
- [28] Jean, F., Bourg-Heckly, G., and Viellerobe, B., “Fibered confocal spectroscopy and multicolor imaging system for in vivo fluorescence analysis,” *Optics Express*, vol. 15, no. 7, p. 4008, 2007. DOI: 10.1364/oe.15.004008. [Online]. Available: <https://doi.org/10.1364/oe.15.004008>.
- [29] Hughes, M. and Yang, G.-Z., “Line-scanning fiber bundle endomicroscopy with a virtual detector slit,” en, *Biomedical Optics Express*, vol. 7, no. 6, pp. 2257–2268, Jun. 2016. DOI: 10.1364/B0E.7.002257. [Online]. Available: <https://doi.org/10.1364/B0E.7.002257>.
- [30] Zhang, H. and Ye, X., “The development and clinical application of microscopic endoscopy for in vivo optical biopsies: Endocytoscopy and confocal laser endomicroscopy,” en, *Photodiagnosis Photodynamic Therapy*, vol. 38, no. 102826, p. 102826, Mar. 2022. DOI: 10.1016/j.pdpdt.2022.102826. [Online]. Available: <https://doi.org/10.1016/j.pdpdt.2022.102826>.
- [31] Koucky, M. H. and Pierce, M. C., “Axial response of high-resolution microendoscopy in scattering media,” *Biomedical Optics Express*, vol. 4, no. 10, p. 2247, Sep. 2013. DOI: 10.1364/boe.4.002247. [Online]. Available: <https://doi.org/10.1364/boe.4.002247>.
- [32] Stelzer, E. H. K. *et al.*, “Light sheet fluorescence microscopy,” *Nature Reviews Methods Primers*, vol. 1, no. 1, Nov. 2021. DOI: 10.1038/s43586-021-00069-4. [Online]. Available: <https://doi.org/10.1038/s43586-021-00069-4>.
- [33] Engelbrecht, C. J., Voigt, F., and Helmchen, F., “Miniaturized selective plane illumination microscopy for high-contrast in vivo fluorescence imaging,” *Optics Letters*, vol. 35, no. 9,

- pp. 1413–1415, Apr. 2010. DOI: 10.1364/o1.35.001413. [Online]. Available: <https://doi.org/10.1364/o1.35.001413>.
- [34] Murayama, M., Pérez-Garci, E., Lüscher, H.-R., and Larkum, M. E., “Fiberoptic System for Recording Dendritic Calcium Signals in Layer 5 Neocortical Pyramidal Cells in Freely Moving Rats,” *Journal of Neurophysiology*, vol. 98, no. 3, pp. 1791–1805, Sep. 2007. DOI: 10.1152/jn.00082.2007. [Online]. Available: <https://doi.org/10.1152/jn.00082.2007>.
- [35] Sacher, W. D. *et al.*, “Implantable photonic neural probes for light-sheet fluorescence brain imaging,” *Neurophotonics*, vol. 8, no. 2, p. 025003, Apr. 2021. DOI: 10.1117/1.nph.8.2.025003.
- [36] Lin, N. C., Zhao, X., Hassan, S., Raghuram, A., Veeraraghavan, A., and Robinson, J. T., “Implantable integrated photonic probe for light sheet brain imaging in vivo,” in *Bio-photonics Congress 2021*, OSA, 2021. DOI: 10.1364/brain.2021.bm3b.3. [Online]. Available: <https://doi.org/10.1364/brain.2021.bm3b.3>.
- [37] Ross, C. A., MacLachlan, D. G., Choudhury, D., and Thomson, R. R., “Optimisation of ultrafast laser assisted etching in fused silica,” *Optics Express*, vol. 26, no. 19, pp. 24343–24356, Sep. 2018. DOI: 10.1364/oe.26.024343. [Online]. Available: <https://doi.org/10.1364/oe.26.024343>.
- [38] Haque, M., Lee, K. K. C., Ho, S., Fernandes, L. A., and Herman, P. R., “Chemical-assisted femtosecond laser writing of lab-in-fibers,” *Lab on a Chip*, vol. 14, no. 19, pp. 3817–3829, 2014. DOI: 10.1039/c4lc00648h.
- [39] Osellame, R., Hoekstra, H. J. W. M., Cerullo, G., and Pollnau, M., “Femtosecond laser microstructuring: An enabling tool for optofluidic lab-on-chips,” *Laser & Photonics Reviews*, vol. 5, no. 3, pp. 442–463, Feb. 2011. DOI: 10.1002/lpor.201000031.
- [40] Choudhury, D., Macdonald, J. R., and Kar, A. K., “Ultrafast laser inscription: Perspectives on future integrated applications,” *Laser & Photonics Reviews*, vol. 8, no. 6, pp. 827–846, 2014. DOI: 10.1002/lpor.201300195. [Online]. Available: <https://doi.org/10.1002/lpor.201300195>.
- [41] Gissibl, T., Thiele, S., Herkommer, A., and Giessen, H., “Two-photon direct laser writing of ultracompact multi-lens objectives,” *Nature Photonics*, vol. 10, no. 8, pp. 554–560, Jun. 2016. DOI: 10.1038/nphoton.2016.121. [Online]. Available: <https://doi.org/10.1038/nphoton.2016.121>.
- [42] Hu, Y. *et al.*, “All-Glass 3D Optofluidic Microchip with Built-in Tunable Microlens Fabricated by Femtosecond Laser-Assisted Etching,” *Advanced Optical Materials*, vol. 6, no. 9, p. 1701299, Feb. 2018. DOI: 10.1002/adom.201701299.
- [43] Wu, D., Xu, J., Niu, L.-G., Wu, S.-Z., Midorikawa, K., and Sugioka, K., “In-channel integration of designable microoptical devices using flat scaffold-supported femtosecond-laser microfabrication for coupling-free optofluidic cell counting,” *Light: Science & Applications*, vol. 4, no. 1, e228–e228, Jan. 2015. DOI: 10.1038/lsa.2015.1.
- [44] Gattass, R. R. and Mazur, E., “Femtosecond laser micromachining in transparent materials,” *Nature Photonics*, vol. 2, no. 4, pp. 219–225, Apr. 2008. DOI: 10.1038/nphoton.2008.47. [Online]. Available: <https://doi.org/10.1038/nphoton.2008.47>.

## References

- [45] Schaffer, C. B., Brodeur, A., and Mazur, E., “Laser-induced breakdown and damage in bulk transparent materials induced by tightly focused femtosecond laser pulses,” *Measurement Science and Technology*, vol. 12, no. 11, pp. 1784–1794, Oct. 2001. DOI: 10.1088/0957-0233/12/11/305. [Online]. Available: <https://doi.org/10.1088/0957-0233/12/11/305>.
- [46] Stuart, B. C., Feit, M. D., Herman, S., Rubenchik, A. M., Shore, B. W., and Perry, M. D., “Nanosecond-to-femtosecond laser-induced breakdown in dielectrics,” *Physical Review B*, vol. 53, no. 4, pp. 1749–1761, Jan. 1996. DOI: 10.1103/physrevb.53.1749. [Online]. Available: <https://doi.org/10.1103/physrevb.53.1749>.
- [47] Casamenti, E., Pollowini, S., and Bellouard, Y., “Few pulses femtosecond laser exposure for high efficiency 3D glass micromachining,” *Optics Express*, vol. 29, no. 22, pp. 35 054–35 066, Oct. 2021. DOI: 10.1364/oe.435163. [Online]. Available: <https://doi.org/10.1364/oe.435163>.
- [48] Thiberville, L., Moreno-Swirc, S., Vercauteren, T., Peltier, E., Cavé, C., and Bourg Heckly, G., “In vivo imaging of the bronchial wall microstructure using fibered confocal fluorescence microscopy,” *American journal of respiratory and critical care medicine*, vol. 175, no. 1, pp. 22–31, 2007. DOI: 10.1164/rccm.200605-6840C. [Online]. Available: <https://www.atsjournals.org/doi/abs/10.1164/rccm.200605-6840C>.
- [49] Hirschman, I. I. and Widder, D. V., *The convolution transform*. Courier Corporation, Mar. 2012, ISBN: 048644175X.
- [50] Schneider, C. A., Rasband, W. S., and Eliceiri, K. W., “NIH image to ImageJ: 25 years of image analysis,” en, *Nature Methods*, vol. 9, no. 7, pp. 671–675, Jul. 2012. DOI: 10.1038/nmeth.2089. [Online]. Available: <https://doi.org/10.1038/nmeth.2089>.
- [51] Virtanen, P. *et al.*, “SciPy 1.0: Fundamental Algorithms for Scientific Computing in Python,” *Nature Methods*, vol. 17, pp. 261–272, 2020. DOI: 10.1038/s41592-019-0686-2. [Online]. Available: <https://doi.org/10.1038/s41592-019-0686-2>.
- [52] <https://www.fujikura.co.uk/>, Accessed: 2022-09-05.
- [53] Thomson, R. R., Psaila, N. D., Bookey, H. T., Reid, D. T., and Kar, A. K., “Controlling the Cross-section of Ultrafast Laser Inscribed Optical Waveguides,” in *Femtosecond Laser Micromachining: Photonic and Microfluidic Devices in Transparent Materials*, Osellame, R., Cerullo, G., and Ramponi, R., Eds. Berlin, Heidelberg: Springer Berlin Heidelberg, 2012, pp. 93–125, ISBN: 978-3-642-23366-1. DOI: 10.1007/978-3-642-23366-1\_5. [Online]. Available: [https://doi.org/10.1007/978-3-642-23366-1\\_5](https://doi.org/10.1007/978-3-642-23366-1_5).
- [54] <https://i-fiberoptics.com/fiber-detail-asahi.php?id=3305&sum=162>, Accesed: 2022-09-01.
- [55] Yavuz, C., Oliaei, S. N. B., Cetin, B., and Yesil-Celiktas, O., “Sterilization of PMMA microfluidic chips by various techniques and investigation of material characteristics,” *The Journal of Supercritical Fluids*, vol. 107, pp. 114–121, Jan. 2016. DOI: 10.1016/j.supflu.2015.08.019.

# 10

## Molecular sensing with Bloch surface waves

---

<b>10.1 Surface waves</b> . . . . .	<b>206</b>
10.1.1 Surface plasmon polaritons (SPPs) . . . . .	207
10.1.2 Bloch surface waves (BSWs) . . . . .	207
<b>10.2 Circular dichroism spectroscopy</b> . . . . .	<b>210</b>
<b>10.3 1DPC for superchiral SWs</b> . . . . .	<b>211</b>
<b>10.4 Optofluidic platform</b> . . . . .	<b>212</b>
10.4.1 Design . . . . .	213
10.4.2 Fabrication . . . . .	215
<b>10.5 Experimental setup</b> . . . . .	<b>216</b>
<b>10.6 Preliminary measurements of molecular chirality</b> . . . . .	<b>218</b>
10.6.1 Chiral molecules . . . . .	218
10.6.2 Measurements . . . . .	218
<b>10.7 Conclusions</b> . . . . .	<b>220</b>
<b>References</b> . . . . .	<b>222</b>

---

**T**HIS chapter explores the promising field of molecular sensing, with a particular emphasis on the use of Bloch surface waves (BSWs). Optical sensors have become indispensable in various domains, notably in medical and life science applications, due to their ability to detect minuscule amounts of analytes. Among the potent tools in this regard are BSWs, which are generated on the surface of a one-dimensional photonic crystal (1DPC). BSWs share similarities with surface plasmon polaritons (SPPs) as both are evanescent surface waves employed in surface-enhanced spectroscopies. Yet, their differences offer diverse application potentials. Unlike SPPs, which are constrained to a metallic surface and a red-near infrared part of the spectrum, BSWs can be finely tuned across the visible-UV range, thereby enabling the investigation of resonant electronic states of molecules.

The chapter further presents an innovative photonic chip, fabricated using ultrafast laser technology, which incorporates a 1DPC. The design enhances the overlap of dispersion relations across a wide spectral range, thereby creating new opportunities in the field of molecular sensing. The work in this chapter is the result of a 3-month research stay at the Institute of Photonics and Nanotechnology (IFN, Istituto di Fotonica e Nanotecnologie) in Milan, part of the National Research Council of Italy (CNR, Consiglio Nazionale delle Ricerche), under the supervision of the researcher Rebeca Martínez-Vázquez. The presented work arises from the collaboration between IFN and the Department of Physics (DFIS) at Politecnico di Milano. The experimental measurements presented here are carried out by Erika Moggi and Paolo Biagioni, both from DFIS, while the fabrication of the photonics chip is performed by Rebeca Martínez Vázquez, from IFN, and the author of this thesis.

## 10.1 Surface waves

A surface wave (SW) represents a type of electromagnetic mode that travels along the boundary between two different media. Characteristically, SWs demonstrate a high level of localisation, with the greatest amplitude of their fields centred near the interface and decaying exponentially with increased distance from it [1, 2]. These waves have been explored in a vast array of materials and structural conditions, further emphasising their versatility and potential.

SWs have the unique ability to manipulate and confine light below the diffraction limit. This field localisation attribute and their unique surface sensitivity have spurred extensive research over recent decades. This has unlocked new opportunities for optical devices and applications including near-field imaging [3], sensing [4, 5], polarisation control [6], light-trapping [7, 8], and nano-guiding [9, 10].

Several kinds of SWs exist, each defined by unique attributes related to the permittivity or permeability of their constituent materials. Existing types of SWs can be grouped into the following categories [11]:

- Surface plasmons: require negative permittivity of one of the media in the interface.
- Bloch SWs: require periodic permittivity of one of the media along the interface.
- Tamm SWs: require periodic permittivity of one of the media truncated by the interface.
- Dyakonov SWs: require linear anisotropy of at least one medium.
- Surface solitons: require non-linear permittivity of one medium.
- Magnetic plasmon: require negative permeability of one medium.
- Other types: Dyakonov plasmons, 2D plasmon waves, surface phonon-polaritons, surface excitons-polaritons, topological SWs, among others.

The two most prevalent types of surface waves in the field of photonics are SPPs and BSWs. Both SWs have become established tools for molecular sensing and surface-enhanced spectroscopy [12, 13]. Brief overviews of these are presented below.

### 10.1.1 Surface plasmon polaritons (SPPs)

SPPs are electromagnetic surface waves that are resonantly coupled to the collective oscillations of electronic charge on the surface of a metal [14]. The excitation of SPPs requires two conditions to be met [14]. Firstly, the sum of the dielectric functions of the incident media ( $\epsilon_1(\omega)$ ) and the external media ( $\epsilon_2(\omega)$ ) must be less than zero (Equation 10.1). Secondly, the product of the dielectric functions must be negative (Equation 10.2).

$$\epsilon_1(\omega) + \epsilon_2(\omega) < 0, \quad (10.1)$$

$$\epsilon_1(\omega) \cdot \epsilon_2(\omega) < 0, \quad (10.2)$$

It is impossible to fulfil the aforementioned conditions with two materials that possess a positive real dielectric function. At least one of the materials must have a negative dielectric constant, which makes metals ideal candidates for satisfying these conditions.

In plasmonic applications, spectral regions are sought where interband transitions are absent, enabling electrons to be treated as free [15]. This characteristic makes metals such as gold optimal for utilisation in the red to near-IR part of the spectrum. A metal–dielectric interface can potentially guide a surface plasmon, but there is a requirement regarding the illumination geometry to excite an evanescent SW. Specifically, the incident beam must be TM polarised as TE polarised waves do not couple with the electron plasma oscillations at the metal surface [14].

### 10.1.2 Bloch surface waves (BSWs)

As mentioned earlier, a platform capable of sustaining SPPs requires a metallic layer, often using gold as a common choice. On the other hand, BSWs are generated at the surface of a truncated one-dimensional photonic crystal (see Fig. 10.1), which is a periodic multilayer structure composed of dielectric materials [17]. Photonic crystals are optical media that exhibit periodic changes in the refractive index. This periodicity of the dielectric function can occur in one (leading to 1DPC), two (2DPC), or three dimensions (3DPC). 1DPCs possess a simple structure but retain the advantages and features of photonic crystals in general. For instance, they can be designed to operate within specific wavelength ranges, exhibit a photonic band gap,

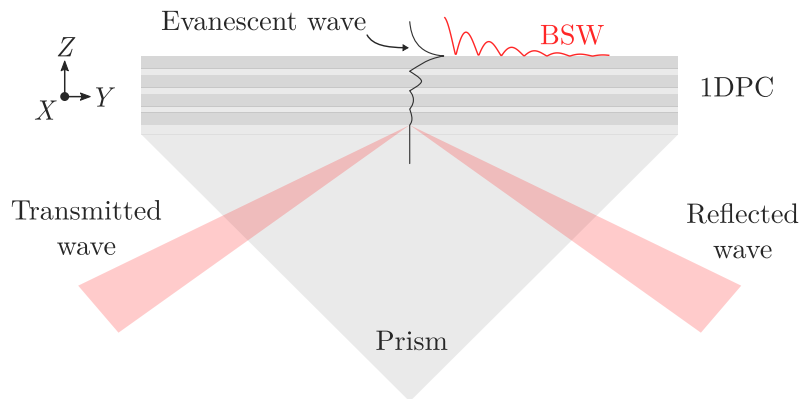


**Figure 10.1.** Illustration of the evanescent wave at the surface of a generic 1DPC in a Kretschmann configuration [16], and the BSW propagating through the interface between the two media.

## 10.1. Surface waves

and support localised modes in the presence of defects [6, 18, 19]. As depicted in Fig. 10.1, a general 1DPC can be seen as a stack of layers, homogeneous in the  $XY$  plane and periodic in the  $Z$  direction, with a certain refractive index contrast.

Modes associated with this particular geometry can be characterised using the Bloch form by the in-plane wavevector  $k_{\parallel}$ , the wavevector along the  $Z$  direction  $k_z$ , and the band number  $m$  [20]. The in-plane wavevector can take any value since the structure is homogeneous in the  $XY$  plane. On the other hand,  $k_z$  has a finite range of possible values. It is constrained within the so-called one-dimensional Brillouin zone, which has a dimension of  $2\pi/d$ , where  $d$  is the periodicity of the crystal over which  $k_z$  repeats.

When considering a homogeneous material, *i.e.*, there is no variation in the refractive index, and focusing on an electromagnetic wave propagating solely along the  $Z$  direction ( $k_{\parallel} = 0$ ), the allowed modes of propagation align with what is known as the light line [21]. The light line represents the boundary between the region where electromagnetic waves can propagate and the region where they cannot. The position and characteristics of the light line are determined by the dielectric function of the material:

$$\omega(k) = \frac{ck_z}{\sqrt{\epsilon}}, \quad (10.3)$$

where  $c$  represents the speed of light in a vacuum, while  $\epsilon$  is the dielectric function of the material through which light is propagating.

On the other hand, in the presence of a heterogeneous crystal composed of different materials with distinct dielectric functions, the band structure exhibits the appearance of a band gap

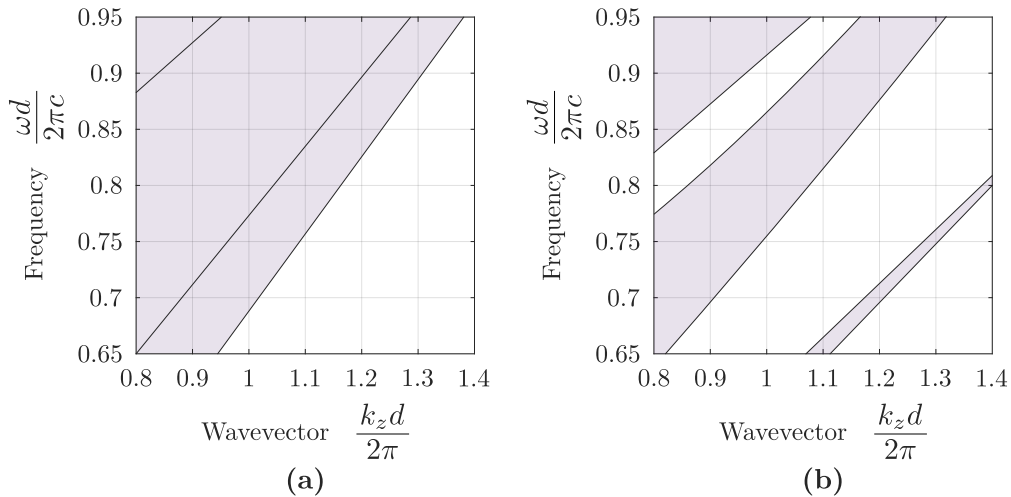


**Figure 10.2.** (a) Dispersion relation (frequency vs. wavevector) of a homogeneous material with a refractive index  $n = 1.45$ . The structure does not exhibit any band gap. (b) Dispersion relation of a 1DPC with a refractive index contrast of  $n_{high}/n_{low} = 1.4$ . The thickness of both materials is equal. The index contrast leads to the formation of a band gap, characterised by frequency ranges where no states exist. In both graphs, the shaded area represents the continuum of allowed bands where electromagnetic waves can propagate, while frequencies within the band gap correspond to evanescent waves. The bottom line is the light line. The MIT Photonic-Bands (MPB) package has been utilised to calculate the definite-frequency eigenstates of Maxwell's equations within a semi-infinite 1DPC. This computation was achieved by applying the supercell method [22] and the plane wave expansion (PWE) method [23].

(Fig. 10.2 b). This phenomenon is directly influenced by the periodic arrangement of the layers and the specific refractive indices of the materials utilised. When the crystal is illuminated with a frequency falling within the band gap, there are no electromagnetic modes, so the resulting wavevector becomes complex, indicating the presence of evanescent modes [24]. These modes experience a decay in amplitude as they propagate within the crystal (see Fig. 10.1). The imaginary part of  $k_z$  determines the length scale associated with the exponential decay in the evanescent wave, as illustrated in Fig. 10.1. By examining the dispersion relation depicted in Fig. 10.2, one can observe the contrast in the band structure between a homogeneous material and a 1DPC.

To achieve localised states at the surface (evanescent waves), two conditions must be met. Firstly, the frequency of the wave must fall within the band gap and be below the light line. Secondly, it is necessary to illuminate the crystal with an angle above the critical angle determined by the Snell's law. When the incident angle exceeds the critical angle, which corresponds to the total internal reflection condition, a complex wavevector  $\mathbf{k}$  is obtained [19]. In this case, the corresponding electromagnetic field exhibits exponential decay as it moves away from the surface of the 1DPC. It is also important to note that total internal reflection occurs when the refractive index of the incident medium is higher than the refractive index of the transmitting medium.

Consequently, the evanescent states under consideration are those that lie below the light line, and the surface wave generate a dip in the reflectivity spectrum [20, 25]. The characteristics of this resonance arise from the interplay between two factors: radiation leakage of the surface mode (radiation losses) and coupling efficiency [20]. When the 1DPC consists of an increased number of layers, the mode becomes narrower spectrally, but its coupling efficiency diminishes as well. Therefore, a compromise must be achieved between these two aspects. Additionally, the inclusion of additional periods in the structure introduces new guided modes, which manifest as weaker dips in the spectra.

Taking into account an illumination with a fixed angle ( $k_{\parallel} \neq 0$ ), the bands of modes polarised in the  $X$  direction (transverse magnetic, TM) or in the  $YZ$  plane (transverse electric, TE) are no longer degenerate, unlike the case when  $k_{\parallel} = 0$ . Consequently, there is no direct correlation between the dispersion relations of TE and TM modes. In general, these modes have different phase velocities during the propagation, indicating their distinct polarisation and propagation characteristics [6, 26].

### Overlapping dispersion relations for TE and TM modes

In the context of a one-dimensional photonic crystals, the reflectivity spectrum may initially suggest that the TE and TM modes exhibit the same dispersion relation [20]. However, upon closer examination at specific wavelengths, it becomes evident that the resonances differ for each mode. This distinction implies that with a perfectly periodic 1DPC, it is not possible to control the polarisation state of the combined surface mode (TE and TM) over a broad spectral range. Instead, the control is limited to adjusting the spectral position of the resonances independently.

In the field of molecular sensing and surface-enhanced spectroscopy, the ability to control the polarisation state of the combined surface mode is highly desirable. To achieve this, a custom-designed structure for the 1DPC is required, leading to overlapping dispersion relations for both

## 10.2. Circular dichroism spectroscopy

TE and TM modes [6, 19, 26]. The key aspect is ensuring that both surface modes possess the same phase velocity. Thus, by carefully engineering the 1DPC structure to achieve overlapping dispersion relations, the control and manipulation of polarisation states become feasible.

For example, the differential signal obtained from the simultaneous TE and TM modes can be utilised to detect the birefringence of a molecular layer situated on the surface of the 1DPC. This capability allows for the determination of molecular orientation within a broad spectral range. Additionally, the superposition of TE and TM modes enables circular dichroism spectroscopy, facilitating the study of molecular interactions and optical properties.

## 10.2 Circular dichroism spectroscopy

In recent years, the pharmaceutical and biochemical industry has recognised the growing importance of analysing and separating chiral molecules [27, 28]. Chiral objects, three-dimensional bodies that are asymmetrical and non-superimposable with its mirror image, play a significant role in various biochemical processes. Enantiomers, which are molecules of opposite chirality, have the same chemical composition and physical properties, except for their ability to rotate the plane of polarised light in opposite directions. Their chiral nature becomes apparent only in the presence of a chiral environment. This geometric characteristic is commonly observed in biomolecules, with DNA serving as a remarkable example [29, 30].

Circular dichroism (CD) is a widely used technique for studying chiral molecules, as it measures the difference in absorption between left and right circularly polarised light. Enantiomer discrimination often relies on CD as a key tool. Nevertheless, CD signals typically exhibit significantly lower intensity compared to standard achiral absorption spectroscopies. This poses a considerable challenge when analysing small quantities of chiral analytes [31], requiring specific approaches to enhance sensitivity and accuracy [32, 33].

In recent times, innovative *superchiral* methods have emerged to amplify the CD signal through the manipulation of the optical chirality of the electromagnetic field using nanostructured systems [34, 35]. The optical chirality ( $C$ ) represents the helicity (*handedness*) of an electromagnetic field, and is defined mathematically through the Equation 10.4.

$$C = -\frac{\epsilon_0\omega}{2}\text{Im}(\mathbf{E}^* \cdot \mathbf{B}), \quad (10.4)$$

where  $\mathbf{E}$  and  $\mathbf{B}$  represent the electric and magnetic fields at the molecule, respectively.  $\omega$  is the frequency of the electromagnetic field, and  $\epsilon_0$  is the permittivity of free space.

The enhancement of optical chirality beyond the values obtained with plane waves has led to the emergence of what is known as the *superchiral* surface wave. This term is now commonly used to describe electromagnetic fields that exhibit a higher degree of optical chirality compared to circularly polarised plane waves [36].

CD signals are characterised by the difference in absorptivity between left-handed ( $\mathcal{A}_L$ ) and right-handed ( $\mathcal{A}_R$ ) circularly polarised light:

$$\Delta\mathcal{A} = \mathcal{A}_L - \mathcal{A}_R = \log_{10}\left(\frac{I_L}{I_R}\right), \quad \text{with} \quad I = I_0 \cdot 10^{-\epsilon l c_{mol}}. \quad (10.5)$$

$$\mathcal{A} = \varepsilon l c_{mol} = \log_{10} \left( \frac{I_0}{I} \right). \quad (10.6)$$

$I_L$  and  $I_R$  denote the intensities of left and right circularly polarised light, respectively. The symbol  $\varepsilon$  represents the molar extinction coefficient,  $l$  represents the path length, and  $c_{mol}$  represents the concentration of the chiral analytes (mol/L).

### 10.3 1DPC for superchiral SWs

Based on previous works conducted by Mogni *et al.* in 2022 [6], the design of the 1DPC utilised throughout the rest of this chapter is presented. The designed 1DPC exhibits the capability to generate superchiral SWs, resulting in an optical chirality enhancement of around  $10^2$  [6], and uniform throughout the structure. The unique feature of this proposed 1DPC design is the inclusion of a defect atop an otherwise perfectly one-dimensional periodic crystal. This arrangement enables the superposition of dispersion relations for TE and TM surface modes across a broad spectral range spanning from the visible to the near-UV, and over a uniform surface.

While the original design comprised 13 layers alternating between  $\text{SiO}_2$  (low RI material,  $n_L = 1.454 + 0.0001i$ ) and  $\text{Ta}_2\text{O}_5$  (high RI material,  $n_H = 2.06 + 0.001i$ ), the improved platform, as documented in [6] and utilised in this chapter, is composed of only 7 layers. This enhanced structure, depicted in Fig. 10.3 **a**, maximises the overlap of TE and TM modes specifically in an aqueous-based environment.

The multilayer platform was manufactured at the Instituto de Ciencia de Materiales de Sevilla (CSIC-Universidad de Sevilla) by layering the different materials on a BK7 standard coverslip substrate. The thin film layers were deposited sequentially using reactive magnetron sputtering (AE Pinnacle Plus), under a base pressure of  $5 \cdot 10^{-8}$  mbar. The thicknesses of each

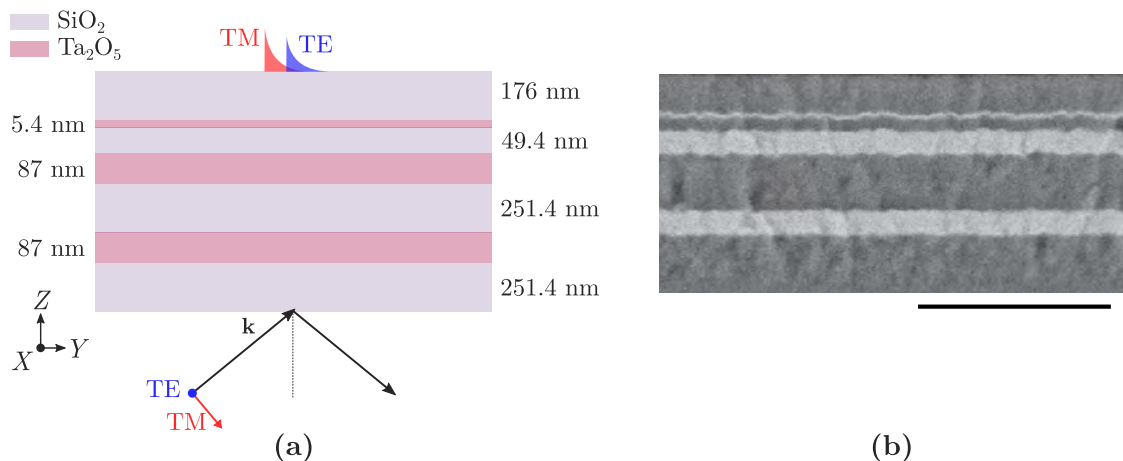


**Figure 10.3.** (a) Diagram illustrating the 1DPC, with the incident TE and TM polarised waves depicted at the lower section, and the corresponding TE and TM surface modes displayed at the upper section. Layers of different RI are distinguished by different colours. (b) Scanning electron microscopy (SEM) image (Hitachi S4800) of the truncated 1DPC, shown in a cross-section view. The brightness contrast between layers arises from the contrasting atomic weights of the  $\text{Ta}_2\text{O}_5$  (lighter) and  $\text{SiO}_2$  (darker). Scale bar in **b** is 500 nm. Adapted from [6].

## 10.4. Optofluidic platform

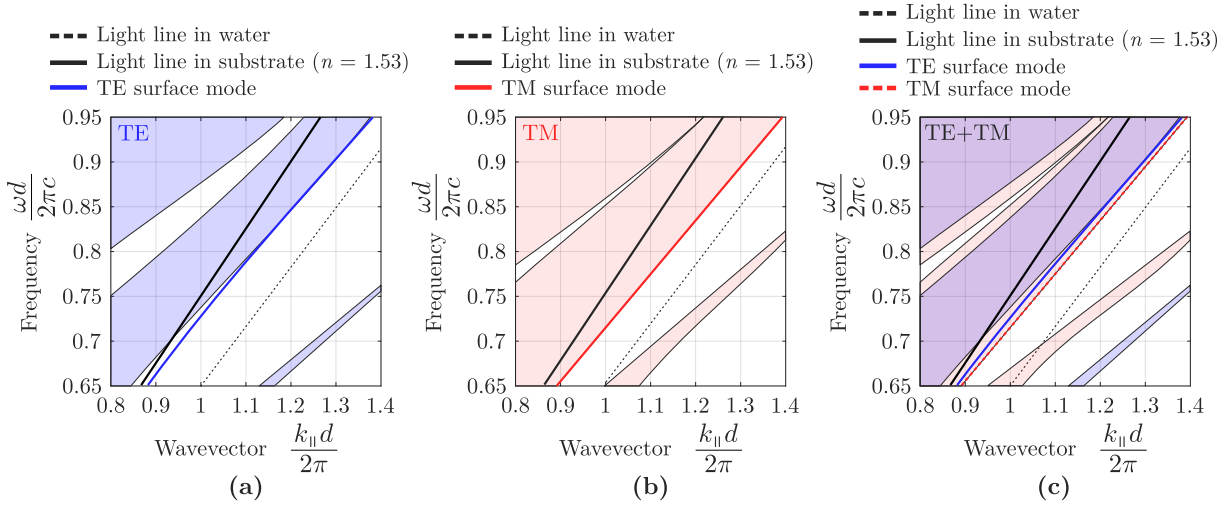


**Figure 10.4.** Dispersion relation of the 1DPC depicted in Fig. 10.3 for (a) TE polarisation, (b) TM polarisation, and (c) the overlap of these two graphs. The shaded area represents the continuum of allowed bands where electromagnetic waves can propagate. Light lines in water and BK7 are also shown. The MPB package has been utilised to calculate the definite-frequency eigenstates of Maxwell’s equations [22, 23]. Adapted from [20].

layer and the cross-section image of the fabricated 1DPC can be observed in Fig. 10.3.

Figures 10.4 a and b show the band diagrams with dispersion relations of both TE and TM modes, respectively. The TM dispersion relation is observed to be closer to the band edge (red continuous line) compared to the TE mode (blue continuous line), indicating higher radiation losses, resulting in a broader mode profile. Figure 10.4 c demonstrates the overlapped band structures achieved by the designed 1DPC. This enables the TE and TM surface mode dispersion relations to nicely overlap in the  $(k_{||}, \omega)$  space. The shaded regions represent the regions where optical modes are allowed to propagate within the 1DPC. These modes can exhibit either extended or exponentially decaying behavior in the upper semispace, depending on their position above or below the light line [19]. This achievement provides the unique opportunity to launch surface modes with arbitrary polarisation states across a wide spectral range, in contrast to isolated BSWs. It is important to note that the illumination is always considered in the Kretschmann configuration [16], with an incident medium having a refractive index of  $n = 1.53$  (BK7). Further characterisation and reflection maps can be accessed in [6, 19, 20]. The designed 1DPC is subsequently utilised for preliminary chiral measurements.

## 10.4 Optofluidic platform

The experimental setup, which will be discussed in the section 10.5, is designed to provide real-time molecular sensing through an optofluidic lab-on-chip where the liquid to be analysed flows over the sensing surface, *i.e.*, the top surface of the 1DPC. The design and fabrication of the photonic chip, which was the primary objective of the author during the research stay at the Institute of Photonics and Nanotechnology (Milan), will be presented next.

### 10.4.1 Design

The platform is composed of various layers or elements, which can be referred to as the 1DPC, SU8 chamber, top plate, and semicylindrical BK7 lens. These components are schematically arranged as shown in Fig. 10.5.

- 1DPC: it refers to the custom 1DPC fabricated as described in section 10.3. The 1DPC is deposited onto a BK7 glass coverslip with dimensions of  $20 \times 20$  mm.
- SU8 chamber: layer that contains the microfluidic chamber. It is made from SU8, an epoxy-based negative photoresist.
- Top plate:  $20 \times 20 \times 1$  mm fused silica plate that contains the 3D *clepsydra* reservoirs, where the inlet and outlet tubes are plugged. Both reservoirs are fabricated using the ULAE technique.
- Semicylindrical BK7 lens: semicylindrical BK7 substrate that acts as the supporting base for the optofluidic chip, with direct contact between the substrate and the 1DPC. The interface between the two surfaces is optically matched using immersion oil ( $n = 1.51$ ). This configuration enables the excitation of SWs through illumination using the Kretschmann configuration.

The key aspect in the design of the photonic chip lies in the microfluidic chamber, particularly in terms of its shape and dimensions. To achieve this, simulations were conducted using the commercial software Comsol, and the shape that provides the most uniform laminar flow across the entire chamber surface was selected. It is important to note that, in steady-state conditions, the entire chamber is filled with fluid, so the simulation study primarily focused on the transient filling phase of the chip. Consequently, the Laminar Flow and Level Set modules of Comsol were utilised to study the two-phase flow problem associated with the filling of the chamber. Water was assumed as the fluid in the simulations, so two phases were present: air and water.

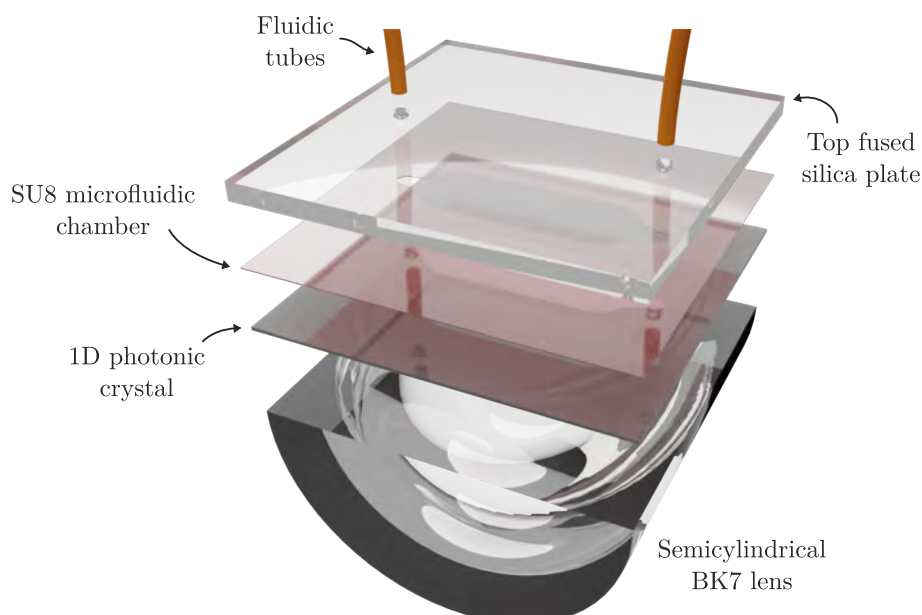


**Figure 10.5.** Physical arrangement of the different elements comprising the sensor platform. The figure is created using Blender 3.2.

#### 10.4. Optofluidic platform

By considering flow rates of 1  $\mu\text{L}/\text{min}$  (slow flow), 10  $\mu\text{L}/\text{min}$ , 25  $\mu\text{L}/\text{min}$ , 50  $\mu\text{L}/\text{min}$ , and 100  $\mu\text{L}/\text{min}$  (fast flow), the chosen shape ensures the absence of turbulence on the walls and promotes a flow velocity as uniform as possible along the axis connecting both reservoirs. Figure 10.6 **a** depicts the physical dimensions of the designed chamber, while Fig. 10.6 **b** illustrates an example of a simulation carried out showing the volume fraction of water filling the chamber with a flow rate of 25  $\mu\text{L}/\text{min}$  after 3.5 seconds.

The chamber, with a center-to-center distance between reservoirs of 14 mm and a width of 4 mm in its central part, will be fabricated using a 100  $\mu\text{m}$  layer of SU8 epoxy, as detailed in the fabrication section. As for the 3D reservoirs located in the top fused silica plate, they feature a *clepsydra* profile, as shown in Fig. 10.7, allowing for easy plug and unplug of microfluidic polyetheretherketone (PEEK) tubes. This design ensures that there are no liquid leakages during the filling process and throughout the entire measurement. The chosen PEEK tubes have an external diameter ( $d_{out}$ ) of 1/32 inches ( $\sim 794 \mu\text{m}$ ) and an internal diameter ( $d_{in}$ ) of 0.02 inches ( $\sim 508 \mu\text{m}$ ) (Ref. 1569 from IDEX Health & Sciences).

In the fabrication process, the *clepsydra* profile of the reservoirs is defined as follows. In the 1 mm thick fused silica plate, the tube will extend to a depth of 0.75 mm, at which point a cylinder with a 600  $\mu\text{m}$  diameter extends to the end of the glass, allowing the passage of the entire fluid as it is larger than the internal diameter of the tube ( $\sim 508 \mu\text{m}$ ). The external diameters of the upper part of the reservoir are fixed at 794  $\mu\text{m}$  (external diameter of the tube), which will be slightly widened after etching. On the other hand, the central part of this *clepsydra* features a diameter 20  $\mu\text{m}$  smaller, in order to keep the tube securely in place once it is plugged.

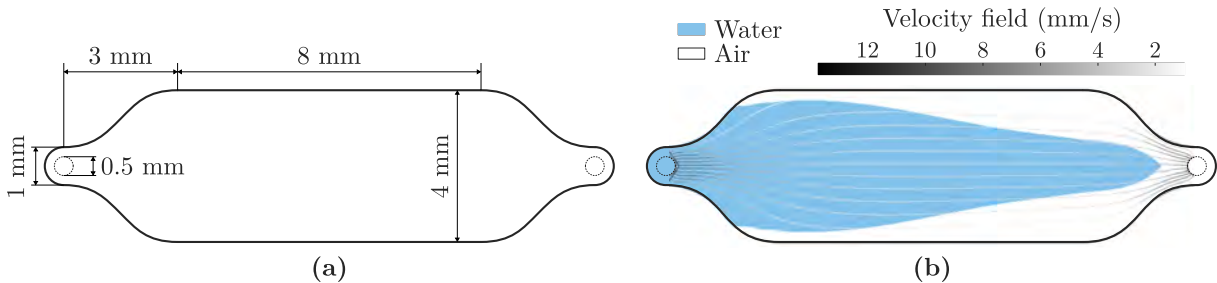


**Figure 10.6.** (a) Physical dimensions of the microfluidic chamber. (b) Two-phase flow simulation of the filling of the chamber with a flow rate of 25  $\mu\text{L}/\text{min}$  after 3.5 seconds. The chamber design was carried out using Solidworks 2019 SP4.0, and the simulation was performed using Comsol Multiphysics.

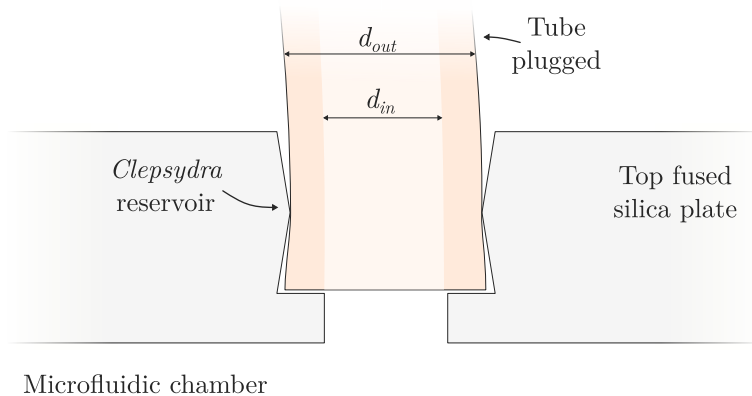


**Figure 10.7.** Illustration of a tube plugged into the 3D reservoir of the top fused silica plate.

### 10.4.2 Fabrication

The fabrication of the photonic chip involves several distinct stages that are carried out sequentially. These stages are listed and described below. It is worth noting that for tasks involving the use of ultrafast laser writing, the Satsuma femtosecond laser (Amplitude System) is employed with a pulse energy of 300 nJ and a repetition rate of 1 MHz. The wavelength used for inscription is 515 nm, achieved by generating the second harmonic from the fundamental wavelength (1030 nm) using a lithium triborate (LBO) crystal. The specific parameters for each inscription are indicated in the corresponding stage.

- (1) Firstly, the top  $20 \times 20 \times 1$  mm fused silica plate of the sensor is fabricated using the fs laser, which includes the two 3D *clepsydra* reservoirs separated by 14 mm with the previously detailed characteristics. The inscription speed is 1 mm/s, with a spacing of 1  $\mu\text{m}$  between scans in the X/Y direction and 5  $\mu\text{m}$  in the Z direction, and the objective lens used is a  $63\times/0.75$  NA from Zeiss. Subsequently, the glass undergoes wet etching for 1 hour in a 20% HF ultrasonic bath at 35  $^{\circ}\text{C}$ . See Fig. 10.8 a.
- (2) The top plate is immersed in a chromic solution ( $\text{CrO}_3$  in a sulfuric acid solvent) for 12 hours to remove any organic residue that may be present. Afterwards, the surface of the plate that will be in contact with the SU8 resin is treated with oxygen plasma cleaning (Zepto M2 from Diener Electronics). This activates the surface, making it more receptive to the photoresist.
- (3) The chamber is contained in a 100  $\mu\text{m}$  thick layer of SU8 epoxy photoresist. Several drops of SU8 are deposited onto the surface of the fused silica plate and spun up according to a specific time and revolutions per minute profile (with a maximum value of 2,000 rpm) using a commercial spin coater (Polos SPIN200i). Through empirical investigation, the parameters are adjusted to achieve a quasi-uniform layer with a thickness of 100  $\mu\text{m}$ .
- (4) The 1DPC, also previously activated through oxygen plasma cleaning, is placed on top of the SU8 layer (on the surface of the photonic crystal, not the BK7 substrate). Subsequently, a soft baking is carried out for 2 hours at 95  $^{\circ}\text{C}$ . See Fig. 10.8 b.
- (5) Using fs laser writing, the shape of the chamber is inscribed on a fused silica plate measuring  $20 \times 20 \times 2$  mm (see Fig. 10.9 a). The inscription includes two small protruding cylinders, which will be aligned with the reservoirs on the top plate. The inscription speed is 2 mm/s, with a scan spacing of 1.7  $\mu\text{m}$  in X/Y and 10  $\mu\text{m}$  in Z. A  $20\times/0.4$  NA Achromatic Zeiss objective lens is used. Subsequently, wet etching is performed for 3 hours using the parameters specified in step (1). The extracted mask is then gold coated with an 80 nm layer using the Cressington 108auto sputter coater. See Fig. 10.8 c.
- (6) Aligning the mask with the corresponding holes of the top plate's reservoirs, the chip is polymerised with UV light for 1 minute. Due to the reflective gold mask, the region corresponding to the chamber is not polymerised. See Fig. 10.8 d.
- (7) Post exposure bake at 95  $^{\circ}\text{C}$  is performed for 3 minutes.
- (8) The uncured resin from the chamber is removed from the chip through the reservoirs using an SU8 developer for 12 hours. See Fig. 10.8 e and Fig. 10.9 b.

## 10.5. Experimental setup

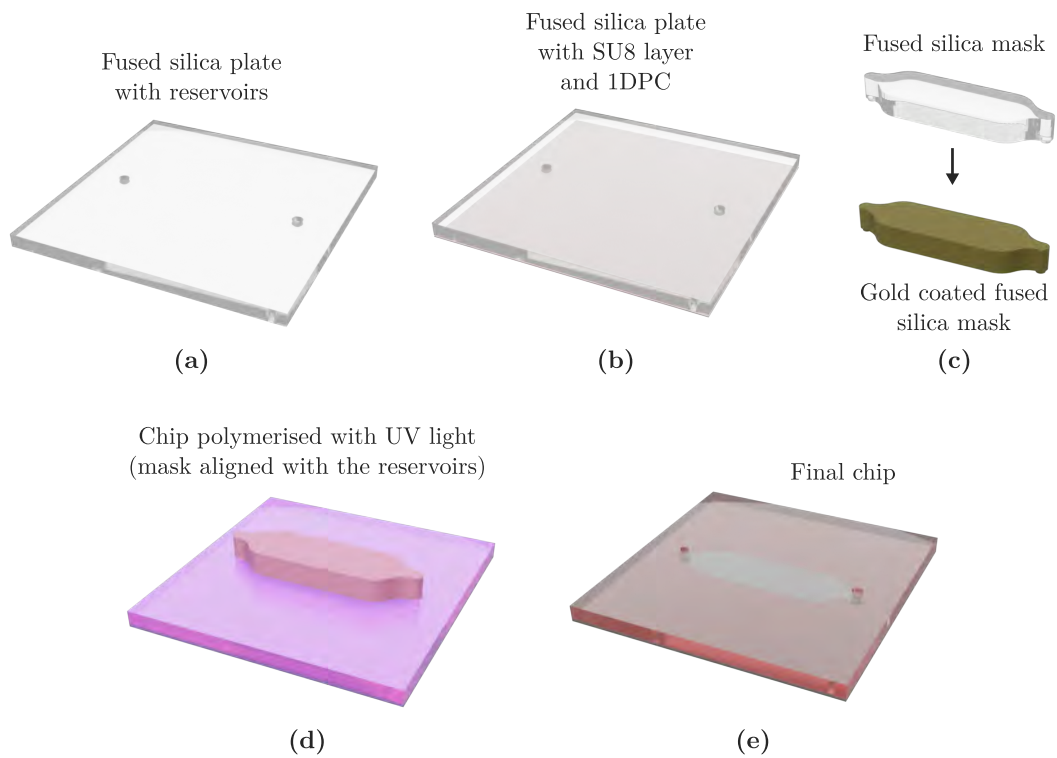


**Figure 10.8.** (a-e) Illustration of some of the different stages involved in the fabrication of the chip. The figures are created using Blender 3.2.

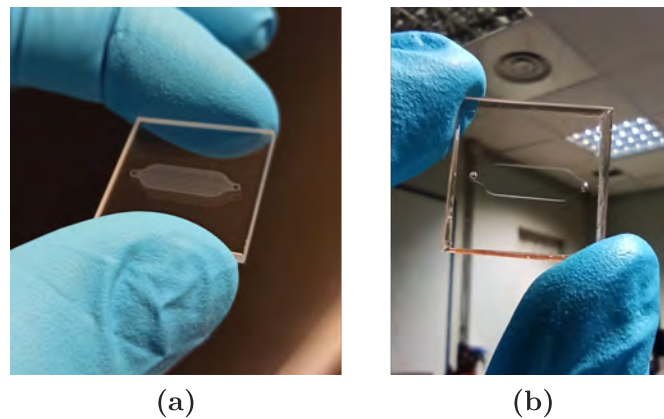


**Figure 10.9.** (a) Image of the  $20 \times 20 \times 2$  mm fused silica glass after the fs laser inscription of the mask used in the UV polymerisation stage of the SU8 layer. (b) Image of the final optofluidic chip. It is equivalent to the illustration in Fig. 10.8 e.

## 10.5 Experimental setup

Circular dichroism measurements are carried out using the experimental setup depicted in Fig. 10.10 a. This setup allows for the acquisition of angular scans of the 1DPC at a wavelength of 405 nm. The fibre laser output is collimated by a lens ( $L_1$ ) and then passes through a quarter waveplate ( $\lambda/4$ ) and a half waveplate ( $\lambda/2$ ) to optimise the intensity of the beam and compensate for polarisation changes in the fibre. A beam splitter (BS) is used to collect the original beam for reference measurements, while a Glan-Taylor polariser (GTP) enables the adjustment of the incident light polarisation between TE and TM.

A photoelastic modulator (PEM) is introduced after the Glan-Taylor polariser. The PEM allows for the modulation of the incoming light between right- and left-circular polarisation states at a frequency of 50 kHz. To demodulate the detected response, a lock-in amplifier (LIA) is employed at the end.

Since the sample is mounted on a semicylindrical BK7 substrate (see Fig. 10.10 b), which also acts as a lens, another semicylindrical BK7 element ( $L_2$ ) is positioned before to ensure a collimated beam in the 1DPC. This guarantees a precisely defined excitation angle (in the Kretschmann configuration) for the SW and maintains a normal illumination in the sample. The sample is optically matched to the prism using immersion oil ( $n = 1.51$ ), and the reflected light is collected by a detector ( $D_2$ ) for further analysis.

The reflected intensity is then processed to obtain reflectivity signal, which is a check on the alignment of the optical elements, and demodulated by the LIA to extract amplitude and phase components. The combination of these two last parameters gives rise to the CD signal, which is an essential parameter for studying the optical properties of the sample and molecular interactions. Figure 10.10 c shows a real image of the photonic chip placed in the actual setup, with the chamber filled with a chiral molecular solution.

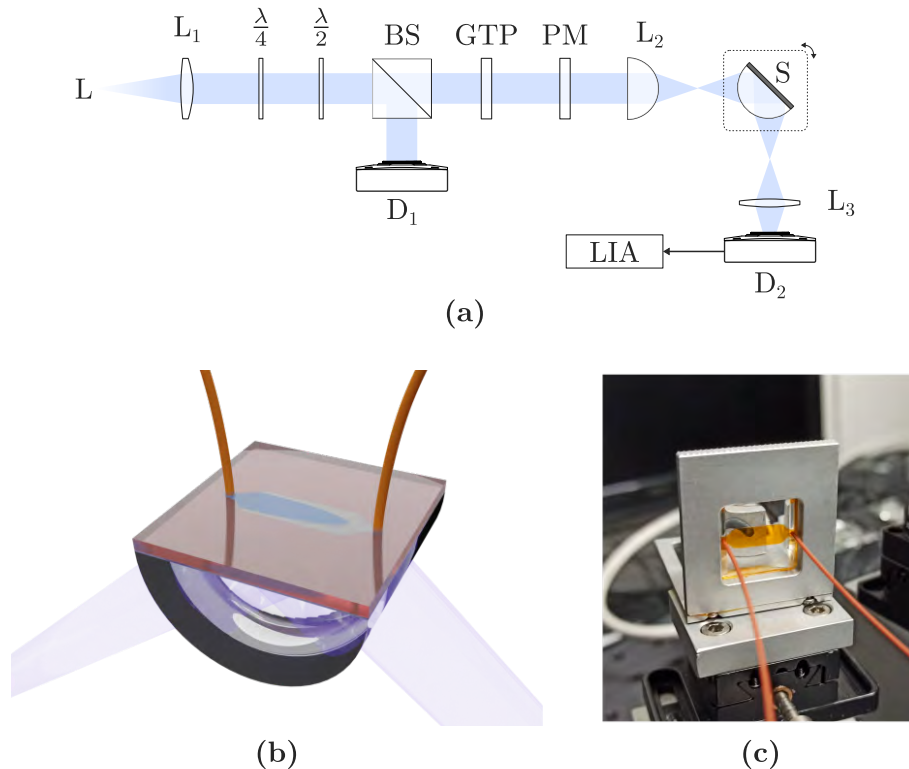


**Figure 10.10.** (a) Schematic of the experimental setup for CD measurements of the sample (Key: L – 405 nm fibre laser,  $L_1$  – collimation lens,  $\lambda/2$  – half waveplate,  $\lambda/4$  – quarter waveplate, BS – beam splitter, GTP – Glan-Taylor polariser, PM – photoelastic modulator,  $L_2$  – semicylindrical BK7 lens, S – sample mounted on a rotating holder,  $L_3$  – signal capture lens,  $D_1$  – intensity detector,  $D_2$  – reflectivity detector, LIA – lock-in amplifier). (b) Illustration of the optofluidic platform assembled with the semicylindrical lens and the microfluidic tubes placed in the reservoirs. The figure is created using Blender 3.2. (c) Image of the photonic chip mounted on the rotating holder in the actual setup. The chamber has been filled with custom chiral molecules o-MR-PEA (o-methyl red conjugates with chiral 1-phenyl-ethylamine).

## 10.6 Preliminary measurements of molecular chirality

In this section, some of the preliminary measurements conducted with chiral molecules are presented. However, ongoing work is still being carried out in order to optimise the setup and achieve real-time molecular chirality sensing using the fabricated optofluidic device. Therefore, the results presented here reflect the current progress rather than the final outcome of the study.

### 10.6.1 Chiral molecules

The chiral molecules used were synthesised at the Department of Chemistry, Materials and Chemical Engineering of Politecnico di Milano following the procedure described in [37]. Enantiomerically pure *o*-MR-PEA (*o*-methyl red conjugated with chiral 1-phenyl-ethylamine) is employed, with the detailed chemical structure shown in Fig. 10.11 **a**.

As depicted in Fig. 10.11 **b**, this molecule absorbs in the blue region of the spectrum, which is the desired range for the designed 1DPC, and it is not soluble in water, requiring highly active solvents. This limitation restricts the use of standard materials in microfluidics, such as PDMS, which is why the chamber has been fabricated using SU8. SU8, which is also another well-established material for fluidic applications, has been proven to be resistant to acetonitrile ( $\text{CH}_3\text{CN}$ ), which is the solvent ultimately used. In fact, the chamber has been filled with acetonitrile overnight, and no defects have been observed at the edges, indicating that its shape and dimensions have remained intact. The reason for choosing SU8 is also its flat and reduced absorption ( $< 10\%$ ) in the spectral range of interest, as well as its very low viscosity, making it suitable for microfluidic chambers.

### 10.6.2 Measurements

The aim of the experimental measurements is to differentiate the chiral signal between the opposite enantiomers of the *o*-MR-(*R*)-PEA molecule. Therefore, circularly polarised light modulated

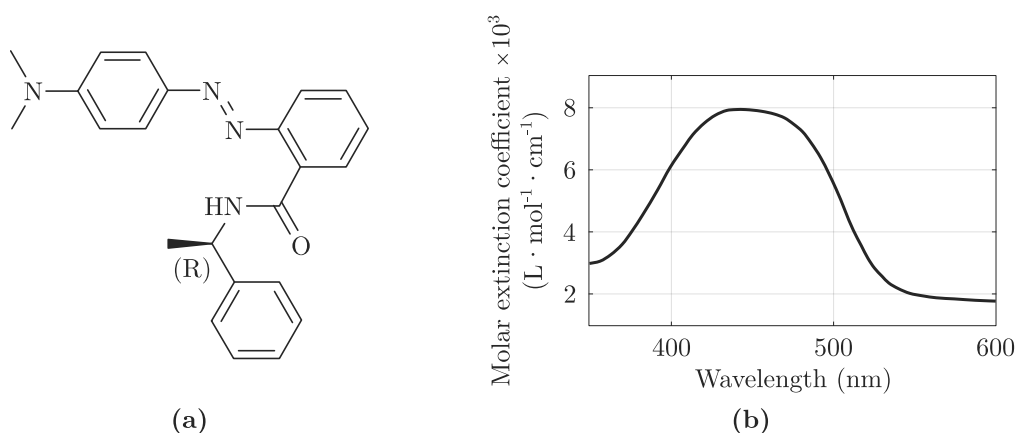


**Figure 10.11.** (a) *o*-MR-(*R*)-PEA molecule represented in a 2D structure. (b) Molar extinction coefficient spectrum obtained from the absorption spectrum of a 200  $\mu\text{M}$  solution of the (*R*) enantiomer. Its peak centred in the blue region of the spectrum, which is the desired range for the 1DPC. Adapted from [20].

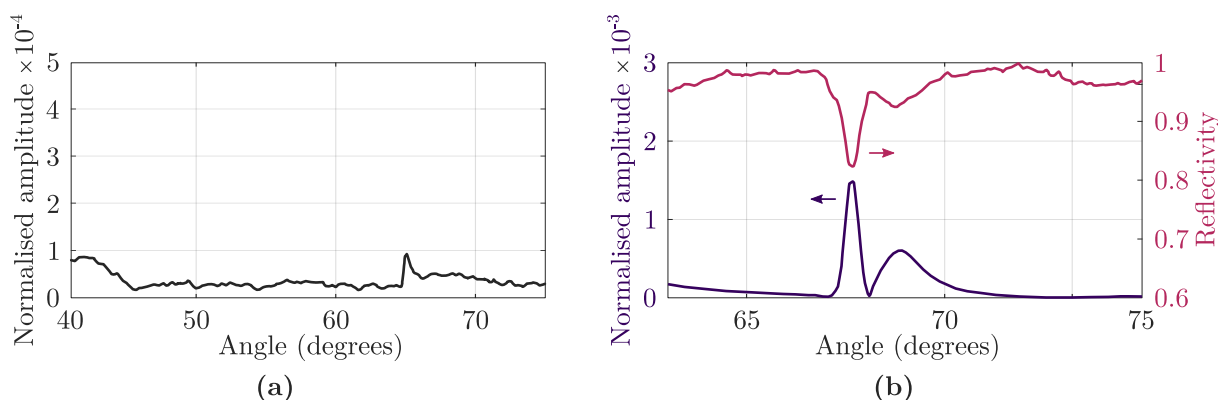


**Figure 10.12.** (a) Optimal amplitude signal of the 1DPC under normal incidence without fluid in the chamber. (b) Optimal amplitude and reflectivity signals of the 1DPC when the chamber is filled with the solvent (acetonitrile). Adapted from [20].

by the PEM is used for illumination and then demodulated into amplitude and phase components by the LIA. The first step is to acquire the baseline signal of the solvent alone. This is crucial as the birefringence of the 1DPC may introduce significant extrinsic chirality, which cannot be observed when acquiring only the reflectivity signal.

Ideally, the amplitude response with no fluid in the chamber should be flat, so adjustments in the position of the 1DPC are made using micropositioners to achieve the flattest response possible. A strong dependence of the tilt of the photonic crystal on the baseline signal is observed, emphasising the need for optimal adjustment. The optimal result achieved is shown in Fig. 10.12 a. The minor peak observed at approximately  $65^\circ$  corresponds to the excitation angle of the SWs in the sample.

In order to further optimise the alignment of the sample in the fluidic environment, it was decided to fill the chamber with the solvent. The results obtained are shown in Fig. 10.12 b. It should be noted that the magnitude of the baseline signal is significantly worse (around 10 times worse) than the signal optimised with the 1DPC alone, as shown in Fig. 10.12 a. This is due to the presence of an absorbing external medium like the acetonitrile. The prominent features can be attributed to the TE and TM surface modes. The correlation between the amplitude peaks and dips in reflectivity is noteworthy. It is observed that both modes are clearly present and partially overlapping when the platform is illuminated with circular polarised light. The tilt optimisation has a slight effect on the position of these features (oscillation around  $0.2^\circ$ ). However, the intensity of the peaks associated with SWs appears to be unaffected. Considering the strong response of the solvent, it was determined that a solution of chiral molecules at a high concentration of 20 mM would be employed, which is two orders of magnitude higher than the 200  $\mu\text{M}$  solution analysed in Fig. 10.11 b. Therefore, a higher absorption is expected.

The amplitude and phase signals derived from the 20 mM solution of chiral molecules are depicted in Fig. 10.13. The amplitude signal for both enantiomers is observed to be higher than that of the solvent, indicating a variation in the signal due to the presence of chiral molecules. However, it is notable that the amplitude and phase signals from (R) and (S) enantiomers exhibit the same shape and are overlapped. Consequently, the CD response is also overlapped.

This suggests that artefacts are still dominant and are further amplified by the absorption of the solution. The absence of distinguishable differences between the signals of both enantiomers

## 10.7. Conclusions

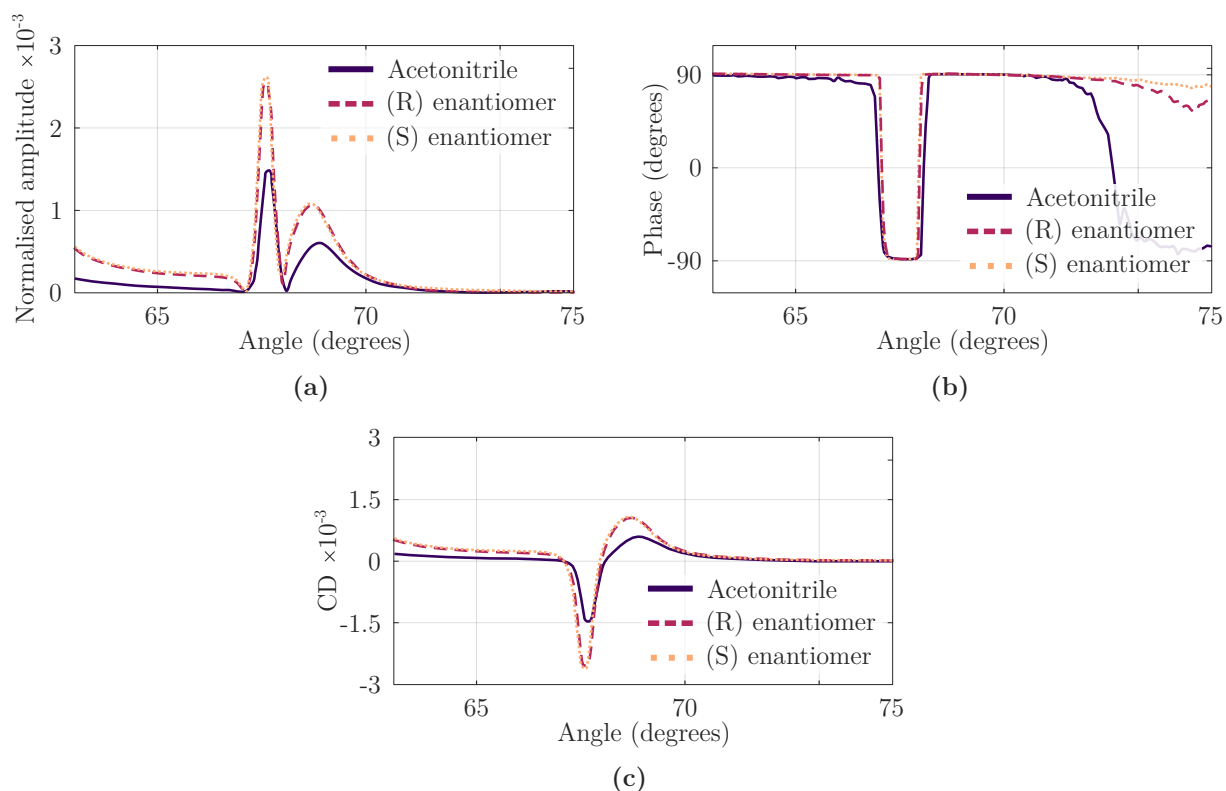


**Figure 10.13.** (a) Amplitude signal, (b) phase, and (c) CD signal from solvent and both (R) and (S) enantiomers. Adapted from [20].

suggests that the artefacts have a stronger influence than the chiral properties of the molecules. The collected surface mode primarily reflects the absorption properties of the crystal materials and the external medium, as the propagation length of the 1DPC surface modes is approximately 100  $\mu\text{m}$  and the diameter of the illumination beam is around 1 mm.

## 10.7 Conclusions

Work is currently ongoing on these preliminary results (June 2023), with the aim of further developing the acquisition technique. One possible approach to collect the CD signal is to reduce the concentration of the molecular solution, which would decrease the level of absorption by the external medium. However, even with a less concentrated solution, the contribution from acetonitrile may still be significant, resulting in only a modest improvement. In order to limit the extrinsic chirality from the platform and allow the intrinsic chirality of the molecules to emerge, it may be necessary to use a crystal with less intense modes. The choice of the photonics crystal for the chiral investigation is crucial: while visible and sharp modes are optimal for optical characterisation of surface modes and proof of concept of the platform, they may not be the most suitable for investigating CD signals. Further exploration and improvement of photonic crystals remains an ongoing area of research, with potential for advancements and investigation in the future.

The investigation demonstrates a pioneering endeavour to employ Bloch surface waves for real-time molecular chirality sensing on a custom ultrafast laser fabricated optofluidic platform.

The 1DPC fabrication process, designed with calculated periodicity, successfully enhanced resonant BSWs. In the developed experimental setup, an innovative coupling of the circularly polarised light mechanism with a photoelastic modulator enabled precise amplitude and phase measurements for circular dichroism. Concurrently, the integrated SU8-based optofluidic device, resistant to the employed solvent acetonitrile, facilitated the study of chiral molecules, specifically *o*-MR-PEA enantiomers. Despite the successful setup, the preliminary measurements highlighted the challenge of artefact interference due to absorption properties of the external medium, overshadowing the intrinsic chiral properties. This multifaceted study serves as a significant foundation for further improvements in BSW-based optofluidic platforms, opening promising avenues in molecular chirality sensing and optofluidics.

## References

- [1] Sinev, I. S. *et al.*, “Chirality Driven by Magnetic Dipole Response for Demultiplexing of Surface Waves,” *Laser & Photonics Reviews*, vol. 11, no. 5, p. 1700168, Sep. 2017. DOI: 10.1002/lpor.201700168.
- [2] Takayama, O., Bogdanov, A. A., and Lavrinenko, A. V., “Photonic surface waves on metamaterial interfaces,” *Journal of Physics: Condensed Matter*, vol. 29, no. 46, p. 463001, Oct. 2017. DOI: 10.1088/1361-648x/aa8bdd.
- [3] Li, Z. *et al.*, “Multi-Wavelength Super-Resolution Imaging by Structured Illumination of Bloch Surface Waves,” *IEEE Photonics Journal*, vol. 14, no. 4, pp. 1–7, Aug. 2022. DOI: 10.1109/jphot.2022.3187508.
- [4] Yu, L., Barakat, E., Sfez, T., Hvozدارa, L., Francesco, J. D., and Herzig, H. P., “Manipulating Bloch surface waves in 2D: a platform concept-based flat lens,” *Light: Science & Applications*, vol. 3, no. 1, e124–e124, Jan. 2014. DOI: 10.1038/lsa.2014.5.
- [5] Sinibaldi, A. *et al.*, “A full ellipsometric approach to optical sensing with Bloch surface waves on photonic crystals,” *Optics Express*, vol. 21, no. 20, pp. 23331–23344, Sep. 2013. DOI: 10.1364/oe.21.023331.
- [6] Mogni, E. *et al.*, “One-Dimensional Photonic Crystal for Surface Mode Polarization Control,” *Advanced Optical Materials*, vol. 10, no. 21, p. 2200759, Aug. 2022. DOI: 10.1002/adom.202200759.
- [7] Bulgakov, E. N. and Sadreev, A. F., “Light trapping above the light cone in a one-dimensional array of dielectric spheres,” *Physical Review A*, vol. 92, no. 2, p. 023816, Aug. 2015. DOI: 10.1103/physreva.92.023816.
- [8] Chen, Z. *et al.*, “Observation of miniaturized bound states in the continuum with ultra-high quality factors,” *Science Bulletin*, vol. 67, no. 4, pp. 359–366, Feb. 2022. DOI: 10.1016/j.scib.2021.10.020.
- [9] Wang, R. *et al.*, “Bloch surface waves confined in one dimension with a single polymeric nanofibre,” *Nature Communications*, vol. 8, no. 1, Feb. 2017. DOI: 10.1038/ncomms14330.
- [10] Yu, L., Barakat, E., Nakagawa, W., and Herzig, H. P., “Investigation of ultra-thin waveguide arrays on a Bloch surface wave platform,” *Journal of the Optical Society of America B*, vol. 31, no. 12, p. 2996, Nov. 2014. DOI: 10.1364/josab.31.002996.
- [11] Takayama, O. *et al.*, “Surface waves on metamaterials interfaces,” in *2016 10th International Congress on Advanced Electromagnetic Materials in Microwaves and Optics (METAMATERIALS)*, IEEE, Sep. 2016. DOI: 10.1109/metamaterials.2016.7746486.
- [12] Aly, A. H., Mohamed, D., Mohaseb, M. A., El-Gawaad, N. S. A., and Trabelsi, Y., “Biophotonic sensor for the detection of creatinine concentration in blood serum based on 1D photonic crystal,” *RSC Advances*, vol. 10, no. 53, pp. 31765–31772, 2020. DOI: 10.1039/d0ra05448h.
- [13] Nouman, W. M., El-Ghany, S. E.-S. A., Sallam, S. M., Dawood, A.-F. B., and Aly, A. H., “Biophotonic sensor for rapid detection of brain lesions using 1D photonic crystal,” *Optical and Quantum Electronics*, vol. 52, no. 6, May 2020. DOI: 10.1007/s11082-020-02409-2.

- [14] Pitarke, J. M., Silkin, V. M., Chulkov, E. V., and Echenique, P. M., “Theory of surface plasmons and surface-plasmon polaritons,” *Reports on Progress in Physics*, vol. 70, no. 1, pp. 1–87, Dec. 2006. DOI: 10.1088/0034-4885/70/1/r01.
- [15] Zayats, A. V., Smolyaninov, I. I., and Maradudin, A. A., “Nano-optics of surface plasmon polaritons,” *Physics Reports*, vol. 408, no. 3-4, pp. 131–314, Mar. 2005. DOI: 10.1016/j.physrep.2004.11.001.
- [16] Kretschmann, E., “Die Bestimmung optischer Konstanten von Metallen durch Anregung von Oberflächenplasmaschwingungen,” *Zeitschrift für Physik A Hadrons and nuclei*, vol. 241, no. 4, pp. 313–324, Aug. 1971. DOI: 10.1007/bf01395428.
- [17] Joannopoulos, J. D., Johnson, S. G., Winn, J. N., and Meade, R. D., *Photonic Crystals: Molding the Flow of Light*. Princeton University Press, Oct. 2011. DOI: 10.2307/j.ctvcm4gz9.
- [18] Novotny, L. and Hecht, B., *Principles of Nano-Optics*. Cambridge University Press, Sep. 2012. DOI: 10.1017/cbo9780511794193.
- [19] Pellegrini, G., Finazzi, M., Celebrano, M., Duò, L., and Biagioni, P., “Chiral surface waves for enhanced circular dichroism,” *Physical Review B*, vol. 95, no. 24, p. 241402, Jun. 2017. DOI: 10.1103/physrevb.95.241402.
- [20] Mogni, E., “Molecular sensing with surface waves,” Ph.D. dissertation, Politecnico di Milano, 2023.
- [21] Kong, W., Sun, Y., and Lu, Y., “Enhanced Goos-Hänchen shift of graphene coated on one-dimensional photonic crystal,” *Results in Physics*, vol. 17, p. 103107, Jun. 2020. DOI: 10.1016/j.rinp.2020.103107.
- [22] Johnson, S. and Joannopoulos, J., “Block-iterative frequency-domain methods for Maxwell’s equations in a planewave basis,” *Optics Express*, vol. 8, no. 3, pp. 173–190, Jan. 2001. DOI: 10.1364/oe.8.000173.
- [23] Veis, M. and Antos, R., “Fourier Factorization in the Plane Wave Expansion Method in Modeling Photonic Crystals,” in *Photonic Crystals - Introduction, Applications and Theory*, InTech, Mar. 2012. DOI: 10.5772/34679.
- [24] Robertson, W. M. and May, M. S., “Surface electromagnetic wave excitation on one-dimensional photonic band-gap arrays,” *Applied Physics Letters*, vol. 74, no. 13, pp. 1800–1802, Mar. 1999. DOI: 10.1063/1.123090.
- [25] Sinibaldi, A. *et al.*, “Direct comparison of the performance of Bloch surface wave and surface plasmon polariton sensors,” *Sensors and Actuators B: Chemical*, vol. 174, pp. 292–298, Nov. 2012. DOI: 10.1016/j.snb.2012.07.015.
- [26] Mogni, E. *et al.*, “One-dimensional photonic crystal for polarization-sensitive surface-enhanced spectroscopy,” *EPJ Web of Conferences*, vol. 266, Costa, M. F., Flores-Arias, M., Pauliat, G., and Segonds, P., Eds., p. 06009, 2022. DOI: 10.1051/epjconf/202226606009.
- [27] Ferenci, P., “Diagnosis and current therapy of Wilson’s disease,” *Alimentary Pharmacology & Therapeutics*, vol. 19, no. 2, pp. 157–165, Nov. 2003. DOI: 10.1046/j.1365-2036.2003.01813.x.
- [28] Smithells, R. W. and Newman, C. G., “Recognition of thalidomide defects,” *Journal of Medical Genetics*, vol. 29, no. 10, pp. 716–723, Oct. 1992. DOI: 10.1136/jmg.29.10.716.

## References

- [29] Meierhenrich, U. J., “Amino Acids and the Asymmetry of Life,” *European Review*, vol. 21, no. 2, pp. 190–199, Apr. 2013. DOI: 10.1017/s106279871200035x.
- [30] Fasman, G. D., Ed., *Circular Dichroism and the Conformational Analysis of Biomolecules*. Springer US, 1996. DOI: 10.1007/978-1-4757-2508-7.
- [31] Tang, Y. and Cohen, A. E., “Enhanced Enantioselectivity in Excitation of Chiral Molecules by Superchiral Light,” *Science*, vol. 332, no. 6027, pp. 333–336, Apr. 2011. DOI: 10.1126/science.1202817.
- [32] Zhang, X., Liu, Y., Han, J., Kivshar, Y., and Song, Q., “Chiral emission from resonant metasurfaces,” *Science*, vol. 377, no. 6611, pp. 1215–1218, Sep. 2022. DOI: 10.1126/science.abq7870.
- [33] Indukuri, S. R. K. C., Frydendahl, C., Sharma, N., Mazurski, N., Paltiel, Y., and Levy, U., “Enhanced Chiral Sensing at the Few-Molecule Level Using Negative Index Metamaterial Plasmonic Nanocuvettes,” *ACS Nano*, vol. 16, no. 10, pp. 17289–17297, Oct. 2022. DOI: 10.1021/acsnano.2c08090.
- [34] Tang, Y. and Cohen, A. E., “Optical Chirality and Its Interaction with Matter,” *Physical Review Letters*, vol. 104, no. 16, p. 163901, Apr. 2010. DOI: 10.1103/physrevlett.104.163901.
- [35] Nesterov, M. L., Yin, X., Schäferling, M., Giessen, H., and Weiss, T., “The Role of Plasmon-Generated Near Fields for Enhanced Circular Dichroism Spectroscopy,” *ACS Photonics*, vol. 3, no. 4, pp. 578–583, Apr. 2016. DOI: 10.1021/acsp Photonics.5b00637.
- [36] Hu, H., Gan, Q., and Zhan, Q., “Generation of a Nondiffracting Superchiral Optical Needle for Circular Dichroism Imaging of Sparse Subdiffraction Objects,” *Physical Review Letters*, vol. 122, no. 22, p. 223901, Jun. 2019. DOI: 10.1103/physrevlett.122.223901.
- [37] Yamamoto, H., Maeda, Y., and Kitano, H., “Molecular Recognition by Self-Assembled Monolayers of Cyclodextrin on Ag,” *The Journal of Physical Chemistry B*, vol. 101, no. 35, pp. 6855–6860, Aug. 1997. DOI: 10.1021/jp963916u.

# PART IV

## FINAL REMARKS AND FUTURE LINES OF WORK

This last part of the document concludes the thesis by highlighting the significant conclusions drawn from the research and outlining future avenues of exploration. The key highlights of the conducted research are summarised, and crucial lines of action based on the findings are identified. This section provides a comprehensive wrap-up of the thesis, emphasising the notable contributions made and suggesting potential directions for further research.

The chapter included in this part is:

- Chapter 11: Conclusions and future lines.

# 11

## Conclusions and future lines

**A**s can be seen at a glance by referring to the table of contents, this thesis delves into a multitude of techniques and methods centred around the processing of transparent materials using ultrafast lasers. The research diversifies in order to propose solutions to existing problems in various fields such as medicine, industry, biochemistry, and healthcare, among others. It is important to highlight that the decision not to restrict the scope to a specific application has required the use of interdisciplinary knowledge, primarily in the intersection of engineering and physics, with some concepts from medicine, biology, and biochemistry also playing a smaller role.

It is worth mentioning the valuable contributions made to this thesis by not only the supervisors at the University of Cantabria but also Robert Thomson (Heriot-Watt University, Edinburgh, UK) and Rebeca Martínez-Vázquez (Institute of Photonics and Nanotechnology, Milan, Italy). Their expertise in the use of chemical etching processes, coupled with ultrafast laser writing, for the fabrication of custom 3D structures in glass has been instrumental in the second half of this thesis. This work forms the foundation for the main research directions pursued by both the Photonics Engineering Group (University of Cantabria) and the author of this thesis.

In this chapter, brief comments will be provided on each relevant area of research covered. While specific conclusions have been drawn for each individual work in this thesis, a concise summary and potential avenues for further research will be highlighted.

**Optical fibre sensors.** This pertains to the field which covered the first two years of the thesis. The three chapters corresponding to Part II are collectively included here. Several sensors have been developed using fibres. In standard telecommunication fibres, notable examples include a hybrid cladding waveguide Mach-Zehnder interferometer sensor and a 200  $\mu\text{m}$  long multi-parameter sensor that houses an in-fibre air cavity alongside a plane-by-plane FBG inscribed in the final part of the fibre. The latter, integrated into a surgical needle, can detect tissue and the surrounding refractive index. On the other hand, in relation to specialty fibres, the

first highlight is a liquid level sensor fabricated in a silica capillary tube through the ablation of the cladding, in which detection is carried out with dynamic Fabry-Perot interferometers. Secondly, a refractometer was made using multimode fibres based on the new material CYTOP for the measurement of aqueous solutions, taking advantage of the specific properties of the fibre, particularly its refractive index ( $n = 1.34$ ).

Future lines of action are quite diverse given the broad nature of this field. It seems clear that the major efforts in optical fibre sensors lie in achieving an extremely low cost, as well as higher precision, miniaturisation, and multiplexing capabilities, with ever-increasing resolution and sensitivity. The use of ultrafast lasers will enable complex microstructure fabrication, and their integration into increasingly smaller spaces, further developing the lab-in-fibre paradigm. Additionally, investigating the incorporation of fs laser-inscribed optical fibre sensors into Internet of Things systems and artificial intelligence platforms for real-time, intelligent monitoring and control offers another promising avenue for research. While it does not correspond to sensors but rather to imaging applications, the use of multimode fibres initially gained importance in photonic lanterns to provide imaging capacity to the multicore fibres within. However, in recent years, notable strides have been made in controlling the propagation of fibre modes and being able to predict their response, largely based on invariant modes. Consequently, there is a substantial area of activity aiming to use multimode fibres to achieve imaging with resolution beyond the diffraction limit. This could be game-changing, especially if integrated into functional catheters or endoscopes, as it would provide the capability to spatially resolve organisms of hundreds of nanometres.

**Polarisation-independent etching in fused silica.** Related to the ULAE-related fundamental research, the achievement of polarisation-independent high etching rates in fused silica is not a new concept. Previous studies have shown quasi-independence from polarisation, either by using very high pulse energies ( $\sim 2 \mu\text{J}$ ), pulse durations in the picosecond range, or specific pulse shaping techniques. However, achieving polarisation-independent etching in the range of hundreds of nJ (pulse energy) and hundreds of fs (pulse duration) with standard pulses is indeed novel. This discovery opens up a new realm of possibilities in the field of ultrafast laser microfabrication. This identified regime brings notable advantages over traditional approaches, including higher fabrication speeds, reduced fluence in etching (thus higher energy efficiency), and simplified optical setups where complete polarisation control is no longer a necessity for creating 3D structures in glass. Nevertheless, the exploration of this femtosecond laser regime not only introduces a new tool in the field of ultrafast laser microfabrication but also gives rise to several questions that have emerged over the past year and continue to arise today.

*What physical mechanism underlies this regime?* This is the fundamental question. It appears likely that it differs from the mechanism governing nanograting formation. The structures generated, with significantly lower anisotropy compared to a nanograting, and the absence of a requirement for  $> 10$  pulses/ $\mu\text{m}$  to achieve high etching rates, suggest that the physical mechanism may differ. However, I hesitate to dismiss the presence of nanopores in an initial stage. Ongoing research on absorption, annealing, and various spectroscopic methods may shed light on whether we are dealing with an etching process dominated by point defects (*e.g.*, NBOHC, E' center, ODCs, among others). Material densification could be another physical mechanism behind the high etching rate in this regime, involving a reduction in bond angles or the appearance of a higher number of 3- and 4-membered rings in the fused silica network. These are conjectures

that, once supported by a precise physical explanation, can lead to process optimisation and ultimately offer high-quality and high-speed etching. *What chemical solution conditions provide improved etching rates or selectivity?* Studies on NaOH are relatively new (since 2021), so further research on solution concentrations and/or temperature could optimise the etching process for fused silica structures. *Can the PRR reduce the energy threshold in the discovered regime while maintaining the fluence? Is it possible to induce the formation of symmetric nanopores that turns into polarisation-independent high etching rates with 1 or 2 pulses per  $\mu\text{m}$ ? How does the etching rate in the discovered regime change when the beam is focused on the substrate with different numerical apertures? What influence does the pulse duration have on the discovered regime? Could other pulse duration values optimise the process? Which combination of laser and/or etching parameters allows us to minimise surface roughness as much as possible?*

**Polymer fibres for lung endomicroscopy.** As an example of a game-changing application of ULAE, a powerful and innovative approach has been demonstrated to enable selective plane illumination microscopy using polymer imaging fibres. This approach utilises a silica-glass end cap, fabricated with ultrafast laser technology, which is passively aligned onto the distal end of the polymer CFB. By spatially separating the pump delivery and fluorescence imaging paths, this novel design effectively circumvents the issue of autofluorescence from the polymer CFBs. The successful implementation of this technology has enabled high-quality endomicroscopic widefield imaging of human lung tissues, free from background autofluorescence signals originating from the polymer CFB. This breakthrough paves the way for the utilisation of polymer CFBs in various clinical and experimental medicine applications.

In the context of respiratory diseases, the COVID-19 pandemic has highlighted the urgent need for safe and effective therapies for respiratory infections. However, traditional pharmaceutical drug development processes are slow and costly. There is a growing recognition that experimental medicine, employing micro-dosing approaches in human patients, can greatly enhance the efficiency of drug-target engagement validation. To fully unlock the potential of experimental medicine for respiratory diseases, new tools are required. The work conducted in this thesis enabled polymer imaging fibres to capture images across a multi-mm field-of-view while maintaining excellent flexibility, thereby providing a new perspective on macroscopic tissue structures and cellular signatures. Future directions include the development of multi-functional catheters that combine pull wires to provide mobility to the catheter tip, as well as the incorporation of additional tools such as micro-dosing of small quantities of experimental medicines, widefield fluorescence lifetime imaging, and gas sensing, among others.

**Multi-functional lab-on-chip devices.** In relation to the lab-on-chip devices manufactured in this thesis, the emphasis has solely been placed on the 1DPC-based optofluidic chip for the detection of molecular chirality. The methodology involved the strategic design of a 1D photonic crystal with a defined periodicity to increase resonant Bloch surface waves. After that, an SU8-based chamber, resilient against the solvent acetonitrile, was leveraged, and the primary focus was given to o-MR-PEA enantiomers. Despite the noteworthy progression, the intrinsic chiral attributes were somewhat eclipsed by the absorption characteristics of the external medium. Current and future endeavours are directed towards improving the data collection method, such as contemplating the reduction of molecular solution concentration and the selection of a photonics crystal with subdued modes. This pioneering research sets a substantial foundation

for forthcoming enhancements in BSW-based optofluidic platforms and the realm of molecular chirality sensing.

Despite not being detailed in this document, the Photonics Engineering Group is currently engaged in a couple of projects related to the creation of lab-on-chip devices. The first one is specifically designed for the detection and analysis of phytoplankton, encompassing everything from taxonomic classification to the assessment of vital conditions. This is achieved through the implementation of in-chip modules that facilitate absorption, fluorescence, and scattering. The other project involves cardiac tissue engineering, a leading research area in regenerative medicine, providing forward-thinking strategies for cardiac disease modelling, cardiotoxicity testing, and cardiovascular repair. The aim is to develop a glass-based lab-on-chip device that can emulate native adult heart tissue, thereby allowing us to evaluate methodologies for potential treatments in the future.

Most of the results obtained during this R&D work and included in this document have been validated by the international community. The industrial application of the obtained results has been previously analysed to be protected before its communication in specialised international conferences and journals. As a result of this thesis work, a UK patent application, 24 articles in journals and more than 35 contributions to conferences have been obtained. In addition, different R&D works are currently being prepared for presentation. Lastly, it is worth highlighting that, according to the Google Scholar database, an h-index of 10 with over 400 citations have been achieved in just 4 years.

I would like to bring this thesis to a close with one last reflection. In order for the research conducted to be truly useful, future research should focus on the translation of these systems, techniques, and devices into real-world applications. Moving beyond the comfort zone of tailor-made laboratory research to adapt to the constantly changing and challenging conditions of the real world is not only motivating but also indispensable for achieving meaningful impact.

# List of publications

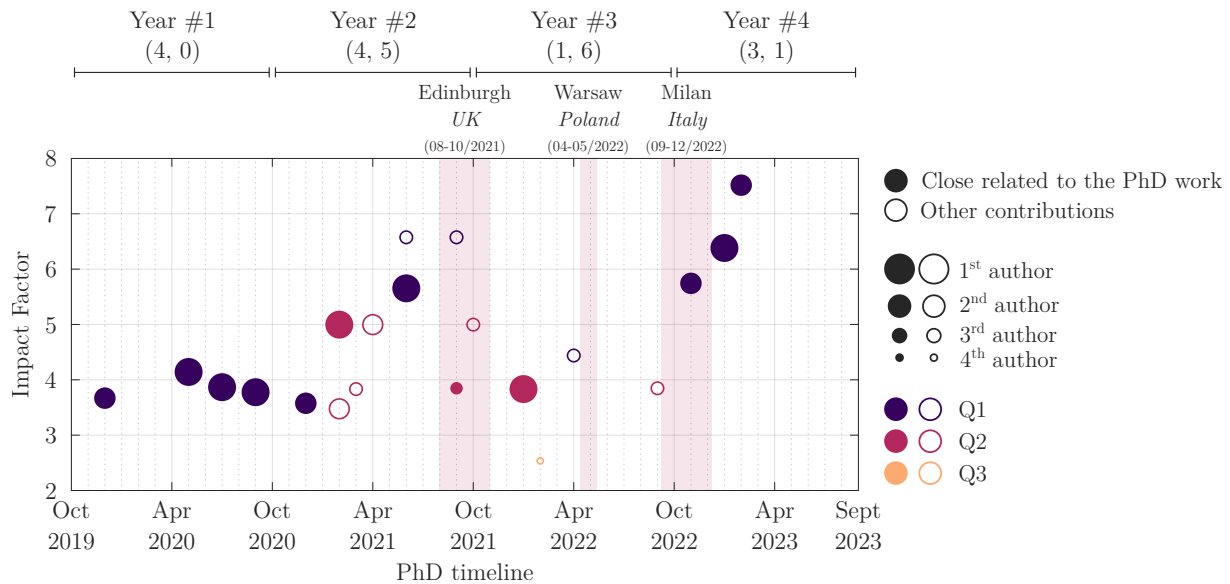


**Figure A.1.** Graph showing relevant information of the journal articles published during the four years of the thesis (from October 2019 to September 2023). Each circle corresponds to the publication of an article. If it is filled, it is a paper related to the PhD work, otherwise it is empty. The size of the circle indicates the authorship order, going from largest (1<sup>st</sup> author) to smallest (4<sup>th</sup> author). The colour refers to the quartile of the journal where it is published. The Y-axis indicates the impact factor of the journal. Similarly, the temporal periods where an international stay was carried out are highlighted, and the number of journal articles published in each of the four years of the thesis is shown in the format  $(\alpha, \beta)$ , where  $\alpha$  is the number of papers related to the PhD work, and  $\beta$  is the rest.

## Close related to the PhD work

### Journal articles

- [Och23a] **Mario Ochoa, Pablo Roldán-Varona, José Francisco Algorri, José Miguel López-Higuera, and Luis Rodríguez-Cobo (2023).** “Polarisation-independent ultrafast laser selective etching processing in fused silica.” *Lab on a Chip*, 23(7), pp. 1752–1757.  
DOI: 10.1039/D3LC00052D
- [Rol23] **Pablo Roldán-Varona, Calum A. Ross, Luis Rodríguez-Cobo, José Miguel López-Higuera, Eric Gaughan, Kevin Dhaliwal, Michael G. Tanner, Robert R. Thomson, and Helen E. Parker (2023).** “Selective Plane Illumination Optical Endomicroscopy with Polymer Imaging Fibres.” *APL Photonics*, 8(1), pp. 016103.  
DOI: 10.1063/5.0130486
- [Alg22a] **José Francisco Algorri, Pablo Roldán-Varona, María Gabriela Fernández-Manteca, José Miguel López-Higuera, Luis Rodríguez-Cobo, and Adolfo**

- Cobo (2022)**. “Photonic Microfluidic Technologies for Phytoplankton Research.” *Biosensors*, 12(11), pp. 1024.  
DOI: 10.3390/bios12111024.
- [Rol22a] **Pablo Roldán-Varona, Mauro Lomer, José Francisco Algorri, Luis Rodríguez-Cobo, and José Miguel López-Higuera (2022)**. “Enhanced refractometer for aqueous solutions based on perfluorinated polymer optical fibres.” *Optics Express*, 30(2), pp. 1397–1409.  
DOI: 10.1364/OE.448111.
- [Och21] **Mario Ochoa, José Francisco Algorri, Pablo Roldán-Varona, Luis Rodríguez-Cobo, and José Miguel López-Higuera (2021)**. “Recent advances in biomedical photonic sensors: A focus on optical fibre-based sensing.” *Sensors*, 21(19), pp. 6469.  
DOI: 10.3390/s21196469. IF (2021): 3.847, Q2 in Instruments & Instrumentation.
- [Rol21a] **Pablo Roldán-Varona, Luis Rodríguez-Cobo, and José Miguel López-Higuera (2021)**. “Slit beam shaping technique for femtosecond laser inscription of symmetric cladding waveguides.” *Journal of Selected Topics in Quantum Electronics*, 27(6), pp. 4400208.  
DOI: 10.1109/JSTQE.2021.3092438. IF (2021): 4.653, Q1 in Optics.
- [Rol21b] **Pablo Roldán-Varona, Rosa Ana Pérez-Herrera, Luis Rodríguez-Cobo, Luis Reyes-González, Manuel López-Amo, and José Miguel López-Higuera (2021)**. “Liquid level sensor based on dynamic Fabry-Perot interferometers in processed hollow-core fibre.” *Scientific Reports*, 11, pp. 3039.  
DOI: 10.1038/s41598-021-82193-5. IF (2021): 4.997, Q2 in Multidisciplinary Sciences.
- [Pal20] **David Pallarés-Aldeiturriaga, Pablo Roldán-Varona, Luis Rodríguez-Cobo, and José Miguel López-Higuera (2020)**. “Optical fibre sensors by direct laser processing: a review.” *Sensors*, 20(23), pp. 6971.  
DOI: 10.3390/s20236971. IF (2020): 3.576, Q1 in Instruments & Instrumentation.
- [Rol20a] **Pablo Roldán-Varona, Luis Rodríguez-Cobo, and José Miguel López-Higuera (2020)**. “Reflection based lab-in-fibre sensor integrated in surgical needle for biomedical applications.” *Optics Letters*, 45(18), pp. 5242–5245.  
DOI: 10.1364/OL.399407. IF (2020): 3.776, Q1 in Optics.
- [Rol20b] **Pablo Roldán-Varona, David Pallarés-Aldeiturriaga, Luis Rodríguez-Cobo, and José Miguel López-Higuera (2020)**. “All-in-fibre multiscan Mach-Zehnder interferometer assisted by core FBG for simultaneous multi-parameter sensing.” *Optics & Laser Technology*, 132, pp. 106459.  
DOI: 10.1016/j.optlastec.2020.106459. IF (2020): 3.867, Q1 in Optics.
- [Rol20c] **Pablo Roldán-Varona, David Pallarés-Aldeiturriaga, Luis Rodríguez-Cobo, and José Miguel López-Higuera (2020)**. “Slit beam shaping technique for femtosecond laser inscription of enhanced plane-by-plane FBGs.” *Journal of Lightwave Technology*, 38(16), pp. 4526–4532.  
DOI: 10.1109/JLT.2020.2992568. IF (2020): 4.142, Q1 in Optics.

- [Laa19] **Ismail Laarossi, Pablo Roldán-Varona, María Ángeles Quintela-Incera, Luis Rodríguez-Cobo, and José Miguel López-Higuera (2019)**. “Ultra-high temperature and strain hybrid integrated sensor system based on Raman and femtosecond FBG inscription in a multimode gold-coated fibre.” *Optics Express*, 27(26), pp. 37122–37130.  
DOI: 10.1364/OE.27.037122. IF (2019): 3.669, Q1 in Optics.

### International conferences

- [Och23b] **Mario Ochoa, Pablo Roldán-Varona, María Gabriela Fernández-Manteca, Adolfo Cobo, José Miguel López-Higuera, and Luis Rodríguez-Cobo (2023)**. “On the mechanisms enabling polarisation-independent high etching rates in fused silica processed by ultrafast laser selective etching.” PULMM 2023, 4th Edition of Progress in Ultrafast Laser Modifications of Materials. Nikko, Japan. June 2023.
- [Gom23] **Celia Gómez-Galdós, Pablo Roldán-Varona, Mario Ochoa, María Gabriela Fernández-Manteca, José Francisco Algorri, José Miguel López-Higuera, Adolfo Cobo, and Luis Rodríguez-Cobo (2023)**. “Lab-on-chip design for multi-parameter phytoplankton analysis.” EWOFs’23 (8th European Workshop of Optical fibre Sensors). Mons, Belgium. May 2023.
- [Och23c] **Mario Ochoa, Pablo Roldán-Varona, José Miguel López-Higuera, and Luis Rodríguez-Cobo (2023)**. “Polarisation-independent ultrafast laser selective etching processing in fused silica.” SPIE Photonic West, Frontiers in Ultrafast Optics: Biomedical, Scientific, and Industrial Applications XXIII. San Francisco, USA. January 2023.
- [Rol22b] **Pablo Roldán-Varona, Nouredine Bennis, Michał Dudek, Anna Spadło, José Francisco Algorri, Luis Rodríguez-Cobo, José Miguel López-Higuera, and Paweł Marć (2022)**. “Fabrication of integrated microlenses in a polymer coherent fibre bundle.” POF 2022, 30th International Conference on Plastic Optical fibres. Bilbao, Spain. September 2022.
- [Rol22c] **Pablo Roldán-Varona, Mario Ochoa, María Gabriela Fernández-Manteca, José Francisco Algorri, Luis Rodríguez-Cobo, Adolfo Cobo, and José Miguel López-Higuera (2022)**. “Ultrafast laser fabricated lab-on-chip for microchannel excitation enhancement.” OFS 2022 (27th International Conference on Optical Fibre Sensors). Alexandria, Virginia, USA. August 2022. Optical Society of America (paper W4.4).  
DOI: 10.1364/OFS.2022.W4.4.
- [Alg22c] **José Francisco Algorri, Pablo Roldán-Varona, Mario Ochoa, Luis Rodríguez-Cobo, and José Miguel López-Higuera (2022)**. “Microfluidic Sensor Based on a Microbubble-Phase-Shifted Fibre Bragg Grating.” OFS 2022 (27th International Conference on Optical Fibre Sensors). Alexandria, Virginia, USA. August 2022. Optical Society of America (paper W4.60).  
DOI: 10.1364/OFS.2022.W4.60.

- [Rol22d] **Pablo Roldán-Varona, Helen E. Parker, Calum A. Ross, Luis Rodríguez-Cobo, José Miguel López-Higuera, Kevin Dhaliwal, Michael G. Tanner, and Robert R. Thomson (2022)**. “Selective Plane Illumination Optical Endomicroscopy with Polymer Imaging Fibres.” 2022 Conference on Lasers and Electro-Optics (CLEO). San José, California, USA. May 2022. Optica Publishing Group (paper SM3L.2). DOI: 10.1364/CLEO\_SI.2022.SM3L.2.
- [Par22] **Helen E. Parker, Pablo Roldán-Varona, Calum A. Ross, Luis Rodríguez-Cobo, José Miguel López-Higuera, Kevin Dhaliwal, Michael G. Tanner, and Robert R. Thomson (2022)**. “Selective Plane Illumination Fluorescence Endomicroscopy using a Polymer Imaging fibre and an End-cap.” 2022 Biophotonics Congress: Biomedical Optics. Fort Lauderdale, Florida, USA. April 2022. Optica Publishing Group (paper TW1B.6). DOI: 10.1364/TRANSLATIONAL.2022.TW1B.6.
- [Rol20d] **Pablo Roldán-Varona, Luis Rodríguez-Cobo, and José Miguel López-Higuera (2020)**. “Lab-In-fibre Sensor integrated in Surgical Needle for Fluid Detection.” OFS 2020 (27th International Conference on Optical Fibre Sensors), Alexandria, Virginia, USA. June 2020. Optical Society of America (paper Th1.4). DOI: 10.1364/OFS.2020.Th1.4.
- [Rol20e] **Pablo Roldán-Varona, David Pallarés-Aldeiturriaga, Luis Rodríguez-Cobo, and José Miguel López-Higuera (2020)**. “A new approach to Optical fibre Sensors: Plane-by-Plane FBGs inscribed using Femtosecond Laser and a Slit.” OFS 2020 (27th International Conference on Optical Fibre Sensors), Alexandria, Virginia, USA. June 2020. Optical Society of America (paper W4.7). DOI: 10.1364/OFS.2020.W4.7.
- [Rol20f] **Pablo Roldán-Varona, David Pallarés-Aldeiturriaga, Luis Rodríguez-Cobo, Rosa Ana Pérez-Herrera, Mikel Bravo Acha, Manuel López-Amo, and José Miguel López-Higuera (2020)**. “Compact Optical fibre Lasers and Optical fibre Sensors assisted by Femtosecond Laser Inscription of Plane-by-Plane FBGs.” OFS 2020 (27th International Conference on Optical Fibre Sensors), Alexandria, Virginia, USA. June 2020. Optical Society of America (paper W4.77). DOI: 10.1364/OFS.2020.W4.77.
- [Rol19a] **Pablo Roldán-Varona, David Pallarés-Aldeiturriaga, Luis Rodríguez-Cobo, and José Miguel López-Higuera (2019)**. “Reflected power-based 2D bending sensor using femtosecond laser FBG inscription in multicore fibre.” EWOFs’19 (7th European Workshop of Optical fibre Sensors). Limassol, Cyprus. October 2019. International Society for Optics and Photonics (Vol. 11199, p. 111992M). DOI: 10.1117/12.2538794.
- [Rol19b] **Pablo Roldán-Varona, David Pallarés-Aldeiturriaga, Luis Rodríguez-Cobo, and José Miguel López-Higuera (2019)**. “Hybrid Mach-Zehnder Interferometer manufactured by femtosecond laser multiscan technique.” EWOFs’19 (7th European Workshop of Optical fibre Sensors). Limassol, Cyprus. October 2019. International Society for Optics and Photonics (Vol. 11199, p. 111992N). DOI: 10.1117/12.2538813.

- [Pal19] **David Pallarés-Aldeiturriaga, Pablo Roldán-Varona, Luis Rodríguez-Cobo, and José Miguel López-Higuera (2019)**. “Astigmatism compensation for waveguide inscription in optical fibre by femtosecond lasers.” EWOFs’19 (7th European Workshop of Optical fibre Sensors). Limassol, Cyprus. October 2019. International Society for Optics and Photonics (Vol. 11199, p. 111992T). DOI: 10.1117/12.2539835.
- [Hig19] **José Miguel López-Higuera, Pablo Roldán-Varona, David Pallarés-Aldeiturriaga, and Luis Rodríguez-Cobo (2019)**. “Tiny fibre Sensors by Laser Processing.” 5th Ed. Smart Materials and Surfaces - 2019 SMS Conference. Lisbon, Portugal. October 2019.

### National conferences

- [Rol21d] **Pablo Roldán-Varona, Rosa Ana Pérez-Herrera, Mauro Lomer, Luis Rodríguez-Cobo, Manuel López-Amo, and José Miguel López-Higuera (2021)**. “Refractómetro optimizado para aplicaciones biomédicas basado en fibras de plástico perfluoradas.” RNO 2021 (XIII Reunión Nacional de Óptica). Online event. November 2021.
- [Rol21e] **Pablo Roldán-Varona, Luis Reyes-González, Marina Martínez-Mincheró, José Francisco Algorri, Luis Rodríguez-Cobo, Adolfo Cobo, and José Miguel López-Higuera (2021)**. “Chemical etching of plastic optical fibres for custom tips.” OPTOEL 2021 (XII Reunión Española de Optoelectrónica). Online event. July 2021.
- [Rol21f] **Pablo Roldán-Varona, Ismail Laarossi, María Ángeles Quintela, Jesús Mirapeix, Luis Rodríguez-Cobo, and José Miguel López-Higuera (2021)**. “Direct femtosecond laser inscription of ytterbium doped fibres for optical fibre sensing.” OPTOEL 2021 (XII Reunión Española de Optoelectrónica). Online event. July 2021.
- [Lom21] **Mauro Lomer, Pablo Roldán-Varona, José Francisco Algorri, Luis Rodríguez-Cobo, Rosa Ana Pérez-Herrera, Manuel López-Amo, and José Miguel López-Higuera (2021)**. “Femtosecond laser inscription of diffraction gratings in CYTOP fibres for optical fibre sensing.” OPTOEL 2021 (XII Reunión Española de Optoelectrónica). Online event. July 2021.
- [Rol19c] **Pablo Roldán-Varona, David Pallarés-Aldeiturriaga, Luis Rodríguez-Cobo, and José Miguel López-Higuera (2019)**. “Sensor de curvatura 2D basado en potencia reflejada por FBGs inscritos en una fibra multinúcleo mediante láser de femtosegundo.” OPTOEL 2019 (XI Reunión Española de Optoelectrónica). Zaragoza, Spain. July 2019.
- [Rol19d] **Pablo Roldán-Varona, Ismail Laarossi, David Pallarés-Aldeiturriaga, Iñaki Aporta, María Ángeles Quintela, Luis Rodríguez-Cobo, and José Miguel López-Higuera (2019)**. “Femtosecond laser fibre Bragg grating inscribed in multi-mode fibres.” OPTOEL 2019 (XI Reunión Española de Optoelectrónica). Zaragoza, Spain. July 2019.

## Others

- [Och23d] **Mario Ochoa and Pablo Roldán-Varona *et al.* (2023)**. Back inside cover related with the article [Och23a] in *Lab on a Chip* journal (Volume 25, Issue 7).
- [Rol21g] **Pablo Roldán-Varona, Luis Rodríguez-Cobo, and José Miguel López-Higuera (2021)**. “Dual optical fiber sensor for in vivo measurements.” *Laser Focus World*. Published on 24<sup>th</sup> March 2021 by Richard Gaughan based on [Rol20a].  
URL: [https://www.laserfocusworld.com/biooptics/article/14197814/dual-optical-fiber-sensor-for-in-vivo-measurements?fbclid=IwAR03E3vkvWlnh\\_qM7JW1YqVfq782GkXR2yZ21rWagNUSonNzHyQTAdCfb8](https://www.laserfocusworld.com/biooptics/article/14197814/dual-optical-fiber-sensor-for-in-vivo-measurements?fbclid=IwAR03E3vkvWlnh_qM7JW1YqVfq782GkXR2yZ21rWagNUSonNzHyQTAdCfb8)

## Industrial publications

- [P2022] **Pablo Roldán-Varona, Calum A. Ross, Michael G. Tanner, Robert R. Thomson, and Helen E. Parker**. End cap for coherent fibre bundle for enabling selective plane illumination microscopy. Patent application filed on 21<sup>st</sup> April 2022 to the UK Intellectual Property Office. The patent application number is (GB2205826.7). Online Patent Information and Document Inspection Service: <https://www.ipo.gov.uk/p-ipsu/Case/ApplicationNumber/GB2205826.7>

## Other contributions

### Journal articles

- [Sie23] **Sergio Sierra, Elena Prado, Luis Rodríguez-Cobo, Carla Quilens-Pons, Pablo Roldán-Varona, David Díaz-Viñolas, Pedro Anuarbe-Cortés, Adolfo Cobo, and Francisco Sánchez (2023)**. “Density estimation of the main structuring sessile species in underwater marine caves with a deep learning approach.” *Journal of Geography and Cartography*, 6(1), pp. 1980.  
DOI: 10.24294/jgc.v6i1.1980.
- [San22a] **Arturo Sánchez-González, Rosa Ana Pérez-Herrera, Pablo Roldán-Varona, Miguel Durán-Escudero, Luis Rodríguez-Cobo, José Miguel López-Higuera, and Manuel López-Amo (2022)**. “A Dual-Wavelength fibre Laser Sensor with Temperature and Strain Discrimination.” *Sensors*, 22(18), pp. 6888.  
DOI: 10.3390/s22186888.
- [Per22a] **Rosa Ana Pérez-Herrera, Pablo Roldán-Varona, Arturo Sánchez-González, Luis Rodríguez-Cobo, José Miguel López-Higuera, and Manuel López-Amo (2022)**. “C and L band fibre lasers enhanced by ultrafast laser inscribed artificial backscatter reflectors.” *Optics Continuum*, 1(9), pp. 1963–1969.  
DOI: 10.1364/OPTCON.458557.
- [San22b] **Arturo Sánchez-González, Rosa Ana Pérez-Herrera, Pablo Roldán-Varona, Luis Rodríguez-Cobo, José Miguel López-Higuera, and Manuel López-Amo**

- (2022). “High Performance fibre Laser Resonator for Dual Band (C and L) Sensing.” *Journal of Lightwave Technology*, 9(3), pp. 130–137.  
DOI: 10.1109/JLT.2022.3170124.
- [Sam22a] **Mohsen Samadi, Fatemeh Abshari, José Francisco Algorri, Pablo Roldán-Varona, Luis Rodríguez-Cobo, José Miguel López-Higuera, José Manuel Sánchez-Pena, Dimitrios C. Zografopoulos, and Francesco Dell’Olio (2022).** “All-Dielectric Metasurface Based on Complementary Split-Ring Resonators for Refractive Index Sensing.” *Photonics*, 9(3), pp. 130–137.  
DOI: 10.3390/photonics9030130.
- [Alg22b] **José Francisco Algorri, Francesco Dell’Olio, Pablo Roldán-Varona, Luis Rodríguez-Cobo, José Miguel López-Higuera, José Manuel Sánchez-Pena, Victor Dmitriev, and Dimitrios C. Zografopoulos (2022).** “Analogue of electromagnetically induced transparency in square slotted silicon metasurfaces supporting bound states in the continuum.” *Optics Express*, 30(3), pp. 4615–4630.  
DOI: 10.1364/OE.446720.
- [Per21a] **Rosa Ana Pérez-Herrera, Mikel Bravo, Pablo Roldán-Varona, Daniel Leandro, Luis Rodríguez-Cobo, José Miguel López-Higuera and Manuel López-Amo (2021).** “Microdrilled tapers to enhance optical fibre lasers for sensing.” *Scientific Reports*, 11, pp. 20408.  
DOI: 10.1038/s41598-021-00046-7. IF (2021): 4.997, Q2 in Multidisciplinary Sciences.
- [Alg21a] **José Francisco Algorri, Mario Ochoa, Pablo Roldán-Varona, Luis Rodríguez-Cobo, and José Miguel López-Higuera (2021).** “Photodynamic Therapy: A compendium of latest reviews.” *Cancers*, 13(17), pp. 4447.  
DOI: 10.3390/cancers13174447. IF (2021): 6.575, Q1 in Oncology.
- [Alg21b] **José Francisco Algorri, Mario Ochoa, Pablo Roldán-Varona, Luis Rodríguez-Cobo, and José Miguel López-Higuera (2021).** “Light Technology for Efficient and Effective Photodynamic Therapy: A Critical Review.” *Cancers*, 13(14), pp. 3484.  
DOI: 10.3390/cancers13143484. IF (2021): 6.575, Q1 in Oncology.
- [Per21b] **Rosa Ana Pérez-Herrera, Pablo Roldán-Varona, Marko Galarza, Silvia Sañudo-Lasagabaster, Luis Rodríguez-Cobo, José Miguel López-Higuera, and Manuel López-Amo (2021).** “Hybrid Raman-Erbium Random fibre Laser with a Half Open Cavity Assisted by Artificially Controlled Backscattering fibre Reflectors.” *Scientific Reports*, 11, pp. 9169.  
DOI: 10.1038/s41598-021-88748-w. IF (2021): 4.997, Q2 in Multidisciplinary Sciences.
- [Alg21c] **José Francisco Algorri, Francesco Dell’Olio, Pablo Roldán-Varona, Luis Rodríguez-Cobo, José Miguel López-Higuera, José Manuel Sánchez-Pena, and Dimitrios C. Zografopoulos (2021).** “Strongly resonant silicon slot metasurfaces with symmetry-protected bound states in the continuum.” *Optics Express*, 29(7), pp. 10374–10385.  
DOI: 10.1364/OE.415377. IF (2021): 3.833, Q2 in Optics.

- [Per21c] **Rosa Ana Pérez-Herrera, Pablo Roldán-Varona, Luis Rodríguez-Cobo, José Miguel López-Higuera, and Manuel López-Amo (2021)**. “Single longitudinal mode lasers by using artificially controlled backscattering erbium doped fibres.” *IEEE Access*, 9, pp. 27428–27433.  
DOI: 10.1109/ACCESS.2021.3058092. IF (2021): 3.476, Q2 in Engineering, Electrical & Electronic.

### International conferences

- [Per22b] **Rosa Ana Pérez-Herrera, Pablo Roldán-Varona, Arturo Sánchez-González, Luis Rodríguez-Cobo, José Miguel López-Higuera, and Manuel López-Amo (2022)**. “Wavelength-switchable L-band fiber laser assisted by ultrafast laser fabricated random reflectors.” EOSAM 2022, European Optical Society Annual Meeting. Porto, Portugal. September 2022.  
DOI: 10.1051/epjconf/202226613026.
- [Per22c] **Rosa Ana Pérez-Herrera, Pablo Roldán-Varona, Arturo Sánchez-González, Miguel Durán, Luis Rodríguez-Cobo, José Miguel López-Higuera, and Manuel López-Amo (2022)**. “Stable L-band fibre Laser Sensor using a Backscattering-Based Multimode fibre Reflector.” OFS 2022 (27th International Conference on Optical Fibre Sensors). Alexandria, Virginia, USA. August 2022. Optical Society of America (paper W4.68).  
DOI: 10.1364/OFS.2022.W4.68.
- [Sam22b] **Mohsen Samadi, Fatemeh Abshari, José Francisco Algorri, Pablo Roldán-Varona, Luis Rodríguez-Cobo, José Miguel López-Higuera, José Manuel Sánchez-Pena, Dimitrios C. Zografopoulos, and Francesco Dell’Olio (2022)**. “Refractive index sensing by all-dielectric metasurfaces supporting quasi-bound states in the continuum.” Laser Resonators, Microresonators, and Beam Control XXIV. San Francisco, California, USA. March 2022. Optica Publishing Group (paper 119870B).  
DOI: 10.1117/12.2608256.
- [Alg22d] **José Francisco Algorri, Francesco Dell’Olio, Pablo Roldán-Varona, Luis Rodríguez-Cobo, José Miguel López-Higuera, José Manuel Sánchez-Pena, and Dimitrios C. Zografopoulos (2022)**. “Double electromagnetically induced transparency resonance in slotted metasurfaces supporting bound states in the continuum.” 2022 Workshop on Recent Advances in Photonics (WRAP). Mumbai, India. March 2022.  
DOI: 10.1109/WRAP54064.2022.97582406.
- [Alg21d] **José Francisco Algorri, Francesco Dell’Olio, Pablo Roldán-Varona, Luis Rodríguez-Cobo, José Miguel López-Higuera, José Manuel Sánchez-Pena, and Dimitrios Zografopoulos (2021)**. “Electromagnetically induced transparency in square slotted dielectric metasurfaces supporting bound states in the continuum.” 2021 IEEE Photonics Conference (IPC). Vancouver, BC, Canada. October 2021.  
DOI: 10.1109/IPC48725.2021.9593077.

- [Alg21e] **José Francisco Algorri, Francesco Dell’Olio, Pablo Roldán-Varona, Luis Rodríguez-Cobo, José Miguel López-Higuera, José Manuel Sánchez-Pena, Victor Dmitriev, and Dimitrios C. Zografopoulos (2021)**. “All-Dielectric Slot Metasurface with Ultra-High-Q resonances.” 2021 Conference on Lasers and Electro-Optics (CLEO). San José, California, USA. May 2021. Optical Society of America (paper JW1A.131).  
DOI: 10.1364/CLEO\_AT.2021.JW1A.131.
- [Laa20] **Ismail Laarossi, Pablo Roldán-Varona, María Ángeles Quintela, Luis Rodríguez-Cobo, and José Miguel López-Higuera (2020)**. “Adaptive Peak-Tracking Algorithm for Multimode fibre Bragg Grating in Ultrahigh Temperature.” OFS 2020 (27th International Conference on Optical Fibre Sensors), Alexandria, Virginia, USA. June 2020. Optical Society of America (paper T3.83).  
DOI: 10.1364/OFS.2020.T3.83.
- [Per20] **Rosa Ana Pérez-Herrera, Mikel Bravo Acha, Pablo Roldán-Varona, Daniel Leandro, Luis Rodríguez-Cobo, José Miguel López-Higuera, and Manuel López-Amo (2020)**. “Enhanced Optical fibre Lasers and Optical fibre Sensors assisted by Micro-Drilled Optical fibres.” OFS 2020 (27th International Conference on Optical Fibre Sensors), Alexandria, Virginia, USA. June 2020. Optical Society of America (paper W4.72).  
DOI: 10.1364/OFS.2020.W4.72.
- [Per19] **Rosa Ana Pérez-Herrera, Mikel Bravo Acha, Pablo Roldán-Varona, Daniel Leandro, Luis Rodríguez-Cobo, José Miguel López-Higuera, and Manuel López-Amo (2019)**. “Micro-drilled optical fibre for enhanced laser strain sensors.” EWOFs’19 (7th European Workshop of Optical fibre Sensors). Limassol, Cyprus. October 2019. International Society for Optics and Photonics (Vol. 11199, p. 111992R).  
DOI: 10.1117/12.2539802.

### National conferences

- [Rol21c] **Pablo Roldán-Varona, Rosa Ana Pérez-Herrera, Arturo Sánchez-González, Luis Rodríguez-Cobo, Manuel López-Amo, and José Miguel López-Higuera (2021)**. “Láser de fibra óptica asistido por un reflector de fibra multimodo con retrodispersión controlada artificialmente.” RNO 2021 (XIII Reunión Nacional de Óptica). Online event. November 2021.
- [San21a] **Arturo Sánchez-González, Rosa Ana Pérez-Herrera, Pablo Roldán-Varona, Luis Rodríguez-Cobo, José Miguel López-Higuera, and Manuel López-Amo (2021)**. “Cavidad láser de fibra óptica multibanda basada en reflectores pseudoaleatorios cuasidistribuidos.” RNO 2021 (XIII Reunión Nacional de Óptica). Online event. November 2021.
- [Rey21] **Luis Reyes-González, Pablo Roldán-Varona, Luis Rodríguez-Cobo, Mauro Lomer, and José Miguel López-Higuera (2021)**. “Increasing SNR of speckle-based ballistocardiogram.” OPTOEL 2021 (XII Reunión Española de Optoelectrónica). Online event. July 2021.

- [Per21d] **Rosa Ana Pérez-Herrera, Pablo Roldán-Varona, Marko Galarza, Silvia Sañudo-Lasagabaster, Luis Rodríguez-Cobo, José Miguel López-Higuera, and Manuel López-Amo (2021).** “Láser random de fibra óptica asistido por reflectores de fibra con retrodispersión controlada artificialmente.” OPTOEL 2021 (XII Reunión Española de Optoelectrónica). Online event. July 2021.
- [San21b] **Arturo Sánchez-González, Rosa Ana Pérez-Herrera, Pablo Roldán-Varona, Luis Rodríguez-Cobo, José Miguel López-Higuera, and Manuel López-Amo (2021).** “Optical fibre lasers based on classic, tapered and micro-drilled mirrors.” OPTOEL 2021 (XII Reunión Española de Optoelectrónica). Online event. July 2021.
- [Gal21] **Marko Galarza, Silvia Sañudo-Lasagabaster, Rosa Ana Pérez-Herrera, Pablo Roldán-Varona, Luis Rodríguez-Cobo, José Miguel López-Higuera, and Manuel López-Amo (2021).** “Diseño y caracterización de reflectores incoherentes de retrodispersión de fibra microperforada para láseres random de fibra óptica.” OPTOEL 2021 (XII Reunión Española de Optoelectrónica). Online event. July 2021.

**Table A.1.** Number of journal articles published during the thesis, highlighting those works that are closely related to the PhD work, as well as the others. The average values of authorship order, impact factor, and quartile are shown.

Works	No.	Average author position	Average impact factor	Average quartile
Related to PhD	12	1.50	4.75	1.25
Non-related to PhD	12	3	4.51	1.80

LIST OF PUBLICATIONS

**Table A.2.** Summary of publications and their relationship with thesis contributions. This table only includes works closely related to the topics conducted in this thesis.

	Work	Review of the state-of-the-art	ULDW		ULAE		
			Technique (Ch. 5)	Fibre sensors (Ch. 6 and 7)	Technique (Ch. 8)	End-cap (Ch. 9)	Lab-on-chip devices
Journal article	[Och23a]				✓		
	[Rol23]					✓	
	[Alg22a]	✓					
	[Rol22a]			✓			
	[Och21]	✓					
	[Rol21a]		✓	✓			
	[Rol21b]			✓			
	[Pal20]						
	[Rol20a]	✓					
	[Rol20b]			✓			
	[Rol20c]		✓				
	[Laa19]			✓			
International conference	[Och23b]				✓		
	[Gom23]						✓
	[Och23c]				✓		
	[Rol22b]					✓	
	[Rol22c]						✓
	[Alg22c]			✓			
	[Rol22d]					✓	
	[Par22]					✓	
	[Rol20d]			✓			
	[Rol20e]		✓	✓			
	[Rol20f]			✓			
	[Rol19a]			✓			
	[Rol19b]		✓	✓			
	[Pal19]		✓				
	[Hig19]	✓					
National conference	[Rol21d]			✓			
	[Rol21e]		✓				
	[Rol21f]		✓	✓			
	[Lom21]			✓			
	[Rol19c]			✓			
	[Rol19d]			✓			
Patent	[P2022]				✓	✓	

# References in alphabetical order

<https://i-fiberoptics.com/fiber-detail-asahi.php?id=3305&sum=162>, Accessed: 2022-09-01.

<https://www.fujikura.co.uk/>, Accessed: 2022-09-05.

<https://www.microsoft.com/en-us/research/project/project-silica/>, Accessed: 2023-05-16.

<https://microrelleus.com/case-studies/>, Accessed: 2023-05-16.

<https://news.microsoft.com/source/features/innovation/ignite-project-silica-superman/>, Accessed: 2023-05-17.

Internal conversations with Peter Kazansky at PULMM 2023, Nikko, Japan.

Internal conversations with Matthieu Lancry at PULMM 2023, Nikko, Japan.

Internal conversations with Saulius Juodkazis at PULMM 2023, Nikko, Japan.

**Adams, C. S., et al.**, *Optics f2f*. Oxford University Press Oxford, Dec. 2018. DOI: 10.1093/oso/9780198786788.001.0001.

**Adams, D. C., et al.**, “Advances in Endoscopic Optical Coherence Tomography Catheter Designs,” *IEEE Journal of Selected Topics in Quantum Electronics*, vol. 22, no. 3, pp. 210–221, May 2016. DOI: 10.1109/jstqe.2015.2510295. [Online]. Available: <https://doi.org/10.1109/jstqe.2015.2510295>.

**Agarwal, A., et al.**, “Correlation of silica glass properties with the infrared spectra,” *Journal of Non-Crystalline Solids*, vol. 209, no. 1-2, pp. 166–174, Jan. 1997. DOI: 10.1016/s0022-3093(96)00542-x.

**Aly, A. H., et al.**, “Biophotonic sensor for the detection of creatinine concentration in blood serum based on 1D photonic crystal,” *RSC Advances*, vol. 10, no. 53, pp. 31 765–31 772, 2020. DOI: 10.1039/d0ra05448h.

**Amin, M. S., et al.**, “Optical transmission filters with coexisting guided-mode resonance and Rayleigh anomaly,” *Applied Physics Letters*, vol. 103, no. 13, p. 131 106, Sep. 2013. DOI: 10.1063/1.4823532.

**Amini, H., et al.**, “Inertial microfluidic physics,” *Lab on a Chip*, vol. 14, no. 15, p. 2739, 2014. DOI: 10.1039/c4lc00128a.

**Ams, M., et al.**, “Slit beam shaping method for femtosecond laser direct-write fabrication of symmetric waveguides in bulk glasses,” *Optics Express*, vol. 13, no. 15, pp. 5676–5681, 2005. DOI: 10.1364/opex.13.005676.

**Ams, M., et al.**, “Study of the influence of femtosecond laser polarisation on direct writing of waveguides,” *Optics Express*, vol. 14, no. 26, pp. 13 158–13 163, 2006. DOI: 10.1364/oe.14.013158.

References in alphabetical order

- Ams, M., et al.**, “Investigation of Ultrafast Laser–Photonic Material Interactions: Challenges for Directly Written Glass Photonics,” *IEEE Journal of Selected Topics in Quantum Electronics*, vol. 14, no. 5, pp. 1370–1381, 2008. DOI: 10.1109/jstqe.2008.925809.
- Anderson, P., et al.**, “Glass: A New Media for a New Era?” In *10th USENIX Workshop on Hot Topics in Storage and File Systems (HotStorage 18)*, Boston, MA: USENIX Association, Jul. 2018. [Online]. Available: <https://www.usenix.org/conference/hotstorage18/presentation/anderson>.
- Arditty, H. J., et al.**, “Sagnac effect in fiber gyroscopes,” *Optics Letters*, vol. 6, no. 8, pp. 401–403, Aug. 1981. DOI: 10.1364/ol.6.000401.
- Arif, M. F. H., et al.**, “Enhancement of relative sensitivity of photonic crystal fiber with high birefringence and low confinement loss,” *Optik*, vol. 131, pp. 697–704, Feb. 2017. DOI: 10.1016/j.ijleo.2016.11.203.
- Awazu, K., et al.**, “Strained Si–O–Si bonds in amorphous SiO<sub>2</sub> materials: A family member of active centers in radio, photo, and chemical responses,” *Journal of Applied Physics*, vol. 94, no. 10, pp. 6243–6262, Nov. 2003. DOI: 10.1063/1.1618351.
- Babu, B. H., et al.**, “Stress-induced optical waveguides written by an ultrafast laser in Nd<sup>3+</sup>, Y<sup>3+</sup> co-doped SrF<sub>2</sub> crystals,” *Applied Optics*, vol. 58, no. 4, pp. 984–990, Jan. 2019. DOI: 10.1364/ao.58.000984.
- Barty, A., et al.**, “Quantitative optical phase microscopy,” *Optics Letters*, vol. 23, no. 11, pp. 817–819, Jun. 1998. DOI: 10.1364/ol.23.000817.
- Bashan, G., et al.**, “A forward Brillouin fibre laser,” *Nature Communications*, vol. 13, no. 1, p. 3554, Jun. 2022. DOI: 10.1038/s41467-022-31246-y.
- Basiri, A., et al.**, “Microfluidic devices for detection of RNA viruses,” *Reviews in Medical Virology*, vol. 31, no. 1, pp. 1–11, Aug. 2020. DOI: 10.1002/rmv.2154.
- Beebe, D. J., et al.**, “Physics and Applications of Microfluidics in Biology,” *Annual Review of Biomedical Engineering*, vol. 4, no. 1, pp. 261–286, Aug. 2002. DOI: 10.1146/annurev.bioeng.4.112601.125916.
- Bellair, C. J., et al.**, “Quantitative phase amplitude microscopy IV: Imaging thick specimens,” *Journal of Microscopy*, vol. 214, no. 1, pp. 62–69, Apr. 2004. DOI: 10.1111/j.0022-2720.2004.01302.x.
- Bellouard, Y., et al.**, “Scanning thermal microscopy and Raman analysis of bulk fused silica exposed to lowenergy femtosecond laser pulses,” *Optics Express*, vol. 16, no. 24, pp. 19 520–19 534, Nov. 2008. DOI: 10.1364/oe.16.019520.
- Bellouard, Y., et al.**, “Fabrication of high-aspect ratio, micro-fluidic channels and tunnels using femtosecond laser pulses and chemical etching,” *Optics Express*, vol. 12, no. 10, pp. 2120–2129, 2004. DOI: 10.1364/opex.12.002120.
- Bellouard, Y., et al.**, “Stress-state manipulation in fused silica via femtosecond laser irradiation,” *Optica*, vol. 3, no. 12, pp. 1285–1293, Nov. 2016. DOI: 10.1364/optica.3.001285.

- Bernard, O., et al.**, “Third-harmonic generation monitoring of femtosecond-laser-induced in-volume functional modifications,” *Optica*, vol. 10, no. 6, pp. 774–782, Jun. 2023. DOI: 10.1364/optica.486746.
- Bertoncini, A., et al.**, “3D printed waveguides based on photonic crystal fiber designs for complex fiber-end photonic devices,” *Optica*, vol. 7, no. 11, pp. 1487–1494, Oct. 2020. DOI: 10.1364/optica.397281.
- Bilro, L., et al.**, “Optical Sensors Based on Plastic Fibers,” *Sensors*, vol. 12, no. 9, pp. 12 184–12 207, Sep. 2012. DOI: 10.3390/s120912184.
- Bisch, N., et al.**, “Adaptive optics aberration correction for deep direct laser written waveguides in the heating regime,” *Applied Physics A*, vol. 125, no. 5, Apr. 2019. DOI: 10.1007/s00339-019-2635-4.
- Bonner, W. A., et al.**, “Fluorescence Activated Cell Sorting,” *Review of Scientific Instruments*, vol. 43, no. 3, pp. 404–409, Mar. 1972. DOI: 10.1063/1.1685647.
- Booth, M. J., et al.**, “Aberration correction for confocal imaging in refractive-index-mismatched media,” *Journal of Microscopy*, vol. 192, no. 2, pp. 90–98, Nov. 1998. DOI: 10.1111/j.1365-2818.1998.99999.x.
- Bragheri, F., et al.**, “Optofluidic integrated cell sorter fabricated by femtosecond lasers,” *Lab on a Chip*, vol. 12, no. 19, p. 3779, 2012. DOI: 10.1039/c2lc40705a.
- Broadway, C., et al.**, “CYTOP Fibre Bragg Grating Sensors for Harsh Radiation Environments,” *Sensors*, vol. 19, no. 13, p. 2853, Jun. 2019. DOI: 10.3390/s19132853.
- Brückner, R.**, “Properties and structure of vitreous silica. I,” *Journal of Non-Crystalline Solids*, vol. 5, no. 2, pp. 123–175, Nov. 1970. DOI: 10.1016/0022-3093(70)90190-0.
- Bulgakov, E. N., et al.**, “Light trapping above the light cone in a one-dimensional array of dielectric spheres,” *Physical Review A*, vol. 92, no. 2, p. 023 816, Aug. 2015. DOI: 10.1103/physreva.92.023816.
- Butcher, H. L., et al.**, “Demonstration and characterization of ultrafast laser-inscribed mid-infrared waveguides in chalcogenide glass IG2,” *Optics Express*, vol. 26, no. 8, pp. 10 930–10 943, Apr. 2018. DOI: 10.1364/oe.26.010930.
- Butkutė, A., et al.**, “Optimization of selective laser etching (SLE) for glass micromechanical structure fabrication,” *Optics Express*, vol. 29, no. 15, pp. 23 487–23 499, Jul. 2021. DOI: 10.1364/oe.430623.
- Canning, J.**, “Fibre gratings and devices for sensors and lasers,” *Laser & Photonics Review*, vol. 2, no. 4, pp. 275–289, Aug. 2008. DOI: 10.1002/lpor.200810010.
- Casamenti, E., et al.**, “Few pulses femtosecond laser exposure for high efficiency 3D glass micromachining,” *Optics Express*, vol. 29, no. 22, pp. 35 054–35 066, Oct. 2021. DOI: 10.1364/oe.435163. [Online]. Available: <https://doi.org/10.1364/oe.435163>.

References in alphabetical order

- Caucheteur, C., et al.**, “Polarization-Assisted Fiber Bragg Grating Sensors: tutorial and Review,” *Journal of Lightwave Technology*, vol. 35, no. 16, pp. 3311–3322, Aug. 2017. DOI: 10.1109/jlt.2016.2585738.
- Cerullo, G., et al.**, “Femtosecond micromachining of symmetric waveguides at 15  $\mu\text{m}$  by astigmatic beam focusing,” *Optics Letters*, vol. 27, no. 21, pp. 1938–1940, Nov. 2002. DOI: 10.1364/ol.27.001938.
- Champion, A., et al.**, “Direct volume variation measurements in fused silica specimens exposed to femtosecond laser,” *Optical Materials Express*, vol. 2, no. 6, pp. 789–798, May 2012. DOI: 10.1364/ome.2.000789.
- Chan, J. W., et al.**, “Structural changes in fused silica after exposure to focused femtosecond laser pulses,” *Optics Letters*, vol. 26, no. 21, pp. 1726–1728, Nov. 2001. DOI: 10.1364/ol.26.001726.
- Chan, J. W., et al.**, “Waveguide fabrication in phosphate glasses using femtosecond laser pulses,” *Applied Physics Letters*, vol. 82, no. 15, pp. 2371–2373, Apr. 2003. DOI: 10.1063/1.1565708.
- Chandrasekharan, H. K., et al.**, “Ultrafast laser ablation of a multicore polymer optical fiber for multipoint light emission,” *Optics Express*, vol. 29, no. 13, pp. 20765–20775, Jun. 2021. DOI: 10.1364/oe.424494. [Online]. Available: <https://doi.org/10.1364/oe.424494>.
- Chatzieleftheriou, A., et al.**, “Could cloud storage be disrupted in the next decade?” In *Proceedings of the 12th USENIX Conference on Hot Topics in Storage and File Systems*, 2020, pp. 25–25.
- Chen, L., et al.**, “Millifluidics, microfluidics, and nanofluidics: Manipulating fluids at varying length scales,” *Materials Today Nano*, vol. 16, p. 100136, Dec. 2021. DOI: 10.1016/j.mtnano.2021.100136.
- Chen, P., et al.**, “Ultra-compact all-in-fiber-core Mach-Zehnder interferometer,” *Optics Letters*, vol. 42, no. 20, pp. 4059–4062, Oct. 2017. DOI: 10.1364/ol.42.004059.
- Chen, Z., et al.**, “Observation of miniaturized bound states in the continuum with ultra-high quality factors,” *Science Bulletin*, vol. 67, no. 4, pp. 359–366, Feb. 2022. DOI: 10.1016/j.scib.2021.10.020.
- Cheng, Y., et al.**, “Control of the cross-sectional shape of a hollow microchannel embedded in photostructurable glass by use of a femtosecond laser,” *Optics Letters*, vol. 28, no. 1, pp. 55–57, Jan. 2003. DOI: 10.1364/ol.28.000055.
- Choudhury, D., et al.**, “Ultrafast laser inscription: Perspectives on future integrated applications,” *Laser & Photonics Reviews*, vol. 8, no. 6, pp. 827–846, 2014. DOI: 10.1002/lpor.201300195. [Online]. Available: <https://doi.org/10.1002/lpor.201300195>.
- Ciriolo, A. G., et al.**, “Microfluidic devices for quasi-phase-matching in high-order harmonic generation,” *APL Photonics*, vol. 7, no. 11, p. 110801, Nov. 2022. DOI: 10.1063/5.0118199.

- Conci, C., et al.**, “A Miniaturized Imaging Window to Quantify Intravital Tissue Regeneration within a 3D Microscaffold in Longitudinal Studies,” *Advanced Optical Materials*, vol. 10, no. 7, p. 2101103, Feb. 2022. DOI: 10.1002/adom.202101103.
- Convery, N., et al.**, “30 years of microfluidics,” *Micro and Nano Engineering*, vol. 2, pp. 76–91, Mar. 2019. DOI: 10.1016/j.mne.2019.01.003.
- Courvoisier, F.**, “Ultrafast Laser Micro-Nano Structuring of Transparent Materials with High Aspect Ratio,” in *Handbook of Laser Micro- and Nano-Engineering*, Springer International Publishing, 2020, pp. 1–37. DOI: 10.1007/978-3-319-69537-2\_33-1.
- Crespi, A., et al.**, “Integrated photonic quantum gates for polarization qubits,” *Nature Communications*, vol. 2, no. 1, Nov. 2011. DOI: 10.1038/ncomms1570.
- Cruz, A. R., et al.**, “Independent control of beam astigmatism and ellipticity using a SLM for fs-laser waveguide writing,” *Optics Express*, vol. 17, no. 23, pp. 20853–20859, Oct. 2009. DOI: 10.1364/oe.17.020853.
- Cui, Z., et al.**, “Dynamic chromatic aberration pre-compensation scheme for ultrashort petawatt laser systems,” *Optics Express*, vol. 27, no. 12, pp. 16812–16822, May 2019. DOI: 10.1364/oe.27.016812.
- Cumming, B. P., et al.**, “Adaptive optics enhanced direct laser writing of high refractive index gyroid photonic crystals in chalcogenide glass,” *Optics Express*, vol. 22, no. 1, pp. 689–698, Jan. 2014. DOI: 10.1364/oe.22.000689.
- Curl, C. L., et al.**, “Refractive index measurement in viable cells using quantitative phase-amplitude microscopy and confocal microscopy,” *Cytometry Part A*, vol. 65A, no. 1, pp. 88–92, 2005. DOI: 10.1002/cyto.a.20134.
- Dakin, J. P., et al.**, “Temperature Distribution Measurement Using Raman Ratio Thermometry,” in *SPIE Proceedings*, SPIE, Jan. 1986. DOI: 10.1117/12.949798.
- Davis, K. M., et al.**, “Writing waveguides in glass with a femtosecond laser,” *Optics Letters*, vol. 21, no. 21, pp. 1729–1731, Nov. 1996. DOI: 10.1364/ol.21.001729.
- Dongre, C., et al.**, “Fluorescence monitoring of microchip capillary electrophoresis separation with monolithically integrated waveguides,” *Optics Letters*, vol. 33, no. 21, pp. 2503–2505, Oct. 2008. DOI: 10.1364/ol.33.002503.
- Dürr, Florian**, “Laser-induced stress changes in optical fibers,” en, 2005. DOI: 10.5075/EPFL-THESIS-3314.
- Eaton, S. M., et al.**, “Fundamentals of Femtosecond Laser Modification of Bulk Dielectrics,” in *Topics in Applied Physics*, Springer Berlin Heidelberg, Dec. 2011, pp. 3–18. DOI: 10.1007/978-3-642-23366-1\_1.
- Eaton, S. M., et al.**, “Fundamentals of femtosecond laser modification of bulk dielectrics,” *Topics in Applied Physics*, vol. 123, pp. 3–18, 2012. DOI: 10.1007/978-3-642-23366-1\_1/COVER. [Online]. Available: [https://link.springer.com/chapter/10.1007/978-3-642-23366-1\\_1](https://link.springer.com/chapter/10.1007/978-3-642-23366-1_1).

- Eaton, S. M., et al.**, “Transition from thermal diffusion to heat accumulation in high repetition rate femtosecond laser writing of buried optical waveguides,” *Optics Express*, vol. 16, no. 13, pp. 9443–9458, Jun. 2008. DOI: 10.1364/oe.16.009443.
- Eijkelenborg, M. A.**, “Imaging with microstructured polymer fibre,” *Optics Express*, vol. 12, no. 2, p. 342, Jan. 2004. DOI: 10.1364/opex.12.000342. [Online]. Available: <https://doi.org/10.1364/opex.12.000342>.
- Engelbrecht, C. J., et al.**, “Miniaturized selective plane illumination microscopy for high-contrast in vivo fluorescence imaging,” *Optics Letters*, vol. 35, no. 9, pp. 1413–1415, Apr. 2010. DOI: 10.1364/ol.35.001413. [Online]. Available: <https://doi.org/10.1364/ol.35.001413>.
- Erdogan, T.**, “Fiber grating spectra,” *Journal of Lightwave Technology*, vol. 15, no. 8, pp. 1277–1294, 1997. DOI: 10.1109/50.618322.
- European Commission**, *Preparing for our future: Developing a common strategy for key enabling technologies in the EU*, 2009.
- European Commission**, *Preparing for our future: Developing a common strategy for key enabling technologies in the EU*, 2009.
- European Commission, et al.**, *Re-finding industry : defining innovation*. Publications Office, 2018. DOI: 10.2777/927953.
- Fasman, G. D., Ed., *Circular Dichroism and the Conformational Analysis of Biomolecules*. Springer US, 1996. DOI: 10.1007/978-1-4757-2508-7.
- Ferenci, P.**, “Diagnosis and current therapy of Wilson’s disease,” *Alimentary Pharmacology & Therapeutics*, vol. 19, no. 2, pp. 157–165, Nov. 2003. DOI: 10.1046/j.1365-2036.2003.01813.x.
- Fernández-Manteca, M. G., et al.**, “Automatic classification of *Candida* species using Raman spectroscopy and machine learning,” *Spectrochimica Acta Part A: Molecular and Biomolecular Spectroscopy*, vol. 290, p. 122270, Apr. 2023. DOI: 10.1016/j.saa.2022.122270.
- Feroldi, F., et al.**, “In vivo multifunctional optical coherence tomography at the periphery of the lungs,” *Biomedical Optics Express*, vol. 10, no. 6, p. 3070, May 2019. DOI: 10.1364/boe.10.003070. [Online]. Available: <https://doi.org/10.1364/boe.10.003070>.
- Ferreira, M. F. S., et al.**, “Roadmap on optical sensors,” *Journal of Optics*, vol. 19, no. 8, p. 083001, Jul. 2017. DOI: 10.1088/2040-8986/aa7419.
- Filippi, A., et al.**, “Multimodal label-free ex vivo imaging using a dual-wavelength microscope with axial chromatic aberration compensation,” *Journal of Biomedical Optics*, vol. 23, no. 09, p. 091403, Mar. 2018. DOI: 10.1117/1.jbo.23.9.091403.
- Flusberg, B. A., et al.**, “Fiber-optic fluorescence imaging,” *Nature Methods*, vol. 2, no. 12, pp. 941–950, Nov. 2005. DOI: 10.1038/nmeth820. [Online]. Available: <https://doi.org/10.1038/nmeth820>.

- “For a brighter tomorrow,” *Nature Photonics*, vol. 7, no. 7, pp. 501–501, Jun. 2013. DOI: 10.1038/nphoton.2013.180.
- Fugazza, A., et al.**, “Confocal Laser Endomicroscopy in Gastrointestinal and Pancreatobiliary Diseases: A Systematic Review and Meta-Analysis,” *BioMed Research International*, vol. 2016, pp. 1–31, 2016. DOI: 10.1155/2016/4638683. [Online]. Available: <https://doi.org/10.1155/2016/4638683>.
- Galarza, M., et al.**, “Spatial-frequency multiplexing of high-sensitivity liquid level sensors based on multimode interference micro-fibers,” *Sensors and Actuators A: Physical*, vol. 307, p. 111985, Jun. 2020. DOI: 10.1016/j.sna.2020.111985.
- Ganziy, D., et al.**, “Dynamic gate algorithm for multimode fiber Bragg grating sensor systems,” *Applied Optics*, vol. 54, no. 18, pp. 5657–5661, Jun. 2015. DOI: 10.1364/ao.54.005657.
- Gattass, R. R., et al.**, “Femtosecond laser micromachining in transparent materials,” *Nature Photonics*, vol. 2, no. 4, pp. 219–225, Apr. 2008. DOI: 10.1038/nphoton.2008.47. [Online]. Available: <https://doi.org/10.1038/nphoton.2008.47>.
- Geng, Q., et al.**, “Ultrafast multi-focus 3-D nano-fabrication based on two-photon polymerization,” *Nature Communications*, vol. 10, no. 1, May 2019. DOI: 10.1038/s41467-019-10249-2.
- Gennes, P.-G., et al.**, *Capillarity and Wetting Phenomena*. Springer New York, 2004. DOI: 10.1007/978-0-387-21656-0.
- Giallorenzi, T., et al.**, “Optical fiber sensor technology,” *IEEE Journal of Quantum Electronics*, vol. 18, no. 4, pp. 626–665, Apr. 1982. DOI: 10.1109/jqe.1982.1071566.
- Gissibl, T., et al.**, “Two-photon direct laser writing of ultracompact multi-lens objectives,” *Nature Photonics*, vol. 10, no. 8, pp. 554–560, Jun. 2016. DOI: 10.1038/nphoton.2016.121. [Online]. Available: <https://doi.org/10.1038/nphoton.2016.121>.
- Glezer, E. N., et al.**, “Three-dimensional optical storage inside transparent materials,” *Optics Letters*, vol. 21, no. 24, pp. 2023–2025, Dec. 1996. DOI: 10.1364/ol.21.002023.
- Gmitro, A. F., et al.**, “Confocal microscopy through a fiber-optic imaging bundle,” *Optics Letters*, vol. 18, no. 8, p. 565, Apr. 1993. DOI: 10.1364/ol.18.000565. [Online]. Available: <https://doi.org/10.1364/ol.18.000565>.
- Goebel, T. A., et al.**, “Realization of aperiodic fiber Bragg gratings with ultrashort laser pulses and the line-by-line technique,” *Optics Letters*, vol. 43, no. 15, pp. 3794–3797, Aug. 2018. DOI: 10.1364/ol.43.003794.
- Gora, M. J., et al.**, “Endoscopic optical coherence tomography: technologies and clinical applications [Invited],” *Biomedical Optics Express*, vol. 8, no. 5, p. 2405, Apr. 2017. DOI: 10.1364/boe.8.002405. [Online]. Available: <https://doi.org/10.1364/boe.8.002405>.
- Grathwohl, P.**, *Diffusion in Natural Porous Media: Contaminant Transport, Sorption/Desorption and Dissolution Kinetics*. Springer US, 1998. DOI: 10.1007/978-1-4615-5683-1.

References in alphabetical order

- Grenier, J. R., et al.**, “Femtosecond Laser Inscription of Photonic and Optofluidic Devices in Fiber Cladding,” in *Planar Waveguides and other Confined Geometries*, Springer New York, Sep. 2014, pp. 67–110. DOI: 10.1007/978-1-4939-1179-0\_4.
- Günter, P., Eds., *Photorefractive Materials and Their Applications 2*. Springer New York, 2007. DOI: 10.1007/0-387-34081-5.
- Häfner, T., et al.**, “Tailored laser beam shaping for efficient and accurate microstructuring,” *Applied Physics A*, vol. 124, no. 2, Jan. 2018. DOI: 10.1007/s00339-017-1530-0.
- Hale, G. M., et al.**, “Optical Constants of Water in the 200-nm to 200- $\mu$ m Wavelength Region,” *Applied Optics*, vol. 12, no. 3, pp. 555–563, Mar. 1973. DOI: 10.1364/ao.12.000555.
- Hamada, T.**, “Determinants of Decision-Makers’ Attitudes toward Industry 4.0 Adaptation,” *Social Sciences*, vol. 8, no. 5, p. 140, May 2019. DOI: 10.3390/socsci8050140.
- Hampson, K. M., et al.**, “Adaptive optics for high-resolution imaging,” *Nature Reviews Methods Primers*, vol. 1, no. 1, Oct. 2021. DOI: 10.1038/s43586-021-00066-7.
- Haque, M.**, “Chemical-Assisted Femtosecond Laser Writing of Lab-in-Fiber Sensors,” Ph.D. dissertation, University of Toronto, 2014.
- Haque, M., et al.**, “Chemical-assisted femtosecond laser writing of lab-in-fibers,” *Lab on a Chip*, vol. 14, no. 19, pp. 3817–3829, 2014. DOI: 10.1039/c4lc00648h.
- Haroun, A., et al.**, “Progress in micro/nano sensors and nanoenergy for future AIoT-based smart home applications,” *Nano Express*, vol. 2, no. 2, p. 022005, Apr. 2021. DOI: 10.1088/2632-959x/abf3d4.
- Harris, C. R., et al.**, “Array programming with NumPy,” *Nature*, vol. 585, no. 7825, pp. 357–362, Sep. 2020. DOI: 10.1038/s41586-020-2649-2. [Online]. Available: <https://doi.org/10.1038/s41586-020-2649-2>.
- Harrison, D. J., et al.**, “Micromachining a Miniaturized Capillary Electrophoresis-Based Chemical Analysis System on a Chip,” *Science*, vol. 261, no. 5123, pp. 895–897, Aug. 1993. DOI: 10.1126/science.261.5123.895.
- Harvey, J. E., et al.**, “Understanding diffraction grating behavior: Including conical diffraction and Rayleigh anomalies from transmission gratings,” *Optical Engineering*, vol. 58, no. 08, p. 087105, Aug. 2019. DOI: 10.1117/1.oe.58.8.087105.
- He, F., et al.**, “Fabrication of microfluidic channels with a circular cross section using spatiotemporally focused femtosecond laser pulses,” *Optics Letters*, vol. 35, no. 7, pp. 1106–1108, Mar. 2010. DOI: 10.1364/ol.35.001106.
- He, F., et al.**, “Independent control of aspect ratios in the axial and lateral cross sections of a focal spot for three-dimensional femtosecond laser micromachining,” *New Journal of Physics*, vol. 13, no. 8, p. 083014, Aug. 2011. DOI: 10.1088/1367-2630/13/8/083014.
- Hering, J., et al.**, “Automated aberration correction of arbitrary laser modes in high numerical aperture systems,” *Optics Express*, vol. 24, no. 25, pp. 28500–28508, Nov. 2016. DOI: 10.1364/oe.24.028500.

- Hermans, M.**, “Selective, Laser-Induced Etching of Fused Silica at High Scan-Speeds Using KOH,” *Journal of Laser Micro/Nanoengineering*, vol. 9, no. 2, pp. 126–131, Jun. 2014. DOI: 10.2961/jlmm.2014.02.0009.
- Hill, K. O., et al.**, “Photosensitivity in optical fiber waveguides: Application to reflection filter fabrication,” *Applied Physics Letters*, vol. 32, no. 10, pp. 647–649, May 1978. DOI: 10.1063/1.89881.
- Hill, K. O., et al.**, “Fiber Bragg grating technology fundamentals and overview,” *Journal of Lightwave Technology*, vol. 15, no. 8, pp. 1263–1276, 1997. DOI: 10.1109/50.618320.
- Hirao, K., et al.**, “Femtosecond laser induced phenomena in glasses and photonic device applications,” *MRS Proceedings*, vol. 850, 2004. DOI: 10.1557/proc-850-mm2.1.
- Hirschman, I. I., et al.**, *The convolution transform*. Courier Corporation, Mar. 2012, ISBN: 048644175X.
- Hirschowitz, B.**, “Endoscopic examination of the stomach and duodenal cap with the fiber-scope,” *The Lancet*, vol. 277, no. 7186, pp. 1074–1078, May 1961. DOI: 10.1016/s0140-6736(61)92308-x. [Online]. Available: [https://doi.org/10.1016/s0140-6736\(61\)92308-x](https://doi.org/10.1016/s0140-6736(61)92308-x).
- Hnatovsky, C., et al.**, “Polarization-selective etching in femtosecond laser-assisted microfluidic channel fabrication in fused silica,” *Optics Letters*, vol. 30, no. 14, pp. 1867–1869, Jul. 2005. DOI: 10.1364/ol.30.001867.
- Hnatovsky, C., et al.**, “Pulse duration dependence of femtosecond-laser-fabricated nanogratings in fused silica,” *Applied Physics Letters*, vol. 87, no. 1, p. 014104, Jul. 2005. DOI: 10.1063/1.1991991.
- Hnatovsky, C., et al.**, “Fabrication of microchannels in glass using focused femtosecond laser radiation and selective chemical etching,” *Applied Physics A*, vol. 84, no. 1-2, pp. 47–61, Apr. 2006. DOI: 10.1007/s00339-006-3590-4.
- Ho, S., et al.**, “Single- and multi-scan femtosecond laser writing for selective chemical etching of cross section patternable glass micro-channels,” *Applied Physics A*, vol. 106, no. 1, pp. 5–13, Dec. 2011. DOI: 10.1007/s00339-011-6675-7.
- Hong, X., et al.**, “Smartphone microendoscopy for high resolution fluorescence imaging,” *Journal of Innovative Optical Health Sciences*, vol. 09, no. 05, p. 1650046, Sep. 2016. DOI: 10.1142/S1793545816500462. [Online]. Available: <https://doi.org/10.1142/S1793545816500462>.
- Hoy, C. L., et al.**, “Clinical Ultrafast Laser Surgery: Recent Advances and Future Directions,” *IEEE Journal of Selected Topics in Quantum Electronics*, vol. 20, no. 2, pp. 242–255, Mar. 2014. DOI: 10.1109/jstqe.2013.2287098.
- Hu, H., et al.**, “Generation of a Nondiffracting Superchiral Optical Needle for Circular Dichroism Imaging of Sparse Subdiffraction Objects,” *Physical Review Letters*, vol. 122, no. 22, p. 223901, Jun. 2019. DOI: 10.1103/physrevlett.122.223901.

- Hu, X., et al.**, “Tilted Bragg gratings in step-index polymer optical fiber,” *Optics Letters*, vol. 39, no. 24, pp. 6835–6838, Dec. 2014. DOI: 10.1364/ol.39.006835.
- Hu, Y., et al.**, “All-Glass 3D Optofluidic Microchip with Built-in Tunable Microlens Fabricated by Femtosecond Laser-Assisted Etching,” *Advanced Optical Materials*, vol. 6, no. 9, p. 1701299, Feb. 2018. DOI: 10.1002/adom.201701299.
- Hughes, M., et al.**, “Line-scanning fiber bundle endomicroscopy with a virtual detector slit,” *Biomedical Optics Express*, vol. 7, no. 6, pp. 2257–2268, Jun. 2016. DOI: 10.1364/BOE.7.002257. [Online]. Available: <https://doi.org/10.1364/BOE.7.002257>.
- Hunter, J. D.**, “Matplotlib: A 2D Graphics Environment,” *Computing in Science and Engineering*, vol. 9, no. 3, pp. 90–95, 2007. DOI: 10.1109/MCSE.2007.55.
- Hwang, J., et al.**, “Microchannel Fabrication on Glass Materials for Microfluidic Devices,” *International Journal of Precision Engineering and Manufacturing*, vol. 20, no. 3, pp. 479–495, Mar. 2019. DOI: 10.1007/s12541-019-00103-2.
- Indukuri, S. R. K. C., et al.**, “Enhanced Chiral Sensing at the Few-Molecule Level Using Negative Index Metamaterial Plasmonic Nanocuvettes,” *ACS Nano*, vol. 16, no. 10, pp. 17289–17297, Oct. 2022. DOI: 10.1021/acsnano.2c08090.
- Ioannou, A., et al.**, “Direct writing of plane-by-plane tilted fiber Bragg gratings using a femtosecond laser,” *Optics Letters*, vol. 42, no. 24, pp. 5198–5201, Dec. 2017. DOI: 10.1364/ol.42.005198.
- Itoh, K., et al.**, “Ultrafast Processes for Bulk Modification of Transparent Materials,” *MRS Bulletin*, vol. 31, no. 8, pp. 620–625, Aug. 2006. DOI: 10.1557/mrs2006.159.
- Jean, F., et al.**, “Fibered confocal spectroscopy and multicolor imaging system for in vivo fluorescence analysis,” *Optics Express*, vol. 15, no. 7, p. 4008, 2007. DOI: 10.1364/oe.15.004008. [Online]. Available: <https://doi.org/10.1364/oe.15.004008>.
- Jesacher, A., et al.**, “Adaptive optics for direct laser writing with plasma emission aberration sensing,” *Optics Express*, vol. 18, no. 2, pp. 656–661, Jan. 2010. DOI: 10.1364/oe.18.000656.
- Joannopoulos, J. D., et al.**, *Photonic Crystals: Molding the Flow of Light*. Princeton University Press, Oct. 2011. DOI: 10.2307/j.ctvc4m4gz9.
- Johnson, S., et al.**, “Block-iterative frequency-domain methods for Maxwell’s equations in a planewave basis,” *Optics Express*, vol. 8, no. 3, pp. 173–190, Jan. 2001. DOI: 10.1364/oe.8.000173.
- Kagermann, H., et al.**, “Ten Years of Industrie 4.0,” *Sci*, vol. 4, no. 3, p. 26, Jun. 2022. DOI: 10.3390/sci4030026.
- Karpinski, P., et al.**, “Laser-writing inside uniaxially birefringent crystals: Fine morphology of ultrashort pulse-induced changes in lithium niobate,” *Optics Express*, vol. 24, no. 7, pp. 7456–7476, Mar. 2016. DOI: 10.1364/oe.24.007456.
- Keahey, P., et al.**, “Differential structured illumination microendoscopy for in vivo imaging of molecular contrast agents,” *Proceedings of the National Academy of Sciences*, vol. 113,

- no. 39, pp. 10 769–10 773, Sep. 2016. DOI: 10.1073/pnas.1613497113. [Online]. Available: <https://doi.org/10.1073/pnas.1613497113>.
- Keldysh, L. V.**, “Ionization in the field of a strong electromagnetic wave,” *Sov. Phys. JETP*, vol. 20, no. 5, pp. 1307–1314, 1965.
- Khalatpour, A., et al.**, “High-power portable terahertz laser systems,” *Nature Photonics*, vol. 15, no. 1, pp. 16–20, Nov. 2020. DOI: 10.1038/s41566-020-00707-5.
- Khaliq, S., et al.**, “Fiber-optic liquid-level sensor using a long-period grating,” *Optics Letters*, vol. 26, no. 16, pp. 1224–1226, Aug. 2001. DOI: 10.1364/ol.26.001224.
- Kiyama, S., et al.**, “Examination of Etching Agent and Etching Mechanism on Femtosecond Laser Microfabrication of Channels Inside Vitreous Silica Substrates,” *The Journal of Physical Chemistry C*, vol. 113, no. 27, pp. 11 560–11 566, Apr. 2009. DOI: 10.1021/jp900915r.
- Kochkina, E.**, “Stigmatic and Astigmatic Gaussian Beams in Fundamental Mode Pathlength Signal Estimates,” Ph.D. dissertation, Leibniz Universität Hannover, 2013.
- Kong, W., et al.**, “Enhanced Goos-Hänchen shift of graphene coated on one-dimensional photonic crystal,” *Results in Physics*, vol. 17, p. 103 107, Jun. 2020. DOI: 10.1016/j.rinp.2020.103107.
- Koucky, M. H., et al.**, “Axial response of high-resolution microendoscopy in scattering media,” *Biomedical Optics Express*, vol. 4, no. 10, p. 2247, Sep. 2013. DOI: 10.1364/boe.4.002247. [Online]. Available: <https://doi.org/10.1364/boe.4.002247>.
- Kretschmann, E.**, “Die Bestimmung optischer Konstanten von Metallen durch Anregung von Oberflächenplasmaschwingungen,” *Zeitschrift für Physik A Hadrons and nuclei*, vol. 241, no. 4, pp. 313–324, Aug. 1971. DOI: 10.1007/bf01395428.
- Krishna, S. G., et al.**, “EUS-guided confocal laser endomicroscopy: Prediction of dysplasia in intraductal papillary mucinous neoplasms (with video),” *Gastrointestinal Endoscopy*, vol. 91, no. 3, 551–563.e5, Mar. 2020. DOI: 10.1016/j.gie.2019.09.014. [Online]. Available: <https://doi.org/10.1016/j.gie.2019.09.014>.
- Krol, D. M.**, “Femtosecond laser modification of glass,” *Journal of Non-Crystalline Solids*, vol. 354, no. 2-9, pp. 416–424, Jan. 2008. DOI: 10.1016/j.jnoncrysol.2007.01.098.
- Krstajic, N., et al.**, “Low-cost high sensitivity pulsed endomicroscopy to visualize tricolor optical signatures,” en, *Journal of Biomedical Optics*, vol. 23, no. 7, pp. 1–12, Jul. 2018. DOI: 10.1117/1.JBO.23.7.076005. [Online]. Available: <https://doi.org/10.1117/1.JBO.23.7.076005>.
- Ku, M. J. H., et al.**, “Imaging viscous flow of the Dirac fluid in graphene,” *Nature*, vol. 583, no. 7817, pp. 537–541, Jul. 2020. DOI: 10.1038/s41586-020-2507-2.
- Kuang, Z., et al.**, “Ultrafast laser beam shaping for material processing at imaging plane by geometric masks using a spatial light modulator,” *Optics and Lasers in Engineering*, vol. 70, pp. 1–5, Jul. 2015. DOI: 10.1016/j.optlaseng.2015.02.004.

- Laarossi, I., et al.**, “Ultrahigh temperature and strain hybrid integrated sensor system based on Raman and femtosecond FBG inscription in a multimode gold-coated fiber,” *Optics Express*, vol. 27, no. 26, pp. 37 122–37 130, Dec. 2019. DOI: 10.1364/oe.27.037122.
- Lacraz, A., et al.**, “Femtosecond Laser Inscribed Bragg Gratings in Low Loss CYTOP Polymer Optical Fiber,” *IEEE Photonics Technology Letters*, vol. 27, no. 7, pp. 693–696, Apr. 2015. DOI: 10.1109/lpt.2014.2386692.
- Lai, Y., et al.**, “Microchannels in conventional single-mode fibers,” *Optics Letters*, vol. 31, no. 17, pp. 2559–2561, Aug. 2006. DOI: 10.1364/ol.31.002559.
- Lai, Y., et al.**, “Low-loss, high reflectivity, first-order, pitch-by-pitch fiber Bragg grating fabrication in truly free-standing single-mode fiber,” *Journal of Physics: Conference Series*, vol. 679, p. 012 055, Feb. 2016. DOI: 10.1088/1742-6596/679/1/012055.
- Lammers, K., et al.**, “Nanograting based birefringent retardation elements in integrated photonic circuits,” in *Laser-based Micro- and Nanoprocessing XIV*, Klotzbach, U., Eds., SPIE, Mar. 2020. DOI: 10.1117/12.2544786.
- Lancry, M., et al.**, “Oriented creation of anisotropic defects by IR femtosecond laser scanning in silica,” *Optical Materials Express*, vol. 2, no. 12, pp. 1809–1821, Nov. 2012. DOI: 10.1364/ome.2.001809.
- Lancry, M., et al.**, “Ultrafast nanoporous silica formation driven by femtosecond laser irradiation,” *Laser & Photonics Reviews*, vol. 7, no. 6, pp. 953–962, Jul. 2013. DOI: 10.1002/lpor.201300043.
- Lancry, M., et al.**, “Fictive temperature in silica-based glasses and its application to optical fiber manufacturing,” *Progress in Materials Science*, vol. 57, no. 1, pp. 63–94, Jan. 2012. DOI: 10.1016/j.pmatsci.2011.05.002.
- Lasi, H., et al.**, “Industry 4.0,” *Business & Information Systems Engineering*, vol. 6, no. 4, pp. 239–242, Jun. 2014. DOI: 10.1007/s12599-014-0334-4.
- Leal-Junior, A. G., et al.**, “Quasi-Distributed Torque and Displacement Sensing on a Series Elastic Actuator’s Spring Using FBG Arrays Inscribed in CYTOP Fibers,” *IEEE Sensors Journal*, vol. 19, no. 11, pp. 4054–4061, Jun. 2019. DOI: 10.1109/jsen.2019.2898722.
- Leal-Junior, A. G., et al.**, “FPI-POFBG Angular Movement Sensor Inscribed in CYTOP Fibers With Dynamic Angle Compensator,” *IEEE Sensors Journal*, vol. 20, no. 11, pp. 5962–5969, Jun. 2020. DOI: 10.1109/jsen.2020.2974931.
- Leal-Junior, A. G., et al.**, “Optimizing Linearity and Sensitivity of 3D-Printed Diaphragms With Chirped FBGs in CYTOP Fibers,” *IEEE Access*, vol. 8, pp. 31 983–31 991, 2020. DOI: 10.1109/access.2020.2973187.
- Lee, C.-L., et al.**, “Dual hollow core fiber-based Fabry-Perot interferometer for measuring the thermo-optic coefficients of liquids,” *Optics Letters*, vol. 40, no. 4, pp. 459–462, Feb. 2015. DOI: 10.1364/ol.40.000459.
- Li, W. W., et al.**, “Fiber inline Mach-Zehnder interferometer based on femtosecond laser inscribed waveguides,” *Optics Letters*, vol. 42, no. 21, pp. 4438–4441, 2017, ISSN: 0146-9592.

- DOI: 10.1364/OL.42.004438. [Online]. Available: <https://www.osapublishing.org/abstract.cfm?URI=ol-42-21-4438>.
- Li, X., et al.**, “Polarization-insensitive space-selective etching in fused silica induced by picosecond laser irradiation,” *Applied Surface Science*, vol. 485, pp. 188–193, Aug. 2019. DOI: 10.1016/j.apsusc.2019.04.211.
- Li, Z., et al.**, “Fully integrated microfluidic devices for qualitative, quantitative and digital nucleic acids testing at point of care,” *Biosensors and Bioelectronics*, vol. 177, p. 112952, Apr. 2021. DOI: 10.1016/j.bios.2020.112952.
- Li, Z., et al.**, “Multi-Wavelength Super-Resolution Imaging by Structured Illumination of Bloch Surface Waves,” *IEEE Photonics Journal*, vol. 14, no. 4, pp. 1–7, Aug. 2022. DOI: 10.1109/jphot.2022.3187508.
- Liang, F., et al.**, “Physical origin of nanograting formation on fused silica with femtosecond pulses,” *Applied Physics Letters*, vol. 105, no. 13, p. 131904, Sep. 2014. DOI: 10.1063/1.4896749.
- Liao, C. R., et al.**, “Optical fiber Fabry-Perot interferometer cavity fabricated by femtosecond laser micromachining and fusion splicing for refractive index sensing,” *Optics Express*, vol. 20, no. 20, pp. 22813–22818, Sep. 2012. DOI: 10.1364/oe.20.022813.
- Liao, C. R., et al.**, “Fiber In-Line Mach-Zehnder Interferometer Embedded in FBG for Simultaneous Refractive Index and Temperature Measurement,” *IEEE Photonics Technology Letters*, vol. 22, no. 22, pp. 1686–1688, Nov. 2010. DOI: 10.1109/lpt.2010.2079924.
- Liao, C., et al.**, “Tunable phase-shifted fiber Bragg grating based on femtosecond laser fabricated in-grating bubble,” *Optics Letters*, vol. 38, no. 21, pp. 4473–4476, Oct. 2013. DOI: 10.1364/ol.38.004473.
- Liao, C., et al.**, “Femtosecond laser micromachining of microfluidic fiber sensors,” in *2016 15th International Conference on Optical Communications and Networks (ICOCN)*, IEEE, Sep. 2016. DOI: 10.1109/icocn.2016.7875603.
- Light Wave Venture, Ed., *Information 2015 Photonic Sensor Consortium Market Survey Report*. Gatekeepers Inc, 2015.
- Light Wave Venture, Ed., *Distributed and Single Point Fiber Optic Sensing Systems Forecast: A PhotonicSensor Consortium Market Survey Report*. Gatekeepers Inc, 2019.
- Lin, N. C., et al.**, “Implantable integrated photonic probe for light sheet brain imaging in vivo,” in *Biophotonics Congress 2021*, OSA, 2021. DOI: 10.1364/brain.2021.bm3b.3. [Online]. Available: <https://doi.org/10.1364/brain.2021.bm3b.3>.
- Liu, D., et al.**, “Sub-micrometer resolution liquid level sensor based on a hollow core fiber structure,” *Optics Letters*, vol. 44, no. 8, pp. 2125–2128, Apr. 2019. DOI: 10.1364/ol.44.002125.
- Liu, J.-J., et al.**, “New optical imaging technologies for bladder cancer: Considerations and perspectives,” in *Journal of Urology*, vol. 188, no. 2, pp. 361–368, Aug. 2012. DOI: 10.1016/

References in alphabetical order

- j.juro.2012.03.127. [Online]. Available: <https://doi.org/10.1016/j.juro.2012.03.127>.
- Liu, S., et al.**, “High-sensitivity strain sensor based on in-fiber rectangular air bubble,” *Scientific Reports*, vol. 5, no. 1, p. 7624, Jan. 2015. DOI: 10.1038/srep07624.
- Liu, S., et al.**, “Temperature Insensitive Liquid Level Sensor Based on Antiresonant Reflecting Guidance in Silica Tube,” *Journal of Lightwave Technology*, vol. 34, no. 22, pp. 5239–5243, Nov. 2016. DOI: 10.1109/jlt.2016.2611007.
- Liu, S., et al.**, “Anti-resonant reflecting guidance in alcohol-filled hollow core photonic crystal fiber for sensing applications,” *Optics Express*, vol. 21, no. 25, pp. 31 690–31 697, Dec. 2013. DOI: 10.1364/oe.21.031690.
- Liu, W., et al.**, “Energetic ultrafast fiber laser sources tunable in 1030–1215 nm for deep tissue multi-photon microscopy,” *Optics Express*, vol. 25, no. 6, pp. 6822–6831, Mar. 2017. DOI: 10.1364/oe.25.006822.
- Liu, Z., et al.**, “Liquid surface tension and refractive index sensor based on a tilted fiber Bragg grating,” *Journal of the Optical Society of America B*, vol. 35, no. 6, pp. 1282–1287, May 2018. DOI: 10.1364/josab.35.001282.
- Lomer, M., et al.**, “A quasi-distributed level sensor based on a bent side-polished plastic optical fibre cable,” *Measurement Science and Technology*, vol. 18, no. 7, pp. 2261–2267, Jun. 2007. DOI: 10.1088/0957-0233/18/7/061.
- Loock, H.-P., et al.**, “Detection limits of chemical sensors: Applications and misapplications,” *Sensors and Actuators B: Chemical*, vol. 173, pp. 157–163, Oct. 2012. DOI: 10.1016/j.snb.2012.06.071.
- Lopez-Higuera, J. M., et al.**, “Fiber Optic Sensors in Structural Health Monitoring,” *Journal of Lightwave Technology*, vol. 29, no. 4, pp. 587–608, Feb. 2011. DOI: 10.1109/jlt.2011.2106479.
- Low, D. K. Y., et al.**, “Femtosecond laser direct writing of embedded optical waveguides in aluminosilicate glass,” *Applied Physics A*, vol. 81, no. 8, pp. 1633–1638, Nov. 2005. DOI: 10.1007/s00339-005-3324-z.
- Lu, P., et al.**, “Plane-by-Plane Inscription of Grating Structures in Optical Fibers,” *Journal of Lightwave Technology*, vol. 36, no. 4, pp. 926–931, Feb. 2018. DOI: 10.1109/jlt.2017.2750490.
- Lu, P., et al.**, “Distributed optical fiber sensing: Review and perspective,” *Applied Physics Reviews*, vol. 6, no. 4, p. 041 302, Sep. 2019. DOI: 10.1063/1.5113955.
- Ma, C., et al.**, “Organ-on-a-Chip: A New Paradigm for Drug Development,” *Trends in Pharmaceutical Sciences*, vol. 42, no. 2, pp. 119–133, Feb. 2021. DOI: 10.1016/j.tips.2020.11.009.
- Ma, X., et al.**, “Single-mode chirally-coupled-core fibers with larger than 50  $\mu\text{m}$  diameter cores,” *Optics Express*, vol. 22, no. 8, pp. 9206–9219, Apr. 2014. DOI: 10.1364/oe.22.009206.

- Madani, A., et al.**, “Optical microtube cavities monolithically integrated on photonic chips for optofluidic sensing,” *Optics Letters*, vol. 42, no. 3, pp. 486–489, Jan. 2017. DOI: 10.1364/ol.42.000486.
- Madsen, L. S., et al.**, “Quantum computational advantage with a programmable photonic processor,” *Nature*, vol. 606, no. 7912, pp. 75–81, Jun. 2022. DOI: 10.1038/s41586-022-04725-x.
- Mahmudlu, H., et al.**, “Fully on-chip photonic turnkey quantum source for entangled qubit/qudit state generation,” *Nature Photonics*, Apr. 2023. DOI: 10.1038/s41566-023-01193-1.
- Malinauskas, M., et al.**, “Ultrafast laser processing of materials: From science to industry,” *Light: Science & Applications*, vol. 5, no. 8, e16133–e16133, Mar. 2016. DOI: 10.1038/lsa.2016.133.
- Marcinkevičius, A., et al.**, “Effect of refractive index-mismatch on laser microfabrication in silica glass,” *Applied Physics A: Materials Science & Processing*, vol. 76, no. 2, pp. 257–260, Feb. 2003. DOI: 10.1007/s00339-002-1447-z.
- Marcinkevičius, A., et al.**, “Femtosecond laser-assisted three-dimensional microfabrication in silica,” *Optics Letters*, vol. 26, no. 5, pp. 277–279, Mar. 2001. DOI: 10.1364/ol.26.000277.
- Marini, M., et al.**, “Microlenses Fabricated by Two-Photon Laser Polymerization for Cell Imaging with Non-Linear Excitation Microscopy,” *Advanced Functional Materials*, p. 2213926, Mar. 2023. DOI: 10.1002/adfm.202213926.
- Martinez, A., et al.**, “Direct writing of fibre Bragg gratings by femtosecond laser,” *Electronics Letters*, vol. 40, no. 19, p. 1170, 2004. DOI: 10.1049/el:20046050.
- Martins, J. P., et al.**, “The importance of microfluidics for the preparation of nanoparticles as advanced drug delivery systems,” *Expert Opinion on Drug Delivery*, vol. 15, no. 5, pp. 469–479, Mar. 2018. DOI: 10.1080/17425247.2018.1446936.
- Mas, S., et al.**, “Biconical Tapered Fibers Manipulation for Refractive Index and Strain Sensing Applications,” *IEEE Sensors Journal*, vol. 15, no. 3, pp. 1331–1335, Mar. 2015. DOI: 10.1109/jsen.2014.2368146.
- Mauclair, C., et al.**, “Ultrafast laser writing of homogeneous longitudinal waveguides in glasses using dynamic wavefront correction,” *Optics Express*, vol. 16, no. 8, pp. 5481–5492, Apr. 2008. DOI: 10.1364/oe.16.005481.
- McArthur, S. R., et al.**, “Ultrafast laser inscription of efficient volume Bragg gratings deep in fused silica using active wavefront shaping,” *Optical Materials Express*, vol. 12, no. 9, pp. 3589–3599, Aug. 2022. DOI: 10.1364/ome.462654.
- McArthur, S. R., et al.**, “Investigating focus elongation using a spatial light modulator for high-throughput ultrafast-laser-induced selective etching in fused silica,” *Optics Express*, vol. 30, no. 11, pp. 18903–18918, May 2022. DOI: 10.1364/oe.454280.
- Mehta, D. S., et al.**, *Quantitative Phase Microscopy and Tomography*. IOP Publishing, Dec. 2022. DOI: 10.1088/978-0-7503-3987-2.

References in alphabetical order

- Meierhenrich, U. J.**, “Amino Acids and the Asymmetry of Life,” *European Review*, vol. 21, no. 2, pp. 190–199, Apr. 2013. DOI: 10.1017/s106279871200035x.
- Méndez, A.**, “Fiber Bragg grating sensors: a market overview,” in *Third European Workshop on Optical Fibre Sensors*, SPIE, Jul. 2007. DOI: 10.1117/12.738334.
- Mihailov, S. J., et al.**, “Bragg Gratings Written in All-SiO<sub>2</sub> and Ge-Doped Core Fibers With 800-nm Femtosecond Radiation and a Phase Mask,” *Journal of Lightwave Technology*, vol. 22, no. 1, pp. 94–100, Jan. 2004. DOI: 10.1109/jlt.2003.822169.
- Millot, G., et al.**, “Frequency-agile dual-comb spectroscopy,” *Nature Photonics*, vol. 10, no. 1, pp. 27–30, Dec. 2015. DOI: 10.1038/nphoton.2015.250.
- Mills, B., et al.**, “Molecular detection of Gram-positive bacteria in the human lung through an optical fiber-based endoscope,” *European Journal of Nuclear Medicine and Molecular Imaging*, vol. 48, no. 3, pp. 800–807, Sep. 2020. DOI: 10.1007/s00259-020-05021-4. [Online]. Available: <https://doi.org/10.1007/s00259-020-05021-4>.
- Miura, K., et al.**, “Three-dimensional deposition of silicon from silicate glass with dispersed metallic aluminum by a femtosecond laser,” in *SPIE Proceedings*, Voelcker, N. H., Ed., SPIE, Dec. 2006. DOI: 10.1117/12.695925.
- Mo, Y., et al.**, “Microfluidic electrochemistry for single-electron transfer redox-neutral reactions,” *Science*, vol. 368, no. 6497, pp. 1352–1357, Jun. 2020. DOI: 10.1126/science.aba3823.
- Mogni, E.**, “Molecular sensing with surface waves,” Ph.D. dissertation, Politecnico di Milano, 2023.
- Mogni, E., et al.**, “One-dimensional photonic crystal for polarization-sensitive surface-enhanced spectroscopy,” *EPJ Web of Conferences*, vol. 266, Costa, M. F., Eds., p. 06 009, 2022. DOI: 10.1051/epjconf/202226606009.
- Mogni, E., et al.**, “One-Dimensional Photonic Crystal for Surface Mode Polarization Control,” *Advanced Optical Materials*, vol. 10, no. 21, p. 2200759, Aug. 2022. DOI: 10.1002/adom.202200759.
- Moh, K. J., et al.**, “Influence of diffraction by a rectangular aperture on the aspect ratio of femtosecond direct-write waveguides,” *Optics Express*, vol. 13, no. 19, pp. 7288–7297, 2005. DOI: 10.1364/opex.13.007288.
- Mulvad, H. C. H., et al.**, “Kilowatt-average-power single-mode laser light transmission over kilometre-scale hollow-core fibre,” *Nature Photonics*, vol. 16, no. 6, pp. 448–453, May 2022. DOI: 10.1038/s41566-022-01000-3.
- Murayama, M., et al.**, “Fiberoptic System for Recording Dendritic Calcium Signals in Layer 5 Neocortical Pyramidal Cells in Freely Moving Rats,” *Journal of Neurophysiology*, vol. 98, no. 3, pp. 1791–1805, Sep. 2007. DOI: 10.1152/jn.00082.2007. [Online]. Available: <https://doi.org/10.1152/jn.00082.2007>.

- Nan, Y.-G., et al.**, “Ultra-fast fiber Bragg grating inscription in CYTOP polymer optical fibers using phase mask and 400 nm femtosecond laser,” *Optics Express*, vol. 29, no. 16, pp. 25 824–25 835, Jul. 2021. DOI: 10.1364/oe.428592.
- Naritomi, M.**, “CYTOP Amorphous Perfluoropolymer for Low Loss POF,” *POF Asia Pacific Forum '96*, 1996. [Online]. Available: <https://ci.nii.ac.jp/naid/10022381823/en/>.
- National Photonics Initiative**, *Lighting the Path to a Competitive Secure Future*, 2014.
- National Photonics Initiative**, *Photonics: Enabling American Innovation, Competition and Security*, 2017.
- National Research Council**, *Optics and Photonics: Essential Technologies for Our Nation*. Washington, DC: The National Academies Press, 2013, ISBN: 978-0-309-26377-1. DOI: 10.17226/13491. [Online]. Available: <https://nap.nationalacademies.org/catalog/13491/optics-and-photonics-essential-technologies-for-our-nation>.
- Nazeer, M., et al.**, “Theoretical study of MHD electro-osmotically flow of third-grade fluid in micro channel,” *Applied Mathematics and Computation*, vol. 420, p. 126 868, May 2022. DOI: 10.1016/j.amc.2021.126868.
- Neil, M. A. A., et al.**, “Method of obtaining optical sectioning by using structured light in a conventional microscope,” *Optics Letters*, vol. 22, no. 24, p. 1905, Dec. 1997. DOI: 10.1364/ol.22.001905. [Online]. Available: <https://doi.org/10.1364/ol.22.001905>.
- Nesterov, M. L., et al.**, “The Role of Plasmon-Generated Near Fields for Enhanced Circular Dichroism Spectroscopy,” *ACS Photonics*, vol. 3, no. 4, pp. 578–583, Apr. 2016. DOI: 10.1021/acsp Photonics.5b00637.
- Ni, W., et al.**, “Simultaneous implementation of enhanced resolution and large dynamic range for fiber temperature sensing based on different optical transmission mechanisms,” *Optics Express*, vol. 26, no. 14, pp. 18 341–18 350, Jul. 2018. DOI: 10.1364/oe.26.018341.
- Niculescu, A.-G., et al.**, “Fabrication and Applications of Microfluidic Devices: A Review,” *International Journal of Molecular Sciences*, vol. 22, no. 4, p. 2011, Feb. 2021. DOI: 10.3390/ijms22042011.
- Norton, S. M., et al.**, “Coupled-mode theory of resonant-grating filters,” *Journal of the Optical Society of America A*, vol. 14, no. 3, pp. 629–639, Mar. 1997. DOI: 10.1364/josaa.14.000629.
- Nouman, W. M., et al.**, “Biophotonic sensor for rapid detection of brain lesions using 1D photonic crystal,” *Optical and Quantum Electronics*, vol. 52, no. 6, May 2020. DOI: 10.1007/s11082-020-02409-2.
- Novotny, L., et al.**, *Principles of Nano-Optics*. Cambridge University Press, Sep. 2012. DOI: 10.1017/cbo9780511794193.
- Ochoa, M., et al.**, “Recent Advances in Biomedical Photonic Sensors: A Focus on Optical-Fibre-Based Sensing,” *Sensors*, vol. 21, no. 19, p. 6469, Sep. 2021. DOI: 10.3390/s21196469.

References in alphabetical order

- Ochoa, M., et al.**, *Data supporting paper: Polarisation-independent ultrafast laser selective etching processing in fused silica*, 2023. DOI: 10.5281/ZENODO.7129527.
- Ochoa, M., et al.**, “Polarisation-independent ultrafast laser selective etching processing in fused silica,” in *Frontiers in Ultrafast Optics: Biomedical, Scientific, and Industrial Applications XXIII*, SPIE, 2023.
- Ochoa, M., et al.**, “Polarisation-independent ultrafast laser selective etching processing in fused silica,” *Lab on a Chip*, vol. 23, no. 7, pp. 1752–1757, 2023. DOI: 10.1039/d3lc00052d.
- Ochoa, M., et al.**, “On the mechanisms enabling polarisation-independent high etching rates in fused silica processed by ultrafast laser selective etching,” in *Progress in Ultrafast Laser Modifications of Materials*, Jun. 2023.
- Ortega-Quijano, N., et al.**, “Optical crosstalk influence in fiber imaging endoscopes design,” *Optics Communications*, vol. 283, no. 4, pp. 633–638, Feb. 2010. DOI: 10.1016/j.optcom.2009.10.075. [Online]. Available: <https://doi.org/10.1016/j.optcom.2009.10.075>.
- Orth, A., et al.**, “Optical fiber bundles: Ultra-slim light field imaging probes,” *Science Advances*, vol. 5, no. 4, Apr. 2019. DOI: 10.1126/sciadv.aav1555.
- Osellame, R., et al.**, “Femtosecond laser microstructuring: An enabling tool for optofluidic lab-on-chips,” *Laser & Photonics Reviews*, vol. 5, no. 3, pp. 442–463, Feb. 2011. DOI: 10.1002/lpor.201000031.
- Osellame, R., et al.**, “Optical properties of waveguides written by a 26 MHz stretched cavity Ti:sapphire femtosecond oscillator,” *Optics Express*, vol. 13, no. 2, pp. 612–620, 2005. DOI: 10.1364/opex.13.000612.
- Osellame, R., Eds., *Femtosecond Laser Micromachining*. Springer Berlin Heidelberg, 2012. DOI: 10.1007/978-3-642-23366-1.
- Osellame, R., et al.**, “Integration of optical waveguides and microfluidic channels both fabricated by femtosecond laser irradiation,” *Applied Physics Letters*, vol. 90, no. 23, p. 231 118, Jun. 2007. DOI: 10.1063/1.2747194.
- Osellame, R., et al.**, “Femtosecond writing of active optical waveguides with astigmatically shaped beams,” *Journal of the Optical Society of America B*, vol. 20, no. 7, p. 1559, Jul. 2003. DOI: 10.1364/josab.20.001559.
- Paiè, P.**, “Femtosecond laser micromachining of optofluidic glass chips for biophotonic applications,” Ph.D. dissertation, Politecnico di Milano, 2016.
- Paiè, P., et al.**, “Microfluidic Based Optical Microscopes on Chip,” *Cytometry Part A*, vol. 93, no. 10, pp. 987–996, Sep. 2018. DOI: 10.1002/cyto.a.23589.
- Pallares-Aldeiturriaga, D., et al.**, “Curvature Sensor Based on In-Fiber Mach-Zehnder Interferometer Inscribed with Femtosecond Laser,” *Journal of Lightwave Technology*, vol. 35, no. 21, pp. 4624–4628, 2017, ISSN: 0733-8724. DOI: 10.1109/JLT.2017.2756103.

- Pallarés-Aldeiturriaga, D., et al.**, “In-fiber Mach-Zehnder interferometer inscribed with femtosecond laser for high temperature sensing,” in *25th International Conference on Optical Fiber Sensors*, Chung, Y., Eds., SPIE, Apr. 2017. DOI: 10.1117/12.2264991.
- Pallarés-Aldeiturriaga, D., et al.**, “Astigmatism compensation for waveguide inscription in optical fiber by femtosecond lasers,” in *Seventh European Workshop on Optical Fibre Sensors*, Kalli, K., Eds., SPIE, Aug. 2019. DOI: 10.1117/12.2539835.
- Pallarés-Aldeiturriaga, D., et al.**, “Optical Fiber Sensors by Direct Laser Processing: A Review,” *Sensors*, vol. 20, no. 23, p. 6971, Dec. 2020. DOI: 10.3390/s20236971.
- Parker, H. E., et al.**, “Core crosstalk in ordered imaging fiber bundles,” *Optics Letters*, vol. 45, no. 23, pp. 6490–6493, Nov. 2020. DOI: 10.1364/ol.405764. [Online]. Available: <https://doi.org/10.1364/ol.405764>.
- Parker, H. E., et al.**, “Fibre-based spectral ratio endomicroscopy for contrast enhancement of bacterial imaging and pulmonary autofluorescence,” *Biomedical Optics Express*, vol. 10, no. 4, pp. 1856–1869, Mar. 2019. DOI: 10.1364/boe.10.001856. [Online]. Available: <https://doi.org/10.1364/boe.10.001856>.
- Parker, H. E., et al.**, “A Lab-in-a-Fiber optofluidic device using droplet microfluidics and laser-induced fluorescence for virus detection,” *Scientific Reports*, vol. 12, no. 1, Mar. 2022. DOI: 10.1038/s41598-022-07306-0. [Online]. Available: <https://doi.org/10.1038/s41598-022-07306-0>.
- Parker, H. E., et al.**, “Selective Plane Illumination Fluorescence Endomicroscopy using a Polymer Imaging Fiber and an End-cap,” in *Biophotonics Congress: Biomedical Optics 2022 (Translational, Microscopy, OCT, OTS, BRAIN)*, Optica Publishing Group, 2022. DOI: 10.1364/translational.2022.tw1b.6.
- Pellegrini, G., et al.**, “Chiral surface waves for enhanced circular dichroism,” *Physical Review B*, vol. 95, no. 24, p. 241402, Jun. 2017. DOI: 10.1103/physrevb.95.241402.
- Perez-Herrera, R. A., et al.**, “Microdrilled tapers to enhance optical fiber lasers for sensing,” *Scientific Reports*, vol. 11, no. 1, p. 20408, Oct. 2021. DOI: 10.1038/s41598-021-00046-7.
- Pérez-Herrera, R. A., et al.**, “Multiplexing optical fiber Fabry-Perot interferometers based on air-microcavities,” in *Seventh European Workshop on Optical Fibre Sensors*, Kalli, K., Eds., SPIE, Aug. 2019. DOI: 10.1117/12.2540150.
- Perperidis, A., et al.**, “Image computing for fibre-bundle endomicroscopy: A review,” *Medical Image Analysis*, vol. 62, p. 101620, 2020, ISSN: 1361-8415. DOI: <https://doi.org/10.1016/j.media.2019.101620>. [Online]. Available: <https://www.sciencedirect.com/science/article/pii/S136184151830639X>.
- Perperidis, A., et al.**, “Characterization and modelling of inter-core coupling in coherent fiber bundles,” *Optics Express*, vol. 25, no. 10, pp. 11932–11953, May 2017. DOI: 10.1364/oe.25.011932. [Online]. Available: <https://doi.org/10.1364/oe.25.011932>.
- Peters, K.**, “Polymer optical fiber sensors—a review,” *Smart Materials and Structures*, vol. 20, no. 1, p. 013002, Dec. 2010. DOI: 10.1088/0964-1726/20/1/013002.

References in alphabetical order

- Pethig, R., et al.**, *Introductory Bioelectronics*. Wiley, Sep. 2012. DOI: 10.1002/9781118443293.
- Photonics21**, *A critical Key Enabling Technology for Europe Role and impact of Photonics in H2020 Report*, 2017.
- Photonics21**, *Europe's age of light! How photonics will power growth and innovation*, 2019.
- Photonics21**, *Market Data and Industry Report 2020. NextPho21: Implementing the European Photonics21 PPP strategy*, 2020.
- Photonics21**, *Update of the Strategic Roadmap Europe's age of light! How photonics will power growth and innovation*, 2020.
- Piacentini, S., et al.**, “Advanced photonic and optofluidic devices fabricated in glass via femtosecond laser micromachining [Invited],” *Optical Materials Express*, vol. 12, no. 10, pp. 3930–3945, Sep. 2022. DOI: 10.1364/ome.463715.
- Pierce, M. C., et al.**, “Low-Cost Endomicroscopy in the Esophagus and Colon,” *American Journal of Gastroenterology*, vol. 106, no. 9, pp. 1722–1724, Sep. 2011. DOI: 10.1038/ajg.2011.140. [Online]. Available: <https://doi.org/10.1038/ajg.2011.140>.
- Pinto, A., et al.**, “Micro-Displacement Sensor Based on a Hollow-Core Photonic Crystal Fiber,” *Sensors*, vol. 12, no. 12, pp. 17497–17503, Dec. 2012. DOI: 10.3390/s121217497.
- Piruska, A., et al.**, “The autofluorescence of plastic materials and chips measured under laser irradiation,” *Lab on a Chip*, vol. 5, no. 12, pp. 1348–1354, 2005. DOI: 10.1039/b508288a. [Online]. Available: <https://doi.org/10.1039/b508288a>.
- Pitarke, J. M., et al.**, “Theory of surface plasmons and surface-plasmon polaritons,” *Reports on Progress in Physics*, vol. 70, no. 1, pp. 1–87, Dec. 2006. DOI: 10.1088/0034-4885/70/1/r01.
- Polglase, A. L., et al.**, “A fluorescence confocal endomicroscope for in vivo microscopy of the upper- and the lower-GI tract,” *Gastrointestinal Endoscopy*, vol. 62, no. 5, pp. 686–695, Nov. 2005. DOI: 10.1016/j.gie.2005.05.021. [Online]. Available: <https://doi.org/10.1016/j.gie.2005.05.021>.
- Pont, M., et al.**, “Quantifying  $n$ -Photon Indistinguishability with a Cyclic Integrated Interferometer,” *Physical Review X*, vol. 12, no. 3, p. 031033, Sep. 2022. DOI: 10.1103/physrevx.12.031033.
- Pshenay-Severin, E., et al.**, “Multimodal nonlinear endomicroscopic imaging probe using a double-core double-clad fiber and focus-combining micro-optical concept,” *Light: Science & Applications*, vol. 10, no. 1, p. 207, Oct. 2021. DOI: 10.1038/s41377-021-00648-w.
- Puig, M.**, “Advanced microscopy to resolve the higher-order organization of the exocyst,” Ph.D. dissertation, Universitat Pompeu Fabra, 2023.
- Qi, J., et al.**, “Fabrication of polarization-independent single-mode waveguides in lithium niobate crystal with femtosecond laser pulses,” *Optical Materials Express*, vol. 6, no. 8, pp. 2554–2559, Jul. 2016. DOI: 10.1364/ome.6.002554.

- Quang, T., et al.**, “A tablet-interfaced high-resolution microendoscope with automated image interpretation for real-time evaluation of esophageal squamous cell neoplasia,” *Gastrointestinal Endoscopy*, vol. 84, no. 5, pp. 834–841, Nov. 2016. DOI: 10.1016/j.gie.2016.03.1472. [Online]. Available: <https://doi.org/10.1016/j.gie.2016.03.1472>.
- Rahman, A., et al.**, *Finite element modeling methods for photonics*. Artech House, 2013.
- Rahman, M., et al.**, “Single-particle analysis with 2D electro-optical trapping on an integrated optofluidic device,” *Optica*, vol. 5, no. 10, pp. 1311–1314, Oct. 2018. DOI: 10.1364/optica.5.001311.
- Rajesh, S., et al.**, “Towards fast femtosecond laser micromachining of fused silica: The effect of deposited energy,” *Optics Express*, vol. 18, no. 20, pp. 21 490–21 497, Sep. 2010. DOI: 10.1364/oe.18.021490.
- Rajesh, S., et al.**, “Towards fast femtosecond laser micromachining of glass, effect of deposited energy.,” in *Conference on Lasers and Electro-Optics 2010*, OSA, 2010. DOI: 10.1364/cleo.2010.jtud18.
- Ramirez, L. P. R., et al.**, “Tuning the structural properties of femtosecond-laser-induced nanogratings,” *Applied Physics A*, vol. 100, no. 1, pp. 1–6, Apr. 2010. DOI: 10.1007/s00339-010-5684-2.
- Regenauer-Lieb, K.**, “An immersed boundary-lattice Boltzmann method for gaseous slip flow,” *Physics of Fluids*, vol. 32, no. 1, p. 012 002, Jan. 2020. DOI: 10.1063/1.5126392.
- Ren, K., et al.**, “Materials for Microfluidic Chip Fabrication,” *Accounts of Chemical Research*, vol. 46, no. 11, pp. 2396–2406, Jun. 2013. DOI: 10.1021/ar300314s.
- Richter, S., et al.**, “Nanogratings in fused silica: Formation, control, and applications,” *Journal of Laser Applications*, vol. 24, no. 4, p. 042 008, Sep. 2012. DOI: 10.2351/1.4718561.
- Roberge, A., et al.**, “Femtosecond laser direct-writing of high quality first-order Bragg gratings with arbitrary complex apodization by phase modulation,” *Optics Express*, vol. 30, no. 17, p. 30 405, Aug. 2022. DOI: 10.1364/oe.465331.
- Robertson, W. M., et al.**, “Surface electromagnetic wave excitation on one-dimensional photonic band-gap arrays,” *Applied Physics Letters*, vol. 74, no. 13, pp. 1800–1802, Mar. 1999. DOI: 10.1063/1.123090.
- Rogers, C., et al.**, “A universal 3D imaging sensor on a silicon photonics platform,” *Nature*, vol. 590, no. 7845, pp. 256–261, Feb. 2021. DOI: 10.1038/s41586-021-03259-y.
- Roldan-Varona, P.**, “Post-processing of optical fibres using femtosecond lasers,” M.S. thesis, Universidad de Cantabria, Jul. 2019. [Online]. Available: <http://hdl.handle.net/10902/16620>.
- Roldan-Varona, P., et al.**, “Slit Beam Shaping Technique for Femtosecond Laser Inscription of Enhanced Plane-by-Plane FBGs,” *Journal of Lightwave Technology*, vol. 38, no. 16, pp. 4526–4532, Aug. 2020. DOI: 10.1109/jlt.2020.2992568.

- Roldán-Varona, P., et al.**, “Slit Beam Shaping Technique for Femtosecond Laser Inscription of Symmetric Cladding Waveguides,” *IEEE Journal of Selected Topics in Quantum Electronics*, vol. 27, no. 6, p. 4400–208, Nov. 2021. DOI: 10.1109/jstqe.2021.3092438.
- Roldán-Varona, P., et al.**, “All-in-fiber multiscan Mach-Zehnder interferometer assisted by core FBG for simultaneous multi-parameter sensing,” *Optics & Laser Technology*, vol. 132, p. 106459, Dec. 2020. DOI: 10.1016/j.optlastec.2020.106459.
- Roldán-Varona, P., et al.**, “Compact Optical Fiber Lasers and Optical Fiber Sensors assisted by Femtosecond Laser Inscription of Plane-by-Plane FBGs,” in *Optical Fiber Sensors Conference 2020 Special Edition*, Optica Publishing Group, 2021. DOI: 10.1364/ofs.2020.w4.77.
- Roldán-Varona, P., et al.**, “Enhanced refractometer for aqueous solutions based on perfluorinated polymer optical fibres,” *Optics Express*, vol. 30, no. 2, pp. 1397–1409, Jan. 2022. DOI: 10.1364/oe.448111.
- Roldán-Varona, P., et al.**, “Hybrid Mach-Zehnder interferometer manufactured by femtosecond laser multiscan technique,” in *Seventh European Workshop on Optical Fibre Sensors*, Kalli, K., Eds., SPIE, Aug. 2019. DOI: 10.1117/12.2538813.
- Roldán-Varona, P., et al.**, “Reflected power-based 2D bending sensor using femtosecond laser FBG inscription in multicore fiber,” in *Seventh European Workshop on Optical Fibre Sensors*, Kalli, K., Eds., SPIE, Aug. 2019. DOI: 10.1117/12.2538794.
- Roldán-Varona, P., et al.**, “Liquid level sensor based on dynamic Fabry-Perot interferometers in processed capillary fiber,” *Scientific Reports*, vol. 11, no. 1, p. 3039, Feb. 2021. DOI: 10.1038/s41598-021-82193-5.
- Roldán-Varona, P., et al.**, “Reflection-based lab-in-fiber sensor integrated in a surgical needle for biomedical applications,” *Optics Letters*, vol. 45, no. 18, pp. 5242–5245, Sep. 2020. DOI: 10.1364/ol.399407.
- Roldán-Varona, P., et al.**, *Data supporting paper: Selective Plane Illumination Optical Endomicroscopy with Polymer Imaging Fibres*, 2022. DOI: 10.17861/31F319C0-66EB-41B0-A586-6F2480C85A47.
- Roldán-Varona, P., et al.**, “Selective Plane Illumination Optical Endomicroscopy with Polymer Imaging Fibres,” in *Conference on Lasers and Electro-Optics*, Optica Publishing Group, 2022. DOI: 10.1364/cleo\_si.2022.sm31.2.
- Roldán-Varona, P., et al.**, “Selective plane illumination optical endomicroscopy with polymer imaging fibers,” *APL Photonics*, vol. 8, no. 1, p. 016103, Jan. 2023. DOI: 10.1063/5.0130486.
- Romero, D., et al.**, “The Operator 4.0: Human Cyber-Physical Systems & Adaptive Automation Towards Human-Automation Symbiosis Work Systems,” in *IFIP Advances in Information and Communication Technology*, Springer International Publishing, 2016, pp. 677–686. DOI: 10.1007/978-3-319-51133-7\_80.
- Ross, C. A., et al.**, “Optimisation of ultrafast laser assisted etching in fused silica,” *Optics Express*, vol. 26, no. 19, pp. 24343–24356, Sep. 2018. DOI: 10.1364/oe.26.024343. [Online]. Available: <https://doi.org/10.1364/oe.26.024343>.

- Ross, C. A., et al.**, “A Miniature Fibre-Optic Raman Probe Fabricated by Ultrafast Laser-Assisted Etching,” *Micromachines*, vol. 11, no. 2, p. 185, Feb. 2020. DOI: 10.3390/mi11020185.
- Roychowdhury, T., et al.**, “Polymethyl methacrylate: Optical properties from 191 to 1688 nm (0.735–6.491 eV) by spectroscopic ellipsometry,” *Surface Science Spectra*, vol. 27, no. 1, p. 016002, Jan. 2020. DOI: 10.1116/1.5095422. [Online]. Available: <https://doi.org/10.1116/1.5095422>.
- Rozhina, E., et al.**, “Comparative cytotoxicity of kaolinite, halloysite, multiwalled carbon nanotubes and graphene oxide,” *Applied Clay Science*, vol. 205, p. 106041, May 2021. DOI: 10.1016/j.clay.2021.106041.
- Sacher, W. D., et al.**, “Implantable photonic neural probes for light-sheet fluorescence brain imaging,” *Neurophotonics*, vol. 8, no. 2, p. 025003, Apr. 2021. DOI: 10.1117/1.nph.8.2.025003.
- Sackmann, E. K., et al.**, “The present and future role of microfluidics in biomedical research,” *Nature*, vol. 507, no. 7491, pp. 181–189, Mar. 2014. DOI: 10.1038/nature13118.
- Sakakura, M., et al.**, “Ultralow-loss geometric phase and polarization shaping by ultrafast laser writing in silica glass,” *Light: Science & Applications*, vol. 9, no. 1, Feb. 2020. DOI: 10.1038/s41377-020-0250-y.
- Sala, F., et al.**, “Effects of Thermal Annealing on Femtosecond Laser Micromachined Glass Surfaces,” *Micromachines*, vol. 12, no. 2, p. 180, Feb. 2021. DOI: 10.3390/mi12020180.
- Salter, P. S., et al.**, “Focussing over the edge: Adaptive subsurface laser fabrication up to the sample face,” *Optics Express*, vol. 20, no. 18, pp. 19978–19989, Aug. 2012. DOI: 10.1364/oe.20.019978.
- Salter, P. S., et al.**, “Adaptive slit beam shaping for direct laser written waveguides,” *Optics Letters*, vol. 37, no. 4, pp. 470–472, Feb. 2012. DOI: 10.1364/ol.37.000470.
- Salter, P. S., et al.**, “Adaptive optics in laser processing,” *Light: Science & Applications*, vol. 8, no. 1, p. 110, Nov. 2019. DOI: 10.1038/s41377-019-0215-1.
- Samokhin, A. S.**, “Syringe Pump Created using 3D Printing Technology and Arduino Platform,” *Journal of Analytical Chemistry*, vol. 75, no. 3, pp. 416–421, Mar. 2020. DOI: 10.1134/s1061934820030156.
- Saunders, J. E., et al.**, “Refractive indices of common solvents and solutions at 1550 nm,” *Applied Optics*, vol. 55, no. 4, pp. 947–953, Feb. 2016. DOI: 10.1364/ao.55.000947.
- Schaffer, C. B., et al.**, “Laser-induced breakdown and damage in bulk transparent materials induced by tightly focused femtosecond laser pulses,” *Measurement Science and Technology*, vol. 12, no. 11, pp. 1784–1794, Oct. 2001. DOI: 10.1088/0957-0233/12/11/305. [Online]. Available: <https://doi.org/10.1088/0957-0233/12/11/305>.
- Schneider, C. A., et al.**, “NIH image to ImageJ: 25 years of image analysis,” en, *Nature Methods*, vol. 9, no. 7, pp. 671–675, Jul. 2012. DOI: 10.1038/nmeth.2089. [Online]. Available: <https://doi.org/10.1038/nmeth.2089>.

References in alphabetical order

- Schulze, C., et al.**, “Mode resolved bend loss in few-mode optical fibers,” *Optics Express*, vol. 21, no. 3, pp. 3170–3181, Feb. 2013. DOI: 10.1364/oe.21.003170.
- Seidel, H., et al.**, “Anisotropic Etching of Crystalline Silicon in Alkaline Solutions: I . Orientation Dependence and Behavior of Passivation Layers,” *Journal of The Electrochemical Society*, vol. 137, no. 11, pp. 3612–3626, Nov. 1990. DOI: 10.1149/1.2086277.
- Shah, L., et al.**, “Waveguide writing in fused silica with a femtosecond fiber laser at 522 nm and 1 MHz repetition rate,” *Optics Express*, vol. 13, no. 6, pp. 1999–2006, 2005. DOI: 10.1364/ope.13.001999.
- Shang, L., et al.**, “Emerging Droplet Microfluidics,” *Chemical Reviews*, vol. 117, no. 12, pp. 7964–8040, May 2017. DOI: 10.1021/acs.chemrev.6b00848.
- Shimotsuma, Y., et al.**, “Self-Organized Nanogratings in Glass Irradiated by Ultrashort Light Pulses,” *Physical Review Letters*, vol. 91, no. 24, p. 247405, Dec. 2003. DOI: 10.1103/physrevlett.91.247405.
- Siebenmorgen, J., et al.**, “Highly efficient Yb:YAG channel waveguide laser written with a femtosecond-laser,” *Optics Express*, vol. 18, no. 15, pp. 16035–16041, Jul. 2010. DOI: 10.1364/oe.18.016035.
- Sima, F., et al.**, “Three-dimensional femtosecond laser processing for lab-on-a-chip applications,” *Nanophotonics*, vol. 7, no. 3, pp. 613–634, Feb. 2018. DOI: 10.1515/nanoph-2017-0097.
- Sinev, I. S., et al.**, “Chirality Driven by Magnetic Dipole Response for Demultiplexing of Surface Waves,” *Laser & Photonics Reviews*, vol. 11, no. 5, p. 1700168, Sep. 2017. DOI: 10.1002/lpor.201700168.
- Singh, A., et al.**, “Development in microreactor technology for nanoparticle synthesis,” *International Journal of Nanoscience*, vol. 09, no. 01n02, pp. 93–112, Feb. 2010. DOI: 10.1142/S0219581X10006557.
- Sinibaldi, A., et al.**, “Direct comparison of the performance of Bloch surface wave and surface plasmon polariton sensors,” *Sensors and Actuators B: Chemical*, vol. 174, pp. 292–298, Nov. 2012. DOI: 10.1016/j.snb.2012.07.015.
- Sinibaldi, A., et al.**, “A full ellipsometric approach to optical sensing with Bloch surface waves on photonic crystals,” *Optics Express*, vol. 21, no. 20, pp. 23331–23344, Sep. 2013. DOI: 10.1364/oe.21.023331.
- Siyu, E., et al.**, “Two-Channel Surface Plasmon Resonance Sensor for Simultaneous Measurement of Seawater Salinity and Temperature,” *IEEE Transactions on Instrumentation and Measurement*, vol. 69, no. 9, pp. 7191–7199, Sep. 2020. DOI: 10.1109/tim.2020.2976405.
- Skuja, L., et al.**, “Defects in oxide glasses,” *physica status solidi (c)*, vol. 2, no. 1, pp. 15–24, Jan. 2005. DOI: 10.1002/pssc.200460102.
- Smithells, R. W., et al.**, “Recognition of thalidomide defects,” *Journal of Medical Genetics*, vol. 29, no. 10, pp. 716–723, Oct. 1992. DOI: 10.1136/jmg.29.10.716.

- Snitzer, E.**, “Proposed Fiber Cavities for Optical Masers,” *Journal of Applied Physics*, vol. 32, no. 1, pp. 36–39, Jan. 1961. DOI: 10.1063/1.1735955.
- Soltsev, A. S., et al.**, “Metasurfaces for quantum photonics,” *Nature Photonics*, vol. 15, no. 5, pp. 327–336, Apr. 2021. DOI: 10.1038/s41566-021-00793-z.
- Song, Y., et al.**, “Fundamental Concepts and Physics in Microfluidics,” in *Microfluidics: Fundamental, Devices and Applications*, Wiley-VCH Verlag GmbH & Co. KGaA, Jan. 2018, pp. 19–111. DOI: 10.1002/9783527800643.ch2.
- Sonn, G. A., et al.**, “Optical biopsy of human bladder neoplasia with in vivo confocal laser endomicroscopy,” en, *Journal of Urology*, vol. 182, no. 4, pp. 1299–1305, Oct. 2009. DOI: 10.1016/j.juro.2009.06.039. [Online]. Available: <https://doi.org/10.1016/j.juro.2009.06.039>.
- Sowa, S., et al.**, “Symmetric waveguides in poly(methyl methacrylate) fabricated by femtosecond laser pulses,” *Optics Express*, vol. 14, no. 1, pp. 291–297, 2006. DOI: 10.1364/opex.14.000291.
- Squires, T. M., et al.**, “Microfluidics: Fluid physics at the nanoliter scale,” *Reviews of Modern Physics*, vol. 77, no. 3, pp. 977–1026, Oct. 2005. DOI: 10.1103/revmodphys.77.977.
- Stelzer, E. H. K., et al.**, “Light sheet fluorescence microscopy,” *Nature Reviews Methods Primers*, vol. 1, no. 1, Nov. 2021. DOI: 10.1038/s43586-021-00069-4. [Online]. Available: <https://doi.org/10.1038/s43586-021-00069-4>.
- Stoian, R., Eds., *Ultrafast Laser Nanostructuring*. Springer International Publishing, 2023. DOI: 10.1007/978-3-031-14752-4.
- Stone, H. A., et al.**, “Engineering Flows in Small Devices: Microfluidics Toward a Lab-on-a-Chip,” *Annual Review of Fluid Mechanics*, vol. 36, no. 1, pp. 381–411, Jan. 2004. DOI: 10.1146/annurev.fluid.36.050802.122124.
- Stone, J. M., et al.**, “Low index contrast imaging fibers,” *Optics Letters*, vol. 42, no. 8, p. 1484, Apr. 2017. DOI: 10.1364/ol.42.001484. [Online]. Available: <https://doi.org/10.1364/ol.42.001484>.
- Stuart, B. C., et al.**, “Nanosecond-to-femtosecond laser-induced breakdown in dielectrics,” *Physical Review B*, vol. 53, no. 4, pp. 1749–1761, Jan. 1996. DOI: 10.1103/physrevb.53.1749. [Online]. Available: <https://doi.org/10.1103/physrevb.53.1749>.
- Su, P., et al.**, “Efficacy of confocal laser endomicroscopy for discriminating colorectal neoplasms from non-neoplasms: A systematic review and meta-analysis,” en, *Colorectal Disease*, vol. 15, no. 1, e1–12, Jan. 2013. DOI: 10.1111/codi.12033. [Online]. Available: <https://doi.org/10.1111/codi.12033>.
- Sudrie, L., et al.**, “Study of damage in fused silica induced by ultra-short IR laser pulses,” *Optics Communications*, vol. 191, no. 3-6, pp. 333–339, May 2001. DOI: 10.1016/s0030-4018(01)01152-x.

References in alphabetical order

- Sugioka, K., et al.**, ““All-in-One” chip fabrication by 3D femtosecond laser microprocessing for biophotonics,” *Journal of Physics: Conference Series*, vol. 59, pp. 533–538, Apr. 2007. DOI: 10.1088/1742-6596/59/1/114.
- Sugioka, K.**, “Hybrid femtosecond laser three-dimensional micro-and nanoprocessing: A review,” *International Journal of Extreme Manufacturing*, vol. 1, no. 1, p. 012003, Apr. 2019. DOI: 10.1088/2631-7990/ab0eda.
- Sugioka, K., Ed., *Handbook of Laser Micro- and Nano-Engineering*. Springer International Publishing, 2021. DOI: 10.1007/978-3-030-63647-0.
- Sugioka, K., et al.**, “Ultrafast lasers – reliable tools for advanced materials processing,” *Light: Science & Applications*, vol. 3, no. 4, e149–e149, Apr. 2014. DOI: 10.1038/lsa.2014.30.
- Sugioka, K., et al.**, “Femtosecond laser 3D micromachining: A powerful tool for the fabrication of microfluidic, optofluidic, and electrofluidic devices based on glass,” *Lab on a Chip*, vol. 14, no. 18, pp. 3447–3458, 2014. DOI: 10.1039/c4lc00548a.
- Sugiura, H., et al.**, “Raman scattering in silica glass in the permanent densification region,” *Journal of Non-Crystalline Solids*, vol. 144, pp. 151–158, Jan. 1992. DOI: 10.1016/s0022-3093(05)80395-3.
- Sun, B., et al.**, “High conductivity micro-wires in diamond following arbitrary paths,” *Applied Physics Letters*, vol. 105, no. 23, p. 231105, Dec. 2014. DOI: 10.1063/1.4902998.
- Sun, K., et al.**, “Three-dimensional direct lithography of stable perovskite nanocrystals in glass,” *Science*, vol. 375, no. 6578, pp. 307–310, Jan. 2022. DOI: 10.1126/science.abj2691.
- Sun, Q., et al.**, “Effect of spherical aberration on the propagation of a tightly focused femtosecond laser pulse inside fused silica,” *Journal of Optics A: Pure and Applied Optics*, vol. 7, no. 11, pp. 655–659, Oct. 2005. DOI: 10.1088/1464-4258/7/11/006.
- Sun, W., et al.**, “Comparative Study on Transmission Mechanisms in a SMF-Capillary-SMF Structure,” *Journal of Lightwave Technology*, vol. 38, no. 15, pp. 4075–4085, Aug. 2020. DOI: 10.1109/jlt.2020.2983910.
- Tadevosyan, K., et al.**, “Engineering and Assessing Cardiac Tissue Complexity,” *International Journal of Molecular Sciences*, vol. 22, no. 3, p. 1479, Feb. 2021. DOI: 10.3390/ijms22031479.
- Takayama, O., et al.**, “Photonic surface waves on metamaterial interfaces,” *Journal of Physics: Condensed Matter*, vol. 29, no. 46, p. 463001, Oct. 2017. DOI: 10.1088/1361-648x/aa8bdd.
- Takayama, O., et al.**, “Surface waves on metamaterials interfaces,” in *2016 10th International Congress on Advanced Electromagnetic Materials in Microwaves and Optics (METAMATERIALS)*, IEEE, Sep. 2016. DOI: 10.1109/metamaterials.2016.7746486.
- Tang, Y., et al.**, “Optical Chirality and Its Interaction with Matter,” *Physical Review Letters*, vol. 104, no. 16, p. 163901, Apr. 2010. DOI: 10.1103/physrevlett.104.163901.

- Tang, Y., et al.**, “Enhanced Enantioselectivity in Excitation of Chiral Molecules by Superchiral Light,” *Science*, vol. 332, no. 6027, pp. 333–336, Apr. 2011. DOI: 10.1126/science.1202817.
- Taylor, R., et al.**, “Applications of femtosecond laser induced self-organized planar nanocracks inside fused silica glass,” *Laser & Photonics Review*, vol. 2, no. 1-2, pp. 26–46, Apr. 2008. DOI: 10.1002/lpor.200710031.
- Taylor, R. S., et al.**, “Femtosecond laser fabrication of nanostructures in silica glass,” *Optics Letters*, vol. 28, no. 12, pp. 1043–1045, Jun. 2003. DOI: 10.1364/ol.28.001043.
- Taylor, R., et al.**, “Ultra-high resolution index of refraction profiles of femtosecond laser modified silica structures,” *Optics Express*, vol. 11, no. 7, p. 775, Apr. 2003. DOI: 10.1364/oe.11.000775.
- Theodosiou, A., et al.**, “Bragg Gratings and Fabry-Perot Cavities in Low-Loss Multimode CYTOP Polymer Fiber,” *IEEE Photonics Technology Letters*, vol. 30, no. 9, pp. 857–860, May 2018. DOI: 10.1109/lpt.2018.2820381.
- Theodosiou, A., et al.**, “All-in-Fiber Cladding Interferometric and Bragg Grating Components Made via Plane-by-Plane Femtosecond Laser Inscription,” *Journal of Lightwave Technology*, vol. 37, no. 18, pp. 4864–4871, Sep. 2019. DOI: 10.1109/jlt.2019.2925263.
- Theodosiou, A., et al.**, “Recent trends and advances of fibre Bragg grating sensors in CYTOP polymer optical fibres,” *Optical Fiber Technology*, vol. 54, p. 102079, Jan. 2020. DOI: 10.1016/j.yofte.2019.102079.
- Theodosiou, A., et al.**, “Plane-by-Plane Femtosecond Laser Inscription Method for Single-Peak Bragg Gratings in Multimode CYTOP Polymer Optical Fiber,” *Journal of Lightwave Technology*, vol. 35, no. 24, pp. 5404–5410, Dec. 2017. DOI: 10.1109/jlt.2017.2776862.
- Theodosiou, A., et al.**, “Modified fs-Laser Inscribed FBG Array for Rapid Mode Shape Capture of Free-Free Vibrating Beams,” *IEEE Photonics Technology Letters*, vol. 28, no. 14, pp. 1509–1512, Jul. 2016. DOI: 10.1109/lpt.2016.2555852.
- Thiberville, L., et al.**, “Human in vivo fluorescence microimaging of the alveolar ducts and sacs during bronchoscopy,” en, *European Respiratory Journal*, vol. 33, no. 5, pp. 974–985, May 2009. DOI: 10.1183/09031936.00083708. [Online]. Available: <https://doi.org/10.1183/09031936.00083708>.
- Thiberville, L., et al.**, “In vivo imaging of the bronchial wall microstructure using fibered confocal fluorescence microscopy,” *American journal of respiratory and critical care medicine*, vol. 175, no. 1, pp. 22–31, 2007. DOI: 10.1164/rccm.200605-6840C. [Online]. Available: <https://www.atsjournals.org/doi/abs/10.1164/rccm.200605-6840C>.
- Thomas, J., et al.**, “Femtosecond pulse written fiber gratings: A new avenue to integrated fiber technology,” *Laser & Photonics Reviews*, vol. 6, no. 6, pp. 709–723, Feb. 2012. DOI: 10.1002/lpor.201100033.
- Thomson, R. R., et al.**, “Shaping ultrafast laser inscribed optical waveguides using a deformable mirror,” *Optics Express*, vol. 16, no. 17, pp. 12786–12793, Aug. 2008. DOI: 10.1364/oe.16.012786.

- Thomson, R. R., et al.**, “Controlling the Cross-section of Ultrafast Laser Inscribed Optical Waveguides,” in *Femtosecond Laser Micromachining: Photonic and Microfluidic Devices in Transparent Materials*, Osellame, R., Eds. Berlin, Heidelberg: Springer Berlin Heidelberg, 2012, pp. 93–125, ISBN: 978-3-642-23366-1. DOI: 10.1007/978-3-642-23366-1\_5. [Online]. Available: [https://doi.org/10.1007/978-3-642-23366-1\\_5](https://doi.org/10.1007/978-3-642-23366-1_5).
- Thoss, A., et al.**, “The age of the laser has only just begun,” *Laser Focus World*, Jan. 2022. [Online]. Available: <https://www.laserfocusworld.com/industrial-laser-solutions/article/14222482/the-age-of-the-laser-has-only-just-begun>.
- Tian, F., et al.**, “Photonic Crystal Fiber as a Lab-in-Fiber Optofluidic Platform,” in *Springer Series in Surface Sciences*, Springer International Publishing, Jul. 2014, pp. 315–334. DOI: 10.1007/978-3-319-06998-2\_15.
- Urrutia, A., et al.**, “A Comprehensive Review of Optical Fiber Refractometers: Toward a Standard Comparative Criterion,” *Laser & Photonics Reviews*, vol. 13, no. 11, p. 1900094, Oct. 2019. DOI: 10.1002/lpor.201900094.
- Valle, G. D., et al.**, “1.5  $\mu\text{m}$  single longitudinal mode waveguide laser fabricated by femtosecond laser writing,” *Optics Express*, vol. 15, no. 6, pp. 3190–3194, 2007. DOI: 10.1364/oe.15.003190.
- Vargas-Ordaz, E. J., et al.**, “Three-dimensional imaging on a chip using optofluidics light-sheet fluorescence microscopy,” *Lab on a Chip*, vol. 21, no. 15, pp. 2945–2954, 2021. DOI: 10.1039/d1lc00098e.
- Vasala, A., et al.**, “Modern Tools for Rapid Diagnostics of Antimicrobial Resistance,” *Frontiers in Cellular and Infection Microbiology*, vol. 10, Jul. 2020. DOI: 10.3389/fcimb.2020.00308.
- Veis, M., et al.**, “Fourier Factorization in the Plane Wave Expansion Method in Modeling Photonic Crystals,” in *Photonic Crystals - Introduction, Applications and Theory*, InTech, Mar. 2012. DOI: 10.5772/34679.
- Virtanen, P., et al.**, “SciPy 1.0: Fundamental Algorithms for Scientific Computing in Python,” *Nature Methods*, vol. 17, pp. 261–272, 2020. DOI: 10.1038/s41592-019-0686-2. [Online]. Available: <https://doi.org/10.1038/s41592-019-0686-2>.
- Vishnubhatla, K. C., et al.**, “Shape control of microchannels fabricated in fused silica by femtosecond laser irradiation and chemical etching,” *Optics Express*, vol. 17, no. 10, pp. 8685–8695, May 2009. DOI: 10.1364/oe.17.008685.
- Vitek, D. N., et al.**, “Spatio-temporally focused femtosecond laser pulses for nonreciprocal writing in optically transparent materials,” *Optics Express*, vol. 18, no. 24, pp. 24673–24678, Nov. 2010. DOI: 10.1364/oe.18.024673.
- Waltermann, C., et al.**, “Cladding waveguide gratings in standard single-mode fiber for 3D shape sensing,” *Optics Letters*, vol. 40, no. 13, pp. 3109–3112, 2015, ISSN: 0146-9592. DOI: 10.1364/OL.40.003109. [Online]. Available: <https://www.osapublishing.org/abstract.cfm?URI=ol-40-13-3109>.

- Wang, A., et al.**, “Mask-Free Patterning of High-Conductivity Metal Nanowires in Open Air by Spatially Modulated Femtosecond Laser Pulses,” *Advanced Materials*, vol. 27, no. 40, pp. 6238–6243, Sep. 2015. DOI: 10.1002/adma.201503289.
- Wang, H., et al.**, “100-Layer Error-Free 5D Optical Data Storage by Ultrafast Laser Nanostructuring in Glass,” *Laser & Photonics Reviews*, vol. 16, no. 4, p. 2100563, Jan. 2022. DOI: 10.1002/lpor.202100563.
- Wang, P., et al.**, “Fabrication of polarization-independent waveguides deeply buried in lithium niobate crystal using aberration-corrected femtosecond laser direct writing,” *Scientific Reports*, vol. 7, no. 1, Jan. 2017. DOI: 10.1038/srep41211.
- Wang, R., et al.**, “Bloch surface waves confined in one dimension with a single polymeric nanofibre,” *Nature Communications*, vol. 8, no. 1, Feb. 2017. DOI: 10.1038/ncomms14330.
- Wang, X., et al.**, “Enhanced cell sorting and manipulation with combined optical tweezer and microfluidic chip technologies,” *Lab on a Chip*, vol. 11, no. 21, p. 3656, 2011. DOI: 10.1039/c1lc20653b.
- Wang, Y., et al.**, “An Overview of the Thermal Erasure Mechanisms of Femtosecond Laser-Induced Nanogratings in Silica Glass,” *physica status solidi (a)*, vol. 218, no. 12, p. 2100023, Apr. 2021. DOI: 10.1002/pssa.202100023.
- Wang, Y., et al.**, “Liquid-level sensing based on a hollow core Bragg fiber,” *Optics Express*, vol. 26, no. 17, pp. 21656–21663, Aug. 2018. DOI: 10.1364/oe.26.021656.
- Wellikoff, A. S., et al.**, “Comparison of in vivo probe-based confocal laser endomicroscopy with histopathology in lung cancer: A move toward optical biopsy,” *Respirology*, vol. 20, no. 6, pp. 967–974, Jun. 2015. DOI: 10.1111/resp.12578. [Online]. Available: <https://doi.org/10.1111/resp.12578>.
- White, I. M., et al.**, “On the performance quantification of resonant refractive index sensors,” *Optics Express*, vol. 16, no. 2, pp. 1020–1028, 2008. DOI: 10.1364/oe.16.001020.
- White, K. I.**, “Practical application of the refracted near-field technique for the measurement of optical fibre refractive index profiles,” *Optical and Quantum Electronics*, vol. 11, no. 2, pp. 185–196, Mar. 1979. DOI: 10.1007/bf00624397.
- Will, M., et al.**, “Optical properties of waveguides fabricated in fused silica by femtosecond laser pulses,” *Applied Optics*, vol. 41, no. 21, pp. 4360–4363, Jul. 2002. DOI: 10.1364/ao.41.004360.
- Williams, R. J., et al.**, “Optimizing the net reflectivity of point-by-point fiber Bragg gratings: The role of scattering loss,” *Optics Express*, vol. 20, no. 12, pp. 13451–13456, May 2012. DOI: 10.1364/oe.20.013451.
- Williams, R. J., et al.**, “Femtosecond direct-writing of low-loss fiber Bragg gratings using a continuous core-scanning technique,” *Optics Letters*, vol. 38, no. 11, pp. 1918–1920, May 2013. DOI: 10.1364/ol.38.001918.

- Witcher, J. J., et al.**, “Thermal annealing of femtosecond laser written structures in silica glass,” *Optical Materials Express*, vol. 3, no. 4, pp. 502–510, Mar. 2013. DOI: 10.1364/ome.3.000502.
- Wood, H. A. C., et al.**, “Tri-mode optical biopsy probe with fluorescence endomicroscopy, Raman spectroscopy, and time-resolved fluorescence spectroscopy,” *Journal of Biophotonics*, vol. 16, no. 2, Sep. 2022. DOI: 10.1002/jbio.202200141.
- Wu, D., et al.**, “In-channel integration of designable microoptical devices using flat scaffold-supported femtosecond-laser microfabrication for coupling-free optofluidic cell counting,” *Light: Science & Applications*, vol. 4, no. 1, e228–e228, Jan. 2015. DOI: 10.1038/lisa.2015.1.
- Wu, J., et al.**, “Lab-on-chip technology for chronic disease diagnosis,” *npj Digital Medicine*, vol. 1, no. 1, pp. 1–11, Apr. 2018. DOI: 10.1038/s41746-017-0014-0.
- Xu, L. D., et al.**, “Industry 4.0: State of the art and future trends,” *International Journal of Production Research*, vol. 56, no. 8, pp. 2941–2962, Mar. 2018. DOI: 10.1080/00207543.2018.1444806.
- Xu, M., et al.**, “Mid-infrared 1 W hollow-core fiber gas laser source,” *Optics Letters*, vol. 42, no. 20, pp. 4055–4058, Oct. 2017. DOI: 10.1364/ol.42.004055.
- Yamamoto, H., et al.**, “Molecular Recognition by Self-Assembled Monolayers of Cyclodextrin on Ag,” *The Journal of Physical Chemistry B*, vol. 101, no. 35, pp. 6855–6860, Aug. 1997. DOI: 10.1021/jp963916u.
- Yan, X., et al.**, “Polarization-independent etching of fused silica based on electrons dynamics control by shaped femtosecond pulse trains for microchannel fabrication,” *Optics Letters*, vol. 39, no. 17, pp. 5240–5243, Aug. 2014. DOI: 10.1364/ol.39.005240.
- Yang, G., et al.**, “Optimized light delivery probe using ball lenses for co-registered photoacoustic and ultrasound endo-cavity subsurface imaging,” *Photoacoustics*, vol. 13, pp. 66–75, Mar. 2019. DOI: 10.1016/j.pacs.2018.12.001. [Online]. Available: <https://doi.org/10.1016/j.pacs.2018.12.001>.
- Yang, J., et al.**, “In-fiber Mach-Zehnder interferometer with piecewise interference spectrum based on hole-assisted dual-core fiber for refractive index sensing,” *Optics Express*, vol. 26, no. 15, pp. 19 091–19 099, Jul. 2018. DOI: 10.1364/oe.26.019091.
- Yao, Q., et al.**, “Polarization-independent microchannel in a high-speed-scan femtosecond laser-assisted etching of fused silica,” *Applied Optics*, vol. 62, no. 2, pp. 291–297, Jan. 2023. DOI: 10.1364/ao.475940.
- Yavuz, C., et al.**, “Sterilization of PMMA microfluidic chips by various techniques and investigation of material characteristics,” *The Journal of Supercritical Fluids*, vol. 107, pp. 114–121, Jan. 2016. DOI: 10.1016/j.supflu.2015.08.019.
- Yerolatsitis, S., et al.**, “Sub millimetre flexible fibre probe for background and fluorescence free Raman spectroscopy,” *Journal of Biophotonics*, vol. 14, no. 10, e202000488, Jul. 2021. DOI: 10.1002/jbio.202000488.

- Yizhar, O., et al.**, “Optogenetics in Neural Systems,” *Neuron*, vol. 71, no. 1, pp. 9–34, Jul. 2011. DOI: 10.1016/j.neuron.2011.06.004.
- Yoo, S. J. B., et al.**, “Heterogeneous 2D/3D photonic integrated microsystems,” *Microsystems & Nanoengineering*, vol. 2, no. 1, Aug. 2016. DOI: 10.1038/micronano.2016.30.
- Yoshihara, N.**, “Low-loss, high-bandwidth fluorinated POF for visible to 1.3- $\mu\text{m}$  wavelengths,” in *OFC '98. Optical Fiber Communication Conference and Exhibit. Technical Digest. Conference Edition. 1998 OSA Technical Digest Series Vol.2 (IEEE Cat. No.98CH36177)*, Opt. Soc. America. DOI: 10.1109/ofc.1998.657428.
- Yu, L., et al.**, “Investigation of ultra-thin waveguide arrays on a Bloch surface wave platform,” *Journal of the Optical Society of America B*, vol. 31, no. 12, p. 2996, Nov. 2014. DOI: 10.1364/josab.31.002996.
- Yu, L., et al.**, “Manipulating Bloch surface waves in 2D: a platform concept-based flat lens,” *Light: Science & Applications*, vol. 3, no. 1, e124–e124, Jan. 2014. DOI: 10.1038/lsa.2014.5.
- Yu, X., et al.**, “Tuning etch selectivity of fused silica irradiated by femtosecond laser pulses by controlling polarization of the writing pulses,” *Journal of Applied Physics*, vol. 109, no. 5, p. 053114, Mar. 2011. DOI: 10.1063/1.3555080.
- Yuan, T., et al.**, “Long period fiber grating in two-core hollow eccentric fiber,” *Optics Express*, vol. 23, no. 26, pp. 33378–33385, Dec. 2015. DOI: 10.1364/oe.23.033378.
- Yun, B., et al.**, “Highly Sensitive Liquid-Level Sensor Based on Etched Fiber Bragg Grating,” *IEEE Photonics Technology Letters*, vol. 19, no. 21, pp. 1747–1749, Nov. 2007. DOI: 10.1109/lpt.2007.905093.
- Zandrini, T., et al.**, “Multi-foci laser microfabrication of 3D polymeric scaffolds for stem cell expansion in regenerative medicine,” *Scientific Reports*, vol. 9, no. 1, Aug. 2019. DOI: 10.1038/s41598-019-48080-w.
- Zayats, A. V., et al.**, “Nano-optics of surface plasmon polaritons,” *Physics Reports*, vol. 408, no. 3-4, pp. 131–314, Mar. 2005. DOI: 10.1016/j.physrep.2004.11.001.
- Zhang, C., et al.**, “A Review of Research Relevant to the Emerging Industry Trends: Industry 4.0, IoT, Blockchain, and Business Analytics,” *Journal of Industrial Integration and Management*, vol. 05, no. 01, pp. 165–180, Feb. 2020. DOI: 10.1142/s2424862219500192.
- Zhang, H., et al.**, “The development and clinical application of microscopic endoscopy for in vivo optical biopsies: Endocytoscopy and confocal laser endomicroscopy,” en, *Photodiagnosis Photodynamic Therapy*, vol. 38, no. 102826, p. 102826, Mar. 2022. DOI: 10.1016/j.pdpdt.2022.102826. [Online]. Available: <https://doi.org/10.1016/j.pdpdt.2022.102826>.
- Zhang, J., et al.**, “Eternal 5D data storage by ultrafast laser writing in glass,” in *SPIE Proceedings*, Klotzbach, U., Eds., SPIE, Mar. 2016. DOI: 10.1117/12.2220600.
- Zhang, J., et al.**, “Seemingly Unlimited Lifetime Data Storage in Nanostructured Glass,” *Physical Review Letters*, vol. 112, no. 3, p. 033901, Jan. 2014. DOI: 10.1103/physrevlett.112.033901.

- Zhang, J., et al.**, “Fundamentals and applications of inertial microfluidics: A review,” *Lab on a Chip*, vol. 16, no. 1, pp. 10–34, 2016. DOI: 10.1039/c51c01159k.
- Zhang, S., et al.**, “Fiber-optic bending vector sensor based on Mach-Zehnder interferometer exploiting lateral-offset and up-taper,” *Optics Letters*, vol. 37, no. 21, pp. 4480–4482, Oct. 2012. DOI: 10.1364/ol.37.004480.
- Zhang, X., et al.**, “Chiral emission from resonant metasurfaces,” *Science*, vol. 377, no. 6611, pp. 1215–1218, Sep. 2022. DOI: 10.1126/science.abq7870.
- Zhang, Y., et al.**, “Femtosecond laser-inscribed fiber interface Mach-Zehnder interferometer for temperature-insensitive refractive index measurement,” *Optics Letters*, vol. 43, no. 18, pp. 4421–4424, 2018, ISSN: 0146-9592. DOI: 10.1364/ol.43.004421.
- Zhang, Y., et al.**, “High sensitivity optical fiber liquid level sensor based on a compact MMF-HCF-FBG structure,” *Measurement Science and Technology*, vol. 29, no. 5, p. 055 104, Mar. 2018. DOI: 10.1088/1361-6501/aaac5c.
- Zhang, Z., et al.**, “Measurement of high pressure and high temperature using a dual-cavity Fabry-Perot interferometer created in cascade hollow-core fibers,” *Optics Letters*, vol. 43, no. 24, pp. 6009–6012, Dec. 2018. DOI: 10.1364/ol.43.006009.
- Zhou, K., et al.**, “Line-by-Line Fiber Bragg Grating Made by Femtosecond Laser,” *IEEE Photonics Technology Letters*, vol. 22, no. 16, pp. 1190–1192, Aug. 2010. DOI: 10.1109/lpt.2010.2050877.
- Zhou, K., et al.**, “Optical fiber micro-devices made with femtosecond laser,” in *Advanced Photonics 2016 (IPR, NOMA, Sensors, Networks, SPPCom, SOF)*, OSA, 2016. DOI: 10.1364/sensors.2016.sew3d.1.
- Zhou, W., et al.**, “A true fiber optic refractometer,” *Laser & Photonics Reviews*, vol. 11, no. 1, p. 1600 157, Jan. 2017. DOI: 10.1002/lpor.201600157.
- Zhou, Z., et al.**, “Towards high-power mid-IR light source tunable from 3.8 to 4.5  $\mu\text{m}$  by HBr-filled hollow-core silica fibres,” *Light: Science & Applications*, vol. 11, no. 1, Jan. 2022. DOI: 10.1038/s41377-021-00703-6.
- Zhu, D., et al.**, “Integrated photonics on thin-film lithium niobate,” *Advances in Optics and Photonics*, vol. 13, no. 2, pp. 242–352, May 2021. DOI: 10.1364/aop.411024.
- Zhu, Y., et al.**, “Design and validation of an angle-resolved low-coherence interferometry fiber probe for in vivo clinical measurements of depth-resolved nuclear morphology,” *Journal of Biomedical Optics*, vol. 16, no. 1, p. 011003, 2011. DOI: 10.1117/1.3520130. [Online]. Available: <https://doi.org/10.1117/1.3520130>.
- Zubia, J., et al.**, “Plastic Optical Fibers: An Introduction to Their Technological Processes and Applications,” *Optical Fiber Technology*, vol. 7, no. 2, pp. 101–140, Apr. 2001. DOI: 10.1006/ofte.2000.0355.